

SUPRAMOLECULAR CHIROGENESIS IN CHEMICAL AND RELATED SCIENCES

EDITED BY: Victor Borovkov, Riina Aav, Yue Sun, Akihiko Tsuda,
Hiroyuki Miyake and Keiji Hirose
PUBLISHED IN: Frontiers in Chemistry





frontiers

Frontiers eBook Copyright Statement

The copyright in the text of individual articles in this eBook is the property of their respective authors or their respective institutions or funders. The copyright in graphics and images within each article may be subject to copyright of other parties. In both cases this is subject to a license granted to Frontiers.

The compilation of articles constituting this eBook is the property of Frontiers.

Each article within this eBook, and the eBook itself, are published under the most recent version of the Creative Commons CC-BY licence.

The version current at the date of publication of this eBook is CC-BY 4.0. If the CC-BY licence is updated, the licence granted by Frontiers is automatically updated to the new version.

When exercising any right under the CC-BY licence, Frontiers must be attributed as the original publisher of the article or eBook, as applicable.

Authors have the responsibility of ensuring that any graphics or other materials which are the property of others may be included in the CC-BY licence, but this should be checked before relying on the CC-BY licence to reproduce those materials. Any copyright notices relating to those materials must be complied with.

Copyright and source acknowledgement notices may not be removed and must be displayed in any copy, derivative work or partial copy which includes the elements in question.

All copyright, and all rights therein, are protected by national and international copyright laws. The above represents a summary only. For further information please read Frontiers' Conditions for Website Use and Copyright Statement, and the applicable CC-BY licence.

ISSN 1664-8714

ISBN 978-2-88966-833-5

DOI 10.3389/978-2-88966-833-5

About Frontiers

Frontiers is more than just an open-access publisher of scholarly articles: it is a pioneering approach to the world of academia, radically improving the way scholarly research is managed. The grand vision of Frontiers is a world where all people have an equal opportunity to seek, share and generate knowledge. Frontiers provides immediate and permanent online open access to all its publications, but this alone is not enough to realize our grand goals.

Frontiers Journal Series

The Frontiers Journal Series is a multi-tier and interdisciplinary set of open-access, online journals, promising a paradigm shift from the current review, selection and dissemination processes in academic publishing. All Frontiers journals are driven by researchers for researchers; therefore, they constitute a service to the scholarly community. At the same time, the Frontiers Journal Series operates on a revolutionary invention, the tiered publishing system, initially addressing specific communities of scholars, and gradually climbing up to broader public understanding, thus serving the interests of the lay society, too.

Dedication to Quality

Each Frontiers article is a landmark of the highest quality, thanks to genuinely collaborative interactions between authors and review editors, who include some of the world's best academicians. Research must be certified by peers before entering a stream of knowledge that may eventually reach the public - and shape society; therefore, Frontiers only applies the most rigorous and unbiased reviews. Frontiers revolutionizes research publishing by freely delivering the most outstanding research, evaluated with no bias from both the academic and social point of view. By applying the most advanced information technologies, Frontiers is catapulting scholarly publishing into a new generation.

What are Frontiers Research Topics?

Frontiers Research Topics are very popular trademarks of the Frontiers Journals Series: they are collections of at least ten articles, all centered on a particular subject. With their unique mix of varied contributions from Original Research to Review Articles, Frontiers Research Topics unify the most influential researchers, the latest key findings and historical advances in a hot research area! Find out more on how to host your own Frontiers Research Topic or contribute to one as an author by contacting the Frontiers Editorial Office: frontiersin.org/about/contact

SUPRAMOLECULAR CHIROGENESIS IN CHEMICAL AND RELATED SCIENCES

Topic Editors:

Victor Borovkov, Tallinn University of Technology, Estonia

Riina Aav, Tallinn University of Technology, Estonia

Yue Sun, South-Central University for Nationalities, China

Akihiko Tsuda, Kobe University, Japan

Hiroyuki Miyake, Osaka City University, Japan

Keiji Hirose, Osaka University, Japan

Citation: Borovkov, V., Aav, R., Sun, Y., Tsuda, A., Miyake, H., Hirose, K., eds. (2021).
Supramolecular Chirogenesis in Chemical and Related Sciences.
Lausanne: Frontiers Media SA. doi: 10.3389/978-2-88966-833-5

Table of Contents

- 05 Editorial: Supramolecular Chirogenesis in Chemical and Related Sciences**
Yue Sun, Riina Aav, Akihiko Tsuda, Hiroyuki Miyake, Keiji Hirose and Victor Borovkov
- 08 Chirogenesis and Pfeiffer Effect in Optically Inactive Eu^{III} and Tb^{III} $\text{Tris}(\beta\text{-diketonate})$ Upon Intermolecular Chirality Transfer From Poly- and Monosaccharide Alkyl Esters and α -Pinene: Emerging Circularly Polarized Luminescence (CPL) and Circular Dichroism (CD)**
Michiya Fujiki, Laibing Wang, Nanami Ogata, Fumio Asanoma, Asuka Okubo, Shun Okazaki, Hiroki Kamite and Abd Jalil Jalilah
- 31 Corrigendum: Chirogenesis and Pfeiffer Effect in Optically Inactive Eu^{III} and Tb^{III} $\text{Tris}(\beta\text{-diketonate})$ Upon Intermolecular Chirality Transfer From Poly- and Monosaccharide Alkyl Esters and α -Pinene: Emerging Circularly Polarized Luminescence (CPL) and Circular Dichroism (CD)**
Michiya Fujiki, Laibing Wang, Nanami Ogata, Fumio Asanoma, Asuka Okubo, Shun Okazaki, Hiroki Kamite and Abd Jalil Jalilah
- 33 Porphyrins Through the Looking Glass: Spectroscopic and Mechanistic Insights in Supramolecular Chirogenesis of New Self-Assembled Porphyrin Derivatives**
Manuela Stefanelli, Marco Savioli, Francesca Zurlo, Gabriele Magna, Sandra Belviso, Giulia Marsico, Stefano Superchi, Mariano Venanzi, Corrado Di Natale, Roberto Paolesse and Donato Monti
- 45 Recent Progress in Optically-Active Phthalocyanines and Their Related Azamacrocycles**
Yusuke Okada, Tomonori Hoshi and Nagao Kobayashi
- 59 Supramolecular Halogen Bonds in Asymmetric Catalysis**
Mikk Kaasik and Tõnis Kanger
- 77 Control and Transfer of Chirality Within Well-Defined Tripodal Supramolecular Cages**
Gege Qiu, Paola Nava, Cédric Colombar and Alexandre Martinez
- 84 Enantioselectivity-Evaluation of Chiral Copper(II) Complexes Coordinated by Novel Chiral Tetradentate Ligands for Free Amino Acids by Mass Spectrometry Coupled With the Isotopically Labeled Enantiomer Method**
Takashi Nakakoji, Kaori Yoshino, Kazuki Izutsu, Hirofumi Sato, Hiroyuki Miyake, Eiko Mieda, Satoshi Shinoda, Hiroshi Tsukube, Hideya Kawasaki, Ryuichi Arakawa, Daisuke Ono and Motohiro Shizuma
- 94 A Chiral Metal-Organic 1D-Coordination Polymer Upon Complexation of Phenylene-Bridged Bipyrrrole and Palladium (II) Ion**
Kumiko Nishinaka, Jiandong Han, Dongli Han, Yue Liu, Yanqing Du, Meiling Wang, Chaolu Eerdun, Nobuyasu Naruse, Yutaka Mera, Yoshio Furusho and Akihiko Tsuda
- 101 Efficient Amplification in Soai's Asymmetric Autocatalysis by a Transient Stereodynamic Catalyst**
Oliver Trapp

- 110** *En Route to a Chiral Melanin: The Dynamic “From-Imprinted-to-Template” Supramolecular Role of Porphyrin Hetero-Aggregates During the Oxidative Polymerization of L-DOPA*
Massimiliano Gaeta, Rosalba Randazzo, Valentina Villari, Norberto Micali, Alessandro Pezzella, Roberto Purrello, Marco d’Ischia and Alessandro D’Urso
- 117** *Polarimetric Measurements of Surface Chirality Based on Linear and Nonlinear Light Scattering*
Ankur Gogoi, Surajit Konwer and Guan-Yu Zhuo
- 141** *Intermolecular Chirality Modulation of Binaphthalene-Bridged Bisporphyrins With Chiral Diamines*
Wenxin Lu, Lei Gong, Chaorui Su, Qibao Wang, Qing Ling, Peng Wang, Dongdong Qi and Yongzhong Bian
- 149** *Aerobic Oxidations in Asymmetric Synthesis: Catalytic Strategies and Recent Developments*
Dzmitry Kananovich, Gábor Zoltán Elek, Margus Lopp and Victor Borovkov
- 171** *CD Imaging at High Spatial Resolution at Diamond B23 Beamline: Evolution and Applications*
Rohanah Hussain, Tamás Jávorfí and Giuliano Siligardi



Editorial: Supramolecular Chirogenesis in Chemical and Related Sciences

Yue Sun^{1*}, Riina Aav², Akihiko Tsuda³, Hiroyuki Miyake⁴, Keiji Hirose⁵ and Victor Borovkov^{2*}

¹ Hubei Key Laboratory of Catalysis and Materials Science, College of Chemistry and Material Sciences, South-Central University for Nationalities, Wuhan, China, ² Department of Chemistry and Biotechnology, School of Science, Tallinn University of Technology, Tallinn, Estonia, ³ Department of Chemistry, Graduate School of Science, Kobe University, Kobe, Japan, ⁴ Department of Chemistry, Graduate School of Science, Osaka City University, Osaka, Japan, ⁵ Department of Materials Engineering Science, Graduate School of Engineering Science, Osaka University, Toyonaka, Japan

Keywords: supramolecular chemistry, chirogenesis, porphyrins, self-assembly, circular dichroism, chirality, circularly polarized luminescence

Editorial on the Research Topic

Supramolecular Chirogenesis in Chemical and Related Sciences

Chirality being a phenomenon of describing the ability of any object to exist as a pair of non-superimposable mirror images has aroused extensive attention as it is directly correlated with numerous biological systems (e.g., transcription, storage, processing of genetic information, and functioning living organisms). Specific to all living organisms, the mentioned microscopic self-assembled nanostructures exhibiting the supramolecular chirogenesis are spontaneously arranged from chiral building blocks through non-covalent interactions or from achiral components being influenced by an external chiral field (Hembury et al., 2008; Liu et al., 2015; Sun et al., 2018a,b). A typical example refers to the conformations of proteins with different chirogenic arrangement (e.g., α -helix, β -sheet, and tertiary structure). An in-depth study on the chirogenesis phenomenon will present more insights into the self-assembly behavior in biological systems, as well as will help expand the application in materials science (Sun et al., 2016).

While the term of supramolecular chirogenesis (**Scheme 1**) was firstly introduced in 2000 (Borovkov et al., 2000), in general, this effect can be generated in two major forms (Morris and Bu, 2010; Zhang et al., 2012). On one hand, chirogenesis contains chiral molecular components and mixed chiral/achiral molecules (Goh et al., 2010; Ie et al., 2015; Nakakoji et al., 2020). On the other hand, it can be arisen from achiral molecules as impacted by the spontaneous symmetry breaking when the self-assembled systems are being formed. Alternatively, it can be also generated from achiral components, which are able to assembly into a chiral system upon external chiral influence. This Research Topic collected 14 original articles from 85 authors on supramolecular chirogenesis in chemical and relevant sciences.

Porphyrins refer to be prominent host molecules, which can be commonly used to study chiral supramolecular systems for their unique planar structures and abundant chemical property. In this respect, Stefanelli et al. reported that porphyrin appended with L- or D-proline is capable of generating remarkable supramolecular chirality, emerging from the stereospecific proline-appended group. Also, Lu et al. prepared corresponding porphyrin dimers linked with 2,2'-diamino-1,1'-binaphthyl. The porphyrin dimers are able to form the 1:1 sandwich host-guest complexes with chiral diamines at low concentrations. It is noteworthy that the

OPEN ACCESS

Edited and reviewed by:

Tony D. James,
University of Bath, United Kingdom

*Correspondence:

Yue Sun
suny@scuec.edu.cn
Victor Borovkov
victor.borovkov@taltech.ee

Specialty section:

This article was submitted to
Supramolecular Chemistry,
a section of the journal
Frontiers in Chemistry

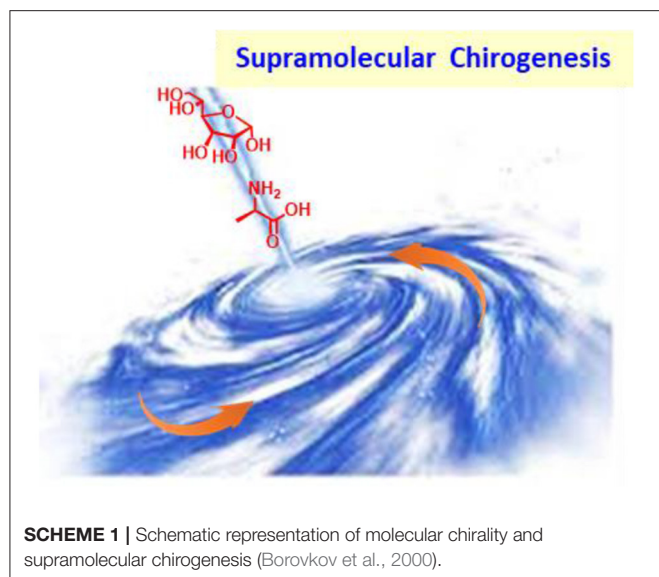
Received: 11 March 2021

Accepted: 12 March 2021

Published: 06 April 2021

Citation:

Sun Y, Aav R, Tsuda A, Miyake H,
Hirose K and Borovkov V (2021)
Editorial: Supramolecular
Chirogenesis in Chemical and Related
Sciences. *Front. Chem.* 9:679332.
doi: 10.3389/fchem.2021.679332



authors could monitor the process of intermolecular chirality attributed to the existence of short chiral linkage units by using circular dichroism (CD) spectroscopy. Furthermore, Gaeta et al. disclosed that chiral porphyrin hetero-aggregates can act as templates to generate the chiral structures during the oxidative conversion of amino acid.

Besides the chirogenic porphyrin chemistry, Fujiki et al. demonstrated that the signal of CPL (circularly polarized luminescence) and CD appeared through the intermolecular chirality transfer upon lanthanide (Eu^{III} and Tb^{III}) tris(β -diketonate) exposed to poly- and monosaccharide alkyl esters and α -pinene. Also, Nakakoji et al. investigated the ability of chiral discrimination between copper(II)-chiral tetradentate ligand and a chiral amino acid with the isotopically labeled/unlabeled enantiomer method. As revealed from this study, the matching steric interaction accounts for the observed chiral recognition. Trapp described that a transient stereodynamic catalyst is capable of efficiently amplifying the Soai's asymmetric autocatalysis. The coordination bond provides a good platform to study the property of materials (Chen et al., 2021; Li et al., 2021). Nishinaka et al. indicated that a novel coordination-driven based polymer composed of phenylene-bridged bipyrrrole and palladium(II) ion achieved the π -electronic communications and exciton coupling in the absorption spectrum.

Numerous fields generated the interest in macrocycles exhibiting the optically-active characteristics (Aav and Mishra,

2018). Okada et al. summarized the synthesis and property of the optically-active phthalocyanines, as well as their related azamacrocycles from 2010 to 2020, which are of high significance for chemists to design highly desirable chiral macrocycles from achiral molecules. As summarized by Qiu et al., the C3 symmetrical cages were employed as efficient scaffolds to study chiral dynamics. With the use of non-linear chiroptical techniques, the chirality at surfaces can be clarified from novel perspectives. Gogoi et al. reviewed that chemists adopted the linear and non-linear optical methods to quantify the surface chirality, as an attempt to solve vital issues in surface biochemistry.

Catalytic asymmetric chemistry is another field of supramolecular chirogenesis. In this respect, halogen bonding, with its high directionality, has been recognized as an attractive interaction for new molecular assemblies and its use in chiral systems just started to emerge. In this respect, Kaasik and Kanger demonstrated the use of halogen bonding in catalytic stereoselective processes. Also, Kananovich et al. highlighted recent achievements in the catalytic enantioselective oxidations utilizing molecular oxygen, which placed the stress on the mechanisms of dioxygen activation and chirogenesis in the mentioned chemical transformations.

In related development Siligardi et al. outlooked that researchers used the CD imaging at high spatial resolution at Diamond B23 beamline to determine the homogeneity of the supramolecular structures of thin films deposited on fused quartz substrates.

In summary, this Research Topic collected various aspects of the supramolecular chirogenesis in chemical and related sciences. To be specific, the topic illustrates the emergence and characterization of chirogenesis and its potential applications. It is expected that this topic will guide the design and functionality of various chiral structures. The field of supramolecular chirogenesis and relevant sciences are significantly promising in understanding the origins of life in nature, as well as in developing novel medicines and smart materials.

AUTHOR CONTRIBUTIONS

All authors listed have made a substantial, direct and intellectual contribution to the work, and approved it for publication.

FUNDING

This work was financially supported by Estonian Research Council through Grant PRG399 and the H2020-FETOPEN 828779 INITIO project.

REFERENCES

- Aav, R., and Mishra, K. A. (2018). The breaking of symmetry leads to chirality in cucurbituril-type hosts. *Symmetry* 10:98. doi: 10.3390/sym10040098
- Borovkov, V. V., Lintuluoto, J. M., and Inoue, Y. (2000). Supramolecular chirogenesis in bis(zinc porphyrin): an absolute configuration probe highly sensitive to guest structure. *Org. Lett.* 2, 1565–1568. doi: 10.1021/ol0000556
- Chen, Z., Sun, Y., and Li, H. (2021). Fabrication of subnanochannels by metal-organic frameworks. *Matter* 4, 772–774. doi: 10.1016/j.matt.2021.02.004
- Goh, M., Matsushita, S., and Akagi, K. (2010). From helical polyacetylene to helical graphite: synthesis in the chiral nematic liquid crystal field and morphology-retaining carbonisation. *Chem. Soc. Rev.* 39, 2466–2476. doi: 10.1039/b907990b

- Hembury, G. A., Borovkov, V. V., and Inoue, Y. (2008). Chirality-sensing supramolecular systems. *Chem. Rev.* 108, 1–73. doi: 10.1021/cr050005k
- Ie, M., Setsune, J., Eda, K., and Tsuda, A. (2015). Chiroptical sensing of oligonucleotides with a cyclic octapyrrole. *Org. Chem. Front.* 2, 29–33. doi: 10.1039/C4QO00268G
- Li, R. H., Feng, X. Y., Zhou, J., Yi, F., Zhou, Z. Q., Men, D., et al. (2021). Rhomboidal Pt(II) metallacycle-based hybrid viral nanoparticles for cell imaging. *Inorg. Chem.* 60, 431–437. doi: 10.1021/acs.inorgchem.0c03095
- Liu, M., Zhang, L., and Wang, T. (2015). Supramolecular chirality in self-assembled systems. *Chem. Rev.* 115, 7304–7397. doi: 10.1021/cr500671p
- Morris, R. E., and Bu, X. (2010). Induction of chiral porous solids containing only achiral building blocks. *Nat. Chem.* 2, 353–361. doi: 10.1038/nchem.628
- Nakakoji, T., Sato, H., Ono, D., Miyake, H., Shinoda, S., Tsukube, H., et al. (2020). Mass spectrometric detection of enantioselectivity in three-component complexation, copper(II)-chiral tetradentate ligand-free amino acid in solution. *Chem. Commun.* 56, 54–57. doi: 10.1039/C9CC07231D
- Sun, Y., Li, S., Zhou, Z., Saha, M. L., Datta, S., Zhang, M., et al. (2018b). Alanine-based chiral metallogels via supramolecular coordination complex platforms: metallogelation induced chirality transfer. *J. Am. Chem. Soc.* 140, 3257–3263. doi: 10.1021/jacs.7b10769
- Sun, Y., Mei, Y., Quan, J., Xiao, X., Zhang, L., Tian, D., et al. (2016). The macroscopic wettable surface: fabricated by calix[4]arene-based host-guest interaction and chiral discrimination of glucose. *Chem. Commun.* 52, 14416–14418. doi: 10.1039/C6CC07956C
- Sun, Y., Zhang, F., Quan, J., Zhu, F., Hong, W., Ma, J., et al. (2018a). A biomimetic chiral-driven ionic gate constructed by pillar[6]arene-based host-guest systems. *Nat. Commun.* 9, 2617. doi: 10.1038/s41467-018-05103-w
- Zhang, M., Qing, G., and Sun, T. (2012). Chiral biointerface materials. *Chem. Soc. Rev.* 41, 1972–1984. doi: 10.1039/C1CS15209B

Conflict of Interest: The authors declare that the research was conducted in the absence of any commercial or financial relationships that could be construed as a potential conflict of interest.

Copyright © 2021 Sun, Aav, Tsuda, Miyake, Hirose and Borovkov. This is an open-access article distributed under the terms of the Creative Commons Attribution License (CC BY). The use, distribution or reproduction in other forums is permitted, provided the original author(s) and the copyright owner(s) are credited and that the original publication in this journal is cited, in accordance with accepted academic practice. No use, distribution or reproduction is permitted which does not comply with these terms.



Chirogenesis and Pfeiffer Effect in Optically Inactive Eu^{III} and Tb^{III} Tris(β -diketonate) Upon Intermolecular Chirality Transfer From Poly- and Monosaccharide Alkyl Esters and α -Pinene: Emerging Circularly Polarized Luminescence (CPL) and Circular Dichroism (CD)

OPEN ACCESS

Edited by:

Keiji Hirose,
Osaka University, Japan

Reviewed by:

Sally Elisabeth Plush,
University of South Australia, Australia
Qionghua Jin,
Capital Normal University, China
Munetaka Iwamura,
University of Toyama, Japan

*Correspondence:

Michiya Fujiki
fujikim@ms.naist.jp;
michiya.fujiki@icloud.com
Abd Jalil Jalilah
jalilahjalil@unimap.edu.my

†ORCID:

Michiya Fujiki
orcid.org/0000-0002-3139-9478
Laibing Wang
orcid.org/0000-0002-3380-7826
Abd Jalil Jalilah
orcid.org/0000-0003-1265-0919

Specialty section:

This article was submitted to
Supramolecular Chemistry,
a section of the journal
Frontiers in Chemistry

Received: 26 April 2020

Accepted: 30 June 2020

Published: 11 August 2020

Citation:

Fujiki M, Wang L, Ogata N,
Asanoma F, Okubo A, Okazaki S,
Kamite H and Jalilah AJ (2020)
Chirogenesis and Pfeiffer Effect in
Optically Inactive Eu^{III} and Tb^{III}
Tris(β -diketonate) Upon Intermolecular
Chirality Transfer From Poly- and
Monosaccharide Alkyl Esters and
 α -Pinene: Emerging Circularly
Polarized Luminescence (CPL) and
Circular Dichroism (CD).
Front. Chem. 8:685.
doi: 10.3389/fchem.2020.00685

Michiya Fujiki^{1*}, Laibing Wang^{1†}, Nanami Ogata¹, Fumio Asanoma¹, Asuka Okubo¹,
Shun Okazaki¹, Hiroki Kamite¹ and Abd Jalil Jalilah^{1,2,3†}

¹ Division of Materials Science, Graduate School of Science and Technology, Nara Institute of Science and Technology, Ikoma, Japan, ² School of Materials Engineering, Universiti Malaysia Perlis, Jejawi, Malaysia, ³ Centre of Excellence Frontier Materials Research, Universiti Malaysia Perlis, Kangar, Malaysia

We report emerging circularly polarized luminescence (CPL) at 4f-4f transitions when lanthanide (Eu^{III} and Tb^{III}) tris(β -diketonate) embedded to cellulose triacetate (**CTA**), cellulose acetate butyrate (**CABu**), *D*-/*L*-glucose pentamethyl esters (**D**-/**L**-**Glu**), and *D*-/*L*-arabinose tetramethyl esters (**D**-/**L**-**Ara**) are in film states. Herein, 6,6,7,7,8,8,8-heptafluoro-2,2-dimethyl-3,5-octanedionate (fod) and 2,2,6,6-tetramethyl-3,5-heptanedione (dpm) were chosen as the β -diketonates. The g_{lum} value of Eu(fod)₃ in **CABu** are +0.0671 at 593 nm (⁵D₀ → ⁷F₁) and −0.0059 at 613 nm (⁵D₀ → ⁷F₂), respectively, while those in **CTA** are +0.0463 and −0.0040 at these transitions, respectively. The g_{lum} value of Tb(fod)₃ in **CABu** are −0.0029 at 490 nm (⁵D₄ → ⁷F₆), +0.0078 at 540 nm (⁵D₄ → ⁷F₅), and −0.0018 at 552 nm (⁵D₄ → ⁷F₅), respectively, while those in **CTA** are −0.0053, +0.0037, and −0.0059 at these transitions, respectively. **D**-/**L**-**Glu** and **D**-/**L**-**Ara** induced weaker g_{lum} values at 4f-4f transitions of Eu(fod)₃, Tb(fod)₃, and Tb(dpm)₃. For comparison, Tb(dpm)₃ in α -pinene showed clear CPL characteristics, though Eu(dpm)₃ did not. A surplus charge neutralization hypothesis was applied to the origin of attractive intermolecular interactions between the ligands and saccharides. This idea was supported from the concomitant opposite tendency in upfield ¹⁹F-NMR and downfield ¹H-NMR chemical shifts of Eu(fod)₃ and the opposite Mulliken charges between *F*-C bonds (fod) and *H*-C bonds (**CTA** and **D**-/**L**-**Glu**). An analysis of CPL excitation (CPLE) and CPL spectra suggests that (+)- and (−)-sign CPL signals of Eu^{III} and Tb^{III} at different 4f-4f transitions in the visible region are the same with the (+)- and (−)-sign exhibited by CPLE bands at high energy levels of Eu^{III} and Tb^{III} in the near-UV region.

Keywords: non-covalent interaction, circularly polarized luminescence, circular dichroism, europium, terbium, cellulose, saccharide, terpene

INTRODUCTION

In recent years, controlled chirogenesis led by several scenarios of intermolecular chirality transfer endowed with natural and human-made resources has become the most popular phenomenon allowing for an efficient generation of the desired optically active substances in the realms of organic chemistry (Bosnich, 1967; Hayward and Totty, 1969; Noack, 1969; Soai et al., 2019), supramolecular chemistry (Kobayashi et al., 1993; Huang et al., 1998; Prince et al., 2000; Borovkov et al., 2004; Hembury et al., 2008; Aida et al., 2012; Borovkov, 2014; Liu et al., 2015; Goto et al., 2017), polymer chemistry (Green et al., 1993; Yashima et al., 1995; Nakashima et al., 2001; Kawagoe et al., 2010; Numata and Shinkai, 2011; Lee et al., 2012; Duan et al., 2014; Fujiki, 2014; Wang et al., 2014; Akagi, 2019), and molecular aggregation/colloidal/gel chemistry (Palmans and Meijer, 2007; Isare et al., 2010; George et al., 2011; Mei et al., 2015; Roose et al., 2016; Sang et al., 2019). Particularly, chirogenesis in metal coordination chemistry by the chirality transfer has long been one of the central subjects in inorganic chemistry (Mason and Norman, 1965; Kirschner and Ahmad, 1968; Kirschner and Bakkar, 1982; Mason, 1982; Brittain, 1983, 1989; Riehl and Richardson, 1986; Tsukube and Shinoda, 2002; Di Bari and Salvadori, 2005; Muller, 2009, 2014; Bünzli, 2010; Carr et al., 2012; Tanner, 2013; Miyake, 2014; Kumar et al., 2015; Zinna and Di Bari, 2015; Kono et al., 2016; Longhi et al., 2016; Lunkley et al., 2018; Wong et al., 2019).

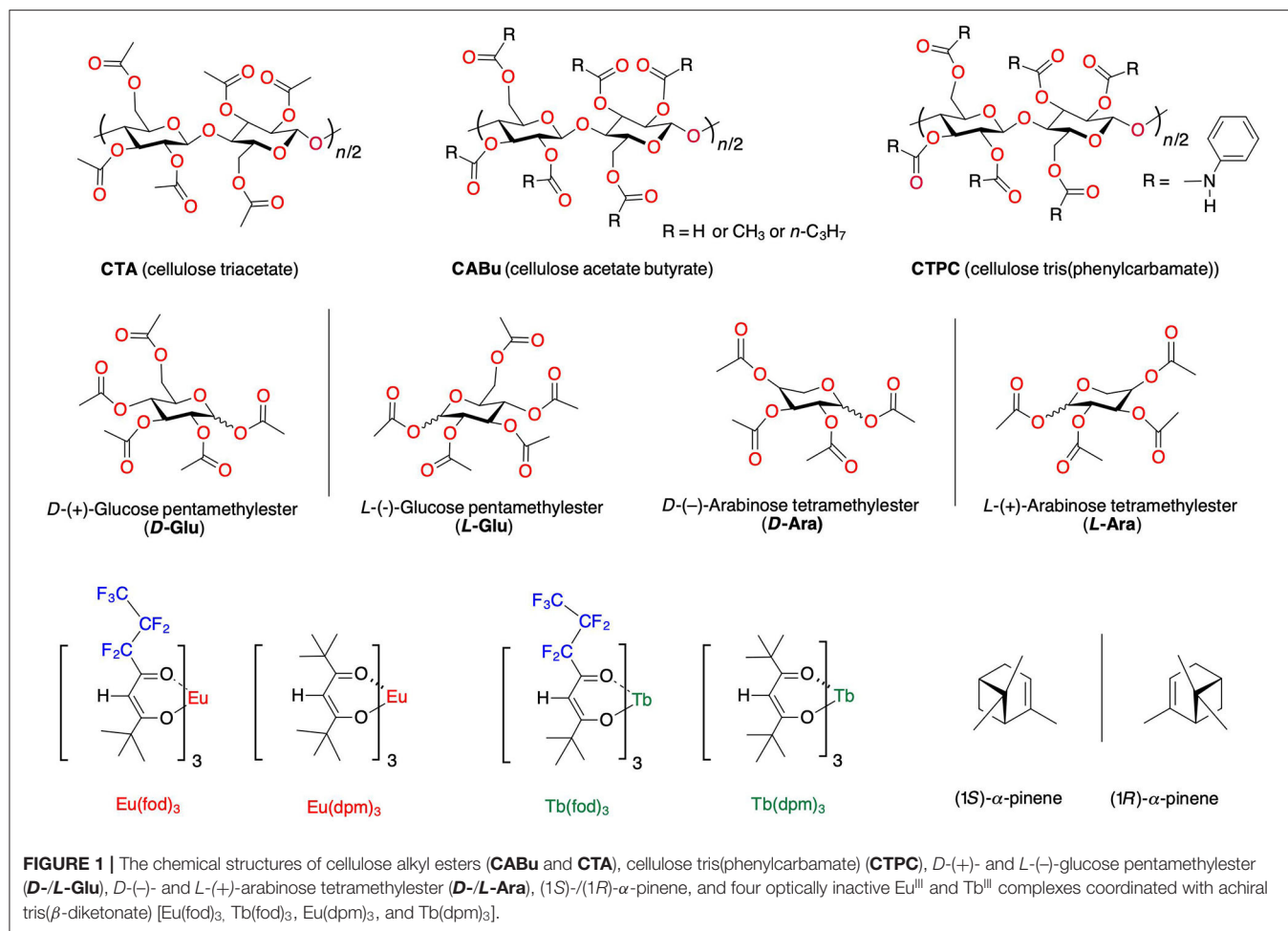
Historically, in 1898, Kipping and Pope investigated the first chirogenesis of *L*-NaClO₃ crystals (*P*₂₁³ space group) in an enantiomer excess (*ee*) of several % that were preferentially grown in a water solution of *D*-glucose and *D*-mannitol (Kipping and Pope, 1898). In 1919, Perucca found the first chirogenesis of triarylmethane textile dye by observing an anomalous optical rotational dispersion (ORD) in visible region when he dispersed an ORD-silent triarylmethane textile dye in polycrystalline *L*-NaClO₃ (Perucca, 1919; Kahr and Gurney, 2001; Jacoby, 2008; Bing et al., 2010). In the early 1930s, Pfeiffer and Quehl were aware that optical rotation of amino acids increased and/or decreased in the presence of racemic labile metal (Zn²⁺, Cd²⁺, and Ni²⁺) complexes (Pfeiffer and Quehl, 1931, 1932). This anomaly is called as the *Pfeiffer effect* (Mayer and Brasted, 1973; Mason, 1982; Brittain, 1983, 1989; Lunkley et al., 2018).

In 1965, Mason and Norman reported the first circular dichroism (CD) signals at *3d-3d* transitions of Co^{III}(NH₃)₆(ClO₄)₃ in the presence of (+)-diethyl tartrate (Mason and Norman, 1965). In 1977, the first circularly polarized luminescence (CPL) spectra from optically inactive Eu^{III}(fod)₃, Eu^{III}(dpm)₃, Tb^{III}(fod)₃, and other two Eu^{II} complexes dissolved in (*R*)-/(*S*)- α -phenylethylamine are reported by hypothesizing the Pfeiffer effect (fod = 6,6,7,7,8,8,8-heptafluoro-2,2-dimethyl-3,5-octanedionate, dpm: dipivaloylmethane or 2,2,6,6-tetramethyl-3,5-heptanedione) (Brittain and Richardson, 1977a; Brittain, 1980). These pioneering CPL studies further stimulated many researchers to investigate CPL and CD spectroscopic characteristics of optically inactive lanthanide complexes in the presence of amino acids, monosaccharides,

malic acid ascorbic acid, cyclic glycols, DNA, and other chiral chemical influences (Luk and Richardson, 1974; Brittain and Richardson, 1977b; Madaras and Brittain, 1980; Brittain, 1981, 1984; Richardson, 1982; Yan et al., 1982; Huskowska and Riehl, 1995; Muller and Riehl, 2005; Muller, 2009; Iwamura et al., 2012, 2016; Miyake et al., 2014; Wu et al., 2016, 2019; Jalilah et al., 2018; Lunkley et al., 2018; Wu and Bouř, 2018; Taniguchi et al., 2019). An outer-sphere intermolecular interaction between the Δ -/ Λ -mixture lanthanide^{III} (Ln^{III}) complex and the chiral additives is responsible for the equilibrium shift, as detectable by emerging CPL spectra. Richardson et al. evaluated that the barrier heights in Δ -/ Λ stereomutation between charged M⁺[Eu(dpa)₃][−] (M⁺; counter cationic species and dpa; dipicolinate) at the photoexcited state (ES) in achiral solvents are in the range of 12 and 17 kcal mol^{−1}; higher viscosity cosolvents of water-ethylene glycol corresponded to higher barrier heights (Glover-Fischer et al., 1998).

New knowledge and understanding of several weak inter- and intramolecular interactions known as C-H/ π , C-H/O-C, C-H/F-C, C-F/H-O, C-F/Si, and π - π (Nishio et al., 1998; Desiraju and Steiner, 1999; Matsuura et al., 2003; Mele et al., 2003; Tsuzuki et al., 2003; Kim et al., 2004; Mahadevi and Sastry, 2016; Pitts et al., 2017) lead us to hypothesize that multiple point chirality and/or main chain helicity of *non-charged* bioresources impose the capability of non-symmetrical force transfer to *non-charged* achiral or optically inactive chromophores and luminophores. *Non-charged* terpene hydrocarbons, e.g., (*S*)-/(*R*)-limonene, (1*S*)-/(1*R*)- α -pinene, and (1*S*)-/(1*R*)- β -pinene, can efficiently work as chiral liquified scaffolds in the ground state (GS) and the ES of several colloidal π -/ σ -conjugated polymers (Kawagoe et al., 2010; Nakano et al., 2010, 2012; Lee et al., 2012; Fujiki, 2014; Wang et al., 2014), colloidal vinyl polymers bearing azobenzene (Jiang et al., 2015), and *non-charged* Eu(fod)₃ (Figure 1; Jalilah et al., 2018). However, to realize practical photonic applications, solution-processable and/or thermoplastic solid materials are inevitably needed because terpenes are volatile, flammable liquids.

Among solidified chiral bioresources, poly- and monosaccharides are incredible biomaterials that are abundant on earth and have a wide variety of functions (Klemm et al., 2005), e.g., allowing growth and maintenance of homochiral life resulting chiral foods (Coulte, 2016), recognition and sorting of enantiomers (Ikai and Okamoto, 2009), service as a building block of optically active supramolecular complexes (Numata and Shinkai, 2011), and fabrication of liquid crystals, solid films, fibers, sheets, and nano-composites for industrial purposes (Dubois et al., 1998; Henriksson et al., 2007; Wang et al., 2007; Iwatake et al., 2008). More recently, poly- and monosaccharides are excellent chiroptical platforms to generate and boost CD/CPL/circularly polarized reflection bands because of their helicoidal and cholesteric higher-order structures (Wilts et al., 2017; De La Cruz et al., 2018; Yu et al., 2018, 2019; Zheng et al., 2018). We have proved that three cellulose derivatives (cellulose triacetate (CTA), cellulose acetate butyrate (CABu), and cellulose tris(phenyl carbamate) (CTPC) in Figure 1 possess



an efficient ambidextrous scaffolding capability toward CD-inactive oligo- and polyfluorenes, leading to the corresponding (+)- or (-)-sign CPL-active/CD-active species as the solid film states (Guo et al., 2017, 2018).

These results encourage us to propose that CTA, CABu, D-/L-glucose permethyl esters (D-Glu/L-Glu), and D-/L-arabinose permethyl esters (D-Ara/L-Ara) should work as chirality transferring solid platforms, enabling several optically inactive and/or racemic Eu^{III} and Tb^{III} complexes to the corresponding CPL-active/CD-active, non-racemic species (Figure 1). For comparison, we tested the chirality transfer capability of (1S)-/(1R)-α-pinene as chiral liquid molecules to Eu(dpm)₃ and Tb(dpm)₃.

Herein, we showcase that Eu(fod)₃, Tb(fod)₃, and Tb(dpm)₃, except Eu(dpm)₃ commonly exhibited CPL signals at 4f-4f transitions and CD bands due to n-π*/π-π* transitions of the ligands when CABu, CTA, D-Glu/L-Glu, and D-Ara/L-Ara were employed as embedding films. In α-pinene, although Tb(dpm)₃ showed clear CPL characteristics, Eu(dpm)₃ did not. Unresolved inherent nature between Eu^{III} and Tb^{III} causes considerable differences of CPL characteristics as well as emission wavelengths at 4f-4f transitions. Although the current g_{lum} values of our

CPL-active lanthanide complex in the films are not very outstanding, the hypothesis of these non-covalent weak chiral intermolecular interactions in the ES and GS led us to freely design solution processible CPL- and/or CD-functioned composite films made of several optically inactive lanthanide complexes coordinated with achiral organic ligands upon chirality/helicity transfer of inexpensive soluble polysaccharide, oligosaccharide, and monosaccharide derivatives as the solidified chiral bioresources, in addition to a conventional multi-step synthesis of optically active lanthanide complexes coordinated with chiral ligands designed strategically.

EXPERIMENTAL

Materials

CTA and CABu

CTA (Wako Pure Chemicals, Osaka, Japan) and CABu (Sigma-Aldrich Japan, Tokyo, Japan) were used without further purification (Figures S1, S2, SM). Chloroform, tetrahydrofuran (THF), methanol (MeOH), and other solvents (Dojindo, Kumamoto, Japan) were used as received. CDCl₃ and hexafluorobenzene (C₆F₆) were purchased from Stable Isotope

Lab (SIL) (Japanese vendor, Wako Pure Chemicals) and Wako Pure Chemicals, respectively. (1S)- and (1R)- α -Pinene (Tokyo Chemical Industry (TCI), Tokyo, Japan) were purified by distillation in a reduced pressure.

Monosaccharide Permethylesters

L-(-)-Glu. To a mixture of *L*-(-)-glucose (0.5 g) and stoichiometric acetic anhydride (4 mL), freshly dried Cu(OTf)₂ (0.03 mol % of *L*-(-)-glucose) at 0°C was added under nitrogen [Scheme S1 in Supplementary Materials (SM)]. The mixture was stirred for 1 h in an ice bath and then stirred at room temperature for 12 h. Methanol (5 mL) was slowly added to quench the acylation reaction, and the mixture was stirred for another 0.5 h, followed by evaporation under reduced pressure. Chloroform (25 mL) was added to dissolve the residue, and the mixture was consecutively washed twice with saturated NaHCO₃ brine and water, respectively. The organic layer was dried over anhydrous Na₂SO₄, and the mixture was filtered. The filtrate was concentrated in a vacuum and purified by silica gel column chromatography, and eluted with petroleum ether/ethyl acetate (v/v, 50/1) to yield a white powder (yield: 0.42 g, 70%; Analysis: calculated (%) for C₁₆H₂₂O₁₁: C, 49.23; H, 5.68; found (%): C, 49.53; H, 5.43. ¹H-NMR (in CDCl₃), FT-IR (onto CaF₂) and ESI (positive mode)-MS spectra of *L*-Glu and *D*-Glu are shown in Figure S3, SM and Figure S4, SM, respectively. Elemental analysis of *L*-Glu and *D*-Glu are given in Figure S5, SM.

D-(+)-Glu. Donated from Prof. Wei Zhang (Soochow University, China) prepared by a similar method. ¹H-NMR, FT-IR, and ESI (positive mode) MS spectra are displayed in Figure S4, SM. Solid-state ¹³C-NMR and ¹H-NMR in CDCl₃ solution are shown in Figures 5, 8A, respectively. Analysis: Calcd (%) for C₁₆H₂₂O₁₁: C, 49.23; H, 5.68; Found (%): C, 49.51; H, 5.40.

D-Ara and L-Ara. *D*-(-)-Arabinose tetramethyl ester and *L*-(+)-arabinose tetramethyl ester were synthesized utilizing the same procedure as described for the synthesis of *L*-Glu. A viscous liquid was obtained as *D*-Ara. Yield: 2.4 g, 32%. Analysis for *D*-Ara: Calcd (%) for C₁₃H₁₈O₉: C, 49.06; H, 5.70, Found (%): C, 48.97; H, 5.56. *L*-Ara. Yield (2.4 g, 32%). Analysis: Calcd (%) for C₁₃H₁₈O₉: C, 49.06; H, 5.70, Found (%): C, 49.01; H, 5.60. ¹H-NMR, FT-IR, and ESI-MS (positive mode) spectra of *D*-Ara and *L*-Ara are shown in Figures S6, S7, SM, respectively. The results of the elemental analysis of *L*-Ara and *D*-Ara are shown in Figure S8, SM.

Tb(fod)₃

The starting material, 0.19 g (0.74 mmol) of TbCl₃ (99% purity, Sigma-Aldrich, now Merck) was dissolved in the minimum amount of methanol (3.0 mL), and 1,1,1,2,2,3,3-heptafluoro-7,7-dimethyl-4,6-octanedione (Hfod, 0.636 g (2.15 mmol, 0.5 mL), TCI) was adjusted to pH 5–6 by adding the required amount of aqueous NaOH solution. The above two solutions were mixed by vigorous stirring with a magnetic stir bar for 10 min, followed by addition of 200 mL distilled water dropwise into the solution. A pale-yellow Tb(fod)₃ was precipitated under vigorous stirring with a magnetic bar for 12 h. The crude product adhered to the bottom of the reaction vessel was purified by a short-column

silica gel chromatography (Wakogel C-200, Chart S1 in SI) as shown below, with chloroform as an eluent to yield a pale yellow oil, followed by drying in a vacuum oven 90°C to obtain a white solid. Yield, 200 mg (40%). The purification of Tb(fod)₃ using a 5 mL pipette tip made of polypropylene, as a short-column apparatus, is illustrated below. Analysis: Calcd (%) for C₃₀H₃₀F₂₁O₆Tb: C, 34.50; H, 2.90. Found (%): C, 34.58; H, 2.80. The elemental analysis suggested that Tb(fod)₃ has no water adducts.

Before we utilized the purification method (see Chart S1, SM) for Tb(fod)₃, we were aware of some impurity peaks approximately 450 nm in the PL spectrum of Tb(fod)₃. After the purification by silica gel column chromatography and elution with chloroform, we obtained a pure Tb(fod)₃ (based on the expected fluorescent emission spectrum). ¹H-NMR (CDCl₃), ¹⁹F-NMR (CDCl₃), FT-IR (CaF₂), and ESI-MS (positive mode) spectra and elemental analysis of Tb(fod)₃ are shown in Figure S9, SM.

Other Lanthanide Complexes

Eu(fod)₃, Eu(dpm)₃, and Tb(dpm)₃ were purchased from Sigma-Aldrich-Merck, TCI, and Sigma-Aldrich-Merck, respectively, and were used as received. ¹H-NMR (CDCl₃) and FT-IR spectra of Eu(fod)₃ are shown in Figure S10, SM. ¹H-NMR and FT-IR spectra of Eu(dpm)₃ are shown in Figure S11, SM. ¹H- and ¹⁹F-NMR (CDCl₃) and FT-IR (CaF₂) spectra of Tb(dpm)₃ are shown in Figure S12, SM.

Instrumentation

The UV-vis and CD spectra of the solutions were measured with a JASCO J-820 spectropolarimeter (Hachioji-Tokyo, Japan) equipped with Peltier-controlled housing units. Synthetic quartz (SQ) cuvette with a 10-mm path length (scanning rate: 100 nm min⁻¹; bandwidth: 1.0 nm; response time: 1.0 s; 0.5-nm interval sampling; single accumulation) at 25°C were used. To avoid second- and third-order stray light due to diffraction grating, CPL and PL spectra were recorded on a JASCO CPL-200, that was designed as a prism-based spectrofluoropolarimeter with a forward scattering of 0° angle equipped with focusing and collecting lenses, and a manually movable film holder onto an optical rail enables to adjust the best focal point to maximize CPL/PL signal amplitudes. Measurement conditions were bandwidths of 10 nm for excitation and emission, a scanning rate of 100 nm min⁻¹, and a data sampling of 0.5 nm interval. IR spectra were measured on CaF₂ plate using a Horiba FT-730 Fourier-transform (FT) infrared (IR) spectrometer (Horiba, Kyoto, Japan) over a wavenumber range between 800 and 4,000 cm⁻¹ with a resolution of 2 cm⁻¹ and a scanning speed of 5 mm s⁻¹ for 128 scans and a Perkin-Elmer Spectrum One/100 FT-IR spectrometer (Winter Street Waltham, MA 02451, USA) over a wavenumber range between 900 and 4,000 cm⁻¹ with a resolution of 4 cm⁻¹ for 64 scans. Electrospray ionization mass spectrometry (ESI-MS) was conducted with a JEOL (Akishima, Tokyo, Japan) AccuTOF JMS-T100 LC mass spectrometer (accelerating voltage,

10 kV). Electron ionization mass spectrometry with high-resolution (HR-EI-MS) mode was recorded with a JEOL JMS-700 double-focusing mass spectrometer (accelerating voltage, 10 kV). The ionic species were often attached with Na^+ ion. The hybridized polymers were characterized by a JEOL JNM-ECX400 cross-polarization (CP) magic-angle-spinning (MAS) solid-state (ss)- $^{13}\text{C}\{\text{H}\}$ -FT-NMR spectrometer (resonance frequency 100.5 MHz, contact time 2.0 ms, 550 scans, relaxation delay 5.0 s, spinning 8.0 kHz, repetition time 5.05 s). Elemental analysis was performed on a Perkin-Elmer 2400II CHNS/O. The solution ^1H - and ^{19}F -FT-NMR spectra were recorded on the JEOL ECP-400 spectrometer. The resonance frequencies of ^{19}F - and ^1H -NMR are 376 MHz and 400 MHz, respectively. Representative measurement conditions for ^{19}F -NMR spectra had an acquisition time of 0.432 sec, 64 acquisitions, a relaxation delay of 4.0 sec, at a temperature of $\sim 20^\circ\text{C}$, a pulse angle of 45° and a pulse width of 7.0 sec were used. Raw NMR data were processed and analyzed by JEOL Delta (Ver. 5) software. Hexafluorobenzene (HFB, -163.0 ppm) and tetramethylsilane (Me_4Si , 0.0 ppm) were used as internal standards for the ^{19}F - and ^1H -NMR measurements, respectively. Photodynamic decay of six solid films ($\text{Eu}(\text{fod})_3$ with **CTA** and **CABu** (detected at 610–620 nm), $\text{Eu}(\text{dpm})_3$ with **CTA** and **CABu** (detected at 610–620 nm), and $\text{Tb}(\text{dpm})_3$ with **CTA** and **CABu** (detected at 542–551 nm) excited by an N_2 laser (Usho KEC-160; wavelength 337.1 nm; pulse width 600 ps; 10 Hz) were measured with the help of streak camera (Hamamatsu, picosecond fluorescence measurement system C4780 with Grating 150 lines per mm and slit width 100 μm). The 337.1 nm of N_2 laser source was used to excite shoulder UV/CD signals of the lanthanide complexes. Photodynamic measurements of other Eu^{III} and Tb^{III} complexes in the *D*-/*L*-**Glu** and *D*-/*L*-**Ara** films excited at 337.1 nm were not successful. For simplicity, the emission lifetime was evaluated by single exponential decay analysis. Quantum yields of the Eu^{III} and Tb^{III} complexes in the solid films were not obtained due to lack of an integrating sphere. The all processed data saved as raw text data were re-organized by KaleidaGraph ver. 4.53 (Synergy software, Reading, PA 19606, USA).

Preparation of the Hybridized Films

In fabricating the hybridized film, 10 mg of lanthanide complexes and 20 mg of saccharide derivatives (**Glu** and **Ara**) or cellulose derivatives (**CABu** and **CTA**) were completely dissolved in 1.0 mL of the desired solvent (chloroform or tetrahydrofuran (THF)) at ambient temperature. The hybridized film was deposited onto a polished circular quartz plate or borosilicate glass (Tempax Float[®], Schott AG, Germany) (25 mm in diameter and 1 mm in thickness) by spin coating using a spin coater (MIKASA, MS-B100, Tokyo, Japan), then, 800 μL of the solution was placed onto the center of the plate and spun at 1,500 rpm for 60 s. The films on the glass were attached on both sides (front and back surfaces) to ensure an *optically symmetrical geometry* with air-sample-(quartz or borosilicate substrate)-sample-air contact by spin coating chloroform or THF solutions that consist of saccharides (chiral host) and lanthanide complex (achiral guest) (Guo et al., 2017, 2018; Yamada et al., 2018). Although the

film thicknesses of both sides were not determined, we assumed to be on the order of several μm for each. The hybridized double-side coating films were scattering-free and transparent by the naked eye. To measure CPL/PL/CPL/PLE/CD/UV-visible spectra, the optical density of the double-side coating specimen was controlled to 0.3–1.0 in the range of 280 and 330 nm. CD, CPL, and CPLE spectra of the hybridized films were measured at ambient temperature (24 – 26°C). The double-sided coating in the symmetrical optical geometry avoids chiroptical inversion artifacts that could be originated from linear dichroism induced by mechanical stress on anisotropic specimens due to spin coating. Based on our experience, single-side coating in the dissymmetrical optical geometry can often cause artifact inversion in signs of CPL and CD signals. In the case of single-side coating, the probability of the chiroptical sign inversion was approximately 2–3 out of 10, while double-side coating prevented the artifact origin sign inversion.

RESULTS AND DISCUSSION

The chirogenesis characteristics of oligo-/polyfluorenes originate from rotatable C–C bonds between fluorene rings and from C–O/C–C bonds of the cellulose derivatives (**Figure 1**) (Guo et al., 2017, 2018; Yamada et al., 2018) in the GS and ES because rotational barrier heights of the single bonds are as small as 1.5 – 2.5 kcal mol^{-1} . Eu^{III} and Tb^{III} complexes with three fod ligands should coexist as racemic mixtures of *D*-/*L*-species of C_3 -symmetrical facial (*fac*)- and C_1 -meridional (*mer*) motifs (Brittain and Richardson, 1977a; Jalilah et al., 2018), while even Eu^{III} and Tb^{III} with three dpm should coexist as a racemic mixture of *D*-/*L*-species of D_3 -geometry. Although barrier heights of *D*-*L* stereomutation and/or *fac*-*mer* isomerisms are considerably high on the order of 10 – 20 kcal mol^{-1} (Glover-Fischer et al., 1998; Carr et al., 2012; Miyake, 2014), multiple intermolecular C–H/O–C, C–H/ π , and C–H/F–C interactions (Murray-Rust et al., 1983; Nishio et al., 1998; Desiraju and Steiner, 1999; Tsuzuki et al., 2003; Yuasa et al., 2011; Koiso et al., 2017; Jalilah et al., 2018) should overcome the barriers when solidified matrices are employed. Note that solidified matrices are regarded as solid-like solvents with a very high viscosity. In this work, we applied a double-side, spin-coating technique (Guo et al., 2017, 2018) to fabricate CPL/CD-functioned films deposited onto fused quartz and/or borosilicate glass to obtain artifact-free CPL/photoluminescence (PL), CPL/PL excitation (PLE), and CD/UV-visible spectra. CPL and CPL spectral characterizations of Eu^{III} and Tb^{III} at 4f–4f transitions were assigned based on the literature (Fulgêncio et al., 2012; Tanner, 2013; Binnemans, 2015; de Queiroz et al., 2015; Xue et al., 2015; Yang et al., 2017). Dimensionless Kuhn's anisotropic ratios in the ES and GS, being popularly known as g_{lum} and g_{abs} , were manually evaluated at a specific extreme wavelength (λ_{ext}) of the corresponding CPL and CD spectral profiles in line with the literature (Eliel and Wilen, 1994). All CPL characteristics (g_{lum} value at λ_{ext}) of Eu^{III} and Tb^{III} complexes are summarized in **Table 1**.

TABLE 1 | CPL characteristics (dissymmetry ratio, g_{lum} in 10^{-2} at specific wavelength) of Eu^{III} and Tb^{III} coordinated with three β -diketonates as achiral ligands embedded in two polysaccharide alkyl esters (**CABu** and **CTA**), *D*-/*L*-glucose pentamethyl esters (**D**-/**L**-**Glu**), and *D*-/*L*-Arabinose tetramethyl esters (**D**-/**L**-**Ara**).

Ln^{III} tris(β -diketonates)	CABu $g_{lum}/10^{-2}$ (nm)	CTA $g_{lum}/10^{-2}$ (nm)	Glu $g_{lum}/10^{-2}$ (nm)		Ara $g_{lum}/10^{-2}$ (nm)		α -pinene $g_{lum}/10^{-2}$ (nm)	
			<i>D</i> -	<i>L</i> -	<i>D</i> -	<i>L</i> -	(1 <i>R</i>)	(1 <i>S</i>)
$Eu(fod)_3$	+6.71 (593) ^a −0.59 (613) ^b	+4.63 (593) ^a −0.40 (613) ^b	+1.05 (594) ^a −0.19 (612) ^b	−0.81 (596) ^a +0.08 (613) ^b	+0.19 (593) ^a −0.02 (607) ^b	−0.30 (591) ^a +0.06 (611) ^b	−0.49 (593) ^f +0.05 (613) ^f	+0.41 (593) ^f −0.04 (613) ^f
$Eu(dpm)_3$	n.d. ^g	n.d. ^g	n.d. ^g	n.d. ^g	n.d. ^g	n.d. ^g	n.d. ^g	n.d. ^g
$Tb(fod)_3$	−0.29 (490) ^c +0.78 (540) ^d −0.18 (552) ^e	−0.10 (490) ^c +0.35 (542) ^d −0.07 (553) ^e	n.d. ^g	n.d. ^g	n.d. ^g	n.d. ^g	n.d. ^g	n.d. ^g
$Tb(dpm)_3$	−0.53 (491) ^c +0.37 (537) ^d −0.59 (547) ^e	−0.44 (489) ^c − +0.80 (547) ^e	n.d. ^g	n.d. ^g	n.d. ^g	n.d. ^g	n.d. ^g (~490) +0.44 ^d (537) −0.13 ^e (547)	n.d. ^g (~490) −0.49 ^d (537) +0.34 ^e (548)

All numerical values in bracket mean wavelength extremum for CPL signals. ^a $Eu^{III} \ ^5D_0 \rightarrow \ ^7F_1$ (593 nm), ^b $Eu^{III} \ ^5D_0 \rightarrow \ ^7F_2$ (613 nm), ^c $Tb^{III} \ ^5D_4 \rightarrow \ ^7F_6$ (490 nm), ^d $Tb^{III} \ ^5D_4 \rightarrow \ ^7F_5$ (l) (540 nm), ^e $Tb^{III} \ ^5D_4 \rightarrow \ ^7F_5$ (ll) (552 nm), ^fData were taken from literature (Jalilah et al., 2018). ^gNot characterized or no data.

Chirality Transfer Capability From Cellulose Alkyl Esters to $Eu(fod)_3$

The normalized CD and UV-visible spectra of $Eu(fod)_3$ in **CABu** and **CTA** films are shown in **Figures 2A,B**, respectively. For comparison, the original raw CD and UV-visible spectra of the $Eu(fod)_3$ -hybridized films were given in **Figure S13A**, SM. Bisignate profile at Cotton CD bands at 290 and 310 nm between **CABu** and **CTA** films are obviously opposite. These Cotton CD bands at 290 and 310 nm, however, do not originate from **CABu** and **CTA**. Broad monosignate CD bands due to $n-\pi^*$ transition from alkyl esters of **CABu** and **CTA** thin films appeared at ~215 nm with (+)-sign and ~205 nm with (−)-sign, respectively (Guo et al., 2018). These (+)- and (−)-sign CD bands at 205 and 215 nm in the solid film reflect from left-handed helicity of **CABu** and right-handed helicity of **CTA** in solutions, respectively (Dubois et al., 1998; Onofrei et al., 2015), though **CABu** and **CTA** are β -(1 \rightarrow 4) linked polymers made of *D*-glucose framework as a common repeating unit.

Although the alkyl ester itself does not have a stereogenic center, the ester can adopt particular chiral conformational geometry by the direct connection of the *D*-glucose ring. Two lone pairs at ethereal “−O−” and two C−H groups at “−CH₂−” are no longer to be equal because of C−O−C single bonds in R−C(=O)−O−CH₂− side group act as pseudochiral stereogenic bonds, similar to gauche *n*-butane. The unequal lone pairs at ethereal oxygen and unequal CH₂ groups may be responsible for the induction of chiral intermolecular C−O/H−C and C−H/F−C interactions between the alkyl ester moieties and lanthanide ligands. However, any CD/CPL signals of $Eu(fod)_3$ in the presence of **CABu** and **CTA** in dilute chloroform solutions (~ 10^{-3} M) were not able to detect because the postulated chiral intermolecular C−O/H−C and C−H/F−C interactions are inherently weak in the fluidic solution. The postulated chiral alkyl esters of **CABu** and **CTA** can thus act efficiently and differently in the solidified films only as external chirality

inducible scaffoldings toward optically inactive $Eu(fod)_3$ and several lanthanide complexes, as discussed in later sections.

The g_{abs} values at λ_{ext} of $Eu(fod)_3$ at 290 and 316 nm in **CABu** film are $+3.5 \times 10^{-4}$ at 280 nm and -3.5×10^{-4} at 310 nm, respectively, while those in **CTA** film are -1.6×10^{-4} at 290 nm and $+1.1 \times 10^{-4}$ at 300 nm, respectively. Note that the λ_{max} values at non-polarized UV-visible spectra of $Eu(fod)_3$ in **CABu** and **CTA** films are commonly ~291 nm. Although these CD bands at ~290 nm and ~310 nm are ascribed to $n-\pi^*/^1\pi-^3\pi^*$ bands of the three fod ligands, their signs appear to be determined solely by preferential helix sense and/or local chirality of multiple alkyl esters of **CABu** and **CTA**.

Contrarily, the normalized bisignate-like CPL spectral profiles between $Eu(fod)_3$ in **CABu** and **CTA** films are apparently the same, as shown in **Figures 2C,D**, respectively. Obviously, bisignate CPL band profiles at ~593 nm and ~613 nm in **CABu** and **CTA** are definitively similar. The g_{lum} values of $Eu(fod)_3$ in **CABu** film are $+6.71 \times 10^{-2}$ at $^5D_0 \rightarrow ^7F_1$ transition (593 nm) and -0.59×10^{-2} at $^5D_0 \rightarrow ^7F_2$ transition (613 nm), respectively, while those in **CTA** film are weaker with $+4.63 \times 10^{-2}$ at $^5D_0 \rightarrow ^7F_1$ transition (593 nm) and -0.40×10^{-2} at $^5D_0 \rightarrow ^7F_2$ transition (613 nm), respectively (**Table 1**).

It is interesting to note that the absolute magnitude $|g_{lum}|$ values at $^5D_0 \rightarrow ^7F_1$ band of $Eu(fod)_3$, 6.7×10^{-2} in **CABu** and 4.6×10^{-2} in **CTA** are considerably boosted by 13–16 times and 9–11 times, respectively, relative to the $|g_{lum}|$ values of $Eu(fod)_3$ in neat (*R*)- and (*S*)- α -pinene (Jalilah et al., 2018). Also, those $|g_{lum}|$ values are enhanced by 2.5–2.7 times and 1.7–1.9 times compared to those of $Eu(fod)_3$ in neat (*R*)- and (*S*)- α -phenylethylamine (Jalilah et al., 2018). Although the $|g_{lum}|$ values of $Eu(fod)_3$ in **CABu** and **CTA** are not outstanding compared to those several Eu^{III} complexes coordinated with well-designed chiral ligands reported recently (Petoud et al., 2007; Lunkley et al., 2008; Leonzio et al., 2017; Yeung et al., 2017; Zhou et al., 2019), the **CABu** and **CTA** have a tremendous benefit as chiral solidified platforms

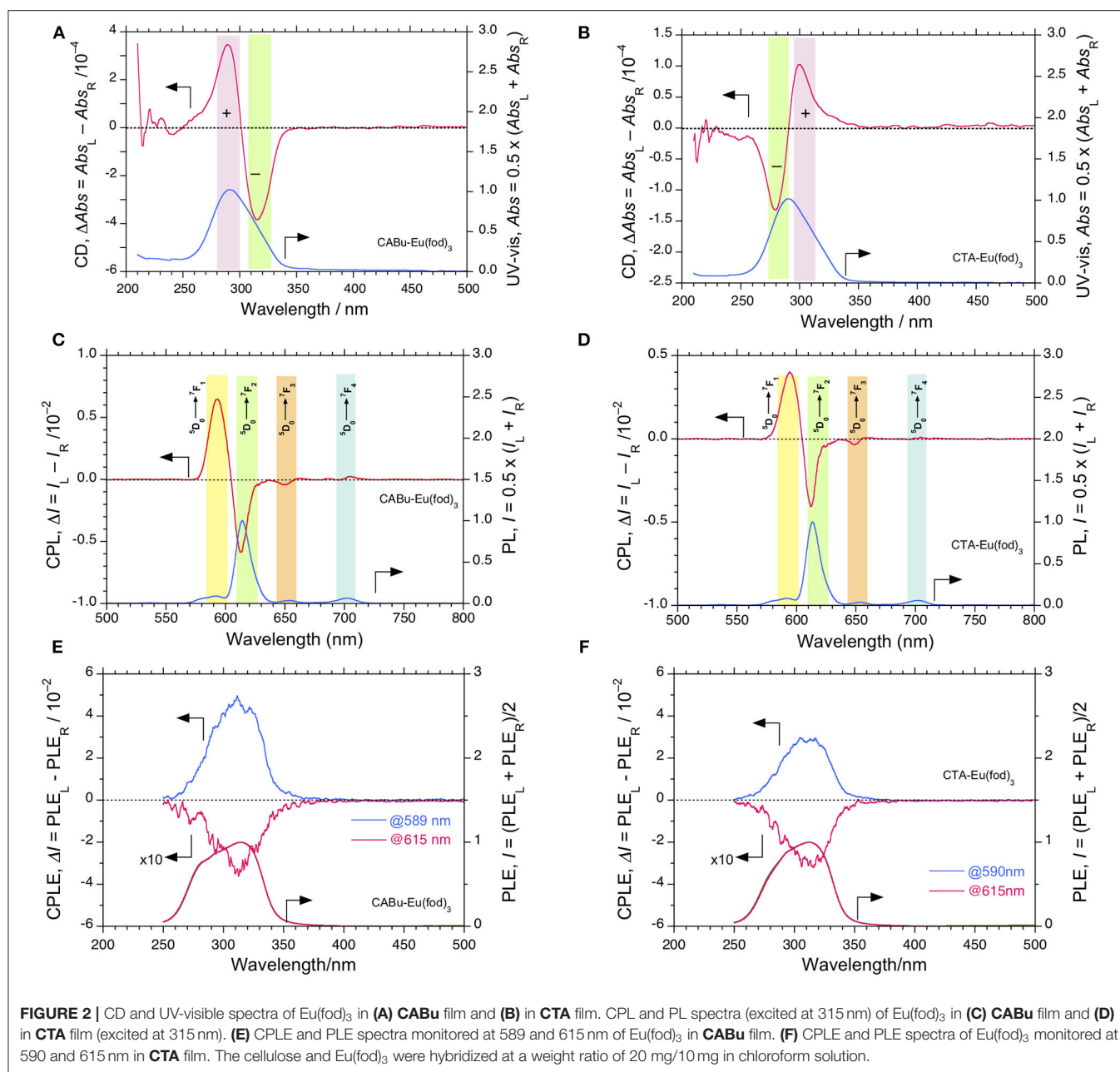


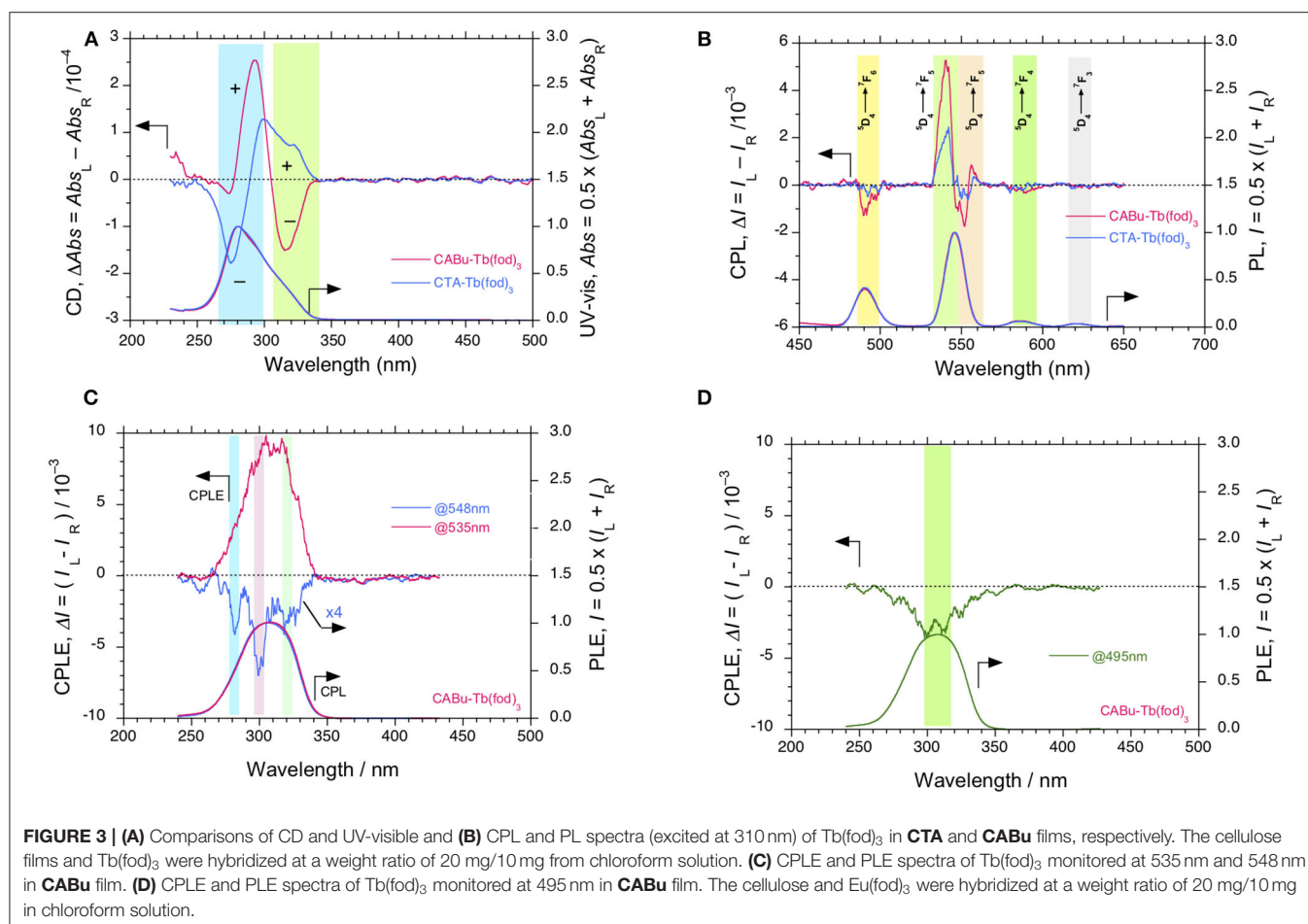
FIGURE 2 | CD and UV-visible spectra of Eu(fod)₃ in (A) CABu film and (B) in CTA film. CPL and PL spectra (excited at 315 nm) of Eu(fod)₃ in (C) CABu film and (D) in CTA film (excited at 315 nm). (E) CPL and PLE spectra monitored at 589 and 615 nm of Eu(fod)₃ in CABu film. (F) CPL and PLE spectra of Eu(fod)₃ monitored at 590 and 615 nm in CTA film. The cellulose and Eu(fod)₃ were hybridized at a weight ratio of 20 mg/10 mg in chloroform solution.

to efficiently induce and magnify $|g_{\text{lum}}|$ values to optically inactive Eu(fod)₃ as a potent CPL emitter regardless of achiral ligands.

To confirm the apparent inconsistency between the retention in CPL bands at $4f-4f$ transitions in CABu and CTA films and between the inversion in CD bands at $n-\pi/\pi-\pi^3\pi^*$ transitions in CABu and CTA films, we applied CPLE and PLE spectroscopy (Duong and Fujiki, 2017) by monitoring at $^5D_0 \rightarrow ^7F_1$ and $^5D_0 \rightarrow ^7F_2$ transitions in CABu and CTA films, as shown in Figures 2E,F, respectively. Disregard of CABu and CTA, it is obvious that the CPLE band at 310 nm is commonly (+)-sign monitored at $^5D_0 \rightarrow ^7F_1$ transition and that the CPLE band at 310 nm is commonly (-)-sign monitored at $^5D_0 \rightarrow ^7F_2$

transition. The magnitudes of the CPLE bands in CABu film are $+4.86 \times 10^{-2}$ monitored at 589 nm and -0.30×10^{-2} monitored at 615 nm, respectively. Similarly, the magnitude of the CPLE bands in CTA film somewhat weaken, and $+2.96 \times 10^{-2}$ monitored at 590 nm and -0.33×10^{-2} monitored at 615 nm, respectively.

The origin of the inconsistency between the sign at the first Cotton CD band (310 nm) and the opposite CPLE sign at this wavelength that depends on the wavelengths monitored at $^5D_0 \rightarrow ^7F_1$ and $^5D_0 \rightarrow ^7F_2$ transitions is an unresolved question and obscure. However, the $n-\pi/\pi-\pi^3\pi^*$ bands at ~310 nm with the opposite sign originates from the three fod ligands, is obviously degenerative, and is responsible for LMCT (from the



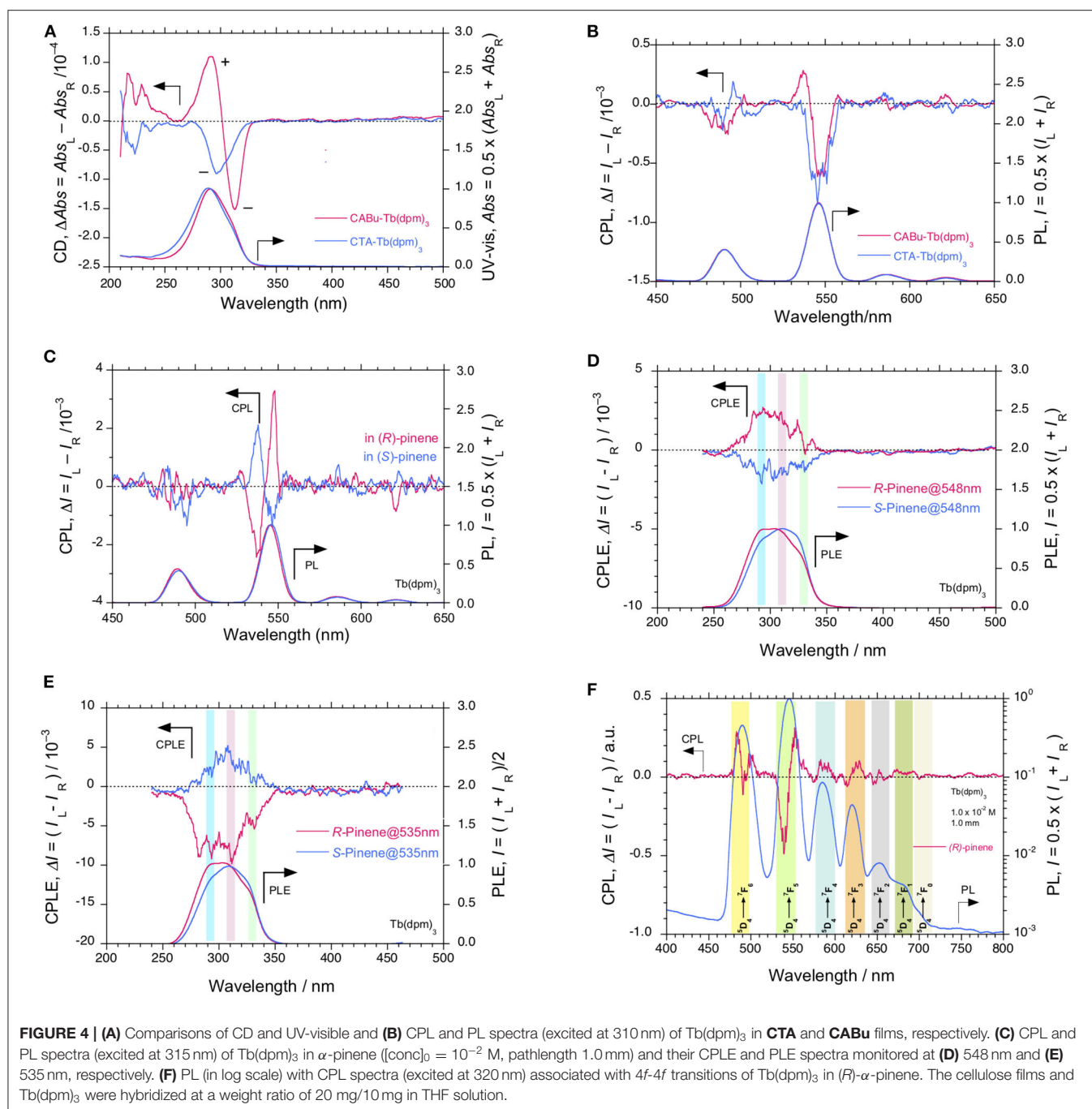
ligands to high energy levels of Eu^{III}, for example, ⁵D₂ state), leading to ⁵D₀ → ⁷F₁ and ⁵D₀ → ⁷F₂ transitions with the opposite CPL sign. The broader ~310 nm transition is likely to be a convolution of two nearly degenerate transitions with an opposite chirality; one (+)-sign band at ~310 nm is responsible for ⁵D₀ → ⁷F₁ and another (-)-sign band at ~310 nm for ⁵D₀ → ⁷F₂ bands. The ⁵D₂ state of Eu^{III} is close to the lowest photoexcited T₁ states of the ligands. When one excite simultaneously at couplet-like ¹π-³π* transitions (~310 nm) of CD-active Eu(fod)₃ using monochromated non-polarized light, the photoexcited Eu(fod)₃ decays into the ⁷F₁ and ⁷F₂ states with two different pathways because ⁵D₀ → ⁷F₁ and ⁵D₀ → ⁷F₂ states are magnetic dipole (MD) allowed transition with an electric dipole (ED) forbidden transition and MD forbidden transition with a forced induced ED transition, so-called, hypersensitive transition, respectively (Tanner, 2013; Binnemans, 2015).

Chirality Transfer Capability From Cellulose Alkyl Esters to Tb(fod)₃

The normalized CD and UV-visible spectra of Tb(fod)₃ in **CTA** and **CABu** films are compared in **Figure 3A**. For comparison, the original CD and UV-visible spectra of the films were given in **Figure S13B**, SM. Unlikely to the case of Eu(fod)₃, trisinate

profile at CD bands appeared at (-)-sign at 315 nm, (+)-sign at 292 nm and (-)-sign at 273 nm in **CABu** while (+)-sign at 322 nm, (+)-sign at 300 nm and (-)-sign at 275 nm in **CTA**. The apparent g_{abs} values at the first Cotton band of Tb(fod)₃ in **CABu** and **CTA** films are -3.5 × 10⁻⁴ at 315 nm and +2.0 × 10⁻⁴ at 324 nm, respectively. **CABu** efficiently induced the Cotton CD band of Tb(fod)₃ rather than **CTA**, similar to the case of Eu(fod)₃.

The different CD inducibility of Tb(fod)₃ between **CABu** and **CTA** reflects the corresponding CPL spectra at 4f-4f transitions of Tb(fod)₃. **Figure 3B** shows the normalized CPL and PL spectra excited at 310 nm of Tb(fod)₃ in **CTA** and **CABu** films. Obviously, three CPL bands are ascribed to ⁵D₄ → ⁷F₆ transition (490 nm) and ⁵D₄ → ⁷F₅ transitions (540 and 552 nm), respectively (**Table 1**). On the other hand, we did not detect any CPL bands at ⁵D₄ → ⁷F₄ transition (585 nm) and ⁵D₄ → ⁷F₃ transition (622 nm) clearly though the corresponding PL band was obvious. The g_{lum} values of Tb(fod)₃ in **CABu** are -2.91 × 10⁻³ at ⁵D₄ → ⁷F₆ transition (490 nm), +7.82 × 10⁻³ at ⁵D₄ → ⁷F₅ transition (540 nm) and -1.75 × 10⁻³ at ⁵D₄ → ⁷F₅ transition (552 nm), respectively (**Table 1**). Those values in **CTA** weaken with -1.01 × 10⁻³ at ⁵D₄ → ⁷F₆ transition (490 nm), +3.53 × 10⁻³ at ⁵D₄ → ⁷F₅ transition (542 nm) and -0.68 × 10⁻³ at ⁵D₄ → ⁷F₅ transition (553 nm), respectively (**Table 1**). Although the origin of the differences in the g_{abs} at



the first Cotton CD bands and g_{lum} values of CPL bands at 4f-4f transitions between Eu(fod)₃ and Tb(fod)₃ remains, CABu and CTA commonly induced clear CD and CPL bands.

Although the $|g_{lum}|$ values ($0.35\text{--}0.78 \times 10^{-2}$ at 540 nm, Table 1) at $^5D_4 \rightarrow ^7F_5$ transition of Tb(fod)₃ in CABu and CTA films are comparable to those (0.83×10^{-2} at 542 nm) of Tb(hfa)₃ (hfa:hexafluoroacetate) with chiral 4,12-bis(diphenylphosphino)-[2.2]-paracyclophane (Taniguchi et al., 2019) and weakened by one order of magnitude compared to those ($4\text{--}8 \times 10^{-2}$ at ~ 540 nm) of Tb^{III} complexes

coordinated with chiral bis(oxazolonyl)pyridine (Yuasa et al., 2011). The well-designed chiral ligands induce CPL-functionality to Tb^{III} complexes in solution more efficiently than solidified polysaccharide alkyl esters.

Chirality Transfer Capability From Cellulose Alkyl Esters to Eu(dpm)₃ and Tb(dpm)₃

The dpm ligand is a symmetrical β-diketonate, in which two methyl groups of acetylacetonate are replaced by two electron-donating (ED) *tert*-butyl groups. Therefore, Tb(dpm)₃ and

Eu(dpm)₃ can adopt a single *D*₃-symmetrical configuration (Brittain and Richardson, 1977a; Brittain, 1980). In a recent paper (Jalilah et al., 2018) and the present work, we confirmed that Eu(fod)₃ in α -pinene has shown clear CPL signals due to the presence of electron-withdrawing (EW) fluoroalkyl groups. Eu(dpm)₃ in α -pinene shows no detectable CPL signals due to the lack of EW fluoroalkyl groups (Figure S14B, SM).

Tb(dpm)₃ in CABu and CTA films shows clear CD and UV-visible spectra in the range of 200 nm and 340 nm, as shown in Figure 4A. For comparison, the original CD and UV-visible spectra of the films are given in Figure S13C, SM. Tb(dpm)₃ in CABu and CTA films, however, showed detectable but weak CPL spectra at 4*f*-4*f* transitions, as shown in Figure 4B. The *g*_{lum} values in CABu film are -0.53×10^{-3} at ⁵D₄ → ⁷F₆ (491 nm), $+0.37 \times 10^{-3}$ at ⁵D₄ → ⁷F₅ (537 nm), -0.59×10^{-3} at ⁵D₄ → ⁷F₅ (547 nm), while the *g*_{lum} values in CTA are -0.44×10^{-3} at ⁵D₄ → ⁷F₆ (489 nm) and -0.80×10^{-3} at ⁵D₄ → ⁷F₅ (547 nm) (Table 1). The absolute magnitudes of *g*_{lum} values with dpm ligands greatly diminished compared to Tb^{III} complexes with fod ligands. Tb(dpm)₃ and Eu(dpm)₃ showed different behaviors toward external chiral chemical perturbations regardless of the same fod and dpm as the ligands. Eu(dpm)₃ in CABu and CTA did not demonstrate obvious CPL spectra although the corresponding PL spectra are evident (Figures S14A,B, SM).

We ascertained many times that there were no detectable CPL signals of Eu(dpm)₃ in CABu films. This could be because Eu(dpm)₃ is lack of EW-fluoroalkyl groups that can cause efficient chiral C-F/H-C interactions. Chiral C-O/H-C interactions seem not efficient to induce the chiral perturbation.

Chirality Transfer Capability From Monosaccharide Permethyl Esters to Eu(fod)₃ and Tb(fod)₃

Kipping and Pope found that preferential crystallization of *L*-NaClO₃ in the presence of naturally occurring *D*-glucose and *D*-mannitol (Kipping and Pope, 1898). Currently, non-naturally occurring *L*-glucose is available commercially, although it is costly. *L*-(+)- and *D*-(-)-arabinose are also available, but the *L*-form is more abundant in nature than the *D*-form due to unknown reasons. To verify whether chirogenesis of Eu(fod)₃ is solely determined by point chirality of monosaccharides, we measured CD and CPL spectra of Eu(fod)₃ embedded in *D*-/*L*-Glu and *D*-/*L*-Ara films, as displayed in Figures 5A–D.

Firstly, CD and UV-visible spectra between Eu(fod)₃ in *D*- and *L*-Glu films are compared in Figure 5A. The original CD and UV-visible spectra of the films are given in Figure S13D, SM. Eu(fod)₃ showed nearly mirror-image bisignate CD bands, though the value of λ_{ext} at the first and second Cotton bands are considerably different from each other. The *g*_{abs} values of Eu(fod)₃ in *D*-Glu film are $+0.89 \times 10^{-4}$ at 321 nm and -0.42×10^{-4} at 284 nm, while in *L*-Glu film, these values are -0.80×10^{-4} at 315 nm and $+0.44 \times 10^{-4}$ at 282 nm (Table 1).

CD and UV-visible spectra between Eu(fod)₃ in *D*- and *L*-Ara films are compared in Figure 5B. The original CD and UV-visible spectra of the films are given in Figure S13E, SM. Similarly, Eu(fod)₃ shows nearly mirror-image bisignate CD bands, though

the value of λ_{ext} at the first and second Cotton bands are subtly different. The *g*_{abs} values of Eu(fod)₃ in *D*-Ara are -0.96×10^{-4} at 321 nm and $+0.55 \times 10^{-4}$ at 281 nm, respectively, while in *L*-Glu film, these values are $+1.08 \times 10^{-4}$ at 316 nm and -0.39×10^{-4} at 275 nm, respectively (Table 1).

Next, we compared CPL and PL spectra excited at 315 nm of Eu(fod)₃ in *D*- and *L*-Glu films, shown in Figure 5C. Eu(fod)₃ displays nearly mirror-image trisignate CPL bands at 4*f*-4*f* transitions associated with emission wavelengths, though the absolute *g*_{lum} values at these transitions are somewhat different. The *g*_{lum} values in *D*-Glu are $+1.05 \times 10^{-2}$ at ⁵D₀ → ⁷F₁ (594 nm), -0.19×10^{-2} at ⁵D₀ → ⁷F₂ (612 nm) and $+0.19 \times 10^{-2}$ at ⁵D₀ → ⁷F₂ (626 nm), while in *L*-Glu, these values are -0.81×10^{-2} at ⁵D₀ → ⁷F₁ (596 nm), $+0.08 \times 10^{-2}$ at ⁵D₀ → ⁷F₂ (613 nm), and -0.04×10^{-2} at ⁵D₀ → ⁷F₂ (627 nm) (Table 1).

For comparison, CPL and PL spectra of Eu(fod)₃ in *D*- and *L*-Ara films were excited at 315 nm, and the results are presented in Figure 5D. Eu(fod)₃ exhibits no longer mirror-image trisignate CPL bands at 4*f*-4*f* transitions, though the absolute *g*_{lum} values at these transitions weaken several times. The *g*_{lum} values in *D*-Ara are $+0.19 \times 10^{-2}$ at ⁵D₀ → ⁷F₁ (593 nm), -0.02×10^{-2} at ⁵D₀ → ⁷F₂ (607 nm), and $+0.42 \times 10^{-2}$ at ⁵D₀ → ⁷F₂ (630 nm), while in *L*-Ara, these values are -0.30×10^{-2} at ⁵D₀ → ⁷F₁ (591 nm), $+0.06 \times 10^{-2}$ at ⁵D₀ → ⁷F₂ (611 nm), and -0.72×10^{-2} at ⁵D₀ → ⁷F₂ (622 nm) (Table 1).

CPL and PL spectra of Tb(fod)₃ excited at 315 nm in *D*-/*L*-Glu and *D*-/*L*-Ara films are given in Figures 5E,F, respectively. Regardless of Glu and Ara, although Tb(fod)₃ shows very weak CPL bands at 4*f*-4*f* transitions, CPL signs are likely to depend on the chirality of Glu and Ara. Because the absolute *g*_{lum} values at these 4*f*-4*f* transitions considerably weaken, the *g*_{lum} values cannot be precisely evaluated.

Although *L*-cellulose is not available on earth, we can conclude that *D*-chirality of CTA, CABu, Glu, and Ara determines the (+)- and (-)-sign CPL characteristics of Eu(fod)₃ at ⁵D₀ → ⁷F₁ and ⁵D₀ → ⁷F₂ transitions. Conversely, (-)- and (+)-signs at these transitions are from the *L*-chirality of Glu and Ara, although the inversion in the bisignate CD bands of Eu(fod)₃ at 280–290 nm and 300–310 nm are considerably dependent on the nature of the alkyl groups of CTA and CABu. Similarly, *D*-chirality of CTA, CABu, Glu, and Ara determines the (+)- and (-)-sign CPL characteristics of Tb(fod)₃ at two ⁵D₄ → ⁷F₅ transitions. Conversely, *L*-chirality of Glu and Ara determines the (-)- and (+)-signs at the transitions.

Chirality Transfer Capability From α -Pinene to Eu(fod)₃, Tb(fod)₃, Eu(dpm)₃, and Tb(dpm)₃

Bicyclic terpenes, (1*S*)-/(1*R*)- α -pinene and (1*S*)-/(1*R*)- β -pinene, are chiral rigid hydrocarbons and are transparent in the near-UV and visible region. This feature is beneficial to gain an insight into higher energy states responsible for CPL transitions by measuring CPLE spectra monitoring at a specific CPL wavelength. Actually, the chirality of α -/ β -pinenes is transferred to achiral or racemic Eu(fod)₃ with considerably large *g*_{lum} values at 4*f*-4*f* transitions,

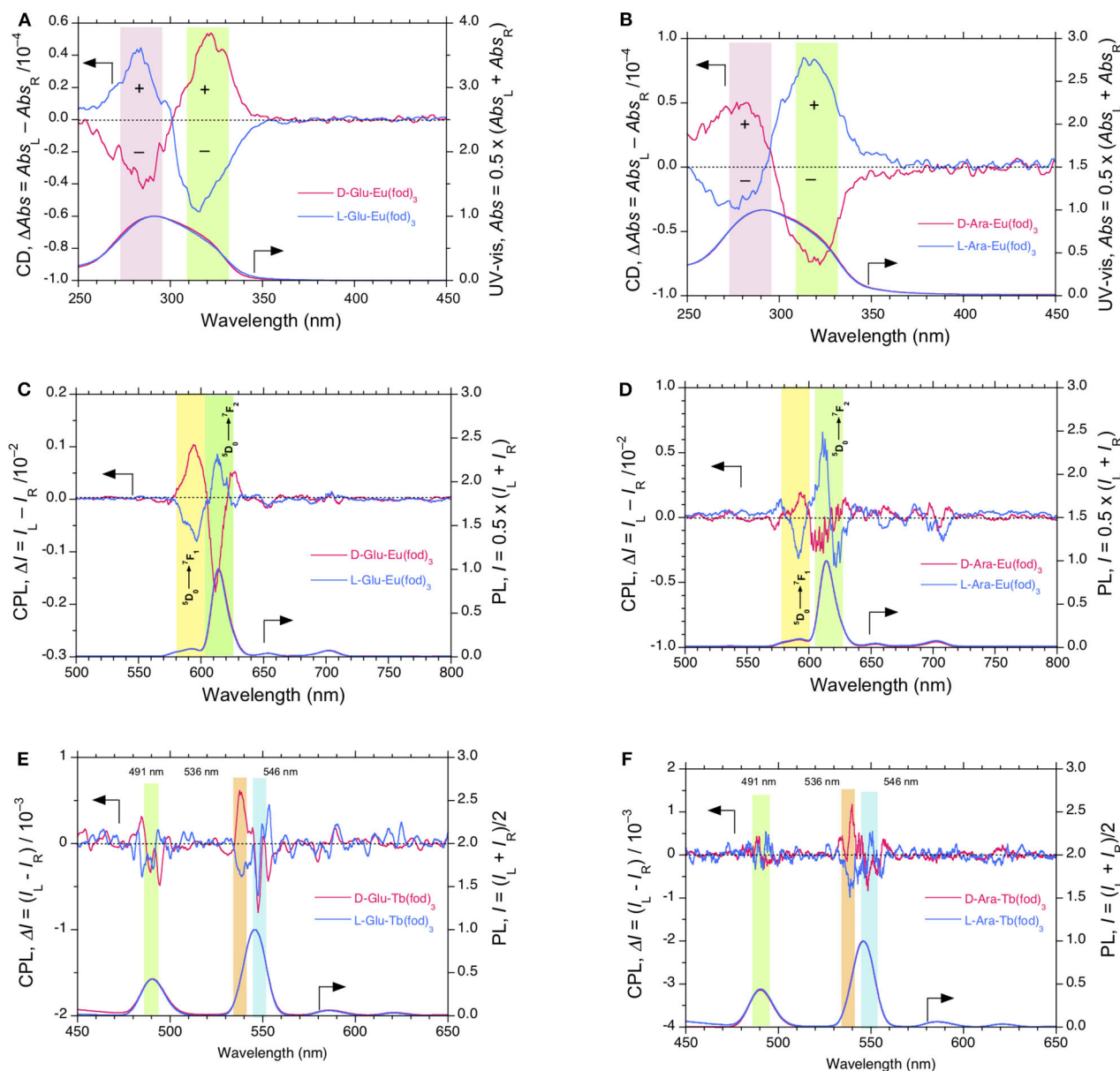


FIGURE 5 | (A) CD and UV-visible spectra and **(C)** CPL and PL spectra (excited at 315 nm) of $Eu(fod)_3$ in **D-/L-Glu** films. **(B)** CD and UV-visible spectra and **(D)** CPL and PL spectra (excited at 315 nm) of $Eu(fod)_3$ in **D-/L-Ara** films. **(E)** CPL and PL spectra (excited at 315 nm) of $Tb(fod)_3$ in **D-/L-Glu** films. **(F)** CPL and PL spectra (excited at 310 nm) of $Tb(fod)_3$ in **D-/L-Ara** films. The saccharide ester and $Eu(fod)_3$ and $Tb(fod)_3$ were hybridized at a weight ratio of 20 mg/10 mg in chloroform solution.

that were verified by CPLE spectra (Jalilah et al., 2018). This result prompted us to test whether $Tb(fod)_3$ in α -pinene reveals CPL signals, although $Tb(fod)_3$ did not show clear CPL signals because of an unknown reason.

On the other hand, $Tb(dpm)_3$ dissolved in α -pinene shows clear CPL signals, in which signs are determined solely by the chirality of the α -pinene (Figure 4C). The g_{lum} values in (1S)- α -pinene are $+4.35 \times 10^{-3}$ at $^5D_4 \rightarrow ^7F_5$ (537 nm) and -1.28×10^{-3} at $^5D_4 \rightarrow ^7F_5$ (547 nm), while in (1R)- α -pinene are -4.94×10^{-3} at $^5D_4 \rightarrow ^7F_5$ (537 nm) and $+3.44 \times 10^{-3}$ at

$^5D_4 \rightarrow ^7F_5$ (548 nm), though the CPL bands at $^5D_4 \rightarrow ^7F_6$ (490 nm) are not obvious (Table 1). Evidently, (+)- and (-)-sign CPL characteristics of $Eu(fod)_3$ at $^5D_0 \rightarrow ^7F_1/5D_0 \rightarrow ^7F_2$ transitions and $Tb(dpm)_3$ at two $^5D_4 \rightarrow ^7F_5$ transitions are determined by S- and R-chirality of α -pinene, respectively. In comparison to $Tb(dpm)_3$, $Eu(dpm)_3$ in α -pinene has shown no detectable CPL signals (Figure S14C, SM). From PL spectrum of $Tb(dpm)_3$ in (R)- α -pinene excited at 320 nm associated with the corresponding CPL signals ranging of 500 and 800 nm (Figure 4F), seven characteristic $4f-4f$ transitions were assigned

to ${}^5D_4 \rightarrow {}^7F_6$ (490.0 nm, 20408 cm^{-1}), ${}^5D_4 \rightarrow {}^7F_5$ (545.5 nm, 18330 cm^{-1}), ${}^5D_4 \rightarrow {}^7F_4$ (584.5 nm, 17,109 cm^{-1}), ${}^5D_4 \rightarrow {}^7F_3$ (620.0 nm, 16129 cm^{-1}), ${}^5D_4 \rightarrow {}^7F_2$ (652.5 nm, 15,326 cm^{-1}), ${}^5D_4 \rightarrow {}^7F_1$ (682.0 nm, 14,663 cm^{-1}), and ${}^5D_4 \rightarrow {}^7F_0$ (702.5 nm, 14,235 cm^{-1}) (Fulgêncio et al., 2012; de Queiroz et al., 2015; Xue et al., 2015; Yang et al., 2017).

We further verified these CPL signals of $\text{Tb}(\text{dpm})_3$ by the broad CPLE spectra centered at ~ 300 nm associated with the corresponding PLE spectra with several shoulders, as marked by blue, pink, and green bars in **Figures 4D,E**. The signs of the CPLE spectra depend on the signs at monitor wavelengths (535 and 548 nm) and α -pinene chirality; (+)-sign in CPLE spectrum is identical to (+)-sign CPL signal at 546 nm in (*R*)-pinene, while (+)-sign in CPLE spectrum is the same of (+)-sign CPL signal at 535 nm in (*S*)-pinene. The broad CPLE/PLE spectra may arise from at least three different origins of $n\text{-}\pi^*/{}^1\pi\text{-}\pi^*$ transitions of three dpm ligands associated with high energy levels (e.g., 5D_1 and 5D_2) of Tb^{III} (Fulgêncio et al., 2012; de Queiroz et al., 2015; Xue et al., 2015). A similar tendency can be seen in the broad CPLE/PLE spectra of $\text{Tb}(\text{fod})_3$ in **CABu**, as marked in blue, pink, and green bars in **Figures 3C,D**.

Unresolved factors between Tb^{III} and Eu^{III} associated with ligands (fod and dpm) and chiral matrices (α -pinene and monosaccharide alkyl esters) are other critical parameters to generate CPL signals and boost g_{lum} characteristics. Although the inherent nature of the differences between Tb^{III} and Eu^{III} is unresolved, we assume that the interactions of $\text{C-H}/\pi$ between $\text{C}(\delta^-)\text{-H}(\delta^+)$ bonds at dpm of $\text{Tb}(\text{dpm})_3$ and $\text{C}(\delta^+)\text{-C}(\delta^-)$ double bond of α -pinene are more crucial while the $\text{C-F}/\text{H-C}$ interactions between $\text{C}(\delta^+)\text{-F}(\delta^-)$ bonds of fod ligands and $\text{H}(\delta^+)\text{-C}(\delta^-)$ bonds of α -pinene are crucial (Jalilah et al., 2018).

Intermolecular Interactions Between $\text{Eu}(\text{fod})_3$ and **CTA/Glu** by Solid-State ${}^{13}\text{C}\{^1\text{H}\}$ -NMR and Solution ${}^1\text{H}/{}^{19}\text{F}$ -NMR Spectra

We do not yet know what kinds of intermolecular noncovalent interactions exist between the lanthanide tris(β -diketonate) and the poly-/monosaccharide alkyl esters. Among lanthanide tris(β -diketonate)s, we chose $\text{Eu}(\text{fod})_3$ for simplicity and excellent solubility in CDCl_3 . The three fod ligands have ${}^1\text{H}$, ${}^{19}\text{F}$, and ${}^{13}\text{C}$ -NMR active elements to discuss the possible interactions. Additionally, we chose **CTA** and **D-/L-Glu** for simplicity in these solid-state (ss)- ${}^{13}\text{C}$ -NMR and solution ${}^1\text{H}/{}^{19}\text{F}$ -NMR spectra. According to the hard-soft-acid-base theory proposed by Pearson (Pearson, 1963), the lone pairs of the hard base O atom(s) of ester groups can coordinate with the hard acid Eu^{III} of $\text{Eu}(\text{fod})_3$. A marked chemical shift in ${}^{13}\text{C}$ -NMR spectra of ester (C=O and O) and ethereal C-O-C atoms was expected.

The ss- ${}^{13}\text{C}\{^1\text{H}\}$ -NMR spectra of $\text{Eu}(\text{fod})_3$, **CTA**, and a mixture of $\text{Eu}(\text{fod})_3$ and **CTA** in 1/1 (w/w) are compared in **Figures 6A,B**. The ss- ${}^{13}\text{C}$ -NMR spectra of the $\text{Eu}(\text{fod})_3$ -**CTA** mixture are merely a convolution of those of **CTA** and $\text{Eu}(\text{fod})_3$. Any noticeable chemical shift in the ${}^{13}\text{C}$ -NMR spectra was not seen. ${}^{13}\text{C}$ -NMR chemical shift at ~ 170 ppm due to O=C-O of **CTA** was unchanged after mixing with $\text{Eu}(\text{fod})_3$.

The ss- ${}^{13}\text{C}\{^1\text{H}\}$ -NMR spectra of $\text{Eu}(\text{fod})_3$, **D-Glu**, and a mixture of $\text{Eu}(\text{fod})_3$ and **D-Glu** in 1/1 (w/w) are compared in **Figures 6C–G**. Similarly, the ss- ${}^{13}\text{C}$ -NMR spectra of the $\text{Eu}(\text{fod})_3$ -**D-Glu** mixture are merely a convolution of those of **D-Glu** and $\text{Eu}(\text{fod})_3$. Any remarkable chemical shift in the ${}^{13}\text{C}$ -NMR spectra was not seen. Even five well-resolved O=C-O peaks of **D-Glu** pentamethyl ester ranging of ~ 169 ppm and ~ 173 ppm showed no detectable chemical shifts (**Figure 6D**). Similarly, no noticeable chemical shifts of three well-resolved methyl groups ranging from ~ 19 ppm to ~ 22 ppm were observed (**Figure 6E**). Among five well-resolved ${}^{13}\text{C}$ peaks assignable to O=C-O of five esters, C-O-C pyranose ring ranging from ~ 64 to ~ 72 ppm and at ~ 83 ppm does not show remarkable chemical shifts of *D*-glucose ring. These ss- ${}^{13}\text{C}\{^1\text{H}\}$ -NMR data led us to the conclusion that any O atom(s) of glucose ring and ester moieties do not coordinate directly to Eu^{III} ions.

On the other hand, alterations in the chemical shifts of the solution ${}^{19}\text{F}$ -NMR spectra of $\text{Eu}(\text{fod})_3$ in the absence and presence of **CTA**, **D-Glu**, and **L-Glu** in CDCl_3 are apparent, as shown in **Figures 7A–C**. The outer CF_3 signal of $\text{Eu}(\text{fod})_3$ in CDCl_3 resonates at -81.73 ppm as a single peak, indicating C_3 -symmetrical geometry (**Figure 7B**). The single peak resonates at -82.21 ppm and -82.26 ppm in the absence and presence of **L-Glu** and **D-Glu**, respectively, and shifts upfield by 0.48 ppm and 0.53 ppm, respectively (**Figure 7B**). In the presence of **CTA**, the CF_3 signal resonates at -82.31 ppm and shifts upfield by 0.58 ppm (**Figure 7B**). Although the middle CF_2 signal of fod ligand resonates broadly at -126 ppm, in the presence of **L-Glu** and **D-Glu**, this signal resonates at -127.4 ppm and -127.5 ppm, that is shifted upfield by 1.4 ppm and 1.5 ppm, respectively (**Figure 7C**). Similarly, the middle CF_2 peak at -127.5 ppm shifts upfield by 1.5 ppm in the presence of **CTA** (**Figure 7C**). The inner CF_2 of fod shows a broad resonance at -129.2 ppm, but this signal appears at -130.1 ppm in the presence of **L-** and **D-Glu** and shifts upfield by 0.9 ppm (**Figure 7C**). Similarly, the signal appears at -130.3 ppm in the presence of **CTA** and shifts upfield by 1.1 ppm. These upfield shifts in the ${}^{19}\text{F}$ -NMR spectra indicate intermolecular interactions between the F atoms and **CTA**, **L-Glu**, and **D-Glu**, possibly, $\text{C-F}(\delta^-)$ (of the three fod ligands)/ $\text{H}(\delta^+)\text{-C}$ (of **CTA** and **Glu**) interactions.

It is thus evident that there were no marked alterations in ss- ${}^{13}\text{C}$ -NMR spectra between CPL-inactive and CPL-active $\text{Eu}(\text{fod})_3$ in **CTA**, **L-Glu**, and **D-Glu**, while the remarkable upfield chemical shifts in ${}^{19}\text{F}$ -NMR of fod ligands in dilute CDCl_3 solution was distinct. These characteristics should arise from outer or second-sphere effects perturbed by chiral chemicals that are non-coordinating to Eu^{III} , the so-called 'Pfeiffer effect'. The multiple $\text{H}(\delta^+)\text{-C}(\delta^-)$ bonds of chiral chemical species (**CTA**, **D-/L-Glu**, possibly, **D-/L-Ara** and **CABu**) interact with multiple $\text{F}(\delta^-)\text{-C}(\delta^+)$ bonds of the three fod ligands but do not directly coordinate with Eu^{III} .

The noticeable downfield chemical shifts in ${}^1\text{H}$ -NMR spectra of **D-Glu** and **CTA** support the postulated $\text{C}(\delta^+)\text{-F}(\delta^-)$ (of fod) and $\text{H}(\delta^+)\text{-C}(\delta^-)$ (of **CTA** and **D-/L-Glu**) interaction. **Figure 8A** displays the changes in ${}^1\text{H}$ -NMR spectra of **D-Glu** in the absence and presence of $\text{Eu}(\text{fod})_3$. All protons are assigned in the inset of the Figure. The degree of the downfield shifts is summarized

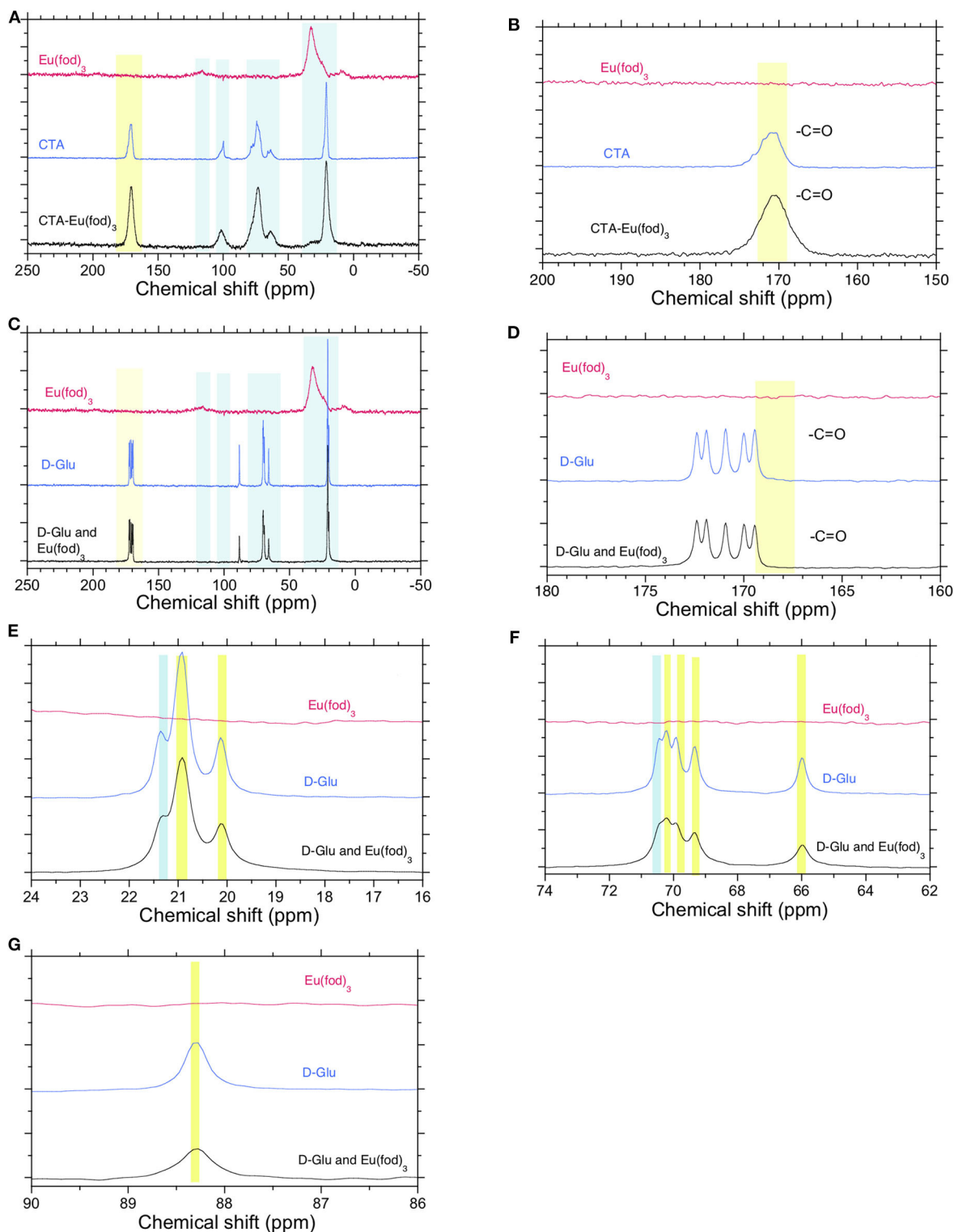
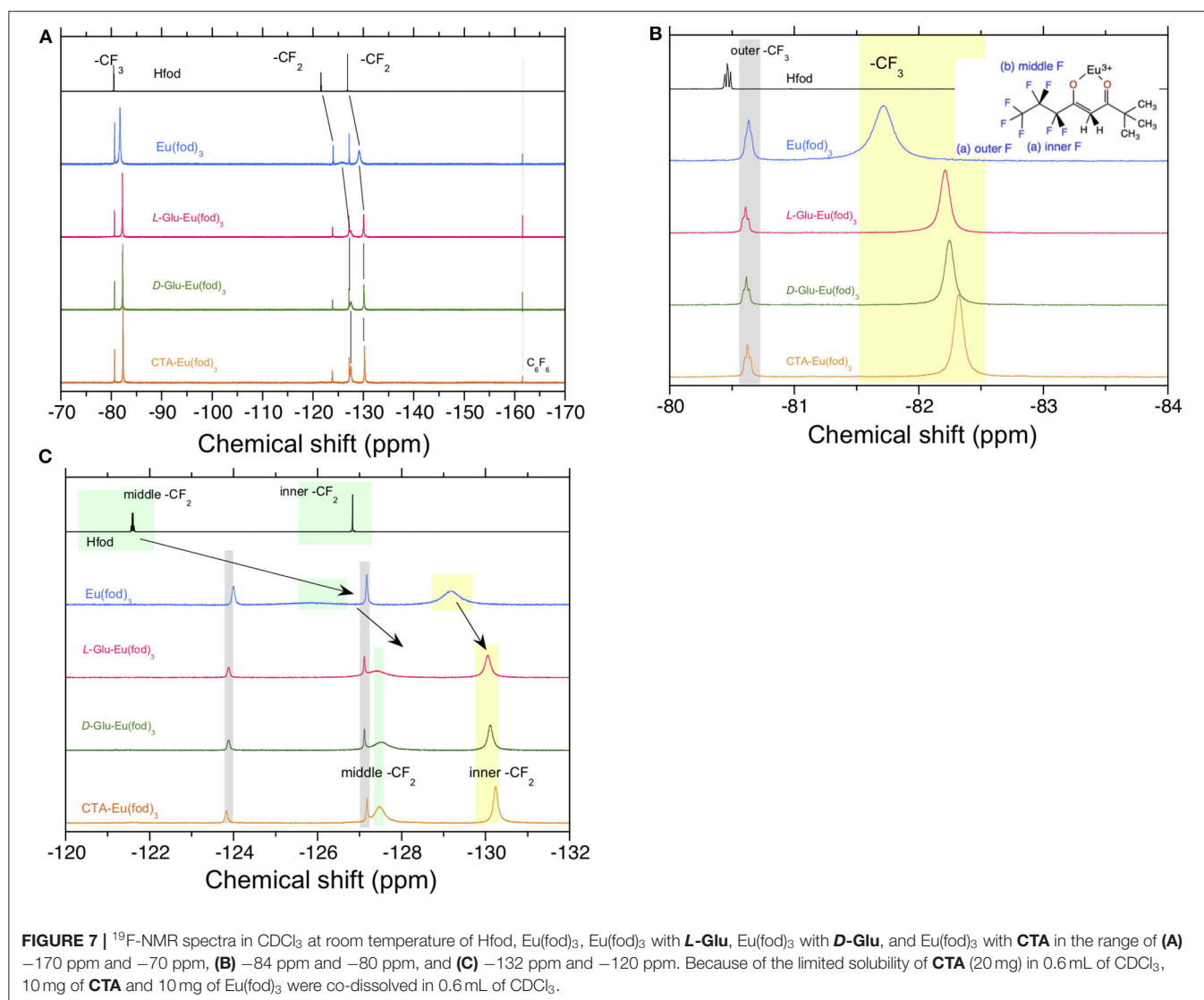


FIGURE 6 | (A) Solid-state (ss)-CP/MAS- $^{13}\text{C}\{^1\text{H}\}$ -NMR spectra of Eu(fod)_3 , CTA, and a mixture of Eu(fod)_3 and CTA in 1/1 (w/w). **(B)** Its magnified spectrum in the range of 150–200 ppm. **(C)** ss- $^{13}\text{C}\{^1\text{H}\}$ -NMR spectra of Eu(fod)_3 , D-Glu, and a mixture of Eu(fod)_3 and D-Glu in 1/1 (w/w) **(D,E)**. Their magnified spectra of methyl groups in D-Glu in the range of 150–200 ppm and 16–24 ppm **(F,G)**. Their magnified spectra of D-glucose ring in the range of 62–90 ppm. A broad ^{13}C -NMR signal at 130 ppm (Figures 5A,C) was attributable to β -diketonate.



in **Table 2**. Notably, protons H1, H3, H5, H6 shift downfield significantly and protons H2, H4, H6 (one of two), H7 also considerably shift downfield. We noticed that H1, H3, H5 are the glucose ring protons and H6 is the CH_2 attached to C5 carbon. Possibly, $\text{Eu}(\text{fod})_3$ molecule is placed on top of the *D*-glucose ring. All H1–H7 protons are close to $\text{Eu}(\text{fod})_3$ molecule with the help of multiple $\text{C}(\delta^+)-\text{F}(\delta^-)/\text{H}(\delta^+)-\text{C}(\delta^-)$ and $\text{C}(\delta^-)-\text{H}(\delta^+)/\text{O}(\delta^-)-\text{C}(\delta^+)$ interactions.

Figure 8B exhibits similar changes in ^1H -NMR spectra of **CTA** in the absence and presence of $\text{Eu}(\text{fod})_3$. Protons are assigned in the insets of the figure. The degree of downfield shifts is summarized in **Table 2**. Notably, protons H1 and H2 shift downfield greatly and protons H3, H4, H5 also shift considerably downfield. H1, H2, H3, and H4 are the glucose ring protons and H5 is the CH_2 attached to C4 carbon. Similarly, $\text{Eu}(\text{fod})_3$ molecule is placed on top of the *D*-glucose ring of **CTA**. All H1–H5 protons are close to $\text{Eu}(\text{fod})_3$ molecule with the

help of multiple $\text{C}(\delta^+)-\text{F}(\delta^-)/\text{H}(\delta^+)-\text{C}(\delta^-)$ and $\text{C}(\delta^-)-\text{H}(\delta^+)/\text{O}(\delta^-)-\text{C}(\delta^+)$ interactions.

For comparison, FT-IR spectra between $\text{Eu}(\text{fod})_3$, **D-Glu**, and $\text{Eu}(\text{fod})_3$ mixed with **D-Glu** in the ranges of 2,700 and 3,700 cm^{-1} , 2,800 and 3,100 cm^{-1} , and 1,000 and 2,000 cm^{-1} are shown in **Figures S15A–C**, SM. We observed no noticeable frequency shifts in $\nu(\text{C-H})$ at 2,850–3,000 cm^{-1} and $\nu(\text{C-F})$ at 1,250–1,050 cm^{-1} . Since the postulated C-F/H-C and C-H/O-C interactions are very weak, the resulting frequency shifts might be minimal, possibly, within 10 cm^{-1} . One $\nu^{\text{as}}(\text{C-H})$ at 2973 cm^{-1} and $\nu^{\text{s}}(\text{C-H})$ at 2873 cm^{-1} due to methyl groups of fod in the absence of **D-Glu** shift to lower frequencies at 2967 cm^{-1} by 7 cm^{-1} and 2871 by 2 cm^{-1} , respectively (**Figure S15B**, SM). These small shifts may be the consequence of the C-H/O-C interactions. On the other hand, $\nu(\text{C=O})$ at $\sim 1,750$ cm^{-1} characteristic of five ester group of **D-Glu** does not coordinate to Eu^{III} directly because there are no noticeable frequency shifts (**Figure S15C**,

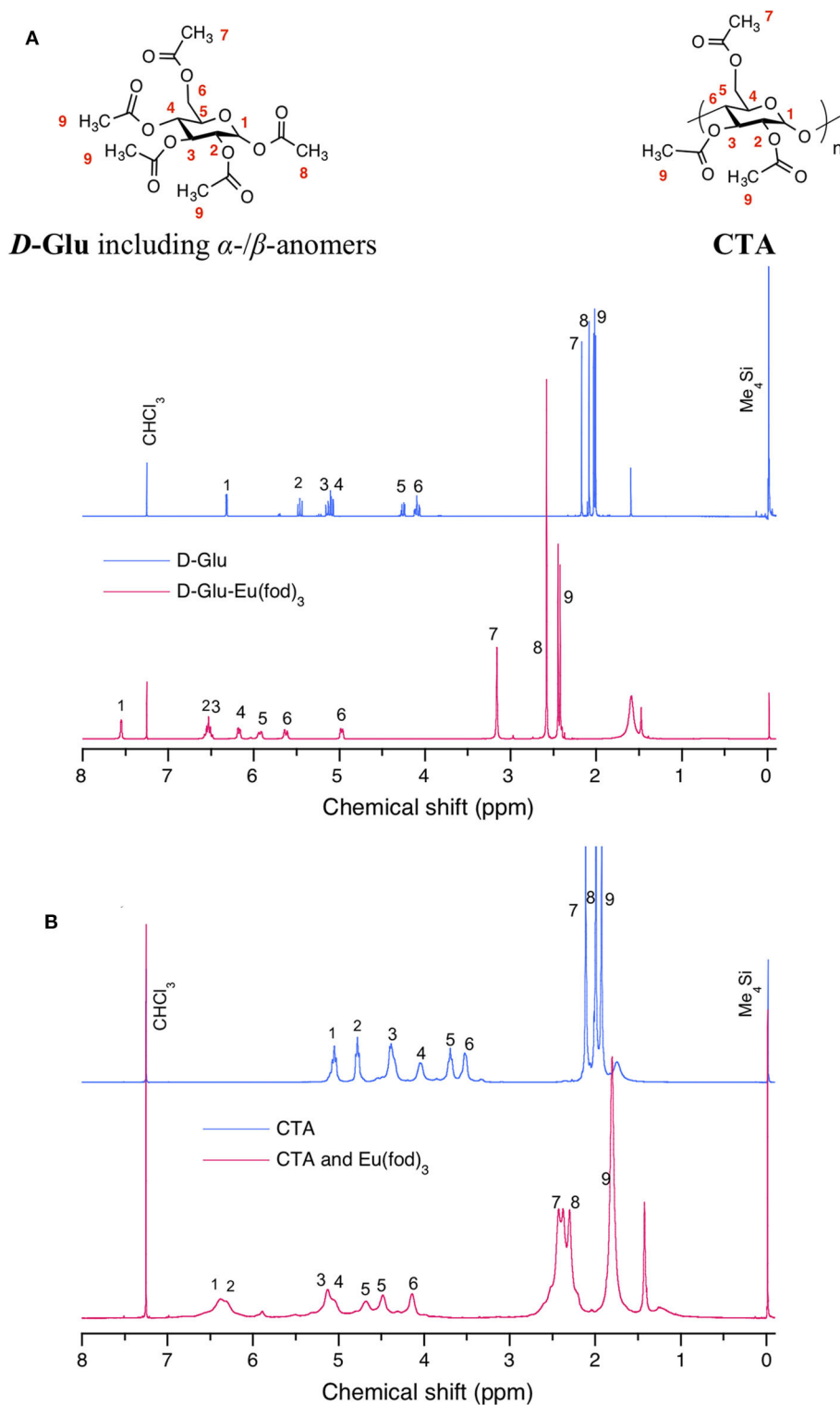


FIGURE 8 | Comparison of ^1H -NMR spectra in CDCl_3 at room temperature between **(A)** *D*-Glu (blue) and $\text{Eu}(\text{fod})_3$ with *D*-Glu (red) and between **(B)** CTA (blue) and $\text{Eu}(\text{fod})_3$ with CTA (red). Sharper and broader ^1H -NMR peaks at ~ 1.5 ppm are assumed to be free water in CDCl_3 and bounded waters at $\text{Eu}(\text{fod})_3$, respectively. Although 20 mg of *D*-Glu and 10 mg of $\text{Eu}(\text{fod})_3$ were able to co-dissolve in 0.6 mL of CDCl_3 , 10 mg of CTA and 10 mg of $\text{Eu}(\text{fod})_3$ were co-dissolved in 0.6 mL of CDCl_3 because of the limited solubility of 20 mg CTA in 0.6 mL of CDCl_3 .

TABLE 2 | Comparison of chemical shifts in the ^1H -NMR spectra in CDCl_3 at room temperature between (a) *D*-Glu without and with $\text{Eu}(\text{fod})_3$ and between (b) CTA without and with $\text{Eu}(\text{fod})_3$, whereas (+)-sign stands for the downfield shift.

	1	2	3	4	5	6	7	8	9
<i>D</i> -Glu	6.31	5.45	5.14	5.09	4.26	4.09	2.17	2.08	2.01
$\text{Eu}(\text{fod})_3$ in <i>D</i> -Glu	7.55	6.53	6.53	6.17	5.93	5.61, 4.99	3.16	2.58	2.44, 2.42
Relative shifts of ^1H -NMR	+1.24	+1.08	+1.39	+1.08	+1.67	+1.52, +0.90	+0.99	+0.50	+0.41, +0.43
CTA	5.05	4.78	4.37	4.04	3.70	3.52	2.10	1.99	1.92
$\text{Eu}(\text{fod})_3$ in CTA	6.38	6.31	5.12	5.05	4.67, 4.49	4.13	2.40	2.31	1.81
Relative shifts of ^1H -NMR	+1.33	+1.53	+0.75	+1.01	+0.93, +0.79	+0.61	+0.30	+0.32	−0.11

TABLE 3 | Lifetimes of photoexcited $\text{Eu}(\text{fod})_3$, $\text{Eu}(\text{dpm})_3$, and $\text{Tb}(\text{dpm})_3$ embedded to CTA and CABu films^a.

Lanthanide complexes	$\text{Eu}(\text{dpm})_3$	$\text{Eu}(\text{dpm})_3$	$\text{Eu}(\text{fod})_3$	$\text{Eu}(\text{fod})_3$	$\text{Tb}(\text{dpm})_3$	$\text{Tb}(\text{dpm})_3$
	CTA	CABu	CTA	CABu	CTA	CABu
Poly(<i>D</i> -saccharide)s						
τ in msec	0.24 ^b	0.29 ^b	0.44 ^b	0.50 ^b	0.59 ^c	0.92 ^c

^aPulsed N_2 laser, 337.1 nm, 10 Hz repetition, Grating 150 lines per mm, slit width 100 μm .^bAt room temperature, detected at 615 nm (collected from 610 to 620 nm), ^cdetected at 546 nm (collected from 542 to 551 nm).

SM). Although, in the absence of *D*-Glu, $\text{Eu}(\text{fod})_3$ has one broad and one shoulder $\nu(\text{C}=\text{O})$ band at 1621 cm^{-1} and 1594 cm^{-1} due to the β -diketonate, in the presence of *D*-Glu, the shoulder $\nu(\text{C}=\text{O})$ may disappear and merge to 1621 cm^{-1} or shift to 1642 cm^{-1} due to specific alteration of β -diketonates. Other frequency shifts such as $\nu(\text{C}-\text{O}-\text{C})$ at $\sim 1200\text{ cm}^{-1}$ and 1150 cm^{-1} of the ester groups and glucose rings of *D*-Glu are not apparent because of significant overlapping with other intense $\nu(\text{C}-\text{F})$ bands. The *C*-*F*/*H*-*C* interactions are not obvious due to the significant overlapping.

Figures S16A–C, SM compare the FT-IR spectra between $\text{Eu}(\text{fod})_3$, CABu, and $\text{Eu}(\text{fod})_3$ with CABu in the ranges of $2,700$ and $3,700\text{ cm}^{-1}$, $2,800$ and $3,100\text{ cm}^{-1}$, and $1,000$ and $2,000\text{ cm}^{-1}$. Similarly, minimal frequency shifts in $\nu(\text{C}-\text{H})$ at $2,850$ – $3,000\text{ cm}^{-1}$ can be seen due to the postulated *C*-*F*/*H*-*C* and *C*-*H*/*O*-*C* interactions (**Figure S16B**, SM). The $\nu^{\text{as}}(\text{C}-\text{H})$ band at $2,973\text{ cm}^{-1}$ and $\nu^{\text{s}}(\text{C}-\text{H})$ at $2,873\text{ cm}^{-1}$ of fod methyl groups in the absence of CABu shift to lower frequencies at $2,967\text{ cm}^{-1}$ by 7 cm^{-1} and conversely higher frequency of $2,878\text{ cm}^{-1}$ by 5 cm^{-1} , respectively (**Figure S16B**, SM). These small shifts may arise from the *C*-*H*/*O*-*C* interactions. On the other hand, a broad $\nu(\text{C}=\text{O})$ band at $\sim 1,630\text{ cm}^{-1}$ characteristic of the β -diketonate split into two $\nu(\text{C}=\text{O})$ bands at $1,643\text{ cm}^{-1}$ and $1,623\text{ cm}^{-1}$, suggesting specific structural alterations of the β -diketonates by the ester groups and/or ethers of CABu. However, no noticeable frequency shifts of $\nu(\text{C}-\text{O}-\text{C})$ at $\sim 1,200\text{ cm}^{-1}$ and $1,150\text{ cm}^{-1}$ of the ester groups of CABu are not seen because of the spectral overlapping with the intense $\nu(\text{C}-\text{F})$ bands (**Figure S16C**, SM).

Photodynamics of $\text{Eu}(\text{fod})_3$, $\text{Eu}(\text{dpm})_3$, and $\text{Tb}(\text{dpm})_3$ in CTA and CABu Films

Lifetimes of $\text{Eu}(\text{fod})_3$, $\text{Eu}(\text{dpm})_3$, and $\text{Tb}(\text{dpm})_3$ species embedded to CTA and CABu films excited at an N_2 pulsed

laser 337.1 nm are summarized in **Table 3** based on decay curves (semilog and linear plots) of these emitters (**Figures S17A–K**, SM). The decay times (τ) of these emitters in CABu are somewhat long by the magnitude of 15–56 % compared to those in CTA. Possibly, these emitters have differently interacted with CTA and CABu, that depends on the nature of alkyl esters. Alternatively, regardless of CTA and CABu, the values of τ belong to in the order of $\text{Eu}(\text{fod})_3$, $\text{Eu}(\text{dpm})_3$, and $\text{Tb}(\text{dpm})_3$, depending on the nature of lanthanides and ligands.

Mulliken Charges of Sc^{III} Tris(β -diketonate) as Models of Eu^{III} / Tb^{III} Tris(β -diketonate), *D*-Glu and *D*-Glu Dimer as a Model of CTA Obtained With MP2 (6-311G) Calculation

To theoretically discuss possible intermolecular interactions, we calculated Mulliken charges (Mulliken, 1955) by the Møller–Plesset second-order perturbation theory (MP2) (Møller and Plesset, 1934; Head-Gordon et al., 1988) (6-311G basis set) method of the model compounds optimized by MM (UFF force field), followed by DFT [6-31G(d)] methods (Frisch et al., 2013). Time-consuming MP2 calculation allows for reliable Mulliken charges compared to DFT calculation. **Figure 9** and **Figure S18**, SM display the numbering for all the atoms in the *D*-Glu and *D*-Glu dimer as a model of CTA. All the peripheral hydrogen atoms of *D*-Glu and *D*-Glu dimer show positive Mulliken charges ranging from $+0.215$ to $+0.261$. The $\text{O}=\text{C}$ atoms of methyl esters have substantial negative Mulliken charges of -0.464 . We observed that the $\text{O}-\text{C}$ atoms of methyl esters and the $\text{C}-\text{O}-\text{C}$ atom in pyranose rings and $\text{C}-\text{O}-\text{C}$ linkage between two pyranose rings show more substantial negative Mulliken charges ranging from -0.652 to -0.690 , respectively. When $\text{C}(\delta^-)-\text{H}(\delta^+)$ bond of the ligands (fod and dpm) feels the force

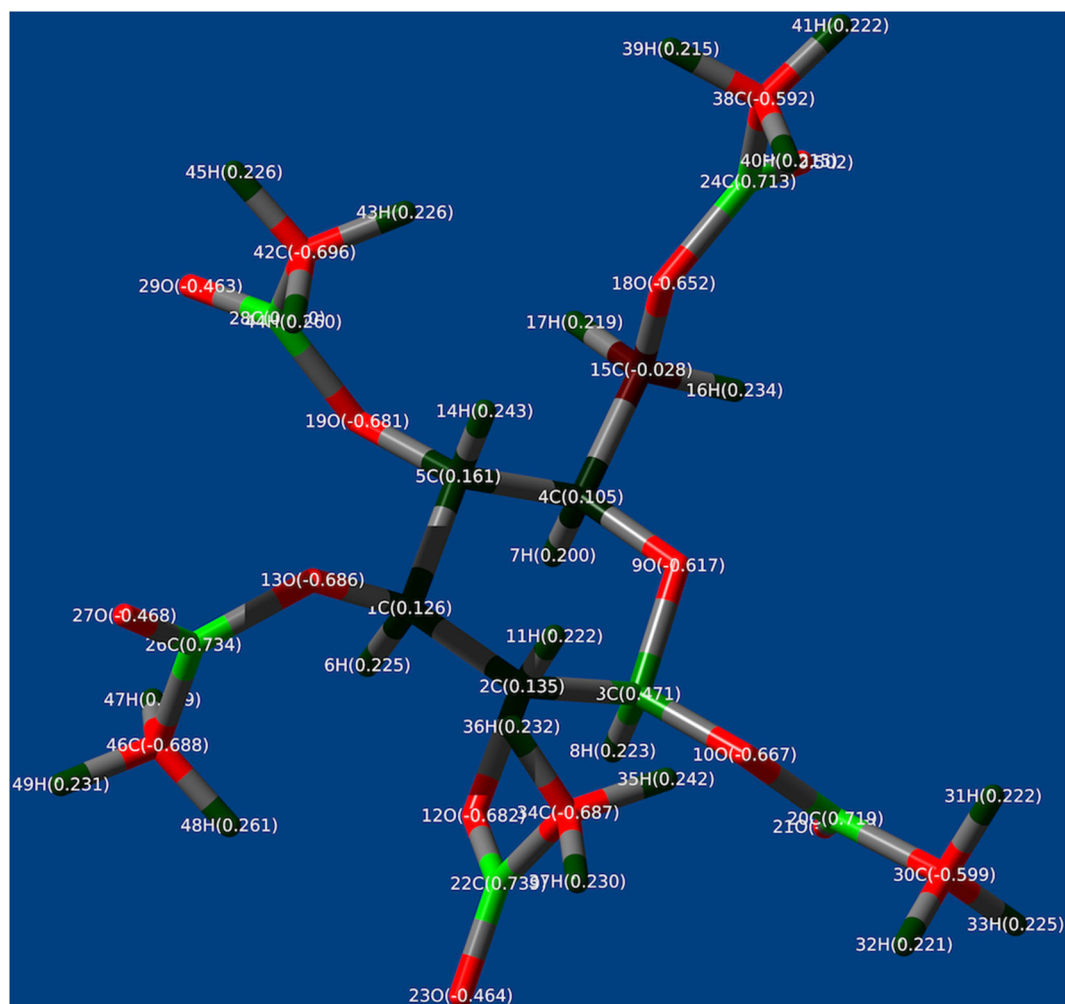


FIGURE 9 | The Mulliken charges of **D-Glu** obtained with MP2 (6-311 G basis set).

of oxygen atoms, the $C(\delta+)-O(\delta-)-C(\delta+)$ and $C(\delta+)-O(\delta-)-C(\delta+)=O(\delta-)$ bonds are more crucial than $O(\delta-)=C(\delta+)$ bond of esters, leading to (ligand, $C-H$)/ O (**D-Glu**, possibly, **CTA**, **CABu**, **Glu**, and **Ara**) interactions.

In the previous paper (Jalilah et al., 2018), we proposed that the surplus charge neutralization obtained with Mulliken charges is a driving force of attractive forces between several ligands in the lanthanide complexes and CPL-inducible chiral substances. The fluorine atoms of $\text{Sc}(\text{fod})_3$ have negative Mulliken charges ranging from -0.341 to -0.373 ; conversely, the hydrogen atoms of $\text{Sc}(\text{fod})_3$ and $\text{Sc}(\text{dpm})_3$ have positive Mulliken charges ranging from $+0.153$ to $+0.193$.

The Mulliken charge neutralization between multiple (δ^-) fluorines of fod and multiple (δ^+) hydrogens of **D-Glu** and the saccharides is possible. Total surplus charge between $C(\delta^+)-F(\delta^-)$ (fod) and $H(\delta^+)-C(\delta^-)$ (saccharides, in this work) is that $3 \times (-0.35) (F_3C) + (4 \sim 5) \times (+0.20 \sim +0.24) (H_3C \text{ or } H_2C) = -0.05 \sim -0.09$. Additionally, the Mulliken charge neutralization between multiple (δ^+) hydrogens of the ligands

(fod and dpm) and multiple (δ^-) oxygen atoms of the saccharides are possible. Total surplus charge between (fod or dpm) $C(\delta^-)-H(\delta^+)$ and $O(\delta^-)-C(\delta^+)$ (saccharides) is that $(4) \times (+0.17) (H-C) + (1) \times (-0.62 \sim -0.69) (O-C \text{ or } O=C=O) = +0.06 \sim -0.01$. Moreover, total surplus charge between (dpm and fod) $C(\delta^-)-H(\delta^+)$ and $C(\delta^-)=C(\delta^+)$ (α -pinene) is that $(1) \times (+0.17) (H-C) + (1) \times (-0.18) (C=C) = -0.01$; $Tb(dpm)_3$ is a dominant factor, while $Eu(dpm)_3$ is unimportant. However, it is reasonably assumed that the same Mulliken charges between multiple (δ^+) hydrogen atoms of ligands (fod and dpm) and multiple (δ^+) hydrogen atoms of the saccharides should cause repulsive interactions.

The Degree of Chirogenesis and the Pfeiffer Effects

Since the serendipitous finding by an anomaly in an optical rotation of chiral substances in the presence of optically inactive labile metal ions in aqueous solutions (Pfeiffer and Quehl, 1931, 1932), the chirogenesis in the GS and ES from

optically inactive labile metal complexes induced by chiral additives has been often appeared in the titles of several papers in the past and currently: e.g., Pfeiffer effect (Kirschner and Ahmad, 1968; Mayer and Brasted, 1973; Schipper, 1978; Brittain, 1982, 1984; Kirschner and Bakkar, 1982; Lunkley et al., 2018); outer-sphere coordination and complexation (Mason and Norman, 1965; Madaras and Brittain, 1980; Kirschner and Bakkar, 1982); second-sphere coordination (Colquhoun et al., 1986). Pfeiffer effect and/or outer-sphere/second-sphere coordination are mainly investigated in their solution states of the metal complexes.

An equilibrium shift from dynamic racemic mixtures ($\Delta:A = 50/50$) of labile metal complexes is responsible for the Pfeiffer effect and chirogenesis by outer-sphere/second-sphere coordination. A barrier height of racemization should be rather small to permit dynamic racemization at ambient temperatures. In 1975, Schipper theoretically discussed chemical discrimination between racemic substances (A' and A'') and chiral substance B surrounded by achiral solvent (Schipper, 1975) as a model of the Pfeiffer effect. In the hypothetical system, an exothermic enthalpic gain Δ_h/T is acquired to compensate an entropic loss Δ_s . The long-range interactions in dynamically dissociate system is needed to overcome thermal fluctuation $k_B T$.

To quantitatively discuss the degree of chirogenesis in six-coordinate labile lanthanide tris(β -diketonate) led by chiral additives in solution, we compare four solution PL spectra of $\text{Eu}(\text{fod})_3$ itself (10 mg, 0.8×10^{-2} M, red line) and in the presence of **D-Glu** (20 mg, 4×10^{-2} M, blue line), **L-Glu** (20 mg, 4×10^{-2} M, green line), and **CTA** (10 mg, 3×10^{-2} M, black line) in 1.2 mL of CDCl_3 (Figure S19, SM). These CDCl_3 solutions were used prior to measurements of ^{19}F - and ^1H -NMR spectra (Figure 7). Among $^5\text{D}_0$ - $^5\text{F}_J$ ($J = 0, 1, 2, 3, 4$) transitions, $^5\text{D}_0$ - $^5\text{F}_1$ transition at 594 nm is known to be susceptible to alterations in molecular symmetry and geometry coordinated with external ligands. Our previous investigation suggests that $\text{Eu}(\text{fod})_3$ is likely to adopt a facial C_3 -symmetrical structure and exists as a mixture of labile Δ - and Λ -isomers in solutions (Jalilah et al., 2018). Similar Pfeiffer effect was reported for D_3 -symmetrical labile $\text{TbIII}(\text{dpa})_3$ in the absence and presence of *L*-histidine, revealing no significant alteration in PL and CPL spectral profiles at 7F_5 - 5D_4 transition (Wu et al., 1989).

From Figure S19A in SM, we can see minimal alterations in magnitudes, wavelengths, and profiles in PL bands of $\text{Eu}(\text{fod})_3$ (non-chiral additive (red line), **D-Glu** (blue line), **L-Glu** (green line), and **CTA** (black line) at the five $^5\text{D}_0$ - $^5\text{F}_J$ ($J = 0, 1, 2, 3, 4$) transitions. Any apparent change in PL wavelength (593.0 nm) of $\text{Eu}(\text{fod})_3$ (non-chiral additive, **D-Glu**, **L-Glu**) is not detectable, while subtle changes in wavelength and magnitude in PL spectra of $\text{Eu}(\text{fod})_3$ (non-chiral (593.0 nm) and **CTA** (592.0 nm)) is discernable. Clearly, PL intensity at $^5\text{D}_0$ - $^5\text{F}_0$ transition (580 nm) of non-chiral additive $\text{Eu}(\text{fod})_3$ increases in the presence of chiral additive in the order of **L-Glu** < **D-Glu** < **CTA**. Similar alterations in subtle increases and subtle spectral shifts at $^5\text{D}_0$ - $^5\text{F}_J$ ($J = 2, 3, 4$) transitions between $\text{Eu}(\text{fod})_3$ (non-chiral additive, **D-Glu**, **L-Glu**, and **CTA**) is observable (Figures S19C-E, SM). We thus conclude that C_3 -symmetrical $\text{Eu}(\text{fod})_3$ in CDCl_3 (0.8

$\times 10^{-2}$ M) maintains in the presence of **L-Glu**, **D-Glu**, **CTA** (3 – 4×10^{-2} M, 4–5-folds excess relative to $\text{Eu}(\text{fod})_3$).

To confirm the dynamic equilibrium shift of the Δ - Λ isomers, we compare CPL and PL spectra of (a) $\text{Eu}(\text{fod})_3$ (0.8×10^{-2} M, 10 mg) and **CTA** (3×10^{-2} M, 20 mg) in 1.2 mL of CDCl_3 (red line) and (b) thin solid films of $\text{Eu}(\text{fod})_3$ (10 mg, $\sim 5 \times 10^{-1}$ M) in **CTA** (20 mg) annealed at 100 °C in a vacuum overnight (blue line).

Previously, a simple thermodynamic analysis confirmed that the binding constant K_b using g_{lum} value at $^5\text{D}_0$ - $^5\text{F}_1$ transition between $\text{Eu}(\text{fod})_3$ and rigid chiral hydrocarbon, α -pinene, was on the order of 10^{-3} M^{-1} ; $0.7 \times 10^{-3} \text{ M}^{-1}$ for (1S)- α -pinene and $1.0 \times 10^{-3} \text{ M}^{-1}$ for (1R)- α -pinene (Jalilah et al., 2018). When a solvent quantity of α -pinene was used, even minimal K_b value was characterized as g_{lum} by CPL spectroscopy.

When a similar analysis was applied to $\text{Eu}(\text{fod})_3$ and non-rigid chiral **CTA**, we obtained $K_b = 0.09 \text{ M}^{-1}$ (Figures S21A,B, SM). This K_b value is more significant than that of α -pinene by two orders of magnitude and it is reasonable because a chiral repeating unit in **CTA** (though non-rigid and floppy) contains five oxygen atoms with the substantial (–)-Mulliken charges responsible for multiple pseudo chiral O/H–C interactions with achiral ligands (Figure 9 and Figure S18, SM). When solidified film and high concentrations of **CTA** were employed as chirality inducible scaffolds and platforms, the degree of chirogenesis was characterizable as g_{lum} values from CPL spectral characteristics. This idea can be extended to **CABu** and other four monosaccharide alkyl esters (Table 1).

CONCLUSION

Two polysaccharide alkyl esters (**CTA** and **CABu**) as the films, two enantiopairs of monosaccharide permethyl esters (**D-/L-Glu** and **D-/L-Ara**) as the films, and (1S)-/(1R)- α -pinene in solution were capable of transferring their chirality to several optically inactive Eu^{III} and Tb^{III} tris(β -diketonate) (= fod and dpm), which impart the shining CPL characteristics at $4f$ - $4f$ transitions. The greatest g_{lum} values at $^5\text{D}_0 \rightarrow ^7\text{F}_1$ transitions ($\lambda_{\text{ex}} = 315 \text{ nm}$) of $\text{Eu}(\text{fod})_3$ in **CABu** and **CTA** films are +0.067 and +0.046, respectively. $\text{Tb}(\text{fod})_3$ in **CABu** and **CTA** exhibited moderately large g_{lum} values of +0.008 and +0.004 at $^5\text{D}_4 \rightarrow ^7\text{F}_5$ transitions ($\lambda_{\text{ex}} = 315 \text{ nm}$), respectively. Meanwhile, **D-/L-Glu** and **D-/L-Ara** films induced weaker g_{lum} values for $\text{Eu}(\text{fod})_3$, $\text{Tb}(\text{fod})_3$, and $\text{Tb}(\text{dpm})_3$. **CTA** and **CABu** induced CPL signals more efficiently for $\text{Eu}(\text{fod})_3$ than **D-/L-Glu** and **D-/L-Ara**. Noticeably, the chirality of α -pinene enabled $\text{Tb}(\text{dpm})_3$ to shine similar CPL characteristics of $\text{Tb}(\text{fod})_3$ in **CABu**. However, $\text{Eu}(\text{dpm})_3$ in **CABu** films and α -pinene did not reveal CPL. From the analyses of solution ^1H -/ ^{19}F -NMR, solid-state ^{13}C -NMR with the help of MP2 (6–311G basis set) calculation, we propose that the surplus charge neutralization evaluated by the opposite Mulliken charges between $H(\delta+)$ - $C(\delta-)$ bonds of the poly- and monosaccharides and $F(\delta-)$ - $C(\delta+)$ bonds of the fluorinated ligands are the attractive driving forces to induce the CPL characteristics of $\text{Tb}(\text{fod})_3$ and $\text{Eu}(\text{fod})_3$. The present knowledge should enable the

fabrication of films, sheets, fibers, and nanocomposites that emit Eu^{III} -origin red-color and Tb^{III} -origin green-color CPL spectra with narrow spectral bandwidths. As demonstrated, $\text{Eu}^{\text{III}}(\text{fod})_3$ and $\text{Tb}^{\text{III}}(\text{dpm})_3$ containing transparent CTA films deposited on the Tempax substrate displayed clear Eu^{III} -origin red-color and Tb^{III} -origin green-color emissions upon 365-nm excitation (see, photographs in **Figure S22**, SM). These materials were obtainable by a chiral ligand-free process at room temperature by co-mixing soluble polysaccharide derivatives (and bacterial cellulose) and several optically inactive $\text{Eu}^{\text{III}}/\text{Tb}^{\text{III}}$ complexes. The challenging issue remains to boost the rather small g_{lum} values [$\text{Eu}(\text{fod})_3$: 6×10^{-2} at 593 nm and $\text{Tb}(\text{fod})_3$: 0.8×10^{-2} at 540 nm] toward an ultimate $g_{\text{lum}} = \pm 2.0$, i.e., obtaining purely left- or right-CPL forms (Eliel and Wilen, 1994). Symmetry-oriented designing of emitters should be considered by precisely controlling topological shape associated with an efficient lens and an optofluidic effect (Wang et al., 2007; Di Pietro and Di Bari, 2012; Kruk et al., 2014; Khorasaninejad et al., 2016; Yeung et al., 2017; Tanaka et al., 2018; Zhou et al., 2019). A deeper understanding of the Pfeiffer effect in the GS and ES, magnetic dipole transitions of Eu^{III} and Tb^{III} complexes, colloidal aggregations, hybridization by other chromophores/luminophores, chain-like polymers, supramolecular motifs and polymers, and nature of oligo- and polysaccharides with conformational freedom are the next challenges (Wormald et al., 2002; Zou et al., 2019) in addition to several approaches to elaborate CPL and CD functions as polymeric colloids, revealing moderately high $|g_{\text{lum}}|$ and $|g_{\text{abs}}|$ values ($>10^{-2}$ – 10^{-1}) in the range of 300 and 800 nm (Nakano and Fujiki, 2011; Duong and Fujiki, 2017; Fujiki and Yoshimoto, 2017; Wang et al., 2017).

However, our approaches of chirogenesis from optically inactive labile Ln^{III} tris(β -diketonate) (Ln : lanthanide) induced by soluble chiral biomaterials is very limited to common organic solvents of Ln^{III} complexes and biomaterials. If water-soluble optically inactive labile Ln^{III} complexes are designed in the future, our approaches are applicable as a thin film state to sense and detect various water-soluble chiral substances including biomaterials, drug, medicine, pesticide, and virus consisting of illness-causing single-strand (ss)/double-strand (ds) RNA.

DATA AVAILABILITY STATEMENT

The raw data supporting the conclusions of this article will be made available by the authors, without undue reservation. Requests for the original CPL/CPL/CD/UV-visible/NMR/IR spectral and photodynamic data sets, followed by the processed data (#.qpc with #.qda and #.txt) using KaleidaGraph (mac, ver 4.53), and the calculation results (#.com, #.log, and #.chk up to 20 GB) of Gaussian09 (mac) to support the conclusion of this article should be sent to MF (fujikim@ms.naist.jp).

AUTHOR CONTRIBUTIONS

All the authors co-designed this work. MF, LW, and AJ co-wrote the paper. LW, NO, AJ, and MF co-measured and co-analyzed

the CPL, CPLE, CD, UV-visible, PL, and PLE spectra of $\text{Tb}(\text{fod})_3$, $\text{Eu}(\text{fod})_3$, $\text{Tb}(\text{dpm})_3$, and $\text{Eu}(\text{dpm})_3$ and other several lanthanide complexes in the presence of chiral additives and chiral solvents. LW and FA co-acquired and co-analyzed ss- $^{13}\text{C}\{^1\text{H}\}$ -FT-NMR and solution ^1H -NMR/ ^{19}F -NMR spectra. FA conducted the elemental analysis of the products. MF performed MP2 and DFT calculations. LW, NO, AJ, AO, SO, HK, and MF contributed to a joint project of emerging CPL spectra from achiral organic, polymeric, and lanthanide luminophores endowed with chiral polymers and chiral solvents. All authors discussed the data and commented on the manuscript. All authors have given approval to the final version of the manuscript. These authors contributed equally. The manuscript was written through contributions of all authors.

FUNDING

MF thanks for the funding from Japan Society for the Promotion of Science (KAKENHI, 16H04155). AJ would like to acknowledge the support from the Fundamental Research Grant Scheme (FRGS) under a grant number of RACER/1/2019/TK05/UNIMAP//1 from the Ministry of Higher Education Malaysia.

ACKNOWLEDGMENTS

MF and AJ owe a debt of gratitude to Prof. Victor Borovcov (South-Central University for Nationalities, Wuhan, China) for giving us the opportunity to contribute to this special issue. LW and MF acknowledge Prof. Wei Zhang (Soochow University, China) for providing **D-Glu**. We thank Dr. Sibio Guo for assisting the chiroptical measurements. We thank Yoshiko Nishikawa for measuring and analyzing mass spectral data sets of **D-/L-Glu**, **D-/L-Ara**, $\text{Tb}(\text{fod})_3$, $\text{Eu}(\text{fod})_3$, $\text{Tb}(\text{dpm})_3$, and $\text{Eu}(\text{dpm})_3$, Yasuo Okajima for measuring photodynamics of $\text{Eu}(\text{fod})_3$, $\text{Eu}(\text{dpm})_3$, and $\text{Tb}(\text{dpm})_3$ embedded to CTA and CABu specimens, and Prof. Tsuyoshi Ando for the permission to use Perkin Elmer FT-IR spectrometer.

SUPPLEMENTARY MATERIAL

The Supplementary Material for this article can be found online at: <https://www.frontiersin.org/articles/10.3389/fchem.2020.00685/full#supplementary-material> Characterization (^1H -/ ^{19}F -NMR, CP-MAS- ^{13}C -FT-NMR, FT-IR, HR-ESI-MS spectra) of CTA, CABu, **D-/L-Glu**, **D-/L-Ara**, $\text{Eu}(\text{fod})_3$, $\text{Tb}(\text{dpm})_3$, and $\text{Eu}(\text{dpm})_3$. Detailed measurement and analytical conditions of all instruments (solution ^1H -/ ^{19}F -FT-NMR, solid-state CP-MAS- ^{13}C -FT-NMR). CPL/PL spectra of $\text{Eu}(\text{dpm})_3$ in CABu and $\text{Eu}(\text{dpm})_3$ in (S)-/(R)- α -pinene. Mulliken charges of **D-Glu dimer** obtained with MP2 (6-311 G basis set) calculation. Photodynamic decay curves of $\text{Eu}(\text{dpm})_3$ in CTA, $\text{Eu}(\text{dpm})_3$ in CABu, $\text{Eu}(\text{fod})_3$ in CTA, $\text{Eu}(\text{fod})_3$ in CABu, $\text{Tb}(\text{dpm})_3$ in CTA, and $\text{Tb}(\text{dpm})_3$ in CABu, raw CD and UV-visible spectra of $\text{Eu}(\text{fod})_3$, $\text{Tb}(\text{fod})_3$, and $\text{Tb}(\text{fod})_3$ in CTA and CABu films and $\text{Eu}(\text{fod})_3$ in **D-/L-Glu** and **D-/L-Glu** films.

REFERENCES

- Aida, T., Meijer, E. W., and Stupp, S. I. (2012). Functional supramolecular polymers. *Science* 335, 813–817. doi: 10.1126/science.1205962
- Akagi, K. (2019). Interdisciplinary chemistry based on integration of liquid crystals and conjugated polymers: development and progress. *Bull. Chem. Soc. Jpn.* 92, 1509–1655. doi: 10.1246/bcsj.20190092
- Bing, Y., Selassie, D., Paradise, R. H., Isborn, C., Kramer, N., Sadilek, M., et al. (2010). Circular dichroism tensor of a triarylmethyl propeller in sodium chlorate crystals. *J. Am. Chem. Soc.* 132, 7454–7465. doi: 10.1021/ja1018892
- Binnemans, K. (2015). Interpretation of europium(III) spectra. *Coord. Chem. Rev.* 295, 1–45. doi: 10.1016/j.ccr.2015.02.015
- Borovkov, V. (2014). Supramolecular chirality in porphyrin chemistry. *Symmetry* 6, 256–294. doi: 10.3390/sym6020256
- Borovkov, V. V., Hembury, G. A., and Inoue, Y. (2004). Origin, control, and application of supramolecular chirogenesis in bisporphyrin-based systems. *Acc. Chem. Res.* 37, 449–459. doi: 10.1021/ar0302437
- Bosnich, B. J. (1967). Asymmetric syntheses, asymmetric transformations, and asymmetric inductions in an optically active solvent. *J. Am. Chem. Soc.* 89, 6143–6148. doi: 10.1021/ja01000a025
- Brittain, H. G. (1980). Correlation of circularly polarized luminescence induced in Tb(dpm)₃ by chiral solvents with the absolute configuration of those solvents. *J. Am. Chem. Soc.* 102, 1207–1208. doi: 10.1021/ja00523a071
- Brittain, H. G. (1981). Optical activity induced in Terbium(III) Tris(Pyridine-2,6-Dicarboxylate) through association with certain chiral amino acids. *Inorg. Chem.* 20, 3007–3013. doi: 10.1021/ic50223a050
- Brittain, H. G. (1982). Studies of the pfeiffer effect developed in tris(pyridine-2,6-dicarboxylato)terbate(III) by phenylalkylamines, phenylalkylamino alcohols, and phenylalkylamino acids. *Inorg. Chem.* 21, 2955–2960. doi: 10.1021/ic00138a009
- Brittain, H. G. (1983). Chiral lanthanide complexes. *Coord. Chem. Rev.* 48, 243–276. doi: 10.1016/0010-8545(83)80004-6
- Brittain, H. G. (1984). Studies of the pfeiffer effect induced in tris(Pyridine-2,6-Dicarboxylato) terbate(III) by monosaccharide aldose sugars. *J. Chem. Soc. Dalton Trans.* 7, 1367–1370. doi: 10.1039/dt9840001367
- Brittain, H. G. (1989). Circularly polarized luminescence studies of chiral lanthanide complexes. *J. Coord. Chem.* 20, 331–347. doi: 10.1080/00958978909408175
- Brittain, H. G., and Richardson, F. S. (1977a). Circularly polarized emission studies on chiral and achiral europium(III) β -diketonate complexes in an optically active solvent. *J. Am. Chem. Soc.* 99, 65–70. doi: 10.1021/ja00443a014
- Brittain, H. G., and Richardson, F. S. (1977b). Circularly polarized emission studies on Tb³⁺ and Eu³⁺ complexes with potentially terdentate amino acids in aqueous solution. *Bioinorg. Chem.* 7, 233–243. doi: 10.1016/S0006-3061(00)80097-6
- Bünzli, J.-C. (2010). Lanthanide luminescence for biomedical analyses and imaging. *Chem. Rev.* 110, 2729–2755. doi: 10.1021/cr900362e
- Carr, R., Evans, N. H., and Parker, D. (2012). Lanthanide complexes as chiral probes exploiting circularly polarized luminescence. *Chem. Soc. Rev.* 41, 7673–7686. doi: 10.1039/c2cs35242g
- Colquhoun, H. M., Stoddart, J. F., and Williams, D. J. (1986). Second-sphere coordination: a novel role for molecular receptors. *Angew. Chem. Int. Ed. Engl.* 25, 487–507. doi: 10.1002/anie.198604873
- Coulate, T. (2016). *Food-The Chemistry of its Components*. 6th Edn. Cambridge: RSC.
- De La Cruz, J. A., Liu, Q., Senyuk, B., Frazier, A. W., Peddireddy, K., and Smalyukh, I. I. (2018). Cellulose-based reflective liquid crystal films as optical filters and solar gain regulators. *ACS Photon.* 5, 2468–2477. doi: 10.1021/acsp Photonics.8b00289
- de Queiroz, T. B., Botelho, M. B. S., Gonçalves, T. S., Dousti, M. R., and de Camargo, A. S. S. (2015). New fluorophosphate glasses co-doped with Eu³⁺ and Tb³⁺ as candidates for generating tunable visible light. *J. Alloys Compd.* 647, 315–321. doi: 10.1016/j.jallcom.2015.06.066
- Desiraju, G. R., and Steiner, T. (1999). *The Weak Hydrogen Bond: In Structural Chemistry and Biology*. Oxford: Oxford University Press.
- Di Bari, L., and Salvadori, P. (2005). Solution structure of chiral lanthanide complexes. *Coord. Chem. Rev.* 249, 2854–2879. doi: 10.1016/j.ccr.2005.03.006
- Di Pietro, S., and Di Bari, L. (2012). The structure of MLn(hfbc)₄ and a key to high circularly polarized luminescence. *Inorg. Chem.* 51, 12007–12014. doi: 10.1021/ic3018979
- Duan, P., Cao, H., Zhang, L., and Liu, M. (2014). Gelation induced supramolecular chirality: chirality transfer, amplification and application. *Soft Matter* 10, 5428–5448. doi: 10.1039/C4SM00507D
- Dubois, J. C., Barny, P. L., Mauzac, M., and Noel, C. (1998). *Handbook of Liquid Crystals, Fundamentals High Regular Weight Liquid Crystal*, Vol. 3. eds D. Demus, J. W. Goodby, G. W. Gray, H. S. Spiess, and V. Vill (New York, NY: Wiley-VCH), 207–269.
- Duong, S. T., and Fujiki, M. (2017). The origin of bisignate circularly polarized luminescence (CPL) spectra from chiral polymer aggregates and molecular camphor: anti-kasha's rule revealed by CPL excitation (CPLE) spectra. *Polym. Chem.* 8, 4673–4679. doi: 10.1039/C7PY00958E
- Eliel, E. L., and Wilen, S. H. (1994). "Chiroptical properties", in *Stereochemistry of Organic Compounds*, eds E. L. Eliel, S. H. Wilen, and L. N. Mander (New York, NY: Wiley-Interscience), 991–1118.
- Frisch, M. J., Trucks, G. W., Schlegel, H. B., Scuseria, G. E., Robb, M. A., Cheeseman, J. R., et al. (2013). *Gaussian 09, Rev. D.01*. Wallingford, CT: Gaussian, Inc.
- Fujiki, M. (2014). Supramolecular chirality: solvent chirality transfer in molecular chemistry and polymer chemistry. *Symmetry* 6, 677–703. doi: 10.3390/sym6030677
- Fujiki, M., and Yoshimoto, S. (2017). Time-evolved, far-red, circularly polarised luminescent polymer aggregates endowed with sacrificial helical Si-Si bond polymers. *Mater. Chem. Front.* 1, 1773–1785. doi: 10.1039/C7QM00096K
- Fulgêncio, F., de Oliveira, F. C., Windmöller, D., Brito, H. F., Malta, O. L., de Sá, G. F., et al. (2012). Evidence of the participation of electronic excited states in the mechanism of positronium formation in substitutional Tb_{1-x}Eu_x(dpm)₃ solid solutions studied by optical and positron annihilation spectroscopies. *Phys. Chem. Chem. Phys.* 14, 9996–10007. doi: 10.1039/c2cp40664k
- George, S. J., Tomovic, Z., Schenning, A. P. H. J., and Meijer, E. W. (2011). Insight into the chiral induction in supramolecular stacks through preferential chiral solvation. *Chem. Commun.* 47, 3451–3453. doi: 10.1039/c0cc04617e
- Glover-Fischer, D. P., Metcalf, D. H., Hopkins, T. A., Pugh, V. J., Chisdes, S. J., Kankare, J., et al. (1998). Excited-state enantiomer interconversion kinetics probed by time-resolved chiroptical luminescence spectroscopy. the solvent and temperature dependence of Δ -Eu(dpa)₃³⁻ \rightleftharpoons Λ -Eu(dpa)₃³⁻ enantiomer interconversion rates in solution. *Inorg. Chem.* 37, 3026–3033. doi: 10.1021/ic9713700
- Goto, T., Okazaki, Y., Ueki, M., Kuwahara, Y., Takafuji, M., Oda, R., et al. (2017). Induction of strong and tunable circularly polarized luminescence of nonchiral, nonmetal, low-molecular-weight fluorophores using chiral nanotemplates. *Angew. Chem. Int. Ed.* 56, 2989–2993. doi: 10.1002/anie.201612331
- Green, M. M., Khatri, C., and Peterson, N. C. (1993). A macromolecular conformational change driven by a minute chiral solvation energy. *J. Am. Chem. Soc.* 115, 4941–4942. doi: 10.1021/ja00064a086
- Guo, G., Suzuki, N., and Fujiki, M. (2017). Oligo- and polyfluorenes meet cellulose alkyl esters: retention, inversion, and racemization of circularly polarized luminescence (CPL) and circular dichroism (CD) via intermolecular C-H/O=C interactions. *Macromolecules* 50, 1778–1789. doi: 10.1021/acs.macromol.6b02762
- Guo, S., Kamite, H., Suzuki, N., Wang, L., Ohkubo, A., and Fujiki, M. (2018). Ambidextrous chirality transfer capability from cellulose tris(phenylcarbamate) to nonhelical chainlike luminophores: achiral solvent-driven helix-helix transition of oligo- and polyfluorenes revealed by sign inversion of circularly polarized luminescence and circular dichroism spectra. *Biomacromolecules* 19, 449–459. doi: 10.1021/acs.biomac.7b01554
- Hayward, L. D., and Totty, R. N. (1969). Induced optical rotation and circular dichroism of symmetric and racemic aliphatic carbonyl compounds. *J. Chem. Soc. D. Chem. Commun.* 676–677. doi: 10.1039/c29690000676
- Head-Gordon, M., Pople, J. A., and Frisch, M. J. (1988). MP2 energy evaluation by direct methods. *Chem. Phys. Lett.* 153, 503–506. doi: 10.1016/0009-2614(88)85250-3

- Hembury, G. A., Borovkov, V. V., and Inoue, Y. (2008). Chirality-sensing supramolecular systems. *Chem. Rev.* 108, 1–73. doi: 10.1021/cr050005k
- Henriksson, M., Henriksson, G., Berglund, L. A., and Lindström, T. (2007). An environmentally friendly method for enzyme-assisted preparation of microfibrillated cellulose (MFC) nanofibers. *Eur. Polym. J.* 43, 3434–3441. doi: 10.1016/j.eurpolymj.2007.05.038
- Huang, X., Rickman, B. H., Borhan, B., Berova, N., and Nakanishi, K. (1998). Zinc porphyrin tweezer in host–guest complexation: determination of absolute configurations of diamines, amino acids, and amino alcohols by circular dichroism. *J. Am. Chem. Soc.* 120, 6185–6186. doi: 10.1021/ja973539e
- Huskowska, E., and Riehl, J. P. (1995). Perturbation of the racemic equilibrium between d_3 lanthanide complexes through the addition of sugars. *Inorg. Chem.* 34, 5615–5621. doi: 10.1021/ic00126a035
- Ikai, T., and Okamoto, Y. (2009). Structure control of polysaccharide derivatives for efficient separation of enantiomers by chromatography. *Chem. Rev.* 109, 6077–6101. doi: 10.1021/cr8005558
- Isare, B., Linares, M., Zargarian, L., Fermandjian, S., Miura, M., Motohashi, S., et al. (2010). Chirality in dynamic supramolecular nanotubes induced by a chiral solvent. *Chem. Eur. J.* 16, 173–177. doi: 10.1002/chem.200902399
- Iwamura, M., Kimura, Y., Miyamoto, R., and Nozaki, K. (2012). Chiral sensing using an achiral europium(III) complex by induced circularly polarized luminescence. *Inorg. Chem.* 51, 4094–4098. doi: 10.1021/ic202355s
- Iwamura, M., Uchida, T.-A., and Nozaki, K. (2016). Chiral sensing of various amino acids using induced circularly polarized luminescence from europium(III) complexes of phenanthroline dicarboxylic acid derivatives. *Chem. Asian J.* 11, 2415–2422. doi: 10.1002/asia.201600798
- Iwatake, A., Nogi, M., and Yano, H. (2008). Cellulose nanofiber-reinforced polylactic acid. *Compos. Sci. Technol.* 68, 2103–2106. doi: 10.1016/j.compscitech.2008.03.006
- Jacoby, M. (2008). Recognizing a pioneer. *Chem. Eng. News* 86, 38–41. doi: 10.1021/cen-v086n033.p038
- Jalilah, A. J., Asanoma, F., and Fujiki, M. (2018). Unveiling controlled breaking of the mirror symmetry of $\text{Eu}(\text{Fod})_3$ with α - β -pinene and BINAP by circularly polarized luminescence (CPL), CPL excitation, and ^{19}F - $^{31}\text{P}\{^1\text{H}\}$ -NMR spectra and Mulliken charges. *Inorg. Chem. Front.* 5, 2718–2733. doi: 10.1039/C8QI00509E
- Jiang, S., Zhao, Y., Wang, L., Yin, L., Zhang, Z., Zhu, J., et al. (2015). Photocontrollable induction of supramolecular chirality in achiral side chain azo-containing polymers through preferential chiral solvation. *Polym. Chem.* 6, 4230–4239. doi: 10.1039/C5PY00496A
- Kahr, B., and Gurney, R. W. (2001). Dyeing crystals. *Chem. Rev.* 101, 893–951. doi: 10.1021/cr980088n
- Kawagoe, Y., Fujiki, M., and Nakano, Y. (2010). Limonene magic: noncovalent molecular chirality transfer leading to ambidextrous circularly polarized luminescent π -conjugated polymers. *New J. Chem.* 34, 637–647. doi: 10.1039/b9nj00733d
- Khorasaninejad, M., Chen, W. T., Zhu, A. Y., Oh, J., Devlin, R. C., Rousso, D., et al. (2016). Multispectral chiral imaging with a metalens. *Nano Lett.* 16, 4595–4600. doi: 10.1021/acs.nanolett.6b01897
- Kim, S. Y., Saxena, A., Kwak, G., Fujiki, M., and Kawakami, Y. (2004). Cooperative C–F...Si interaction in optically active helical polysilanes. *Chem. Commun.* 2004, 538–539. doi: 10.1039/b314723a
- Kipping, F. S., and Pope, W. J. (1898). LXIII.—enantiomorphism. *J. Chem. Soc., Trans.* 73, 606–617. doi: 10.1039/CT8987300606
- Kirschner, S., and Ahmad, M. (1968). The Application of the Pfeiffer effect to the resolution of dissymmetric coordination compounds. *J. Am. Chem. Soc.* 90, 1910–1911. doi: 10.1021/ja01009a047
- Kirschner, S., and Bakkar, I. (1982). Utilization of the Pfeiffer effect and outer-sphere complexation for the prediction of absolute configurations of optically active metal complexes. *Coord. Chem. Rev.* 43, 325–335. doi: 10.1016/S0010-8545(00)82103-7
- Klemm, D., Heublein, B., Fink, H.-P., and Bohn, A. (2005). Cellulose: fascinating biopolymer and sustainable raw material. *Angew. Chem. Int. Ed.* 44, 3358–3393. doi: 10.1002/anie.200460587
- Kobayashi, K., Asakawa, Y., Kikuchi, Y., Toi, H., and Aoyama, Y. (1993). CH- π interaction as an important driving force of host-guest complexation in apolar organic media. binding of monools and acetylated compounds to resorcinol cyclic tetramer as studied by ^1H NMR and circular dichroism spectroscopy. *J. Am. Chem. Soc.* 115, 2648–2654. doi: 10.1021/ja00060a013
- Koiso, N., Kitagawa, Y., Nakanishi, T., Fushimi, K., and Hasegawa, Y. (2017). Eu(III) Chiral coordination polymer with a structural transformation system. *Inorg. Chem.* 56, 5741–5747. doi: 10.1021/acs.inorgchem.7b00337
- Kono, Y., Nakabayashi, K., Kitamura, S., Shizuma, M., Fujiki, M., and Imai, Y. (2016). Can chiral P(III) coordinate Eu(III)? unexpected solvent dependent circularly polarized luminescence of BINAP and Eu(III)(hfa) $_3$ in chloroform and acetone. *RSC Adv.* 6, 40219–40224. doi: 10.1039/C6RA05856F
- Kruk, S. S., Decker, M., Staude, I., Schlecht, S., Greppmair, M., Neshev, D. N., et al. (2014). Spin-polarized photon emission by resonant multipolar nanoantennas. *ACS Photonics* 1, 1218–1223. doi: 10.1021/ph500288u
- Kumar, J., Nakashima, T., and Kawai, T. (2015). Circularly polarized luminescence in chiral molecules and supramolecular assemblies. *J. Phys. Chem. Lett.* 6, 3445–3452. doi: 10.1021/acs.jpclett.5b01452
- Lee, D., Jin, Y.-J., Suzuki, N., Fujiki, M., Sakaguchi, T., Kim, S., et al. (2012). Solvent-to-polymer chirality transfer in intramolecular stack structure. *Macromolecules* 45, 5379–5386. doi: 10.1021/ma300976r
- Leonzio, M., Melchior, A., Faura, G., Tolazzi, M., Zinna, F., Di Bari, L., et al. (2017). Strongly circularly polarized emission from water-soluble Eu(III)- and Tb(III)-based complexes: a structural and spectroscopic study. *J. Am. Chem. Soc.* 139, 4413–4421. doi: 10.1021/acs.inorgchem.7b00430
- Liu, M., Zhang, L., and Wang, T. (2015). Supramolecular chirality in self-assembled systems. *Chem. Rev.* 115, 7304–7397. doi: 10.1021/cr500671p
- Longhi, G., Castiglioni, E., Koshoubu, J., Mazzeo, G., and Abbate, S. (2016). Circularly polarized luminescence: a review of experimental and theoretical aspects. *Chirality* 28, 696–707. doi: 10.1002/chir.22647
- Luk, C. K., and Richardson, F. S. (1974). Circularly polarized luminescence of terbium (III) complexes in solution. *Chem. Phys. Lett.* 25, 215–220. doi: 10.1016/0009-2614(74)89121-9
- Lunkley, J. L., Nguyen, N. M., Tuminaro, K. M., Margittai, D., and Muller, G. (2018). The importance of solvent effects on the mechanism of the Pfeiffer effect. *Inorganics* 6, 87. doi: 10.3390/inorganics6030087
- Lunkley, J. L., Shirotani, D., Yamanari, K., Kaizaki, S., and Muller, G. (2008). Extraordinary circularly polarized luminescence activity exhibited by cesium Tetrakis(3-heptafluorobutylryl-+)-camphorato) Eu(III) complexes in EtOH and CHCl_3 solutions. *J. Am. Chem. Soc.* 130, 13814–13815. doi: 10.1021/ja805681w
- Madaras, J. S., and Brittain, H. G. (1980). Induced optical activity in the Tb(III) complex of Pyridine-2,6-Dicarboxylic acid through outer-sphere coordination with L-Ascorbic acid. *Inorg. Chim. Acta* 42, 109–113. doi: 10.1016/S0020-1693(00)88894-5
- Mahadevi, A. S., and Sastry, G. N. (2016). Cooperativity in noncovalent interactions. *Chem. Rev.* 116, 2775–2825. doi: 10.1021/cr500344e
- Mason, S. F. (1982). *Molecular Optical Activity and the Chiral Discrimination*, 353–367, Cambridge: Cambridge University Press, 208–210.
- Mason, S. F., and Norman, B. J. (1965). Outer-sphere co-ordination and optical activity in transition-metal complexes. *Chem. Commun.* 335–336. doi: 10.1039/c19650000335
- Matsuura, H., Yoshida, H., Hieda, M., Yamanaka, S.-Y., Harada, T., Shin-ya, K., et al. (2003). Experimental evidence for intramolecular blue-shifting C–H...O hydrogen bonding by matrix-isolation infrared spectroscopy. *J. Am. Chem. Soc.* 125, 13910–13911. doi: 10.1021/ja030538f
- Mayer, L. A., and Brasted, R. C. (1973). Further evidence on the origins of the Pfeiffer effect using circular dichroism. *J. Coord. Chem.* 3, 85–89. doi: 10.1080/00958977308073791
- Mei, J., Leung, N. L. C., Kwok, R. T. K., Lam, J. W. Y., and Tang, B. Z. (2015). Aggregation-induced emission: together we shine, united we soar! *Chem. Rev.* 115, 11718–11940. doi: 10.1021/acs.chemrev.5b00263
- Mele, A., Tran, C. D., and De Pauli Lacerda, S. H. (2003). The structure of a room-temperature ionic liquid with and without trace amounts of water: the role of C–H...O and C–H...F interactions in 1-n-Butyl-3-methylimidazolium tetrafluoroborate. *Angew. Chem. Int. Ed.* 42, 4364–4366. doi: 10.1002/anie.200351783
- Miyake, H. (2014). Supramolecular chirality in dynamic coordination chemistry. *Symmetry* 6, 880–895. doi: 10.3390/sym6040880

- Miyake, H., Terada, K., and Tsukube, H. (2014). Lanthanide Tris(β -diketonates) as useful probes for chirality determination of biological amino alcohols in vibrational circular dichroism: ligand to ligand chirality transfer in lanthanide coordination sphere. *Chirality* 26, 293–299. doi: 10.1002/chir.22319
- Møller, C., and Plesset, M. S. (1934). Note on an approximation treatment for many-electron systems. *Phys. Rev.* 46, 618–622. doi: 10.1103/PhysRev.46.618
- Muller, G. (2009). Luminescent chiral lanthanide (III) complexes as potential molecular probes. *Dalton Trans.* 9692–9707. doi: 10.1039/b909430j
- Muller, G. (2014). “Circularly polarised luminescence,” in *Luminescence of Lanthanide Ions in Coordination Compounds and Nanomaterials*, ed A. de Bettencourt-Dias (Chichester: Wiley), 77–123. doi: 10.1002/9781118682760.ch03
- Muller, G., and Riehl, J. P. (2005). Use of induced circularly polarized luminescence (CPL) from racemic D_3 lanthanide complexes to determine the absolute configuration of amino acids. *J. Fluor.* 15, 553–558. doi: 10.1007/s10895-005-2828-4
- Mulliken, R. S. (1955). Electronic population analysis on LCAO–MO molecular wave functions. I. *J. Chem. Phys.* 23, 1833–1840. doi: 10.1063/1.1740588
- Murray-Rust, P., Stallings, W. C., Monti, C. T., Preston, R. K., and Glusker, J. P. (1983). Intermolecular interactions of the C–F bond: The crystallographic environment of fluorinated carboxylic acids and related structures. *J. Am. Chem. Soc.* 105, 3206–3214. doi: 10.1021/ja00348a041
- Nakano, Y., and Fujiki, M. (2011). Circularly polarized light enhancement by helical polysilane aggregates suspension in organic optofluid. *Macromolecules* 44, 7511–7519. doi: 10.1021/ma201665n
- Nakano, Y., Ichihara, F., Naito, M., Yang, Y., and Fujiki, M. (2012). Chiroptical generation and inversion during the mirror-symmetry-breaking aggregation of dialkylpolysilanes due to limonene chirality. *Chem. Commun.* 48, 6636–6638. doi: 10.1039/c2cc17845a
- Nakano, Y., Liu, Y., and Fujiki, M. (2010). Ambidextrous circular dichroism and circularly polarised luminescence from Poly(9,9-di-*n*-decylfluorene) by terpene chirality transfer. *Polym. Chem.* 1, 460–469. doi: 10.1039/B9PY00288J
- Nakashima, H., Koe, J. R., Torimitsu, K., and Fujiki, M. (2001). Transfer and amplification of chiral molecular information to polysilylene aggregates. *J. Am. Chem. Soc.* 123, 4847–4848. doi: 10.1021/ja010119n
- Nishio, M., Hirota, M., and Umezawa, Y. (1998). *The CH/ π Interaction. Evidence, Nature, and Consequences*. New York, NY: Wiley-VCH.
- Noack, K. (1969). Induktion von circulardichroismus in einer optisch inaktiven Verbindung durch zwischenmolekulare Wechselwirkung mit einem optisch aktiven Lösungsmittel. *Helv. Chim. Acta* 52, 2501–2507. doi: 10.1002/hlca.19690520833
- Numata, N., and Shinkai, S. (2011). ‘Supramolecular wrapping chemistry’ by helix-forming polysaccharides: a powerful strategy for generating diverse polymeric nano-architectures. *Chem. Commun.* 47, 1961–1975. doi: 10.1039/c0cc03133j
- Onofrei, M. D., Dobos, A. M., and Ioan, S. (2015). In *Polymer Nanocomposites: Fundamentals and Applications* ed V. K. Thakur (Weinheim: Wiley), 355–391.
- Palmans, A. R. A., and Meijer, E. W. (2007). Amplification of chirality in dynamic supramolecular aggregates. *Angew. Chem. Int. Ed.* 46, 8948–8968. doi: 10.1002/anie.200701285
- Pearson, R. G. (1963). Hard and soft acids and bases. *J. Am. Chem. Soc.* 85, 3533–3539. doi: 10.1021/ja00905a001
- Perucca, E. (1919). Nuove osservazioni e misure su cristalli otticamente attivi (NaClO_3). *II Nuovo Cimento*, 18, 112–154. doi: 10.1007/BF02959865
- Petoud, S., Muller, G., Moore, E. G., Xu, J., Sokolnicki, J., Riehl, J. P., et al. (2007). Brilliant Sm, Eu, Tb, and Dy chiral lanthanide complexes with strong circularly polarized luminescence. *J. Am. Chem. Soc.* 129, 77–83. doi: 10.1021/ja064902x
- Pfeiffer, P., and Quehl, K. (1931). Über einen neuen effekt in lösungen optischaktiver substanzen (I. Mitteil). *Chem. Ber.* 64, 2667–2671. doi: 10.1002/cber.19310641015
- Pfeiffer, P., and Quehl, K. (1932). Aktivierung von Komplexsalzen in wässriger Lösung (II. Mitteil). *Chem. Ber.* 65, 560–565. doi: 10.1002/cber.19320650410
- Pitts, C. R., Siegler, M. A., and Lectka, T. (2017). Intermolecular aliphatic C–F...H–C interaction in the presence of “stronger” hydrogen bond acceptors: crystallographic, computational, and IR studies. *J. Org. Chem.* 82, 3996–4000. doi: 10.1021/acs.joc.7b00268
- Prince, R. B., Barnes, S. A., and Moore, J. S. (2000). Foldamer-based molecular recognition. *J. Am. Chem. Soc.* 122, 2758–2762. doi: 10.1021/ja993830p
- Richardson, F. S. (1982). Terbium(III) and europium(III) Ions as luminescent probes and stains for biomolecular systems. *Chem. Rev.* 82, 541–552. doi: 10.1021/cr00051a004
- Riehl, J. P., and Richardson, F. S. (1986). Circularly polarized luminescence spectroscopy. *Chem. Rev.* 86, 1–16. doi: 10.1021/cr00071a001
- Roose, J., Tang, B. Z., and Wong, K. S. (2016). Circularly-polarized luminescence (CPL) from chiral AIE molecules and macrostructures. *Small* 12, 6495–6512. doi: 10.1002/smll.201601455
- Sang, Y., Han, Y. J., Zhao, T., Duan, P. and Liu, M. (2019). Circularly polarized luminescence in nanoassemblies: generation, amplification, and application. *Adv. Mater.* doi: 10.1002/adma.201900110. [Epub ahead of print].
- Schipper, P. E. (1975). On the chemical consequences of long-range interactions in chiral systems. *Aust. J. Chem.* 28, 1161–1168. doi: 10.1071/CH9751161
- Schipper, P. E. (1978). Induced equilibrium shifts in labile racemates. The nature of the discriminatory interactions in the Pfeiffer effect. *J. Am. Chem. Soc.* 100, 1079–1084. doi: 10.1021/ja00472a010
- Soai, K., Kawasaki, T., and Matsumoto, A. (2019). Role of asymmetric autocatalysis in the elucidation of origins of homochirality of organic compounds. *Symmetry* 11:694. doi: 10.3390/sym11050694
- Tanaka, H., Ikenosako, M., Kato, Y., Fujiki, M., Inoue, Y., and Mori, T. (2018). Symmetry-based rational design for boosting chiroptical responses. *Comm. Chem.* 1:38. doi: 10.1038/s42004-018-0035-x
- Taniguchi, A., Hara, N., Shizuma, M., Tajima, N., Fujiki, M., and Imai, Y. (2019). Circularly polarised luminescence from planar-chiral phanephos/Tb(III)(hfa)₃ hybrid luminophores. *Photochem. Photobiol. Sci.* 18, 2859–2864. doi: 10.1039/C9PP00296K
- Tanner, P. A. (2013). Some misconceptions concerning the electronic spectra of tri-positive europium and cerium. *Chem. Soc. Rev.* 42, 5090–5101. doi: 10.1039/c3cs60033e
- Tsukube, H., and Shinoda, S. (2002). Lanthanide complexes in molecular recognition and chirality sensing of biological substrates. *Chem. Rev.* 102, 2389–2403. doi: 10.1021/cr010450p
- Tsuzuki, S., Uchamaru, T., Mikami, M., and Urata, S. (2003). Ab Initio calculations of intermolecular interaction of CHF_3 dimer: origin of attraction and magnitude of CH/F interaction. *J. Phys. Chem. A* 107, 7962–7968. doi: 10.1021/jp035531z
- Wang, L., Suzuki, N., Liu, J., Matsuda, T., Abdul Rahim, N. A., Zhang, W., et al. (2014). Limonene induced chiroptical generation and inversion during aggregation of achiral polyfluorene analogs: structure-dependence and mechanism. *Polym. Chem.* 5, 5920–5920. doi: 10.1039/C4PY00865K
- Wang, L., Yin, L., Zhang, W., Zhu, X., and Fujiki, M. (2017). Circularly polarized light with sense and wavelengths to regulate azobenzene supramolecular chirality in optofluidic medium. *J. Am. Chem. Soc.* 139, 13218–13226. doi: 10.1021/jacs.7b07626
- Wang, Z., Teh, B. H., Wang, Y., Adamo, G., Teng, J., and Sun, H. (2007). Enhancing circular dichroism by super chiral hot spots from a chiral metasurface with apices. *Appl. Phys. Lett.* 110, 221108. doi: 10.1063/1.4984920
- Wilts, B. D., Dumanli, A. G., Middleton, R., Vukusic, P., and Vignolini, S. (2017). Chiral optics of helicoidal cellulose nanocrystal films. *APL Photonics* 2:040801. doi: 10.1063/1.4978387
- Wong, H.-Y., Lo, W.-S., Yim, K.-H., and Law, G.-L. (2019). Chirality and chiroptics of lanthanide molecular and supramolecular assemblies. *Chem* 5, 3058–3095. doi: 10.1016/j.chempr.2019.08.006
- Wormald, M. R., Petrescu, A. J., Pao, J.-L., Glithero, A., Elliott, T., and Dwek, R. (2002). A conformational studies of oligosaccharides and glycopeptides: complementarity of NMR, X-ray crystallography, and molecular modelling. *Chem. Rev.* 102, 371–386. doi: 10.1021/cr990368i
- Wu, S., Hilmes, G. L., and Riehl, J. P. (1989). Nature of chiral-induced equilibrium shifts in racemic labile lanthanide complexes. *J. Phys. Chem.* 93, 2307–2310. doi: 10.1021/j100343a022
- Wu, T., and Bouř, P. (2018). Specific circularly polarized luminescence of Eu(III), Sm(III), and Er(III) induced by *N*-acetylneuraminic acid. *Chem. Commun.* 54, 1790–1792. doi: 10.1039/C7CC09463A
- Wu, T., Bouř, P., and Andrushchenko, V. (2019). Europium (III) as a circularly polarized luminescence probe of DNA structure. *Sci. Rep.* 9:1068. doi: 10.1038/s41598-018-37680-7
- Wu, T., Průša, J., Kessler, J., Dračinský, M., Valenta, J., and Bour, P. (2016). Detection of sugars via chirality induced in europium(III)

- compounds. *Anal. Chem.* 88, 8878–8885. doi: 10.1021/acs.analchem.6b02505
- Xue, X., Cheng, T., Suzuki, T., and Ohishi, Y. (2015). Upconversion emissions from high energy levels of Tb^{3+} under near-infrared laser excitation at 976 nm. *Opt. Mater. Exp.* 5, 2768–2776. doi: 10.1364/OME.5.002768
- Yamada, T., Nomura, K., and Fujiki, M. (2018). Noticeable chiral center dependence of signs and magnitudes in circular dichroism (CD) and circularly polarized luminescence (CPL) spectra of all-trans poly(9,9-dialkylfluorene-2,7-vinylene)s bearing chiral alkyl side chains in solution, aggregates, and in thin films. *Macromolecules* 51, 2377–2387. doi: 10.1021/acs.macromol.8b00241
- Yan, F., Copeland, R. A., and Brittain, H. G. (1982). Optical activity induced in the terbium(III) and europium(III) tris complexes of pyridine-2,6-dicarboxylate through association with monoamino- and diaminocarboxylic acids. *Inorg. Chem.* 21, 1180–1185. doi: 10.1021/ic00133a059
- Yang, X., Lin, X., Zhao, Y., Zhao, Y. S., and Yan, D. (2017). Lanthanide metal-organic framework microrods: colored optical waveguides and chiral polarized emission. *Angew. Chem. Int. Ed.* 56, 7853–7857. doi: 10.1002/anie.201703917
- Yashima, E., Matsushima, T., and Okamoto, Y. (1995). Poly((4-carboxyphenyl)acetylene) as a probe for chirality assignment of amines by circular dichroism. *J. Am. Chem. Soc.* 117, 11596–11597. doi: 10.1021/ja00151a032
- Yeung, C.-T., Yim, K.-H., Wong, H.-Y., Pal, R., Lo, W.-S., Yan, S.-C., et al. (2017). Chiral transcription in self-assembled tetrahedral Eu_4L_6 chiral cages displaying sizable circularly polarized luminescence. *Nat. Commun.* 8:1128. doi: 10.1038/s41467-017-01025-1
- Yu, H., Pan, K., and Deng, J. (2018). Cellulose concurrently induces predominantly one-handed helicity in helical polymers and controls the shape of optically active particles thereof. *Macromolecules* 51, 5656–5664. doi: 10.1021/acs.macromol.8b01282
- Yu, Y., Gim, S., Kim, D., Arnon, Z. A., Gazit, E., Seeberger, P. H., et al. (2019). Oligosaccharides self-assemble and show intrinsic optical properties. *J. Am. Chem. Soc.* 2019, 141, 4833–4838. doi: 10.1021/jacs.8b11882
- Yuasa, J., Ohno, T., Miyata, K., Tsumatori, H., Hasegawa, Y., and Kawai, T. (2011). Noncovalent ligand-to-ligand interactions alter sense of optical chirality in luminescent $Tris(\beta\text{-diketonate})$ Lanthanide(III) complexes containing a chiral bis(oxazolonyl) pyridine ligand. *J. Am. Chem. Soc.* 133, 9892–9902. doi: 10.1021/ja201984u
- Zheng, H., Li, W., Li, W., Wang, X., Tang, Z., Zhang, S. X.-A., et al. (2018). Uncovering the circular polarization potential of chiral photonic cellulose films for photonic applications. *Adv. Mater.* 30:1705948. doi: 10.1002/adma.201705948
- Zhou, Y., Li, H., Zhu, T., Gao, T., and Yan, P. A. (2019). Highly luminescent chiral tetrahedral $Eu_4L_4(L')_4$ cage: chirality induction, chirality memory, and circularly polarized luminescence. *J. Am. Chem. Soc.* 141, 19634–19643. doi: 10.1021/jacs.9b07178
- Zinna, F., and Di Bari, L. (2015). Lanthanide circularly polarized luminescence: bases and applications. *Chirality* 27, 1–13. doi: 10.1002/chir.22382
- Zou, C., Qu, D., Jiang, H., Lu, D., Ma, X., Zhao, Z., et al. (2019). Bacterial cellulose: a versatile chiral host for circularly polarized luminescence. *Molecules* 24:1008. doi: 10.3390/molecules24061008

Conflict of Interest: The authors declare that the research was conducted in the absence of any commercial or financial relationships that could be construed as a potential conflict of interest.

Copyright © 2020 Fujiki, Wang, Ogata, Asanoma, Okubo, Okazaki, Kamite and Jalilah. This is an open-access article distributed under the terms of the Creative Commons Attribution License (CC BY). The use, distribution or reproduction in other forums is permitted, provided the original author(s) and the copyright owner(s) are credited and that the original publication in this journal is cited, in accordance with accepted academic practice. No use, distribution or reproduction is permitted which does not comply with these terms.



Corrigendum: Chirogenesis and Pfeiffer Effect in Optically Inactive Eu^{III} and Tb^{III} Tris(β -diketonate) Upon Intermolecular Chirality Transfer From Poly- and Monosaccharide Alkyl Esters and α -Pinene: Emerging Circularly Polarized Luminescence (CPL) and Circular Dichroism (CD)

OPEN ACCESS

Edited and reviewed by:

Keiji Hirose,
Graduate School of Engineering
Science, Osaka University, Japan

*Correspondence:

Michiya Fujiki
fujikim@ms.naist.jp;
michiya.fujiki@icloud.com
Abd Jalil Jalilah
jalilahjalil@unimap.edu.my

†ORCID:

Michiya Fujiki
orcid.org/0000-0002-3139-9478
Laibing Wang
orcid.org/0000-0002-3380-7826
Abd Jalil Jalilah
orcid.org/0000-0003-1265-0919

Specialty section:

This article was submitted to
Supramolecular Chemistry,
a section of the journal
Frontiers in Chemistry

Received: 25 August 2020

Accepted: 31 August 2020

Published: 02 October 2020

Citation:

Fujiki M, Wang L, Ogata N,
Asanoma F, Okubo A, Okazaki S,
Kamite H and Jalilah AJ (2020)
Corrigendum: Chirogenesis and
Pfeiffer Effect in Optically Inactive Eu^{III}
and Tb^{III} Tris(β -diketonate) Upon
Intermolecular Chirality Transfer From
Poly- and Monosaccharide Alkyl
Esters and α -Pinene: Emerging
Circularly Polarized Luminescence
(CPL) and Circular Dichroism (CD).
Front. Chem. 8:598729.
doi: 10.3389/fchem.2020.598729

Michiya Fujiki^{1*†}, Laibing Wang^{1†}, Nanami Ogata¹, Fumio Asanoma¹, Asuka Okubo¹,
Shun Okazaki¹, Hiroki Kamite¹ and Abd Jalil Jalilah^{1,2,3†}

¹ Division of Materials Science, Graduate School of Science and Technology, Nara Institute of Science and Technology, Ikoma, Japan, ² School of Materials Engineering, Universiti Malaysia Perlis, Jejawi, Malaysia, ³ Centre of Excellence Frontier Materials Research, Universiti Malaysia Perlis, Kangar, Malaysia

Keywords: non-covalent interaction, circularly polarized luminescence, circular dichroism, europium, terbium, cellulose, saccharide, terpene

A Corrigendum on

Chirogenesis and Pfeiffer Effect in Optically Inactive Eu^{III} and Tb^{III} Tris(β -diketonate) Upon Intermolecular Chirality Transfer From Poly- and Monosaccharide Alkyl Esters and α -Pinene: Emerging Circularly Polarized Luminescence (CPL) and Circular Dichroism (CD)

by Fujiki, M., Wang, L., Ogata, N., Asanoma, F., Okubo, A., Okazaki, S., et al. (2020). Front. Chem. 8:685. doi: 10.3389/fchem.2020.00685

In the original article, there were mistakes in **Table 1** as published. **Table 1** aimed to compare all g_{lum} values at specific wavelengths of four Ln^{III} tris(β -diketonates) (Ln^{III}: Eu^{III} and Tb^{III}) upon intermolecular chirality transfer from CABu, CTA, Glu (*D*- and *L*-), Ara (*D*- and *L*-), and α -pinene for clarity and readability. However, although the g_{lum} values described in the main text are correct, most data in the three right-side columns of **Table 1** are incorrectly displayed. Also, in **Table 1** caption, *D*-/*L*-glucose pentamehyl esters should be *D*-/*L*-glucose pentamethyl esters. The corrected **Table 1** with corrected numerical values in the three right-side columns and corrected caption appears below.

Also, there was an error in Introduction. The sentence starting with “Particularly, chirogenesis in metal coordination chemistry by the chirality transfer has long been one of the central subjects in inorganic chemistry 1 (Mason and Norman, 1965...)” should read as follows: “Particularly, chirogenesis in metal coordination chemistry by the chirality transfer has long been one of the central subjects in inorganic chemistry (Mason and Norman, 1965...)”.

The authors apologize for these errors and state that this does not change the scientific conclusions of the article in any way. The original article has been updated.

TABLE 1 | CPL characteristics (dissymmetry ratio, g_{lum} in 10^{-2} at specific wavelength) of Eu^{III} and Tb^{III} coordinated with three β -diketonates as achiral ligands embedded in two polysaccharide alkyl esters (**CABu** and **CTA**), *D*-/L-glucose pentamethyl esters (**D-/L-Glu**), and *D*-/L-Arabinose tetramethyl esters (**D-/L-Ara**).

Ln ^{III} tris(β -diketonates)	CABu $g_{lum}/10^{-2}$ (nm)	CTA $g_{lum}/10^{-2}$ (nm)	Glu $g_{lum}/10^{-2}$ (nm)		Ara $g_{lum}/10^{-2}$ (nm)		α -pinene $g_{lum}/10^{-2}$ (nm)	
			D-	L-	D-	L-	(1R)	(1S)
Eu(fod) ₃	+6.71 (593) ^a	+4.63 (593) ^a	+1.05 (594) ^a	−0.81 (596) ^a	+0.19 (593) ^a	−0.30 (591) ^a	−0.49 (593) ^f	+0.41 (593) ^f
	−0.59 (613) ^b	−0.40 (613) ^b	−0.19 (612) ^b	+0.08 (613) ^b	−0.02 (607) ^b	+0.06 (611) ^b	+0.05 (613) ^f	−0.04 (613) ^f
Eu(dpm) ₃	n.d. ^g	n.d. ^g	n.d. ^g	n.d. ^g	n.d. ^g	n.d. ^g	n.d. ^g	n.d. ^g
Tb(fod) ₃	−0.29 (490) ^c	−0.10 (490) ^c	n.d. ^g	n.d. ^g	n.d. ^g	n.d. ^g	n.d. ^g	n.d. ^g
	+0.78 (540) ^d	+0.35 (542) ^d						
	−0.18 (552) ^e	−0.07 (553) ^e						
Tb(dpm) ₃	−0.53 (491) ^c	−0.44 (489) ^c	n.d. ^g	n.d. ^g	n.d. ^g	n.d. ^g	n.d. ^g (~490)	n.d. ^g (~490)
	+0.37 (537) ^d	−					+0.44 ^d (537)	−0.49 ^d (537)
	−0.59 (547) ^e	+0.80 (547) ^e					−0.13 ^e (547)	+0.34 ^e (548)

All numerical values in bracket mean wavelength extremum for CPL signals. ^a $Eu^{III} \ ^5D_0 \rightarrow \ ^7F_1$ (593 nm), ^b $Eu^{III} \ ^5D_0 \rightarrow \ ^7F_2$ (613 nm), ^c $Tb^{III} \ ^5D_4 \rightarrow \ ^7F_6$ (490 nm), ^d $Tb^{III} \ ^5D_4 \rightarrow \ ^7F_5$ (I) (540 nm), ^e $Tb^{III} \ ^5D_4 \rightarrow \ ^7F_5$ (II) (552 nm), ^fData were taken from literature (Jalilah et al., 2018). ^gNot characterized or no data.

REFERENCES

Jalilah, A. J., Asanoma, F., and Fujiki, M. (2018). Unveiling controlled breaking of the mirror symmetry of Eu(Fod)₃ with α -/ β -pinene and BINAP by circularly polarised luminescence (CPL), CPL excitation, and ¹⁹F-/³¹P{¹H}-NMR spectra and mulliken charges. *Inorg. Chem. Front.* 5, 2718–2733. doi: 10.1039/C8QI00509E

Mason, S. F., and Norman, B. J. (1965). Outer-sphere co-ordination and optical activity in transition-metal complexes. *Chem. Commun.* 335–336. doi: 10.1039/c19650000335

Copyright © 2020 Fujiki, Wang, Ogata, Asanoma, Okubo, Okazaki, Kamite and Jalilah. This is an open-access article distributed under the terms of the Creative Commons Attribution License (CC BY). The use, distribution or reproduction in other forums is permitted, provided the original author(s) and the copyright owner(s) are credited and that the original publication in this journal is cited, in accordance with accepted academic practice. No use, distribution or reproduction is permitted which does not comply with these terms.



Porphyrins Through the Looking Glass: Spectroscopic and Mechanistic Insights in Supramolecular Chirogenesis of New Self-Assembled Porphyrin Derivatives

Manuela Stefanelli^{1†}, Marco Savioli^{1†}, Francesca Zurlo¹, Gabriele Magna¹, Sandra Belviso², Giulia Marsico², Stefano Superchi², Mariano Venanzi¹, Corrado Di Natale³, Roberto Paolesse¹ and Donato Monti^{1,4*}

OPEN ACCESS

Edited by:

Victor Borovkov,
South-Central University for
Nationalities, China

Reviewed by:

Minghua Liu,
Institute of Chemistry (CAS), China
Michiya Fujiki,
Nara Institute of Science and
Technology (NAIST), Japan
Roberto Purrello,
University of Catania, Italy

*Correspondence:

Donato Monti
monti@stc.uniroma2.it
donato.monti@uniroma2.it

[†]These authors have contributed
equally to this work

Specialty section:

This article was submitted to
Supramolecular Chemistry,
a section of the journal
Frontiers in Chemistry

Received: 27 July 2020

Accepted: 09 September 2020

Published: 15 October 2020

Citation:

Stefanelli M, Savioli M, Zurlo F,
Magna G, Belviso S, Marsico G,
Superchi S, Venanzi M, Di Natale C,
Paolesse R and Monti D (2020)
Porphyrins Through the Looking
Glass: Spectroscopic and Mechanistic
Insights in Supramolecular
Chirogenesis of New Self-Assembled
Porphyrin Derivatives.
Front. Chem. 8:587842.
doi: 10.3389/fchem.2020.587842

¹ Department of Science and Chemical Technologies, University of Rome "Tor Vergata", Rome, Italy, ² Department of Sciences, University of Basilicata, Potenza, Italy, ³ Department of Electronic Engineering, University of Rome Tor Vergata, Rome, Italy, ⁴ Department of Chemistry, University La Sapienza, Rome, Italy

The solvent driven aggregation of porphyrin derivatives, covalently linked to a L- or D-proline enantiomer, results in the stereospecific formation of species featuring remarkable supramolecular chirality, as a consequence of reading and amplification of the stereochemical information stored in the proline-appended group. Spectroscopic, kinetic, and topographic SEM studies gave important information on the aggregation processes, and on the structures of the final chiral architectures. The results obtained may be the seeds for the construction of stereoselective sensors aiming at the detection, for example, of novel emergent pollutants from agrochemical, food, and pharmaceutical industry.

Keywords: porphyrins, circular dichroism, supramolecular chemistry, supramolecular chirogenesis, self-assembly, chirality

INTRODUCTION

Porphyrin-based chiral supramolecular systems are of great importance owing to their potential application in wide fields of science and technology (Cui et al., 2015; Paolesse et al., 2017; Lee et al., 2018), and for the implication on the emergence of homochirality in Life (Guijarro and Yus, 2009). Addressed protocols pursued for the formation of such a species usually rely on the use of either chiral or achiral platforms (Monti, 2014; Liu et al., 2015; Magna et al., 2019). In the former case, the stereochemical course of the self-assembling process is governed by the presence of chiral groups linked on the porphyrin peripheral frame (Oliveira-González et al., 2015; van der Weegen et al., 2017). In the latter issue, final chiral suprastructures are obtained by interaction of achiral substrates with external physical effectors, such as hydrodynamic directional forces (Sorrenti et al., 2012; Arteaga et al., 2016); magnetic fields (Micali et al., 2012); LB and LS techniques (Chen et al., 2011), or chiral molecular templates, such as surfactants (El-Hachemi et al., 2008), chiral polymeric matrices (D'Urso et al., 2012), chiral ligands (Borovkov and Inoue, 2006; Berova et al., 2007) or carboxylic acids (Castriciano et al., 2011). With this regard, Monsù Scolaro showed that the assembly of a non-chiral porphyrin derivative templated by the two different enantiomers of tartaric acid proceeds

with different kinetics and results in final chiral suprastructures with highly different anisotropy factors, which are strictly dependent on the enantiomer used as a templating agent (Castriciano et al., 2012). These findings indicate the complexity of factors that play a crucial role in the formation of such chiral species. As a part of our studies dedicated to the construction of chiral porphyrin aggregates (Monti et al., 2010; Zelenka et al., 2011), we investigated the self-assembly behavior of intrinsically chiral zinc-tetraphenylporphyrin derivatives, characterized by the presence of covalently linked enantiomers of L- or D-proline groups on the molecular frame (**Scheme 1**). The molecular information stored on the periphery of the macrocycles, besides inferring key amphiphilic properties to the monomers, can be effectively read out during the self-assembly of the aromatic platforms, once steered by hydrophobic effect, owing to the conformational rigidity, and robustness toward adventitiously caused racemization of the proline residues. This, in certain aspects, unique aminoacid has been recently found to play a role in asymmetric aminocatalysis (Mathew et al., 2004). We may anticipate that the process follows a highly stereospecific multistep mechanism, to give assemblies with specular CD features, indicating the formation of aggregate structures with opposite supramolecular chirality, dictated by the type of stereocenter present on the macrocycle. Further kinetic and topographic SEM investigations gave clear cut insights on the mechanism and the morphology of the chiral supramolecular structures formed. The results obtained are of great importance for the fabrication of sensors featuring stereoselective properties. We recently found, for example, that hybrid organic-inorganic materials, constituted by ZnO nanoparticles covalently linked to a porphyrin enantiomer studied in detail in the present work, are able to selectively detect the different enantiomers of chiral analytes, such as limonene and other terpenes (Stefanelli et al., 2019).

RESULTS AND DISCUSSION

Synthesis of Porphyrin Derivatives

Synthesis of the title porphyrins has been accomplished by following the path reported in **Scheme 1**, which relies on straightforward procedures used in peptide chemistry. As a first stage, the 5-(4-carboxyphenyl)-10,15,20-triphenylporphyrin **pCTPP** was reacted with (L)- or (D)-proline *tert*-butyl ester using the EDCl/HOBT coupling reagents, providing the corresponding prolinated derivatives which were subsequently hydrolyzed in a TFA/CH₂Cl₂ mixture to give the amphiphilic compounds (L)**H₂P**(-) and (D)**H₂P**(-). The further metalation with an excess of zinc acetate in CHCl₃/MeOH afforded the corresponding (L)**ZnP**(-) and (D)**ZnP**(-) complexes (Stefanelli et al., 2019).

Aggregation Studies

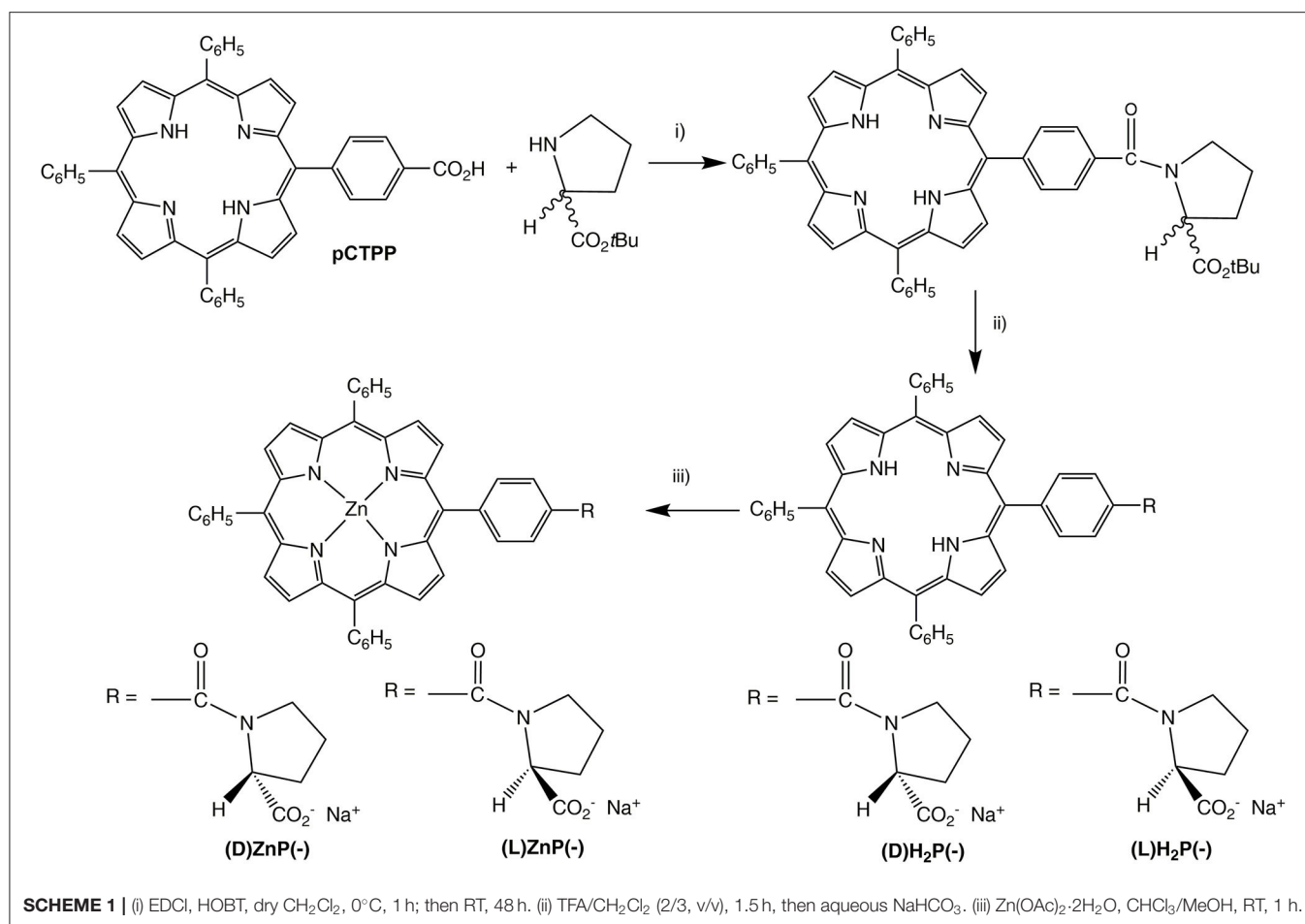
Spectroscopic Investigations

Aggregation of title porphyrins has been carried out in aqueous ethanol solutions (EtOH/H₂O 25:75 v:v; 298 K) typically at 5 μ M concentration, by strictly following a “porphyrin first” protocol, as reported in the Experimental Section. Previously published studies, carried out by our group and by others,

pointed out the strong dependence of the aggregation process on the experimental conditions, such as the order in which the reagents are mixed (Micali et al., 2000). Moreover, the chiral induction exerted by homochiral dopants can be effectively modulated during the early milliseconds mixing stage (i.e., standard flask preparation vs. microfluidic mixing; Sorrenti et al., 2016). However, within the standard playground of solutions preparation, the peculiar solvent mixture used allows for a good reproducibility of the results and a convenient time of reaction, to be followed by conventional spectroscopic techniques. It is important to remark that the preparation of the samples requires also an additional step of sonication and microfiltration of the solutions, to ensure an optimal reproducibility of the results obtained, in terms of spectral features (UV-Vis and CD band intensities) and kinetic parameters (for a brief discussion see **Supplementary Material**). Sonication steps have been demonstrated to feature a key role in supramolecular chirogenesis of porphyrin macrocycles and related structures (Liu et al., 2015; El-Hachemi et al., 2016). The protocol followed is described in full details in the Experimental Section.

In ethanol, the title amphiphilic macrocycles are in monomeric form ($\lambda_{\text{max}} = 424 \text{ nm}$; **Figure 1A**, trace a); the addition of a proper amount of water steers the self-aggregation process driven by hydrophobic effect, as indicated by the typical UV-Vis spectral changes (**Figure 1A**, trace b), which is complete within the time of mixing, likely driven by π - π interactions (Type-I aggregates). The corresponding spectral pattern indicates a hypochromic effect with a concomitant broadening and small red-shift of the Soret B band to 427 nm. CD spectroscopy reveals that these species feature, although of low intensities, appreciable supramolecular chirality of opposite sign, depending on the configuration of the appended groups. In particular, the aggregates of (D)**ZnP**(-) show a positive (+/-) bisignate spectrum, whereas those of the (L)**ZnP**(-) enantiomer show a mirrored, negative pattern (-/+), as reported in **Figure 2A**. The reproducibility of the results, along with the specularity of the dichroic bands, safely rules out any effect due to the presence of adventitious chiral residues in the medium (El-Hachemi et al., 2009), also upon using of distilled water from different sources and time of storage. Interestingly, these species show a further slow evolution, which is generally completed within few weeks, into structures of different morphology (Type-II aggregates; **Figure 1A**, trace c). Accordingly, the UV-Vis spectra of the solutions show a further slow decrease of intensity of the Soret bands, evolving at final equilibrium into a double peaked coupled B band ($\lambda_{\text{max}} = 422$ and 443 nm) in the case of both (L)**ZnP**(-) and its (D)**ZnP**(-) stereoisomer, with a clear isosbestic point at 439 nm (**Figure 1B**).

Again, CD experiments gave insights on this phenomenon. In the cases of both of the enantiomers, the spectra show remarkable evolution of the initial features, with the gradual formation of multi-patterned coupled bands featuring intensities increased by two order of magnitude, with crossover points in correspondence of the UV-Vis absorption maxima (**Figure 2B,C**). This complex pattern has been ascribed to the formation of J-type aggregates of complex morphology, with excitonic coupling along two preferential space directions (Ohno et al., 1993). In particular, the



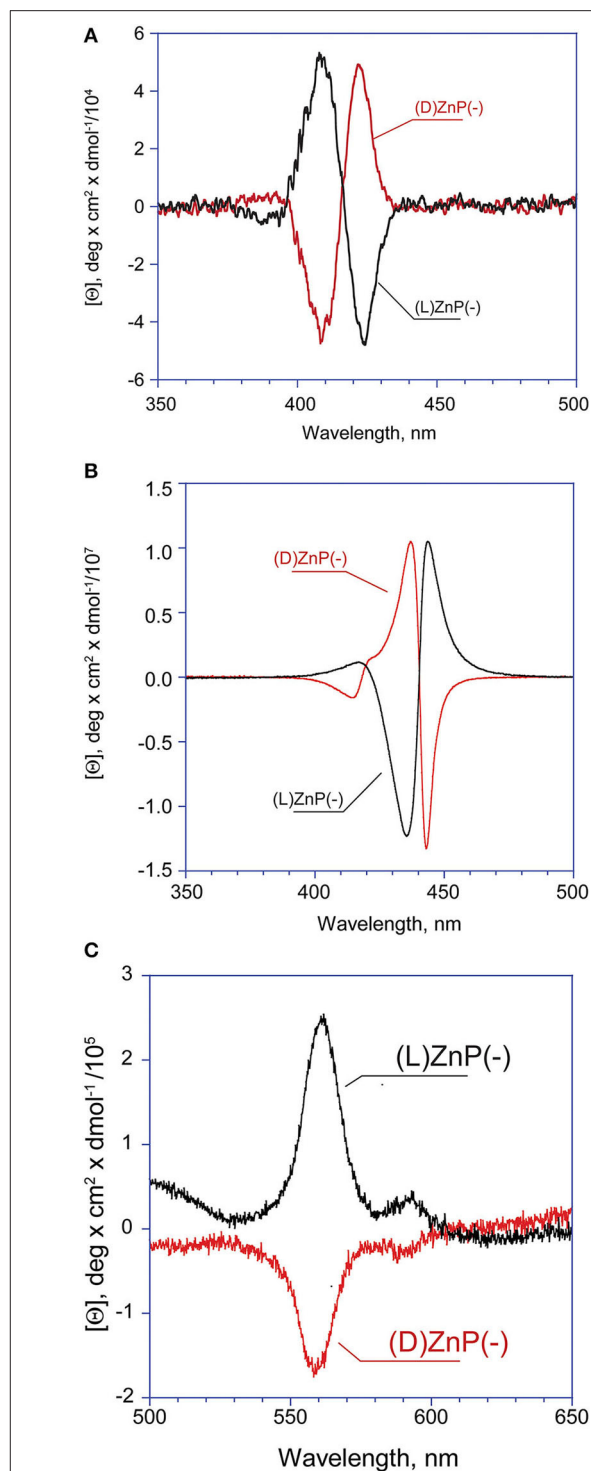
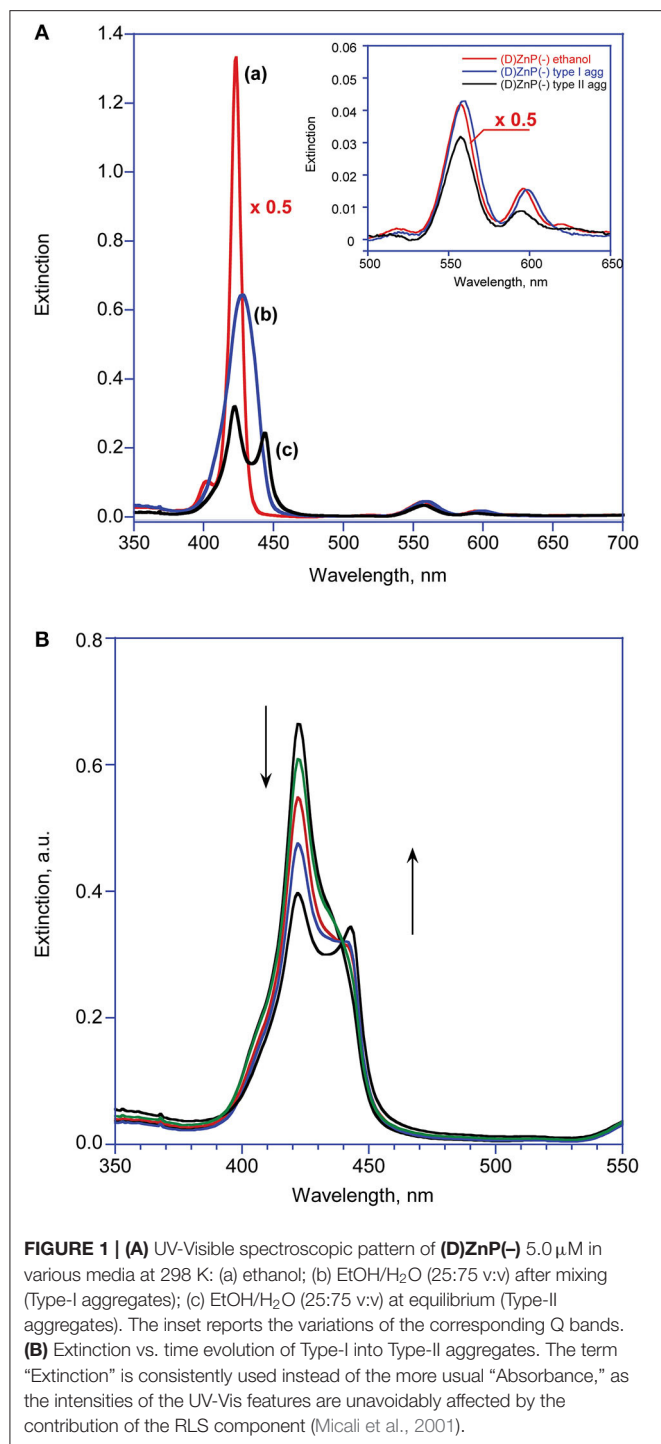
supramolecular structures derived from the **(L)ZnP(-)** species, show a $+/-/+$ pattern, while those of the **(D)ZnP(-)** forms show a specular $-/+/-$ sign. Accordingly, the calculated anisotropy factors g (Berova et al., 2000) are $9.5 (\pm 0.5) \times 10^{-5}$ for both the initial (Type-I) aggregates; $0.068 (\pm 0.005)$ and $0.071 (\pm 0.008)$ for **(L)ZnP(-)** and **(D)ZnP(-)** respectively, at equilibrium (Type-II species; $5 \mu\text{M}$ initial concentration). These values indicate an enhancement of the intrinsic chirality on going to the larger, more structured Type-II species.

Accordingly, Type-II aggregates showed quenching of fluorescence emission (**Supplementary Figure 1A**), and intense Resonance Light Scattering features (**Supplementary Figures 1B,C**), as a consequence of an efficient delocalization of porphyrin exciton momenta over a large number of electronically coupled monomers, with respect to those featured in the first aggregation stage, indicating the formation of larger and strongly coupled self-assembled structures (Pasternack et al., 1993). Finally, the corresponding excitation spectra, carried out at both the emission wavelength maxima (i.e., at 604 or 650 nm) gave the exact reproduction of the UV-Vis Type-II spectral pattern, ruling out the formation of distinct families of H and J aggregates

(**Supplementary Figure 1D**). The supramolecular structures formed at $10 \mu\text{M}$ concentration featured a somewhat reduced g -value to about $0.049 (\pm 0.006)$, indicating a lesser degree of order of the final structures. Analogous and even more dramatic effect, has been previously reported (Romeo et al., 2014), pointing out the importance of the initial nucleation stage preceding the ordered growth of final structures.

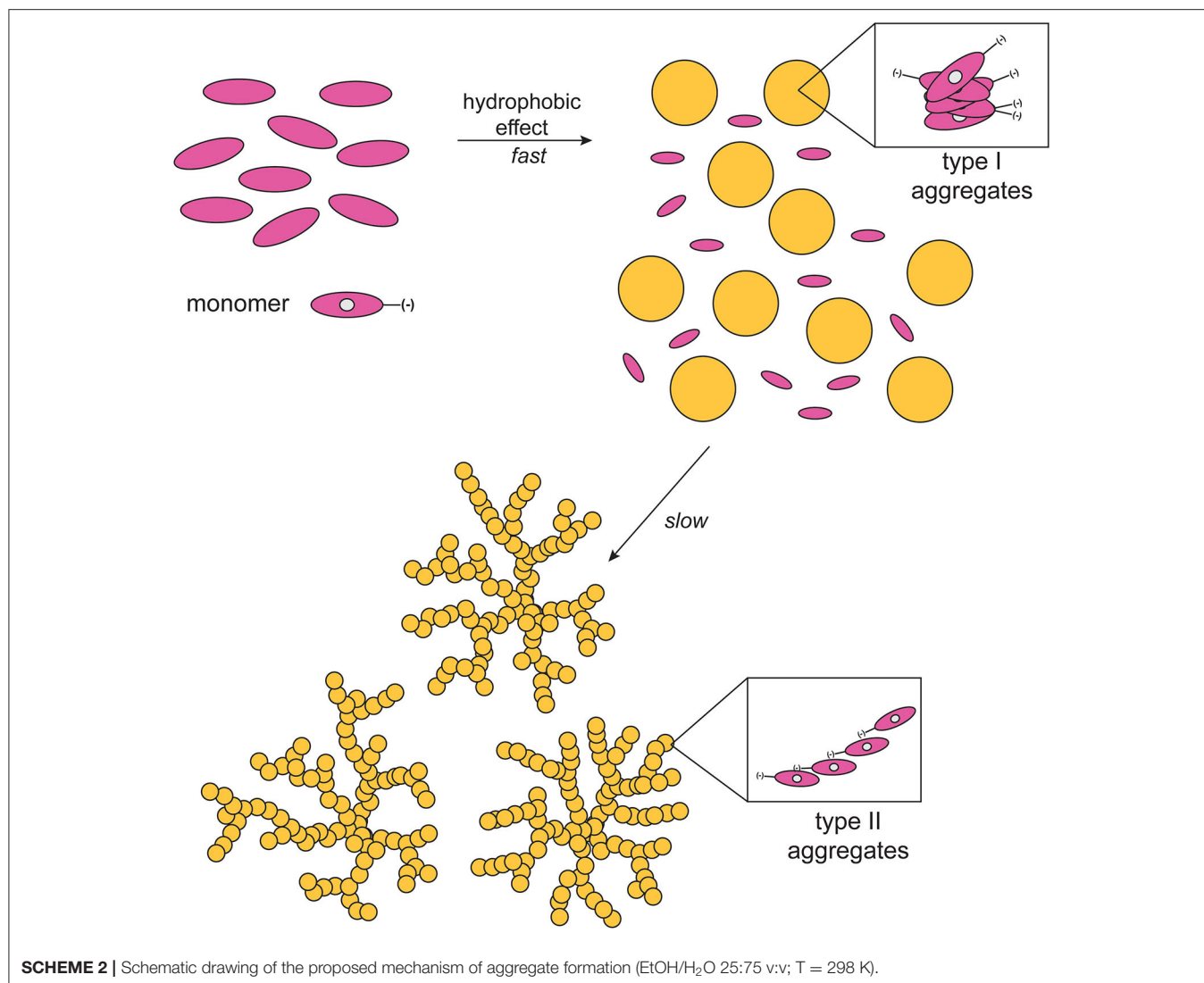
The results obtained showed good reproducibility well within a factor of two, also with porphyrins from different synthetic batches, although a strong decrease of the overall CD spectral intensities of the aggregates is generally observed when aged porphyrins stock solutions are used (time of storage longer than 1 month). Conversely, studies carried out at $1 \mu\text{M}$ concentration did not give evidences of complete formation of Type-II chiral aggregates, resulting in corresponding dichroic bands of very low intensity, which in some cases were difficult to be disentangled from the background noise. Prolonged standing of these solutions merely resulted in the flocculation of uncharacterized material.

It should be emphasized that in all of the cases observed the final CD spectra feature a sign inversion of the main lower energy bands, with respect to the blue-shifted coupled pattern. Inversion of these J-band has been also found by others in



the case of the formation of chiral porphyrin aggregates upon symmetry breaking induced by rotary evaporation (Sorrenti et al., 2012), and has been ascribed to a distortion from the planarity of the macrocycles due to steric hindrance. Similar results have been reported by Micali and Monsù Scolaro (Micali et al., 2006), for the case of chiral fractal structures of a water-soluble tetrakis(*p*-sulphonatophenyl)porphyrin derivative,

assembled in the presence of D- and L-tartaric acid as chiral effectors. In the present case, this effect may arise from a coordination of the Zn ion by the proline carboxylate



group, and this event would likely constitute the driving force for the evolution toward the final Type-II species. The involvement of Zn-coordination is also suggested by the fact that the free-base analogs of the title porphyrins [(D)- and (L)H₂P(-); **Scheme 1**] show different aggregation behavior with different CD spectral features, which are composed by simple mirrored bisignated bands, with constant intensity and pattern throughout the whole temporal window examined and, relevantly, with same signs of that of the Type-I species (**Supplementary Figure 2**). As far as the macrocycles intimate molecular level structure is concerned, a metastable mutual *syn* configuration for the Type-I aggregates, and a thermodynamically stable extended *anti* configuration could be proposed. This suggestion was made on the basis of strong similarities of both Soret band and CD profiles of the aggregates to those of chiral *syn*- or *anti*-geometry of bis-(Zn)porphyrin derivatives with several chiral ligands (Borovkov et al., 2000, 2001). A pictorial representation of the mechanism is reported in **Scheme 2**. Furthermore, if the aggregation of

the title Zn porphyrins is carried out in the presence of an excess of benzylamine, a competing achiral nitrogen ligand, the aggregation occurs with the formation of final achiral, CD silent, aggregate structures (results not shown), confirming the key role of the coordination on the formation of the final structures.

As far as the overall aggregation process is concerned, we recently found an analogous two-step process in the aggregation of related cationic L-proline-porphyrin derivatives in analogous aqueous media (Lorecchio et al., 2014; Caroleo et al., 2019), and also in the study of the interaction of a chiral Zn-porphyrin derivative with chiral anionic surfactants in water, that results in the rapid formation of small sized aggregates, followed by a slower step in which the initial species rearrange in more ordered and specific structures driven by Zn-coordination (Simoncini et al., 2014). Same phenomenon has been also observed by others in organic solvent (Feldborg et al., 2011), in the case of water-soluble tetrapyrrolic macrocycles

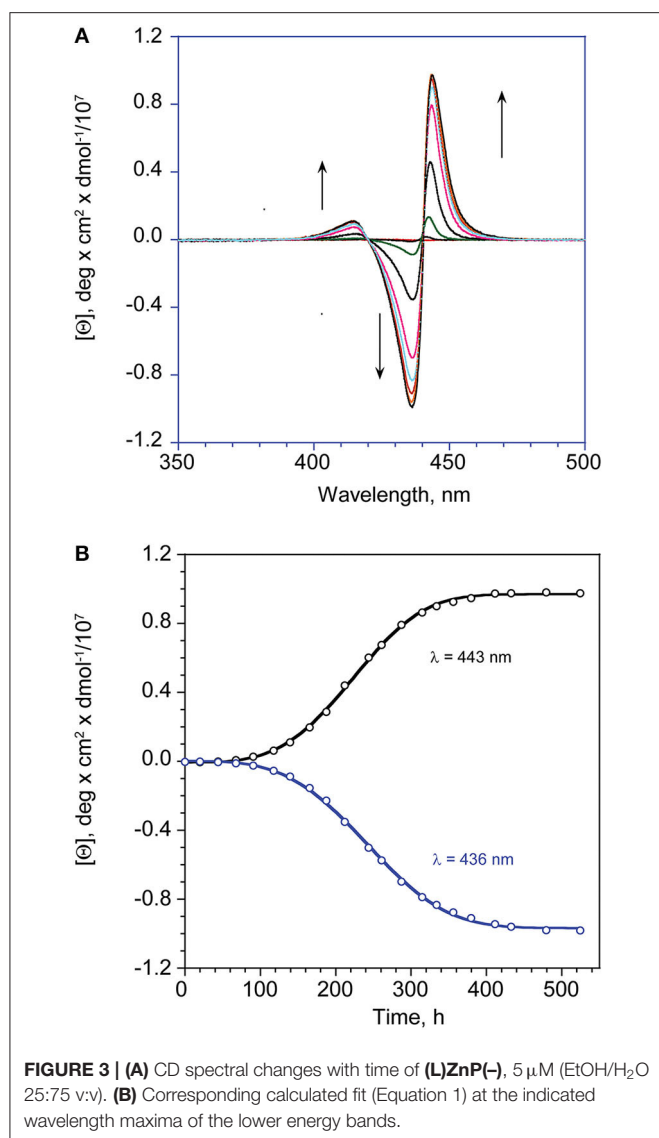


FIGURE 3 | (A) CD spectral changes with time of **(L)ZnP(–)**, 5 μ M (EtOH/H₂O 25:75 v/v). **(B)** Corresponding calculated fit (Equation 1) at the indicated wavelength maxima of the lower energy bands.

(El-Hachemi et al., 2016) or, amazingly, even in solid state (Borovkov et al., 2003).

Finally, when the aggregation experiment was carried out on the racemic mixture (i.e., 5 μ M of both the enantiomers) only a broadening and hypochromic effect of the Soret bands and silent CD spectra are obtained, indicating the formation of non-specific achiral structures, likely due to the mismatching of the chiral proline groups during the key molecular recognition event.

Kinetic Studies

Kinetic studies, carried out on the slow formation step of Type-II aggregates, allowed to get more insights on the intimate mechanism of formation of such important chiral architectures. In all of the case examined, the kinetic profiles [i.e., molar ellipticity $[\Theta]$ vs. time] followed a sigmoidal autocatalytic behavior (**Figures 3A,B**) that could be successfully modeled

by a “fractal-type” exponential equation (Equation 1) formerly developed by Pasternack et al. (2002) for the case of disassembly of porphyrin aggregates by cyclodextrins. The equation used is of the form:

$$[\Theta] = [\Theta]_{eq} + ([\Theta]_0 - [\Theta]_{eq})e^{\left[\frac{-(kt)^{n+1}}{(n+1)}\right]} \quad (1)$$

In this equation, $[\Theta]$, $[\Theta]_0$, and $[\Theta]_{eq}$ are the molar ellipticity values at time t , time $= 0$, and at equilibrium, respectively; n is the “aggregate growth rate” parameter, and k the kinetic constant. We consistently found values of $n > 1$, indicating that the interaction between monomers and the growing structures become increasingly favored with time, i.e., with the increase of their surface area.

It is worthwhile of noting that this equation is a reduced form of a more general non-conventional equation previously developed by Pasternack himself (Pasternack et al., 2000), employed in the kinetic studies of fractal growth of porphyrin aggregates onto DNAs. This latter equation includes, beside a kinetic constant for an uncatalyzed path (k_0), a further parameter (m) related to the number of monomers forming the aggregation nuclei with catalytic activity (nucleation seeds). The equation reduces to Equation 1 in the case of $m = 1$, implying that the rate-determining step is the adhesion of the monomer to the growing assemblies, and not the formation of catalytically-active nucleation seeds. In our case the initial oligo-assemblies formed (Type-I species) should act as *single-site enantiomorphous surfaces* (i.e., a collection of uniform and independent chiral interaction sites), that promote the catalyzed growth of the final suprastructures with high stereospecificity. The legitimacy of this hypothesis is corroborated by the fact that the fit of the experimental values with the original “full-form equation” always gave m -values very close to 1 (i.e., from 0.95 to 1.1 ± 0.2) and negligible values of k_0 that faded within their experimental errors, along with a lower adherence to the experimental data points and higher uncertainties of the obtained kinetic parameters. The results have been reported in **Table 1**.

From the inspection of the table, the second step kinetic constant has been found to be in the order of 10^{-4} min^{-1} for the process carried out at 5 μ M, for both of the enantiomers, with n -values of *ca* 2 (entry 1). Kinetic experiments carried out at 10 μ M concentration resulted in an increase of the rate constant within one order of magnitude, along with an exponential growing factor of $n = 4$ (entry 3), which should arise from both the increase of the number of the initial nucleation structures, and on their increased size (i.e., area of the catalytic surfaces). Same results, in good agreement within experimental errors, have been obtained by UV-Vis spectroscopy, by following the slow decay with time of the Soret band of the Type-I species (see **Table 1**, entry 2, and **Supplementary Figure 3**).

Interestingly, experiments carried out at 1 μ M concentration revealed that the formed aggregates featured very low supramolecular chirality. However, the lower aggregation rate observed at this concentration regime, allowed for shedding light on the initial fast aggregation stage (i.e., formation of Type-I molecular structures) by UV-Vis technique. Remarkably,

TABLE 1 | Kinetic parameters for the aggregation reaction of (L)ZnP(-) and (D)ZnP(-) in EtOH/H₂O (25:75 v:v; 298 K) at different concentrations.

Concentration, M	(L)ZnP(-)		(D)ZnP(-)	
	k, min^{-1}	n	k, min^{-1}	n
(1) $5.0 \times 10^{-6} \text{ M}^{(a)}$	$9.3 (\pm 0.8) \times 10^{-5}$	2.3 ± 0.7	$9.0 (\pm 0.8) \times 10^{-5}$	2.7 ± 0.6
(2) $5.0 \times 10^{-6} \text{ M}^{(b)}$	$9.7 (\pm 0.6) \times 10^{-5}$	1.8 ± 0.3	$8.5 (\pm 0.4) \times 10^{-5}$	1.7 ± 0.2
(3) $1.0 \times 10^{-5} \text{ M}^{(a)}$	$8.4 (\pm 0.7) \times 10^{-4}$	4.8 ± 0.9	$7.3 (\pm 0.6) \times 10^{-4}$	4.0 ± 0.6
(4) $1.0 \times 10^{-6} \text{ M}^{(c)}$	$6.0 (\pm 0.5) \times 10^{-2}$	0.12 ± 0.05	$5.0 (\pm 0.4) \times 10^{-2}$	0.11 ± 0.03

(a) Followed by CD spectroscopy, fitted by Equation 1; (b) Followed by UV-Vis spectroscopy ($\lambda = 423 \text{ nm}$), fitted by Equation 1; (c) Followed by UV-Vis spectroscopy ($\lambda = 422 \text{ nm}$), fitted by Equation 2.

the extinction vs. time plot revealed a Diffusion Limited Cluster-Cluster Aggregation kinetic (DLCCA; **Figure 4**), which entails the rapid formation of small clusters, that subsequently slowly stick together forming larger structures (Monsù Scolaro et al., 2002). The equation used is of the form

$$[E] = [E]_o + ([E]_{eq} - [E]_o)(1 - e^{(-kt)^n}) \quad (2)$$

where E is the extinction values of the Soret band of the monomeric forms ($\lambda = 424 \text{ nm}$) at time t , at time $t = 0$ and at equilibrium, respectively; k is the apparent first-order reaction constant, and n , the so called “stretching factor,” modulates the diffusion growth of the aggregates, which in the case of this observed mechanism is strictly required to be $n < 1$. Due to the fast decay of the Soret intensity, the value at time $t = 0$ is calculated in the closest non-aggregative conditions (EtOH/H₂O 50% v:v).

The corresponding fit gave an estimation of the calculated rate constant values in the order of 10^{-2} min^{-1} , whereas the n -values are about 0.1 for both (L)ZnP(-) and (D)ZnP(-) (entry 4, **Table 1**).

Topographic SEM Investigations

The structural features of the supramolecular species, have been investigated by Scanning Electron Microscopy (SEM) of drop-casted equilibrium solutions. Micrographies show the formation of regular finely branched fractal structures of about $5\text{--}10 \mu\text{m}$ of diameter, throughout the surface investigated, for both the (L)ZnP(-) and (D)ZnP(-) derivatives (**Figures 5A–C**), in agreement with the peculiar kinetic process found for the formation of these supramolecular self-assembled chiral structures. Interestingly, racemic mixtures resulted in the formation of small globular structure only (**Figure 5D**), according to the negligible stereospecificity of the supramolecular assemblies. We previously found in fact that, in peptide self-assembly, globular structures predominate when the process is driven by non-specific interactions (e.g., hydrophobic effect). Where specific interactions between ordered structures predominate, the formation of fibrillar structures is then observed (Caruso et al., 2013).

CONCLUSIONS AND FUTURE PERSPECTIVES

In summary, the self-assembly process of amphiphilic porphyrin derivatives, functionalized by the two different stereoisomers

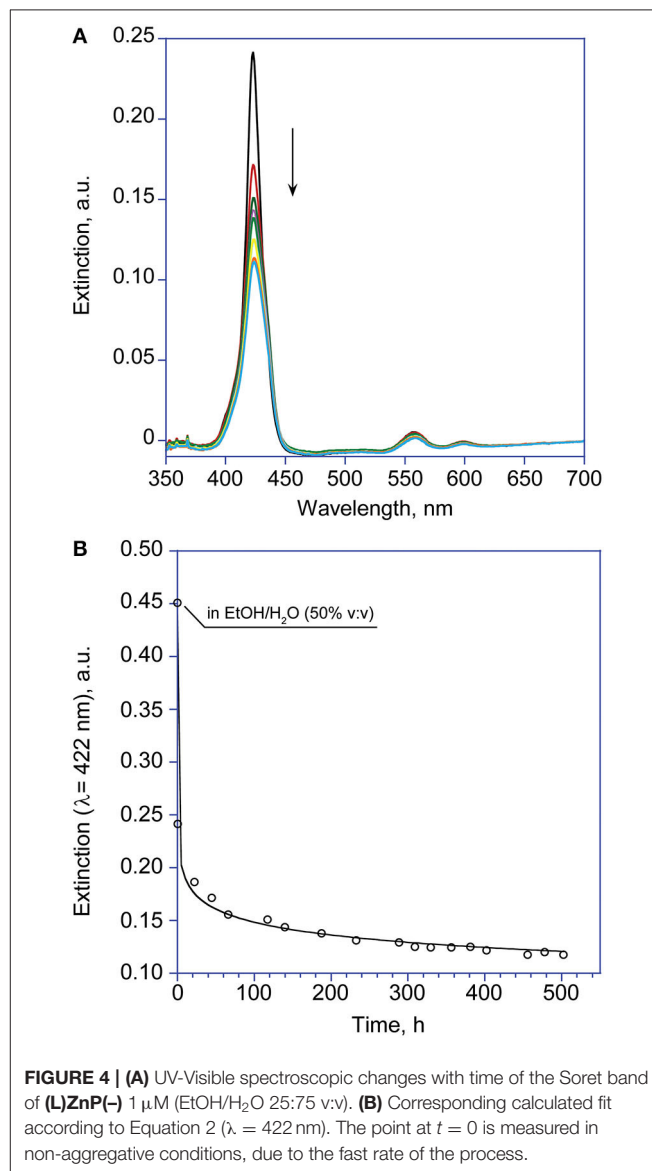


FIGURE 4 | (A) UV-Visible spectroscopic changes with time of the Soret band of (L)ZnP(-) $1 \mu\text{M}$ (EtOH/H₂O 25:75 v:v). (B) Corresponding calculated fit according to Equation 2 ($\lambda = 422 \text{ nm}$). The point at $t = 0$ is measured in non-aggregative conditions, due to the fast rate of the process.

of proline, results in fractal architectures featuring specular chiroptical properties, and alike morphology. Combined spectroscopic and kinetic studies pointed out the occurrence of a two-step process, in which an initial fast and chaotic assembly is followed by a slower stereospecific growth of fractal

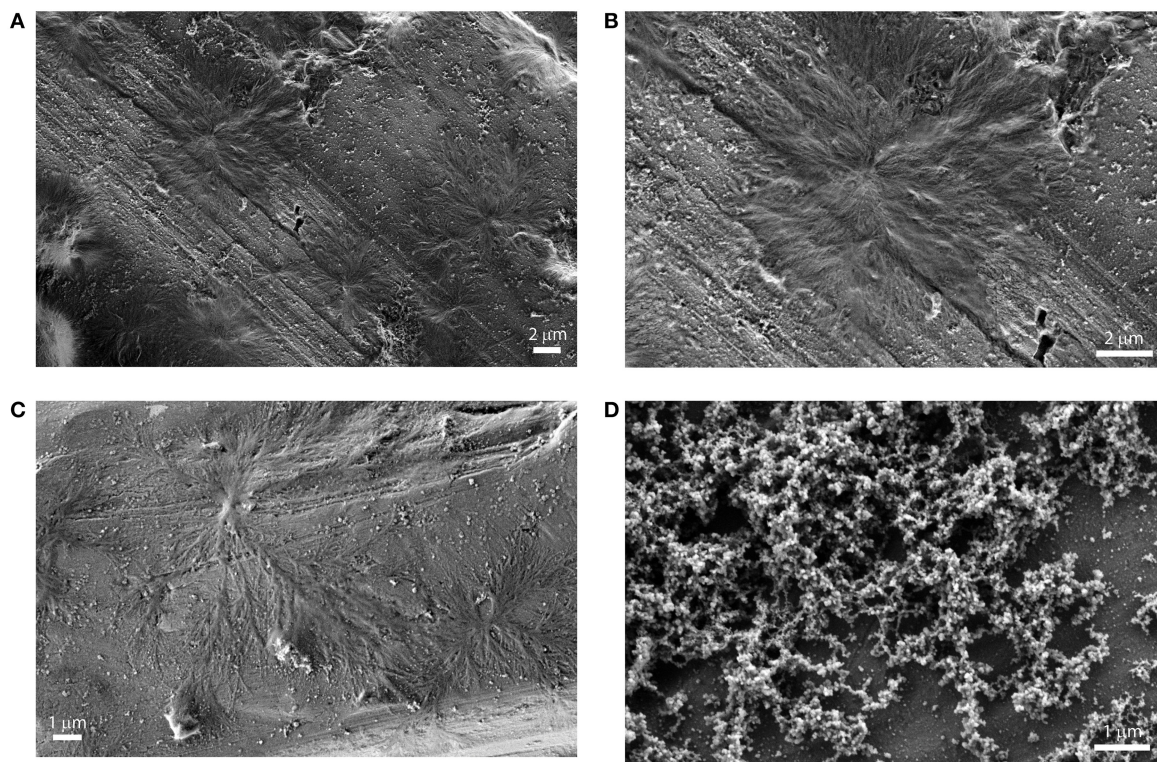


FIGURE 5 | SEM images of drop casted equilibrium solutions of porphyrin aggregates (5 μ M (EtOH/H₂O 25:75 v:v). (A): (L)ZnP(-); (B): (L)ZnP(-) enlargement of 5A; (C): (D)ZnP(-); (D) racemic mixture.

architectures, featuring intense coupled CD bands. Careful choice of experimental conditions gave a good control on the spectroscopic and morphological features of the final species. Detailed Scanning Electron Microscopy studies confirmed the complex peculiar structures of the obtained species. These findings would be of importance for understanding the fundamental process of evolution of homochirality at biological level (Guijarro and Yus, 2009), and for the development of chiral materials that, coupled with nanotechnology, constitutes a deeply pursued target with a wide range of exploitation in many important areas such as catalysis (Yoon et al., 2012), non-linear optics (Valev et al., 2014), materials science (Wang et al., 2013), sensors (Paolesse et al., 2011; Labuta et al., 2015; Intrieri et al., 2018), and catalysis (Zhou et al., 2018).

EXPERIMENTAL SECTION

General

Reagents and solvents were of commercial sources, in the highest degree of purity and were used as received. (D)-proline *tert*-butyl ester was purchased from Chem Impex International, Inc (USA). Thin-layer chromatography (TLC) was performed on Merck silica gel plates. Chromatographic purification on column was accomplished by using silica gel 60 (70–230 mesh, Sigma Aldrich) as the stationary phase. ¹H NMR spectra of the new porphyrin derivatives (D)H₂P(-) and (D)ZnP(-) were recorded

with a Bruker AV300 spectrometer (300 MHz) in CDCl₃ and THF-d₈ and are internally referenced to residual proton solvent signals (CDCl₃: δ = 7.24 ppm, THF-d₈: δ = 1.73 and 3.58 ppm). FAB mass spectra were obtained with a VG-Quattro spectrometer in the positive-ion mode by using CHCl₃ as the solvent and *m*-nitrobenzyl alcohol (Sigma Aldrich) as the matrix. Solvents used for spectroscopic measurements were of spectroscopic grade. UV/Vis spectra were recorded on a Cary 100 spectrophotometer.

CD spectra were performed on a JASCO J-1500, equipped with a thermostated cell holder set at 298 K, and purged with ultra-pure nitrogen gas. Linear Dichroism contribution (LD) has been found to be in all of the cases examined < 0.0004 DOD units, in all of the case examined. Fluorescence emission and Resonance Light Scattering measurements were performed on a Fluoromax-4 (HORIBA Scientific) spectrofluorimeter, in a synchronous scan mode, in which the emission and excitation monochromators are pre-set to identical wavelengths. Microstructural analysis of (D)- and (L)- porphyrin aggregates was carried out by using a Field Emission Scanning Electron Microscope FE-SEM, SUPRATM 35, Carl Zeiss SMT, Oberkochen, Germany. Samples have been prepared by slow evaporation of 20 μ L of the proper solution, on a previously cleaned aluminum stub (MeOH; N₂ flow). Sonication of the prepared solutions have been performed by ultrasound thermostath Fisher Scientific FB 15047, 90 W power supply, ultrasonic frequency of 37 kHz. Chiral HPLC analyses were performed

with a JASCO PU-1580 intelligent HPLC pump equipped with a Rheodyne model 7725i 20 μ L injector and coupled with a Varian 2,550 UV detector. Data were collected by using the Borwin software (Jasco, Japan). The Lux i-Amylose-1 [amylose tris(3,5-dimethylphenylcarbamate)] chiral chromatographic column (250 mm \times 4.6 mm I.D., 5 μ m particle size) was purchased from Phenomenex (Torrance, CA, USA). HPLC runs were performed eluting with a mixture *n*-Hexane:EtOH (80:20, v/v) at flow rates of 0.7 mL min⁻¹ and monitoring by UV detection at 350 nm. Samples were dissolved in the eluent, briefly sonicated, and filtered through a 0.45 μ m membrane (Whatman, UK) prior to injection.

Synthesis and Characterization of Porphyrin Derivatives

The chiral porphyrin derivatives investigated were prepared as outlined in **Scheme 1**. The synthesis and characterization of the (L)-prolinated porphyrins was recently reported (Stefanelli et al., 2019). Thus, herein we report the experimental details to prepare the (D)- counterpart. As expected, the spectroscopic characterization of these new compounds is fully in agreement with those just reported for the corresponding (L)-analogs.

Synthesis of (D)H₂P(–)

To a stirred solution of 5-(4-carboxyphenyl)-10,15,20-triphenylporphyrin (**pCTPP**) (104 mg, 0.158 mmol) in dry CH₂Cl₂ (25 mL) kept at 0°C, 1-ethyl-3-(3-dimethylaminopropyl)carbodiimide hydrochloride (EDCI) (30 mg, 0.156 mmol), hydroxybenzotriazole (HOBT) (22 mg, 0.162 mmol) and *N*-methylmorpholine (82 μ L, 0.746 mmol) were added. The resulting solution was stirred under N₂ for 1 h, then (D)-proline *tert*-butyl ester (97 μ L, 0.474 mmol) was added. The ice bath was removed and the reaction was allowed to reach the room temperature, then stirred for 48 h. Afterwards, the solvent was evaporated and the reaction crude was dissolved in chloroform and washed with brine (3 \times 100 mL). The organic phases were collected, dried over anhydrous Na₂SO₄ and then purified on silica chromatographic column, eluting with CHCl₃. In a second step, the obtained porphyrin was dissolved in TFA/CH₂Cl₂ mixture (2/3 v/v; 25 mL). The reaction was stirred at room temperature for 1.5 h. After the solvent removal under reduced pressure, the green residue was dissolved in CHCl₃ and neutralized with a saturated solution of NaHCO₃. The organic phase was dried over Na₂SO₄, concentrated and crystallized by adding an equal volume of *n*-pentane. Porphyrin was obtained as bright purple crystals (81 mg, 0.107 mmol; 68% yield). UV-Vis (CHCl₃): λ_{\max} (ϵ , M⁻¹ cm⁻¹) = 419 (125,900), 515 (6,310), 547 (6,290), 585 (5,010), 640 (3,160) nm. ¹H NMR (300 MHz, CDCl₃): 8.80 (br s, 8 H, β -pyrr), 8.19 (m, 4H, ArH), 8.17 (m, 6H, ArH), 7.71 (m, 3H, ArH), 7.60 (m, 6H, ArH), 4.5 (m, 1 H, proline α -H), 3.97 (m, 2 H, proline δ -H), 2.44 (m, 2 H, proline β -H), 2.07 (m, 2 H, proline γ -H), -2.79 (s, 2H, NH). FAB-MS (NBA), *m/z*: 756 [M]⁺.

Synthesis of (D)ZnP(–)

To a stirred solution of porphyrin (D)H₂P(–) (90 mg, 0.119 mmol) dissolved in CHCl₃ (15 mL) an excess of a methanolic

solution of Zn(OAc)₂·2H₂O (43 mg, 0.234 mmol dissolved in 3 mL of MeOH) was added. The progress of metal insertion was followed by UV-Vis spectroscopy (Soret and Q visible band changes). After 1 h of stirring at room temperature, the complex was quantitatively formed and obtained as a cherry-purple solid after solvent evaporation. Pure purple crystals of the desired compound was obtained after crystallization from CHCl₃/*n*-pentane (93 mg, 0.114 mmol; 96% yield). UV-Vis (THF): λ_{\max} (ϵ , M⁻¹ cm⁻¹) = 424 (451,000), 556 (15,500), 595 (5,600) nm. ¹H NMR (300 MHz, THF-*d*₈): 8.83 (m, 8 H, β -pyrr), 8.21 (m, 4H, ArH), 8.19 (m, 6H, ArH), 7.76 (m, 3H, ArH), 7.65 (m, 6H, ArH), 3.99 (m, 1 H, proline α -H), 3.89 (m, 2 H, proline δ -H), 2.34 (m, 2 H, proline β -H), 2.18 (m, 2 H, proline γ -H). FAB-MS (NBA), *m/z*: 818 [M]⁺.

Determination of Enantiomeric Purity of (D)- and (L)ZnP(–)

The enantiomeric purity of (D)ZnP(–) and (L)ZnP(–) was checked by HPLC chromatography on a chiral stationary phase (c.s.p.), a method which has proved to be efficient for enantioseparation of chiral tetrapyrrole macrocycles (Belviso et al., 2018a,b). Accordingly, the racemic mixture and the two enantiomers were eluted on amylose tris(3,5-dimethylphenylcarbamate) c.s.p. This c.s.p. allowed separation of the racemic mixture into the two enantiomers (D)ZnP(–) and (L)ZnP(–) (see **Supplementary Figure 4**) even if a peak overlap occurs as a consequence of a peak tailing probably due to aggregation phenomena in the required elution mixture. In particular, (L)ZnP(–) showed a retention time of 28.90 min, while (D)ZnP(–) a retention time of 36.70 min. Comparison of the racemic mixture chromatogram with those of the single enantiomers allowed to establish that both samples were enantiomerically pure, showing no traces of the other stereoisomer.

Aggregation Studies

All the spectroscopic studies have been carried out at 298 K. Solutions suitable for the aggregation studies were prepared as follows. Porphyrin stock solutions in ethanol (*ca.* 10⁻⁴ M concentration) were gently warmed, then briefly sonicated and finally filtered through a 0.22 μ m Nylon® membrane (HahnemÅ1/4le Albet® Syringe Filters), prior to use. These precautions have been taken to avoid uncontrolled nucleation of porphyrin protoaggregates that would affect the reproducibility of the experiments. Check of the effective concentration was made by UV-Vis spectroscopy in pure ethanol (Soret band intensity of the porphyrins in monomeric form; ϵ = 4.51 \times 10⁵ M⁻¹ cm⁻¹). Aggregation of title porphyrins has been carried out in aqueous ethanol solutions (EtOH/H₂O 25:75 v/v; 298 K) at 1, 5 and 10 μ M concentration, by strictly following a “porphyrin first” protocol. Namely, a proper aliquot of a stock solution of porphyrin (10–100 μ L), was added to the required amount of ethanol (final volume of 1.0 mL) in an 8 mL glass vial, and briefly sonicated. To this solution 3.0 mL of water were then slowly added, again under sonication, to give 4.0 mL of resulting solution with 25% v:v solvent proportion, with the required porphyrin concentration. A *ca.*

2.5 mL portion was finally transferred into a quartz cuvette and the relative spectra were then acquired at different time in order to monitoring the temporal evolution of the systems. This second sonication step appears to be of crucial importance for a good reproducibility of the results, that depends on the homogeneity of the morphology of the initially formed porphyrin clusters, which would be detrimentally affected by the unavoidable occurrence of both gradient of concentration and solvent polarity changes, during the mixing with water. The porphyrin stock solutions should be used within 2 weeks from preparation, to ensure optimal reproducibility of the results.

Kinetic Studies

Kinetic studies on the aggregation process of the title porphyrins, have been carried out in EtOH/H₂O (75:25 v:v) and followed by CD spectroscopy. In all of the case examined, the first aggregation stage (Type-I aggregate formation) was in general too fast to be followed by conventional spectroscopic techniques. As far as the second process is concerned (Type-II aggregate formation) autocatalytic-type behavior of the molar ellipticity [θ] vs. time profiles have been obtained. The experimental data have been fitted by the Equation 1, reported in the Results and Discussion section of the text. The kinetic parameters were obtained by non-linear regression fit (KaleidaGraph 4.1, Synergy Software, 2011), over tens of data points. Entry values of k and n were initially obtained by running the program with fixed initial and equilibrium experimental values (theta molar or extinction). Final regressions were operated with “free” initial and final parameters to give final calculated values, that have been found to be always in good agreement with the experimental ones. The final kinetic data, reported in **Table 1**, are the averaged values obtained over at least three different runs, and for both minimum and maximum wavelength of lower

energy, most intense coupled bands at 436 and 443 nm, of the CD spectra.

DATA AVAILABILITY STATEMENT

The original contributions presented in the study are included in the article/**Supplementary Material**, further inquiries can be directed to the corresponding author/s.

AUTHOR CONTRIBUTIONS

DM contributed to conception and design of the study. MSt synthesized the title porphyrins. FZ performed SEM characterization of samples. DM, GMag, and MSa performed the Circular Dichroism measurements. MSa and MV performed the fluorescence spectroscopy studies. SB, GMar, and SS performed chiral HPLC analysis. DM organized the database and performed the fitting and statistical analysis. GMag performed the editing of the figures and plots. MSt, DM, MV, CD, SS, and RP wrote sections of the manuscript. RP was responsible for the financial support to the work. All authors contributed to the discussion and interpretation of the results and to manuscript revision, and read and approved the submitted version.

FUNDING

This research was funded by the European Community, H2020-FETOPEN, 828779, INITIO project.

SUPPLEMENTARY MATERIAL

The Supplementary Material for this article can be found online at: <https://www.frontiersin.org/articles/10.3389/fchem.2020.587842/full#supplementary-material>

REFERENCES

- Arteaga, O., El-Hachemi, Z., Canillas, A., Crusats, J., Rovira, M., and Ribó, J. M. (2016). Reversible and irreversible emergence of chiroptical signals in J-aggregates of achiral 4-sulfonatophenyl substituted porphyrins: intrinsic chirality vs. chiral ordering in the solution. *Chem. Commun.* 52, 10874–10877. doi: 10.1039/C6CC05709H
- Belviso, S., Capasso, S., Santoro, E., Najafi, L., Lelj, F., Superchi, S., et al. (2018a). Thioethyl-porphyrazine/nanocarbon hybrids for photoinduced electron transfer. *Adv. Funct. Mater.* 28, 1705418. doi: 10.1002/adfm.201705418
- Belviso, S., Santoro, E., Lelj, F., Casarini, D., Villani, C., Franzini, R., et al. (2018b). Stereochemical stability and absolute configuration of atropisomeric thioalkyl-porphyrazines by dynamic NMR and HPLC studies and computational analysis of HPLC-ECD recorded spectra. *Eur. J. Org. Chem.* 4029–4037. doi: 10.1002/ejoc.201800553
- Berova, N., Di Bari, L., and Pescitelli, G. (2007). Application of electronic circular dichroism in configurational and conformational analysis of organic compounds. *Chem. Soc. Rev.* 36, 914–931. doi: 10.1039/b515476f
- Berova, N., Nakanishi, K., and Woody, R. W. (2000). *Circular Dichroism: Principles and Applications*, 2nd Edn. Weinheim: Wiley-WCH.
- Borovkov, V. V., Harada, T., Hembury, G. A., and Inoue, Y. (2003). Solid-state supramolecular chirogenesis: high optical activity and gradual development of zinc octaethylporphyrin aggregates. *Angew. Chem. Int. Ed.* 42, 1746–1749. doi: 10.1002/anie.200250524
- Borovkov, V. V., and Inoue, Y. (2006). Supramolecular chirogenesis in host-guest systems containing porphyrinoids. *Top. Curr. Chem.* 265, 89–146. doi: 10.1007/128_037
- Borovkov, V. V., Lintuluoto, J. M., Fujiki, M., and Inoue, Y. (2000). Temperature effect on supramolecular chirality induction in bis(zinc porphyrin). *J. Am. Chem. Soc.* 122, 4403–4407. doi: 10.1021/ja9936971
- Borovkov, V. V., Lintuluoto, J. M., and Inoue, Y. (2001). Supramolecular Chirogenesis in zinc porphyrins: mechanism, role of guest structure, and application for the absolute configuration determination. *J. Am. Chem. Soc.* 123, 2979–2989. doi: 10.1021/ja0032982
- Caroleo, F., Stefanelli, M., Magna, G., Venanzi, M., Paolesse, R., Sennato, S., et al. (2019). Kinetic and spectroscopic studies on the chiral self-aggregation of amphiphilic zinc and copper (L)-prolinato-tetraarylporphyrin derivatives in different aqueous media. *Org. Biomol. Chem.* 17, 1113–1120. doi: 10.1039/C8OB02689K
- Caruso, M., Gatto, E., Mazzuca, C., Stella, L., Bocchinfuso, G., Palleschi, A., et al. (2013). Fibrils or globules? Tuning the morphology of peptide aggregates from helical building blocks. *J. Phys. Chem. B* 117, 5448–5459. doi: 10.1021/jp400009j
- Castriciano, M. A., Romeo, A., De Luca, G., Villari, V., Monsù Scolaro, L., and Micali, N. (2011). Scaling the chirality in porphyrin J-nanoaggregates. *J. Am. Chem. Soc.* 133, 765–767. doi: 10.1021/ja110028g
- Castriciano, M. A., Romeo, A., Zagami, R., and Micali, N. (2012). Kinetic effects of tartaric acid on the growth of chiral J-aggregates of

- tetrakis(4-sulfonatophenyl)porphyrin. *Chem. Commun.* 48, 48722–48724. doi: 10.1039/c2cc00028h
- Chen, P., Ma, X., Hu, K., Rong, Y., and Liu, M. (2011). Left or right? The direction of compression-generated vortex-like flow selects the macroscopic chirality of interfacial molecular assemblies. *Chem. Eur. J.* 17, 12108–12114. doi: 10.1002/chem.201101322
- Cui, L., Tokarz, D., Cisek, R., Ng, K. K., Wang, F., Chen, J., et al. (2015). Organized aggregation of porphyrins in lipid bilayers for third harmonic generation microscopy. *Angew. Chem. Int. Ed.* 54, 13928–13932. doi: 10.1002/anie.201506171
- D'Urso, A., Fragalà, M. E., and Purrello, R. (2012). From self-assembly to noncovalent synthesis of programmable porphyrins' arrays in aqueous solution. *Chem. Commun.* 48, 8165–8176. doi: 10.1039/c2cc31856c
- El-Hachemi, Z., Balaban, T. S., Campos, J. L., Cespedes, S., Crusats, J., Escudero, C., et al. (2016). Effects of hydrodynamic forces on meso-(4-sulfonatophenyl)-substituted porphyrin J-aggregate nanoparticles: elasticity, plasticity and breaking. *Chem. Eur. J.* 22, 9740–9749. doi: 10.1002/chem.201600874
- El-Hachemi, Z., Escudero, C., Arteaga, O., Canillas, A., Crusats, J., Mancini, G., et al. (2009). Chiral sign selection on the J-aggregates of deprotonated tetrakis(4-sulfonatophenyl)porphyrin by traces of unidentified chiral contaminants present in the ultra-pure water used as solvent. *Chirality* 21, 408–412. doi: 10.1002/chir.20602
- El-Hachemi, Z., Mancini, G., Ribó, J. M., and Sorrenti, A. (2008). Role of the hydrophobic effect in the transfer of chirality from molecules to complex systems: from chiral surfactants to porphyrin/surfactant aggregates. *J. Am. Chem. Soc.* 130, 15176–15184. doi: 10.1021/ja805669v
- Feldborg, L. N., Saletta, W. J., Iavicoli, P., and Amabilino, D. B. (2011). Central metal ion determined self-assembly of intrinsically chiral porphyrins. *J. Porphyrins Phthalocyanines* 15, 995–1003. doi: 10.1142/S108842461100394X
- Guijarro, A., and Yus, M. (2009). *The Origin of Chirality in the Molecules of Life*. Cambridge: RSC Publishing.
- Intrieri, D., Damiano, C., Rizzato, S., Paolesse, R., Venanzi, M., Monti, D., et al. (2018). Sensing of diclofenac by a porphyrin-based artificial receptor. *New J. Chem.* 42, 15778–15783. doi: 10.1039/C8NJ02737D
- Labuta, J., Hill, J. P., Ishihara, S., Hanykova, L., and Ariga, K. (2015). Chiral sensing by nonchiral tetrapyrroles. *Acc. Chem. Res.* 48, 521–259. doi: 10.1021/acs.accounts.5b00005
- Lee, H., Hong, K.-I., and Jang, W.-D. (2018). Design and applications of molecular probes containing porphyrin derivatives. *Coord. Chem. Rev.* 354, 46–73. doi: 10.1016/j.ccr.2017.06.008
- Liu, M., Zhang, L., and Wang, T. (2015). Supramolecular chirality in self-assembled systems. *Chem. Rev.* 115, 7304–7397. doi: 10.1021/cr500671p
- Lorecchio, C., Venanzi, M., Mazzuca, C., Lettieri, R., Palleschi, A., Thi, T. H. N., et al. (2014). Tuning the chiroptical and morphological properties of steroidal-porphyrin aggregates: a mechanistic, structural, and MM investigation. *Org. Biomol. Chem.* 12, 3956–3963. doi: 10.1039/C4OB00134F
- Magna, G., Monti, D., Di Natale, C., Paolesse, R., and Stefanelli, M. (2019). The assembly of porphyrin systems in well-defined nanostructures: an update. *Molecules* 24:4307. doi: 10.3390/molecules24234307
- Mathew, S. P., Iwamura, H., and Blackmond, D. G. (2004). Amplification of enantiomeric excess in a proline-mediated reaction. *Angew. Chem. Int. Ed.* 43, 3317–3321. doi: 10.1002/anie.200453997
- Micali, N., Engelkamp, H., van Rhee, P. G., Christianen, P. C. M., Monsù Scolaro, L., and Maan, J. C. (2012). Selection of supramolecular chirality by application of rotational and magnetic forces. *Nat. Chem.* 4, 201–207. doi: 10.1038/nchem.1264
- Micali, N., Mallamace, F., Castriciano, M., Romeo, A., and Monsù Scolaro, L. (2001). Separation of scattering and absorption contributions in UV/Visible spectra of resonant systems. *Anal. Chem.* 73, 4958–4963. doi: 10.1021/ac010379n
- Micali, N., Mallamace, F., Romeo, A., Purrello, R., and Monsù Scolaro, L. (2000). Mesoscopic structure of meso-tetrakis(4-sulfonatophenyl)porphyrin J-aggregates. *J. Phys. Chem. B* 104, 5897–5904. doi: 10.1021/jp991909a
- Micali, N., Villari, V., Castriciano, M. A., Romeo, A., and Monsù Scolaro, L. (2006). From fractal to nanorod porphyrin J-aggregates. Concentration-induced tuning of the aggregate size. *J. Phys. Chem. B* 110, 8289–8295. doi: 10.1021/jp060730e
- Monsù Scolaro, L., Castriciano, M., Romeo, A., Mazzaglia, A., Mallamace, F., and Micali, N. (2002). Nucleation effects in the aggregation of water-soluble porphyrin aqueous solutions. *Physica A* 304, 158–169. doi: 10.1016/S0378-4371(01)00547-7
- Monti, D. (2014). Recent advancements in chiral porphyrin self-assembly. *Top. Heterocycl. Chem.* 33, 231–292. doi: 10.1007/7081_2013_110
- Monti, D., De Rossi, M., Sorrenti, A., Laguzzi, G., Gatto, E., Stefanelli, M., et al. (2010). Supramolecular Chirality in solvent-promoted aggregation of amphiphilic porphyrin derivatives: kinetic studies and comparison between solution behavior and solid-state morphology by AFM topography. *Chem. Eur. J.* 16, 860–870. doi: 10.1002/chem.200901964
- Ohno, O., Kaizu, Y., and Kobayashi, H. (1993). J-aggregate formation of a water-soluble porphyrin in acidic aqueous media. *J. Chem. Phys.* 99, 4128–4139. doi: 10.1063/1.466109
- Oliveira-González, C., Di Meo, F., González-Campo, A., Beljonne, D., Norman, P., Simeón-Sorbed, M., et al. (2015). Bottom-up hierarchical self-assembly of chiral porphyrins through hydrogen bonds. *J. Am. Chem. Soc.* 137, 15795–15808. doi: 10.1021/jacs.5b08081
- Paolesse, R., Monti, D., Dini, F., and Di Natale, C. (2011). Fluorescence based sensor arrays. *Top. Curr. Chem.* 300, 139–174. doi: 10.1007/128_2010_97
- Paolesse, R., Nardis, S., Monti, D., Stefanelli, M., and Di Natale, C. (2017). Porphyrinoids for chemical sensor applications. *Chem. Rev.* 117, 2517–2583. doi: 10.1021/acs.chemrev.6b00361
- Pasternack, R., Gibbs, E. J., Bruzewicz, D., Stewart, D., and Engstrom, K. S. (2002). Kinetics of disassembly of a DNA-bound porphyrin supramolecular array. *J. Am. Chem. Soc.* 124, 3533–3539. doi: 10.1021/ja0124820
- Pasternack, R. F., Bustamante, C., Collings, P. J., Giannetto, A., and Gibbs, E. J. (1993). Porphyrin assemblies on DNA as studied by a Resonance Light-Scattering technique. *J. Am. Chem. Soc.* 115, 5393–5399. doi: 10.1021/ja00066a006
- Pasternack, R. F., Fleming, C., Herring, S., Collings, P. J., dePaula, J., DeCastro, G., et al. (2000). Aggregation kinetics of extended porphyrins and cyanine dyes assemblies. *Biophys. J.* 79, 550–560. doi: 10.1016/S0006-3495(00)76316-8
- Romeo, A., Castriciano, M. A., Occhiuto, I., Zagami, R., Pasternack, R. F., and Monsù Scolaro, L. (2014). Kinetic control of chirality in porphyrin J-aggregates. *J. Am. Chem. Soc.* 136, 40–43. doi: 10.1021/ja410514k
- Simoncini, E., Caroleo, F., Ceccacci, F., Mancini, G., Stefanelli, M., Paolesse, R., et al. (2014). Surfactant-induced chirality on reluctant aggregates of a chiral amphiphilic cationic (L)-proline-Zn(II)porphyrin conjugate in water. *RSC Adv.* 4, 55362–55366. doi: 10.1039/C4RA05870D
- Sorrenti, A., El-Hachemi, Z., Arteaga, O., Canillas, A., Crusats, J., and Ribó, J. M. (2012). Kinetic control of the supramolecular chirality of porphyrin J-aggregates. *Chem. Eur. J.* 18, 8820–8826. doi: 10.1002/chem.201200881
- Sorrenti, A., Rodríguez-Trujillo, R., Amabilino, D. B., and Puigmartí-Luis, J. (2016). Milliseconds make the difference in far-from-equilibrium self-assembly of supramolecular chiral nanostructures. *J. Am. Chem. Soc.* 138, 6920–6923. doi: 10.1021/jacs.6b02538
- Stefanelli, M., Magna, G., Zurlo, F., Caso, F. M., Di Bartolomeo, E., Antonaroli, S., et al. (2019). Chiral selectivity of porphyrin-ZnO nanoparticle conjugates. *ACS Appl. Mater. Interfaces* 11, 12077–12087. doi: 10.1021/acsami.8b22749
- Valev, V. K., Baumberg, J. J., De Clercq, B., Braz, N., Zheng, X., Osley, E. J., et al. (2014). Nonlinear superchiral meta-surfaces: tuning chirality and disentangling non-reciprocity at the nanoscale. *Adv. Mater.* 26, 4074–4081. doi: 10.1002/adma.201401021
- van der Weegen, R., Teunissen, A. J. P., and Meijer, E. W. (2017). Directing the self-assembly behavior of porphyrin-based supramolecular systems. *Chem. Eur. J.* 23, 3773–3783. doi: 10.1002/chem.201605872
- Wang, Y., Xu, J., Wang, Y., and Chen, H. (2013). Emerging chirality in nanoscience. *Chem. Soc. Rev.* 42, 2930–2962. doi: 10.1039/C2CS35332F
- Yoon, M., Srirambalaji, R., and Kim, K. (2012). Homochiral metal-organic frameworks for asymmetric heterogeneous catalysis. *Chem. Rev.* 112, 1196–1231. doi: 10.1021/cr2003147
- Zelenka, K., Trnka, T., Tislerová, I., Monti, D., Cinti, S., Naitana, M. L., et al. (2011). Spectroscopic, morphological, and mechanistic investigation of the solvent-promoted aggregation of porphyrins modified in meso-positions by glucosylated steroids. *Chem. Eur. J.* 17, 13743–13753. doi: 10.1002/chem.201101163

Zhou, C., Feng, X., Wang, R., Yang, G., Wang, T., and Jiang, J. (2018). Hierarchical assembly of L-phenylalanine-terminated bolaamphiphile with porphyrin show tunable nanostructures and photocatalytic properties. *ACS Omega* 3, 10638–10646. doi: 10.1021/acsomega.8b01822

Conflict of Interest: The authors declare that the research was conducted in the absence of any commercial or financial relationships that could be construed as a potential conflict of interest.

Copyright © 2020 Stefanelli, Savioli, Zurlo, Magna, Belviso, Marsico, Superchi, Venanzi, Di Natale, Paolesse and Monti. This is an open-access article distributed under the terms of the Creative Commons Attribution License (CC BY). The use, distribution or reproduction in other forums is permitted, provided the original author(s) and the copyright owner(s) are credited and that the original publication in this journal is cited, in accordance with accepted academic practice. No use, distribution or reproduction is permitted which does not comply with these terms.



Recent Progress in Optically-Active Phthalocyanines and Their Related Azamacrocycles

Yusuke Okada¹, Tomonori Hoshi² and Nagao Kobayashi^{1*}

¹ Faculty of Textile Science and Technology, Shinshu University, Ueda, Japan, ² Clinical Research, Innovation and Education Center, Tohoku University Hospital, Sendai, Japan

OPEN ACCESS

Edited by:

Victor Borovkov,
South-Central University for
Nationalities, China

Reviewed by:

Tomas Torres,
Autonomous University of
Madrid, Spain
Norio Shibata,
Nagoya Institute of Technology, Japan
Dmitry Valentinovich Konarev,
Institute of Problems of Chemical
Physics (RAS), Russia

*Correspondence:

Nagao Kobayashi
nagaok@shinshu-u.ac.jp;
nagaok@m.tohoku.ac.jp

Specialty section:

This article was submitted to
Supramolecular Chemistry,
a section of the journal
Frontiers in Chemistry

Received: 18 August 2020

Accepted: 28 September 2020

Published: 19 October 2020

Citation:

Okada Y, Hoshi T and Kobayashi N
(2020) Recent Progress in
Optically-Active Phthalocyanines and
Their Related Azamacrocycles.
Front. Chem. 8:595998.
doi: 10.3389/fchem.2020.595998

Optically-active phthalocyanines (Pcs) and related macrocycles reported in the 2010–2020 period are introduced in this review. They are grouped into several categories: (1) chiral binaphthyl-containing Pcs, (2) optically active alkyl chain-containing Pcs, (3) chiral axial ligand-coordinated or -linked Pcs, (4) chiral subphthalocyanines (SubPcs), and (5) related azamacrocycles. For each compound, the structure and important characteristics are summarized.

Keywords: chiral, optically active, phthalocyanine, binaphthyl, circular dichroism, porphyrin

INTRODUCTION

Optically-active or chiral macrocycles of azaporphyrinoids have attracted the attention of synthetic and theoretical chemists, as well as researchers in the fields of applied chemistry and physics, and natural science (Kadish et al., 2003a). Although some small chiral molecules including porphyrins have been studied due to their relatively easy synthesis and specific optical, medicinal, and catalytic properties (Kadish et al., 2000, 2003b), optically active azaporphyrins including phthalocyanines (Pcs) have mainly been introduced by researchers who want to have intense CD signal in the visible region, since azaporphyrins have theoretically more intense absorption band than normal porphyrins in the visible region (the so-called Q band). In the twenty-first century, several review articles have already been published (Kobayashi, 2001, 2010, 2012; Lu and Kobayashi, 2016). However, in this review, we summarize the reports on chiral Pcs and their related macrocycles published in the last 10 years, between 2010 and 2020. After collecting papers on chiral, i.e., optically-active Pcs and related macrocycles, we observed that they are roughly grouped into five categories: (1) chiral binaphthyl (Binap) and related aromatic molecule-containing Pcs, (2) optically-active alkyl chain-containing Pcs, (3) chiral axial ligand-coordinated or -linked Pcs, (4) chiral subphthalocyanines (SubPcs), and (5) related azamacrocycles. Papers containing chiral binaphthyls number more than half of these publications, and this may be due to several factors: easy preparation of binaphthyl-linked precursors, very little possibility of racemization under the experimental conditions, and an expected large circular dichroism (CD) intensity. Reports on optically-active alkyl chain-containing Pcs are also frequently seen, and these are generally used to examine liquid crystalline properties, since long alkyl chain (generally more than 10 carbon)-containing Pcs are known to form liquid crystals (= mesophase) by varying the temperature. Other interesting azamacrocycles which can be congeners of or related to Pcs have also appeared from several groups across the world. We introduce these in order in this review.

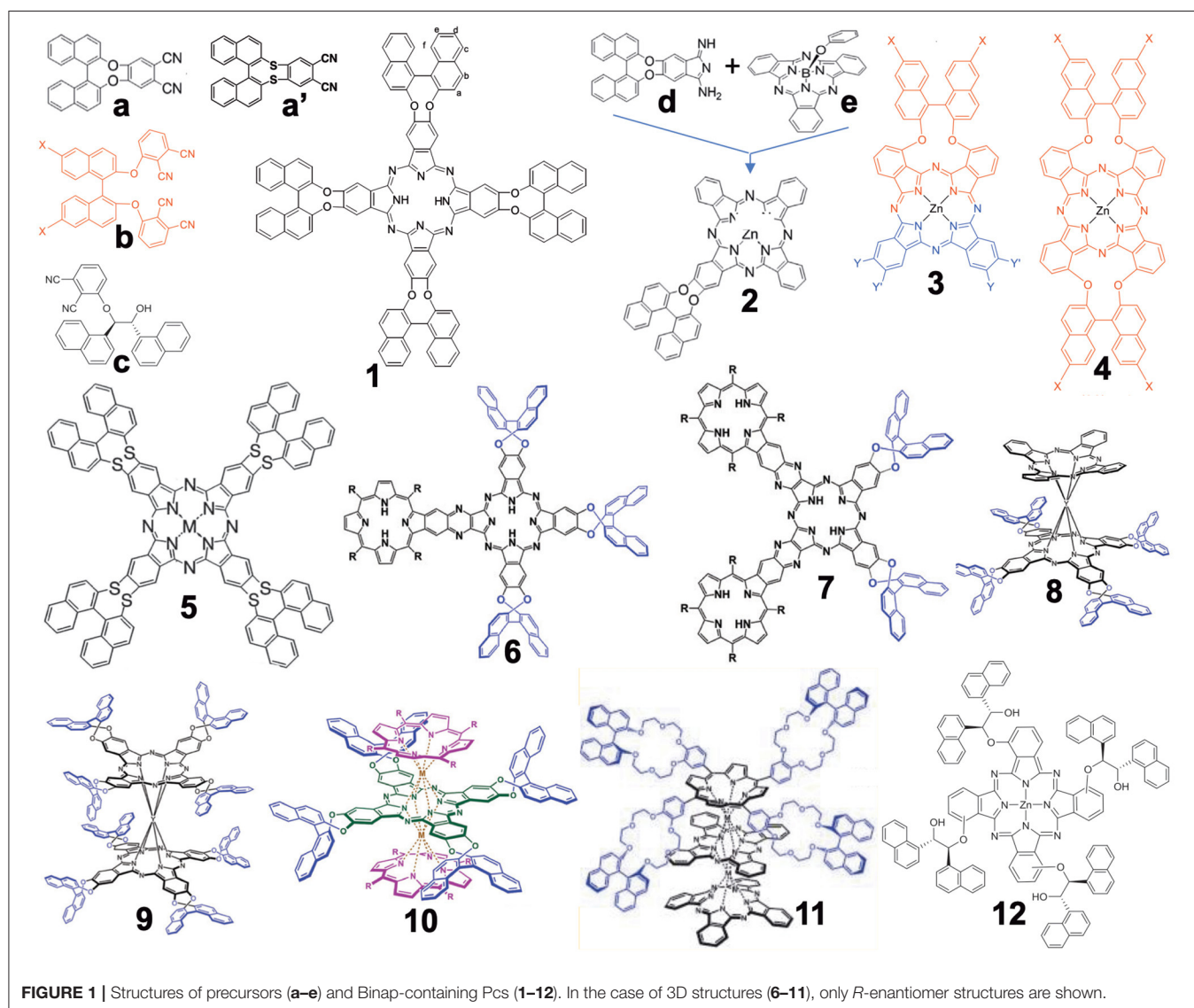
BINAP AND BINAP-RELATED SUBSTITUENT-LINKED SYSTEMS

Synthesis

Figure 1 summarizes the structures grouped into this category (in the case of 3D-structures, **6–11**, only *R*-enantiomers which have an anti-clockwise binaphthyl structure are shown). In 2012, the synthesis of compound **1** from precursor **a** was reported (Wang et al., 2012). Previously, similar compounds **4** had been reported from a precursor containing sulfur instead of oxygen in **a** (i.e., **a'**) (Kobayashi et al., 1999a) due to the then-known low racemization probability of **a'** under the experimental conditions. However, it was possible to prepare **a** from commercially available 2,2'-dihydroxybinaphthyl and 4,5-dichlorophthalonitrile in one step without racemization, while the cyclic tetramerization step leading to **1** was also free from racemization. Accordingly, both **a** and **1** were later used in chiral Pc chemistry. For

example, the zinc complex of **1** could form a cofacial dimer by stepwise coordination of two quinuclidine molecules (Giménez-Agulló et al., 2016), which was confirmed by the change of absorption spectra and $^1\text{H-NMR}$ signal. In addition, **1** was used to construct chiral bis(phthalocyaninato)yttrium double-decker complexes **8** and **9** (Zhou et al., 2014), as well as a porphyrin-Pc heteroleptic rare-earth triple-decker complex **10** (Wang et al., 2014). These were synthesized by metal-free **1** and $\text{Y}(\text{acac})_3 \cdot n\text{H}_2\text{O}$ or **1** and metal-free porphyrin or Pc in the presence of $\text{Y}(\text{acac})_3 \cdot n\text{H}_2\text{O}$ or $\text{Dy}(\text{acac})_3 \cdot n\text{H}_2\text{O}$, followed by purification using column chromatography.

Compound **2** was obtained by ring-expansion reaction of a SubPc with isoindole derivative **d** which was obtained by bubbling ammonia gas to dinitrile **a** (Zhao et al., 2015). The ring-expansion using SubPc and isoindoline derivatives *per se* was introduced in 1990 as a means to obtain mono-substituted ABBB-type Pcs (Kobayashi et al., 1990, 1999b). Since then,



more than 300 papers have appeared on the use of this method (Claessens et al., 2002, 2014; Kobayashi, 2002). Compounds **3** and **4** containing long alkyl chains were prepared by Torres' group in order to study their aggregation (Revuelta-Maza et al., 2019). The precursor **b** was reported as early as 1998 as a stable phthalonitrile which does not racemize under normal Pc formation conditions (Kobayashi, 1998), so that the reaction of **b** and long-alkyl chain-containing phthalonitrile afforded Pc **3** preferentially, and reactions of only **b** produced **4** in relatively high yield.

Compounds **6** and **7** contain porphyrin units. In order to synthesize these compounds, mixed condensation between **a** and pyrazinonitrile fused to a trimethylphenylporphyrin was performed in the presence of lithium in refluxing pentanol, and **6** and **7** were separated after purification using column chromatography in ca. 6–10% yield (Zhang et al., 2017). Triple-decker compound **11** containing both porphyrin and two Pc units were prepared in ca. 40% yield by reacting the corresponding metal-free crowned binaphthyl-linked porphyrin and substituent-free H₂Pc in the presence of a rare-earth metal, Mt(acac)₃·nH₂O (Mt = Eu, Y), in refluxing trichlorobenzene (Lu et al., 2011). Although the reaction temperature was 218°, no racemization of the binaphthyl unit occurred.

Compound **12** was synthesized from precursor **c** which was prepared from 3-nitrophthalonitrile and (1*R*,2*R*)-1,2-di(naphthalen-1-yl) ethane-1,2-diol in the presence of Zn(OAc)₂·nH₂O and a catalytic amount of DBU (1,8-dia-zabicyclo[5.4.0]undec-7-ene) by a Turkish group (Gok et al., 2018).

Spectroscopic Properties

It is important to show at least the electronic absorption, circular dichroism (CD), and magnetic circular dichroism (MCD) spectra of representative compounds. **Figure 2** shows some spectra of compounds **1**, **5**, **9**, and **10**. The absorption and MCD spectra of **1** are typical of those of metal-free Pcs, in that it shows four Q-band peaks and Faraday B-term MCD (Fukuda and Kobayashi, 2010). (*R*)- and (*S*)-enantiomers show mainly positive and negative CD, respectively, similarly to **5** (Kobayashi et al., 1999a). A small negative CD trough observed at 782 nm for the (*R*)-enantiomer suggests that **1** is not completely planar. **9** is a cofacial rare-earth double decker. The interpretation of the spectra of these types of double-decker Pcs and porphyrins was already reported in 2005 (Muranaka et al., 2005). Similarly to **1**, (*R*)- and (*S*)-enantiomers show positive and negative CD, respectively, associated with each absorption peak. Although the apparent absorption coefficient of the Q band is larger than that in the Soret region, inversely, the Soret band CD intensity is much larger than the Q band CD intensity, which is due to the energy difference in the binaphthyl absorption (ca. 220–250 nm) and the Soret (ca. 330–350 nm) or Q band (ca. 670 nm). Here, since the induced CD intensity is proportional to $1/(\nu_N^2 - \nu_{Pc}^2)$, where ν_N and ν_{Pc} are the frequencies of the absorption of naphthalene and Pc, respectively, the Soret band CD becomes stronger than the Q band CD (Kobayashi et al., 2012).

The curves in **Figure 2C** are both the fluorescence-detected CD (FDICD) (ca. 200–270 nm) and FD “induced” CD (FDICD) spectra (ca. 270–700 nm) observed for the metal-free and zinc complexes of **5**, of which the latter FDICD data are the only

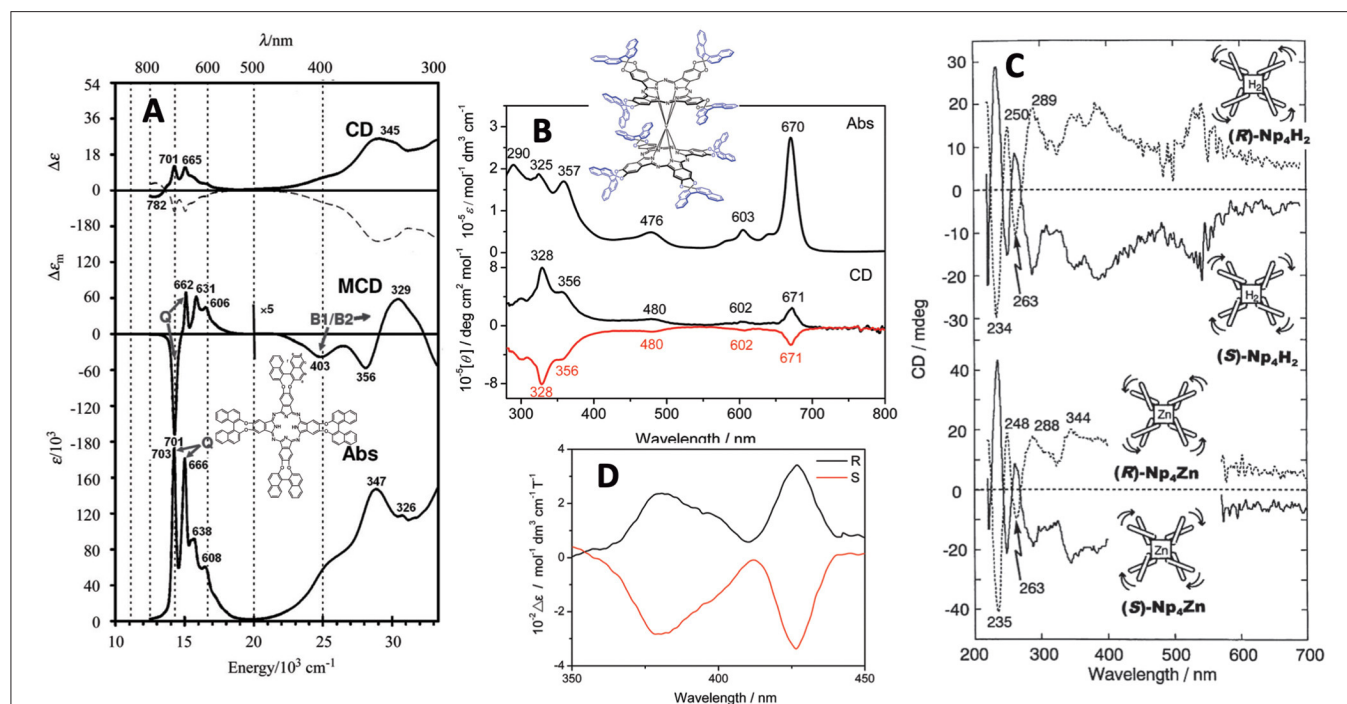


FIGURE 2 | (A) Absorption, MCD and CD spectra of **1** [solid and broken lines are for (*R*)- and (*S*)-enantiomer, respectively], **(B)** Absorption and CD spectra of **9** [black and red lines are for (*R*)- and (*S*)-enantiomer, respectively], **(C)** FDICD (ca. 220–270 nm) and FDICD spectra (ca. 270–700 nm) for metal-free (top) and zinc (bottom) derivatives of **5**, and **(D)** magnet-chiral dichroism spectra of **10**. Adapted from Kobayashi (2012) and Wang et al. (2012, 2014).

published data for any compound (Kobayashi, 2012). The FDICD signal was positive for (*R*)-binaphthyl linked species (left-handed conformer), while negative for (*S*)-binaphthyl linked Pcs, suggesting that the (*S*) species (right-handed conformer) absorbs right-circularly polarized light more than the left, and *vice versa* for the (*R*) species (left-handed conformer).

The spectra in **Figure 2D** are the rare magnet-chiral dichroism spectra of **10** in the 360–450 nm region where strong ICD and MCD signs were detected. The value of $\Delta\epsilon$ ($= 10^2 \text{ mol}^{-1}\text{dm}^3\text{cm}^{-1}\text{T}^{-1}$), was comparable to those reported previously in porphyrinoids (Kitagawa et al., 2011, 2012).

Comparing the absorption spectra of **6** and **7**, the Q band of **6** splits, while that of **7** does not, as proven by group theory (Kobayashi and Konami, 1996). In these cases, the absorptions are roughly expressed as a summation of the spectra of porphyrin and Pc, but the Q band region is mainly the contribution from the Pc moiety. Viewing from the Pc structure, **6** is mono-substituted type Pc, while **7** is adjacent-type di-substituted Pc, so that Q band of Pc **6** splits. In both cases, the (*R*)- and (*S*)-enantiomer showed mainly positive and negative CD, respectively. The Q-band MCD of **7** is dispersion type pseudo Faraday A term, since the splitting of the Q_x and Q_y bands is small. The CD spectra of **11** are noisy, due to the long distance of the perturber (binaphthyl units) from the macrocyclic chromophore. Faraday A-term MCD curves were observed corresponding to each absorption peak, since the excited state of this type of porphyrinoid is orbitally doubly degenerate (Muranaka et al., 2005). Compound **12** was prepared only from 3-((1'*R*,2'*R*)-2-hydroxy-1',2'-dinaphthylethoxy)phthalonitrile **c**, and no Pc from the corresponding (1'*S*,2'*S*)-enantiomer was reported. Its absorption spectrum is normal, similar to that of regular Pcs, and weak negative CD envelopes were detected associated with the Q and Soret bands.

OPTICALLY-ACTIVE ALKYL CHAIN-CONTAINING PHTHALOCYANINES

Synthesis

Chiral alkyl chain-containing Pcs have often been prepared in order to examine their liquid crystalline properties (Ohta et al., 2011; Basova et al., 2016). The structures of Pc compounds categorized in this group are shown in **Figure 3**, which are all reported from Zhang's group. As seen in the figure, all substituents contain chiral (*S*)-2-methylbutoxy moieties next to the Pc skeleton or at the outer end of substituent groups. The reaction of 3-nitrophthalonitrile with (*S*)-2-methylbutanol in the presence of K_2CO_3 produced 3-((*S*)-2-methylbutoxy)phthalonitrile, whose cyclic tetramerization performed using lithium or in the presence of $\text{Zn}(\text{OAc})_2 \cdot 2\text{H}_2\text{O}$ or $\text{Cu}(\text{OAc})_2 \cdot n\text{H}_2\text{O}$ and DBU produced **13**((*S*)-**H₂Pc**-, **13**(**ZnPc**-, or **13**(**CuPc**($\alpha\text{-OC}_5\text{H}_{11}$)₄), respectively (Tian et al., 2013a).

A similar reaction between (*S*)-4-hydroxy-4'-(2-methylbutoxy)biphenyl and 4,5-dichloro-1,2-dicyanobenzene in the presence of K_2CO_3 in DMF produced 1,2-dicyano-4,5-bis[(*S*)-4'-(2-methylbutoxy)biphenyl]benzene, which was then tetramerized similarly, to yield octa-substituted H_2 - and ZnPc s at β -positions, i.e., **14**((*S*)-**H₂Pc**-A) and **14**((*S*)-**ZnPc**-A) (Zhang et al., 2013). **14**((*S*)-**H₂Pc**-B) and **14**((*S*)-**CuPc**-B) were similarly prepared using a phthalonitrile having a long alkyl chain at the 4,5-positions, which was synthesized in four steps starting from catechol (Tian et al., 2013b). **14**((*S*)-**Cu**- and -**CoPc**($\beta\text{OC}_5\text{H}_{11}$)₈) were synthesized using 4,5-di-((*S*)-2-methylbutoxy)phthalonitrile that was prepared by reacting (*S*)-2-methylbutanol with 4,5-dichlorophthalonitrile. **15**(**CoPc**($\alpha\text{OC}_5\text{H}_{11}$)₈) was prepared using 3,6-di-((*S*)-2-methylbutoxy)phthalonitrile which was prepared by reaction

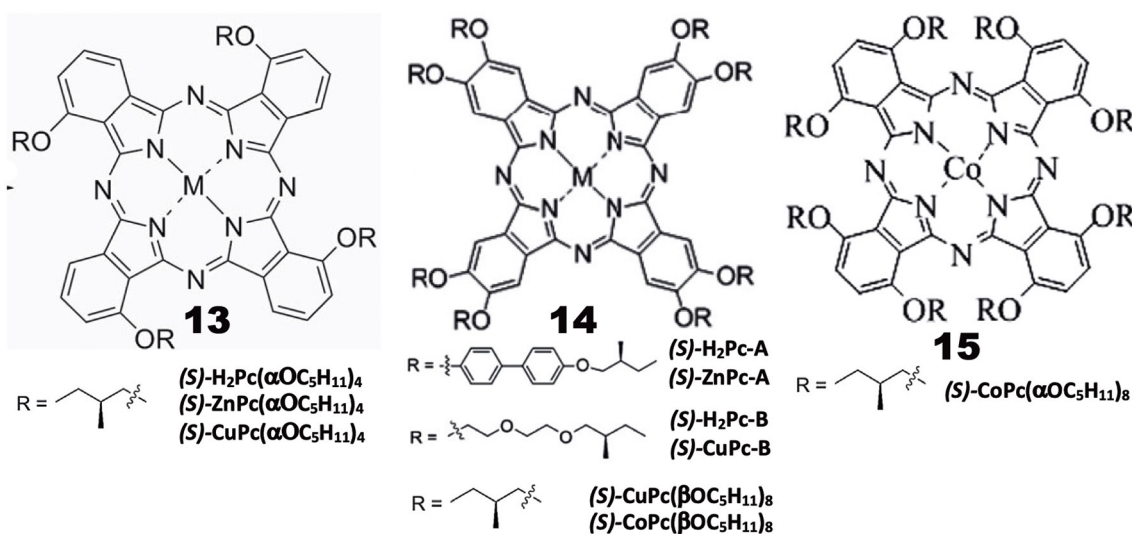


FIGURE 3 | Structures of optically-active alkyl chain-containing phthalocyanines.

between (*S*)-2-methylbutanol and 3,6-dihydroxyphthalonitrile (Lin et al., 2015).

Properties

Induced CD spectra due to optically-active carbon is generally very weak (Kobayashi et al., 2012), and is not well-reproduced by theoretical calculations. Indeed, although most of the Pc compounds in **Figure 3** showed weak, noisy CD signals in the Q-band region, their sign is different from compound to compound, irrespective of containing only (*S*)-2-methylbutoxy moieties, i.e., **13**((*S*)-MtPc(α OC₅H₁₁)₄) (Mt = H₂, Zn, Cu), **14**((*S*)-CuPc(α OC₅H₁₁)₈), **14**((*S*)-H₂Pc-A), **14**((*S*)-ZnPc-A), **14**((*S*)-Cu- and **14**((*S*)-CoPc(β OC₅H₁₁)₈), exhibited a positive sign, and the intensity of **15**((*S*)-CoPc(α OC₅H₁₁)₈) is almost zero, while both **14**((*S*)-H₂- and **14**((*S*)-ZnPc-B) showed a negative sign in dilute solutions where aggregation can be neglected. The absorption and CD spectra of aggregates became broader and the CD intensity is stronger than in solution. However, no interpretation is given. It is a pity that the authors did not try similar experiments using compounds containing (*R*)-2-methylbutoxy groups. It is interesting to examine whether the CD of (*R*)-enantiomers always produce signals having a mirror image relationship to those of (*S*)-enantiomers, particularly since Pc compounds containing only (*S*)-2-methylbutoxy groups show both positive and negative CD signs depending on the system.

Investigation of the self-assembled **13**((*S*)-H₂Pc- and **13**((*S*)-ZnPc(α -OC₅H₁₁)₄) by IR and X-ray photoelectron spectroscopies (XPS), and by transmission electronic- (TEM) and scanning electronic (SEM) microscopies, revealed that the metal-free **13**((*S*)-H₂Pc(α -OC₅H₁₁)₄) gets together to form a nanocube, while its zinc derivative, **13**((*S*)-ZnPc(α -OC₅H₁₁)₄), gets together to produce assembly of helical nanobelts, which implies that the morphology and handedness of the self-assembled nano-structures are affected by metal coordination (Tian et al., 2013a). Similarly, with respect to **14**((*S*)-H₂Pc-A) and **14**((*S*)-ZnPc-A), it was found that the molecular packing in the nano-structures is influenced by the metal-coordination bond, resulting in nano-structured assembly with different morphologies, ranging from nanosheet for **14**((*S*)-H₂Pc-A) to helical nanofibers for **14**((*S*)-ZnPc-A). In the cases of **14**((*S*)-H₂Pc-B) and **14**((*S*)-CuPc-B), the former H₂Pc self-assembles into clockwise right-handed screw-like

fibers (ca. 10 μ m length, 6 μ m width, and 1.5 μ m helical pitch), while the latter CuPc self-assembly into anti-clockwise left-handed aggregates of fibers (ca. 25 μ m length, 1 μ m width, and 0.7 μ m helical pitch) (Tian et al., 2013b). In the mesophase, **15**((*S*)-CuPc(α OC₅H₁₁)₄) gathers into rectangular columnar liquid crystals with anti-clockwise fan textured structure. However, from **14**((*S*)-CuPc(β OC₅H₁₁)₈), hexagonal columnar liquid crystals with well-ordered, rare, clockwise spherulites were produced. The helical self-assembly and non-linear optical properties of (*S*)-CoPc(α OC₅H₁₁)₈ were comparatively investigated with its analog having the same chiral moieties linked by substituents at β -positions, i.e., **15**((*S*)-CoPc(β OC₅H₁₁)₈) (Lin et al., 2015). Although these two compounds have the identical chiral functional group, they showed different CD signals in the Q absorption region of the corresponding complex, and gathered into different morphologies. At the initial stage, they got together into clockwise ribbon-like structures, while in the further later stage of assembly, they formed either clockwise or anti-clockwise fibrous structures.

CHIRAL SUBPHTHALOCYANINE SYSTEMS

General Pcs consist of four isoindoline units and are almost flat, but subphthalocyanine (SubPc) is a Pc congener consisting of three isoindoline units and boron coordinated with an axial ligand (**Figure 4**). Accordingly, it has a cone-shaped structure and blue-shifted Soret and Q bands. As a chiral SubPc, peripherally chiral binaphthyl-linked SubPc **16** has been known since 2014 (Zhao et al., 2014). The starting materials are (*S*)- and (*R*)-**a** in **Figure 1**. By refluxing these in the presence of BCl₃ in 1,2,4-trichlorobenzene, the target SubPcs **16** were obtained in ca. 33% yield. Even the ¹H-NMR spectra are interesting in that the ring-current effect is different between the *endo* and *exo* sides (the ring current of the SubPc ring is stronger in the concave side of the bowl than the convex side) (Shimizu et al., 2012). Thus, since one binaphthyl unit lies on the *exo* side while the other lies on the *endo* side, the ¹H proton signals of binaphthyl appeared far away from each other.

Subnaphthalocyanine (SubNc) can be obtained by reacting naphthalonitrile in the presence of a boron compound, such as

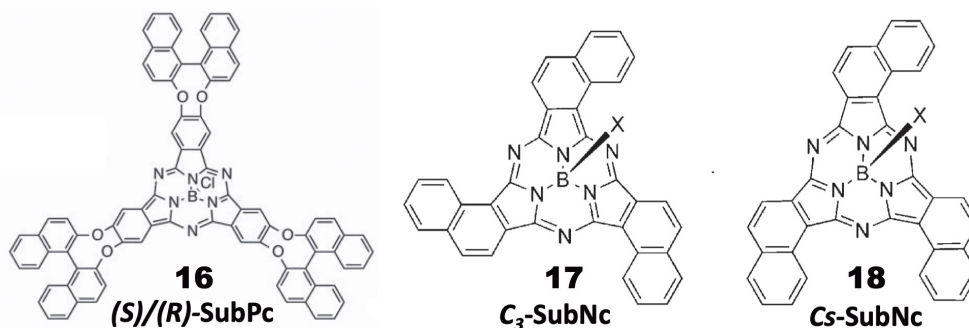


FIGURE 4 | Structures of (*S*)- or (*R*)-binaphthyl-linked SubPc **16** and C₃- **17** and C_s-subnaphthalocyanine (SubNc) **18**.

BCl_3 in a solvent, such as dimethylbenzene or trimethylbenzene (Kobayashi, 2002). If 1,2-dicyanonaphthalonitrile is used as a starting material, the product is a mixture of inherently chiral C_3 -SubNc **17** and C_s -SubNc **18** isomers, which can be separated by column chromatography. Further, each isomer can be resolved, by using chiral columns, to clockwise and anti-clockwise enantiomers viewing from the axial ligand (Shimizu et al., 2011).

Figure 5 shows the absorption, fluorescence, CD and MCD spectra of SubPc with chiral binaphthyl-linked SubPc and C_3 -SubNc **17**. The Q and Soret bands of SubPc generally appear at 570 and 280–300 nm, blue-shifted compared with those of Pcs [ca. 650–680 and 330–350 nm, respectively (Fukuda and Kobayashi, 2010)]. The Q-band MCD signals are mainly a contribution of Faraday C terms, since the SubPc chromophore itself can be approximated as having C_{3v} symmetry, i.e., the first excited state is doubly degenerate. The enantiomer with (*R*)- and (*S*)-chirality in the binaphthyl moiety produced plus and minus CD signs, respectively, over the whole window region. The angle between the two naphthyl units in binaphthyl is about 66 degrees, and the sign and intensity of CD can be reasonably explained similarly to the chiral binaphthyl-linked Pc systems (Kobayashi et al., 1999a), although the SubPc system might be slightly more difficult due to its bowl-shaped structure. Nevertheless, molecular orbital calculations using the TD-DFT method succeeded in reproducing the minus CD signals associated with the Q and Soret bands of the (*S*)-SubPc **16** compound. The absorption spectrum (particularly wavelengths) of 1,2-SubNc does not differ significantly from that of SubPc, since outer benzene rings are not fused in a radial direction, viewing from the central boron

of the molecule (Kobayashi and Konami, 1996). The two peaks on the longer-wavelength side of the Soret band are characteristic of naphthalocyanine derivatives (Kobayashi, 2002). Although not shown in this review, the absorption spectrum of the C_s -isomer **18** is almost identical to that of the C_3 -isomer **17** in **Figure 5B**, so that the MCD spectra of the two isomers also have very similar band shape to each other. However, the CD intensity of these isomers are quite different, where that of the C_3 -isomer **17** is about three times stronger than for the C_s -isomer **18**. Theoretically, the CD intensity (rotational strength) is directly proportionate to the product of the transition electric moment (μ) and the transition magnetic moment (m), i.e., μm , whilst the absorption intensity (oscillator strength) is proportionate to the square of μ , i.e., μ^2 (Kobayashi et al., 2012). The fact that the absorption spectra of the C_3 - **17** and C_s -isomers **18** are almost identical means that the μ values of these two compounds are also considered almost identical. Therefore, we can attribute the CD intensity difference between the C_3 - **17** and C_s -isomers **18** to m . The transition magnetic moment m is generated along the *z*-direction when charge is rotated in the *x-y* plane. If we compare the geometrical structures of the C_3 - **17** and C_s -isomers **18** of 1,2-SubNcs, it sounds feasible that the net m values of the C_3 -isomer **17** are lessened to one-third in C_s -isomer **18** by one oppositely-arranged naphthalene moiety in the latter isomer. Thus, this is a very rare but exemplary system which certifies that the magnitude of m is really parallels the rotation of charge. The absolute structure of C_3 -SubNcs **17** elucidated by X-ray crystallography led to a comprehensive understanding of the structure-chirality relationship of 1,2-SubNcs; i.e., the minus CD signals in the Q-band region indicate a molecular structure where

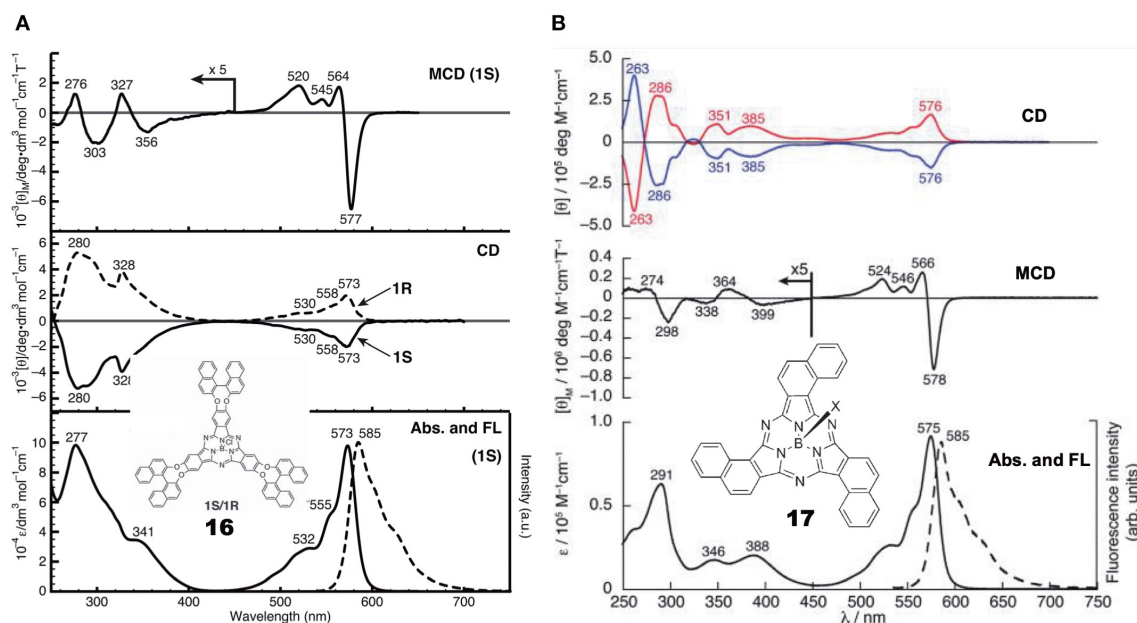


FIGURE 5 | Electronic absorption, fluorescence, CD, and MCD spectra of **(A)** chiral binaphthyl-linked SubPc **16**, and **(B)** C_3 -SubNc **17**. In the CD of C_3 -SubNc **17**, the red and blue lines are from enantiomers whose naphthalene rings are arranged anti-clockwise and clockwise, respectively. Adapted from Shimizu et al. (2011) and Zhao et al. (2014).

the naphthalene moieties are arranged right-handed, whilst the plus CD signals in the same region indicate an left-handed arrangement viewing from the axial ligand side.

OPTICALLY-ACTIVE SYSTEMS DUE TO COORDINATION OF CHIRAL LIGANDS

Many chromophores are not optically active, but by coordination of an extraneous chiral ligand, the system becomes optically active. Zhang et al. (2011) added equimolar amounts of chiral diamine to tetracarboxyphthalocyanine metal complexes (MtTCPc, Mt = Cu, Ni) in DMSO/CHCl₃ mixed solvent, and succeeded in inducing CD signals in the region of the absorption spectrum. The diamines used were: (1*R*,2*R*)-(-)- and (1*S*,2*S*)-(+)-1,2-diaminocyclohexane, (1*R*,2*R*)-(+)- and (1*S*,2*S*)-(+)-1,2-diphenyl-1,2-ethylenediamine (DPEA), (*R*)-1,1'- and (*S*)-1,1'-binaphthyl-2,2'-diamine, in addition to (*R*)-1-phenylethanamine, (*R*)-1-(naphthalene-1-yl)-ethanamine, and (-)-sparteine. The CD signal induced by adding (1*R*,2*R*)- and (1*S*,2*S*)-diamine exhibited a mirror-symmetry structure in relation to the signal intensity = zero line, and its intensity was largest when the amount of diamine was equimolar to that of MtTCPc. By increasing CHCl₃ (poor solvent) in DMSO (good solvent) from 1:1 (v/v), the absorption spectrum changed to

that of cofacial aggregates, and concomitantly the CD intensity decreased. Surprisingly, in the presence of (*R*)- or (*S*)-DPEA, MtTCPc (M = Ni, Cu) showed no significant CD and UV/Vis spectral changes before and after the addition of an equimolar amount of the corresponding antipode ((*S*)- or (*R*)-DPEA, totally, *R*/*S* or *S*/*R* = 1:1), implying a very quick self-gathering ability of MtTCPc that produces highly stable optically-active MtTCPc π - π stacks whose chirality is immobilized firmly.

The aggregate's morphology of supramolecular MtTCPc was studied by high resolution TEM. Samples on a carbon-coated copper minigrid were prepared by casting a drop of MtTCPc solution onto its surface. This showed that supramolecular MtTCPcs (M = Ni, Cu) adopted an entangled structure composed of nano-structural fibers of about 10 nm diameter and 150–700 nm length.

CHIRAL CONGENERS OF PHTHALOCYANINE-RELATED COMPOUNDS

Four papers reporting various types of hemiporphyrazine (Figure 6) were found in this category, and they are introduced in chronological order. *anti*-19 and *syn*-19 were prepared at a ratio of ca. 1:1 by heating an equimolar amount of isoindoleidiimine

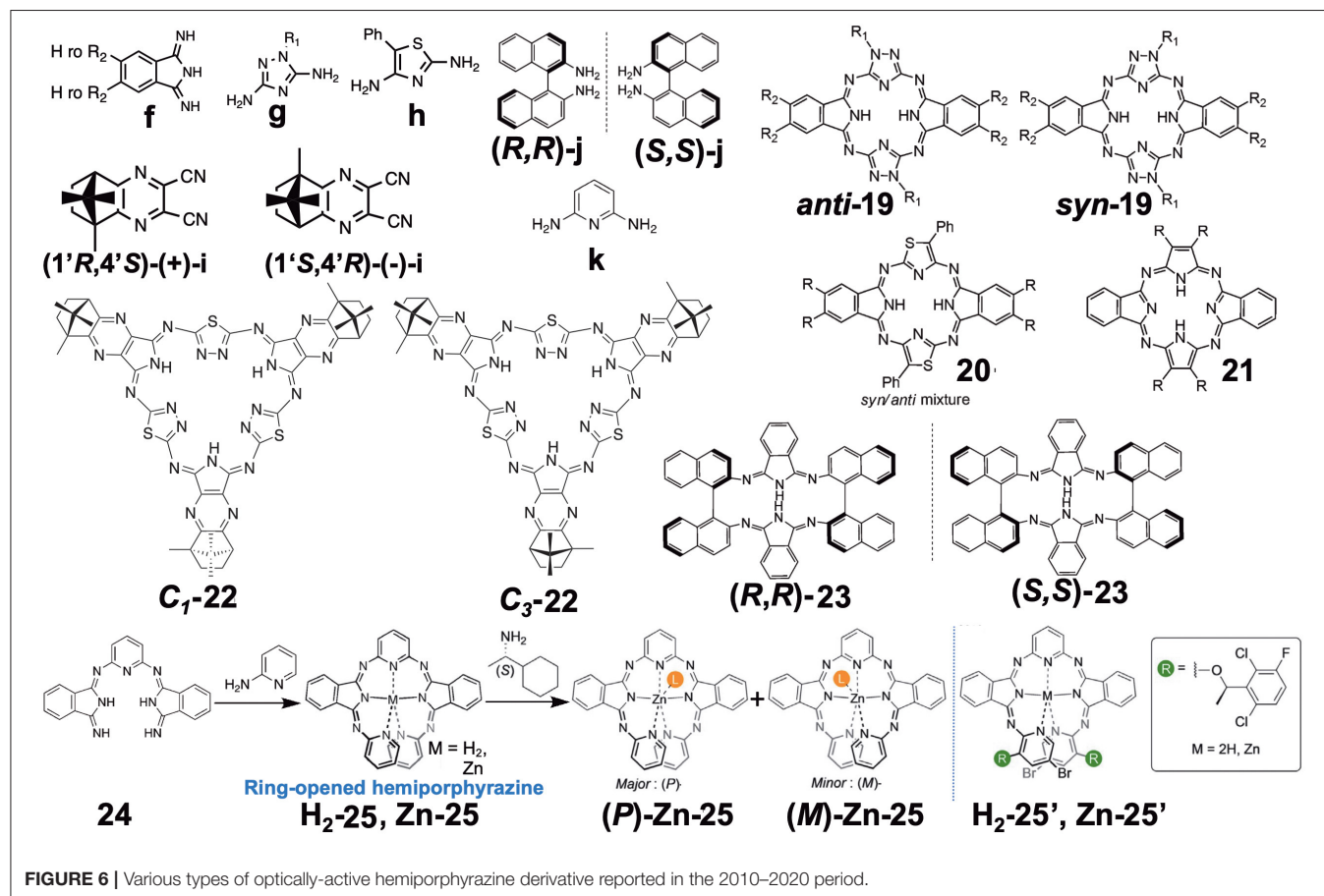


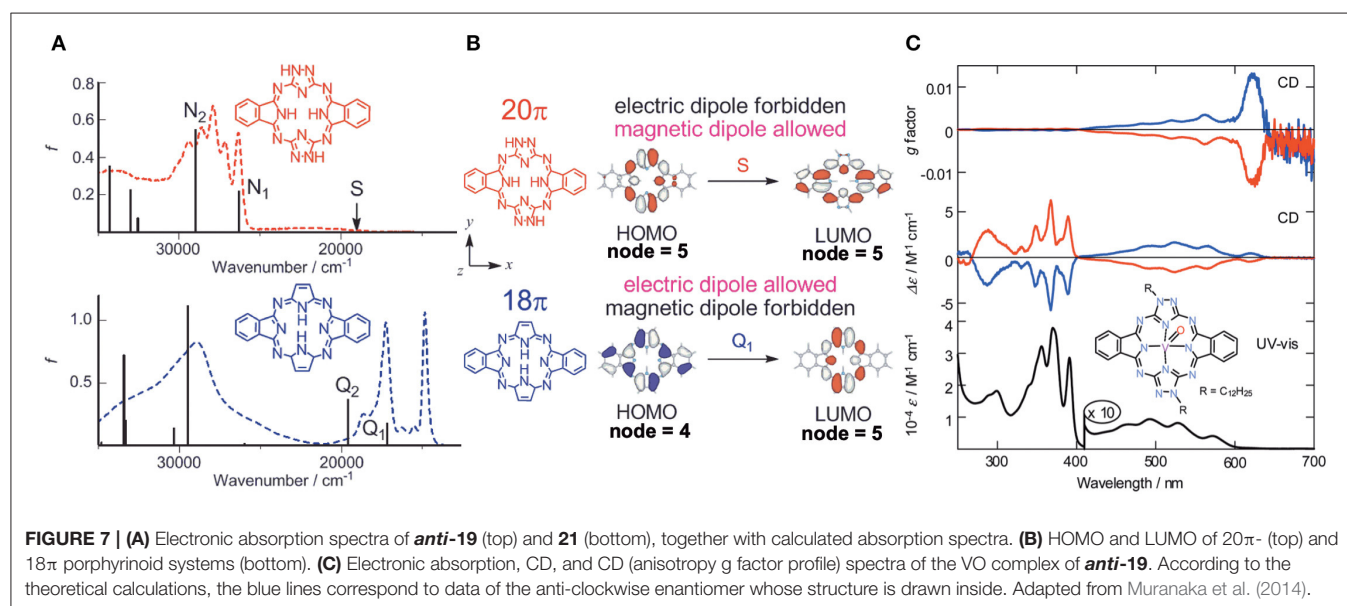
FIGURE 6 | Various types of optically-active hemiporphyrazine derivative reported in the 2010–2020 period.

f and triazole diamine **g** (Muranaka et al., 2014). *anti* and *syn* structures were confirmed from ^1H -NMR and IR spectra: The pyrrole proton signal appeared at around 15 ppm, but as a singlet for *anti*-**19** and two singlets for *syn*-**19**, and in the powder state, the former showed a single NH stretching vibration at $3,298\text{ cm}^{-1}$, while two peaks were detected for the latter at $3,363$ and $3,291\text{ cm}^{-1}$. Insertion of VO to *anti*-**19** was performed in order to obtain intrinsically-chiral triazolehemiporphyrizine (Kobayashi et al., 2009), whose resolution was achieved by high-performance liquid chromatography. In order to compare the properties of **19** with those of congeners, **20** and **21** were synthesized from isoindoleimine **f** and thiazole diamine **h** in 2-ethoxyethanol at 135°C , and isoindoleimine **f** and 4,5-dicyano-4-octene in the presence of magnesium in butanol at boiling temperature, respectively. Pyrrole proton ^1H NMR signals of **20** and **21** were observed at ca. 13.6–14.2 and -1.93 ppm, respectively, suggesting that **20** is anti-aromatic while **21** is aromatic.

Molecular orbitals (MOs) of these molecules were calculated, and it was found that the *anti*-forms of **19** and **20** have HOMO and LUMO with five nodal patterns, while those of **21** have four and five nodal patterns, respectively. Obviously, the nodal patterns of the HOMO–1, HOMO, and LUMO of the *anti*-**19** and **20** were respectively in connection with the HOMO, LUMO, and LUMO+1 of the 18π -electron dibenzotetraazaporphyrin **21**. The LUMO and HOMO of **19** and **20** are derived from a pair of degenerate LUMOs of the 18π -electron perimeter model, while from one of the degenerate HOMOs, the HOMO–1 is derived. Accordingly, together with the pyrrole proton ^1H NMR data at very low field, **19** and **20** were judged to be 20π anti-aromatic [$4n\pi$]-electron systems. This kind of system can be analyzed using Michl's perimeter model (Fleischhauer et al., 2000, 2004, 2005; Muranaka et al., 2009). **Figure 7A** shows the experimental and calculated absorption spectra of *anti*-**19** and **21**. The spectral pattern of **21** retains characteristic features of a low-symmetrical tetraazaporphyrin with D_{2h} symmetry

(Kobayashi and Konami, 1996; Kobayashi, 2002), showing two prominent, split Q envelopes with coupled Faraday B-terms in the visible region (not shown). *anti*-**19**, on the other hand, revealed a weak absorption band with a pronounced vibronic progression in ca. 400–600 nm region, followed by stronger bands in the UV region of $<400\text{ nm}$. If we pay attention to the HOMO-LUMO transition, it is an intrashell $\Delta M_L = 0$ forbidden transition for *anti*-**19** and an $\Delta M_L = \pm 1$ allowed transition for **21**, so that the longest wavelength region of *anti*-**19** is very weak, while **21** has some intensity. Indeed, as seen in **Figure 7B**, the HOMO-LUMO transition accompanies a rotation of charge for a 20π system (magnetic dipole allowed), but a translation of charge for 18π system (electric dipole allowed). The spectra of two enantiomers of the VO complex of *anti*-**19** are collected in **Figure 7C**. Most notably, a large g-factor associated with the electric dipole forbidden band in the 400–650 nm region was detected. The value of g-factor associated with the lowest-energy S band at ca. 615–620 nm was larger than 0.01, in accord with the rotation of charge produced by intrashell forbidden transitions. This was the first report of unambiguous spectral fact that cyclic [$4n\pi$]-electron molecules have indeed a large transition magnetic dipole moment in the region of the lowest π - π^* transition with forbidden character. The g-factor spectrum ends at ca. 420 nm, where the electric dipole allowed transitions start to appear.

Filatov et al. reported the so-called 3+3 compound **22** in 2014 (Filatov et al., 2014). The starting compounds, (1'R,4'S)-(+)-**i** and (1'S,4'R)-(-)-**i** were synthesized by reacting (1S)-(+)- or (1R)-(-)-camphorquinone and diaminomaleonitrile in acetic acid at 50°C (Kobayashi and Nevin, 1998). Compound **22** was obtained by heating (1'R,4'S)-(+)-**i** and (1'S,4'R)-(-)-**i** together with 2,5-diamino-1,3,4-thiadiazole in either butanol in the presence of CH_3ONa at ca. 100°C (yield 10%) or in ethylene glycol in the absence of CH_3ONa at refluxing temperature (yield 30%). Separation of C_1 and C_3 symmetry regioisomers was carried out using chiral columns. The ratio of regioisomer, $C_1:C_3$



was 57:43 for the reaction in butanol and 76:24 in ethylene glycol. In ^1H NMR spectra, the pyrrole NH signal of the C_3 isomer appeared as a singlet at 12.44 ppm, and as three singlets at 12.45, 12.43, and 12.42 ppm for the C_1 isomer, confirming an insignificant, if any, diatomic ring current.

Figure 8A shows the absorption and CD spectra of **22**. Absorption peaks appeared at 515, 474, 421, and 399 nm, of which two peaks at longer wavelength are weak, while those at shorter wavelength are intense. According to MO calculations

recently performed, these are 30π -electron, $4n+2$ aromatic systems (Bacilla et al., 2020). Both the HOMO and LUMO are doubly degenerate, so that these are grouped into “double-soft chromophore” systems (Michl, 1978a,b,c; Michl, 1980). The two weak bands at longer wavelength correspond to transitions from $M_L = -7$ to $+8$ and 7 to -8 (i.e., $\Delta M_L = \pm 15$) transitions with forbidden character, whereas the intense bands in the ca. 380–440 nm correspond to allowed transitions with $\Delta M_L = \pm 1$. Concerning the CD spectra of $\text{C}_3(\text{S})$ - and $\text{C}_3(\text{R})$ -**22** which

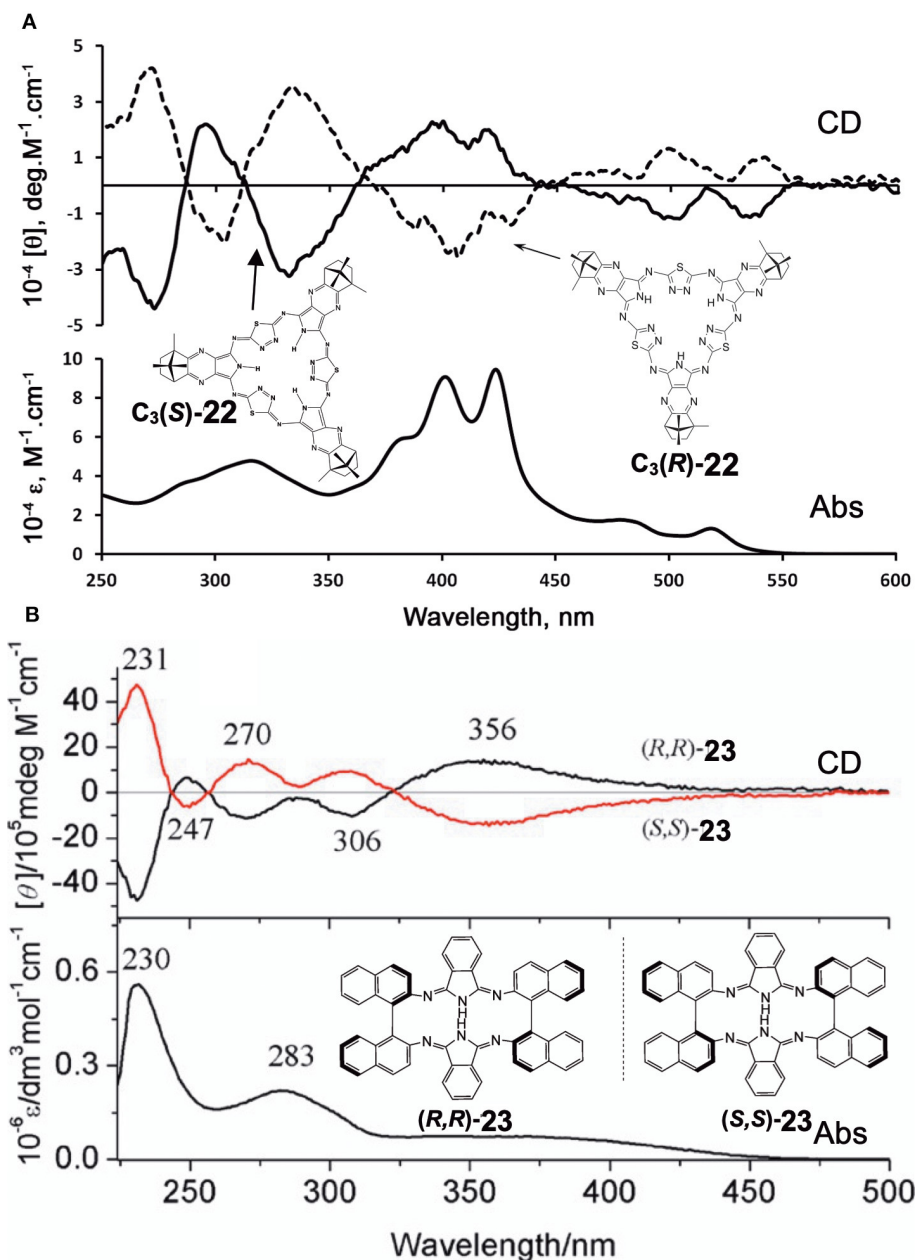


FIGURE 8 | Electronic absorption and MCD spectra of (A) $\text{C}_3(\text{S})$ - and $\text{C}_3(\text{R})$ -**22** and (B) (R,R) -**23** and (S,S) -**23**. Adapted from Filatov et al. (2014) and Wu et al. (2016).

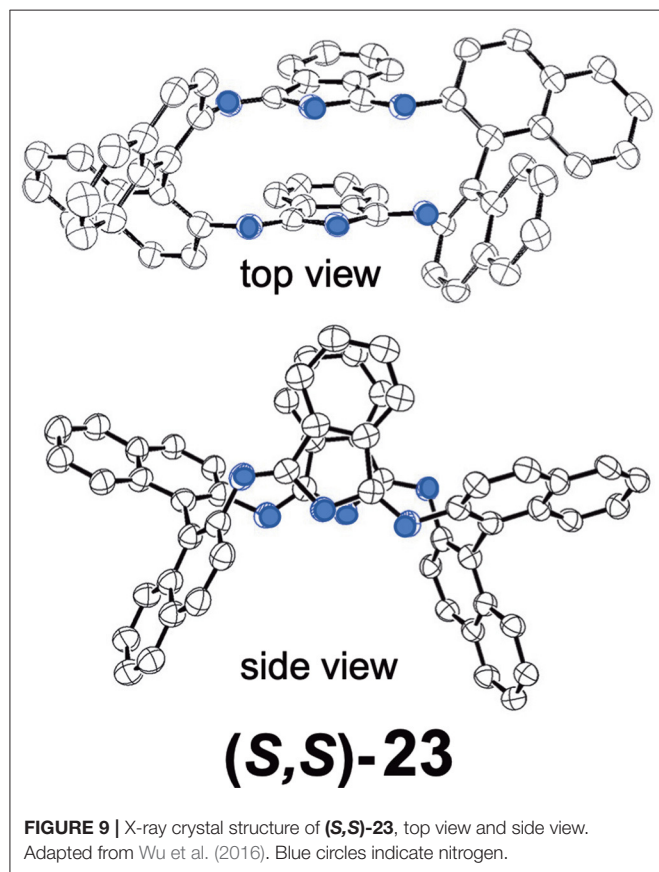
exhibit a mirror-symmetry pattern in relation to the $[\theta] = 0$ line, no interpretation was attempted. Since CD in this system is generated only by optically-active carbons, its shape and intensity cannot be explained at least using the concept of CD (Kobayashi et al., 2012).

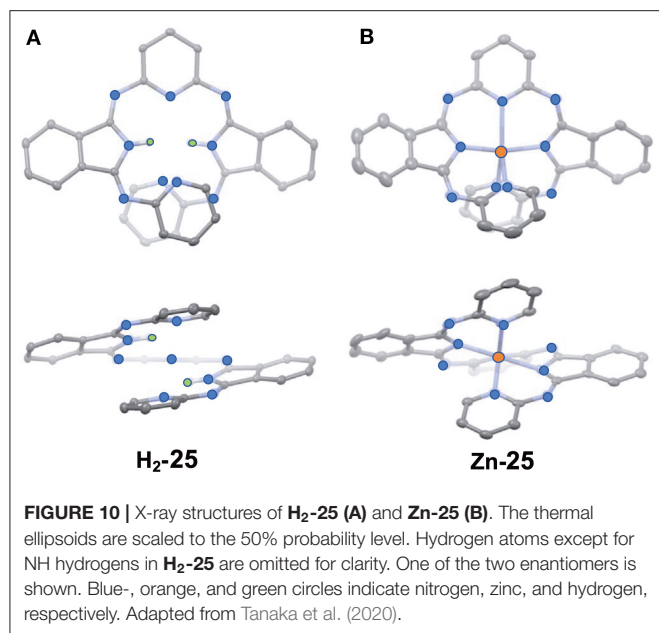
Shen et al. reported compound **23**, which is a kind of hemiporphyrazine that was prepared via core modification of the macrocycle adopting an intrinsically chiral ring molecule as a part of the inner perimeter of the macrocycle (Wu et al., 2016). A condensation reaction of enantiopure chiral diamine, (*R,R*)-**j** or (*S,S*)-**j** and isoindolediimine **f** was performed in *n*-butanol at 150°C for 12 h to give the (*R,R*)-**23** and (*S,S*)-**23** target compounds as yellow solids in ca. 3–7% yield. Although their mass and ^1H NMR data were in accordance with the structure shown in **Figure 8**, single crystal X-ray analysis further confirmed the structure of (*S,S*)-**23**, where the two naphthyl moieties lie around a pseudo C_2 axis and are inflexible, with an angle of ca. 85 degrees. The two isoindole moieties at opposite positions lie parallel to each other forming a kite-like conformation, so that the two nitrogen atoms in the isoindoline moiety point in the same direction (**Figure 9**). Thus, although previously reported himiporphyrazines have roughly planar structures, in compounds **23**, all constituting chromophores are quite strongly deviated from the inner perimeter plane, but still exhibit absorption bands in the longer-wavelength region

(ca. 260–500 nm) that the constituting chromophore units do not show (**Figure 8B**). Here, in the absorption spectra, a broad intense band is seen at 283 nm, in addition to a weaker band envelope in the 325–500 nm region, which is in agreement with what is generally observed for non-aromatic hemiporphyrazines. (*R,R*)-**23** and (*S,S*)-**23** molecules contain 18 atoms and 20- π -electrons along their inner perimeter, so the authors inferred that a Mobius strip type structure could conceivably result in Mobius aromaticity. Since the isoindoline and binaphthyl moieties are severely deviated from planarity of the macrocycle, the calculated frontier π MOs of **23** were predicted to be significantly localized on either the 1,1'-binaphthyl or isoindoline moieties, so that the spectral bands could not be easily assigned using Michl's 4N perimeter model (Howeler et al., 1998; Fleischhauer et al., 2000, 2004, 2005). Nevertheless, both the CD and absorption spectra predicted by TD-DFT calculations on the X-ray structure of (*S,S*)-**23**, were in close agreement with those recorded experimentally.

Muranaka and Uchiyama et al. recently reported ring-opened helical hemiporphyrazines, **H₂-25** and **Zn-25**, exhibiting circularly-polarized luminescence (CPL) (Tanaka et al., 2020). CPL-active compounds have attracted the attention of scientists, not only due to purely scientific interest, but also due to their potential applications. In order to obtain strong CPL signals accompanying a high luminescence dissymmetry factor (g_{lum}), it is important to design molecules with a large transition magnetic dipole moment (m) compared to the transition electric dipole moment (μ). Since many fluorescent organic molecules have a small m and large μ for the S_1 - S_0 transition, their g_{lum} is low ($g_{\text{lum}} = 10^{-5}$ – 10^{-3}). This is quite different from the f - f transition in lanthanide metal complexes and the π^* - n (S_1 - S_0) transition in carbonyl-containing compounds, since they have an almost zero μ and a large m (Riehl and Richardson, 1986; Lunkley et al., 2008). The latter case led to a relatively high luminescence dissymmetry factor ($g_{\text{lum}} = 10^{-3}$ – 10^0), but unfortunately in these systems, the emission quantum yield is very low due to the very small μ . If we design hemiporphyrazine which is considered to be a 20π system, the absorption at the longest wavelength accompanies rotation of charge, as shown in **Figure 7B**, meaning that the m of this transition is large. However, in order to obtain stronger fluorescence and CD spectra, an intense μ is also desirable. Accordingly, planar molecules do not generally satisfy these two requirements. Compounds **H₂-25** and **Zn-25** are helical molecules due to steric interaction of the pyridine moiety, so that they may satisfy these requirements after resolution of the enantiomers. Their precursor **24** was first prepared by reacting 2,6-diaminopyridine and substituent-free isoindolediimine **f** at a ratio of 1:2, which was then reacted with two equivalents of 2-aminopyridine, to afford **H₂-25**. Resolution of **H₂-25** into its enantiomers was unsuccessful, but after insertion of a Zn ion, **Zn-25** was resolved into its *P*- and *M*-enantiomers at 0°C, due to relatively high solubility in a range of solvents. However, at room temperature, the enantiomers were racemized immediately due to a low energy barrier for racemization.

Figure 10 shows the X-ray structure of one enantiomer of each of **H₂-25** and **Zn-25**, which have helical geometry due to





steric repulsion between the pyridine moieties. All five nitrogen atoms in the pyridine and isoindoline moieties coordinate to the Zn(II) ion so that the central part is in a distorted trigonal bipyramidal geometry.

Figure 11A shows the absorption spectra of **H₂-25** and **Zn-25**. **H₂-25** exhibited a shoulder absorption at 380–500 nm, and a similar weak band appeared for **Zn-25** in 420–540 nm which could be assigned to a (S_0 - S_1) π - π^* transition (Muranaka et al., 2014). The molar extinction coefficient of **H₂-25** at 430 nm was ca. 3–4 times larger than that of conventional hemiporphyrazines, plausibly by ring-opening, suggesting that μ became larger. The calculated absorption spectra also support the observed spectra to a fair extent, and the oscillator strengths for the S_0 - S_1 transition of **H₂-25** and **Zn-25** were 0.16 and 0.11, respectively, in comparison with 0.00 for hemiporphyrazine. As shown in **Figure 11B**, resolved enantiomers of **Zn-25** exhibited CD and CPL envelopes of mirror symmetry in connection to the intensity = 0 line. The g_{lum} value of **Zn-25** at 535 nm was estimated by calculation to be $\pm 2.1 \times 10^{-2}$, representing one of the largest values among to date reported small helical molecules (Sanchez-Carnerero et al., 2015). The value of absorbance dissymmetry factor, $g_{abs} = \pm 2.6 \times 10^{-2}$, obtained experimentally from CD spectra at 520 nm, was very close to the g_{lum} value in CPL spectra, suggesting that structural change was small upon excitation.

In order to elucidate the origin of the CPL properties, they performed MO analysis for the optimized S_1 state geometry of **Zn-25** and hemiporphyrazine zinc complex as a reference. The properties of the associated HOMOs and LUMOs, such as coefficient values and nodal patterns and numbers, were retained even after structural modification to the helical geometry, and the estimated values of transition magnetic dipole moment (m) for the S_0 - S_1 transition of (*P*)-**Zn-25** was 3.64 au,

which was close to that of zinc hemiporphyrazine (4.35 au). The large g_{lum} value for **Zn-25** was, therefore, taken to be related to the peculiar molecular orbital feature of the ring-opened hemiporphyrazines.

A rigid CPL-active ring-unclosed hemiporphyrazine (**H₂-25'**) and its zinc complex (**Zn-25'**) (**Figure 6**) were also synthesized by using 2-aminopyridine accompanying a chiral structure. As seen in **Figure 11C-a**, compounds **H₂-25'** and **Zn-25'** showed positive CPL spectra at ambient temperature without chiral HPLC separation (**H₂-25'**: $g_{lum} = +6.5 \times 10^{-3}$ at 587 nm in toluene; **Zn-25'**: $g_{lum} = +1.0 \times 10^{-2}$ at 573 nm in $CHCl_3$), indicating that the ring-unclosed hemiporphyrazines with the right-handed (*P*)-helical structure were successfully obtained in a diastereoselective manner by covalently linking the chiral subgroup to the skeleton. The chiral recognition ability of (*R*)- and (*S*)-**Zn-25** was then examined by means of CPL spectroscopy since they racemized rapidly at ambient temperature. Here, when (*R*)- or (*S*)-cyclohexylamine was added to a CH_2Cl_2 solution of **Zn-25**, a minus or plus CPL signal with a g_{lum} value of $\pm 1.3 \times 10^{-3}$ at 541 nm was recorded (**Figure 11C-b**), depending on the chirality of amine. Afterall, this phenomenon could be rationalized by means of the induction of helical chirality via ligation of the chiral amine to the central zinc ion. Thus, since the helical structure of **Zn-25** is flexible, it can be utilized as a dynamic chiral recognition/sensing tool.

CONCLUSIONS AND OUTLOOK

Optically-active Pcs and their congeners are expected to be the subject of ongoing reports. As seen in this review, those containing chiral binaphthyls may become an important topic in future publications, for several conceivable reasons: easy and high-yield preparation of precursors from commercially available compounds, i. e. **a** and **b** in **Figure 1**; no racemization of **a** and **b** during macrocyclic formation reaction; and anticipated strong CD and ICD intensity and relatively easy theoretical analysis of the spectroscopic properties of the resultant compounds. In particular, since enantiopure (*R,R*)- and (*S,S*)-2,2'-dihydroxybinaphthyl are commercially available, researchers will continue to use these precursors often. Since the synthesis and CD properties of normal compounds are no longer uniquely interesting, because two enantiomers always afford CD of mirror image with respect to the $[\theta] = 0$ line, it is important to produce compounds which have spectroscopically intriguing properties, and to analyze the data theoretically if needed with the help of quantum chemical calculations. In most papers including chiral binaphthyl units published over the past decade, however, no analysis of CD spectra has been given, unfortunately.

The studies of Pc derivatives substituted by long alkyl chains have mostly been related to liquid crystals. Interestingly, it was found and established by Ohta et al. that some of the achiral dyads based on Pc and fullerene (Pc- C_{60}) show a unique helical structure in the liquid crystalline phases (= mesophases) (Tauchi

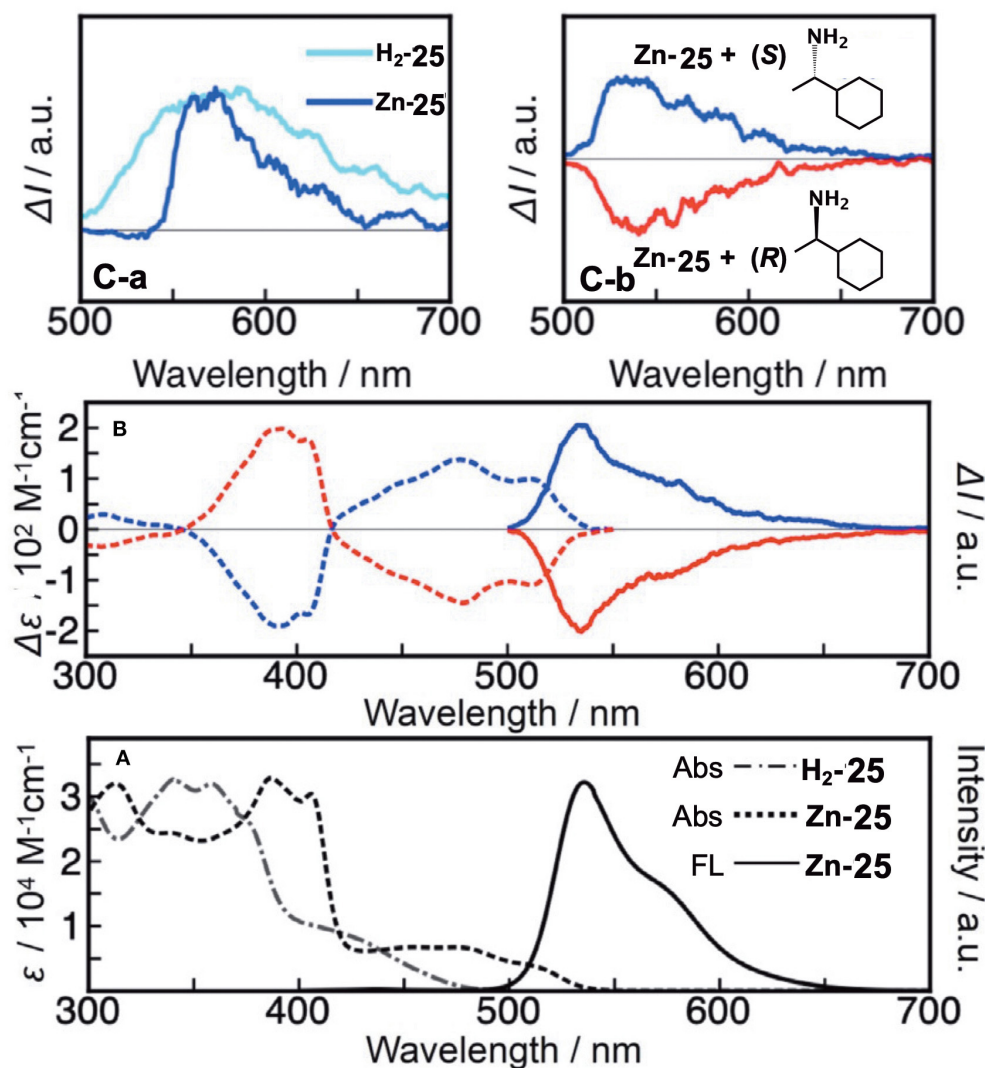


FIGURE 11 | (A) Electronic absorption and fluorescence spectra of H_2-25 and $Zn-25$ in CH_2Cl_2 at ambient temperature. **(B)** CD and CPL signals of $Zn-25$ in n -hexane/THF/diethylamine = 80:20:0.1 (v/v/v) (first fraction, blue line; second fraction, red line). According to the TDDFT calculations, the first and second fractions were respectively assigned as right-handed (*P*)- and left-handed (*M*)- $Zn-25$. **(C-a)** CPL signals of ring-unclosed hemiporphyrazines bearing chiral units (H_2-25' in toluene and $Zn-25'$ in $CHCl_3$) at ambient temperature. **(C-b)** CPL signals of $Zn-25$ in the presence of (S)- or (R)-1-cyclohexylethylamine.

et al., 2010). However, a problem is that some researchers did not have enough expertise on the mesophase structural analysis. For example, a paper from a high-level university reported that other Pc- C_{60} based-dyads exhibit the helicity, although their assigned mesophase cannot show theoretically a homeotropic alignment necessary for the establishment of the helicity (Hayashi et al., 2011, 2017). The authors assigned a faint shoulder in a diagram of temperature-variable X-ray diffraction measurements (XRD pattern) to the helicity, but the homeotropic alignment should not appear theoretically for their assigned mesophase. This assignment was later shown to be false in a detailed study using compounds having similar structures by a group of liquid

crystal specialists (Ishikawa et al., 2018). Thus, researchers of liquid crystals are recommended to learn more about the analysis of mesophase data. In this respect, a nice textbook was published recently (Ohta, 2020).

In the work introduced here as Pc congeners, for example, Muranaka's **19–21** were interesting. Although the structures were similar, depending on the element included, the spectra changed between those of $4n\pi$ and $(4n+2)\pi$ systems, and in the case of the VO complex of $4n\pi$ *anti*-**19**, the two enantiomers showed an intense CD in the region where rotation of charge is expected theoretically. This became possible since in $4n\pi$ compounds, the HOMO-LUMO transition has essentially an intrashell nature

(magnetic dipole allowed transition), and this kind of theme cannot be easily pursued without having some knowledge on spectroscopy. Rather than Pc itself, attractive compounds may be found more easily in Pc-related congeners, since structural modification possibilities are huge, and new ideas can come easily from researchers who always seek for fantastic azamacrocycles. In addition, the formation of some achiral dyad and triad systems that form helicity or chirality appears to be a challenging theme to be pursued going forward, in order to elucidate its driving force.

REFERENCES

- Bacilla, A. C. C., Okada, Y., Yoshimoto, S., Islyaikin, M. K., Koifman, K. I., and Kobayashi, N. (2020). Triangular expanded hemiporphyrines: electronic structures and nanoscale characterization of their adlayers on Au(111). *Bull. Chem. Soc. Jpn.* 93. doi: 10.1246/bcsj.20200188
- Basova, T., Hassan, A., Durmus, M., Gurek, A. G., and Ahsen, V. (2016). Liquid crystalline metal phthalocyanines: structural organization on the substrate surface. *Coord. Chem. Rev.* 310, 131–153. doi: 10.1016/j.ccr.2015.11.005
- Claessens, C. G., Gonzales-Rodriguez, D., Rodriguez-Morgade, M. S., Medina, A., and Torres, T. (2014). Subphthalocyanines, subporphyrines, and subporphyrins: singular nonplanar aromatic systems. *Chem. Rev.* 114, 2192–2277. doi: 10.1021/cr400088w
- Claessens, C. G., Gonzales-Rodriguez, D., and Torres, T. (2002). Subphthalocyanines: singular nonplanar aromatic compounds—synthesis, reactivity, and physical properties. *Chem. Rev.* 102, 835–854. doi: 10.1021/cr0101454
- Filatov, M. S., Trukhina, O. N., Rodriguez-Morgade, M. S., Islyaikin, M. K., Koifman, O. I., and Torres, T. (2014). Synthesis and spectroscopic properties of chiral bornane[2,3-*b*]pyrazino-fused [30]trithiadodecaazahexaphyrins. *J. Porphyrins Phthalocyanines* 18, 1014–1020. doi: 10.1142/1088424614500771
- Fleischhauer, J., Höweler, U., and Michl, J. (2000). MCD of nonaromatic cyclic π -electron systems. 3. The perimeter model for low-symmetry “unaromatic” and “ambiaromatic” molecules derived from 4N-electron [n]annulenes. *J. Phys. Chem. A* 104, 7762–7775. doi: 10.1021/jp000116h
- Fleischhauer, J., Höweler, U., Spanget-Larsen, J., Raabe, G., and Michl, J. (2004). MCD of nonaromatic cyclic π -electron systems. 5. Biphenylene and its aza analogues. *J. Phys. Chem. A* 108, 3225–3234. doi: 10.1021/jp037806g
- Fleischhauer, U., Raabe, G., Klingensmit, K. A., Höweler, U., Chattrjee, R. K., Hafner, K., et al. (2005). MCD of nonaromatic cyclic π -electron systems. Part 6: pentalenes and heptalenes. *Int. J. Quantum Chem.* 102, 925–939. doi: 10.1002/qua.20453
- Fukuda, T., and Kobayashi, N. (2010). “Electronic absorption spectra—phthalocyanines,” in *Handbook of Porphyrin Science*, Vol. 9, Chapter 42, eds K. M. Kadish, K. M. Smith, and R. Guilard (Singapore: World Scientific), 1–650.
- Giménez-Agulló, N., Aragay, G., Galán-Mascarós, J. R., and Ballester, P. (2016). Study of the Coordination of Quinuclidine to a Chiral Zinc Phthalocyanine Dimer. *J. Porphyrins Phthalocyanines* 20, 1224–1232. doi: 10.1142/S1088424616500929
- Gok, Y., Gok, H. Z., and Karayigit, I. U. (2018). Synthesis, characterization and aggregation properties of non-peripherally (1*R*,2*R*)-1,2-Di(naphthalen-1-yl)ethane-1,2-diol substituted optically active zinc phthalocyanine and its catalytic application in enantioselective ethylation of aldehydes. *J. Orgmet. Chem.* 873, 43–49. doi: 10.1016/j.jorganchem.2018.07.033
- Hayashi, H., Nishashi, W., Ueyama, T., Matano, Y., Seki, S., Shimizu, Y., et al. (2011). Segregated donor–acceptor columns in liquid crystals that exhibit highly efficient ambipolar charge transport. *J. Am. Chem. Soc.* 133, 10736–10739. doi: 10.1021/ja203822q
- Hayashi, H., Nishashi, W., Ueyama, T., Matano, Y., Seki, S., Shimizu, Y., et al. (2017). Correction to “segregated donor–acceptor columns in liquid crystals that exhibit highly efficient ambipolar charge transport”. *J. Am. Chem. Soc.* 139, 13957–13957. doi: 10.1021/jacs.7b09424
- Howeler, U., Downing, J. W., Fleischhauer, J., and Michl, J. (1998). MCD of non-aromatic cyclic π -electron systems. Part 1. The perimeter model for antiaromatic 4N-electron [n]annulene biradicals. *J. Chem. Soc. Perkin Trans.* 2, 1101–1117. doi: 10.1039/A800088C
- Ishikawa, K., Watarai, A., Yasugatake, M., and Ohta, K. (2018). Discotic liquid crystals of transition metal complexes 56: synthesis of mesogenic phthalocyanine-fullerene dyads and Influence of the substitution position of alkoxy chains and the kind of terminal groups on appearance of the helical supramolecular structure. *J. Porphyrins Phthalocyanines* 22, 693–715. doi: 10.1142/S108842461850092X
- Kadish, K. M., Smith, K. M., and Guilard, R. (2000). *The Porphyrin Handbook*, Vol. 6, eds K. M. Kadish, K. M. Smith, and R. Guilard (New York, NY: Academic Press), 1–346.
- Kadish, K. M., Smith, K. M., and Guilard, R. (2003a). *The Porphyrin Handbook*, Vol. 19, eds K. M. Kadish, K. M. Smith, and R. Guilard (New York, NY: Academic Press), 1–194.
- Kadish, K. M., Smith, K. M., and Guilard, R. (2003b). *The Porphyrin Handbook*, Vol. 14, eds K. M. Kadish, K. M. Smith, and R. Guilard (New York, NY: Academic Press), 1–347.
- Kitagawa, Y., Miyatake, T., and Ishii, K. (2012). Magneto-chiral dichroism of artificial light-harvesting antenna. *Chem. Commun.* 48, 5091–5093. doi: 10.1039/C2CC30996C
- Kitagawa, Y., Segawa, H., and Ishii, K. (2011). Magneto-chiral dichroism of organic compounds. *Angew. Chem.* 123, 9299–9302. doi: 10.1002/ange.201101809
- Kobayashi, N. (1998). Optically active ‘adjacent’ type non-centrosymmetrically substituted phthalocyanines. *Chem. Commun.* 1998, 487–488. doi: 10.1039/A708343B
- Kobayashi, N. (2001). Optically active phthalocyanines. *Coord. Chem. Rev.* 221/222, 99–123. doi: 10.1016/S0010-8545(01)00323-X
- Kobayashi, N. (2002). “Synthesis and spectroscopic properties of phthalocyanine analogues,” in *Handbook of Porphyrins and Related Macrocycles*, Vol. 15, Chapter 100, eds K. M. Kadish, K. M. Smith, and R. Guilard (New York, NY: Academic Press), 161–262.
- Kobayashi, N. (2010). “Optically active porphyrin systems analyzed by circular dichroism,” in *Handbook of Porphyrin Science*, Vol. 7, Chapter 33, eds K. M. Kadish, K. M. Smith, and R. Guilard (Singapore: World Scientific), 147–245.
- Kobayashi, N. (2012). “Synthesis and characterization of chiral phthalocyanines,” in *Handbook of Porphyrin Science*, Vol. 23, Chapter 110, eds K. M. Kadish, K. M. Smith, and R. Guilard (Singapore: World Scientific), 373–440.
- Kobayashi, N., Higashi, R., Titeca, B. C., Lamote, F., and Ceulemans, A. (1999a). Substituent induced circular dichroism in phthalocyanines. *J. Am. Chem. Soc.* 121, 12018–12028. doi: 10.1021/ja992556w
- Kobayashi, N., Ishizaki, T., Ishii, K., and Konami, H. (1999b). Synthesis, spectroscopy, and molecular orbital calculations of subzaporphyrins, subphthalocyanines, subnaphthalocyanines, and compounds derived therefrom by ring expansion. *J. Am. Chem. Soc.* 121, 9096–9110. doi: 10.1021/ja983325c
- Kobayashi, N., and Konami, H. (1996). “Electronic spectra and molecular orbitals of phthalocyanines,” in *Phthalocyanines-Properties and Applications*, Vol. IV, Chapter 6, eds C. C. Leznoff and A. B. P. Lever (New York, NY: Weinheim; Cambridge: VCH), 343–404.
- Kobayashi, N., Kondo, R., Nakajima, S., and Osa, T. (1990). New route to unsymmetrical phthalocyanine analogues by the use of structurally distorted subphthalocyanines. *J. Am. Chem. Soc.* 112, 9640–9641. doi: 10.1021/ja00182a034

AUTHOR CONTRIBUTIONS

YO prepared the figures. TH collected the reference papers. NK wrote the text. All authors contributed to the article and approved the submitted version.

FUNDING

This work was supported in part by JSPS KAKENHI, grant number 18K05076.

- Kobayashi, N., Muranaka, A., and Mack, J. (2012). *Circular Dichroism and Magnetic Circular Dichroism Spectroscopy for Organic Chemists*. London: Royal Society of Chemistry.
- Kobayashi, N., Narita, F., Ishii, K., and Muranaka, A. (2009). Optically active oxo(phthalocyaninato)vanadium(IV) with geometric asymmetry: synthesis and correlation between the circular dichroism sign and conformation. *Chem. Eur. J.* 15, 10173–10181. doi: 10.1002/chem.200901306
- Kobayashi, N., and Nevin, W. A. (1998). Optically active tetrapyrroloporphyrins and their circular dichroism in monomeric and dimeric forms. *Chem. Lett.* 1998, 851–852. doi: 10.1246/cl.1998.851
- Lin, S., Ji, L., Jing, L., Lu, J., Wang, H., Sun, S., et al. (2015). Helical self-assembly and nonlinear optical properties of two optically active phthalocyanine derivatives with the same chiral substituents on the a or b position. *Inorg. Chim. Acta* 434, 24–30. doi: 10.1016/j.ica.2015.05.006
- Lu, H., and Kobayashi, N. (2016). Optically active porphyrin and phthalocyanine systems. *Chem. Rev.* 116, 6184–6261. doi: 10.1021/acs.chemrev.5b00588
- Lu, J., Deng, Y., Zhang, X., Kobayashi, N., and Jiang, J. (2011). Optically Active Mixed (Phthalocyaninato)(Porphyrinato) Rare Earth Triple-Decker Complexes. *Synthesis, Spectroscopy, and Effective Chiral Information Transfer*, *Inorg. Chem.*, 50, 2562–2567. doi: 10.1021/ic102393c
- Lunkley, J. L., Shirota, D., Yamanari, K., Kaizaki, S., and Muller, G. (2008). Extraordinary circularly polarized luminescence activity exhibited by cesium tetrakis(3-heptafluoro-butylryl-(+)-camphorato) Eu(III) complexes in EtOH and CHCl₃ solutions. *J. Am. Chem. Soc.* 130, 13814–13815. doi: 10.1021/ja805681w
- Michl, J. (1978a). Magnetic circular dichroism of cyclic p-electron systems. 1. Algebraic solution of the perimeter model for the A and B terms of high-symmetry systems with a (4N + 2) p-electron [n]annulene perimeter. *J. Am. Chem. Soc.* 100, 6801–6811. doi: 10.1021/ja00490a001
- Michl, J. (1978b). Magnetic circular dichroism of cyclic π -electron systems. 3. Classification of cyclic π chromophores with a (4N + 2) π -electron [n]annulene perimeter and general rules for substituent effects on the MCD spectra of soft chromophores. *J. Am. Chem. Soc.* 100, 6819–6824. doi: 10.1021/ja00490a003
- Michl, J. (1978c). Magnetic circular dichroism of cyclic π -electron systems. 2. Algebraic solution of the perimeter model for the B terms of systems with a (4N + 2) π -electron [n]annulene perimeter. *J. Am. Chem. Soc.* 100, 6812–6818. doi: 10.1021/ja00490a002
- Michl, J. (1980). Electronic structure of aromatic π -electron systems as reflected in their MCD spectra. *Pure Appl. Chem.* 52, 1549–1563. doi: 10.1351/pac198052061549
- Muranaka, A., Matsumoto, Y., Uchiyama, M., Jiang, J., Bian, Y., Ceulemans, A., et al. (2005). Definitive assignments of the visible-near-IR bands of porphyrin-naphthalocyanine rare-earth sandwich double- and triple-decker compounds by magnetic circular dichroism spectroscopy. *Inorg. Chem.* 44, 3818–3826. doi: 10.1021/ic0502325
- Muranaka, A., Matsushita, O., Yoshida, K., Mori, S., Suzuki, M., Furuyama, T., et al. (2009). Application of the perimeter model to the assignment of the electronic absorption spectra of gold(III) hexaphyrins with [4n + 2] and [4n] π -electron systems. *Chem. Eur. J.* 15, 3744–3751. doi: 10.1002/chem.200801742
- Muranaka, A., Ohira, S., Toriumi, N., Hirayama, M., Kyoutani, F., Mori, Y., et al. (2014). Unraveling the electronic structure of azolehemiporphyrins: direct spectroscopic observation of magnetic dipole allowed nature of the lowest π - π^* transition of 20 π -electron porphyrinoids. *J. Phys. Chem. A* 118, 4415–4424. doi: 10.1021/jp5001557
- Ohta, K. (2020). *Physics and Chemistry of Molecular Assemblies*. Singapore: World Scientific.
- Ohta, K., Nguyen-Tran, H. -D., Tauchi, L., Kanai, Y., Megumi T, and Takagi, Y. (2011). “Liquid crystals of phthalocyanines, porphyrins and related compounds,” in *Handbook of Porphyrin Science With Applications to Chemistry, Physics, Materials Science, Engineering, Biology and Medicine*, Volume 12: Applications, Chapter 53, eds K. M. Kadish, K. M. Smith, and R. Guillard (Singapore: World Scientific), 1–120. doi: 10.1142/9789814322386_0005
- Revuelta-Maza, M. A., Torres, T., and Torre, G. (2019). Synthesis and aggregation studies of functional binaphthyl-bridged chiral phthalocyanines. *Org. Lett.* 21, 8183–8186. doi: 10.1021/acs.orglett.9b02718
- Riehl, J. P., and Richardson, F. S. (1986). Circularly polarized luminescence spectroscopy. *Chem. Rev.* 86, 1–16. doi: 10.1021/cr00071a001
- Sanchez-Carnerero, E. M., Agarrabeitia, A. R., Moreno, F., Maroto, B. L., Muller, G., Ortiz, M. J., et al. (2015). Circularly polarized luminescence from simple organic molecules. *Chem. Eur. J.* 21, 13488–13500. doi: 10.1002/chem.201501178
- Shimizu, S., Miura, A., Khene, S., Nyokong, T., and Kobayashi, N. (2011). Chiral 1,2-subnaphthalocyanines. *J. Am. Chem. Soc.* 133, 17322–17328. doi: 10.1021/ja2052667
- Shimizu, S., Otaki, T., Yamazaki, Y., and Kobayashi, N. (2012). Synthesis and properties of β,β -sp³-hybridized subphthalocyanine analogues. *Chem. Commun.* 48, 34100–34002. doi: 10.1039/c2cc30511a
- Tanaka, Y., Maruyama, T., Mureanaka, A., Imai, E., and Uchiyama, M. (2020). Ring-opened hemiporphyrins: helical molecules exhibiting circularly polarized luminescence. *Chem. Eur. J.* 26, 1768–1771. doi: 10.1002/chem.201905246
- Tauchi, L., Shimizu, M., Fujii, T., Nguyen-Tran, H. -D., Kamei, T., and Ohta, T. (2010). “Mesogenic phthalocyaninefullerene dyad showing homeotropic alignment and helical structure,” in *23rd International Liquid Crystal Conference* (Krakow), P1.106.
- Tian, J., Jing, L., Zhang, C., Ji, L., Zhu, P., and Zhang, X. (2013a). Helical self-assembly of optically active phthalocyanine derivatives bearing four optically active (S)-2-methylbutoxy moieties at the α position of the phthalocyanine ring. *Eur. J. Inorg. Chem.* 2013, 5281–5287. doi: 10.1002/ejic.201300564
- Tian, J., Jing, L., Ji, L., Zhang, C., Liu, Q., and Zhang, X. (2013b). Helical self-assembly and nonlinear optical properties of optically active phthalocyanine derivatives bearing eight optically active diethyleneglycol mono-(S)-2-methylbutyl ether moieties on the β -position of the phthalocyanine ring. *RSC Adv.* 3, 22461–22468. doi: 10.1039/c3ra44164d
- Wang, K., Wang, H., Li, W., Kobayashi, N., and Jiang, J. (2012). Chiral phthalocyanine with unambiguous absolute molecular structures for both enantiomers. *Acta Chim. Sin.* 70, 1791–1797. doi: 10.6023/A12050262
- Wang, K., Zeng, S., Wang, H., Dou, J., and Jiang, J. (2014). Magneto-chiral dichroism in chiral mixed (phthalocyaninato)(porphyrinato) rare earth triple-decker SMMs. *Inorg. Chem. Front.* 1, 167–171. doi: 10.1039/c3qi00097d
- Wu, Y., Gai, L., Xiao, X., Lu, H., Li, Z., Mack, J., et al. (2016). A chiral hemiporphyrin derivative: synthesis and chiroptical properties. *Chem. Asian. J.* 11, 2113–2116. doi: 10.1002/asia.201600754
- Zhang, C., Jing, L., Lin, S., Hao, Z., Tian, J., Zhang, X., et al. (2013). Helical self-assembly of optically active phthalocyanine derivatives: effect of Zn-O coordination bond on morphology and handedness of nanostructures. *ChemPhysChem* 14, 3827–3833. doi: 10.1002/cphc.201300604
- Zhang, W., Fujiki, M., and Zhu, X. (2011). Chiroptical nanofibers generated from achiral metallophthalocyanines induced by diamine homochirality. *Chem. Eur. J.* 17, 10628–10635. doi: 10.1002/chem.201100208
- Zhang, Y., Zhao, L., Wang, K., and Jiang, J. (2017). Unprecedented phthalocyanine-porphyrin-fused oligomers with induced chirality nature. *Inorg. Chem. Front.* 4, 104–109. doi: 10.1039/c6qi00496b
- Zhao, L., Wang, K., Furuyama, T., Jiang, J., and Kobayashi, N. (2014). Synthesis and spectroscopic properties of chiral binaphthyl-linked subphthalocyanines. *Chem. Commun.* 50, 7663–7665. doi: 10.1039/c4cc03426k
- Zhao, L., Wang, K., Shang, H., and Jiang, J. (2015). Novel chiral ABBB-type unsymmetrical phthalocyanine. Ring-expansion synthesis, spectroscopic, and electrochemical properties. *Dyes Pigments* 120, 52–56. doi: 10.1016/j.dyepig.2015.04.009
- Zhou, H., Wang, K., Qi, D., and Jiang, J. (2014). Chiral bis(phthalocyaninato) yttrium double-decker complexes. Synthesis, structure, spectroscopy, and electrochemistry. *Dalton Trans.* 43, 1699–1705. doi: 10.1039/c3dt52611a

Conflict of Interest: The authors declare that the research was conducted in the absence of any commercial or financial relationships that could be construed as a potential conflict of interest.

Copyright © 2020 Okada, Hoshi and Kobayashi. This is an open-access article distributed under the terms of the Creative Commons Attribution License (CC BY). The use, distribution or reproduction in other forums is permitted, provided the original author(s) and the copyright owner(s) are credited and that the original publication in this journal is cited, in accordance with accepted academic practice. No use, distribution or reproduction is permitted which does not comply with these terms.



Supramolecular Halogen Bonds in Asymmetric Catalysis

Mikk Kaasik and Tõnis Kanger*

Department of Chemistry and Biotechnology, Tallinn University of Technology, Tallinn, Estonia

Halogen bonding has received a significant increase in attention in the past 20 years. An important part of this interest has centered on catalytic applications of halogen bonding. Halogen bond (XB) catalysis is still a developing field in organocatalysis, although XB catalysis has outgrown its proof of concept phase. The start of this year witnessed the publication of the first example of a purely XB-based enantioselective catalytic reaction. While the selectivity can be improved upon, there are already plenty of examples in which halogen bonds, among other interactions, play a crucial role in the outcome of highly enantioselective reactions. This paper will give an overview of the current state of the use of XBs in catalytic stereoselective processes.

Keywords: halogen bond, asymmetric catalysis, bifunctional catalyst, organocatalysis, metal-catalyzed reactions

OPEN ACCESS

Edited by:

Victor Borovkov,
South-Central University for
Nationalities, China

Reviewed by:

Lingpeng Meng,
Hebei Normal University, China
Mate Erdelyi,
Uppsala University, Sweden

*Correspondence:

Tõnis Kanger
tonis.kanger@taltech.ee

Specialty section:

This article was submitted to
Supramolecular Chemistry,
a section of the journal
Frontiers in Chemistry

Received: 26 August 2020

Accepted: 15 September 2020

Published: 21 October 2020

Citation:

Kaasik M and Kanger T (2020)
Supramolecular Halogen Bonds in
Asymmetric Catalysis.
Front. Chem. 8:599064.
doi: 10.3389/fchem.2020.599064

INTRODUCTION

Halogen bonding is an attractive interaction between an electrophilic region associated with a halogen atom and a nucleophilic region (Desiraju et al., 2013). While the exact origin of this interaction is still under debate, the distribution of electron density on the halogen atom is anisotropic, leading to the formation of an electropositive region, often referred to by the term “ σ -hole” (Brinck et al., 1992). Although the first evidence of this phenomenon dates to the early nineteenth century (Colin and de Claubry, 1814), halogen bonding has gained considerable attention only in the last two decades (for selected reviews, see: Gilday et al., 2015; Cavallo et al., 2016; Wang et al., 2016; Montaña, 2017). While solid state applications have been predominant (for selected reviews, see: Troff et al., 2013; Li et al., 2016; Christopherson et al., 2018), halogen bonding has gained wider use in the solution phase as well (for selected reviews, see: Beale et al., 2013; Jentzsch, 2015; Tepper and Schubert, 2018).

Halogen bonds (XBs) are often compared to hydrogen bonds (HBs), with XB strengths ranging from 5 to 180 kJ/mol (Metrangolo et al., 2005). However, XBs have several beneficial characteristics which contribute to the growing interest in XB applications. An XB is formed on the elongation of the covalent bond to the halogen and, therefore, XBs are very linear, with angles near 180° (Metrangolo et al., 2005; Rissanen, 2008). Compared to hydrogen bonding, a wider range of donor atoms can be used from the seventh row, although in reality chlorine, bromine and iodine are typically used (Cavallo et al., 2016). The halogen atoms can be ranked by their XB donor ability in the order of F < Cl < Br < I, which corresponds to the increase in the polarizability of the halogen atoms (Clark et al., 2007). Also, the substituent attached covalently to the halogen atom can be varied to tune the XB donor ability (Nepal and Scheiner, 2015). Based on the “hard and soft (Lewis) acids and bases” theory (Pearson, 1963), hydrogen is a hard atom, while halogens are softer atoms. Therefore, XBs and HBs should have different preferences toward acceptor atoms (Robertson et al., 2014). In addition, it has been demonstrated that XBs are not as sensitive to solvent effects as HBs are (Robertson et al. (2014, 2017).

The deliberate use of XBs for a catalytic purpose was realized by Bruckmann et al. (2008). 1-Iodoperfluorooctane was used to activate quinolines in their reduction with a Hantzsch ester. This opened the door for the development of a new field in organocatalysis and since then a growing number of publications have dealt with catalytic applications of XBs (for recent reviews, see: Bamberger et al., 2019; Sutar and Huber, 2019; Breugst and Koenig, 2020; Yang and Wong, 2020). Thus, far, considerable effort has gone into proving the catalytic viability of XBs and as a result, a set of benchmark reactions (Michael, aza-Diels Alder, and the halogen abstraction reaction) for XB catalysis has emerged. Since neutral XB acceptors are generally quite weak, the design and use of charge-assisted XB catalysts based on azolium-cores is very dominant in studies. Asymmetric XB catalysis has been an exciting prospect for some time (Kniep et al., 2013). However, considerable advancements in the field have been made only in the past 2 years.

This review will explore the use of XBs in catalytic enantioselective transformations in which XBs have been demonstrated to influence the outcome of the reaction (Figure 1). With a few exceptions, examples of transient halogen bonding (an XB to a Lewis base leads to the cleavage of the covalent bond with the halogen atom) are omitted from the review, as in these instances the XB donors are usually used as reagents. In addition, by focusing the discussion on examples in which the inert Lewis acid nature of the XB donor is utilized, the discussion will also better reflect the most prominent trends in XB catalysis.

Halogen-bonded adducts have been demonstrated to be on the reaction pathways of halogenation reactions of aromatic and other unsaturated systems (Brown, 1997; Lenoir and Chiappe, 2003; Figure 2A). Over the years, several asymmetric variants of these reactions (for example: halogenations, halocyclizations) have been developed (for selected reviews, see: Murai and Fujioka, 2013; Cheng et al., 2014; Cresswell et al., 2015; Cai et al., 2019; Kristianslund et al., 2019). However, the term halogen bonding is only rarely used in association with these processes. The transient nature of these XBs also place the reactions out of the focus of this review. As the field of asymmetric halogenation reactions is well-established, the reader is referred to previous reviews. Nonetheless, some papers have addressed the issue of halogen bonding in enantioselective halogenation reactions in

more detail, and three particular cases are included in the later part of this review.

Chiral hypervalent organoiodine reagents have been used in different oxidative transformations in which the reagent is temporally inserted into a suitable substrate and is afterwards displaced by a nucleophilic species (Figure 2B; for recent reviews, see: Claraz and Masson, 2018; Flores et al., 2019; Parra, 2019). Typically, these reagents are generated *in situ* from chiral iodoarenes by sacrificial oxidants, which are also used to regenerate the hypervalent organoiodine. Thus, only catalytic quantities of iodoarenes are needed. As the coordination patterns in hypervalent iodine species can be viewed as special cases of halogen bonding (Heinen et al., 2020; Turunen and Erdélyi, 2020) and as XBs can contribute to halogen insertions, it is pertinent to mention this type of catalysis in the review. Nevertheless, the contribution of XBs to these catalytic processes are again rarely acknowledged and the topic has been thoroughly reviewed in recent years by experts in the field. Therefore, the reader is referred to the previously mentioned reviews.

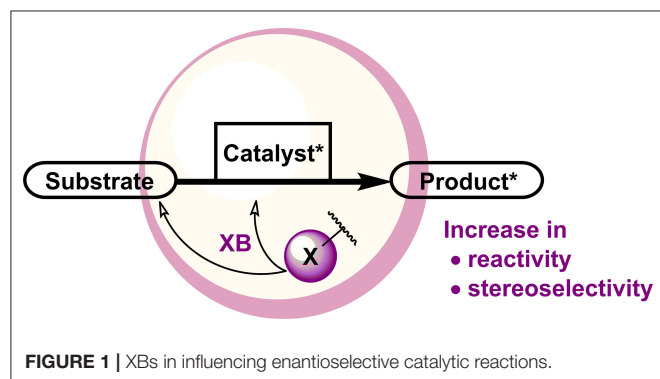
For the following discussion, the review will be divided into three parts, based on how the XBs in the catalytic system affect the outcome of the enantioselective reaction by enhancing:

- reactivity
- both reactivity and stereoselectivity
- stereoselectivity.

A valid argument can be made that reactivity and stereoselectivity are connected to each other and therefore should not be separated from one another. However, the examples encompass very different types of reactions, activation modes, roles of the halogen etc., to make a division based on a more traditional reasoning. The division of the review is based on the observable outcomes of the reactions.

XBs IN ENHANCING REACTIVITY

Through the years several reagents have been used in halogenation reactions. Interestingly, it has been noted that combinations of halogenating agents give better results than the use of a single reagent. The increase in reactivity can be reasoned to come from XBs. For instance, molecular iodine (or ICl) and haloimides (such as **4**, Figure 3A; Nakatsuji et al., 2014) formed XB-based complexes **5** in the iodolactonization of 4-arylmethyl-4-pentenoic acids. The formation of complex **5** was postulated based on the appearance of new bands in the Raman spectrum of the mixture of I₂ and **4** compared to the spectra of individual components. In addition, the lactonization was accelerated when I₂ and **4** were premixed for 1 h prior to the addition of catalyst **3** and acid **1**, which also supported the formation of a complex. The haloimide **4** and iodine were consumed in the course of the reaction, and therefore both were actually reagents. However, the generation of ICl made it possible to use catalytic amounts of I₂ in the reaction. According to the proposed mechanism, complex **5** reacted with the chiral triaryl phosphate **3**, which led to the formation of an active iodinating species (Figure 3B).



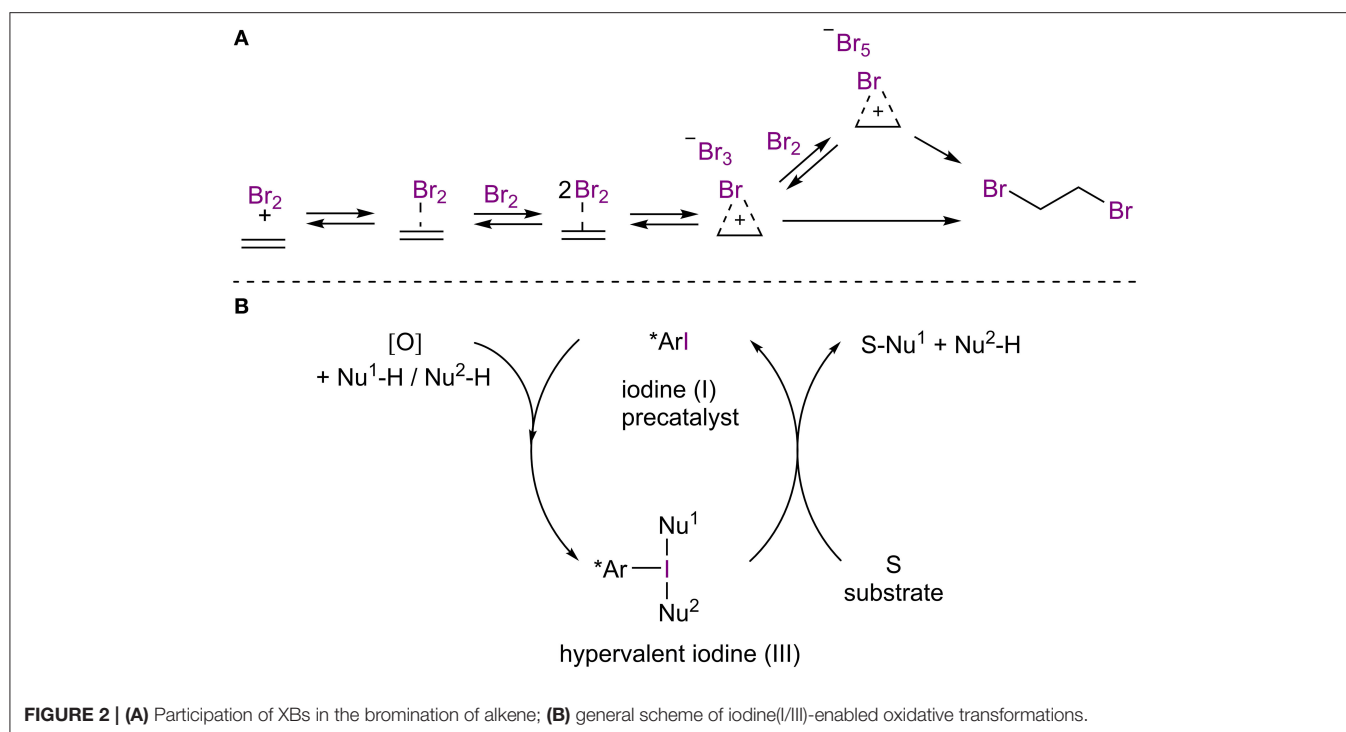


FIGURE 2 | (A) Participation of XBs in the bromination of alkene; **(B)** general scheme of iodine(I/III)-enabled oxidative transformations.

This in turn reacted with the double bond of **1** resulting in a chiral iodonium ion due to the presence of **3**. Intramolecular ring closure by the carboxyl group gave product **2**. The halogenating complex **5** is much more reactive than I_2 or **4** alone and made it possible to conduct the reaction at -78°C , which resulted in higher selectivities. Under optimized conditions, γ -lactones **2** were obtained in moderate to excellent yields (63–99%), with up to excellent enantioselectivities (2–99% *ee*). Similar halogenating complexes have been successfully used in other applications as well. However, often the XB contribution in these systems is not discussed (Kwon et al., 2008; Veitch and Jacobsen, 2010; Tungen et al., 2012; Arai et al., 2013, 2015a,b), or is only mentioned in passing, without in-depth studies resulting in new knowledge on the XB contribution (Mizar et al., 2014; Lu et al., 2018).

The definition of halogen bonding is inclusive of hypervalent halogens, although monovalent halogens have found wider use in catalytic applications. As one of the first examples, diaryliodonium salts were used as catalysts in a three-component Mannich reaction (Figure 4; Zhang et al., 2015). A very low level of enantioinduction was achieved with the use of salt **6** containing a chiral BINOL-based phosphate as the counterion. The Lewis acidic diaryliodonium cation was assumed to activate either the carbonyl or the imine group of the substrates through lowering their LUMO. Thus, the counterion was responsible for enantioinduction and this example is representative of asymmetric counterion-directed catalysis (ACDC; Mahlau and List, 2013). Although the authors did not mention the term XB catalysis and presented the work as an example of Lewis acid catalysis, then due to the nature of XBs it is pertinent to include the example in this review. Catalytic activity of the salts was inferred from

a few comparative experiments. For example, no reaction took place without the diaryliodonium salts and Brønsted acids were less efficient than the achiral salts in facilitating the reaction and provided comparable yields of product if at least one equivalent of the acid was used. Unfortunately, the mechanism of the reaction and the exact cause of enantioinduction were not elaborated, leaving unclear the true nature of the catalysis.

Arai et al. reasoned the importance of the formation of an XB network in the metal acetate-catalyzed asymmetric halolactonization reaction (Figure 5A; Arai et al., 2019) with DFT calculations. The use of I_2 (or Br_2) as an additive helped to facilitate the formation of an XB network with NIS/NBS, which resulted in the acceleration of the reaction, without affecting the stereochemical control (Figure 5B). In the case of bromolactonization a similar effect could be obtained with an increase in reaction temperature from -78 to -40°C . DFT calculations of the transition state (TS) of the iodolactonization revealed that alkene activation and iodine transfer occurred from NIS in the absence of I_2 and from I_2 when it was present (Figure 5C). The addition of I_2 did not significantly influence the organization of the TS, but in the presence of the XB network the TS was greatly stabilized (by 12.6 kcal/mol), leading to a faster reaction. As I_2 was regenerated in the process, it could be used in catalytic quantities. Under optimized conditions, δ -lactones were obtained in moderate to excellent yields (I: 74–99%, Br: 56–99%) with moderate to excellent enantioselectivities (I: 45–99% *ee*, Br: 72–99% *ee*), and γ -lactones were obtained in good to excellent yields (I: 80–99%), with excellent diastereoselectivities (I: dr 96:4–99:1) and good to excellent enantioselectivities (I: 79–99% *ee*).

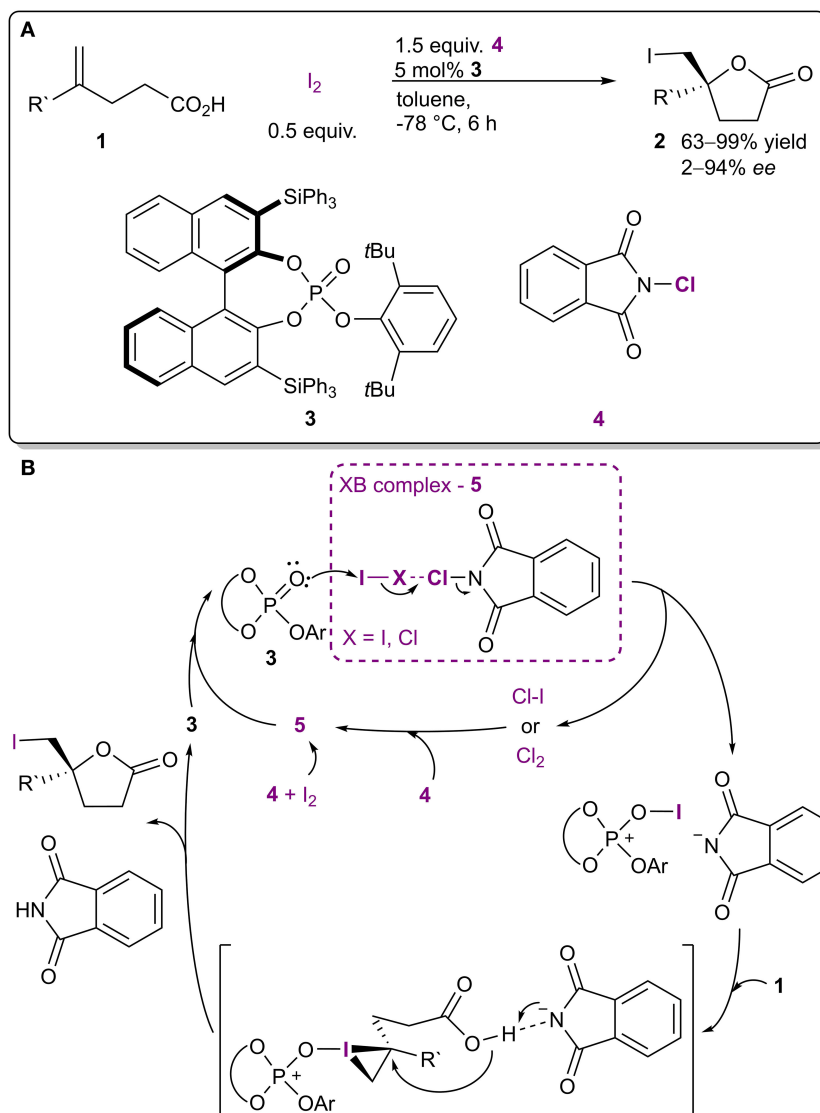


FIGURE 3 | (A) Lewis base-catalyzed halocyclization utilizing the complex **5** as a halogenating agent; **(B)** proposed mechanism of the reaction.

Recently, XBs were utilized in an enantioselective dehydrative cyclization of allylic alcohols **8** *N*-tethered to pyrroles (**Figure 6A**; Iwase et al., 2020). The authors proposed a mechanism in which the allylic alcohol **8** was activated by both the Brønsted acid fragment and the ruthenium species of the catalyst **9** (**Figure 6B**). At the same time, the XB donor fragment of the catalyst stabilized the substrate/catalyst complex through a σ - π XB to a pyrrole core and also brought the nucleophilic and electrophilic parts of the substrate closer together. These effects in turn led to an S_N2' -type cyclization. Interestingly, the choice of the XB donor atom had almost no influence on the selectivity of the reaction (94%/96%/98% ee respectively for I/Br/Cl). On the other hand, the activity was greatly affected by this choice and aligned with the XB donor ability of the halogens (99%/65%/9% conversion after 30 min for I/Br/Cl, respectively). This trend was used to

support the XB-involved mechanism. The scope of the reaction revealed that in almost all of the cases the cyclic products **10** were obtained with high yields (up to 99%) and excellent selectivities (up to 98% ee). Interestingly, the catalytic system and its analogs were first developed ten years ago by Kitamura et al. and have been used in similar asymmetric intramolecular dehydrative allylations (**Figure 6C**; Tanaka et al., 2009; Seki et al., 2012; Suzuki et al., 2015). In the initial publication, the chloro group seemed to play a more crucial role than just a steric control unit and it was speculated that the chloro group helped to stabilize the TS by lowering the LUMO level (Tanaka et al., 2009). Nevertheless, the possibility of XB participation in these cyclizations was only proposed in their most recent study. Another implication of the series of publications is the fact that XBs might also be operable in other catalytic systems that could have gone unnoticed since

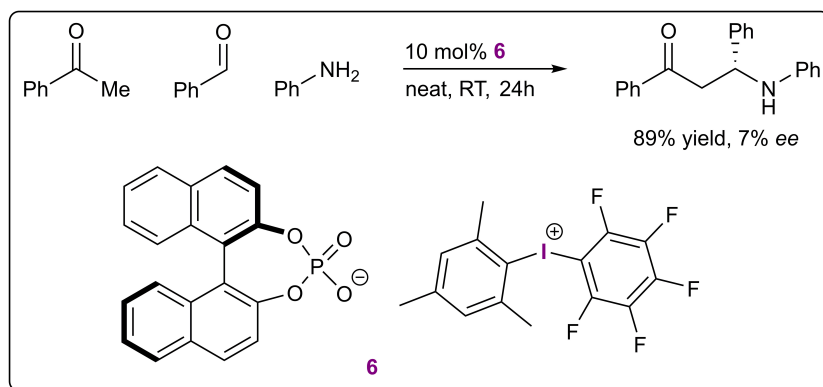


FIGURE 4 | Three-component Mannich reaction catalyzed by diaryliodonium salt **6**.

information about XBs has reached a wider audience only in the past 20 years.

XBs IN ENHANCING BOTH REACTIVITY AND STEREOSELECTIVITY

Chiral pentanidium salts **13** containing an XB donor fragment were used as phase-transfer catalysts (PTCs) in the enantioselective alkylation of sulfonate anions (**Figure 7A**; Zong et al., 2014). First, cesium hydroxide converted the β -sulfinyl methyl ester **11** into the corresponding enolate, which decomposed into methyl acrylate **15** and a sulfonate anion that formed a chiral complex **14** with the cationic part of the PTC (**Figure 7B**). Molecular mechanics calculations revealed that a halogen bond (**Figure 7C**) along with hydrogen bonds were formed between the catalyst and the leaving halide group of the alkylating agent in the TS, resulting in the enantioselective formation of the sulfoxide **12**. The presence of this XB was used to rationalize some of the observed trends. Initial optimization reactions revealed that if the leaving group was a bromide anion, the presence of a halogen atom in the catalyst had a more profound influence on the stereoselectivity than on the reactivity (76% yield and 61% *ee* compared to 72% yield and 81% *ee* if the non-halogenated or the brominated analog was used, respectively). On the other hand, when the leaving group was a chloride anion, the presence of a halogen atom in catalyst **13** had a more profound influence on the reactivity than on the selectivity (27% of only side product **16** obtained after 48 h compared to 29% yield of product **12** with 90% *ee* after 24 h if the non-halogenated or the iodinated analog was used, respectively). The formation of the side product **16** took place when the anionic intermediate attacked the initially released methyl acrylate **15** if the alkyl halide was omitted from the reaction mixture or when a less active electrophile was used along with the non-halogenated or chlorinated version of the PTC **13**. It was also demonstrated that, although the iodinated catalyst gave the best results, in specific cases the brominated analog should be used instead. With the optimized

conditions, a set of products **12** were obtained in moderate to high yields (65–88%) and high to excellent stereoselectivities (77–94% *ee*). In 2016 Tan et al. used the same catalyst family to achieve enantioselective alkylation of dihydrocoumarins (Teng et al., 2016). Major differences in the selectivity and the reactivity of the reaction using the halogenated catalysts were not observed, but all of the halogenated catalysts showed higher selectivities compared to the corresponding hydrogenated and methylated analogs. In 2015 Tan et al. used similar catalysts **18**, in which only some of the R substituents on the nitrogen atoms of the pentanidium contained halogen atoms, to achieve an enantioselective conjugate addition between oxindoles **17** and vinyl sulfones (**Figure 7D**; Zong et al., 2015). A slight increase in the selectivity of the reaction was observed with the variation of halogen atoms corresponding to the size/polarizability order (as $F < Cl < Br < I$ with 78% < 80% < 83% < 90% *ee* of **19**). Unfortunately, neither of the studies explored the role of the halogen atom or the participation of XBs on the outcome of the reaction.

The Arai research group combined a Brønsted base fragment and an XB donor motif into a bifunctional organocatalyst **22**, which was used in an enantioselective Mannich reaction (**Figure 8A**; Kuwano et al., 2018). This example is also important for the fact that from the outset of the study, the XB donating core was a key design element of an asymmetric catalyst which was successfully used to achieve high levels of enantioinduction. Different catalyst core structures were explored and in the case of two such cores (**22** and **24**), a comparison between the non-halogenated and the halogenated systems was made. When non-halogenated analogs of the catalysts were used containing either an isosteric methyl group or a hydrogen atom, both the activity and the selectivity dropped significantly (from 92%/74% yield and 82%/85% *ee* for the iodinated catalysts **22a/24a** to 47%/41% yield and 12%/8% *ee* for the hydrogen analogs **22b/24b** and -/56% yield and -/24% *ee* for the methylated analog **24c**; **Figure 8B**). NMR experiments were also conducted with truncated analogs of **22**, containing only a part of the catalyst, to determine the most plausible interaction sites in catalyst **22a** and the substrates. Shift changes observed in the NMR spectra indicated the formation of

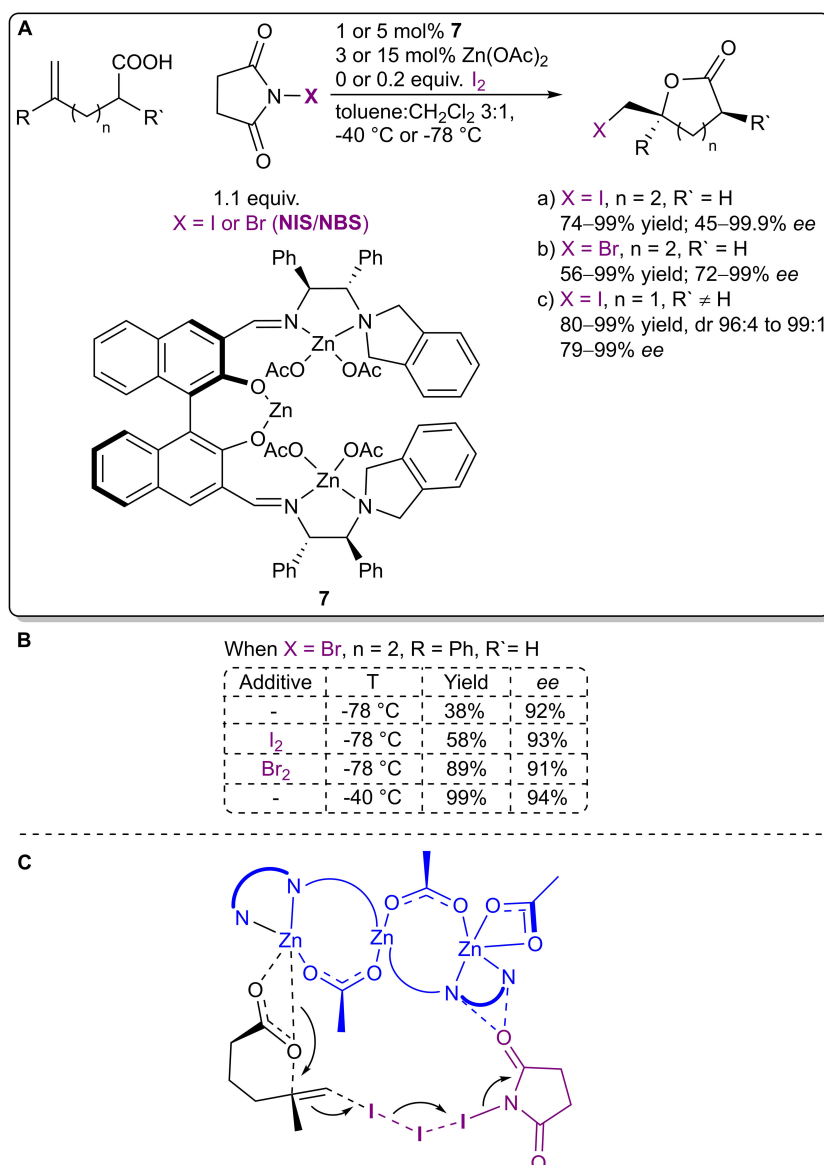


FIGURE 5 | (A) Zinc acetate-catalyzed asymmetric halolactonization using the I₂-NIS/NBS complex as a halogenating agent; **(B)** the influence of additives and temperature on the bromolactonization; **(C)** the proposed transition state for the iodolactonization.

an XB between imine **21** and the XB donor motif of **22a**. Based on the observations, a likely mechanism was proposed in which the base was used to deprotonate and activate the nucleophilic malononitrile **20** and the XB donor motif was used to activate and coordinate the imine **21** through its carbonyl group (**Figure 8C**). Several substituents on the imine **21** were tolerated, which led to products **23** with excellent yields and stereoselectivities (up to 99% yield and 98% ee). It was also demonstrated that the new bifunctional XB catalyst **22a** was superior to a known chiral thiourea catalyst acting mainly through HBs.

The next two examples are again representative of asymmetric counterion-directed catalysis. Iodo-imidazolium salts **25a** were used to activate *N*-acyliminium ions in a halogen abstraction

type reaction (**Figure 9A**; Chan and Yeung, 2019). It was postulated that the catalyst transformed an initially formed *N*-acyliminium chloride into a more reactive triflate intermediate by binding the chloride ions through XBs. In a preliminary experiment (**Figure 9C**), a low level of asymmetric induction was achieved with the use of salt **27** containing a chiral BINOL-based phosphate as the counterion. It should be noted that the corresponding phosphoric acid **28** also demonstrated catalytic activity with a somewhat higher level of activity and a lower level of selectivity (**Figure 9D**). Therefore, XBs seem to have influenced both the reactivity and selectivity of the reaction, although in theory the latter should have only been affected by the chiral counterion. The exact nature of the asymmetric induction

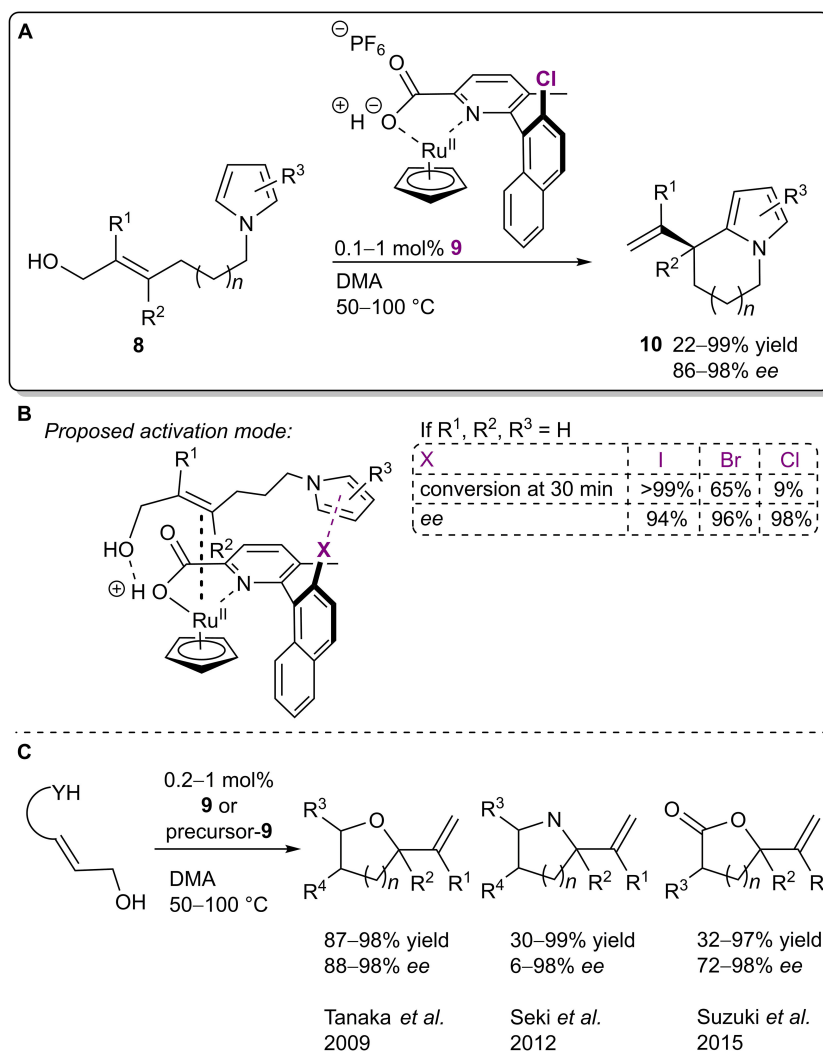


FIGURE 6 | (A) Ruthenium-catalyzed dehydrative cyclization of allylic alcohols **8**; **(B)** proposed activation mode and influence of the halogen atom on the reaction; **(C)** other dehydrative cyclizations performed in the presence of **9** or its precursors.

was not further explored, although control experiments carried out with an achiral analog of the catalyst **27** supported an activation mode by halogen bonding in general (**Figure 9B**). First, the hydrogen analog **25b** was inactive in the reaction. Next, ^{13}C NMR experiments revealed a significant interaction between catalyst **25a** and chloride anions and demonstrated that **25a** did not substantially interact with TMS-Cl, ruling out the activation of it. Finally, the reaction could be shut down with the use of excess chloride anions, which was not possible when TfOH was used to catalyze the reaction.

In the same year, 1,2,4-triazolium salts were used to catalyze a Michael reaction between indole **29** and *trans*-crotonophenone **30** (**Figure 10A**; Squitieri *et al.*, 2019). The use of enantiopure catalysts with chiral cationic backbones did not result in the formation of enantioenriched product **31** (catalysts **32** and **33**; **Figure 10B**). On the other hand, a low level of asymmetric induction was achieved using salt **34**

with an achiral cationic backbone and a chiral BINOL-based phosphate as the counterion. Similar to the previous example, the BINOL-based phosphoric acid **35** yielded the product **31** in a somewhat lower selectivity. The activation of the carbonyl group of **30** was envisioned to come from the XB and ^{13}C NMR experiments revealed that the 1,2,4-triazolium salts can interact with some Lewis bases, including carbonyl compounds. Both the selectivity and reactivity seemed to be affected by the presence of the iodoazolum part of the catalyst **34**. However, control experiments carried out with the corresponding phosphoric acid **35** and in the presence of proton scavengers did not support an activation mode by XBs. It was concluded that the true catalytic activity was the result of hidden Brønsted acid catalysis. This is a constant danger associated with the development of XB catalysis, as sufficient levels of catalytic activity are often achieved only with the use of charged azolum-type XB donors. In addition, a recent computational publication

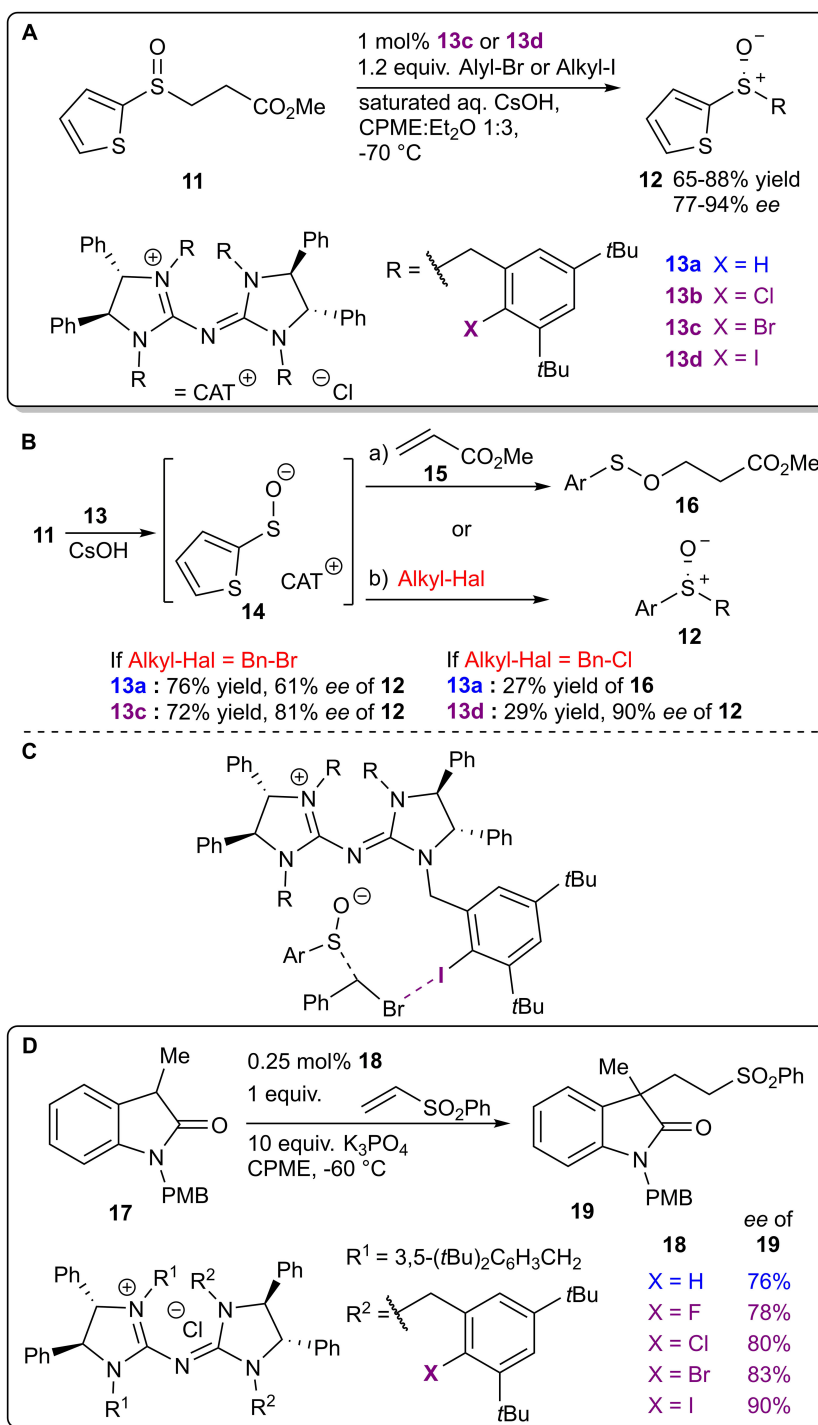


FIGURE 7 | (A) Enantioselective alkylation of sulfenate anions; **(B)** alternative reaction pathways and influence of halogen atoms on the reaction outcome; **(C)** proposed XB participation in the TS leading to product **12**; **(D)** chiral pentanidium salt-catalyzed enantioselective Michael reaction.

explored quinone activation by XBs in a Hantzsch ester reduction reaction (He et al., 2014) and demonstrated that a Brønsted acid-catalyzed pathway should be more favorable (Ser et al., 2019). These examples highlight the importance of control

experiments in catalyst development to confirm a mode of activation by XBs.

It should be noted that several chiral XB donors have been featured in publications on XB catalysis (Kniep et al., 2012;

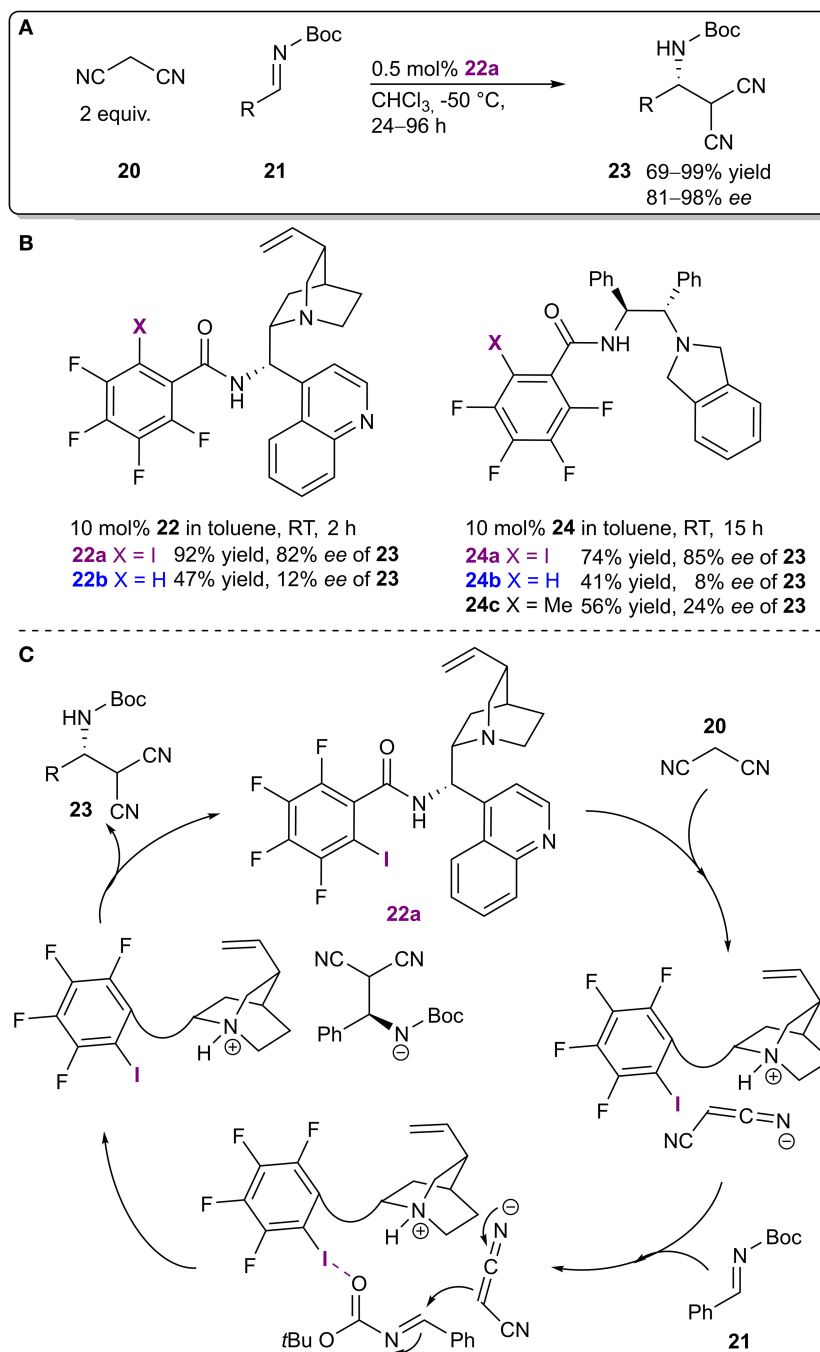


FIGURE 8 | (A) Enantioselective Mannich reaction; **(B)** catalysts probed to determine the influence of the halogen atom on the reaction; **(C)** proposed catalytic cycle.

He et al., 2014; Kaasik et al., 2019). However, the presence of asymmetric induction was not observed or discussed in these publications. Kaasik et al. (2019) used chiral 1,2,3-triazolium salts to activate imines in an aza-Diels-Alder reaction, which provided a racemic product. Similar XB donors had previously been demonstrated to discriminate between the enantiomers of a chiral thiourea (Kaasik et al., 2017). However, the discrimination

of enantiomers of a chiral imine and a chiral amine by these donors was not observed (Peterson et al., 2019). Based on these reports, the authors reasoned that additional noncovalent interactions were also needed to facilitate enantiodiscrimination. In addition, Beer et al. demonstrated the possibility of using XBs to discriminate between chiral anions if bidentate XB donors were used (Lim et al., 2016, 2018; Borissov et al., 2017).

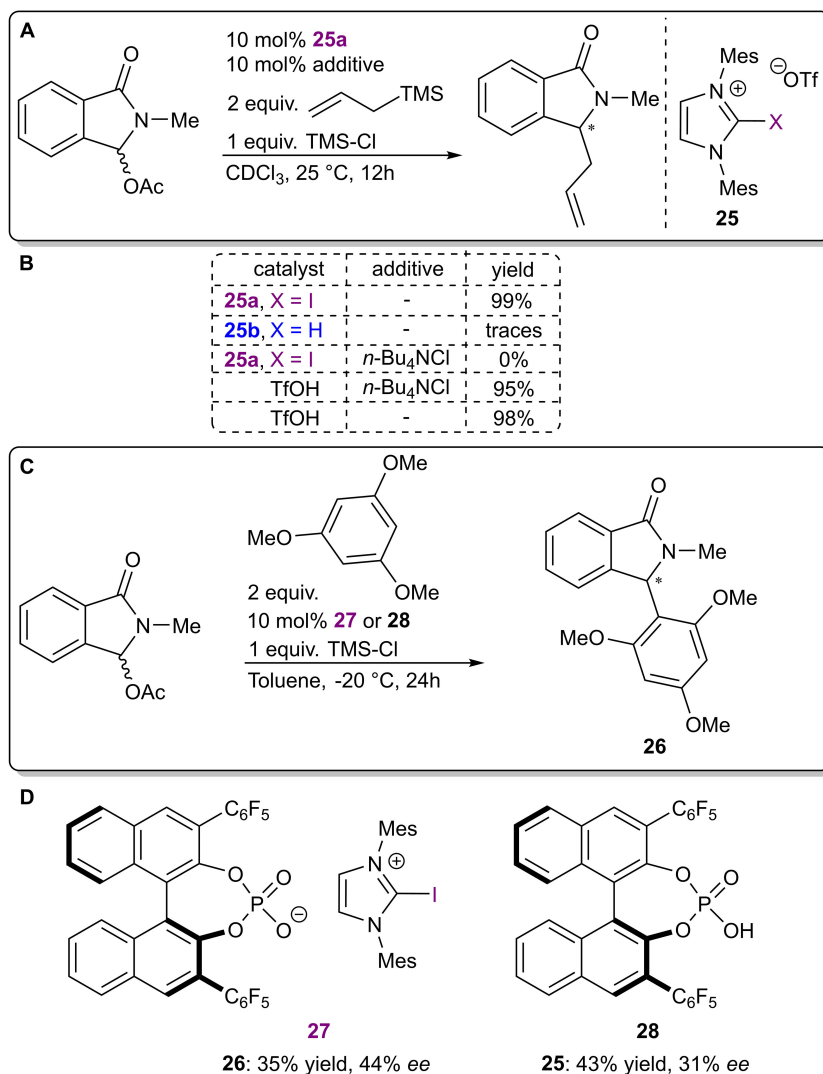


FIGURE 9 | (A) Iodo-imidazolium triflate-catalyzed nucleophilic addition to α -oxo-lactams; **(B)** control experiments used to determine the influence of the halogen atom; **(C)** reaction conditions used in the asymmetric variant; **(D)** catalytic systems used in the asymmetric reaction.

Recently the Huber group published the first example of a purely XB-based catalyst achieving enantioinduction in a reaction (**Figure 11A**; Sutar et al., 2020). The novel catalyst **39** featured a bidentate iodoimidazolium core for substrate activation with rigidly fixed “chiral” sidearms to achieve enantioinduction. The performance of the catalyst was improved further by pre-organizing the XB-donating sidearms into the syn configuration by placing a methyl group in the phenyl linker unit. ^1H NMR experiments confirmed that the chiral XB donor could discriminate between enantiomers of a chiral bidentate diamine. These observations were supported by DFT calculations, which indicated that the differentiation was the result of different spatial orientations of the acceptors toward the XB donor. Therefore, bidentate acceptors **36** featuring adjacent carbonyl groups were used as substrates in a Mukayama aldol reaction with silyl enol ethers **37**. No reaction took place in the

absence of the catalyst and in the case of the hydrogen analog of the catalyst (**Figure 11B**). Furthermore, possible decomposition products of the catalyst were either inactive or less active. These results supported the hypothesis of activation by XBs. The authors proposed that the bidentate nature of the substrate **36** was important both for the activity and the selectivity, as monocarbonyl electrophiles (benzaldehyde and *o*-anisaldehyde) led to products with a decreased selectivity or yield. With the use of the more active prefixed catalyst variant, the enantioselectivity of **38** was increased to 33% ee at -70°C . Although quite low in the sense of traditional asymmetric catalysis, this is an important milestone in the development of asymmetric XB catalysis.

The Arai group has recently published a paper on an enantioselective haloesterification reaction between styrenes **40** and benzoic acids **41** utilizing a chiral dinuclear zinc complex formed *in situ* from chiral ligand **42** and zinc carboxylate **43**

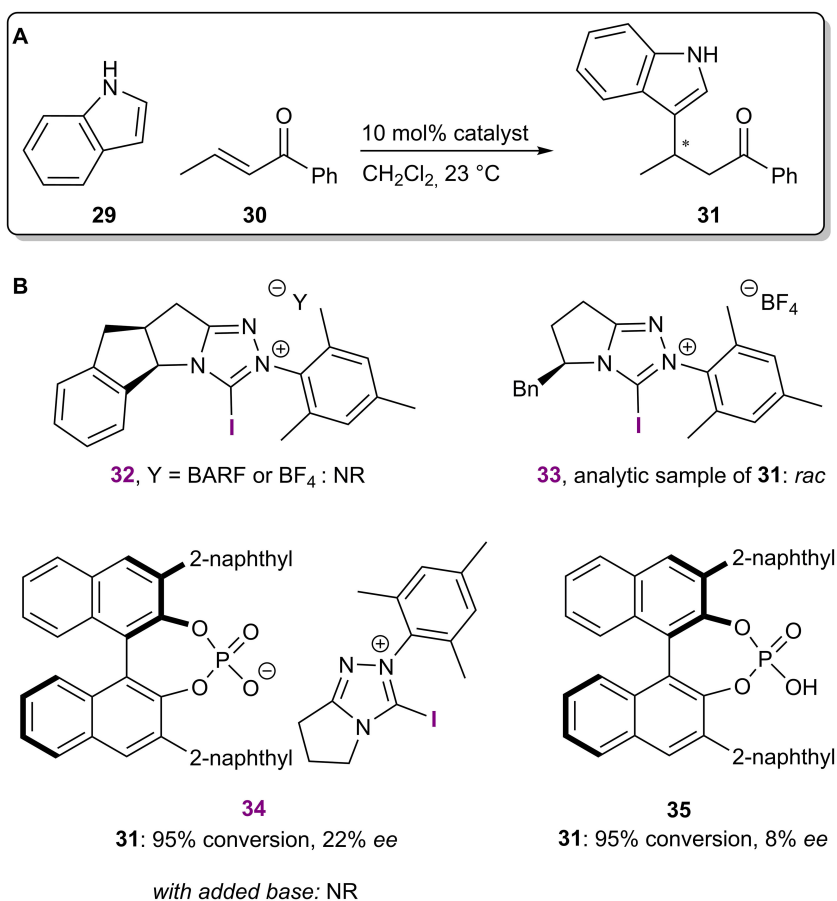


FIGURE 10 | (A) Iodo-1,2,4-triazolium salt-catalyzed Michael reaction; **(B)** chiral catalytic systems used in the reaction.

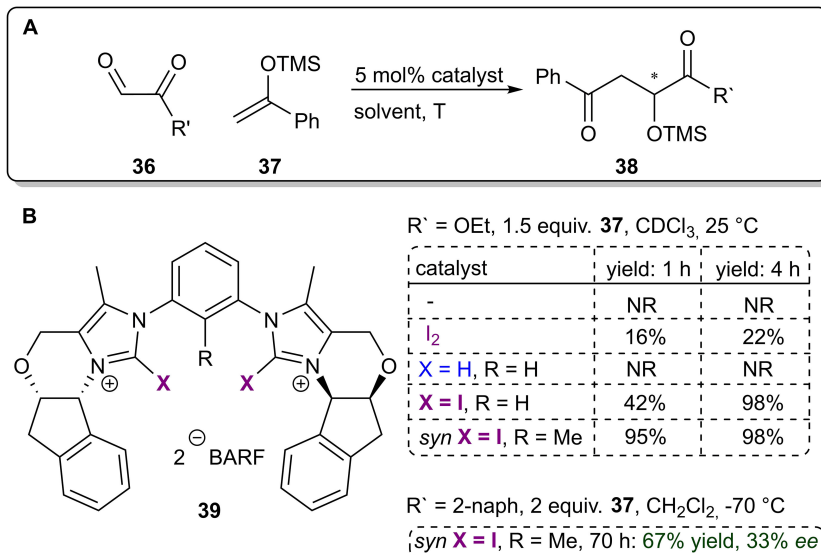


FIGURE 11 | (A) Enantioselective XB-catalyzed Mukayama aldol reaction, yields refer to approximate values from Figure 6 in the publication (Sutar et al., 2020); **(B)** influence of the structure of the catalyst and reaction conditions on the reaction outcome.

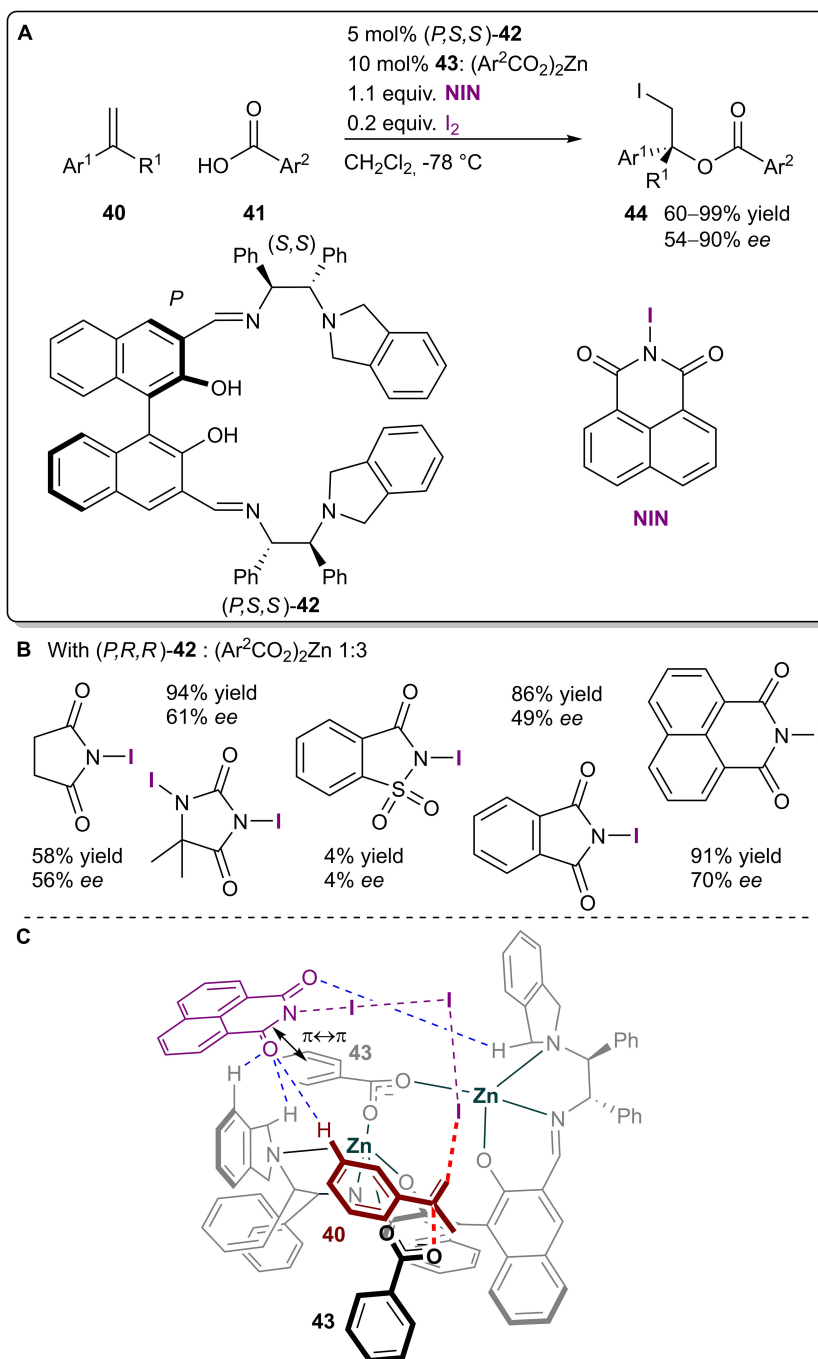


FIGURE 12 | (A) Zinc-catalyzed asymmetric iodoesterification utilizing the I₂-**NIN** complex as a halogenating agent; **(B)** comparison of the influence of the different halogen sources on the reaction; **(C)** proposed TS structure leading to the major product.

(Figure 12A; Arai et al., 2020). XBs were again used for the generation of active iodinating species. The use of different iodoimides affected both the yield and selectivity of the reaction (Figure 12B). Based on DFT calculations and their earlier study (Arai et al., 2019), the authors proposed a transition state structure, in which a halogen-bonding network activated the styrene **40** from the *Re*-face, while the nucleophilic zinc

carboxylate **43** attacked the double bond from the other side, giving the *R*-iodoester (Figure 12C). Hydrogen bonding and π - π interactions were also crucial for the organization of the 3D transition structure. As the exact influence of the different halogenating complexes on the enantioselectivity was not explored, it could be that the π - π stacking ability of the haloimide had a more profound role on stereoselectivity than the

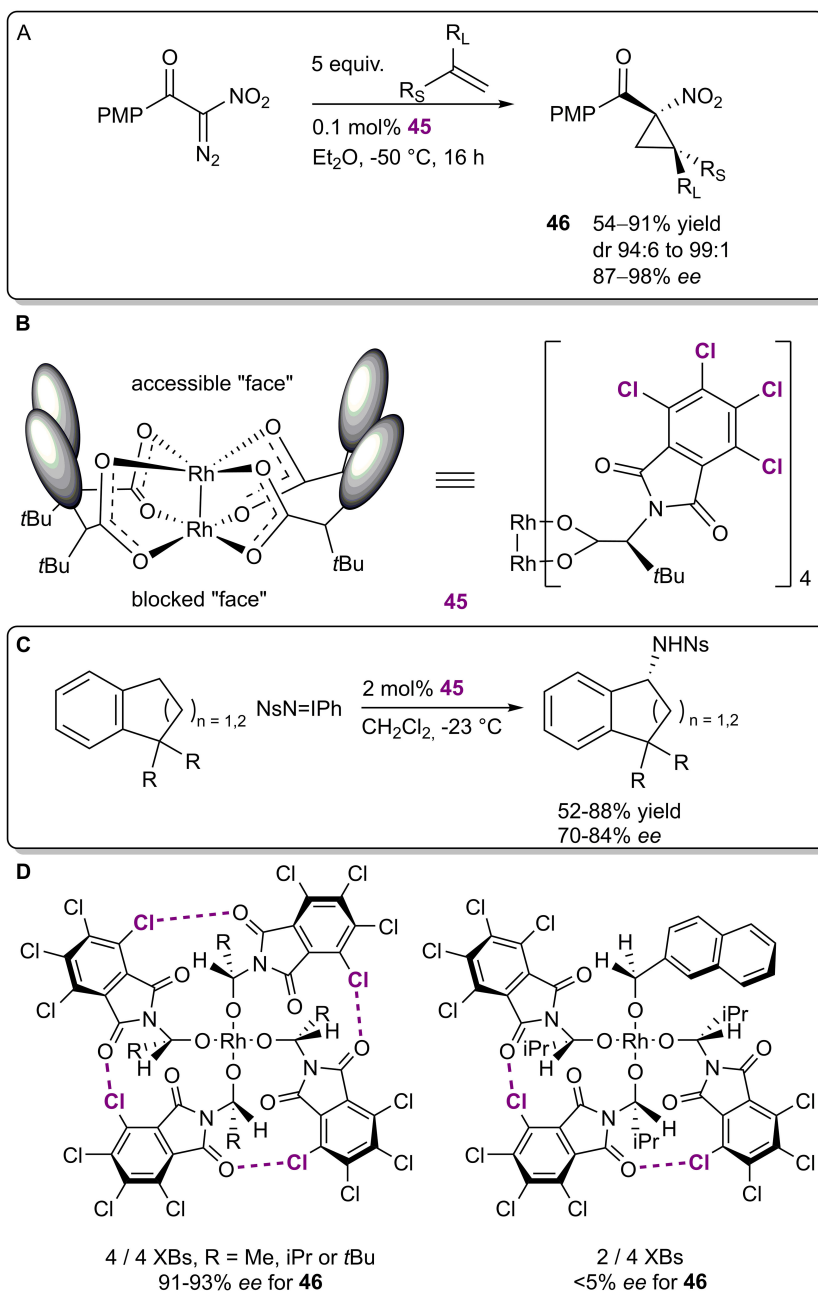


FIGURE 13 | (A) Enantioselective Ru-catalyzed cyclopropanation; **(B)** structure of the Ru-catalyst **45**; **(C)** enantioselective Ru-catalyzed amidation; **(D)** top view of two Ru-catalysts depicting the XB networks and their influence on the selectivity of the cyclopropanation.

XB donor ability of the haloimide. With the optimized conditions at hand, iodoesters **44** were obtained in moderate to excellent yields (60–99%) and moderate to good selectivities (54–90% *ee*).

XBs IN ENHANCING SELECTIVITY

In 2009, the Charette group published an example of an enantioselective Ru-catalyzed cyclopropanation (Figure 13A;

Lindsay et al., 2009) in which halogen bonds were used to fix the ligands of the ruthenium species **45** into a bowl shape (Figure 13B). The cyclopropanes **46** were obtained in moderate to excellent yields (54–91%), excellent diastereoselectivities (94:6–99:1) and good to excellent enantioselectivities (87–98% *ee*). Interestingly, the catalyst **45** was designed and successfully used in an enantioselective amidation reaction by the Hashimoto group as early as 2002 (Figure 13C; Yamawaki et al., 2002). At the time, it was reasoned that the chlorine atoms had a primarily

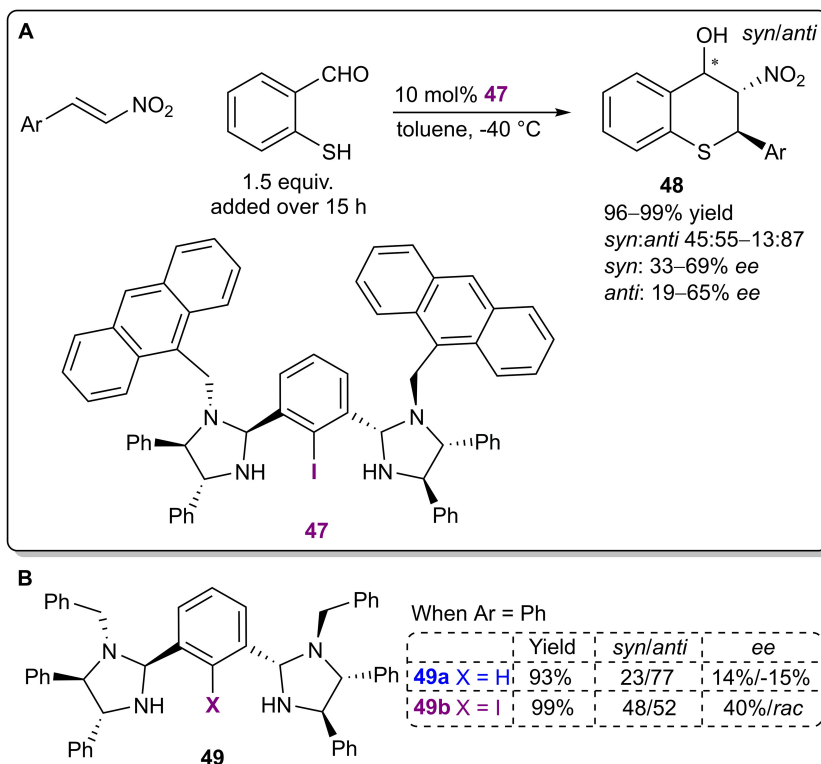


FIGURE 14 | (A) Bis(imidazolidine)iodobenzene- catalyzed enantioselective Michael/Henry cascade reaction; **(B)** influence of the halogen atom of the catalyst **49** on the reaction.

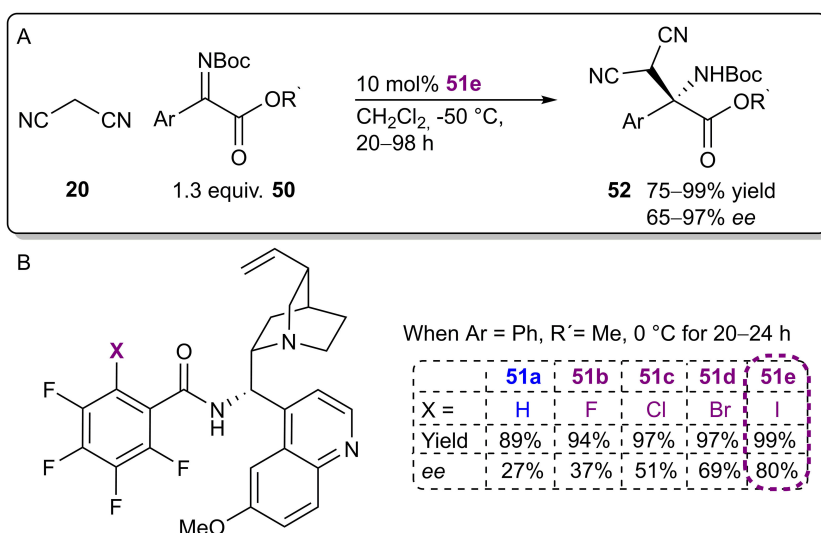


FIGURE 15 | (A) Enantioselective Mannich reaction catalyzed by bifunctional Brønsted base/XB catalyst **51e**; **(B)** influence of the halogen atom of the catalyst **51** on the reaction.

electronic influence on the catalyst, resulting in improved performance compared to other non-halogenated analogs. In contrast, Charette et al. obtained X-ray crystal structures of catalyst **45** and its non-halogenated version, and both had similar

bowl-shaped structures. ¹H-¹³C heteronuclear NOESY NMR experiments revealed that the halogenated version retained its shape in solution, leaving only one ruthenium atom accessible for catalysis, while the non-halogenated analog was more flexible.

The difference in flexibility was primarily attributed to the XBs formed among the ligands as observed in crystal structures. In a follow-up report, Charette et al. demonstrated that (by omitting XB acceptor or donor fragments from the catalyst) at least three XBs must form among the ligands to obtain high levels of selectivity, leaving room for catalyst design (Figure 13D; Lindsay and Charette, 2012). In the years since then, catalyst **45** or its analogs have been used in other enantioselective transformations, but catalytic applications have been the focus of the research (for selected examples, see: Goto et al., 2011; Liao et al., 2017; Rodriguez et al., 2018). As the shape of the catalyst and its effect on selectivity have been determined, the importance of the halogen bonding network has not been explored further and often is not mentioned in publications at all.

The Arai research group developed a chiral bis(imidazolidine)iodobenzene catalyst **47** based on the core of similar NCN-pincer metal complexes (Figure 14A; Arai et al., 2017). The organocatalysts were used in a Michael/Henry cascade reaction to obtain thiochromanes **48** with excellent yields (up to 99%), moderate diastereoselectivities (up to 13:87 *syn:anti*) and moderate enantioselectivities (up to 65% *ee* for the major *anti* diastereoisomer). Although the authors have stated that halogen bonding was an important catalyst design element, the exact mode of activation was not discussed, and not enough control experiments were conducted. A difference in stereoselectivity between the iodinated catalyst **49b** and its non-halogenated analog **49a** (40% *ee* and 14% *ee*, respectively, for the minor *syn* diastereomer during initial catalyst screening; Figure 14B) was observed, which can also be attributed to the steric influence of iodine. Notably, it is quite unlikely that an iodophenyl fragment without electron-withdrawing substituents forms a strong enough XB with the formyl group to single-handedly activate it. Due to the slow addition of the aldehyde throughout the reaction, the activity of the catalysts is also difficult to establish. In both cases the product was obtained in excellent yields (99 and 93%, respectively). Further catalyst optimization resulted in an increase in the previously mentioned selectivities with the use of sterically larger substituents in the catalyst instead of the benzyl substituents.

The Arai group continued research on their bifunctional Brønsted base/XB catalyst and recently published an example in which the catalysts were used to activate malononitrile **20** and ketiminoesters **50** in a Mannich reaction (Figure 15A; Kuwano et al., 2020). Catalyst optimization studies revealed a significant dependence between the donor atom and reaction selectivity that corresponded to the polarizability order of the halogens (82% > 69% > 51% > 37% > 27% *ee* for I > Br > Cl > F > H; Figure 15B). However, in contrast to their first study utilizing this catalytic system, the activity of the catalyst **51** was not greatly affected by this change (yields ranged from 89 to 99%). ¹⁹F NMR titration experiments also supported the participation of XBs. A truncated analog of catalyst **51e** without a chiral alkaloid fragment interacted more strongly with the imine than did the non-halogenated analog (affinity constant with values of K_a 0.90 M⁻¹ and K_a 0.17 M⁻¹, respectively). Based on these observation, a catalytic cycle

similar to the one described in their earlier publication was proposed: the electrophilic imine was activated by an XB to its carbonyl group (see Figure 8C). In future studies, it would be of interest to ascertain the role of the acidic amid NH proton. All in all, under optimized conditions enantioenriched products **52** were obtained in good to excellent yields (75–99%) and moderate to excellent selectivities (65–97% *ee*) using catalyst **51e**.

CONCLUSION AND PERSPECTIVE

About half of the examples, that received an in dept examination, have been published in the past 2 years, which demonstrates a significant increase in the interest in asymmetric XB catalysis. As mentioned throughout the review, the participation of XBs has not been acknowledged in several instances or in initial studies. This leads to the realization that there could be other examples in the literature in which the crucial role of XBs has remained unnoticed. Nevertheless, both the acknowledgment that XBs could participate in catalytic enantioselective processes and the deliberate use of XBs in these processes has increased.

So far, the use of cationic XB donors to achieve asymmetric induction has not been very successful, leading to at best moderate stereoselectivities. One would have to concur with the statement by Huber (Sutar and Huber, 2019) that the combination of the size of the halogen substituent, the length of its covalent bond and the linearity requirements of the corresponding XB make the task of achieving asymmetric induction very difficult. In principle, the relevance of XBs in purely XB-based catalysts should be simpler to confirm than the relevance of XBs in bifunctional catalysts. However, the possibility of other competing pathways in the case of charge-assisted XB catalysis hinders its development further. In contrast, bifunctional systems that have not utilized XBs as the primary mode of activation, but as secondary elements (that is, as organizing units or as secondary activating units) have led to better results. More surprisingly, the weaker neutral XB donor motifs are prevalent in these examples compared to charge-assisted XB donor motifs. With the publication of the first example utilizing only XBs to achieve asymmetric induction, the field might have reached a turning point in its development with new purely XB catalytic examples hopefully following in the near future.

It is also noteworthy that XB-donating units have been used in, or in combination with, very different catalyst types (Lewis bases, PTCs, Brønsted bases, and metal catalysts), demonstrating the wide reach of XBs. In addition, the examples discussed in this review cover a wide range of different reactions. Therefore, XBs have a lot of potential for applications in asymmetric catalysis. However, as the relevant information is scattered among a diverse set of examples it will not be a trivial task to use this knowledge successfully and this will depend on the ingenuity of the scientist. Acknowledging the influence of XBs on the reactivity or the selectivity of the reaction after the fact is much simpler than predicting this influence beforehand and then applying it successfully.

AUTHOR CONTRIBUTIONS

Both authors contributed substantially to the work reported, have read, and agreed to the published version of the manuscript.

REFERENCES

- Arai, T., Horigane, K., Suzuki, T. K., Itoh, R., and Yamanaka, M. (2020). Catalytic asymmetric iodoesterification of simple alkenes. *Angew. Chem. Int. Ed.* 59, 12680–12683. doi: 10.1002/anie.202003886
- Arai, T., Horigane, K., Watanabe, O., Kakino, J., Sugiyama, N., Makino, H., et al. (2019). Association of halogen bonding and hydrogen bonding in metal acetate-catalyzed asymmetric halolactonization. *iScience* 12, 280–292. doi: 10.1016/j.isci.2019.01.029
- Arai, T., Kajikawa, S., and Matsumura, E. (2013). The role of ni-carboxylate during catalytic asymmetric iodolactonization using pyridine-ni(OAc). *Synlett* 24, 2045–2048. doi: 10.1055/s-0033-1339676
- Arai, T., Kojima, T., Watanabe, O., Itoh, T., and Kanoh, H. (2015a). Recyclable Poly-Zn₃(OAc)₄-3,3'-Bis(aminoimino)binaphthoxide catalyst for asymmetric iodolactonization. *ChemCatChem* 7, 3234–3238. doi: 10.1002/cctc.201500842
- Arai, T., Suzuki, T., Inoue, T., and Kuwano, S. (2017). Chiral Bis(imidazolidine)iodobenzene (I-Bidine) organocatalyst for thiochromane synthesis using an asymmetric michael/henry reaction. *Synlett* 28, 122–127. doi: 10.1055/s-0036-1588614
- Arai, T., Watanabe, O., Yabe, S., and Yamanaka, M. (2015b). Catalytic asymmetric iodocyclization of N-tosyl alkenamides using aminoiminophenoxy copper carboxylate: a concise synthesis of chiral 8-Oxa-6-azabicyclo[3.2.1]octanes. *Angew. Chem. Int. Ed.* 54, 12767–12771. doi: 10.1002/anie.201505748
- Bamberger, J., Ostler, F., and Mancheño, O. G. (2019). Frontiers in halogen and chalcogen-bond donor organocatalysis. *ChemCatChem* 11, 5198–5211. doi: 10.1002/cctc.201901215
- Beale, T. M., Chudzinski, M. G., Sarwar, M. G., and Taylor, M. S. (2013). Halogen bonding in solution: thermodynamics and applications. *Chem. Soc. Rev.* 42, 1667–1680. doi: 10.1039/C2CS35213C
- Borissav, A., Lim, J. Y. C., Brown, A., Christensen, K. E., Thompson, A. L., Smith, M. D., et al. (2017). Neutral iodotriazole foldamers as tetradentate halogen bonding anion receptors. *Chem. Commun.* 53, 2483–2486. doi: 10.1039/C7CC00727B
- Breugst, M., and Koenig, J. J. (2020). σ -Hole interactions in catalysis. *Eur. J. Org. Chem.* 2020, 5473–5487. doi: 10.1002/ejoc.202000660
- Brinck, T., Murray, J. S., and Politzer, P. (1992). Surface electrostatic potentials of halogenated methanes as indicators of directional intermolecular interactions. *Int. J. Quantum Chem.* 44, 57–64. doi: 10.1002/qua.560440709
- Brown, R. S. (1997). Investigation of the early steps in electrophilic bromination through the study of the reaction with sterically encumbered olefins. *Acc. Chem. Res.* 30, 131–137. doi: 10.1021/ar960088e
- Bruckmann, A., Pena, M. A., and Bolm, C. (2008). Organocatalysis through halogen-bond activation. *Synlett* 2008, 900–902. doi: 10.1055/s-2008-1042935
- Cai, Y., Liu, X., Zhou, P., and Feng, X. (2019). asymmetric catalytic halofunctionalization of α,β -unsaturated carbonyl compounds. *J. Org. Chem.* 84, 1–13. doi: 10.1021/acs.joc.8b01951
- Cavallo, G., Metrangolo, P., Milani, R., Pilati, T., Priimagi, A., Resnati, G., et al. (2016). The halogen bond. *Chem. Rev.* 116, 2478–2601. doi: 10.1021/acs.chemrev.5b00484
- Chan, Y. C., and Yeung, Y. Y. (2019). Halogen-bond-catalyzed addition of carbon-based nucleophiles to n-acyliminium ions. *Org. Lett.* 21, 5665–5669. doi: 10.1021/acs.orglett.9b02006
- Cheng, Y. A., Yu, W. Z., and Yeung, Y. Y. (2014). Recent advances in asymmetric intra- and intermolecular halofunctionalizations of alkenes. *Org. Biomol. Chem.* 12, 2333–2343. doi: 10.1039/c3ob42335b
- Christopherson, J. C., Topić, F., Barrett, C. J., and Friščić, T. (2018). Halogen-bonded cocrystals as optical materials: next-generation control over light-matter interactions. *Cryst. Growth Des.* 18, 1245–1259. doi: 10.1021/acs.cgd.7b01445
- Claraz, A., and Masson, G. (2018). Asymmetric iodine catalysis-mediated enantioselective oxidative transformations. *Org. Biomol. Chem.* 16, 5386–5402. doi: 10.1039/C8OB01378K
- Clark, T., Hennemann, M., Murray, J. S., and Politzer, P. (2007). “Halogen bonding: the σ -hole,” in *Proceedings of “Modeling interactions in biomolecules II”*, Prague, September 5–9th, 2005. *J. Mol. Model.* 13, 291–296. doi: 10.1007/s00894-006-0130-2
- Colin, J. J., and de Claubry, H. (1814). Sur le combinaisons de l'iode avec les substances végétales et animales. *Ann. Chim* 90, 87–100.
- Cresswell, A. J., Eey, S. T. C., and Denmark, S. E. (2015). Catalytic, Stereoselective dihalogenation of alkenes: challenges and opportunities. *Angew. Chem., Int. Ed.* 54, 15642–15682. doi: 10.1002/anie.201507152
- Desiraju, G. R., Shing Ho, P., Kloo, L., Legon, A. C., Marquardt, R., Metrangolo, P., et al. (2013). Definition of the halogen bond (IUPAC recommendations 2013). *Pure Appl. Chem.* 85, 1711–1713. doi: 10.1351/PAC-REC-12-05-10
- Flores, A., Cots, E., Bergès, J., and Muñiz, K. (2019). Enantioselective Iodine(I/III) catalysis in organic synthesis. *Adv. Synth. Catal.* 361, 2–25. doi: 10.1002/adsc.201800521
- Gilday, L. C., Robinson, S. W., Barendt, T. A., Langton, M. J., Mullaney, B. R., and Beer, P. D. (2015). Halogen bonding in supramolecular chemistry. *Chem. Rev.* 115, 7118–7195. doi: 10.1021/cr500674c
- Goto, T., Takeda, K., Shimada, N., Nambu, H., Anada, M., Shiro, M., et al. (2011). Highly enantioselective cyclopropanation reaction of 1-alkynes with α -alkyl- α -diazoesters catalyzed by dirhodium(II) carboxylates. *Angew. Chem. Int. Ed.* 50, 6803–6808. doi: 10.1002/anie.201101905
- He, W., Ge, Y. C., and Tan, C. H. (2014). Halogen-bonding-induced hydrogen transfer to C=N bond with hantzsch ester. *Org. Lett.* 16, 3244–3247. doi: 10.1021/ol501259q
- Heinen, F., Engelage, E., Cramer, C. J., and Huber, S. M. (2020). Hypervalent Iodine(III) compounds as biaxial halogen bond donors. *J. Am. Chem. Soc.* 142, 8633–8640. doi: 10.1021/jacs.9b13309
- Iwase, S., Suzuki, Y., Tanaka, S., and Kitamura, M. (2020). CpRu/Brønsted acid-catalyzed enantioselective dehydrative cyclization of pyrroles n-tethered with allylic alcohols. *Org. Lett.* 22, 1929–1933. doi: 10.1021/acs.orglett.0c00290
- Jentzsch, A. V. (2015). Applications of halogen bonding in solution. *Pure Appl. Chem.* 87, 15–41. doi: 10.1515/pac-2014-0807
- Kaasik, M., Kaabel, S., Kriis, K., Järving, I., Aav, R., Rissanen, K., et al. (2017). Synthesis and characterisation of chiral triazole-based halogen-bond donors: halogen bonds in the solid state and in solution. *Chem. Eur. J.* 23, 7337–7344. doi: 10.1002/chem.201700618
- Kaasik, M., Metsala, A., Kaabel, S., Kriis, K., Järving, I., and Kanger, T. (2019). Halo-1,2,3-triazolium salts as halogen bond donors for the activation of imines in dihydropyridinone synthesis. *J. Org. Chem.* 84, 4295–4303. doi: 10.1021/acs.joc.9b00248
- Kniep, F., Jungbauer, S. H., Zhang, Q., Walter, S. M., Schindler, S., Schnapperelle, I., et al. (2013). Organocatalysis by neutral multidentate halogen-bond donors. *Angew. Chem. Int. Ed.* 52, 7028–7032. doi: 10.1002/anie.201301351
- Kniep, F., Rout, L., Walter, S. M., Bensch, H. K. V., Jungbauer, S. H., Herdtweck, E., et al. (2012). 5-Iodo-1,2,3-triazolium-based multidentate halogen-bond donors as activating reagents. *Chem. Commun.* 48, 9299–9301. doi: 10.1039/c2cc34392d
- Kristianslund, R., Tungen, J. E., and Hansen, T. V. (2019). Catalytic enantioselective iodolactonization reactions. *Org. Biomol. Chem.* 17, 3079–3092. doi: 10.1039/C8OB03160F
- Kuwano, S., Nishida, Y., Suzuki, T., and Arai, T. (2020). Catalytic asymmetric mannich-type reaction of malononitrile with N-Boc α -ketiminoesters using chiral organic base catalyst with halogen bond donor

- functionality. *Adv. Synth. Catal.* 362, 1674–1678. doi: 10.1002/adsc.202000092
- Kuwano, S., Suzuki, T., Hosaka, Y., and Arai, T. (2018). A chiral organic base catalyst with halogen-bonding-donor functionality: asymmetric Mannich reactions of malononitrile with: N -Boc aldimines and ketimines. *Chem. Commun.* 54, 3847–3850. doi: 10.1039/C8CC00865E
- Kwon, H. Y., Park, C. M., Lee, S. B., Youn, J. H., and Kang, S. H. (2008). Asymmetric iodocyclization catalyzed by salen-CrIII/Cl: its synthetic application to swainsonine. *Chem. Eur. J.* 14, 1023–1028. doi: 10.1002/chem.200701199
- Lenoir, D., and Chiappe, C. (2003). What is the nature of the first-formed intermediates in the electrophilic halogenation of alkenes, alkynes, and allenes? *Chem. Eur. J.* 9, 1036–1044. doi: 10.1002/chem.200390097
- Li, B., Zang, S.-Q., Wang, L.-Y., and Mak, T. C. W. (2016). Halogen bonding: a powerful, emerging tool for constructing high-dimensional metal-containing supramolecular networks. *Coord. Chem. Rev.* 308, 1–21. doi: 10.1016/j.ccr.2015.09.005
- Liao, K., Pickel, T. C., Boyarskikh, V., Bacsá, J., Musaev, D. G., and Davies, H. M. L. (2017). Site-selective and stereoselective functionalization of non-activated tertiary C-H bonds. *Nature* 551, 609–613. doi: 10.1038/nature24641
- Lim, J. Y. C., Marques, I., Félix, V., and Beer, P. D. (2018). Chiral halogen and chalcogen bonding receptors for discrimination of stereo- and geometric dicarboxylate isomers in aqueous media. *Chem. Commun.* 54, 10851–10854. doi: 10.1039/C8CC06400H
- Lim, J. Y. C., Marques, I., Ferreira, L., Félix, V., and Beer, P. D. (2016). Enhancing the enantioselective recognition and sensing of chiral anions by halogen bonding. *Chem. Commun.* 52, 5527–5530. doi: 10.1039/C6CC01701K
- Lindsay, V. N. G., and Charette, A. B. (2012). Design and synthesis of chiral heteroleptic rhodium(II) carboxylate catalysts: experimental investigation of halogen bond rigidification effects in asymmetric cyclopropanation. *ACS Catal.* 2, 1221–1225. doi: 10.1021/cs300214v
- Lindsay, V. N. G., Lin, W., and Charette, A. B. (2009). Experimental evidence for the all-up reactive conformation of chiral rhodium(II) carboxylate catalysts: enantioselective synthesis of cis-cyclopropane α -amino acids. *J. Am. Chem. Soc.* 131, 16383–16385. doi: 10.1021/ja9044955
- Lu, Y., Nakatsuji, H., Okumura, Y., Yao, L., and Ishihara, K. (2018). Enantioselective halo-oxy- and halo-azacyclizations induced by chiral amidophosphate catalysts and halo-lewis acids. *J. Am. Chem. Soc.* 140, 6039–6043. doi: 10.1021/jacs.8b02607
- Mahlau, M., and List, B. (2013). Asymmetric counteranion-directed catalysis: Concept, definition, and applications. *Angew. Chem., Int. Ed.* 52, 518–533. doi: 10.1002/anie.201205343
- Metrangolo, P., Neukirch, H., Pilati, T., and Resnati, G. (2005). Halogen bonding based recognition processes: a world parallel to hydrogen bonding. *Acc. Chem. Res.* 38, 386–395. doi: 10.1021/ar0400995
- Mizar, P., Burrelli, A., Günther, E., Söftje, M., Farooq, U., and Wirth, T. (2014). Organocatalytic stereoselective iodoamination of alkenes. *Chem. Eur. J.* 20, 13113–13116. doi: 10.1002/chem.201404762
- Montaña, Á. M. (2017). The σ and π Holes. *The halogen and tetrel bondings: their nature, importance and chemical, biological and medicinal implications.* *ChemistrySelect* 2, 9094–9112. doi: 10.1002/slct.201701676
- Murai, K., and Fujioka, H. (2013). Recent progress in organocatalytic asymmetric halocyclization. *Heterocycles* 87, 763–805. doi: 10.3987/REV-12-762
- Nakatsuji, H., Sawamura, Y., Sakakura, A., and Ishihara, K. (2014). Cooperative activation with chiral nucleophilic catalysts and n-haloimides: enantioselective iodolactonization of 4-arylmethyl-4-pentenoic acids. *Angew. Chem. Int. Ed.* 53, 6974–6977. doi: 10.1002/anie.201400946
- Nepal, B., and Scheiner, S. (2015). Substituent effects on the binding of halides by neutral and dicationic bis(triazolium) receptors. *J. Phys. Chem. A* 119, 13064–13073. doi: 10.1021/acs.jpca.5b09738
- Parra, A. (2019). Chiral hypervalent iodines: active players in asymmetric synthesis. *Chem. Rev.* 119, 12033–12088. doi: 10.1021/acs.chemrev.9b00338
- Pearson, R. G. (1963). Hard and soft acids and bases. *J. Am. Chem. Soc.* 85, 3533–3539. doi: 10.1021/ja00905a001
- Peterson, A., Kaasik, M., Metsala, A., Järving, I., Adamson, J., and Kanger, T. (2019). Tunable chiral triazole-based halogen bond donors: assessment of donor strength in solution with nitrogen-containing acceptors. *RSC Adv.* 9, 11718–11721. doi: 10.1039/C9RA01692A
- Rissanen, K. (2008). Halogen bonded supramolecular complexes and networks. *CrystEngComm* 10, 1107–1113. doi: 10.1039/b803329n
- Robertson, C. C., Perutz, R. N., Brammer, L., and Hunter, C. A. (2014). A solvent-resistant halogen bond. *Chem. Sci.* 5, 4179–4183. doi: 10.1039/C4SC01746C
- Robertson, C. C., Wright, J. S., Carrington, E. J., Perutz, R. N., Hunter, C. A., and Brammer, L. (2017). Hydrogen bonding: vs. halogen bonding: the solvent decides. *Chem. Sci.* 8, 5392–5398. doi: 10.1039/C7SC01801K
- Rodriguez, K. X., Pilato, T. C., and Ashfeld, B. L. (2018). An unusual stereoretentive 1,3-quaternary carbon shift resulting in an enantioselective RhII-catalyzed formal [4+1]-cycloaddition between diazo compounds and vinyl ketenes. *Chem. Sci.* 9, 3221–3226. doi: 10.1039/C8SC00020D
- Seki, T., Tanaka, S., and Kitamura, M. (2012). Enantioselective synthesis of pyrrolidine-, Piperidine-, and azepane-type N -heterocycles with α -alkenyl substitution: the CpRu-catalyzed dehydrative intramolecular N -allylation approach. *Org. Lett.* 14, 608–611. doi: 10.1021/ol203218d
- Ser, C. T., Yang, H., and Wong, M. W. (2019). Iodoimidazolium-catalyzed reduction of quinoline by hantzsch ester: halogen bond or brønsted acid catalysis. *J. Org. Chem.* 84, 10338–10348. doi: 10.1021/acs.joc.9b01494
- Squiteri, R. A., Fitzpatrick, K. P., Jaworski, A. A., and Scheidt, K. A. (2019). Synthesis and evaluation of azolium-based halogen-bond donors. *Chem. Eur. J.* 25, 10069–10073. doi: 10.1002/chem.201902298
- Sutar, R., and Huber, S. M. (2019). Catalysis of organic reactions through halogen bonding. *ACS Catal.* 9, 9622–9639. doi: 10.1021/acscatal.9b02894
- Sutar, R. L., Engelage, E., Stoll, R., and Huber, S. M. (2020). Bidentate chiral bis(imidazolium)-based halogen-bond donors: synthesis and applications in enantioselective recognition and catalysis. *Angew. Chem. Int. Ed.* 59, 6806–6810. doi: 10.1002/anie.201915931
- Suzuki, Y., Seki, T., Tanaka, S., and Kitamura, M. (2015). Intramolecular tsujitrost-type allylation of carboxylic acids: asymmetric synthesis of highly π -allyl donative lactones. *J. Am. Chem. Soc.* 137, 9539–9542. doi: 10.1021/jacs.5b05786
- Tanaka, S., Seki, T., and Kitamura, M. (2009). Asymmetric dehydrative cyclization of ω -hydroxy allyl alcohols catalyzed by ruthenium complexes. *Angew. Chem. Int. Ed.* 48, 8948–8951. doi: 10.1002/anie.200904671
- Teng, B., Chen, W., Dong, S., Kee, C. W., Gandamana, D. A., Zong, L., et al. (2016). Pentanidium- and bisguanidinium-catalyzed enantioselective alkylations using silylamide as brønsted probase. *J. Am. Chem. Soc.* 138, 9935–9940. doi: 10.1021/jacs.6b05053
- Tepper, R., and Schubert, U. S. (2018). Halogen bonding in solution: anion recognition, templated self-assembly, and organocatalysis. *Angew. Chem. Int. Ed.* 57, 6004–6016. doi: 10.1002/anie.201707986
- Troff, R. W., Mäkelä, T., Topic, F., Valkonen, A., Raatikainen, K., and Rissanen, K. (2013). Alternative motifs for halogen bonding. *Eur. J. Org. Chem.* 2013, 1617–1637. doi: 10.1002/ejoc.201201512
- Tungen, J. E., Nolsoe, J. M. J., and Hansen, T. V. (2012). Asymmetric iodolactonization utilizing chiral squaramides. *Org. Lett.* 14, 5884–5887. doi: 10.1021/ol302798g
- Turunen, L., and Erdélyi, M. (2020). Halogen bonds of halonium ions. *Chem. Soc. Rev.* 49, 2688–2700. doi: 10.1039/D0CS00034E
- Veitch, G. E., and Jacobsen, E. N. (2010). Tertiary aminourea-catalyzed enantioselective iodolactonization. *Angew. Chem. Int. Ed.* 49, 7332–7335. doi: 10.1002/anie.201003681
- Wang, H., Wang, W., and Jin, W. J. (2016). σ -hole bond vs π -hole bond: a comparison based on halogen bond. *Chem. Rev.* 116, 5072–5104. doi: 10.1021/acs.chemrev.5b00527
- Yamawaki, M., Tsutsui, H., Kitagaki, S., Anada, M., and Hashimoto, S. (2002). Dirhodium(II) tetrakis[N-tetrachlorophthaloyl-(S)-tert-leucinate]: a new chiral Rh(II) catalyst for enantioselective amidation of C-H bonds. *Tetrahedron Lett.* 43, 9561–9564. doi: 10.1016/S0040-4039(02)02432-2
- Yang, H., and Wong, M. W. (2020). Application of halogen bonding to organocatalysis: a theoretical perspective. *Molecules* 25:1045. doi: 10.3390/molecules25051045

- Zhang, Y., Han, J., and Liu, Z. J. (2015). Diaryliodonium salts as efficient Lewis acid catalysts for direct three component mannich reactions. *RSC Adv.* 5, 25485–25488. doi: 10.1039/C5RA00209E
- Zong, L., Ban, X., Kee, C. W., and Tan, C. H. (2014). Catalytic enantioselective alkylation of sulfenate anions to chiral heterocyclic sulfoxides using halogenated pentanidium salts. *Angew. Chem. Int. Ed.* 53, 11849–11853. doi: 10.1002/anie.201407512
- Zong, L., Du, S., Chin, K. F., Wang, C., and Tan, C. H. (2015). Enantioselective synthesis of quaternary carbon stereocenters: addition of 3-substituted oxindoles to vinyl sulfone catalyzed by pentanidiums. *Angew. Chem. Int. Ed.* 54, 9390–9393. doi: 10.1002/anie.201503844

Conflict of Interest: The authors declare that the research was conducted in the absence of any commercial or financial relationships that could be construed as a potential conflict of interest.

The handling editor declared a shared affiliation, though no other collaboration, with the authors MK and TK.

Copyright © 2020 Kaasik and Kanger. This is an open-access article distributed under the terms of the Creative Commons Attribution License (CC BY). The use, distribution or reproduction in other forums is permitted, provided the original author(s) and the copyright owner(s) are credited and that the original publication in this journal is cited, in accordance with accepted academic practice. No use, distribution or reproduction is permitted which does not comply with these terms.



Control and Transfer of Chirality Within Well-Defined Tripodal Supramolecular Cages

Gege Qiu, Paola Nava, Cédric Colombari* and Alexandre Martinez*

Aix Marseille Univ, CNRS, Centrale Marseille, iSm2, Marseille, France

OPEN ACCESS

Edited by:

Victor Borovkov,
South-Central University for
Nationalities, China

Reviewed by:

Tianyu Wang,
University of Science and Technology
Beijing, China
Zhengbiao Zhang,
Soochow University, China
Li Zhang,
Institute of Chemistry (CAS), China

*Correspondence:

Cédric Colombari
cedric.colombari@univ-amu.fr
Alexandre Martinez
alexandre.martinez@
centrale-marseille.fr

Specialty section:

This article was submitted to
Supramolecular Chemistry,
a section of the journal
Frontiers in Chemistry

Received: 28 August 2020

Accepted: 29 September 2020

Published: 03 November 2020

Citation:

Qiu G, Nava P, Colombari C and
Martinez A (2020) Control and
Transfer of Chirality Within
Well-Defined Tripodal Supramolecular
Cages. *Front. Chem.* 8:599893.
doi: 10.3389/fchem.2020.599893

The development of new strategies to turn achiral artificial hosts into highly desirable chiral receptors is a crucial challenge in order to advance the fields of asymmetric transformations and enantioselective sensing. Over the past few years, C_3 symmetrical cages have emerged as interesting class of supramolecular hosts that have been reported as efficient scaffolds for chirality dynamics (such as generation, control, and transfer). On this basis, this mini review, which summarizes the existing examples of chirality control and propagation in tripodal supramolecular cages, aims at discussing the benefits and perspectives of this approach.

Keywords: cages, chirality, transfer, tripodal, supramolecular

INTRODUCTION

Stereoselective bindings are essential events for biochemical functions such as enzymatic catalysis and recognition of natural metabolites. In order to reproduce the efficiency of the stereoselective receptors found in the biological world, the synthesis of chiral artificial hosts has attracted considerable attentions over the past few decades. In this context, the supramolecular approach appears as particularly promising as it allows for the construction of tridimensional hosts that could, for example, mimic enzyme cavities (Liu et al., 2015). Among supramolecular hosts, organic or self-assembled cages built from chiral building blocks are of particular interest due to their ability to bind guests within their interior. A variety of chiral organic (Brotin et al., 2013), or metallo-cages (Hardie, 2016; Chen et al., 2017) have been constructed over the past years, via covalent bond or coordination driven assembly processes, respectively. Such supramolecular cages have found a wide range of applications from selective recognition and separation of hydrocarbon derivatives (Zhang et al., 2018, 2019), chiral molecules (Brotin and Dutasta, 2009) and noble gases (Mastalerz, 2018), to drug delivery (Sepehrpour et al., 2019; Samanta and Isaacs, 2020), photophysical and CPL properties (Saha et al., 2016; Feng et al., 2018; Jing et al., 2019; Zhou et al., 2019), functional molecular machines (Oldknow et al., 2018; Elemans and Nolte, 2019), stabilization of reactive species (Mal et al., 2009) and catalysis in confined spaces (Hong et al., 2018; Mouarrawis et al., 2018; Roland et al., 2018).

However, being able to induce chirality dynamics (generation and propagation) within supramolecular cages and their related host-guest complexes remains a highly challenging task. In this line, C_3 symmetrical cages present a structural advantage due to their propensity to form triple-stranded helix or propeller-like structures (Yamakado et al., 2013; Míguez-Lago et al., 2015; Malik et al., 2018; Sato et al., 2018). Aiming at providing a general view about recent progress in the preparation of chiral tripodal cages displaying chirality dynamics, this mini-review summarizes current knowledge on how the chiral information can propagate along such tridimensional

architectures. Control of the chirality within tripodal cages upon chiral sorting (Henkelis et al., 2014; Schaly et al., 2016; Jedrzejewska and Szumna, 2017; Schulte et al., 2019; Séjourné et al., 2020), or guest binding (You et al., 2012; Bravin et al., 2019; Pavlovic et al., 2019) are beyond the scope of this work.

The first part of the mini-review will be devoted to examples of propagation of the stereochemical information from one chiral unit to linkers of C_3 symmetrical cages. Its second part will describe how the chiral unit can control and induce a chiral arrangement of another tripodal unit included in the cage structure.

CONTROL OF THE CHIRAL ARRANGEMENT OF THE LINKERS IN TRIPODAL CAGES

A straightforward strategy to generate chiral hosts consists in the covalent substitution of a chiral precursor, to create an inner cavity. In particular, chiral C_3 symmetrical cages have been obtained by connecting one chiral moiety with another tripodal unit, by three linkers. The presence of three identical linkers connected to one chiral component can interestingly lead to the formation of triple-stranded helical structures with a controlled orientation. It has been indeed observed that the stereochemical information of the chiral unit could propagate along the structure to (i) induce a controlled propeller-like arrangement of the linkers or (ii) turn the other opposite moiety into a chiral structure with a controlled orientation.

Chirality transfer events within tripodal hosts were firstly evidenced between the chiral unit and its nearest linkers, resulting in a remote control of their helical arrangement (Figure 1). For example, Badjic et al. reported the preparation and characterization of the gated stereoisomeric basket (**1**) (Hu et al., 2015). Such C_3 symmetrical cavitand was built from a basket unit owning a *P*- or *M*-twisted structure, decorated by three aminopyridine gates at its rim. The authors demonstrated, through a combination of $^1\text{H}/^{13}\text{C}$ -NMR analysis and computational results, that the aminopyridine substituents display a right- or left-handed propeller like arrangement maintained by an intramolecular $\text{N-H}\cdots\text{N}$ hydrogen-bond network. Interestingly, the unidirectional orientation of the gate folding is dictated by the chirality (*P*- or *M*-) of the southern twisted chiral basket. Computational studies further suggest that the *P*-basket framework imposes an anti-clockwise orientation while the *M*-basket results in a clockwise arrangement. By replacing aminopyridines by quinolone gates, the same team reported, 1 year later, the enantiopure basket (**2**), which displays a solvent dependent transfer of the stereochemical information from the basket to the rim (Pratumyot et al., 2016). By comparison with **1**, **2** exhibits π -stacked gates instead of hydrogen-bonded ones. 2D ^1H -NMR characterizations, exciton-coupled circular dichroism (ECD) analysis, and computational modeling, reveal that the clockwise and/or anticlockwise orientations of the quinolone gates exist in acetonitrile while the three substituents remain randomly oriented in the non-polar dichloromethane solvent.

In the same vein, hemicryptophanes are organic cages built from a northern bowl-shaped, C_3 symmetrical cyclotrivierylene (CTV) unit, connected to another tripodal moiety by three spacers (Zhang et al., 2017). Due to the inherent chirality of the CTV unit, hemicryptophanes are chiral cages with *M* or *P* configuration. Enantiopure versions of this kind of host are commonly obtained following two main strategies: (i) the chiral HPLC resolution of a racemic mixture of *P* and *M* structures and (ii) the addition of another chiral moiety and separation of the resulting diastereoisomers (Colomban et al., 2019). Hemicryptophane (**3**), which connects a CTV unit and a phosphotrihydrazone moiety through three butylene ($-\text{C}_4\text{H}_8-$) linkers, was reported in 2016 as ligand for Ga^{III} and Fe^{III} metal ions (Gosse et al., 2016). The authors observed, through XRD analysis, that the butylene linkers of **3** displayed a clockwise/anticlockwise helical orientation (α or β helicity). Interestingly, for both **3** and its corresponding Ga^{III} and Fe^{III} complexes, such solid-state helical arrangement of the linkers (α or β) was imposed by the configuration of the CTV unit. Indeed only (*M*)-CTV-(β)-helix and (*P*)-CTV-(α)-helix pairs of enantiomers were observed. In 2018, the group of Martinez reported a new example of hemicryptophane cages displaying a remote control of the linkers' helical arrangement, dictated by the CTV unit (Long et al., 2018a). The hemicryptophane **4**, which displays linkers constituted of both amine and amide groups, was prepared. Analysis of its X-ray molecular structure reveals H-bond interactions between the amide and the amine function of each arm resulting in a triple-stranded helical arrangement of the linkers (Figure 1D). Interestingly, the chirality of such triple helices was dictated by the chirality of the CTV unit (*P*- or *M*-). Hemicryptophane (*P*)-**4** indeed displayed a Δ propeller-like arrangement of the linkers while (*M*)-**4** revealed a Λ orientation. Moreover, careful ^1H -NMR analyses allow the authors to suggest that the controlled arrangement observed in the solid state may be retained in solution. This example highlights the remarkable flexibility of the whole organic structure that is strongly twisted and displays a propagation of the CTV chirality over nine bonds.

CONTROL OF THE CHIRAL ARRANGEMENT OF AN OTHER C_3 UNIT IN TRIPODAL CAGES

Based on these interesting examples of chirality transfer between chiral unit and linkers, the supramolecular chemists asked themselves: could this phenomenon be extended in order to induce and control the helical arrangement of another C_3 symmetrical unit? The remote control of the helical arrangement of some tripodal units is indeed of particular interest, as it might allow turning achiral artificial ligands into enantiomerically-pure binding sites. For example, the control of the helicity of the C_3 symmetrical tris(2-pyridylmethyl)amine (TPA) ligand as attracted considerable attention due to its versatile applications ranging from bio-inspired models (Borrell et al., 2019), catalysts (Peterson et al., 2011), to chiral sensors (You et al., 2011). This ligand could display a propeller-like arrangement of its pyridine units that rapidly interconvert between clockwise

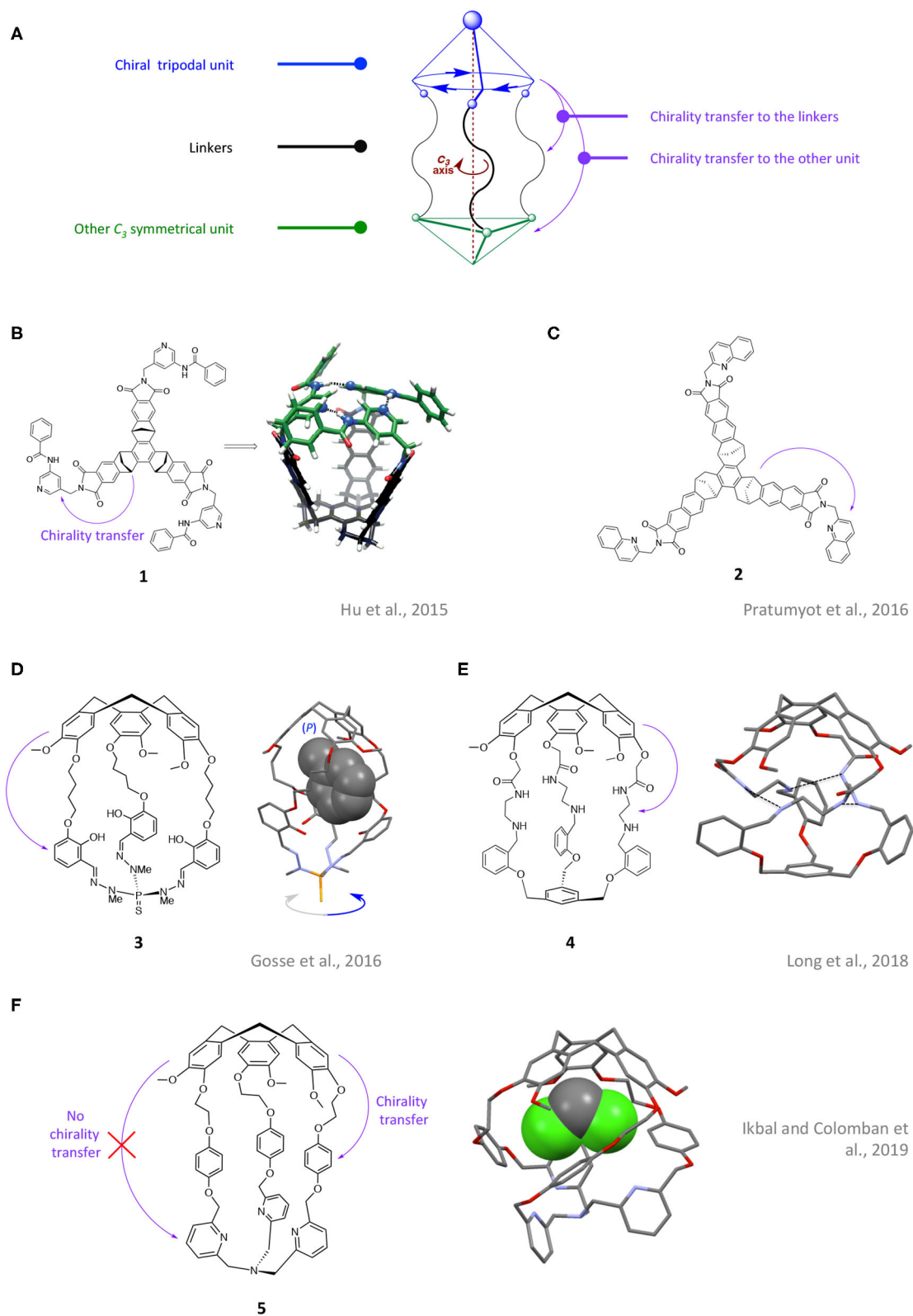
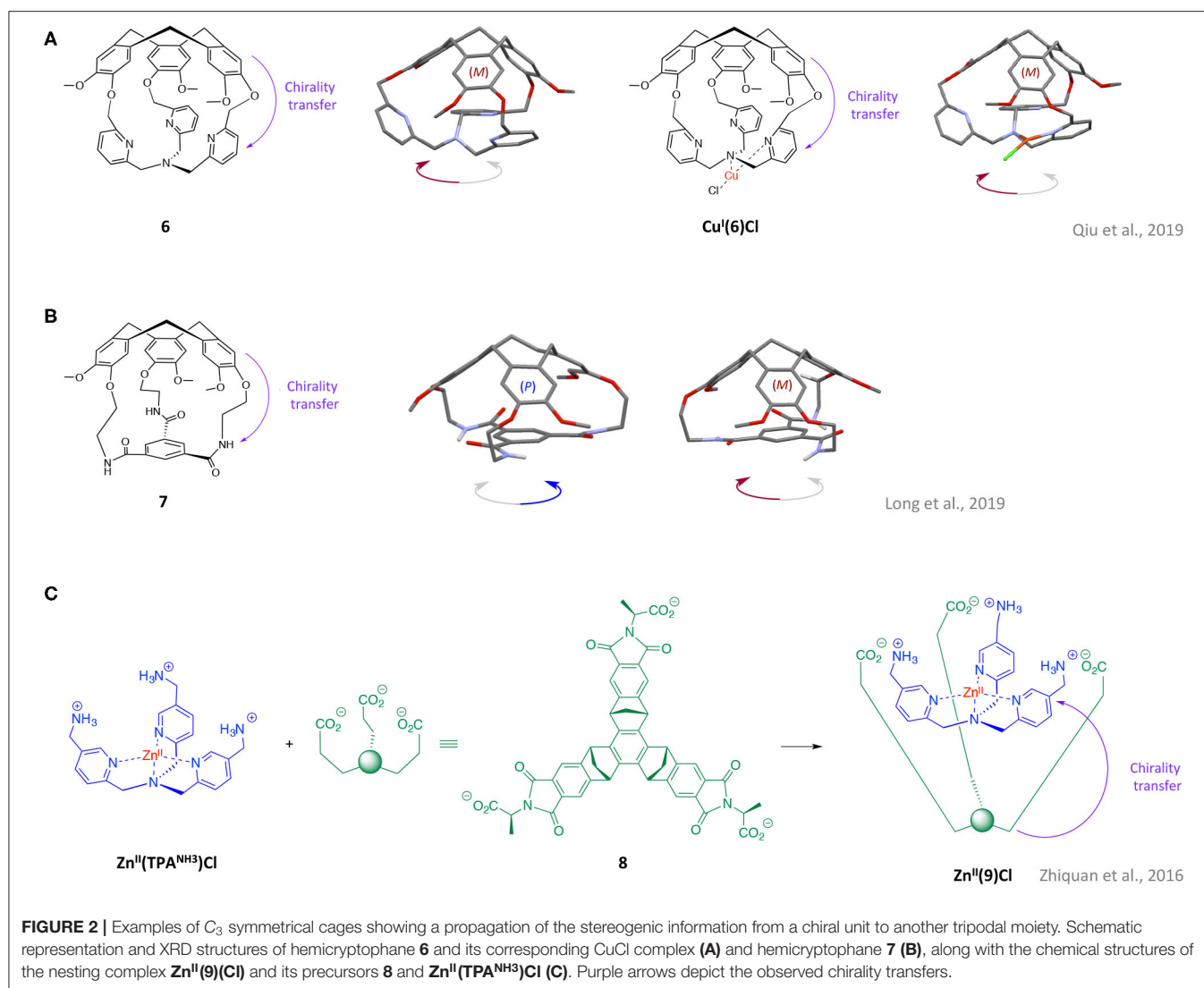


FIGURE 1 | (A) Schematic representation of the structural characteristics of the chiral cages depicted in this review. Examples of tripodal cages displaying a transfer of chirality between a chiral unit and its side arms: schematic representation and computed structures of open cages **1** (B) and **2** (C) together with the schematic representation and XRD structures of hemicryptophanes **3** (D), **4** (E) and **5** (F) (the XRD structure of **3** and **5** displays an entrapped molecule of toluene and CH_2Cl_2 respectively). Purple arrows depict the observed chirality transfers.



and anticlockwise enantiomeric conformations. Therefore, by controlling the sense of the pyridines twist, the achiral TPA could be switched into highly desirable chiral coordinating structures. In 2019, the X-ray structure of the TPA-based hemicryptophane **5** was reported during the study of this cage-ligand for selective metal-based methane oxidation (Ikbal et al., 2019). This solid-state structure reveals a CTV-dictated triple-stranded helical arrangement of the phenyl linkers of **5**, but no orientation of the southern TPA part was observed (Figure 1E). On this basis, Colomban, Martinez and co-workers have designed the structurally contracted cage **6** (Qiu et al., 2019) where the phenyl linkers are replaced by single methylene $-\text{CH}_2-$ (Figure 2A). The authors resonated that a closer proximity between the chiral northern CTV cap and the southern TPA ligand would result on the propagation of the chirality to the ligand, allowing for a predictable control of its helicity. These expectations turn out to be accurate since, remarkably, the organic cage **6** displays a controlled clockwise/anticlockwise propeller arrangement of

the TPA unit, dictated by the chirality of the CTV unit. The covalent capping with a *M*-CTV unit indeed results in a left-handed propeller arrangement of the TPA (while the *P*-CTV leads to a right-handed propeller arrangement). It should be noted that enantiopure versions of (*M*)-**6** and (*P*)-**6** were obtained in a highly efficient purification step based on the chiral-HPLC resolution of the racemic mixture (\pm)-**6** (ee values >99.5%). Importantly, this strong chirality transfer is maintained upon metallation of the TPA moiety with the Cu(I) metal ion. The resulting complex $\text{Cu}^{\text{I}}(6)\text{Cl}$, (Figure 2A) displays a rare T-shaped coordination geometry along with a controlled helicity of the TPA unit that both occur in solution and solid state (XRD, ^1H -NMR, ECD analysis). The design of the cage-ligand **6** therefore allowed the authors to report an unprecedented Cu(I) complex with a controlled helicity of the TPA-Cu(I) core, highlighting the promises of the approach for the preparation of novel optically pure metal-based catalysts and receptors.

This strategy combining a chiral CTV cap and short spacers to control the chirality of another C_3 symmetrical unit, has been further exemplified by Martinez and his team through the preparation of the hemicryptophane **7** (Long et al., 2019). Due to its ability to engage strong hydrogen bonds, the benzene-1,3,5-tricarboxamide (BTA) unit has been widely reported as useful building block for the preparation of supramolecular assemblies (Kulkarni and Palmans, 2017; Zimbron et al., 2017). Therefore, methods able to tune and control its structural properties are of particular interest. With such considerations in mind, **7** was built aiming at controlling the sense of rotation of the three amides of the BTA unit. This cage consists in a southern BTA covalently linked to a chiral CTV cap by three ethylene $-C_2H_4-$ linkers (Figure 2B). Interestingly, the close proximity between CTV and BTA unit in **7**, results in a remote control of the Δ/Λ orientation of the three amides of the south part dictated by the chirality of the CTV cap. It was indeed demonstrated, through XRD analysis of the racemic mixture of (\pm)**7**, that the BTA unit capped with a *M*-CTV displays a Λ orientation of their amides, while its *P* analog displays a Δ arrangement. It was shown that the enantiopure cages (*M*- Λ)-**7** and (*P*- Δ)-**7** could be easily obtained, with excellent *ee* values (*ee* > 97.5 %) through straightforward chiral-HPLC resolution of the racemic mixture. Finally, the authors proposed, based on 1H -NMR observations, that the transfer of chirality observed in the solid states might be retained in solution. Interestingly, this cage **7**, was used as the chain capper of BTA based supramolecular polymers allowing to control their length: whereas the external face of the BTA unit of **7** interacts with the polymer, the CTV unit crowds the other face, preventing further polymerization (ter Huurne et al., 2020).

Another remarkable strategy to generate and control chirality on an achiral tripodal ligand consists in its non-covalent wrapping with a chiral concave open-cage structure, through intermolecular ionic contacts. This so-called “Russian nesting doll” approach have been reported in 2016 by Badjic et al. which used the chiral molecular baskets developed in their team to create and control a propeller-like arrangement of a TPA-based Zinc complex (Zhiquan et al., 2016). The self-assembled architecture $Zn^{II}(\mathbf{9})(Cl)$ is based on supramolecular ionic interactions between a zinc complex substituted with three positively charged ammonium groups $Zn^{II}(TPA^{NH_3})Cl$, and the chiral molecular nest **8** (displaying three negatively charged carboxylates at its rim) (Figure 2C). Formation of the entrapped Zn complex $Zn^{II}(\mathbf{9})(Cl)$ in its nesting form, was confirmed by 1H -NMR titration, ESI-MS analysis, and computational simulations. The preferential formation of the Russian nesting dolls conformation of $Zn^{II}(\mathbf{9})(Cl)$ was explained by both hydrophobic effect and non-polar interactions between the two hydrophobic shell of **8** and $Zn^{II}(TPA^{NH_3})$. It was observed that the chirality of the anionic basket **8**, which displays (S)-alanine amino acids groups at its rim, is efficiently transfer to the cationic $Zn^{II}(TPA^{NH_3})Cl$ moiety, resulting in a controlled propeller-like arrangement of the TPAs pyridines. Careful analysis of computed structures and the circular dichroism (CD) spectrum, indeed demonstrated that the supramolecular interactions between the three carboxylates of **8** and the ammoniums of $Zn^{II}(TPA^{NH_3})Cl$ were responsible for the exclusive formation of a left-handed

(*M*) Zn -TPA core. Interestingly, this study allowed the authors to demonstrate that a predictable control of the helical arrangement of TPA-based complexes, could be achieved by an ionic contract-based transfer of chirality. In 2017, the same group further exemplified the approach by studying the capture of several metallated and non-metallated TPA derivatives by both anionic and cationic molecular baskets (Zhiquan et al., 2017).

CONCLUSION, DISCUSSION, AND FUTURE DIRECTIONS

To summarize, this mini-review highlights recent advances related to chirality dynamics within tripodal supramolecular cages in terms of induction, transfer and control of the chiral information. Various hosts of C_3 symmetrical type, displaying a predictable and robust control of the chirality, have been recently prepared. The tendency of tripodal structures to form triple-stranded helix or propeller-like arrangements has been exploited to prepare architectures displaying an internal transfer of the stereogenic information from one chiral unit to (i) its nearest linkers or (ii) another C_3 symmetrical unit. This predictable way to generate and control chirality on another linked unit was found to arise from non-covalent interactions of different nature, such as hydrogen-bonding or steric repulsion. Interestingly, this approach has been used to turn achiral ligand into highly valuable coordinating structures, leading to metal complexes with controlled chiral environments. These strategies open new ways in four main research topics. The propagation of the chirality along linkers and even to the opposite face of the cage could lead to highly efficient enantioselective sensors, due to the presence of a strongly controlled chiral environment around the guest-binding site. Indeed, although examples of C_3 -symmetrical cages displaying enantioselectivity in the recognition of chiral guests remain rare (Sambasivan et al., 2010; De Rycke et al., 2018), it has been recently shown that remarkable enantioselective recognition of chiral neurotransmitters or carbohydrates can be reached by hemicryptophane cages presenting a C_3 symmetrical axis (Long et al., 2018b; Yang et al., 2020). Secondly, by controlling the chirality at both first and second coordination sphere levels of metal complexes, promising chiral confined catalysts for enantioselective transformations could be obtained. This represents a highly challenging goal since, to the best of our knowledge, there is no example of chiral C_3 symmetrical cages able to induce enantiomeric excess when used as asymmetric catalyst. This approach could also provide new tools for controlling the chirality and the length of helical supramolecular polymers by acting as enantiopure cappers. Finally, the combination of chiral C_3 units with achiral fluorescence units, or lanthanide complexes, could lead to the construction of new fluorescent hosts with a chiral environment around the fluorophore that is fully imposed by the enantiopure tripodal unit (chirality transfer), giving new structures for CPL applications.

Altogether, these examples of preparation of enantiopure chiral C_3 symmetrical supramolecular cages have led to the discovery and understanding of the mechanisms that result in

chirality dynamics. It is therefore reasonable to expect that such way of generating, controlling, and propagate chirality will be further applied to other class of supramolecular architectures, and will result in the preparation of new kinds of stereoselective and adaptive hosts. In particular, aiming at mimicking the allosteric properties of biological receptors, the chirality dynamics in well-defined cages is the key to develop challenging on-demand control of the hosts chirality, dictated by the nature of the encapsulated guest (Bravin et al., 2019; Pavlovic et al., 2019).

REFERENCES

- Borrell, M., Andris, E., Navrátil, R., Roithová J., and Costas, M. (2019). Characterized cis-FeV(O)(OH) intermediate mimics enzymatic oxidations in the gas phase. *Nat. Commun.* 10:90. doi: 10.1038/s41467-019-08668-2
- Bravin, C., Mason, G., Licini, G., and Zonta, C. (2019). A Diastereodynamic Probe Transducing Molecular Length into Chiroptical Readout. *J. Am. Chem. Soc.* 141, 11963–11969. doi: 10.1021/jacs.9b04151
- Brotin, T., and Dutasta, J.-P. (2009). Cryptophanes and their complexes—present and future. *Chem. Rev.* 109, 88–130. doi: 10.1021/cr0680437
- Brotin, T., Guy, L., Martinez, A., and Dutasta, J.-P. (2013). Enantiopure supramolecular cages: synthesis and chiral recognition properties. *Top. Curr. Chem.* 341, 177–230. doi: 10.1007/128_2013_487
- Chen, L. J., Yang, H. B., and Shionoya, M. (2017). Chiral metallosupramolecular architectures. *Chem. Soc. Rev.* 46, 2555–2576. doi: 10.1039/C7CS00173H
- Colomban, C., Châtelet, B., and Martinez, A. (2019). Different strategies for obtaining enantiopure hemicryptophanes. *Synthesis* 51, 2081–2099. doi: 10.1055/s-0037-1612420
- De Rycke, N., Jean, M., Vanthuyne, N., Buffeteau, T., and Brotin, T. (2018). Enantioselective complexation of chiral oxirane derivatives by an enantiopure cryptophane in water. *Eur. J. Org. Chem.* 2018, 1601–1607. doi: 10.1002/ejoc.201800142
- Elemans, J. A. A. W., and Nolte, R. J. M. (2019). Porphyrin cage compounds based on glycoluril –from enzyme mimics to functional molecular machines. *Chem. Commun.* 55, 9590–9605. doi: 10.1039/C9CC04372A
- Feng, H.-T., Yuan, Y.-X., Xiong, J.-B., Zheng, Y.-S., and Tang, B. Z. (2018). Macrocycles and cages based on tetraphenylethylene with aggregation-induced emission effect. *Chem. Soc. Rev.* 47, 7452–7476. doi: 10.1039/C8CS00444G
- Gosse, I., Robeyns, K., Bougault, C., Martinez, A., Tinant, B., and Dutasta, J. P. (2016). Synthesis and structural studies of gallium(III) and iron(III) hemicryptophane complexes. *Inorg. Chem.* 55, 1011–1013. doi: 10.1021/acs.inorgchem.5b02750
- Hardie, M. J. (2016). Self-assembled cages and capsules using cyclotrimeratrylene-type scaffolds. *Chem. Lett.* 45, 1336–1346. doi: 10.1246/cl.160780
- Henkelis, J. J., Carruthers, C. J., Chambers, S. E., Clowes, R., Cooper, A. I., Fisher, J., et al. (2014). Metallo-cryptophanes decorated with bis-N-heterocyclic carbene ligands: self-assembly and guest uptake into a nonporous crystalline lattice. *J. Am. Chem. Soc.* 136, 14393–14396. doi: 10.1021/ja508502u
- Hong, C. M., Bergman, R. G., Raymond, K. N., and Toste, F. D. (2018). Self-assembled tetrahedral hosts as supramolecular catalysts. *Acc. Chem. Res.* 51, 2447–2455. doi: 10.1021/acs.accounts.8b00328
- Hu, L., Polen, S., Hardin, A. M., Pratumyot, Y., Hadad, C. M., and Badjić, J. D. (2015). On the transfer of chirality, thermodynamic stability, and folding characteristics of stereoisomeric gated baskets. *Eur. J. Org. Chem.* 6832–6840. doi: 10.1002/ejoc.201501071
- Ikkal, S. A., Colomban, C., Zhang, D., Delecluse, M., Brotin, T., Dufaud, V., et al. (2019). Bioinspired oxidation of methane in the confined spaces of molecular cages. *Inorg. Chem.* 58, 7220–7228. doi: 10.1021/acs.inorgchem.9b00199
- Jedrzejewska, H., and Szumna, A. (2017). Making a right or left choice: chiral self-sorting as a tool for the formation of discrete complex structures. *Chem. Rev.* 117, 4863–4899. doi: 10.1021/acs.chemrev.6b00745
- Jing, X., He, C., Zhao, L., and Duan, C. (2019). Photochemical properties of host–guest supramolecular systems with structurally confined metal–organic capsules. *Acc. Chem. Res.* 52, 100–109. doi: 10.1021/acs.accounts.8b00463
- Kulkarni, C., Meijer, E. W., and Palmans, A. R. A. (2017). Cooperativity scale: a structure–mechanism correlation in the self-assembly of benzene-1,3,5-tricarboxamides. *Acc. Chem. Res.* 50, 1928–1936. doi: 10.1021/acs.accounts.7b00176
- Liu, M., Zhang, L., and Wang, T. (2015). Supramolecular chirality in self-assembled systems. *Chem. Rev.* 115, 7304–7397. doi: 10.1021/cr500671p
- Long, A., Jean, M., Albalat, M., Vanthuyne, N., Giorgi, M., Górecki, M., et al. (2019). Synthesis, resolution, and chiroptical properties of hemicryptophane cage controlling the chirality of propeller arrangement of a C₃ triamide unit. *Chirality* 31, 910–916. doi: 10.1002/chir.23131
- Long, A., Perraud, O., Albalat, M., Robert, V., Dutasta, J.-P., and Martinez, A. (2018b). Helical chirality induces a substrate-selectivity switch in carbohydrates recognitions. *J. Org. Chem.* 83, 6301–6306. doi: 10.1021/acs.joc.8b00276
- Long, A., Perraud, O., Jeanneau, E., Aronica, C., Dutasta, J. P., and Martinez, A. (2018a). A hemicryptophane with a triple-stranded helical structure. *Beilstein J. Org. Chem.* 14, 1885–1889. doi: 10.3762/bjoc.14.162
- Mal, P., Breiner, B., Rissanen, K., and Nitschke, J. R. (2009). White phosphorus is air-stable within a self-assembled tetrahedral capsule. *Science* 324, 1697–1699. doi: 10.1126/science.1175313
- Malik, A. U., Gan, F., Shen, C., Yu, N., Wang, R., Crassous, J., et al. (2018). Chiral organic cages with a triple-stranded helical structure derived from helicene. *J. Am. Chem. Soc.* 140, 2769–2772. doi: 10.1021/jacs.7b13512
- Mastalerz, M. (2018). Porous shape-persistent organic cage compounds of different size, geometry, and function. *Acc. Chem. Res.* 51, 2411–2422. doi: 10.1021/acs.accounts.8b00298
- Míguez-Lago, S., Llamas-Saiz, A. L., Magdalena Cid, M., and Alonso-Gómez, J. L. (2015). A covalent organic helical cage with remarkable chiroptical amplification. *Chem. Eur. J.* 21, 18085–18088. doi: 10.1002/chem.201503994
- Mouarravis, V., Plessius, R., van der Lugt, J. I., and Reek, J. N. H. (2018). Confinement effects in catalysis using well-defined materials and cages. *Front. Chem.* 6, 623–643. doi: 10.3389/fchem.2018.00623
- Oldknow, S., Rota Martir, D., Pritchard, V. E., Blitz, M. A., Fishwick, C. W. G., Zysman-Colman, E., et al. (2018). Structure-switching M3L₂ Ir(III) coordination cages with photo-isomerising azo-aromatic linkers. *Chem. Sci.* 9, 8150–8159. doi: 10.1039/C8SC03499K
- Pavlovic, R. Z., Zhiquan, L., Güney, M., Lalis, R. F., Hopf, R. G., Gallucci, J., et al. (2019). Multivalent C-H···Cl/Br···C interactions directing the resolution of dynamic and twisted capsules. *Chem. Eur. J.* 25, 13124–13130. doi: 10.1002/chem.201903006
- Peterson, R. L., Himes, R. A., Kotani, H., Suenobu, T., Tian, L., Siegler, M. A., et al. (2011). Cupric superoxo-mediated intermolecular C–H activation chemistry. *J. Am. Chem. Soc.* 133, 1702–1705. doi: 10.1021/ja110466q
- Pratumyot, Y., Chen, S., Hu, L., Polen, S. M., Hadad, C. M., and Badjić, J. D. (2016). Assembly and folding of twisted baskets in organic solvents. *Org. Lett.* 18, 4238–4244. doi: 10.1021/acs.orglett.6b01976
- Qiu, G., Colomban, C., Vanthuyne, N., Giorgi, M., and Martinez, A. (2019). Chirality transfer in a cage controls the clockwise/anticlockwise propeller arrangement of the tris(2-pyridylmethyl)amine ligand. *Chem. Commun.* 55, 14158–14161. doi: 10.1039/C9CC07244F

AUTHOR CONTRIBUTIONS

GQ, PN, CC, and AM have co-written the paper. All authors discussed the results and commented on the manuscript.

FUNDING

This research was supported by the French National Research Agency (ANR, France, OH Risque grant ANR-14-OHRI-0015-03).

- Roland, S., Suarez, J. M., and Sollogoub, M. (2018). Confinement of metal–N-heterocyclic carbene complexes to control reactivity in catalytic reactions. *Chem. Eur. J.* 24, 12464–12473. doi: 10.1002/chem.201801278
- Saha, M. L., Yan, X., and Stang, P. J. (2016). Photophysical properties of organoplatinum(II) compounds and derived self-assembled metallacycles and metallacages: fluorescence and its applications. *Acc. Chem. Res.* 49, 2527–2539. doi: 10.1021/acs.accounts.6b00416
- Samanta, S. K., and Isaacs, L. (2020). Biomedical applications of metal organic polygons and polyhedra (MOPs). *Coord. Chem. Rev.* 410, 213181–213197. doi: 10.1016/j.ccr.2020.213181
- Sambasivan, S., Kim, S. G., Choi, S. M., Rhee, Y. M., and Ahn, K. (2010). C₃-symmetric cage-like receptors: chiral discrimination of α -chiral amines in a confined space. *Org. Lett.* 12, 4228–4231. doi: 10.1021/ol1015527
- Sato, H., Bender, J. A., Roberts, S. T., and Krische, M. J. (2018). Helical rod-like phenylene cages via ruthenium catalyzed diol-diene benzannulation: a cord of three strands. *J. Am. Chem. Soc.* 140, 2455–2459. doi: 10.1021/jacs.8b00131
- Schaly, A., Roussel, Y., Chambron, J.-C., Aubert, E., and Espinosa, E. (2016). The stereoselective self-assembly of chiral metallo-organic cryptophanes. *Eur. J. Inorg. Chem.* 2016, 832–843. doi: 10.1002/ejic.201501446
- Schulte, T. R., Holstein, J. J., and Clever, G. H. (2019). Chiral self-discrimination and guest recognition in helicene-based coordination cages. *Angew. Chem. Int. Ed.* 58, 5562–5566. doi: 10.1002/anie.201812926
- Séjourné, S., Labrunie, A., Dalinot, C., Benchohra, A., Carré, V., Aubriet, F., et al. (2020). Chiral self-sorting in truxene-based metallacages. *Inorganics* 8, 1–12. doi: 10.3390/inorganics8010001
- Sepehrpour, H., Fu, W., Sun, Y., and Stang, P. J. (2019). Biomedically relevant self-assembled metallacycles and metallacages. *J. Am. Chem. Soc.* 141, 14005–14020. doi: 10.1021/jacs.9b06222
- ter Huurne, G. M., Chidchob, P., Long, A., Martinez, A., Palmans, A. R. A., and Vantomme, G. (2020). Controlling the length of cooperative supramolecular polymers with chain cappers. *Chem. Eur. J.* 26, 9964–9970. doi: 10.1002/chem.202001293
- Yamakado, R., Mikami, K., Takagi, K., Azumaya, I., Sugimoto, S., Matsuoka, S.-I., et al. (2013). Helicity induction in three π -conjugated chromophores by planar chirality of calixamide. *Chem. Eur. J.* 19, 11853–11857. doi: 10.1002/chem.201301198
- Yang, J., Chatelet, B., Dufaud, V., Héroult, D., Jean, M., Vanthuyne, N., et al. (2020). Enantio- and substrate-selective recognition of chiral neurotransmitters with C₃-symmetric switchable receptors. *Org. Lett.* 22, 891–889. doi: 10.1021/acs.orglett.9b04440
- You, L., Berman, J. S., and Anslyn, E. V. (2011). Dynamic multi-component covalent assembly for the reversible binding of secondary alcohols and chirality sensing. *Nat. Chem.* 3, 943–948. doi: 10.1038/nchem.1198
- You, L., Pescitelli, G., Anslyn, E. V., and Di Bari, L. (2012). An exciton-coupled circular dichroism protocol for the determination of identity, chirality, and enantiomeric excess of chiral secondary alcohols. *J. Am. Chem. Soc.* 134, 7117–7125. doi: 10.1021/ja301252h
- Zhang, D., Martinez, A., and Dutasta, J.-P. (2017). Emergence of hemicryptophanes: from synthesis to applications for recognition, molecular machines, and supramolecular catalysis. *Chem. Rev.* 117, 4900–4942. doi: 10.1021/acs.chemrev.6b00847
- Zhang, D., Ronson, T. K., Lavendomme, R., and Nitschke, J. R. (2019). Selective separation of polyaromatic hydrocarbons by phase transfer of coordination cages. *J. Am. Chem. Soc.* 141, 18949–18953. doi: 10.1021/jacs.9b10741
- Zhang, D., Ronson, T. K., and Nitschke, J. R. (2018). Functional capsules via subcomponent self-assembly. *Acc. Chem. Res.* 51, 2423–2436. doi: 10.1021/acs.accounts.8b00303
- Zhiquan, L., Polen, S. M., Hadad, C., RajanBabu, T. V., and Badjic, J. D. (2016). Russian nesting doll complexes of molecular baskets and zinc containing TPA ligands. *J. Am. Chem. Soc.* 138, 8253–8258. doi: 10.1021/jacs.6b04436
- Zhiquan, L., Polen, S. M., Hadad, C. M., RajanBabu, T. V., and Badjic, J. D. (2017). Examining the scope and thermodynamics of assembly in nesting complexes comprising molecular baskets and TPA ligands. *Org. Lett.* 19, 4932–4935. doi: 10.1021/acs.orglett.7b02391
- Zhou, Y., Li, H., Zhu, T., Gao, T., and Yan, P. (2019). A highly luminescent chiral tetrahedral Eu₄L₄(L')₄ cage: chirality induction, chirality memory, and circularly polarized luminescence. *J. Am. Chem. Soc.* 141, 19634–19643. doi: 10.1021/jacs.9b07178
- Zimbron, J. M., Caumes, X., Li, Y., Thomas, C. M., Raynal, M., and Bouteiller, L. (2017). Real-time control of the enantioselectivity of a supramolecular catalyst allows selecting the configuration of consecutively formed stereogenic centres. *Angew. Chem.* 56, 14016–14019. doi: 10.1002/anie.201706757

Conflict of Interest: The authors declare that the research was conducted in the absence of any commercial or financial relationships that could be construed as a potential conflict of interest.

Copyright © 2020 Qiu, Nava, Colombari and Martinez. This is an open-access article distributed under the terms of the Creative Commons Attribution License (CC BY). The use, distribution or reproduction in other forums is permitted, provided the original author(s) and the copyright owner(s) are credited and that the original publication in this journal is cited, in accordance with accepted academic practice. No use, distribution or reproduction is permitted which does not comply with these terms.



Enantioselectivity-Evaluation of Chiral Copper(II) Complexes Coordinated by Novel Chiral Tetradentate Ligands for Free Amino Acids by Mass Spectrometry Coupled With the Isotopically Labeled Enantiomer Method

OPEN ACCESS

Edited by:

Carmine Gaeta,
University of Salerno, Italy

Reviewed by:

Grzegorz Schroeder,
Adam Mickiewicz University, Poland
Carmen Talotta,
University of Salerno, Italy

*Correspondence:

Hiroyuki Miyake
miyake@sci.osaka-cu.ac.jp
Motohiro Shizuma
shizuma@omtri.or.jp

Specialty section:

This article was submitted to
Supramolecular Chemistry,
a section of the journal
Frontiers in Chemistry

Received: 25 August 2020

Accepted: 31 October 2020

Published: 30 November 2020

Citation:

Nakakoji T, Yoshino K, Izutsu K,
Sato H, Miyake H, Mieda E,
Shinoda S, Tsukube H, Kawasaki H,
Arakawa R, Ono D and Shizuma M
(2020) Enantioselectivity-Evaluation of
Chiral Copper(II) Complexes
Coordinated by Novel Chiral
Tetradentate Ligands for Free Amino
Acids by Mass Spectrometry Coupled
With the Isotopically Labeled
Enantiomer Method.
Front. Chem. 8:598598.
doi: 10.3389/fchem.2020.598598

Takashi Nakakoji¹, Kaori Yoshino¹, Kazuki Izutsu¹, Hirofumi Sato², Hiroyuki Miyake^{1*}, Eiko Mieda¹, Satoshi Shinoda¹, Hiroshi Tsukube¹, Hideya Kawasaki³, Ryuichi Arakawa³, Daisuke Ono² and Motohiro Shizuma^{2*}

¹ Department of Chemistry, Graduate School of Science, Osaka City University, Osaka, Japan, ² Osaka Research Institute of Industrial Science and Technology, Osaka, Japan, ³ Faculty of Chemistry, Materials and Bioengineering, Kansai University, Suita, Japan

A series of copper(II) complexes with chiral tetradentate ligands, *N,N'*-ethylene- bis(*S*-amino acid methyl amide or methyl ester) prepared from *S*-alanine, *S*-phenylalanine, *S*-valine or *S*-proline, was generated in methanol. The copper complexes provided three component complexes in the presence of a free chiral amino acid. The enantioselectivity for the amino acid was evaluated by electrospray ionization-mass spectrometry coupled with the deuterium-labeled enantiomer method and these copper complexes were found to exhibit high enantioselectivity for free amino acids having bulky side chains. This result suggests that steric interaction between the tetradentate ligand and free amino acid was a major factor in chiral recognition. The copper complex with a chiral tetradentate ligand prepared from *S*-proline showed opposite enantioselectivity to copper complexes consisting of tetradentate ligands prepared from other *S*-amino acids. The conformational difference of the tetradentate ligand in the copper complex was found to be significant for enantioselectivity.

Keywords: chiral metal complex, free amino acid, electrospray ionization mass spectrometry, isotopic labeling, chiral tetradentate ligand, enantioselective complexation

INTRODUCTION

Chiral recognition is one of the essential and fundamental processes in living systems. Particularly, chiral discrimination of α -amino acids and their derivatives has been paid great attention since they are among the most significant compound groups in bioscience. Organometallics and metal complexes can play a special role to detect the chirality of amino acids (Severin et al., 1998; Chin et al., 1999).

For example, chiral lanthanoid complexes were useful to determine enantiomeric excess (*ee*) and the absolute configuration of α -amino acids by using them as nuclear magnetic resonance (NMR) shift reagents (Kabuto and Sasaki, 1987; Takemura et al., 2001). In ligand exchange chromatography using a stationary phase fixed with metal ion such as copper or nickel, enantiomers of chiral amino acids were separated by using a chiral selector as the mobile phase (Brückner et al., 1990). By reversed-phase chromatography, optical separation of chiral amino acids was achieved by using a mobile phase including a chiral selector and copper salts (Gil-Av et al., 1980). Tao et al. used a metal complex with three amino acids including one enantiopure amino acid and two *ee*-unknown amino acids to evaluate the *ee* value of the amino acid with high accuracy by mass spectrometry coupled with collision induced dissociation in the ion trap (Tao et al., 1999, 2000; Tao and Cooks, 2003). Thus, the optical isomerism of chiral amino acids has been examined by various instrumental analysis methods by utilizing the complexation of chiral organometallics or metal complexes with amino acids. However, the details of the complexation and the mechanism of chiral discrimination have not been clarified due to the complicated complexation behaviors in the solution state. Therefore, detailed investigation of complexation of chiral metal complexes with amino acids leads to finding new designs for molecular recognition systems, which can spread to a wide range of fields such as organic, inorganic, analytical, and biological chemistries.

Recently, we have reported the enantioselective coordination of chiral α -amino acids in solution to a copper(II) complex consisting of chiral tetradentate ligand (**L1** or **L2**) (Nakakoji et al., 2020) in which two alanine methyl esters or amides are linked via an ethylene bridge (Miyake et al., 2004). The chiral copper complex produced three-component complex with an amino acid and its enantioselectivity was evaluated by electrospray ionization mass spectrometry coupled with the deuterium-labeled/unlabeled enantiomer guest method. Complex formation behavior observed by spectroscopic methods such as CD and UV, and by DFT calculations. It was clarified that the steric intramolecular interaction between the sidearm of the chiral ligand and that of the amino acid in the three-component complex was the primary factor in the chiral amino acid discrimination by the MS method. It is of interest to clarify the steric factors by altering the steric effects of the side chain of the chiral tetradentate ligand since controlling the enantioselectivity in the coordination of amino acids to the copper(II) complex is one of the significant issues. In this report, we synthesized chiral tetradentate ligands (**L3–L8**) with different sidearms in occupancy space size or flexibility (Figure 1) and evaluated the enantioselectivity of amino acid coordination with the copper complexes by electrospray ionization.

MATERIALS AND METHODS

General

^1H NMR (270 or 300 MHz) and ^{13}C NMR (67.5 or 75 MHz) spectra were taken with a JEOL JNM EX-270 FT-NMR spectrometer or a JEOL JNM AL300 FT-NMR spectrometer,

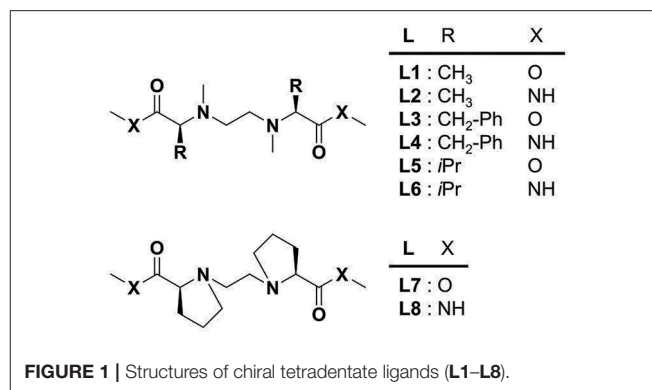


FIGURE 1 | Structures of chiral tetradentate ligands (**L1–L8**).

respectively. Tetramethylsilane (TMS, δ 0 ppm) was used as the internal standard in CDCl_3 . The solvent signal (δ 4.8 ppm) was used as the internal standard in D_2O . High resolution mass spectra (ESI, positive ion mode) were measured with a JEOL AccuTOF LC-plus 4G mass spectrometer and the JEOL YOKUDELNA ion peak $[\text{M} + \text{Na}]^+$ (m/z 430.9141952) was used as an internal standard for mass calibration. IR spectra were taken with a HORIBA FT-IR 730 in the range of 650–4,000 cm^{-1} . Elemental analysis was measured with a CE INSTRUMENTS EA-1110 CHNS-O or J-Science MICRO CORDER JM10. Melting points were measured with a SEIKO DSC SSC/5200. Optical rotation was measured with a Jasco P-1020 with a 10 cm quartz cell irradiating the sodium D line. TLC was performed by using Merck TLC Silica gel 60 F_{254} 25 glass plates detected by a UV lamp (254 nm) or iodine as indicator.

Materials

Chiral tetradentate ligands having *S*-alanine units (**L1** and **L2**) were synthesized according to previous reports (Miyake et al., 2004). ^1H NMR and mass spectra of the products are shown in **Supplementary Figures 1, 2**. The synthesized compounds were purified by column chromatography using silica gel 60 (Merck) and silica gel 60N (Merck) as the stationary phase. Methanol for synthesis was distilled over quicklime as a desiccant.

LC/MS grade methanol (Fujifilm Wako Pure Chem. Co.) was purchased and used for ESI-MS. Ethylene glycol bistosylate was prepared from ethylene glycol and *p*-toluenesulfonyl chloride. Boc-*N*-methyl-*S*-valine methyl amide was prepared by the reported procedures (Bronner et al., 2011; Faggi et al., 2013). All other reagents containing metal salts and amino acids (AAs) were purchased from commercial suppliers and used without further purification. The structures of given deuterium-labeled amino acids (CDN ISOTOPES and ISOTEC, Inc.) are shown in **Supplementary Table 1**.

Preparation of Chiral Ligands

N,N'-Dimethyl-*N,N'*-Ethylene-Bis(*S*-Phenylalanine Methyl Ester) (**L3**) (Olsen, 1970; Insaf and Witiak, 1999)

Dimethylformamide (30 mL) was added to a mixture of *N*-Boc-*S*-phenylalanine (2.0 g, 7.5 mmol) and silver oxide (5.2 g, 23 mmol) in an ice bath. Methyl iodide (4.3 g, 30 mmol) was

added dropwise to the mixture in the ice bath, and the resulting mixture was stirred at room temperature overnight. The mixture was further stirred at 50°C for 3 h and then cooled to room temperature. The mixture was filtered through celite on the glass filter. The filtrate was mixed with chloroform which was washed with 10% Na₂S₂O₃ aqueous solution and the organic layer was dried over anhydrous sodium sulfate. The solution was evaporated and the residue purified with flash column chromatography (silica gel, ethyl acetate:*n*-hexane = 1:4, v/v) to give *N*-Boc-*N*-methyl-*S*-phenylalanine methyl ester (**1**) as a colorless liquid (1.70 g, 79.0%). ¹H NMR (270 MHz, CDCl₃): δ 7.33–7.14 (m, 5H, Ar-*H*), 4.94 (m, 0.5H, CH), 4.54 (m, 0.5H, CH), 3.74 (s, 6H, OCH₃), 3.29 (m, 1H, CH₂), 3.01 (ddd, ³*J* = 11.0 Hz, ²*J* = 14.5 Hz, 1H, CH₂), 2.72 (s, 3H, NCH₃), 1.33 (s, 9H, CH₃); ¹³C NMR (67.5 MHz, CDCl₃): δ 28.2, 35.5, 52.0, 61.6, 128.6, 128.5, 129.0; IR (neat, cm⁻¹): 2976, 1745, 1697, 1392, 1171, 1146; elemental analysis, calcd. for C₁₆H₂₃NO₄: C, 65.5%; H, 7.9%; N, 4.8%; Found: C, 65.5%; H, 7.9%; N, 4.8%; HRMS (ESI) calculated for C₁₆H₂₂NO₄ [M + Na]⁺ *m/z* 316.1525, found *m/z* 316.1542; [α]_D^{26.5} –90.9 (c 0.1, CHCl₃).

Compound **1** (1.0 g, 3.4 mmol) was dissolved in excess TFA, and the solution was stirred for 1 h at room temperature. After the starting material disappeared on TLC (silica gel, ethyl acetate: *n*-hexane = 1:4, v/v), the solution was evaporated to give *N*-methyl-*S*-phenylalanine methyl ester TFA salt. The TFA salt was treated with K₂CO₃ aqueous solution. The obtained *N*-methyl-*S*-phenylalanine methyl ester (0.41 g, 2.1 mmol), ethylene glycol bistosylate (0.39 g, 1.1 mmol), and 1,2,2,6,6-pentamethylpiperidine (PMP) (0.39 g, 2.6 mmol) were dissolved in toluene, and the resulting mixture was stirred at 80°C for 4 days. After cooling to room temperature, diethylether was added to the mixture. The precipitate was removed by filtration, the filtrate was evaporated and purified with flash column chromatography (silica gel, ethyl acetate:*n*-hexane = 1:1, v/v) to give **L3** as a colorless liquid (0.26 g, 29.0%). ¹H NMR (270 MHz, CDCl₃): δ 7.30–7.15 (m, 5H, Ar-*H*), 3.60 (s, 6H, OCH₃), 3.53 (dd, ³*J* = 6.06 Hz, ²*J* = 8.57 Hz, 2H, CH), 2.97 (ddd, ³*J* = 9.15 Hz, ³*J* = 13.6 Hz, ²*J* = 47.9 Hz, 2H, CH₂), 2.63 (m, 4H, ethylene-CH₂), 2.36 (s, 6H, N-CH₃); ¹³C NMR (67.5 MHz, CDCl₃): δ 35.9, 38.7, 51.0, 52.8, 68.5, 126.3, 128.3, 129.1, 138.4, 172.2; IR (neat, cm⁻¹): 2951, 1732, 1456, 1213, 1196, 1165; elemental analysis, calcd. for C₂₄H₃₂N₂O₄: C, 69.9%; H, 7.8%; N, 6.8%; Found: C, 69.6%; H, 7.7%; N, 6.7%; (ESI) calculated for C₂₄H₃₂N₂O₄ [M + H]⁺ *m/z* 413.2440, found *m/z* 413.2437; [α]_D^{26.5} –52.2 (c 0.1, CHCl₃).

***N,N'*-Dimethyl-*N,N'*-Ethylene-Bis(*S*-Phenylalanine Methyl Amide) (**L4**)**

L3 (0.10 g, 0.24 mmol) was dissolved in an excess amount of 40% methylamine solution in methanol, and the solution was stirred at 60°C for 2 days and room temperature for a day. The solution was evaporated, and the residue was purified with flash column chromatography (silica gel, chloroform: methanol = 1:9, v/v) to give **L4** as a white solid (0.05 g, 47.2%). ¹H NMR (300 MHz, CDCl₃): δ 7.27–7.16 (m, 12H, Ar-*H* and N-*H*), 3.45 (dd, ³*J* = 7.0 Hz, ³*J* = 7.4 Hz, 2H, -CH-CH₂), 3.32 (dd, ²*J* = 7.0 Hz, ²*J* = 15.7 Hz, 2H, CHH'-Ar), 2.85 (dd, ³*J* = 7.4 Hz, ²*J* = 15.7 Hz, 2H,

CHH'-Ar), 2.74 (d, ³*J* = 5.3 Hz, 6H, NH-CH₃), 2.56 (m, 2H, -CHH'-NCH₃), 2.45 (m, 2H, -CHH'-NCH₃), 2.25 (s, 6H, N-CH₃); ¹³C NMR (75 MHz, CDCl₃): δ 26.8, 33.5, 40.4, 52.5, 71.1, 126.8, 129.1, 129.9, 141.0, 173.6; IR (KBr, cm⁻¹): 3313, 2979, 1641, 1562, 1454, 1412, 1252, 1120, 1047, 750, 696; elemental analysis, calcd. for C₂₄H₃₄N₄O₂: C, 70.2%; H, 8.4%; N, 13.7%; Found: C, 70.0%; H, 8.4%; N, 13.6%; HRMS (ESI) calculated for C₂₄H₃₄N₄O₂ [M + Na]⁺ *m/z* 433.2579, found *m/z* 433.2582; [α]_D^{26.6} –33.7 (c 0.08, CHCl₃); mp, 101°C.

***N,N'*-Dimethyl-*N,N'*-Ethylene-Bis(*S*-Valine Methyl Ester) (**L5**)**

(*S*)-Valine methyl ester hydrochloride (0.51 g, 3.0 mmol) was dissolved in methanol, and 40% glyoxal aqueous solution was added to the solution. The mixture was stirred at room temperature for 2.5 h. NaBH₃CN (0.75 g, 11.9 mmol) was added to the mixture keeping the pH at 4.0–5.0 by addition of 30% trimethylamine aqueous solution, and the resulting solution was stirred for 2 weeks. The solution was extracted with chloroform and the organic layer was washed with sat. NaHCO₃ aq. and dried over anhydrous sodium sulfate. The solution was evaporated, and 0.67 mol/L diethylether hydrochloride was added to give *N,N'*-ethylene-bis(*S*-valine methyl ester) dihydrochloride as a white solid. The solid was purified by recrystallization from chloroform/methanol to yield 0.14 g (16.0%) of *N,N'*-ethylene-bis(*S*-valine methyl ester) dihydrochloride. The physical and spectral properties of the product were as follows: ¹H NMR (270 MHz, D₂O): δ 3.97 (d, ³*J* = 3.92 Hz, 2H, CH), 3.78 (s, 6H, OCH₃), 3.40 (s, 4H, CH₂), 2.28 (m, 2H, (CH₃)₂-CH), 0.95 (dd, ³*J* = 6.92 Hz, ²*J* = 18.1 Hz, 12H, CH₃); ¹³C NMR (67.5 MHz, D₂O): δ 18.8, 30.5, 54.3, 67.0; IR (KBr, cm⁻¹): 3464, 2954, 2725, 2679, 1743, 1473, 1442, 1234; elemental analysis, calcd. C₁₄H₂₈N₂O₄·4HCl for C, 38.72%; H, 7.43%; N, 6.45%; found C, 38.73%; H, 6.77%; N, 6.35%; HRMS (ESI, positive), calculated for C₁₄H₂₉N₃O₄ (M + H) *m/z* 289.212, found *m/z* 289.212; specific rotation, [α]_D^{26.5} –9.35 (c 0.1, H₂O); mp, 99.5°C.

N,N'-Ethylene-bis(*S*-valine methyl ester) hydrochloride (0.1 g, 0.28 mmol) was dissolved in methanol, and 37% formaldehyde aqueous solution (0.090 g, 1.1 mmol) was added to the solution, and the mixture was stirred at room temperature at 0.5 h. NaBH₃CN (0.75 g, 11.9 mmol) was added to the mixture keeping the pH at 4.0 by addition 30% trimethylamine aqueous solution, and the resulting mixture was stirred overnight. The solution was extracted with chloroform and the organic layer was washed with saturated NaHCO₃ aqueous solution, and dried over anhydrous sodium sulfate. The solution was evaporated and the residue was purified with flash column chromatography (silica gel, ethylacetate: *n*-hexane = 1: 3, v/v) to give **L5** as colorless liquid (0.070 g, 80.0%). The physical and spectral properties of the product were as follows: ¹H NMR (300 MHz, CDCl₃): δ 3.68 (s, 6H, OCH₃), 2.78 (d, ³*J* = 10.5 Hz, 2H, CH), 2.54 (m, 4H, CH₂), 2.26 (s, 6H, N-CH₂), 2.00 (m, 2H, (CH₃)₂-CH), 0.90 (dd, ³*J* = 6.56 Hz, ²*J* = 34.3 Hz, 12H, CH₃); ¹³C NMR (75 MHz, CDCl₃): δ 19.3, 19.8, 27.5, 38.2, 50.4, 52.9, 73.9, 172.5; IR (KB/cm⁻¹): 2962, 1732, 1456, 1178, 1149; elemental analysis, calcd. C₁₆H₃₂N₂O₄ C, 60.7%; H, 10.2%; N, 8.9%; found C, 60.4%; H, 10.3%; N, 8.7%; HRMS (ESI, positive) calculated for C₁₆H₃₂N₂O₄ [M +

$[H]^+ m/z$ 317.2440, found m/z 317.2466; specific rotation, $[\alpha]_D^{26.6}$ -78.6 (c 0.1, $CHCl_3$).

N,N'-Dimethyl-N,N'-Ethylene-Bis(S-Valine Methyl Amide) (L6)

A solution of 4N HCl in ethyl acetate (ca. 10 mL) was added to Boc-N-methyl-S-valine methyl amide (1.03 g, 4.24 mmol) which was stirred for 1 h at room temperature. After evaporation of the solvent, dry diethyl ether was added to the residue to give hydrochloride salt of N-methyl-S-valine methyl amide as a white solid, which was separated by filtration and dried in vacuo for several hours (yield 0.626 g, 3.48 mmol). To a solution of N-methyl-S-valine methyl amide hydrochloride (0.626 g, 3.48 mmol) in 20 mL of methanol, 37% formaldehyde aqueous solution (0.252 g, 1.74 mmol) was added, and the mixture was stirred at room temperature for 2.5 h. Ninety percentage $NaBH_3CN$ (0.253 g, 3.61 mmol) was added to the mixture and the resulting mixture was stirred overnight. The product was extracted with chloroform and the organic layer was washed with saturated $NaHCO_3$ aqueous solution three times, and then dried over anhydrous sodium sulfate. The solution was removed and the residue was purified with column chromatography (silica gel, chloroform: methanol = 20:1, v/v) and recycle HPLC (JAIGEL-1H, -2H, chloroform) to give **L6** as a white solid (0.053 g, 9.6%). The physical and spectral properties of the product were as follows: 1H NMR (300 MHz, $CDCl_3$): δ H 6.55 (brs, 2H, NH_2), 2.82 (d, J = 4.8 Hz, 6H, $NHCH_3$), 2.68 (d, J = 6.79 Hz, 2H, CH), 2.49 (dd, 3J = 120.7 Hz, 2J = 8.57 Hz, 4H, CH_2), 2.25 (s, 6H, N- CH_2), 2.14 (ddd, J = 6.98 Hz, 2H, $(CH_3)_2-CH$), 0.95 (dd, 3J = 6.79 Hz, 2J = 47.1 Hz, 12H, CH_3); ^{13}C NMR (75 MHz, $CDCl_3$): δ 18.8, 20.9, 26.4, 28.2, 39.7, 54.1, 76.0, 172.8; IR (KBr, cm^{-1}): 3300, 3093, 2971, 1639, 1564, 1468, 1412, 1232, 1161, 1109, 1034; elemental analysis, calcd. for $C_{14}H_{34}N_4O_2$: C, 61.1%; H, 10.9%; N, 17.8%; Found: C, 61.0%; H, 10.9%; N, 17.7%; HRMS (ESI) calculated for $C_{16}H_{34}N_4O_2$ $[M + Na]^+ m/z$ 337.2579, found m/z 337.2604; $[\alpha]_D^{26.6}$ -71.1 (c 0.1, $CHCl_3$); mp, 168°C.

N,N'-Dimethyl-N,N'-Ethylene-Bis(S-Proline Methyl Ester) (L7) (Insaf and Witiak, 1999)

S-Proline methyl ester hydrochloride was treated with K_2CO_3 aqueous solution. S-proline methyl ester (0.50 g, 3.8 mmol), ethylene glycol bistosylate (0.70 g, 0.19 mmol) and PMP (0.71 g, 4.6 mmol) was dissolved in toluene, and the resulting mixture was refluxed for 2 days. After cooling to room temperature, diethylether was added to the mixture. The obtained precipitate was removed by filtration, and the filtrate was evaporated and purified with flash column chromatography (silica gel, chloroform:methanol = 1:9, v/v) to give **L7** as a yellow syrup (0.26 g, 25.0%). 1H NMR (300 MHz, $CDCl_3$): δ 3.71 (s, 6H, OCH_3), 3.20 (m, 4H, 2H (CH), 2H (1- CH_2)), 2.65 (m, 4H, ethylene- CH_2), 2.42 (q, J = 8.0 Hz, 2H, 1- CH_2), 2.18–1.72 (m, 8H, 2- CH_2 , 3- CH_2); ^{13}C NMR (75 MHz, $CDCl_3$): δ 23.2, 29.2, 51.7, 53.4, 53.6, 66.0, 174.6; IR (neat, cm^{-1}): 2952, 2817, 1734, 1435, 1198, 1171; elemental analysis, calcd. for $C_{14}H_{24}N_2O_4 \cdot 0.25CO_2$: C, 58.0%; H, 8.2%; N, 9.5%; Found: C, 57.9%; H, 8.3%; N, 9.3%; HRMS (ESI) calculated for $C_{14}H_{24}N_2O_4$

$[M + H]^+ m/z$ 285.1814, found m/z 285.1849; $[\alpha]_D^{26.6}$ -106.8 (c 0.1, $CHCl_3$).

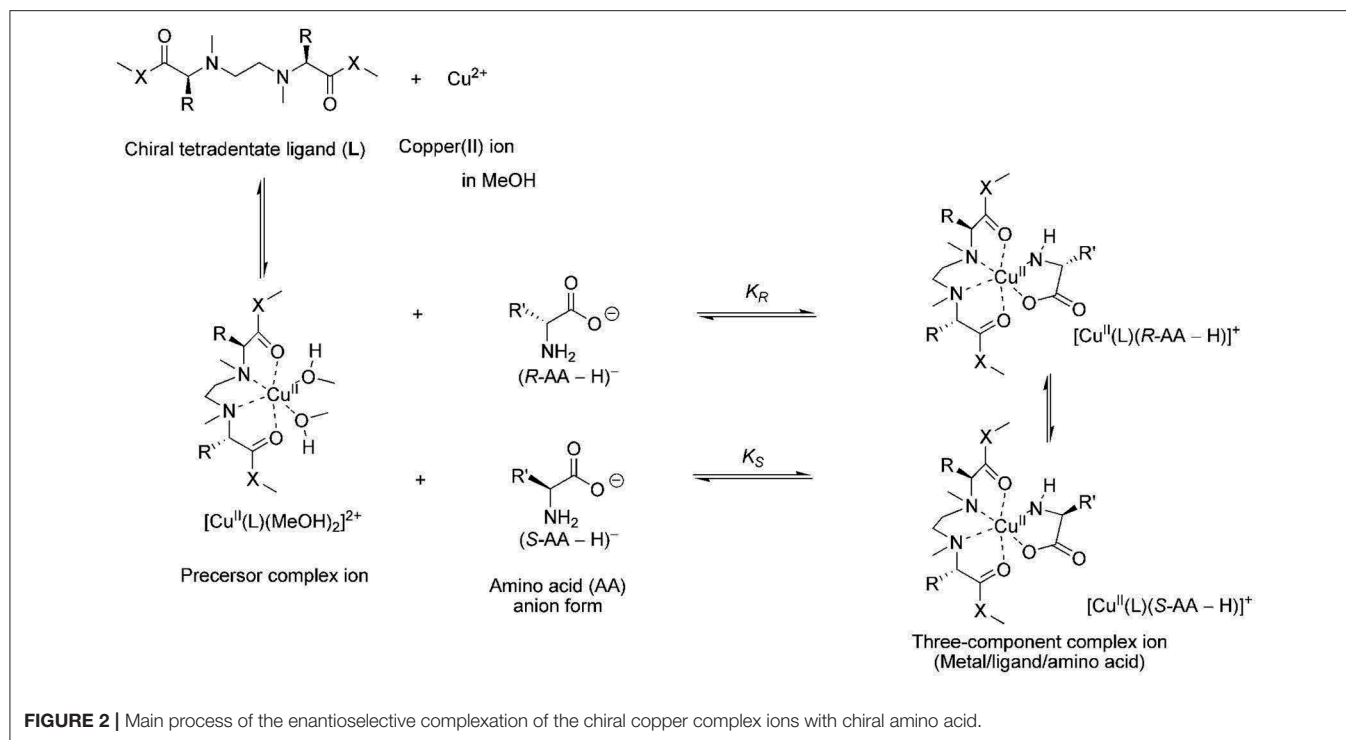
N,N'-Dimethyl-N,N'-Ethylene-Bis(S-Proline Methyl Amide) (L8)

L8 was synthesized by the same procedures as **L4**. The product (0.08 g, 80.6%) was afforded from **L7** (0.10 g, 0.35 mmol). The physical and spectral properties of the product were as follows: 1H NMR (300 MHz, $CDCl_3$): δ H 7.72 (brs, 2H, NH), 3.18 (m, 4H, CH, 1- CHH'), 2.82 (m, 8H, CH_3 and ethylene- CHH'), 2.49 (d, J = 8.6 Hz, 4H, ethylene- CHH'), 2.30 (m, 4H, 1- CHH' , 3- CHH'), 1.99–1.66 (m, 6H, 2- CH_2 , 3- CHH'); ^{13}C NMR (75 MHz, $CDCl_3$): δ 24.7, 26.6, 31.0, 54.7, 55.5, 68.6, 175.7; IR (KBr, cm^{-1}): 3477, 3305, 2960, 2831, 1836, 1537, 1404, 1302, 1155, 1061, 872, 739; elemental analysis, calcd. for $C_{14}H_{26}N_4O_2 \cdot 0.5H_2O$: C, 57.7%; H, 9.3%; N, 19.2%; Found: C, 57.8%; H, 9.3%; N, 19.1%; HRMS (ESI) calculated for $C_{14}H_{26}N_4O_2$ $[M + Na]^+ m/z$ 305.1953, found m/z 305.1977; $[\alpha]_D^{26.6}$ -171.6 (c 0.05, $CHCl_3$); mp, 122°C.

Mass Spectrometry

The instrumental conditions for ESI mass spectral measurements (positive ion mode) with a JEOL AccuTOF LC-plus 4G mass spectrometer were optimized to detect the metal complex ions with high sensitivity as follows: voltage of spray needle, 1 kV; orifice1, 50 V; orifice2, 1 V; ring lens, 5 V; temperature of desolvation chamber, 100°C; temperature of orifice1, 50°C; mass range, m/z 150–1,000. The mass spectral data were collected under the following conditions: acquisition time, 0.397 s (wait time = 0.003 s, recording time = 0.4 s); measurement time, 2 min.

The accuracy of the 1:1 equivalent of the R-AA and deuterium-labeled S-AA was calibrated based on the I_R/I_S values obtained by the copper complex with achiral tetradentate ligand. I_R/I_S measurements of Cu^{II} -**L3** and Cu^{II} -**L8** were carried out under optimized conditions by controlling the amount of amino acid determined from the relative peak intensity of the complex ions in the mass spectra shown in **Supplementary Figures 19–26**. I_R/I_S measurements of Cu^{II} -**L1** was carried out under conditions optimized in a previous report (Nakakoji et al., 2020). The sample solutions used for mass spectral measurements shown in **Figure 3** and **Supplementary Figures 27–42** were prepared as follows: solution (1) 1.20 mL of copper(II) chloride (2.00×10^{-3} M) in methanol and 1.00 mL of **L** (2.00×10^{-3} M) in methanol were mixed, which was then diluted to 20 mL in a volumetric flask by adding methanol; solution (2-1) In the case of Cu^{II} -**L3** and Cu^{II} -**L8** as chiral hosts, 1.00 mL of solution (1) and 0.1 mL of an equimolar mixture of R-AA and deuterium-labeled S-AA (5.00×10^{-4} M each) containing K_2CO_3 (equimolar for carboxyl group) in water were mixed to prepare the final solution (mole ratio: $CuCl_2/(L)/R-AA/S-AA-d_n = 1.2/1.0/0.5/0.5$); (2-2) In the case of Cu^{II} -**L1** as chiral host, 1.00 mL of solution (1) and 0.4 mL of an equimolar mixture of R-enantiomer and deuterium-labeled S-enantiomer (5.00×10^{-4} M each) containing K_2CO_3 (1.00×10^{-3} M) in water were mixed to prepare the final solution (mole ratio: $CuCl_2/(L)/R-AA/S-AA-d_n = 1.2/1.0/2.0/2.0$).



DFT Calculations

Density Functional Theory (DFT) calculations were performed using a Material Studio version 2018 (Dassault Systems Biovia) on a Windows workstation (Delley, 1990, 2000). The X-ray crystalline structure of copper(II) complex [Cu^{II}(L2)(MeOH)₂]²⁺ (Nakakoji et al., 2020) was used as the initial structure and the ligand (L2) was modified to build other ligands (L1, L3–L8) using the Visualizer module in Material Studio. The geometry of each complex [Cu^{II}(L)(MeOH)₂]²⁺ in methanol was optimized using a DMol3 module (density functional, B3LYP; basis set, DNP) (Vosko et al., 1980; Lee et al., 1988; Weinert and Davenport, 1992; Becke, 1993; Stephens et al., 1994; Delley, 1995, 2006).

RESULTS AND DISCUSSION

Detection of Three-Component Complex Ions by Mass Spectrometry

In this study the ligand exchange reaction of a copper(II) complex ion between chiral amino acids (AAs) in solution was examined (Figure 2). The chiral discrimination abilities of the copper(II) complexes with novel chiral ligands (L3–L8) toward free amino acids were evaluated using electrospray ionization mass spectrometry coupled with the deuterium-labeled/unlabeled enantiomer method (the MS/EL method) (Sawada et al., 1995; Sawada, 1997; Shizuma, 2010). In this method, the chiral discrimination ability was estimated on the basis of the relative peak intensity of the three-component complex ions, [Cu^{II}(L)(R-AA-H)]⁺ and [Cu^{II}(L)(S-AA-*d_n*-H)]⁺ (*n*, number of deuterium atoms). The complex ions were generated by mixing the copper

salt, the chiral ligand, and an equimolar mixture of deuterium-labeled *S*-AA and unlabeled *R*-AA at the following mole ratio: Cu/L/*S*-AA-*d_n*/*R*-AA = 1.2:1.0:2.0:2.0. Addition of excess AA induced competitive coordination of AAs to the precursor complex ion [Cu^{II}(L)(solvent)₂]²⁺ (Nakakoji et al., 2020). The relative peak intensity of the complex ions, $I[\text{Cu}^{\text{II}}(\text{L})(\text{R-AA-H})]^+ / I[\text{Cu}^{\text{II}}(\text{L})(\text{S-AA-}d_n\text{-H})]^+ (=I_R/I_S, I: \text{peak intensity})$, under the competitive coordination equilibrium conditions becomes nearly equal to the ratio of association constants in the complexation equilibrium system (K_R/K_S) (Shizuma et al., 2002, 2005). Copper(II) chloride was chosen as the copper salt since very few peaks of ion species except the three-component complex ions consisting of one chiral ligand L1 or L2 were observed in the mass spectra (Nakakoji et al., 2020).

Since detecting the three-component complex ion by mass spectrometry is required to evaluate the chiral discrimination ability, the ion species observed in the mass spectrum were examined. Mass spectra of the mixtures of copper salt, chiral ligands and *S*-alanine are shown in Figure 3. When the pH was <7, the three-component complex ion peak containing coordinated amino acid was not observed. Since the three-component complex ion was observed with high sensitivity by adding potassium carbonate equal to or more than the amino acid, it is required the amino acid in a carboxylate state to form the three-component complex ion. In all chiral ligand cases, the peaks of the three-component complex ions [Cu^{II}(L)(*S*-AA-H)]⁺ were observed in the mass spectra under the following concentration conditions: [CuCl₂]₀, 1.09 × 10⁻⁴ M; [L]₀, 9.09 × 10⁻⁵ M; [*S*-Ala]₀, 9.09 × 10⁻⁵ M; [K₂CO₃]₀, 9.09 × 10⁻⁵ M. However, in the cases of Cu^{II}/L5, Cu^{II}/L6, and Cu^{II}/L7, the intensity of the complex ion [Cu^{II}(L)(*S*-AA-H)]⁺

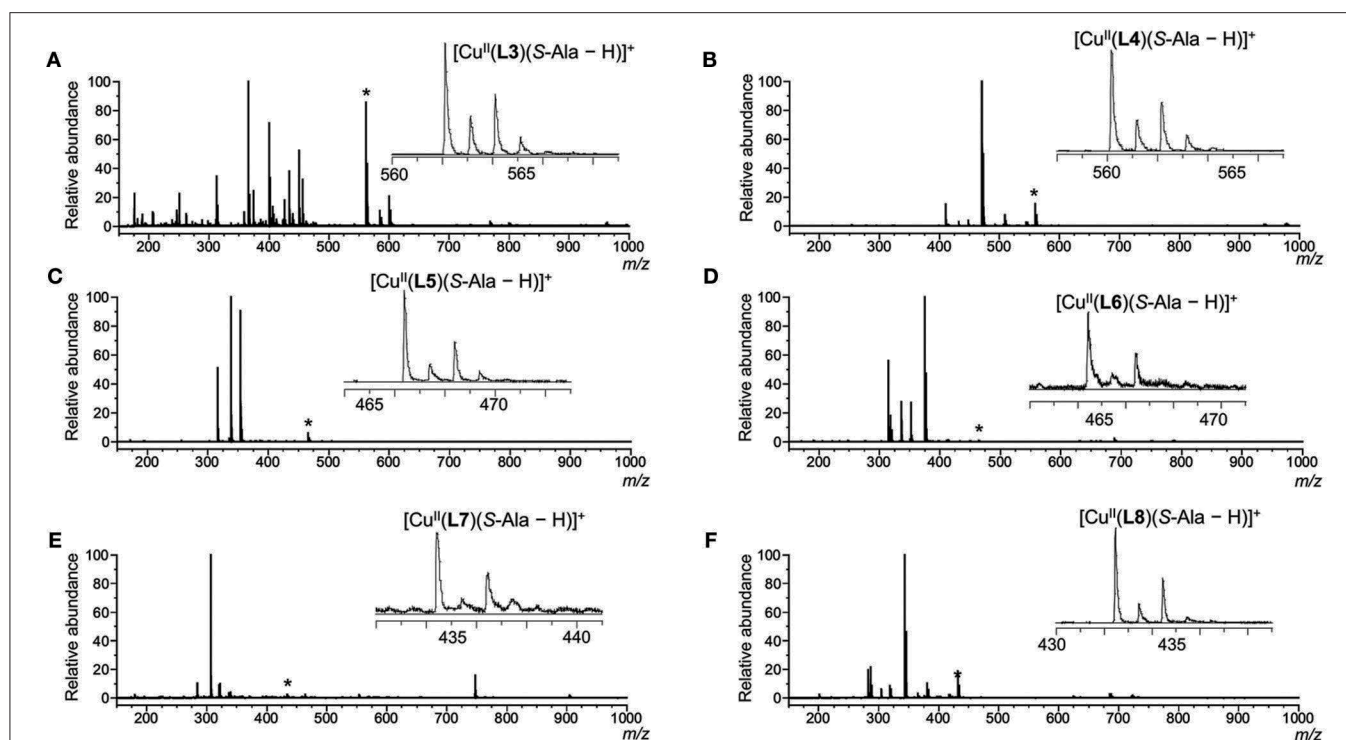


FIGURE 3 | ESI mass spectra of $\text{CuCl}_2/\text{L}/\text{S-Ala}$ in water/methanol (1/10, v/v). Each signal marked with an asterisk (*) shows $[\text{Cu}^{\text{II}}(\text{L})(\text{S-Ala-H})]^+$ and the expanded signal is shown in each spectrum. $[\text{CuCl}_2]_0 = 1.09 \times 10^{-4}$ M and $[\text{L}]_0 = [\text{S-Ala}]_0 = [\text{K}_2\text{CO}_3]_0 = 9.09 \times 10^{-5}$ M. $[\text{CuCl}_2]_0/[\text{L}]_0/[\text{S-Ala}]_0 = 1.2/1.0/1.0$. L: (A) L3; (B) L4; (C) L5; (D) L6; (E) L7; (F) L8.

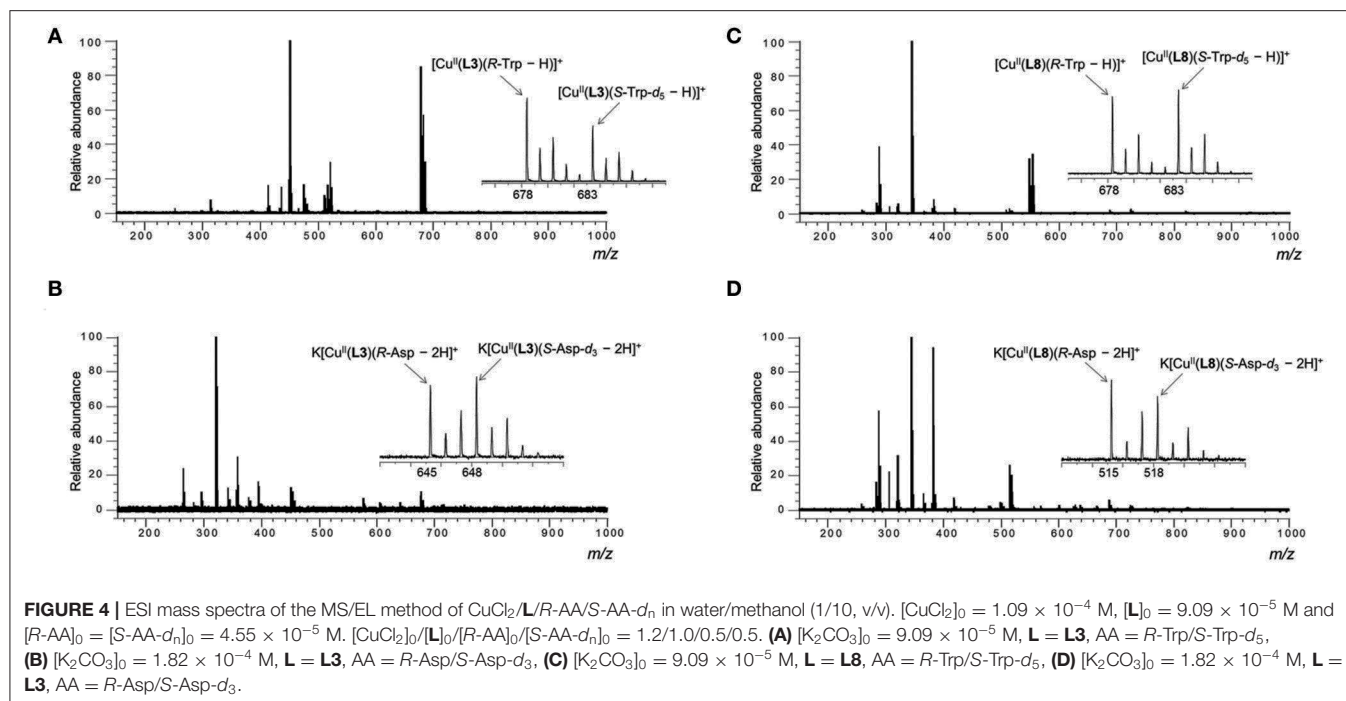
was very low. It was suggested that the isopropyl units of S-valine moieties were too bulky to incorporate S-Ala. The three-component complex ions $[\text{Cu}^{\text{II}}(\text{L})(\text{S-AA-H})]^+$ were detected for the $\text{Cu}^{\text{II}}/\text{L3}$, $\text{Cu}^{\text{II}}/\text{L4}$, and $\text{Cu}^{\text{II}}/\text{L8}$ systems. The peak intensity of complex ion $[\text{Cu}^{\text{II}}(\text{L3})(\text{S-AA-H})]^+$ (ester type ligand) was higher than that of complex ion $[\text{Cu}^{\text{II}}(\text{L4})(\text{S-AA-H})]^+$ (amide type ligand), and $[\text{Cu}^{\text{II}}(\text{L8})(\text{S-AA-H})]^+$ (amide type ligand) was higher than $[\text{Cu}^{\text{II}}(\text{L7})(\text{S-AA-H})]^+$. Thus, the systems of $\text{Cu}^{\text{II}}/\text{L3}$ and $\text{Cu}^{\text{II}}/\text{L8}$ were chosen for further evaluation of the I_R/I_S value.

Evaluation of Chiral Discrimination Ability Toward AA

Tetradentate ligands **L3** and **L8** were chosen for enantioselectivity evaluation of the copper(II) complex toward chiral AAs by mass spectrometry, since three-component complex ions $[\text{Cu}(\text{L})(\text{AA-H})]^+$ were detected with high intensity. Each ligand was mixed with copper(II) chloride in methanol, and then an aqueous solution of an equimolar mixture of a deuterium-labeled S-Val (d_8) and unlabeled R-Val containing potassium carbonate was added to the methanol solution. The mass spectra of the prepared solutions were measured. In the resulting mass spectra, two complex ions, $[\text{Cu}(\text{L})(\text{R-Val-H})]^+$ and $[\text{Cu}(\text{L})(\text{S-Val-}d_8\text{-H})]^+$, were observed (Supplementary Figures 19–26). Under competitive complexation conditions with large excess of AA for the copper(II)-L complex ($[\text{AA}]_0 \gg [\text{Cu}^{2+}(\text{L})(\text{MeOH})_2]_0$), the relative peak intensity of the complex ions ($I[\text{Cu}(\text{L})(\text{R-Val-H})]^+ / I[\text{Cu}(\text{L})(\text{S-Val-}d_8\text{-H})]^+ = I_R/I_S$ value, I : intensity)

was regarded as the chiral discrimination ability. The larger the concentration of Val relative to that of the copper(II)-L complex, the larger the relative ratio of I_R and I_S values. Finally, the I_R/I_S reached a certain value. In the case where there was a much larger concentration of Val relative to the copper(II)-L complex, the signal of $[\text{L} + \text{Na}]^+$ was detected as the base peak, suggesting decomposition of copper(II)-L complex (Supplementary Figures 22, 26). The final sample preparation conditions were determined based on the effect of the contamination peak and the I_R/I_S value. The final concentrations of each component of the sample solution used for the MS measurement were as follows: $[\text{CuCl}_2]_0$: $[\text{L}]_0$: $[\text{R-AA}]_0$: $[\text{S-AA-}d_n]_0$: $[\text{K}_2\text{CO}_3]_0 = 1.2 \times 10^{-4}$ M: 1.0×10^{-4} M: 5.0×10^{-4} M: 5.0×10^{-4} M: 1.0×10^{-3} M in methanol/water (10/1).

Sample solutions for various amino acids were prepared under the condition described above, and their mass spectra were measured. Two three-component complex ion peaks were observed in all measured mass spectra. As a typical mass spectrum, the mass spectrum of the sample solution using **L3** as the ligand and Val as the AA is shown in Figure 4A. In the case of Asp, the three-component complex ion peak was detected as a potassium ion adduct $\text{K}[\text{Cu}(\text{L})(\text{Asp-2H})]^+$ (Figure 4B). The mass spectra of other sample solutions are shown in the Supplementary Figures 27–42. As shown in the enlarged view in Figure 4, two complex ion peaks with isotope distributions characteristic of copper were observed. In the case of **L3** and Trp (Figure 4A), the signal intensity on the low mass side was large,



suggesting that the *R*-amino acid coordinates with the complex ion preferentially. The I_R/I_S value was 1.64. In the case of **L8** and Asp, the I_R/I_S value was 1.31 (*R*-preference).

The relative intensity (I_R/I_S) values of the two complex ions are summarized in **Table 1**, and the values are corrected for the contribution of the isotope peaks of the complex ions on the low mass side to the peak intensity on the high mass side. The complex containing **L3** showed high chiral discriminating ability for Phe, Val, Hyp, and Trp, and its enantioselectivity preference was the *R*-amino acid. On the other hand, in the complex ions containing **L8**, a high chiral discrimination ability was observed for Hyp and Asp and its enantioselectivity was *S*-selective for Hyp and *R*-selective for Asp.

As described in previous reports, detailed investigations for copper(II) complex containing **L1** or **L2** as tetradentate ligands and amino acid confirmed that the complexation observed by mass spectrometry took place in the solution, not in the gas phase (Nakakoji et al., 2020). In this study using ligands with similar structures, it seems that the ligand exchange reaction in solution was observed by mass spectrometry.

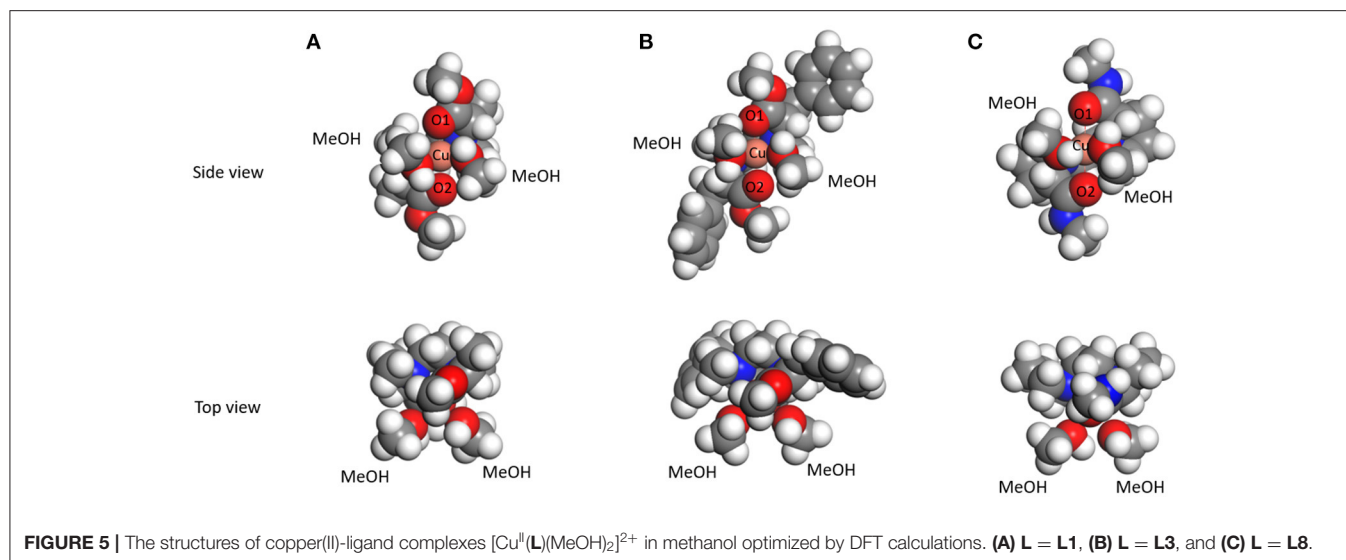
Structure of Complex Ions and Enantioselectivity

To clarify the chiral discrimination mechanism, it is necessary to investigate the complex structure. For the complex structure, a spectroscopic approach based on the absorption spectrum or the circular dichroism spectrum is desirable. However, since the complexation equilibrium system of this study contains many ionic species (see Nakakoji et al., 2020), it shows complicated spectral changes. Therefore, it is difficult to evaluate the structure by spectroscopy. Furthermore, since divalent

copper ions are paramagnetic, it is difficult to analyze the complex structure by the nuclear magnetic resonance (NMR) method. Therefore, we adopted DFT method for optimization of their structures.

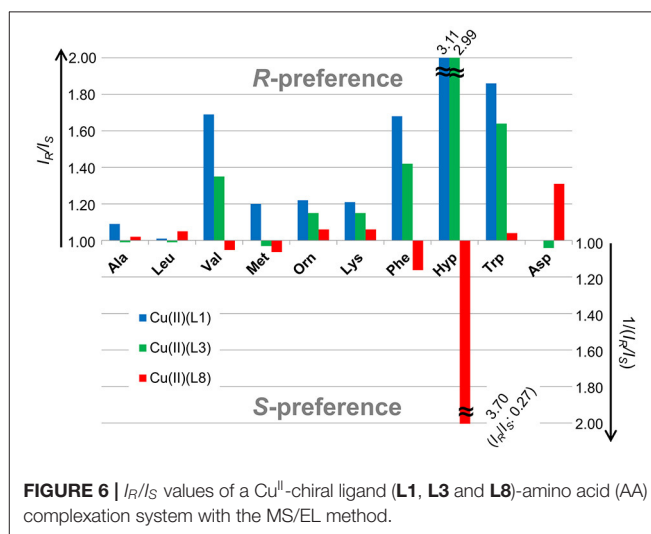
TABLE 1 | I_R/I_S values of a Cu^{II} -chiral ligand (**L3** and **L8**)-amino acid (AA) complexation system in the MS/EL method.

Ligand	Amino acid (AA)	I_R/I_S	Enantioselectivity
L3	Ala	0.99	–
L3	Leu	0.99	–
L3	Val	1.35	<i>R</i>
L3	Met	0.97	–
L3	Orn	1.15	<i>R</i>
L3	Lys	1.15	<i>R</i>
L3	Phe	1.42	<i>R</i>
L3	Hyp	2.99	<i>R</i>
L3	Trp	1.64	<i>R</i>
L3	Asp	0.96	–
L8	Ala	1.02	–
L8	Leu	1.05	–
L8	Val	0.95	–
L8	Met	0.94	<i>S</i>
L8	Orn	1.06	<i>R</i>
L8	Lys	1.06	<i>R</i>
L8	Phe	0.86	<i>S</i>
L8	Hyp	0.27	<i>S</i>
L8	Trp	1.04	–
L8	Asp	1.31	<i>R</i>



The structure of the complex $[\text{Cu}(\text{L})(\text{MeOH})_2]^{2+}$ in methanol, which is the precursor to generate the three-component complex $[\text{Cu}(\text{L})(\text{AA} - \text{H})]^+$, was investigated by DFT calculations. The amino acid could occupy the *cis* position on the copper(II) ion as a bidentate ligand by replacing the two methanol molecules. X-ray crystalline structure analysis of the complex $[\text{Cu}(\text{L2})(\text{MeOH})_2]^{2+}$ revealed that the chiral tetradentate ligand is coordinated in *cis*- α form (Nakakoji et al., 2020). The initial structures of the complexes for DFT calculations were built based on the crystalline structure. The structures of the complexes $[\text{Cu}(\text{L})(\text{MeOH})_2]^{2+}$ ($\text{L} = \text{L1}$, L3 , and L8) obtained by DFT calculations are shown in Figure 5 (The results of L2 , L4 – L7 are shown in Supplementary Figure 43). The complexes $[\text{Cu}(\text{L})(\text{MeOH})_2]^{2+}$ (L : L1 – L8) had slightly twisted *cis*- α structures with C_2 -symmetry similar to the complex $[\text{Cu}(\text{L2})(\text{MeOH})_2]^{2+}$ whose crystal structure was reported. The bond length between copper ion and the oxygen atom of the carbonyl of the tetradentate ligand in $[\text{Cu}(\text{L1})(\text{MeOH})_2]^{2+}$ and $[\text{Cu}(\text{L3})(\text{MeOH})_2]^{2+}$ was 2.15 Å (Supplementary Table 2). On the other hand, the bond length (2.5 Å) of Cu–O in $[\text{Cu}(\text{L8})(\text{MeOH})_2]^{2+}$ was longer than this. This is considered to be the effect of strain due to the rigid structure of the proline ring in the chiral tetradentate ligand. The side chains of the ligand in the complex ions $[\text{Cu}(\text{L1})(\text{MeOH})_2]^{2+}$ and $[\text{Cu}(\text{L3})(\text{MeOH})_2]^{2+}$ are free to rotate, whereas this is difficult for the ligand in the complex ion $[\text{Cu}(\text{L8})(\text{MeOH})_2]^{2+}$. This structural divergence of the complexes suggests that the complexes $[\text{Cu}(\text{L1})(\text{MeOH})_2]^{2+}$ and $[\text{Cu}(\text{L3})(\text{MeOH})_2]^{2+}$ provide similar large spaces to coordinate AA, and $[\text{Cu}(\text{L8})(\text{MeOH})_2]^{2+}$ provides a different space due to the rigidity of the Pro moieties.

As shown in Figure 6, the enantioselectivity in the complexation of $[\text{Cu}(\text{L1})(\text{AA} - \text{H})]^+$ (blue block) and $[\text{Cu}(\text{L3})(\text{AA} - \text{H})]^+$ (green block) with each AA was similar, while that of $[\text{Cu}(\text{L8})(\text{AA} - \text{H})]^+$ (red block) was quite different. Thus, it is considered that the slight difference of



the coordination structure of the copper(II) complex with the tetradentate ligand, which is calculated by DFT, is the main factor that determines the enantioselectivity for amino acids. The magnitude of the chiral discrimination ability for amino acids is considered to depend on the steric interaction between the side chain of the chiral tetradentate ligand and that of the amino acid. In fact, a large chiral discrimination ability was observed for AAs such as Phe, Val, Hyp, and Trp, which have large side chains.

The selectivity in reactions such as asymmetric catalytic reactions or ligand-exchange of metal complexes was investigated on the basis of the steric parameters (Sigman and Miller, 2009). The Taft steric parameters (Taft, 1952, 1953) have been applied to various fields such as quantitative structure-activity relationship (QSAR) in medicinal chemistry (Unger and Hansch, 1979; Huang et al., 2014). The ordering of the Taft steric

parameter (E_S) was $-\text{CH}_3$ (0) > $-\text{CH}_2\text{C}_6\text{H}_5$ (−0.38) > $-\text{CH}(\text{CH}_3)_2$ (−0.47). The ordering shows agreement with that of the intensity of the three-component complex ion $[\text{Cu}(\text{L})(\text{AA} - \text{H})]^+$ in mass spectrometry. The coordination of the AA to $[\text{Cu}(\text{L})(\text{MeOH})_2]^{2+}$ suggests a dependence on the steric interaction between the side arms of AA and the precursor complex ion.

Thus, the binding ability with AA and the chiral AA discrimination ability of copper(II)-tetradentate ligand complex ions were controlled by the steric effect of the side arms of the ligand.

SUMMARY

In this paper, we evaluated the chiral discrimination ability in the enantioselective complexation of a copper(II)-chiral tetradentate ligand with a chiral amino acid as a second ligand by electrospray ionization mass spectrometry coupled with the isotopically labeled/unlabeled enantiomer method and clarified the following facts. (i) In the chiral tetradentate ligands **L5** and **L6** where the sidearms are sterically bulky, it is difficult to form the three-component complex with an amino acid. (ii) The complex ions with chiral tetradentate ligands **L1** and **L3**, which coordinate to the copper ion in pseudo *cis*- α type fashion, are similar in enantioselectivity toward amino acids. (iii) In the case of ligand **L8**, which has proline rings in the skeleton, the pseudo *cis*- α type of structure cannot be maintained due to the rigidity, and the enantioselectivity of the copper complex for amino acids are different from those of the complexes with **L1** or **L3**. In the case of amino acid having bulky side arm such as Val, Phe, Hyp, $\text{Cu}^{\text{II}}/\text{L8}$ complex showed opposite enantioselectivity to $\text{Cu}^{\text{II}}/\text{L2}$ complexes. It was clarified that the enantioselectivity for amino acids is controlled by the slight difference in the coordination form of the copper(II) complex with chiral tetradentate ligand, and the magnitude of the chiral discrimination ability depends on the steric interaction between the sidearms of the chiral tetradentate ligand and the side chain of the amino acid.

Mass spectrometry coupled with the isotopically labeled enantiomer method can be applied to a method for determination of the enantiomeric excess of chiral guests by using an isotopically labeled/unlabeled enantiomer pair for the chiral host (Sawada et al., 1998; Shizuma et al., 2000).

REFERENCES

- Becke, A. D. (1993). Density-functional thermochemistry. III. The role of exact exchange. *J. Chem. Phys.* 98, 5648–5652. doi: 10.1063/1.464913
- Bronner, S. M., Goetz, A. E., and Garg, N. K. (2011). Overturning indolyne regioselectivities and synthesis of indolactam V. *J. Am. Chem. Soc.* 133, 3832–3835. doi: 10.1021/ja200437g
- Brückner, H., Sorsche, B., Esna-Ashari, A., and Jöster, R. (1990). “Chiral ligand-exchange chromatography of amino acid derivatives,” in: *Amino Acids*, eds G. Lubec and G. A. Rosenthal (Leiden: ESCOM Science Publisher B. V.), 152–158.
- Chin, J., Lee, S. S., Lee, K. J., Park, S., and Kim, D. H. (1999). A metal complex that binds α -amino acids with high and predictable stereospecificity. *Nature* 401, 254–257. doi: 10.1038/45751

Remarkably, it was revealed that the copper(II) complex with ligand **L8** has enantioselectivity for Asp, of which racemization in the human body has been reported to be related to various diseases (Man et al., 1983; Fujii et al., 1994; Fujii, 2005; Xin et al., 2007). Therefore, the copper(II)-chiral tetradentate ligand-amino acid three-component complexation equilibrium system proposed in this study can be applied to a method that can determine the optical purity of Asp simply, quickly and with high sensitivity by mass spectrometry alone. The knowledge obtained in this research will contribute to the future technological development of disease diagnosis.

DATA AVAILABILITY STATEMENT

The datasets generated for this study can be found in online repositories. The names of the repository/repositories and accession number(s) can be found in the article/**Supplementary Material**.

AUTHOR CONTRIBUTIONS

TN, HS, HM, and MS conceived and designed the study. TN, HS, HM, SS, and HT designed the metal-chiral ligand complexes. TN, KY, KI, EM, and HS synthesized and purified them. TN and MS measured the spectral data. HK, RA, and MS conceived the mass spectrometric experiments. TN prepared sample solutions and measured mass spectra. HM and MS performed the molecular simulations. HM, SS, HT, HK, RA, DO, and MS verified and discussed the results. TN, HM, and MS wrote the paper. All authors contributed to the article and approved the submitted version.

FUNDING

This work was partially supported by JSPS KAKENHI Grant Numbers JP18K0595 to MS and JP19K05505 to HM.

SUPPLEMENTARY MATERIAL

The Supplementary Material for this article can be found online at: <https://www.frontiersin.org/articles/10.3389/fchem.2020.598598/full#supplementary-material>

- Delley, B. (1990). An all-electron numerical method for solving the local density functional for polyatomic molecules. *J. Chem. Phys.* 92, 508–517. doi: 10.1063/1.458452
- Delley, B. (1995). in *Modern Density Functional Theory—A Tool for Chemistry*, Vol. 2, eds J. M. Seminario and P. Politzer (Amsterdam: Elsevier), 221.
- Delley, B. (2000). From molecules to solids with the DMol 3. *J. Chem. Phys.* 113, 7756–7764. doi: 10.1063/1.1316015
- Delley, B. (2006). The conductor-like screening model for polymers and surfaces. *Mol. Simul.* 32, 117–123. doi: 10.1080/08927020600589684
- Faggi, E., Luis, S. V., and Alfonso, I. (2013). Minimalistic amino amides as models to study N–H $\cdots \pi$ interactions and their implication in the side chain folding of pseudopeptidic molecules. *RSC Adv.* 3, 11556–11565. doi: 10.1039/c3ra41843j

- Fujii, N. (2005). D-Amino acid in elderly tissues. *Biol. Pharm. Bull.* 28, 585–1589. doi: 10.1248/bpb.28.1585
- Fujii, N., Satoh, K., Harada, K., and Ishibashi, Y. (1994). Simultaneous stereoinversion and isomerization at specific aspartic acid residues in α A-crystallin from human lens. *J. Biochem.* 116, 663–669. doi: 10.1093/oxfordjournals.jbchem.a124577
- Gil-Av, E., Tishbee, A., and Hare, P. E. (1980). Resolution of underivatized amino acids by reversed-phase chromatography. *J. Am. Chem. Soc.* 102, 5115–5117. doi: 10.1021/ja00535a059
- Huang, H., Zong, H., Shen, B., Yue, H., Bian, G., and Song, L. (2014). QSAR analysis of the catalytic asymmetric ethylation of ketone using physical steric parameters of chiral ligand substituents. *Tetrahedron* 70, 1289–1297. doi: 10.1016/j.tet.2013.12.054
- Insaf, S. S., and Witiak, D. T. (1999). Facile non-racemizing route for the N-alkylation of hindered secondary amines. *Synthesis* 3, 435–440. doi: 10.1055/s-1999-3399
- Kabuto, K., and Sasaki, Y. (1987). Highly consistent correlation between absolute configuration of α -amino acids and their shift induced by the n.m.r. chiral shift reagent propylenediaminetetra-acetateeuropium(III) in aqueous solution. *J. Chem. Soc. Chem. Commun.* 670–671. doi: 10.1039/C39870000670
- Lee, C., Yang, W., and Parr, R. G. (1988). Development of the Colle-Salvetti correlation-energy formula into a functional of the electron density. *Phys. Rev. B* 37, 785–789. doi: 10.1103/PhysRevB.37.785
- Man, E. H., Sandhouse, M. E., Burg, J., and Fisher, G. H. (1983). Accumulation of D-aspartic acid with age in the human brain. *Science* 220, 1407–1408. doi: 10.1126/science.6857259
- Miyake, H., Yoshida, K., Sugimoto, H., and Tsukube, H. (2004). Dynamic helicity inversion by achiral anion stimulus in synthetic labile cobalt(II) complex. *J. Am. Chem. Soc.* 126, 6524–6525. doi: 10.1021/ja049130o
- Nakakoji, T., Sato, H., Ono, D., Miyake, H., Shinoda, S., Tsukube, H., et al. (2020). Mass spectrometric detection of enantioselectivity in three-component complexation, copper(ii)-chiral tetradentate ligand-free amino acid in solution. *Chem. Commun.* 56, 54–57. doi: 10.1039/C9CC07231D
- Olsen, R. K. (1970). Synthesis of protected N-methylamino acid derivatives. *J. Org. Chem.* 35, 1912–1915. doi: 10.1021/jo00831a042
- Sawada, M. (1997). Chiral recognition detected by fast atom bombardment mass spectrometry. *Mass Spectrom. Rev.* 16, 73–90. doi: 10.1002/(SICI)1098-2787(1997)16:2<73::AID-MAS2>3.0.CO;2-6
- Sawada, M., Takai, Y., Yamada, H., Hirayama, S., Kaneda, T., Tanaka, T., et al. (1995). Chiral recognition in host-guest complexation determined by the enantiomer-labeled guest method using fast atom bombardment mass spectrometry. *J. Am. Chem. Soc.* 117, 7726–7736. doi: 10.1021/ja00134a017
- Sawada, M., Takai, Y., Yamada, H., Yamaoka, H., Azuma, T., Fujioka, T., et al. (1998). Determination of enantiomeric excess for amino acid ester salts using FAB mass spectrometry. *Chem. Commun.* 1569–1570. doi: 10.1039/a802029I
- Severin, K., Bergs, R., and Beck, W. (1998). Bioorganometallic chemistry-transition metal complexes with α -amino acids and peptides. *Angew. Chem. Int. Ed.* 37, 1635–1654. doi: 10.1002/(SICI)1521-3773(19980703)37:12<1634::AID-ANIE1634>3.0.CO;2-C
- Shizuma, M. (2010). “Chiral recognition in mass spectrometry, focusing on FAB mass spectrometry,” in *Chiral Recognition in the Gas Phase Chap. 5*, ed A. Zehnacker (Boca Raton: CRC Press), 26–45.
- Shizuma, M., Imamura, H., Takai, Y., Yamada, H., Takeda, T., Takahashi, S., et al. (2000). A new reagent to evaluate optical purity of organic amines by FAB mass spectrometry. *Chem. Lett.* 29, 1292–1293. doi: 10.1246/cl.2000.1292
- Shizuma, M., Kadoya, Y., Takai, Y., Imamura, H., Yamada, H., Takeda, T., et al. (2002). New artificial host compounds containing galactose end groups for binding chiral organic amine guests: chiral discrimination and their complex structures. *J. Org. Chem.* 67, 4795–4807. doi: 10.1021/jo011137q
- Shizuma, M., Yamada, H., Takai, Y., and Sawada, M. (2005). Estimation of thermodynamic parameters on enantioselective complexation equilibria by temperature-dependent FAB mass spectrometry. *Chem. Lett.* 34, 1182–1183. doi: 10.1246/cl.2005.1182
- Sigman, M. S., and Miller, J. J. (2009). Examination of the role of Taft-type steric parameters in asymmetric catalysis. *J. Org. Chem.* 74, 7633–7643. doi: 10.1021/jo901698t
- Stephens, P. J., Devlin, F. J., Chabalowski, C. F., and Frisch, M. J. (1994). Ab initio calculation of vibrational absorption and circular dichroism spectra using density functional force fields. *J. Phys. Chem.* 98, 11623–11627. doi: 10.1021/j100096a001
- Taft, R. W. Jr. (1952). Linear free energy relationships from rates of esterification and hydrolysis of aliphatic and ortho-substituted benzoate esters. *J. Am. Chem. Soc.* 74, 2729–2732. doi: 10.1021/ja01131a010
- Taft, R. W. Jr. (1953). Linear steric energy relationships. *J. Am. Chem. Soc.* 75, 4538–4539. doi: 10.1021/ja01114a044
- Takemura, M., Yamato, K., Doe, M., Watanabe, M., Miyake, H., Kikunaga, T., et al. (2001). Europium(III)-N,N'-ethylenebis(L-amino acid) complexes as new chiral NMR lanthanide shift reagents for unprotected α -amino acids in neutral aqueous solution. *Bull. Chem. Soc. Jp.* 74, 707–715. doi: 10.1246/bcsj.74.707
- Tao, W. A., and Cooks, R. G. (2003). Chiral analysis by MS. *Anal. Chem.* 75, 25A–31A. doi: 10.1021/ac0312110
- Tao, W. A., Zhang, D., Nikolaev, E. N., and Cooks, R. G. (2000). Copper(II)-assisted enantiomeric analysis of D,L-amino acids using the kinetic method: chiral recognition and quantification in the gas phase. *J. Am. Chem. Soc.* 122, 10598–10609. doi: 10.1021/ja000127o
- Tao, W. A., Zhang, D., Wang, F., Thomas, P. D., and Cooks, R. G. (1999). Kinetic resolution of D,L-amino acids based on gas-phase dissociation of copper(II) complexes. *Anal. Chem.* 71, 4427–4429. doi: 10.1021/ac990530h
- Unger, S. H., and Hansch, C. (1979). Quantitative models of steric effects. *Prog. Phys. Org. Chem.* 12, 91–118. doi: 10.1002/9780470171912.ch4
- Vosko, S. H., Wilk, L., and Nusair, M. (1980). Accurate spin-dependent electron liquid correlation energies for local spin density calculations: a critical analysis. *Can. J. Phys.* 58, 1200–1211. doi: 10.1139/p80-159
- Weinert, M., and Davenport, J. W. (1992). Fractional occupations and density-functional energies and forces. *Phys. Rev. B* 45, 13709–13712. doi: 10.1103/PhysRevB.45.13709
- Xin, L., Jie, L., Liu, C. -W., and Zhao, S.-L. (2007). Determination of D-aspartic acid and D-glutamic acid in midbrain of parkinson's disease mouse by reversed phase high performance liquid chromatography. *Chinese J. Anal. Chem.* 35, 1151–1154. doi: 10.1016/S1872-2040(07)60076-0

Conflict of Interest: The authors declare that the research was conducted in the absence of any commercial or financial relationships that could be construed as a potential conflict of interest.

Copyright © 2020 Nakakoji, Yoshino, Izutsu, Sato, Miyake, Mieda, Shinoda, Tsukube, Kawasaki, Arakawa, Ono and Shizuma. This is an open-access article distributed under the terms of the Creative Commons Attribution License (CC BY). The use, distribution or reproduction in other forums is permitted, provided the original author(s) and the copyright owner(s) are credited and that the original publication in this journal is cited, in accordance with accepted academic practice. No use, distribution or reproduction is permitted which does not comply with these terms.



A Chiral Metal-Organic 1D-Coordination Polymer Upon Complexation of Phenylene-Bridged Bipyrrrole and Palladium (II) Ion

Kumiko Nishinaka¹, Jiandong Han², Dongli Han², Yue Liu¹, Yanqing Du², Meiling Wang², Chaolu Eerdun^{2*}, Nobuyasu Naruse³, Yutaka Mera³, Yoshio Furusho³ and Akihiko Tsuda^{1,2,3*}

¹ Department of Chemistry, Graduate School of Science, Kobe University, Kobe, Japan, ² Department of Pharmaceutical Sciences, Inner Mongolia Medical University, Hohhot, China, ³ Department of Chemistry, Shiga University of Medical Science, Otsu, Japan

OPEN ACCESS

Edited by:

Cheng Yang,
Sichuan University, China

Reviewed by:

Zong-Quan Wu,
Hefei University of Technology, China
Xiaobin Peng,
South China University of
Technology, China

*Correspondence:

Chaolu Eerdun
20030091@immu.edu.cn
Akihiko Tsuda
tsuda@harbor.kobe-u.ac.jp

Specialty section:

This article was submitted to
Supramolecular Chemistry,
a section of the journal
Frontiers in Chemistry

Received: 04 October 2020

Accepted: 06 November 2020

Published: 01 December 2020

Citation:

Nishinaka K, Han J, Han D, Liu Y,
Du Y, Wang M, Eerdun C, Naruse N,
Mera Y, Furusho Y and Tsuda A (2020)
A Chiral Metal-Organic
1D-Coordination Polymer Upon
Complexation of Phenylene-Bridged
Bipyrrrole and Palladium (II) Ion.
Front. Chem. 8:613932.
doi: 10.3389/fchem.2020.613932

Metal-organic 1D-coordination polymers, having unique electronic and optical properties, are expected to be a novel advanced functional material capable of fabricating smart plastics, films, and fibers. In this study, we have synthesized a novel metal-organic 1D-coordination polymer composed of a phenylene-bridged bipyrrrole bearing *N*-alkylimino groups (BPI) and palladium(II) ion. The BPI and Pd(II) form square planar bis(bidentate) complex to form a metal coordinated π -conjugation polymer (Poly-BPI/Pd). It is stable in solutions at room temperature, and allowed measurement of its average molecular weight in SEC ($M_w = 106,000$ and $M_n = 18,000$, $M_w/M_n = 5.88$). It also provided a reversible multi redox profile in cyclic voltammetry, most likely originating from strong π -electronic interactions between the BPI components via Pd ion. A variety of substituent groups can be attached to the imino-nitrogens of BPI. A coordination polymer composed of a BPI derivative bearing chiral alkyl chains and Pd(II) showed strong circular dichroism (CD) in the solution due to the unidirectional chiral conformation of the BPI components in the polymer backbone.

Keywords: coordination polymer, helical polymer, complex, π -conjugation, chirality

INTRODUCTION

Coordination polymers (CPs) having two- and three-dimensional network structures such as nanosheets, metal-organic frameworks (MOFs), and porous coordination polymers (PCPs) have been actively studied (Wang et al., 2017; Sahadevan et al., 2018; Gu et al., 2019). These materials have attracted intense interests in terms of potential wide applications in catalysis, magnetism, luminescence, electrical conduction, chemical sensing, and especially in gas storage and separation (Sahay et al., 2014; Stavila et al., 2014; Kirchon et al., 2018). On the other hand, less attention has been paid to one-dimensional coordination polymer (1D-CP), which is expected to have characteristic molecular functions originating from its repetitive metal-organic components and softness of the linear polymers (Noro et al., 2009; Liu et al., 2017). In the reported examples, the 1D-CPs appear mainly in the solid-state, but readily dissociate into the constitutive ligands and metals and/or aggregate randomly in solution. For this reason, it is a challenging subject to isolate and functionalize the metal-organic 1D-CP in the solution. As a limited example, Nishihara and

coworkers reported 1D-CPs comprising bridging dipyrin ligands and divalent metal ions (Zn^{2+} , Ni^{2+} , and Cu^{2+}) (Matsuoka et al., 2015). Their 1D-CPs are stable in solution but include a non-conjugated chromophoric ligand that allows weak electronic communications over the polymer backbone. In the present study, with an expectation to increase the electronic interactions between the components, which provides unique electronic and optical properties, we have designed a novel metal-organic 1D-CP with a π -conjugated ligand and metal ion.

We previously reported the synthesis of a π -conjugated phenylene-bridged bipyrrrole bearing *N*-alkylimino groups (**BPI-1**), and found that it is an acid-responsive single trichromatic luminescent dye capable of emitting pure white light (WL) (Imamura et al., 2017). The blue-light-emitting **BPI-1** exhibits dramatic color changes in fluorescence to orange and green upon mono- and diprotonation, respectively, providing a wide emission band in the range of $\lambda = 400\text{--}800\text{ nm}$ that provide WL when the compound is in a dynamic equilibrium between the three states. With this **BPI-1** and its derivatives as a π -conjugated organic component (bis-bidentate ligand), we have newly designed and synthesized metal-organic 1D-CPs upon complexation with palladium(II) ion (Poly-**BPI**/Pd). *N*-Substituted pyrrole-2-aldehydes are known to form metal complexes with transition metal ions (Figure 1A) (Holm et al., 1966; Yeh and Barker, 1967). We expected that the **BPI** monomers are directly connected with Pd(II) ions to form square-planar bis(bidentate) complexes to form a metal coordinated π -conjugation polymer (Figure 1B). We found, herein, that Poly-**BPI**/Pd is stable in the solutions at room temperature and shows a reversible multi redox behavior. Further, its derivative having chiral alkyl chains shows strong circular dichroism (CD) in the solution due to the unidirectional chiral conformation of the **BPI** components in the polymer backbone.

RESULTS AND DISCUSSION

Synthesis and Characterization of Metal-Organic Coordination Polymers

We synthesized imino-substituted bipyrrrole derivatives **BPI-1–4**, containing a 1,4-phenylene spacer according to the previously reported procedures Scheme 1 (Setsune et al., 2015). **BPF** bearing formyl groups at pyrrolic α -positions were synthesized in advance. Then, the formyl groups were converted to the corresponding imines bearing various functional groups on the nitrogen atom through condensation reactions with the amine in the presence or absence of an acid catalyst (isolated yields 75–96 %).

We initially attempted the synthesis of 1D-CPs with **BPI-1**, bearing *N*-benzyl groups, and transition metal salts such as $\text{Zn}(\text{OAc})_2$, $\text{Cu}(\text{OAc})_2$, and $\text{Pd}(\text{OAc})_2$. **BPI-1** and metal salt were mixed in a 1:1 ratio in a mixture solution of $\text{CH}_2\text{Cl}_2/\text{CH}_3\text{OH}$ (5:1) and stirred overnight at room temperature. In these experiments, only the sample solution containing **BPI-1** and $\text{Pd}(\text{OAc})_2$ provided a precipitate, which is slightly soluble into organic solvents such as CHCl_3 and CH_2Cl_2 , likely due to the

complexation. ^1H NMR spectrum of **BPI-1** in CDCl_3 provides characteristic singlet signals corresponding to the protons on imine, phenylene, and benzyl groups at $\delta = 8.27$, 7.49, and 4.73 ppm, respectively (Figure 2). These peaks become broad and are shifted to the higher magnetic field region at 8.01, 7.33–6.97, and 3.36 ppm, respectively, upon complexation with Pd(II) ion. Similar changes were observed for other peaks corresponding to the phenyl and ethyl exteriors. These ^1H NMR spectral features indicate the formation of the certain polymers (Berl et al., 2002).

On the other hand, in UV-Vis absorption spectroscopy, **BPI-1** showed a large red-shift of its lowest energy absorption band from $\lambda_{\text{max}} = 368\text{ nm}$ to 419 nm in CH_2Cl_2 upon complexation with Pd(II) (Figure 3), which may mainly originate from exciton coupling of **BPI-1** array, owing to the electric transition dipole for the long-axis polarized $\pi\text{--}\pi^*$ transition (*vide infra*) (Ahmad et al., 2009; Li et al., 2019). Further, the emission spectrum of **BPI-1**, observed at 400–600 nm with $\lambda_{\text{max}} = 426$ and 450 nm, disappeared upon the complexation. This observed quenching behavior may be ascribed to the heavy atom effect due to Pd ion (Drzewiecka-Matuszek et al., 2005). These observed spectral features strongly indicate the formation of a metal-organic CP. However, its low solubility into organic solvents does not allow measurement of the average molecular weight in SEC.

We then synthesized **BPI-2**, having *N*-dodecyl chains, to increase the solubility of the product into organic solvents. **BPI-2** was mixed with 2 equiv. amounts of $\text{Pd}(\text{OAc})_2$ in CH_2Cl_2 , and stirred for 2 days at room temperature to give the complex soluble into organic solvents such as CHCl_3 and CH_2Cl_2 . The **BPI-2**/Pd complex was thus isolated through extraction with CH_2Cl_2 and water to give a film-like solid after evaporation of the solvent (Figure 4A). Spectral changes of **BPI-2** in ^1H NMR, UV-Vis absorption, and fluorescence spectroscopies upon complexation with Pd(II) were almost the same as those observed in **BPI-1** as described above (Supplementary Figures 1, 2). **BPI-2**/Pd is stable in solutions and was subjected to the SEC measurements to estimate average molecular weight. SEC was conducted with CHCl_3 as an eluent, and it revealed that **BPI-2**/Pd complex has shorter retention time (13.4 min) than **BPI-2** monomer (23.5 min) (Figure 4B). The average molecular weight of **BPI-2**/Pd complex was estimated to be $M_w = 106,000$ (corresponding to 130 mer) and $M_n = 18,000$, $M_w/M_n = 5.88$ compared to polystyrene standards. As an experimental reference data, dynamic light scattering (DLS) measurement of **BPI-2**/Pd complex provided an average particle size of 372 nm with a size distribution of 143–2,114 nm in CHCl_3 (Supplementary Figure 3). These results indicate that **BPI**/Pd complexes have polymeric structures.

Cyclic Voltammetry

The electrochemical properties, especially for oxidation, of the metal-organic 1D-CP, were studied by cyclic voltammetry (CV) in CH_2Cl_2 containing 0.1 M tetrabutylammonium perchlorate (Bu_4NClO_4) as supporting electrolyte. The cyclic voltammograms (V vs. Fc/Fc^+) of **BPI-2** monomer and **BPI-2**/Pd polymer are shown in Figure 5. **BPI-2** showed an irreversible oxidation peak at around 0.8 V, where the oxidation may bring about the chemical reaction and/or

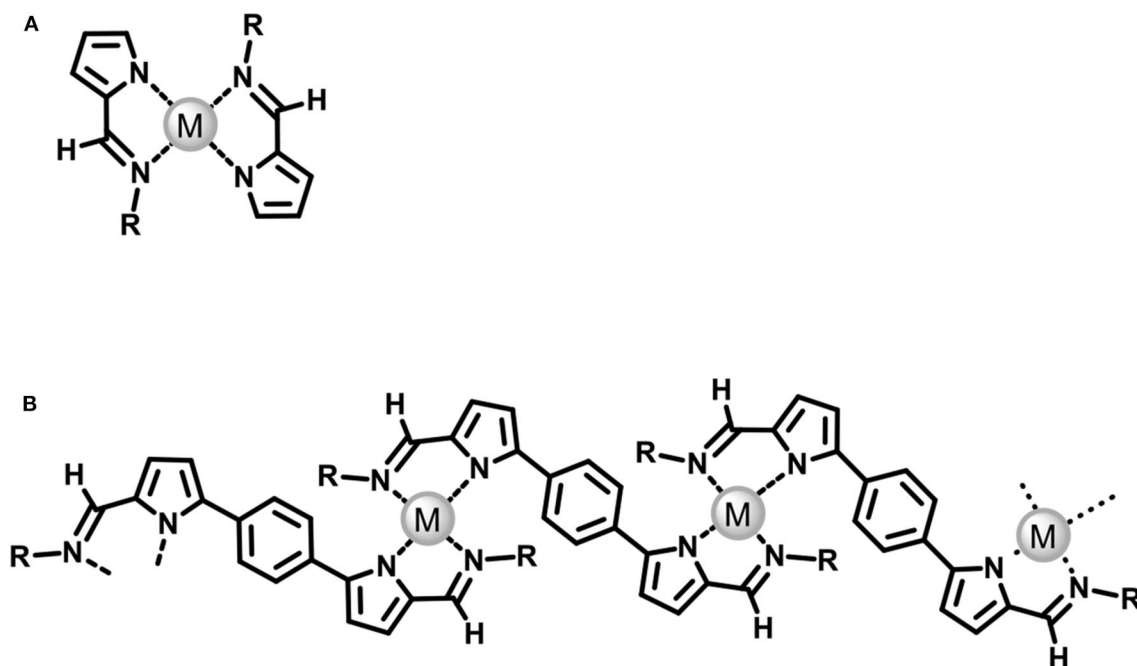
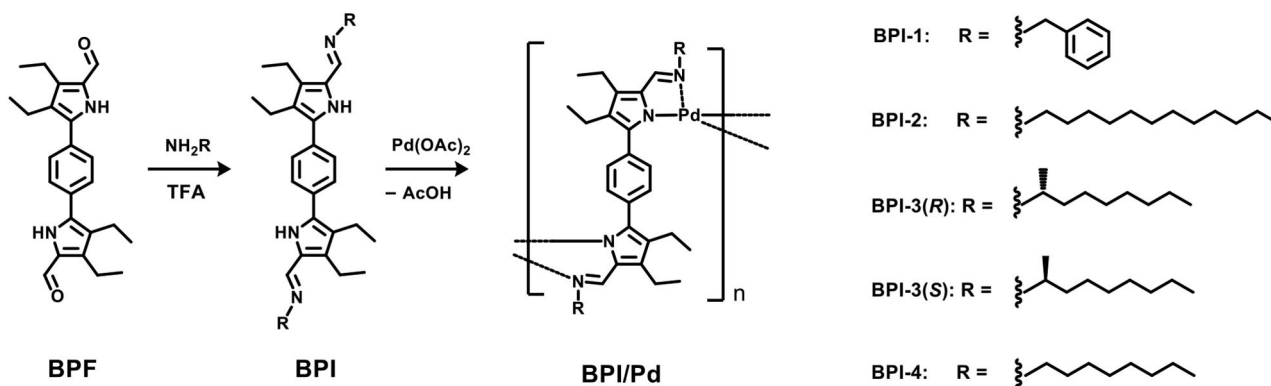


FIGURE 1 | (A) 2:1 complex of *N*-substituted pyrrole-2-aldimines and transition metal ion reported previously, (B) 1:1 complex of bis(*N*-substituted pyrrole-2-aldimines) and transition metal ion studied in this study.



SCHEME 1 | Synthesis of a series of **BPI** and **BPI/Pd** polymers.

decomposition of the imine groups. Differential pulse voltammetry (DPV) also provided the corresponding peak at 0.78 V (**Supplementary Figure 4A**). However, in sharp contrast, **BPI-2/Pd** polymer provided reversible multi redox peaks in CV at around $E_{1/2} = 0.35$ and 0.5 V, where the electrochemical properties of imino group may be changed upon complexation with Pd(II) ion. DPV also provided the corresponding two peaks at 0.33 and 0.50 V, respectively (**Supplementary Figure 4B**). This observed multi-redox behavior of **BPI-2/Pd** polymer could be explained by the π -electronic interactions between bipyrrrole ligands via Pd(II) ion (Hildebrandt et al., 2011). The positive charge generated upon first oxidation on the polymer backbone withdraw π -electrons of other **BPI** ligands via the metal ions,

resulting in a positive shift of their oxidation potential to give the multi redox profile.

Chirality Induction in BPI-3/Pd Polymer

BPI can attach a variety of substituent groups on imino-nitrogens. We have previously synthesized *N*-hexyl **BPI** and found in the crystal structure that two pyrrole components adopt a twisted geometry with an anti-folded confirmation through the phenylene spacer (Ie et al., 2015). The dihedral angle of pyrrole and phenylene components is 33.3° on average, owing to the steric repulsions between the ethyl group attached to the pyrrole- β and phenylene ring (Li et al., 2020). This observed twisted structure allows our

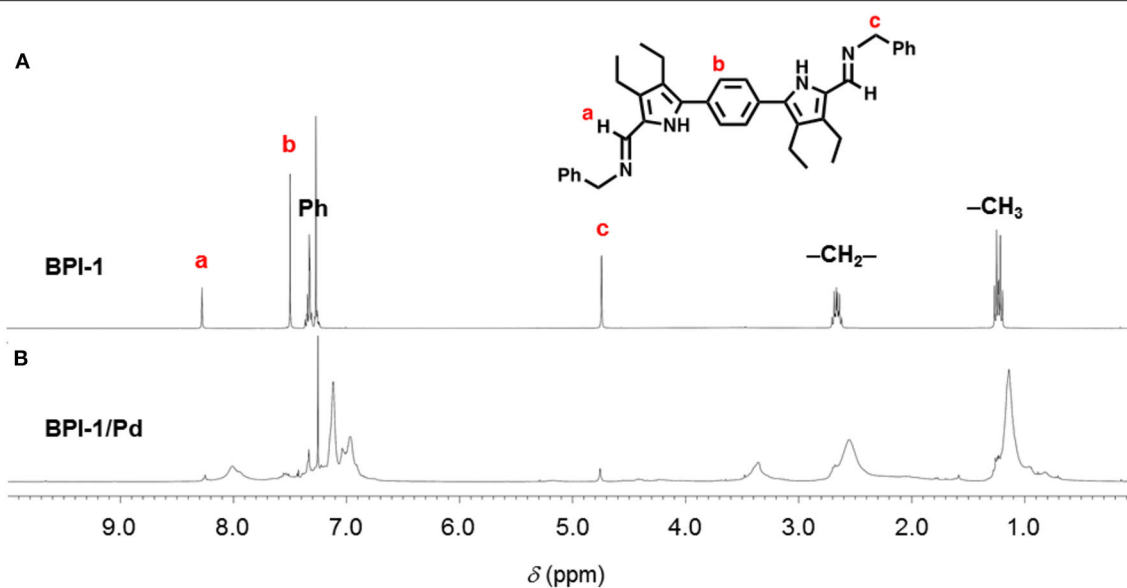


FIGURE 2 | ^1H NMR spectra (400 MHz, CDCl_3) of (A) BPI-1 and (B) a product formed upon mixing BPI-1 and $\text{Pd}(\text{OAc})_2$ at 1:1 ratio.

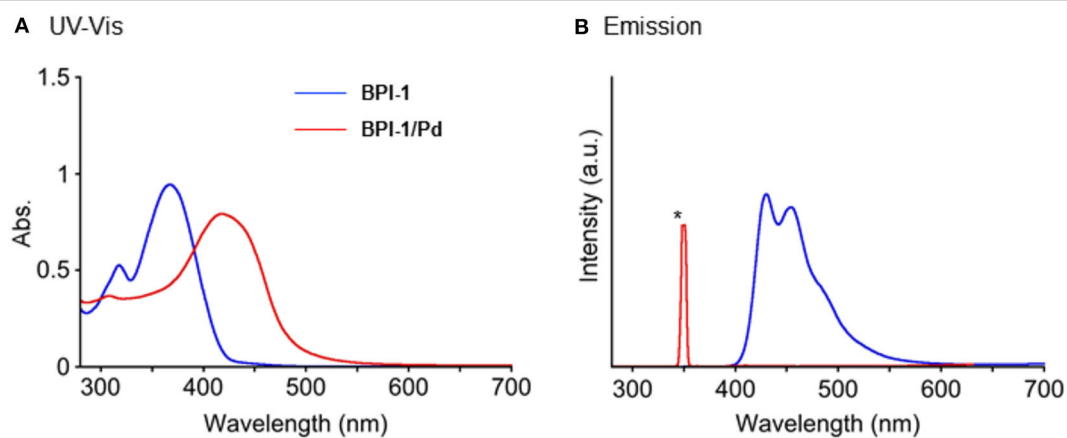


FIGURE 3 | (A) UV-Vis absorption spectra and (B) fluorescence spectra upon excitation at 350 nm of BPI-1 and BPI-1/Pd complex in CH_2Cl_2 at 25°C. [BPI-1] = 2.28×10^{-5} M, [BPI-1/Pd complex] = 1.92×10^{-5} M. *Stray light.

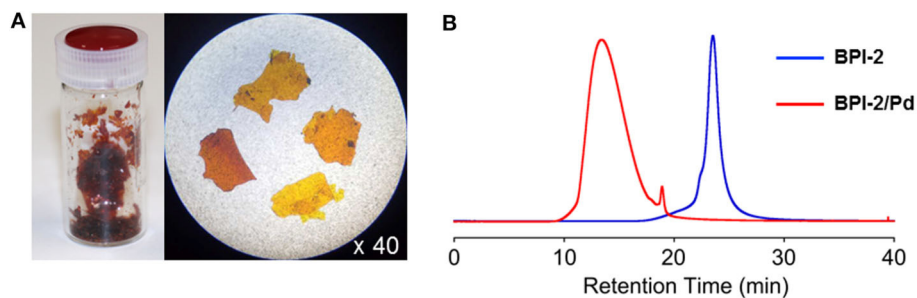


FIGURE 4 | (A) Photos of film-like solid samples of BPI-2/Pd complex. (B) SEC profiles of BPI-2 and BPI-2/Pd complex monitored at 424 and 420 nm, respectively, in SEC. [Conditions] Column: TOSOH TSKgel G4000H_{XL} + G4000H_{HR}, Solvent: CHCl_3 , Flow speed: 1 mL/min, Temperature: 20°C.

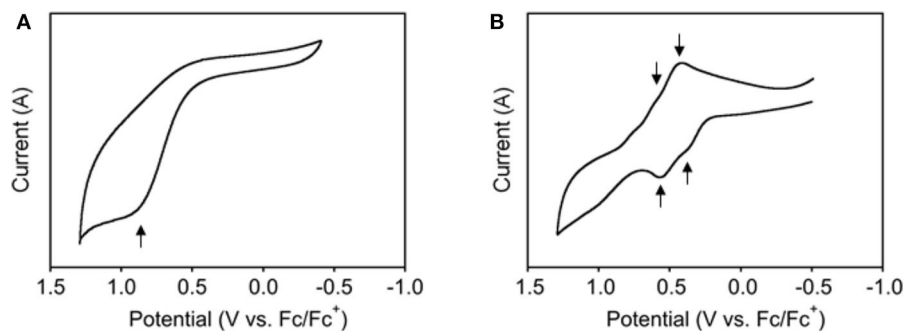


FIGURE 5 | Cyclic voltammograms (V vs. Fc/Fc^+) of (A) **BPI-2** and (B) **BPI-2/Pd** polymer in CH_2Cl_2 . Scan rate, 100 mV/s; working electrode, Pt; supporting electrolyte, 0.1 M Bu_4NClO_4 .

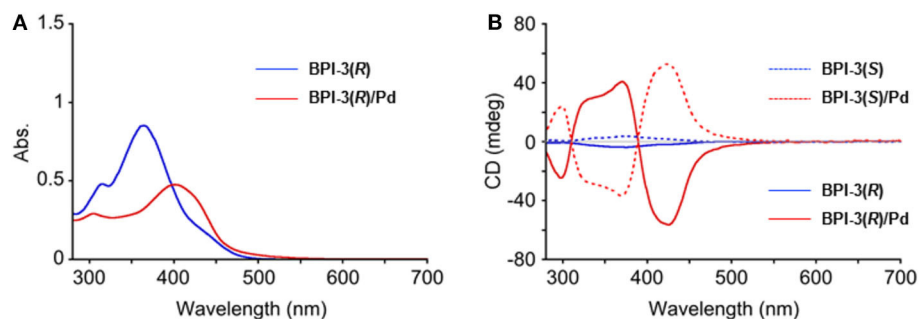


FIGURE 6 | (A) UV-Vis absorption spectra of **BPI-3(R)** and **BPI-3(R)/Pd** polymer and (B) CD spectra of **BPI-3(R)**, **BPI-3(S)**, **BPI-3(R)/Pd** polymer, and **BPI-3(S)/Pd** polymer in CH_2Cl_2 at 25°C. $[\text{BPI-3}] = 3.29 \times 10^{-5} \text{ M}$, $[\text{BPI-3/Pd polymer (monomer)}] = 3.11 \times 10^{-5} \text{ M}$.

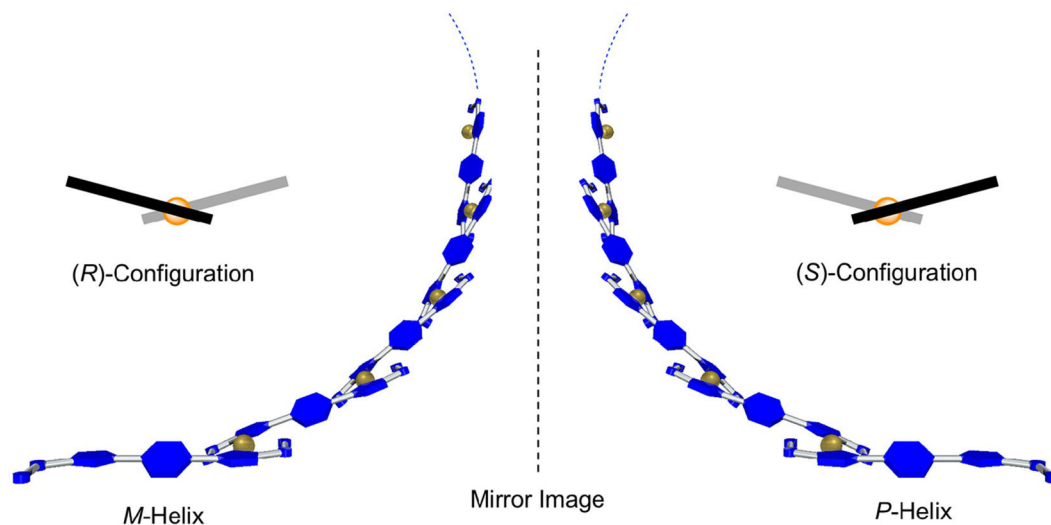


FIGURE 7 | Schematic illustrations of helical polymer structures of **BPI-3(R)/Pd** (Right) and **BPI-3(S)/Pd** (Left) expected from exciton coupled CD spectra in Figure 6B.

expectation that **BPI/Pd** polymer can form a helical CP by attachment of chiral substituent groups on imino-nitrogens (Huang et al., 2018; Wang et al., 2019; Zhou et al., 2020).

We then synthesized **BPI-3(R)** and **BPI-3(S)**, having chiral alkyl chains on imino-nitrogens. **BPI-3**, upon mixing with $\text{Pd}(\text{OAc})_2$, also formed the coordination polymer under the same conditions of synthesizing **BPI-2/Pd** polymer

(Supplementary Figure 5). However, their average molecular weights [BPI-3(R)/Pd, $M_w = 10,900$, $M_n = 6,800$, $M_w/M_n = 1.60$; BPI-3(S)/Pd, $M_w = 8,600$, $M_n = 4,700$, $M_w/M_n = 1.80$] are clearly lower than that of BPI-2/Pd polymer (Supplementary Figure 6). The 1-methyl group attached to the *N*-alkyl chain may increase steric crowding around metal-ligand coordination bonds to decrease the polymerization degree of the CP (Guzei and Wendt, 2006; Talarico and Budzelaar, 2008). Here, BPI components may adopt a chiral conformation in the resulting polymer structure.

In circular dichroism (CD) spectroscopy, BPI-3(R) and BPI-3(S) ligands showed weak CD spectra with λ_{\max} at 425 nm (Figure 6). However, interestingly, strong CD responses with Cotton effects appeared in their coordination polymers. BPI-3(R)/Pd and BPI-3(S)/Pd showed negative to positive and positive to negative Cotton effects, respectively, at the lowest energy absorption band to give the mirror-imaged CD profiles in each other. These observed spectral features may originate from exciton-coupled CD owing to the helical orientation of BPI-3 ligands in the 1D-polymeric structure as schematically illustrated in Figure 7. Their Cotton effects allow empirical estimation of their absolute configurations (Gonnella et al., 1982; Furo et al., 2005; Telfer et al., 2011). BPI-3(R)/Pd and BPI-3(S)/Pd may dominantly adopt (S)- and (R)-configuration, which allows the formation of *P*- and *M*-helical coordination polymer, respectively.

Next, we synthesized a coordination copolymer (CCP) with a 1:5 mixture of chiral BPI-3(R) and achiral BPI-4 upon mixing with Pd(OAc)₂ through the similar procedures to the synthesis of the above polymers. The polymer was obtained in 72% yield and characterized using ¹H NMR, UV-Vis absorption, and CD spectra and SEC. The SEC profile provided only a broad single peak, a typical polydispersion profile of the polymer, indicating random copolymerization. Its average molecular weight is estimated to be $M_w = 11,100$ and $M_n = 6,300$, $M_w/M_n = 1.76$ compared to polystyrene standards in SEC. Hence, its sample solution in CH₂Cl₂ was CD active, and the spectral pattern observed was essentially the same as that of BPI-3(R)/Pd polymer. However, since the spectral intensity is ~4–5 times smaller, it seems that the local chiral twisted conformations occurred in BPI-3(R)/Pd complexation in the copolymer is not amplified on the resulting polymer backbone. The *p*-phenylene-spacer of BPI unit, which provides a distance between its substituent groups, likely allows the polymerization

without steric repulsions and/or interactions of the chiral metal-coordination moieties.

CONCLUSION

In this study, we have synthesized a novel metal-organic 1D-coordination polymer composed of a phenylene-bridged bipyrrrole bearing *N*-alkylimino groups and palladium(II) ion. Although most of 1D-CPs reported are unstable in solutions, BPI and Pd(II) ion form a metal coordinated π -conjugation polymer, which is stable in the solutions. BPI/Pd polymer showed π -electronic communications between the BPI components via Pd(II) ion in its polymer structure to give exciton coupling in the absorption spectrum. Further it allowed a reversible multi redox in cyclic voltammetry. BPI-3/Pd polymer having chiral alkyl chains on the imino-nitrogen showed strong circular dichroism (CD) owing to its one-handedly twisted helical polymer structure. We can expect a variety of the molecular functions through structural modifications of *N*-substituent groups, metal ion, and aromatic spacer, and control of the polymerization degree of this metal-organic 1D-coordination polymer.

DATA AVAILABILITY STATEMENT

The raw data supporting the conclusions of this article will be made available by the authors, without undue reservation.

AUTHOR CONTRIBUTIONS

All authors listed have made a substantial, direct and intellectual contribution to the work, and approved it for publication.

FUNDING

This present work was sponsored by Grants-in-Aid for Scientific Research (B) (No. 17H02740) from the Ministry of Education, Science, Sports, and Culture, Japan, and National Natural Science Foundation of China (No. 21961026) from the Ministry of Science and Technology, China.

SUPPLEMENTARY MATERIAL

The Supplementary Material for this article can be found online at: <https://www.frontiersin.org/articles/10.3389/fchem.2020.613932/full#supplementary-material>

REFERENCES

- Ahmad, R., Wong-Foy, A. G., and Matzger, A. J. (2009). Microporous coordination polymers as selective sorbents for liquid chromatography. *Langmuir* 25, 11977–11979. doi: 10.1021/la902276a
- Berl, V., Schmutz, M., Krische, M. J., Khoury, R. G., and Lehn, J. M. (2002). Supramolecular polymers generated from heterocomplementary monomers linked through multiple hydrogen-bonding arrays-formation, characterization, and properties. *Chem. Eur. J.* 8, 1227–1244. doi: 10.1002/1521-3765(20020301)8:5<1227::AID-CHEM1227>3.0.CO;2-0
- Drzewiecka-Matuszek, A., Skalna, A., Karocki, A., Stochel, G., and Fiedor, L. (2005). Effects of heavy central metal on the ground and excited states of chlorophyll. *J. Biol. Inorg. Chem.* 10, 453–462. doi: 10.1007/s00775-005-0652-6
- Furo, T., Mori, T., Wada, T., and Inoue, Y. (2005). Absolute configuration of chiral [2.2] paracyclophanes with intramolecular charge-transfer interaction. Failure of the exciton chirality method and use of the sector rule applied to the cotton effect of the CT transition. *J. Am. Chem. Soc.* 127, 8242–8243. doi: 10.1021/ja0508323
- Gonnella, N. C., Nakanishi, K., Martin, V. S., and Sharpless, K. B. (1982). General method for determining absolute configuration of acyclic

- allylic alcohols. *J. Am. Chem. Soc.* 104, 3775–3776. doi: 10.1021/ja00377a063
- Gu, J., Wen, M., Cai, Y., Shi, Z., Nesterov, D. S., Kirillova, M. V., et al. (2019). Cobalt (II) coordination polymers assembled from unexplored pyridine-carboxylic acids: structural diversity and catalytic oxidation of alcohols. *Inorg. Chem.* 58, 5875–5885. doi: 10.1021/acs.inorgchem.9b00242
- Guzei, I. A., and Wendt, M. (2006). An improved method for the computation of ligand steric effects based on solid angles. *Dalton Trans.* 33, 3991–3999. doi: 10.1039/b605102b
- Hildebrandt, A., Pfaff, U., and Lang, H. (2011). 5-Membered heterocycles with directly-bonded sandwich and half-sandwich termini as multi-redox systems: synthesis, reactivity, electrochemistry, structure and bonding. *Rev. Inorg. Chem.* 31, 111–141. doi: 10.1515/REVIC.2011.008
- Holm, R. H., Chakravorty, A., and Theriot, L. J. (1966). The synthesis, structures, and solution equilibria of bis(pyrrole-2-aldimino)metal(II) complexes. *Inorg. Chem.* 5, 625–635. doi: 10.1021/ic50038a028
- Huang, J., Shen, L., Zou, H., and Liu, N. (2018). Enantiomer-selective living polymerization of rac-phenyl isocyanide using chiral palladium catalyst. *Chinese J. Polym. Sci.* 36, 799–804. doi: 10.1007/s10118-018-2136-5
- Ie, M., Setsune, J., Eda, K., and Tsuda, A. (2015). Chiroptical sensing of oligonucleotides with a cyclic octapyrrole. *Org. Chem. Front.* 2, 29–33. doi: 10.1039/C4QO00268G
- Imamura, K., Ueno, Y., Akimoto, S., Eda, K., Du, Y., Eerdun, C., et al. (2017). An acid-responsive single trichromatic luminescent dye that provides pure white-light emission. *ChemPhotoChem.* 1, 427–431. doi: 10.1002/cptc.201700108
- Kirchon, A., Feng, L., Drake, H. F., Joseph, E. A., and Zhou, H.-C. (2018). From fundamentals to applications: a toolbox for robust and multifunctional MOF materials. *Chem. Soc. Rev.* 47, 8611–8638. doi: 10.1039/C8CS00688A
- Li, C., Zhang, K., Ishida, M., Li, Q., Shimomura, K., Baryshnikov, G., et al. (2020). Tripyrrin-armed isosmaragdyrins: synthesis, heterodinuclear coordination, and protonation-triggered helical inversion. *Chem. Sci.* 11, 2790–2795. doi: 10.1039/C9SC06197E
- Li, G., Fan, C., Cheng, G., Wu, W., and Yang, C. (2019). Synthesis, enantioseparation and photophysical properties of planar-chiral pillar [5] arene derivatives bearing fluorophore fragments. *Beilstein J. Org. Chem.* 15, 1601–1611. doi: 10.3762/bjoc.15.164
- Liu, M., Quah, H. S., Wen, S., Wang, J., Kumar, P. S., Eda, G., et al. (2017). Nonlinear optical properties of a one-dimensional coordination polymer. *J. Mater. Chem. C* 5, 2936–2941. doi: 10.1039/C6TC05372F
- Matsuoka, R., Toyoda, R., Sakamoto, R., Tsuchiya, M., Hoshiko, K., Nagayama, T., et al. (2015). Bis(dipyrrinato) metal (II) coordination polymers: crystallization, exfoliation into single wires, and electric conversion ability. *Chem. Sci.* 6, 2853–2858. doi: 10.1039/C5SC00273G
- Noro, S., Tanaka, D., Sakamoto, H., Shimomura, S., Kitagawa, S., Takeda, S., et al. (2009). Selective gas adsorption in one-dimensional, flexible Cu^{II} coordination polymers with polar units. *Chem. Mater.* 21, 3346–3355. doi: 10.1021/cm9012969
- Sahadevan, S. A., Monni, N., Abhervé, A., Marongiu, D., Sarritzu, V., and Sestu, N., et al. (2018). Nanosheets of two-dimensional neutral coordination polymers based on near-infrared-emitting lanthanides and a chlorocyananilate ligand. *Chem. Mater.* 30, 6575–6586. doi: 10.1021/acs.chemmater.8b03399
- Sahay, R., Reddy, V. J., and Ramakrishna, S. (2014). Synthesis and applications of multifunctional composite nanomaterials. *Int. J. Mech. Mater. Eng.* 9:25. doi: 10.1186/s40712-014-0025-4
- Setsune, J., Toda, M., Yoshida, T., Imamura, K., and Watanabe, K. (2015). The synthesis and dynamic structures of multinuclear complexes of large porphyrinoids expanded by phenylene and thienylene spacers. *Chem. Eur. J.* 21, 12715–12727. doi: 10.1002/chem.201501570
- Stavila, V., Talin, A. A., and Allendorf, M. D. (2014). MOF-based electronic and opto-electronic devices. *Chem. Soc. Rev.* 43, 5994–6010. doi: 10.1039/C4CS00096J
- Talarico, G., and Budzelaar, P. H. M. (2008). Variability of chain transfer to monomer step in olefin polymerization. *Organometallics* 27, 4098–4107. doi: 10.1021/om800313n
- Telfer, S. G., McLean, T. M., and Waterland, M. R. (2011). Exciton coupling in coordination compounds. *Dalton Trans.* 40, 3097–3108. doi: 10.1039/c0dt01226b
- Wang, H.-Y., Cui, L., Xie, J.-Z., Leong, C. F., D'Alessandro, D. M., and Zuo, J.-L. (2017). Functional coordination polymers based on redox-active tetrathiafulvalene and its derivatives. *Coord. Chem. Rev.* 345, 342–361. doi: 10.1016/j.ccr.2016.10.011
- Wang, Y., Chen, Y., Jiang, Z., Liu, F., Liu, F., Zhu, Y., et al. (2019). Halogen effects on phenylethynyl palladium (II) complexes for living polymerization of isocyanides: a combined experimental and computational investigation. *Sci. China Chem.* 62, 491–499. doi: 10.1007/s11426-018-9415-8
- Yeh, K.-N., and Barker, R. H. (1967). Synthesis and properties of some metal chelates of 2-pyrrole aldimines. *Inorg. Chem.* 6, 830–833. doi: 10.1021/ic50050a037
- Zhou, L., Xu, X.-H., Jiang, Z.-Q., Xu, L., and Chu, B.-F., Liu, N., et al. (2020). Selective synthesis of single-handed helical polymers from achiral monomer and a mechanism study on helix-sense-selective polymerization. *Angew. Chem. Int. Ed.* 59, 2–9. doi: 10.1002/anie.202011661

Conflict of Interest: The authors declare that the research was conducted in the absence of any commercial or financial relationships that could be construed as a potential conflict of interest.

Copyright © 2020 Nishinaka, Han, Han, Liu, Du, Wang, Eerdun, Naruse, Mera, Furusho and Tsuda. This is an open-access article distributed under the terms of the Creative Commons Attribution License (CC BY). The use, distribution or reproduction in other forums is permitted, provided the original author(s) and the copyright owner(s) are credited and that the original publication in this journal is cited, in accordance with accepted academic practice. No use, distribution or reproduction is permitted which does not comply with these terms.



Efficient Amplification in Soai's Asymmetric Autocatalysis by a Transient Stereodynamic Catalyst

Oliver Trapp^{1,2*}

¹ Department of Chemistry, Ludwig-Maximilians-University Munich, Munich, Germany, ² Max-Planck-Institute for Astronomy, Heidelberg, Germany

OPEN ACCESS

Edited by:

Keiji Hirose,
Osaka University, Japan

Reviewed by:

Arimasa Matsumoto,
Nara Women's University, Japan
Patrick Walsh,
University of Pennsylvania,
United States

*Correspondence:

Oliver Trapp
oliver.trapp@cup.uni-muenchen.de

Specialty section:

This article was submitted to
Supramolecular Chemistry,
a section of the journal
Frontiers in Chemistry

Received: 09 October 2020

Accepted: 16 November 2020

Published: 09 December 2020

Citation:

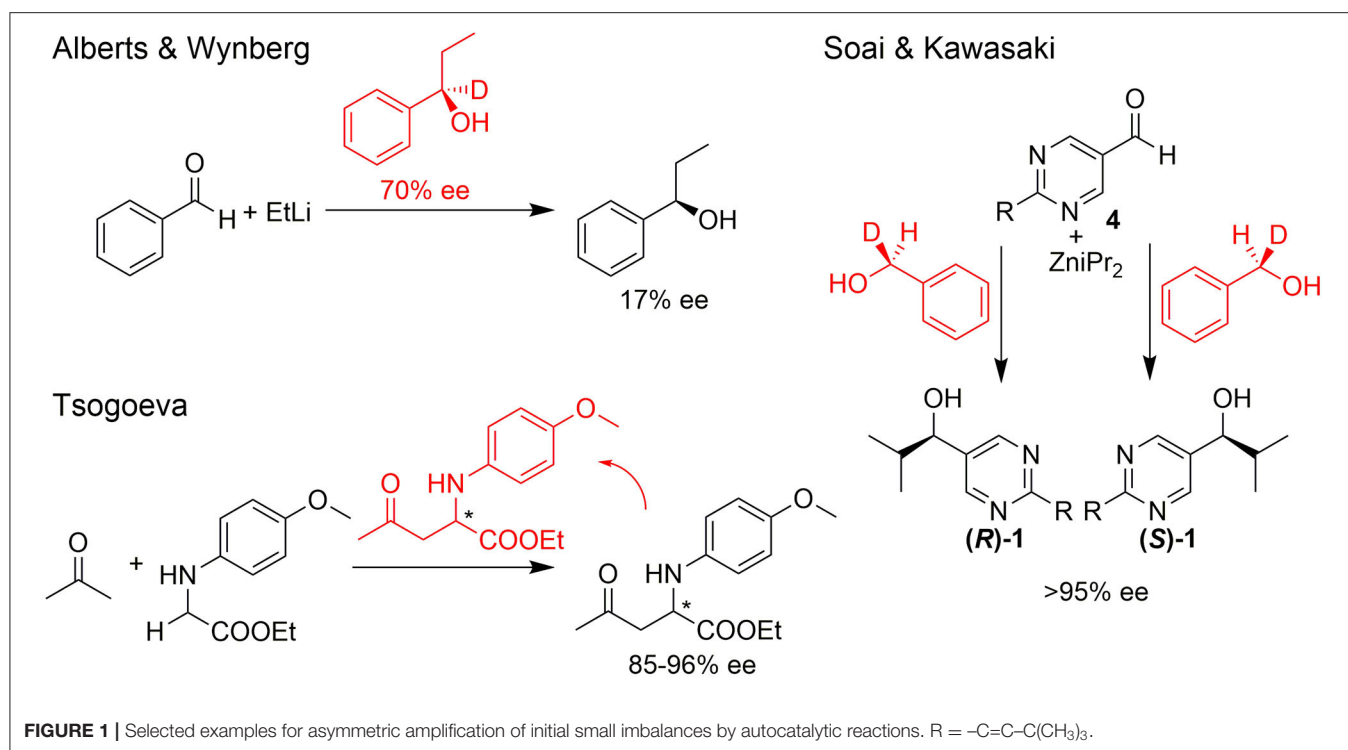
Trapp O (2020) Efficient Amplification
in Soai's Asymmetric Autocatalysis by
a Transient Stereodynamic Catalyst.
Front. Chem. 8:615800.
doi: 10.3389/fchem.2020.615800

Mechanisms leading to a molecular evolution and the formation of homochirality in nature are interconnected and a key to the underlying principles that led to the emergence of life. So far proposed mechanisms leading to a non-linear reaction behavior are based mainly on the formation of homochiral and heterochiral dimers. Since homochiral and heterochiral dimers are diastereomers of each other, the minor enantiomer is shifted out of equilibrium with the major enantiomer by dimer formation and thus a reaction or catalysis can be dominated by the remaining molecules of the major enantiomer. In this article a mechanism is shown that leads to homochirality by the formation of a highly catalytically active transient intermediate in a stereodynamically controlled reaction. This is demonstrated by Soai's asymmetric autocatalysis, in which aldehydes are transformed into the corresponding alcohols by addition of dialkylzinc reagents. The mechanism of chirogenesis proposed here shows that an apparently inefficient reaction is the best prerequisite for a selection mechanism. In addition, stereodynamic control offers the advantage that the minor diastereomeric intermediate can be interconverted into the major diastereomer and thus be stereoeconomically efficient. This is supported by computer simulation of reaction kinetics.

Keywords: asymmetric autocatalysis, non-linear effects, kinetics, organometallic chemistry, Soai's reaction

INTRODUCTION

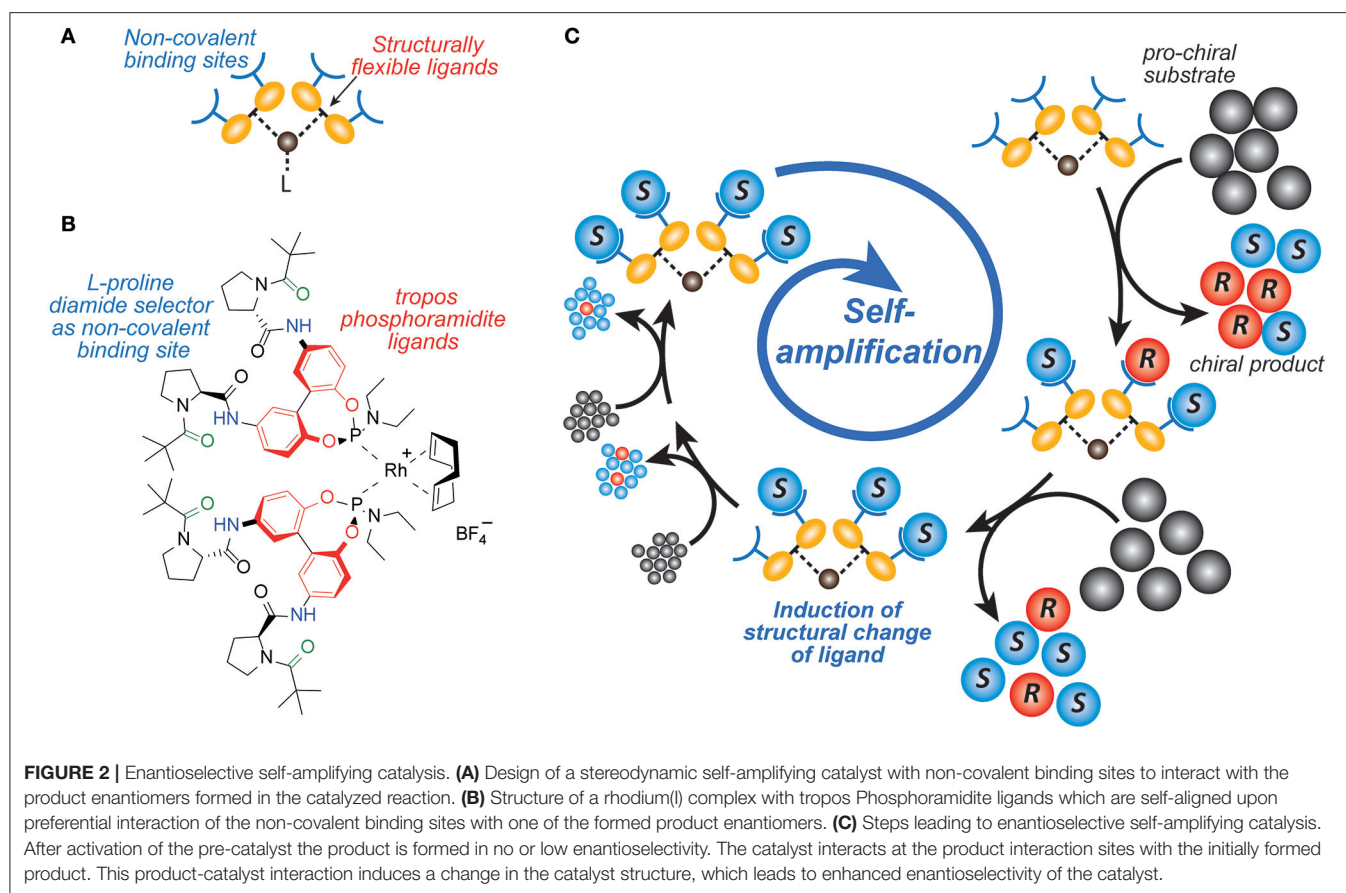
The single-handedness of molecular building blocks, such as amino acids and sugars, in biologically relevant metabolisms and (polymeric) structures is considered the signature of life and an important prerequisite for the emergence of life (Hegstrom, 1984; Blackmond, 2004, 2011; Kawasaki et al., 2008; Hawbaker and Blackmond, 2019; Karunakaran et al., 2019; Teichert et al., 2019). In the absence of chiral directing forces, an abiotic process provides a racemic mixture. Therefore, one of the most exciting questions is how biological homochirality developed from a predominantly achiral environment. Several theoretical approaches to this question have been investigated experimentally over the last decades and many findings show how enantiomer enrichment may have occurred by physical processes or chemical reactions. Some of the most promising theoretical proposals for asymmetric amplification of initial small imbalances are autocatalytic reactions (cf. **Figure 1**) (Alberts and Wynberg, 1989; Soai and Kawasaki, 2008; Tsogoeva, 2010; Bissette and Fletcher, 2013). A comprehensive review of such processes was recently compiled by Blackmond (2020).



Early mechanistic concepts of such reactions with positive nonlinear effects (Blackmond, 2010) were discussed by Noyori (Kitamura et al., 1989; Mikami et al., 2000) and Kagan (Girard and Kagan, 1998; Satyanarayana et al., 2009). Predominantly the formation of reversible monomer-dimer association complexes was considered. Frank postulated a theoretical model (Frank, 1953) that leads to a spontaneous asymmetric synthesis by forming dimers from their monomer building blocks, for example by intermolecular interaction. If these monomers have the same configuration, the dimers are homochiral, or if the monomers have opposite configurations, heterochiral dimers are obtained. Since these dimers are diastereoisomeric to each other, they have different intrinsic properties, which are reflected for example in their formation and decomposition rates, their solubilities, their chiroptic properties. Thus, the formation of a heterochiral dimer from an enantiomerically enriched mixture can increase the enantiomeric excess of the free monomers. Ideally, this process could even lead to the result that only the main enantiomer remains monomeric in a solution and the heterochiral dimer precipitates as insoluble solid. If the remaining major enantiomer is catalytically active, this process can lead to the starting point of a highly efficient amplification. However, this would be an exceptionally rare case. In recent years, we have developed catalysts decorated with chiral recognition units to recognize and transfer the chirality of the reaction product generated in the catalysis to the stereodynamic unit of the catalyst (Maier and Trapp, 2014; Storch and Trapp, 2015, 2017, 2018; Storch et al., 2015, 2016a,b; Scholtes and Trapp, 2019a,b,c,d). This induces a shift in the equilibrium of the stereodynamic catalyst by the recognized chirality (cf. **Figure 2**).

In this way, it was possible to develop self-amplifying catalytic systems which aligned their configuration dynamically during catalysis and thus formed a preferred enantiomer from the prochiral substrate (Scholtes and Trapp, 2020). In the course of this research we have been working intensively on the elucidation of the mechanism of the Soai reaction (Trapp et al., 2020). Soai's asymmetric autocatalysis (Soai et al., 1995; Shibata et al., 1997) is a highly unusual reaction. In this reaction pyrimidine-5-carbaldehydes **4** are reacted with diisopropyl zinc in the presence of catalytic amounts of the corresponding pyrimidine alcohol **1** with low *ee*. Asymmetric autocatalytic amplification of the enriched enantiomer yields the pyrimidine alcohol **1** with enhanced *ee*. Several mechanistic models were proposed to explain the extraordinary behavior of this reaction (Blackmond et al., 2001; Blackmond, 2006; Ercolani and Schiaffino, 2011; Gehring et al., 2012; Micheau et al., 2012; Gridnev and Vorobiev, 2015; Athavale et al., 2020).

By comprehensive kinetic and mass spectrometry experiments, we recently identified and monitored the formation of a transient catalyst that forms a hemiacetalate-zinc complex **5** by reaction of pyrimidine-5-carbaldehyde **4** with the corresponding pyrimidine alcoholate **2** (Trapp et al., 2020). The dynamic behavior of the formed hemiacetals **5** is of particular interest and was investigated by dynamic HPLC (DHPLC). The mass spectrometric detection of the substrates and the product as well as the intermediates occurring during the reaction enabled the derivation of a reaction mechanism (cf. **Figure 3**). First of all, the alcoholate **2** is formed from the alcohol added as an additive to diisopropyl zinc, which can form homochiral (**R**,



R)-3/(*S*, *S*)-3 or heterochiral dimers (*R*, *S*)-3. The zinc alcoholate **2** reacts slowly with the aldehyde **4** in an equilibrium reaction to form the hemiacetalate **5**, which first adds another molecule of diisopropyl zinc and aldehyde **4** to form complex **6** and is then enantioselectively alkylated to complex **7**. In a further step, another molecule of aldehyde is added and forms a dimeric hemiacetalate complex **8** that decomposes into its monomeric hemiacetalates **5**, establishing an autocatalytic cycle. The reaction product, the alcoholate **2** and its dimers **3**, is continuously formed by the back reaction of the hemiacetalate **5**/alcoholate-aldehyde (**2–4**) equilibrium.

This contribution will focus on the dynamics of hemiacetal formation and will investigate the influence of reaction kinetics and equilibrium on the autocatalytic reaction and the enantiomeric excess *ee*.

MATERIALS AND METHODS

General

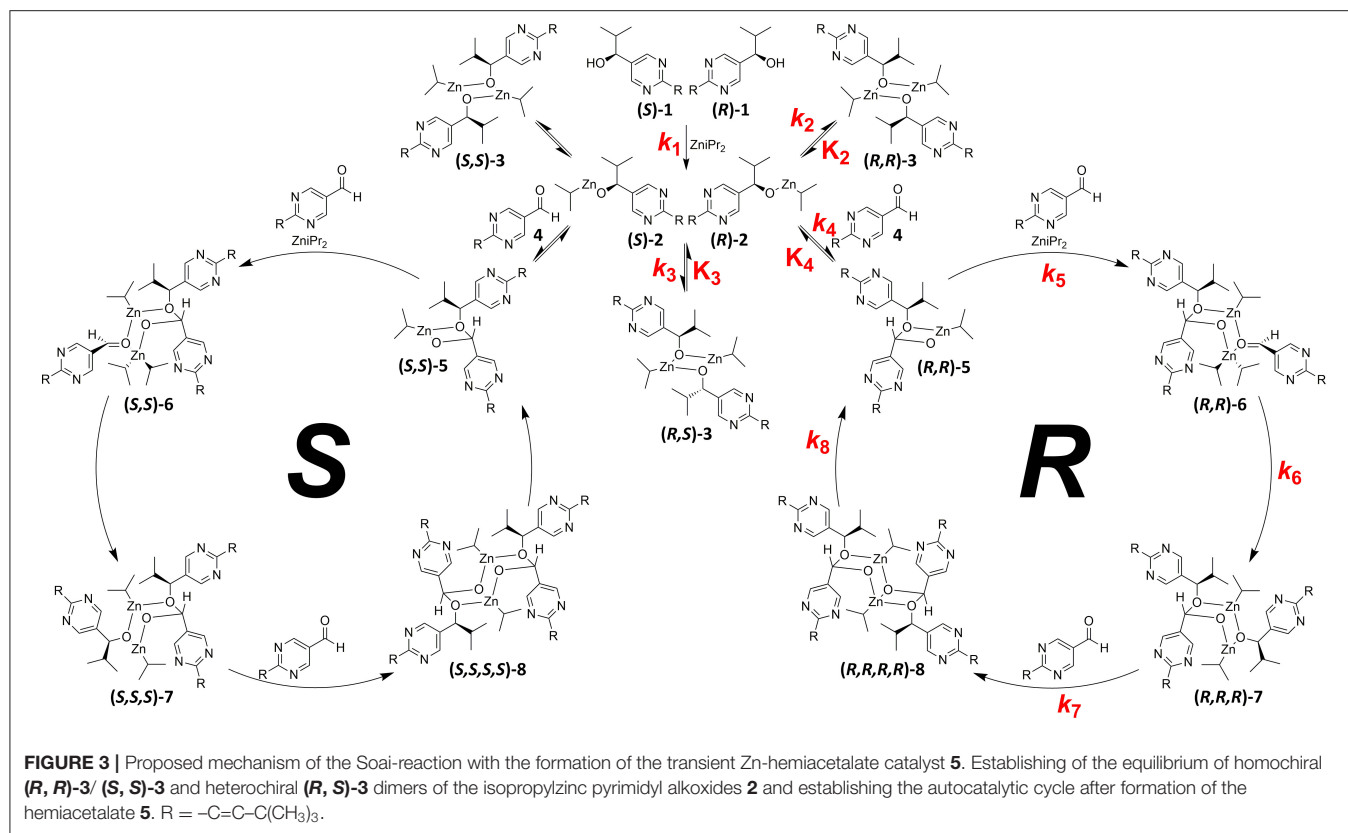
Reagents and solvents were obtained from Sigma-Aldrich (Taufkirchen, Germany), ABCR (Karlsruhe, Germany), and Alfa Aesar (Karlsruhe, Germany) and were used without further purification. Standard Schlenk techniques were used for air sensitive reactants. Glass ware was heated prior to use and the syntheses were carried out under an argon atmosphere.

NMR spectra were recorded on Bruker Avance 600 and 500 MHz spectrometers.

HPLC and HPLC-MS measurements were performed on an Agilent 1200 Infinity HPLC equipped with a binary pump, an autosampler (Agilent HiP+), a thermostatted column oven and a photodiode array detector (DAD). All operations were controlled by the Agilent Chemstation software. Enantioselective separations were performed on an immobilized chiral stationary phase (CSP) cellulose tris(3,5-dichlorophenylcarbamate), Chiralpak IC-3 (15 cm, I.D. 4.6 mm, particle size 3 μm , Chiral Technologies, Parc d'Innovation, Bd Gonthier d'Andernach, 67400 Illkirch Cedex, France) using *n*-hexane/2-propanol 60:40 (v/v) as mobile phase at a flow rate of 1.0 mL·min⁻¹.

Evaluation of the Dynamic HPLC Profiles

Dynamic HPLC traces were analyzed by the unified equation, which allows the direct calculation of reaction rate constants k_1 and k_{-1} and Gibbs activation energies ΔG^\ddagger for all types of (pseudo) first-order reactions taking place in chromatographic systems, regardless of the initial concentrations of the interconverting analytes A and B and the equilibrium constant $K_{A/B}$. A detailed description of the derivation is given in literature (Trapp, 2006a,b,c,d; Trapp et al., 2009).



RESULTS AND DISCUSSION

During the HPLC separation of pyrimidine-5-carbaldehyde **4** with 2-propanol in the mobile phase a second peak is observed which is connected to the peak of pyrimidine-5-carbaldehyde **4** by a plateau formation. If this separation is performed using a chiral stationary phase, e.g., with Chiralpak IC-3, then the separation of the newly formed peak into two peaks is observed, which indicates, that enantiomers have been formed (cf. **Figure 4**). Using HPLC-MS, the newly formed peaks can be clearly assigned to the hemiacetals **(R)-5_{iPr}** or **(S)-5_{iPr}** formed from the 2-propanol of the mobile phase and the pyrimidine-5-carbaldehyde **4**. The observation of hemiacetals is important because chromatographic techniques can be used to study and screen the reactivity of the formation of hemiacetals from aldehydes and alcohols. It can be expected that the formation of hemiacetalates **5** from aldehydes **4** and zinc alcoholates **2** occurs with similar reactivity due to the electronic properties of the aldehydes **4** and therefore the ability of formation can be directly correlated.

To determine the reaction rate of the hemiacetal formation and decomposition of the aldehyde **4** in presence of 2-propanol, we performed temperature-dependent enantioselective dynamic HPLC (DHPLC) (Trapp et al., 2001; D'Acquarica et al., 2006; Wolf, 2008; Trapp, 2013) measurements. As can be seen from

the elution profiles (cf. **Figure 5**) a pronounced plateau formation with increasing reaction temperature can be observed.

The kinetic analysis was performed by analysis with the unified equation of chromatography considering a pseudo-first-order reaction because of the excess of 2-propanol in the mobile phase. This allowed the determination of the reaction rate constants, e.g., k_1 (293 K) = $4.1 \times 10^{-3} \text{ (mol} \times \text{s)}^{-1}$ and k_{-1} (293 K) = $1.3 \times 10^{-2} \text{ s}^{-1}$ and the determination of the activation enthalpies ΔH^\ddagger for the hemiacetal **5_{iPr}** formation and decomposition via the slope and the activation entropies ΔS^\ddagger via the intercept of the Eyring plots [$\ln(k/T)$ vs. $1/T$] (cf. **Figure 6A**). Deviations of the activation parameters ΔH^\ddagger and ΔS^\ddagger have been calculated by error band analysis of the linear regression with a level of confidence of 95%. The activation parameters of the hemiacetal **5_{iPr}** formation were determined to be $\Delta H^\ddagger = 26.3 \pm 0.2 \text{ kJ/mol}$ and $\Delta S^\ddagger = -195 \pm 34 \text{ J/(K} \times \text{mol)}$ ($r = 0.9990$, residual deviation $s_y = 0.0306$) and for the backward reaction, the hemiacetal **5_{iPr}** decomposition, the activation parameters were determined to be $\Delta H^\ddagger = 47.7 \pm 0.2 \text{ kJ/mol}$ and $\Delta S^\ddagger = -112 \pm 1 \text{ J/(K} \times \text{mol)}$ ($r = 0.9994$, $s_y = 0.0630$). These activation parameters indicate, that the formation of hemiacetal **5_{iPr}** from **4** is an endergonic process, which is highly dynamic. The thermodynamic parameters of the formation of the hemiacetal **5_{iPr}** were determined by linear regression of the thermodynamic Gibbs free energies $\Delta G(T)$, obtained from the equilibrium constants K , vs. the temperatures

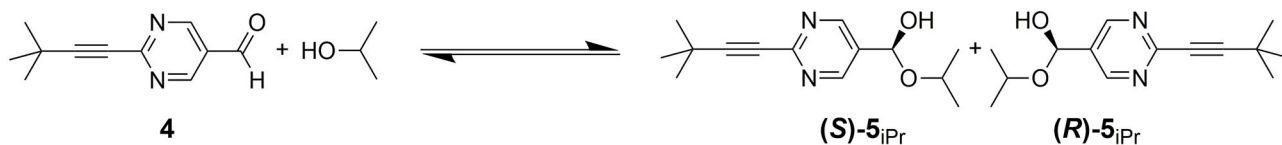


FIGURE 4 | Hemiacetal formation of 2-(*tert*-butylacetylene-1-yl)pyrimidin-5-carbaldehyde 4 with 2-propanol.

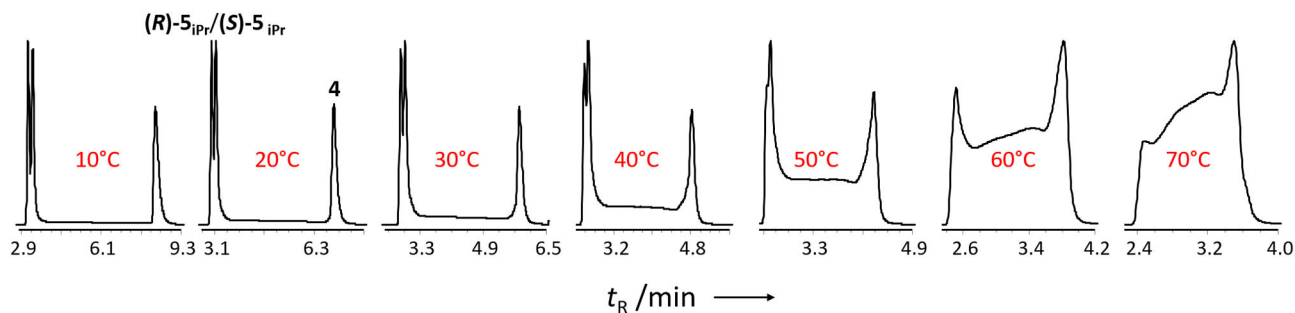


FIGURE 5 | Temperature-dependent enantioselective DHPLC measurements of the formation of the hemiacetal starting from 2-(*tert*-butylacetylene-1-yl)pyrimidin-5-carbaldehyde 4 with 2-propanol. Experimental conditions: Chiralpak IC-3 (15 cm, I.D. 4.6 mm, particle size 3 μm), *n*-hexane/2-propanol 60:40 (v/v), flow 1.0 mL·min⁻¹.

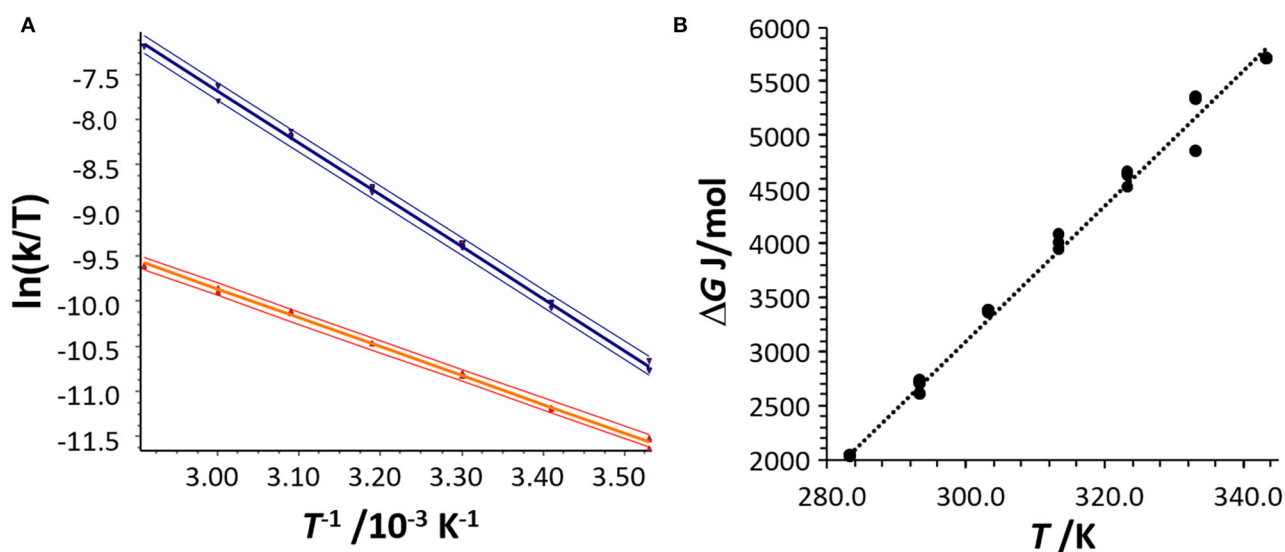


FIGURE 6 | **(A)** Eyring plot for the determination of the activation parameters ΔH^\ddagger and ΔS^\ddagger of the hemiacetal formation (red data points) and the hemiacetal decomposition (blue data points) obtained from the DHPLC experiment considering the concentration of 2-propanol. The upper and lower curves represent the error bands of the linear regression with a level of confidence of 95%. For the linear regression 21 data points were considered. **(B)** Determination of the thermodynamic parameters ΔH and ΔS by plotting the Gibbs free energy ΔG as a function of T .

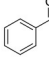
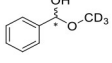
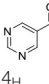
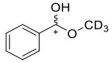
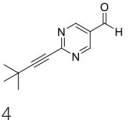
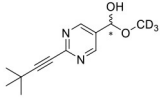
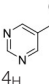
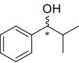
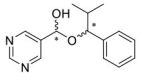
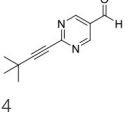
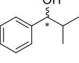
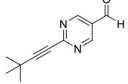
T (correlation coefficient $r = 0.9949$) to be $\Delta G^0 = 3 \text{ kJ/mol}$, $\Delta H^0 = -15.6 \text{ kJ/mol}$ and $\Delta S^0 = -62.5 \text{ J/(K} \times \text{mol)}$ (cf. **Figure 6B**).

It is important to note that this reversible process of hemiacetal formation creates a stereocenter, which leads to the formation of diastereomers in the case of the reaction with a chiral alcohol. It is therefore obvious that a reaction with the corresponding alcohol or alcoholate in the Soai reaction leads to

diastereomeric hemiacetals or hemiacetalates 5. This endergonic process leads to the formation of more hemiacetal, which are well coordinating chiral ligands, at low temperature. This is consistent with the higher reaction rates observed at low temperatures in the Soai reaction.

We have extended the investigation of hemiacetal formation to ^1H NMR studies of the chemical equilibrium. For this

TABLE 1 | Determination of equilibrium constants of the formation of hemiacetals from benzaldehyde and pyrimidyl-5-carbaldehydes by reaction with alcohols.

Aldehyde	Alcohol	Hemiacetal	Yield (%)	K (M^{-1})	K_{minor} (M^{-1})	K_{major} (M^{-1})
	CD_3OH		9	0.0040		
 4 _H	CD_3OH		95	0.7733		
 4	CD_3OH		95	0.7722		
 4 _H			9	0.0544	0.0151	0.0393
 4			11	0.1195	0.0193	0.1002

Quantification was performed by 1H NMR spectroscopy.

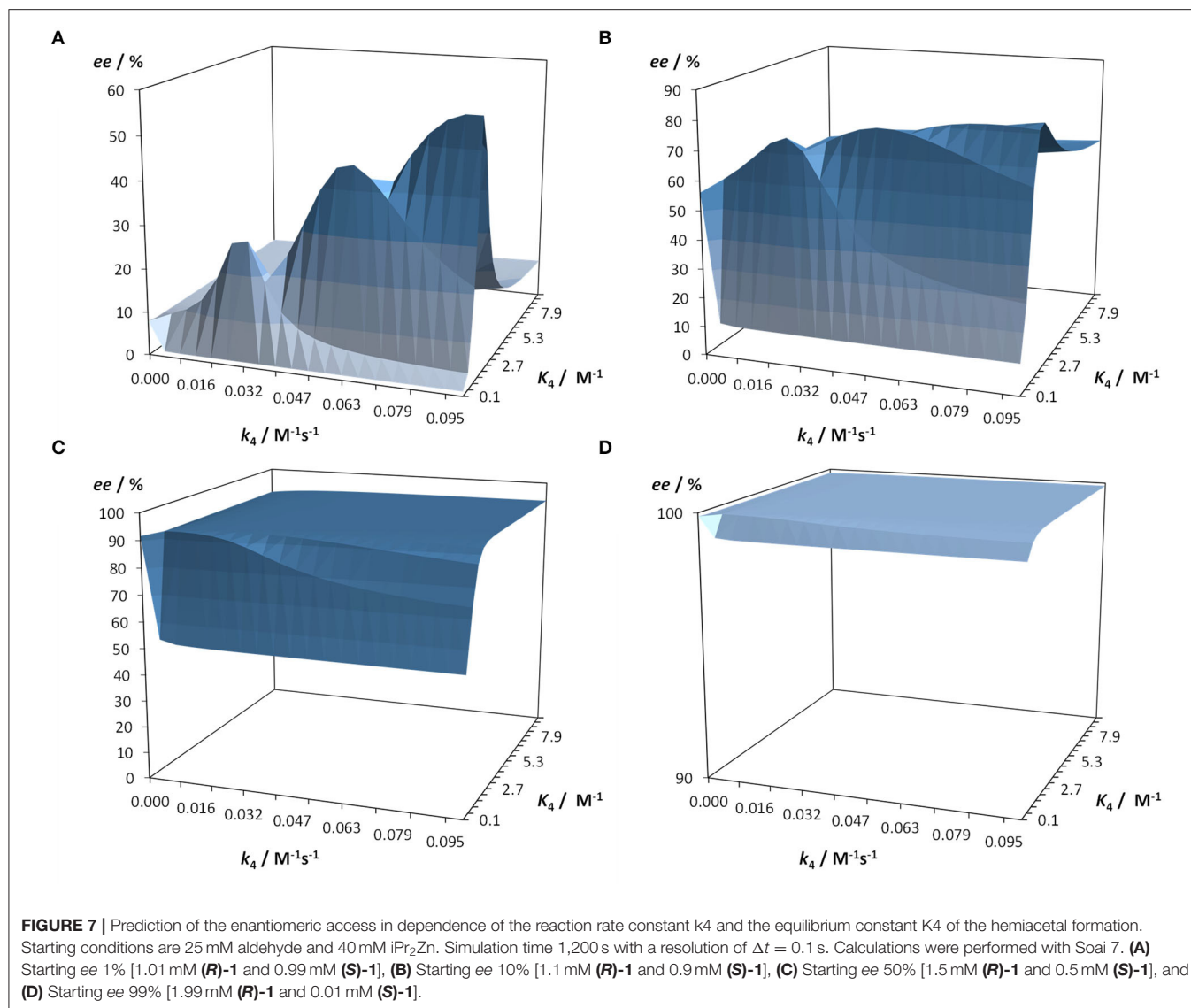
TABLE 2 | Kinetic data of the Soai-reaction of aldehyde **4** with iPr_2Zn forming alcohol **1** determined by comprehensive reaction networks analysis.

n	k_n	K_n	k_{-n}
1	$1.5 \cdot 10^2 \pm 7 M^{-1}s^{-1}$		
2	$7.0 \cdot 10^2 \pm 32 M^{-1}s^{-1}$	$81 \pm 4 M^{-1}$	$8.6 \pm 0.8 s^{-1}$
3	$7.0 \cdot 10^2 \pm 32 M^{-1}s^{-1}$	$162 \pm 8 M^{-1}$	$4.3 \pm 0.4 s^{-1}$
4	$1.7 \cdot 10^{-3} \pm 1.2 \cdot 10^{-4} M^{-1}s^{-1}$	$0.136 \pm 0.001 M^{-1}$	$1.3 \cdot 10^{-2} \pm 1.0 \cdot 10^{-3} s^{-1}$
5	$63 \pm 5 M^{-2}s^{-1}$		
6	$0.11 \pm 0.01 s^{-1}$		
7	$13.2 \pm 0.2 M^{-1}s^{-1}$		
8	$0.23 \pm 0.02 s^{-1}$		

purpose, 5 mg each of benzaldehyde, pyrimidyl-5-carbaldehyde **4_H** and 2-(*tert*-butylacetylene-1-yl)pyrimidyl-5-carbaldehyde **4** were mixed with 0.5 ml methanol- d_3 . The results of the equilibrium adjustment after 6 h are summarized in **Table 1**. As can be clearly seen, the hemiacetals are formed with yields of 9% in the case of benzaldehyde and, remarkably, 95% of the corresponding hemiacetals of pyrimidyl-5-carbaldehydes **4_H** and 2-(*tert*-butyl acetylene-1-yl)pyrimidyl-5-carbaldehyde **4**, respectively. This reveals the unique properties of pyrimidine-5-carbaldehydes, which are excellent at forming hemiacetals. In a further experiment, 20 mg each of pyrimidyl-5-carbaldehyde **4_H** and 2-(*tert*-butyl acetylene-1-yl)pyrimidyl-5-carbaldehyde **4** were mixed with 5 eq. 2-methyl-1-phenyl propanol in anhydrous

toluene- d_8 . Toluene was chosen as solvent to achieve reaction conditions comparable to the Soai reaction. The corresponding diastereomeric hemiacetals are obtained in 9 and 11% yield, respectively. The equilibrium constants K of the formation of the hemiacetals described here are summarized in **Table 1**. It is important to note that we focused here on the analysis of the hemiacetals instead of the hemiacetalates **5**, which can be observed by *in-situ* mass spectrometric investigation of the Soai reaction. In the case of the diastereomeric hemiacetals **5**, the formation of a major and a minor diastereomer is observed, for which respective equilibrium constants can be determined. These equilibrium constants are in line with the equilibrium constant K_4 for the formation of the hemiacetal **5** in the proposed mechanism of the Soai reaction (cf. **Figure 3** and **Table 2**), which have been determined by comprehensive reaction networks analysis.

This reaction network analysis was performed by using 26 differential equations describing the reaction kinetics of the reaction mechanism of the Soai reaction depicted in **Figure 3** (see details in reference Trapp et al., 2020). These equations are implemented in a software program (Soai 7; Trapp, 2020). This program allows to calculate kinetic reaction profiles using an adaptive Runge-Kutta routine to solve the system of differential equations with the initial input concentrations of the enantiomers of the additive alcohol **1**, aldehyde **4**, and iPr_2Zn . The kinetic model allows to calculate kinetic reaction profiles of the conversion of the pyrimidine-5-carbaldehyde **4** into the



reaction product **1** of the Soai reaction and the precise prediction of the non-linear amplification of the *ee* and the induction period in dependence on the *ee*.

This kinetic model and software Soai 7 were used to investigate the influence of the reaction kinetics and equilibrium of the hemiacetal formation on the autocatalytic reaction and the enantiomeric excess *ee*. For this purpose the kinetic and thermodynamic parameters summarized in Table 2 were used and the parameters for the hemiacetal formation were varied in 20 steps each for k_4 from 0.0001 to $0.1 \text{ M}^{-1}\text{s}^{-1}$ and for K_4 from 0.05 to 10 M^{-1} . Four scenarios were considered with increasing starting enantiomeric excess *ee*: *ee* 1% [1.01 mM (**R**)-**1** and 0.99 mM (**S**)-**1**] (cf. Figure 7A), *ee* 10% [1.1 mM (**R**)-**1** and 0.9 mM (**S**)-**1**] (cf. Figure 7B), *ee* 50% [1.5 mM (**R**)-**1** and 0.5 mM (**S**)-**1**] (cf. Figure 7C), and *ee* 99% [1.99 mM (**R**)-**1** and 0.01 mM (**S**)-**1**] (cf. Figure 7D). The predicted final high *ee*'s starting from already very high *ee*'s

are not surprising. In this case the amplification (difference between final product *ee* and initial *ee*) is low. However, the simulation predicts that there are scenarios, which lead to a very amplification in a single step with proper k_4 and K_4 values. The result is, that a high stereodynamics with reaction rates $k_4 > 0.08 \text{ M}^{-1}\text{s}^{-1}$ paired with an equilibrium constant K_4 in the range between 0.06 and 2.7 M^{-1} gives an immediate jump in the *ee* starting at 1% to an *ee* between 29 and 57%!

CONCLUSIONS

By means of enantioselective dynamic HPLC (DHPLC) and ^1H NMR studies the hemiacetal formation was investigated kinetically and thermodynamically. On the one hand, it could be shown that the formation process of the hemiacetal is endergonic

and that there is a rapid conversion equilibrium between the hemiacetals. Simulations with the kinetic model of the Soai reaction under variation of the kinetics and thermodynamics of the hemiacetal formation allowed the prediction of the amplification of the enantiomeric excess depending on the addition of the alcohol as additive. The results show that in the underlying mechanism of the Soai reaction by the formation of transient stereodynamic hemiacetal catalysts the stereodynamics has an important influence on the resulting enantiomeric excess *ee*. It is remarkable that a high stereodynamics and equilibrium in favor of the alcohol and aldehyde compared to the hemiacetal leads to an enormous amplification of the enantiomeric excess *ee*. This leads to the conclusion that apparently inefficient processes lead to an optimal selection and amplification and thus to chirogenesis and homochirality. Furthermore, it can be concluded that maintaining homochirality is much more robust and tolerates wider ranges of kinetic and thermodynamic parameters.

REFERENCES

- Alberts, A. H., and Wynberg, H. (1989). The role of the product in asymmetric carbon-carbon bond formation: stoichiometric and catalytic enantioselective autoinduction. *J. Am. Chem. Soc.* 111, 7265–7266. doi: 10.1021/ja00200a059
- Athavale, S. V., Simon, A., Houk, K. N., and Denmark, S. E. (2020). Demystifying the asymmetry-amplifying, autocatalytic behaviour of the Soai reaction through structural, mechanistic and computational studies. *Nat. Chem.* 12, 412–423. doi: 10.1038/s41557-020-0421-8
- Bissette, A. J., and Fletcher, S. P. (2013). Mechanisms of Autocatalysis. *Angew. Chem. Int. Ed.* 52, 12800–12826. doi: 10.1002/anie.201303822
- Blackmond, D. G. (2004). Asymmetric autocatalysis and its implications for the origin of homochirality. *Proc. Natl. Acad. Sci. U.S.A.* 101, 5732–5736. doi: 10.1073/pnas.0308363101
- Blackmond, D. G. (2006). Mechanistic study of the Soai autocatalytic reaction informed by kinetic analysis. *Tetrahedron: Asymmetry* 17, 584–589. doi: 10.1016/j.tetasy.2006.01.012
- Blackmond, D. G. (2010). Kinetic aspects of non-linear effects in asymmetric synthesis, catalysis, and autocatalysis. *Tetrahedron: Asymmetry* 21, 1630–1634. doi: 10.1016/j.tetasy.2010.03.034
- Blackmond, D. G. (2011). The origin of biological homochirality. *Phil. Trans. R. Soc. B* 366, 2878–2884. doi: 10.1098/rstb.2011.0130
- Blackmond, D. G. (2020). Autocatalytic models for the origin of biological homochirality. *Chem. Rev.* 120, 4831–4847. doi: 10.1021/acs.chemrev.9b00557
- Blackmond, D. G., McMillan, C. R., Ramdeehul, S., Schorm, A., and Brown, J. M. (2001). Origins of asymmetric amplification in autocatalytic alkylzinc additions. *J. Am. Chem. Soc.* 123, 10103–10104. doi: 10.1021/ja0165133
- D'Acquarica, I., Gasparini, F., Pierini, M., Villani, C., and Zappia, G. (2006). Dynamic HPLC on chiral stationary phases: a powerful tool for the investigation of stereomutation processes. *J. Sep. Sci.* 29, 1508–1516. doi: 10.1002/jssc.200600129
- Ercolani, G., and Schiaffino, L. (2011). Putting the mechanism of the Soai reaction to the test: DFT study of the role of aldehyde and dialkylzinc structure. *J. Org. Chem.* 76, 2619–2626. doi: 10.1021/jo102525t
- Frank, F. C. (1953). On spontaneous asymmetric synthesis. *Biochim. Biophys. Acta* 11, 459–463. doi: 10.1016/0006-3002(53)90082-1
- Gehring, T., Quaranta, M., Odell, B., Blackmond, D. G., and Brown, J. M. (2012). Observation of a transient intermediate in Soai's asymmetric autocatalysis: insights from 1H NMR turnover in real time. *Angew. Chem. Int. Ed.* 51, 9539–9542. doi: 10.1002/anie.201203398
- Girard, C., and Kagan, H. B. (1998). Nonlinear effects in asymmetric synthesis and stereoselective reactions: ten years of investigation. *Angew. Chem. Int. Ed.* 37, 2922–2959. doi: 10.1002/(SICI)1521-3773(19981116)37:21<2922::AID-ANIE2922>3.0.CO;2-1
- Gridnev, I. D., and Vorobiev, A. K. (2015). On the origin and structure of the recently observed acetal in the Soai reaction. *Bull. Chem. Soc. Jpn.* 88, 333–340. doi: 10.1246/bcsj.20140341
- Hawbaker, N. A., and Blackmond, D. G. (2019). Energy threshold for chiral symmetry breaking in molecular self-replication. *Nat. Chem.* 11, 957–962. doi: 10.1038/s41557-019-0321-y
- Hegstrom, R. A. (1984). Parity nonconservation and the origin of biological chirality: theoretical calculations. *Origins life.* 14, 405–411. doi: 10.1007/BF00933684
- Karunakaran, S. C., Cafferty, B. J., Weigert-Muñoz, A., Schuster, G. B., and Hud, N. V. (2019). Spontaneous symmetry breaking in the formation of supramolecular polymers: implications for the origin of biological homochirality. *Angew. Chem. Int. Ed.* 58, 1453–1457. doi: 10.1002/anie.201812808
- Kawasaki, T., Suzuki, K., Hakoda, Y., and Soai, K. (2008). Achiral nucleobase cytosine acts as an origin of homochirality of biomolecules in conjunction with asymmetric autocatalysis. *Angew. Chem. Int. Ed.* 47, 496–499. doi: 10.1002/anie.200703634
- Kitamura, M., Okada, S., Suga, S., and Noyori, R. (1989). Enantioselective addition of dialkylzinc to aldehydes promoted by chiral amino alcohols. Mechanism and Nonlinear Effect. *J. Am. Chem. Soc.* 111, 4028–4036. doi: 10.1021/ja00193a040
- Maier, F., and Trapp, O. (2014). Selector-induced dynamic deracemization of a selectand-modified tropes BIPHEPO-ligand: application in the organocatalyzed asymmetric double-aldol-reaction. *Angew. Chem. Int. Ed.* 53, 8756–8760. doi: 10.1002/anie.201402293
- Micheau, J.-C., Coudret, C., Cruz, J.-M., and Buhse, T. (2012). Amplification of enantiomeric excess, mirror-image symmetry breaking and kinetic proofreading in Soai reaction models with different oligomeric orders. *Phys. Chem. Chem. Phys.* 14, 13239–13248. doi: 10.1039/c2cp42041d
- Mikami, K., Korenaga, T., Ohkuma, K., and Noyori, R. (2000). Asymmetric activation/deactivation of racemic Ru catalysts for highly enantioselective hydrogenation of ketonic substrates. *Angew. Chem. Int. Ed.* 39, 3707–3710. doi: 10.1002/1521-3773(20001016)39:20<3707::AID-ANIE3707>3.0.CO;2-M
- Satyanarayana, T., Abraham, S., and Kagan, H. B. (2009). Nonlinear effects in asymmetric catalysis. *Angew. Chem. Int. Ed.* 48, 456–494. doi: 10.1002/anie.200705241
- Scholtes, J. F., and Trapp, O. (2019a). Design and synthesis of a stereodynamic catalyst with reversal of selectivity by enantioselective self-inhibition. *Chirality* 31, 1028–1042. doi: 10.1002/chir.23132

DATA AVAILABILITY STATEMENT

The original contributions presented in the study are included in the article/supplementary materials, further inquiries can be directed to the corresponding author/s.

AUTHOR CONTRIBUTIONS

OT designed and performed the experiments and analysis, programmed the software application and wrote the manuscript.

ACKNOWLEDGMENTS

I acknowledge financial support from the Max-Planck-Society (Max-Planck-Fellow Research Group Origins of Life) the VolkswagenStiftung (Initiating Molecular Life), the DFG for financial support by the SFB 235 (Emergence of Life), and the Cluster of Excellence ORIGINS (EXC 2094–390783311).

- Scholtes, J. F., and Trapp, O. (2019b). Enantioselectivity induced by stereoselective interlocking: a novel core motif for tropos ligands. *Chem. Eur. J.* 25, 11707–11714. doi: 10.1002/chem.201902017
- Scholtes, J. F., and Trapp, O. (2019c). Inducing enantioselectivity in a dynamic catalyst by supramolecular interlocking. *Angew. Chem. Int. Ed.* 58, 6306–6310. doi: 10.1002/anie.201901175
- Scholtes, J. F., and Trapp, O. (2019d). Supramolecular interlocked biphenyl ligands for enantioselective Ti-catalyzed alkylation of aromatic aldehydes. *Organometallics* 38, 3955–3960. doi: 10.1021/acs.organomet.9b00262
- Scholtes, J. F., and Trapp, O. (2020). *Stereinduction and -Amplification in Stereodynamic Systems by Non-Covalent Interactions*. Synlett. doi: 10.1055/a-1274-2777
- Shibata, T., Takahashi, T., Konishi, T., and Soai, K. (1997). Asymmetric self-replication of chiral 1,2-amino alcohols by highly enantioselective autoinductive reduction. *Angew. Chem. Int. Ed.* 36, 2458–2460. doi: 10.1002/anie.199724581
- Soai, K., and Kawasaki, T. (2008). Asymmetric autocatalysis with amplification of chirality. *Top. Curr. Chem.* 284, 1–33. doi: 10.1007/128_2007_138
- Soai, K., Shibata, T., Morioka, H., and Choji, K. (1995). Asymmetric autoanalysis and amplification of enantiomeric excess of a chiral molecule. *Nature* 378, 767–768. doi: 10.1038/378767a0
- Storch, G., Deberle, L., Menke, J.-M., Rominger, F., and Trapp, O. (2016a). A stereodynamic phosphoramidite ligand derived from 3,3'-functionalized ortho-biphenol and its rhodium(I) complex. *Chirality* 28, 744–748. doi: 10.1002/chir.22655
- Storch, G., Pallmann, S., Rominger, F., and Trapp, O. (2016b). Stereodynamic tetrahydro-bisindole “NU-BIPHEP(O)” s: functionalization, rotational barriers and non-covalent interactions. *Beilstein J. Org. Chem.* 12, 1453–1458. doi: 10.3762/bjoc.12.141
- Storch, G., Siebert, M., Rominger, F., and Trapp, O. (2015). 5,5'-diamino-BIPHEP ligands bearing small selector units for non-covalent binding of chiral analytes in solution. *Chem. Commun.* 51, 15665–15668. doi: 10.1039/C5CC06306J
- Storch, G., and Trapp, O. (2015). Temperature controlled bidirectional enantioselectivity in a dynamic catalyst for asymmetric hydrogenation. *Angew. Chem. Int. Ed.* 54, 3580–3586. doi: 10.1002/anie.201412098
- Storch, G., and Trapp, O. (2017). By-design enantioselective self-amplification based on non-covalent product-catalyst interactions. *Nat. Chem.* 9, 179–187. doi: 10.1038/nchem.2638
- Storch, G., and Trapp, O. (2018). Supramolecular chirality transfer in a stereodynamic catalysts. *Chirality* 30, 1150–1160. doi: 10.1002/chir.23007
- Teichert, J. S., Kruse, F. M., and Trapp, O. (2019). Direct prebiotic pathway to DNA nucleosides. *Angew. Chem. Int. Ed.* 58, 9944–9947. doi: 10.1002/anie.201903400
- Trapp, O. (2006a). Fast and precise access to enantiomerization rate constants in dynamic chromatography. *Chirality* 18, 489–497. doi: 10.1002/chir.20276
- Trapp, O. (2006b). The unified equation for the evaluation of degenerated first order reactions in dynamic electrophoresis. *Electrophoresis* 27, 2999–3006. doi: 10.1002/elps.200500907
- Trapp, O. (2006c). The unified equation for the evaluation of first order reactions in dynamic electrophoresis. *Electrophoresis* 27, 534–541. doi: 10.1002/elps.200500708
- Trapp, O. (2006d). Unified Equation for access to rate constants of first-order reactions in dynamic and on-column reaction chromatography. *Anal. Chem.* 78, 189–198. doi: 10.1021/ac051655r
- Trapp, O. (2013). Interconversion of stereochemically labile enantiomers (enantiomerization). *Top. Curr. Chem.* 341, 231–270. doi: 10.1007/128_2013_453
- Trapp, O. (2020). *Soai 7, Compatible With Microsoft Windows 7, 8 and 10*. The compiled executable program can be obtained from the author upon request.
- Trapp, O., Bremer, S., and Weber, S. K. (2009). accessing reaction rate constants in on-column reaction chromatography: an extended unified equation for reaction educts and products with different response factors. *Anal. Bioanal. Chem.* 395, 1673–1679. doi: 10.1007/s00216-009-2993-4
- Trapp, O., Lamour, S., Maier, F., Siegle, A., Zawatzky, K., and Straub, B. F. (2020). *In situ* mass spectrometric and kinetic investigations of Soai's asymmetric autocatalysis. *Chem. Eur. J.* 26. (in press). doi: 10.1002/chem.202003260
- Trapp, O., Schoetz, G., and Schurig, V. (2001). Determination of enantiomerization barriers by dynamic and stopped flow chromatographic methods. *Chirality* 13, 403–414. doi: 10.1002/chir.1052
- Tsogoeva, S. B. (2010). When chiral product and catalyst are the same: discovery of asymmetric organoautocatalysis. *Chem. Commun.* 46, 7662–7669. doi: 10.1039/c0cc02305a
- Wolf, C. (2008). *Dynamic Stereochemistry of Chiral Compounds - Principles and Applications*. Cambridge: RSC Publishing.

Conflict of Interest: The author declares that the research was conducted in the absence of any commercial or financial relationships that could be construed as a potential conflict of interest.

Copyright © 2020 Trapp. This is an open-access article distributed under the terms of the Creative Commons Attribution License (CC BY). The use, distribution or reproduction in other forums is permitted, provided the original author(s) and the copyright owner(s) are credited and that the original publication in this journal is cited, in accordance with accepted academic practice. No use, distribution or reproduction is permitted which does not comply with these terms.



En Route to a Chiral Melanin: The Dynamic “From-Imprinted-to-Template” Supramolecular Role of Porphyrin Hetero-Aggregates During the Oxidative Polymerization of L-DOPA

Massimiliano Gaeta¹, Rosalba Randazzo¹, Valentina Villari², Norberto Micali², Alessandro Pezzella³, Roberto Purrello¹, Marco d'Ischia^{4*} and Alessandro D'Urso^{1*}

OPEN ACCESS

Edited by:

Victor Borovkov,
South-Central University for
Nationalities, China

Reviewed by:

Claudio Baggiani,
University of Turin, Italy
Andrea Romeo,
University of Messina, Italy
Silvano Geremia,
University of Trieste, Italy

*Correspondence:

Marco d'Ischia
dischia@unina.it
Alessandro D'Urso
adurso@unict.it

Specialty section:

This article was submitted to
Supramolecular Chemistry,
a section of the journal
Frontiers in Chemistry

Received: 13 October 2020

Accepted: 23 November 2020

Published: 21 December 2020

Citation:

Gaeta M, Randazzo R, Villari V,
Micali N, Pezzella A, Purrello R,
d'Ischia M and D'Urso A (2020) En
Route to a Chiral Melanin: The
Dynamic
“From-Imprinted-to-Template”
Supramolecular Role of Porphyrin
Hetero-Aggregates During the
Oxidative Polymerization of L-DOPA.
Front. Chem. 8:616961.
doi: 10.3389/fchem.2020.616961

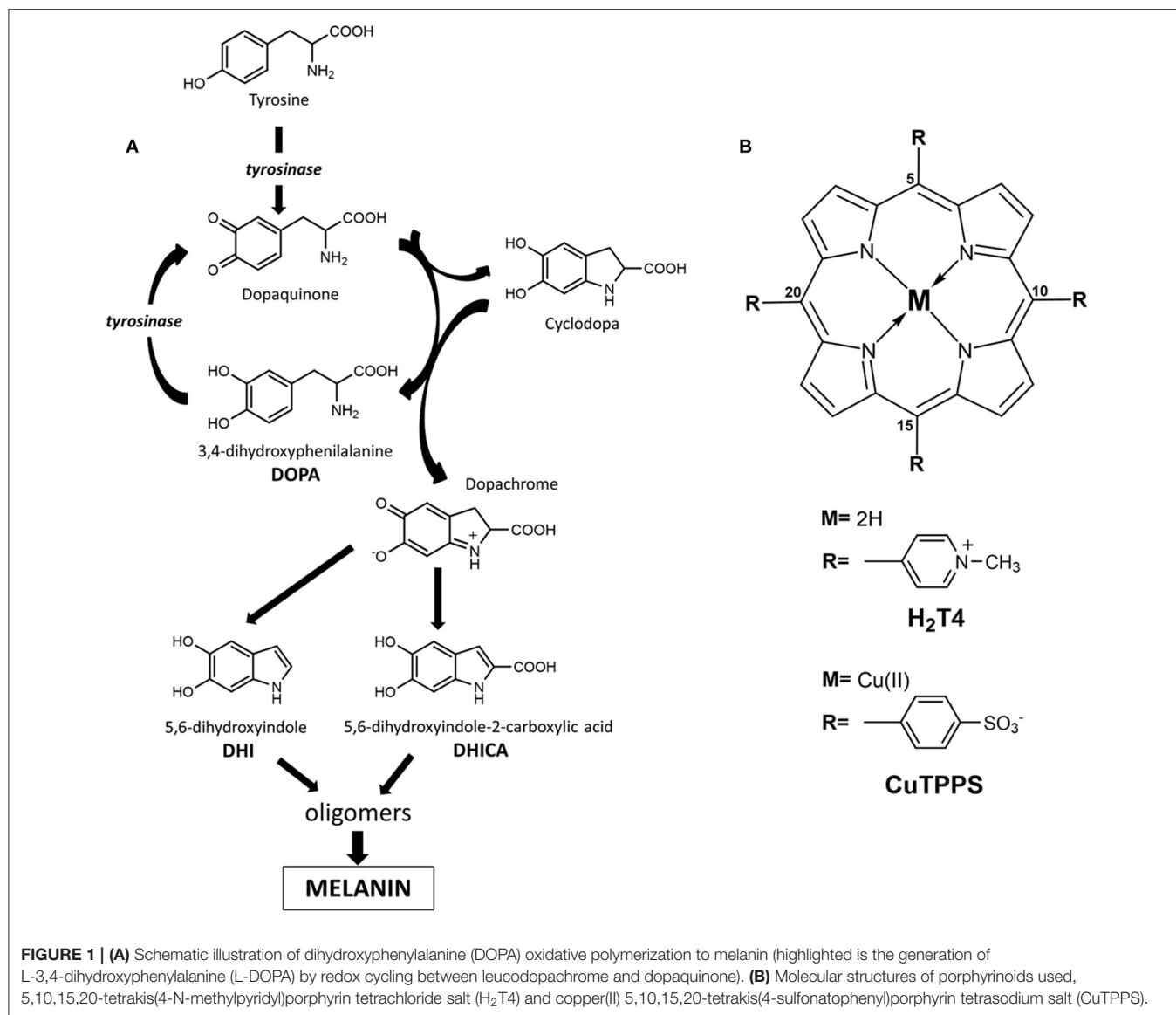
¹ Dipartimento di Scienze Chimiche, Università degli Studi di Catania, Catania, Italy, ² Consiglio Nazionale delle Ricerche-IPCF Istituto per i Processi Chimico-Fisici, Messina, Italy, ³ Department of Physics “Ettore Pancini,” University of Naples “Federico II,” Naples, Italy, ⁴ Department of Chemical Sciences, University of Naples “Federico II,” Naples, Italy

Chiral porphyrin hetero-aggregates, produced from meso-tetrakis(4-N-methylpyridyl) porphyrin H₂T4 and copper(II) meso-tetrakis(4-sulfonatophenyl)porphyrin CuTPPS by an imprinting effect in the presence of L-3,4-dihydroxyphenylalanine (L-DOPA), are shown herein to serve as templates for the generation of chiral structures during the oxidative conversion of the amino acid to melanin. This remarkable phenomenon is suggested to involve the initial role of L-DOPA and related chiral intermediates like dopachrome as templates for the production of chiral porphyrin aggregates. When the entire chiral pool from DOPA is lost, chiral porphyrin hetero-aggregate would elicit axially chiral oligomer formation from 5,6-dihydroxyindole intermediates in the later stages of melanin synthesis. These results, if corroborated by further studies, may open unprecedented perspectives for efficient strategies of asymmetric melanin synthesis with potential biological and technological applications.

Keywords: eumelanin, DOPA, porphyrin, supramolecular aggregates, circular dichroism

INTRODUCTION

L-3,4-Dihydroxyphenylalanine (L-DOPA; **Figure 1A**) is an aromatic amino acid produced in various organisms by the oxidative modification of L-tyrosine (Raper, 1927; Mason and Wright, 1949; Haneda and Watanabe, 1971; Protá, 1995; Ito, 2003; Slominski et al., 2012; Marchiosi et al., 2020). In the skin and other organs, like the ink sac of cephalopods, L-DOPA is an early intermediate in the synthesis of black eumelanin pigments from L-tyrosine by the action of the copper enzyme tyrosinase (Slominski et al., 2004; Ito and Wakamatsu, 2007; Simon et al., 2009; Della Vecchia et al., 2013; d'Ischia et al., 2014). *In vivo*, the process involves the oxidation of tyrosine to dopaquinone followed by intramolecular cyclization to an indoline intermediate, termed leucodopachrome or cyclodopa, which can enter a redox cycle by exchanging electrons with dopaquinone to produce L-DOPA and L-dopachrome. The latter, then, undergoes isomerization with or without decarboxylation and loss of the chiral center to give 5,6-dihydroxyindole (DHI)



and/or 5,6-dihydroxyindole-2-carboxylic acid (DHICA), respectively (Pezzella et al., 1996; Edge et al., 2006; Ito and Wakamatsu, 2007, 2008; Ito et al., 2011; d'Ischia et al., 2013; Panzella et al., 2018). The oxidative polymerization of these latter intermediates leads to the deposition of black insoluble melanin polymers (Figure 1A). So far, knowledge of the intrinsic chiroptical features of melanin polymers is scant, and little attention has been paid to the possible generation of chiral structures under *in vivo* or *in vitro* conditions. The only evidence for the possible occurrence of chirality in melanins is due to the demonstration that oligomers from DHICA may display atropisomerism caused by hindered rotation about interunit bonds (Pezzella et al., 2003). However, current information on the chirality of DHICA oligomers during the polymerization process remains limited.

Recently, a systematic investigation of the effect of porphyrin aggregation on melanin synthesis was undertaken, exploiting the well-known tendency of porphyrins to interact with amino acids (Angelini et al., 2005; Uemori et al., 2012; Charalambidis et al., 2016; Gaeta et al., 2016; Rananaware et al., 2016; Ryu et al., 2018) and polymeric chains (Borovkov et al., 2002a,b; De Luca et al., 2010; Occhiuto et al., 2015; Zhao et al., 2015; Gaeta et al., 2018), with a view to generating new bioinspired functional materials with tailored optical and chiral properties. Water-soluble porphyrins maintain their tendency to aggregate owing to the hydrophobic aromatic macrocycle, whereby binding suitable functional groups to the porphyrin ring may allow to realize self-assembled porphyrin systems in aqueous solution. Although supramolecular arrangements of achiral porphyrins in aqueous solution result in achiral supramolecular structures,

chiral aggregates of porphyrins can be formed in the presence of chiral templates (Bellacchio et al., 1998; Onouchi et al., 2006; Toyofuku et al., 2007; Lauceri et al., 2008; Helmich et al., 2010).

Noteworthy, as a consequence of extensive network of interactions (electrostatic, solvophobic, etc.) that trap porphyrin aggregates in a quite deep local energy minimum ensuring kinetic inertia, the porphyrin supramolecular assembly is able to *memorize* the chiral information imprinted by the chiral template in aqueous solution (Mammana et al., 2007; Gaeta et al., 2016). In this context, porphyrin hetero-aggregates (built by opposite-charged porphyrins) proved to be an ideal system to store chiral information and may offer the possibility of designing switch of memory (Mammana et al., 2007). In this work, we show that porphyrin hetero-aggregates made up of 5,10,15,20-tetrakis(4-N-methylpyridyl)porphyrin H_2T4 (Figure 1B) and copper(II) 5,10,15,20-tetrakis(4-sulfonatophenyl)porphyrin CuTPPS (Figure 1B) can drive the oxidative polymerization of DOPA to melanins with the unexpected generation of asymmetric structures.

MATERIALS AND METHODS

5,10,15,20-Tetrakis(4-N-methylpyridyl)porphyrin tetrachloride salt (H_2T4) and copper(II) 5,10,15,20-tetrakis(4-sulfonatophenyl)porphyrin tetrasodium salt (CuTPPS) were purchased from Mid-Century Company and used without further purification. Porphyrin mother solutions (about 4×10^{-4} M, stored in the dark at room temperature) were prepared dissolving the solid in ultrapure water obtained from Elga Purelab Flex system by Veolia. Then, the concentration was checked by spectrophotometric methods in water solution at neutral pH by means of their molar extinction coefficients at maximum of the Soret band: $\lambda_{\max}(H_2O) = 423$ nm ($\epsilon = 224,000$ M $^{-1}$ cm $^{-1}$) for H_2T4 and $\lambda_{\max}(H_2O) = 412$ nm ($\epsilon = 416,000$ M $^{-1}$ cm $^{-1}$) for CuTPPS.

The phosphate buffered saline (PBS) tablets were purchased from Sigma-Aldrich Company, and the stock solution was prepared by dissolving one tablet in 200 ml of ultrapure water. PBS buffer (pH = 7.4) contains 10 mM of phosphate buffer sodium salt, 137 mM of sodium chloride, and 2.7 mM of potassium chloride.

L-DOPA and the respective D-enantiomer [D-3,4-dihydroxyphenylalanine (D-DOPA)] were purchased from Sigma-Aldrich Company and used without further purification. Solutions of both DOPA enantiomers were freshly prepared by solubilizing the proper amount of solid in PBS buffer in order to attain a final concentration of 0.5 mM.

The porphyrin hetero-aggregates in PBS buffer were obtained by filling with 2 ml of PBS solution a quartz cuvette (path length = 1 cm), then the proper volume of H_2T4 mother solution was added to reach a 2 μ M concentration of H_2T4 in the sample solution. After 5 min, the amount of CuTPPS was added in order to reach again a 2 μ M concentration of CuTPPS in the sample solution. After an additional 20 min, other aliquots of H_2T4 and CuTPPS were added as illustrated before. The

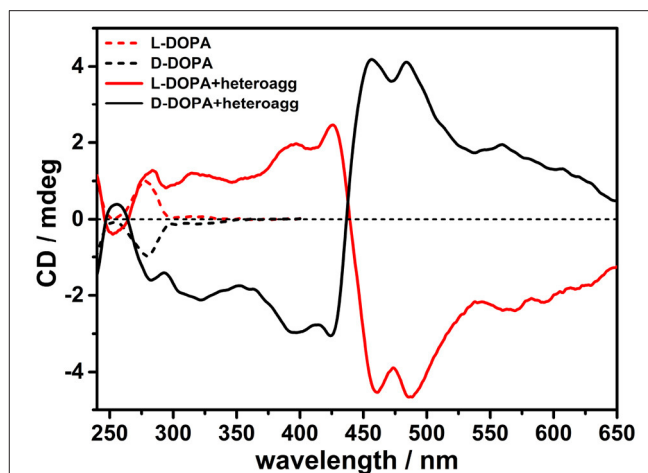


FIGURE 2 | Circular dichroism (CD) spectra in phosphate buffered saline (PBS) buffer (pH = 7.4) of porphyrin hetero-aggregates [5,10,15,20-tetrakis(4-N-methylpyridyl)porphyrin tetrachloride salt (H_2T4) = 4 μ M, copper(II) 5,10,15,20-tetrakis(4-sulfonatophenyl)porphyrin tetrasodium salt (CuTPPS) = 4 μ M] in the presence of L-3,4-dihydroxyphenylalanine (L-DOPA; red solid curve) and D-3,4-dihydroxyphenylalanine (D-DOPA; black solid curve) as prepared. The CD spectra for dihydroxyphenylalanine (DOPA) alone in PBS buffer are graphed in red dashed curve for L-enantiomer and in black dashed curve for D-enantiomer. In all samples, the concentration of DOPA was 0.5 mM.

final work solution thus obtained was kept for 20 min before spectroscopic investigations.

The porphyrin hetero-aggregates in the presence of D- and L-DOPA were obtained by using the corresponding DOPA solution (0.5 mM in PBS) following the aforementioned procedure. In detail, the proper volume of H_2T4 mother solution was added to D- or L-DOPA solution to reach a 2 μ M concentration of H_2T4 , then after 5 min, the proper amount of CuTPPS was added to the sample solution in order to reach again a 2 μ M concentration of CuTPPS. After an additional 20 min, other aliquots of H_2T4 and CuTPPS were added as illustrated before. The final work solution thus obtained was kept for 20 min before spectroscopic investigations. For the long incubation time, each solution of DOPA and porphyrin hetero-aggregates was stored in sealed plastic cuvettes in order to limit the adhesion of both porphyrins and DOPA on the cuvette walls.

All solutions, both stock and sample solutions, are prepared in ultraclean conditions: (i) the operators wore a lab coat, hair cap, gloves, and mask during the preparation of samples and (ii) the tips of the pipettes and the plastic cells were washed three times with ultrapure water before being used.

Circular dichroism (CD) and Uv/Vis measurements were carried out at room temperature (quartz cuvette path length 1 cm) on a JASCO J-710 spectropolarimeter and JASCO V-530 spectrophotometer, respectively. Linear dichroism (LD) measurements were carried out on a modified JASCO J-500A spectropolarimeter (Micali et al., 2015) after proper calibration with an oriented polarizer. Linear birefringence of the instrument

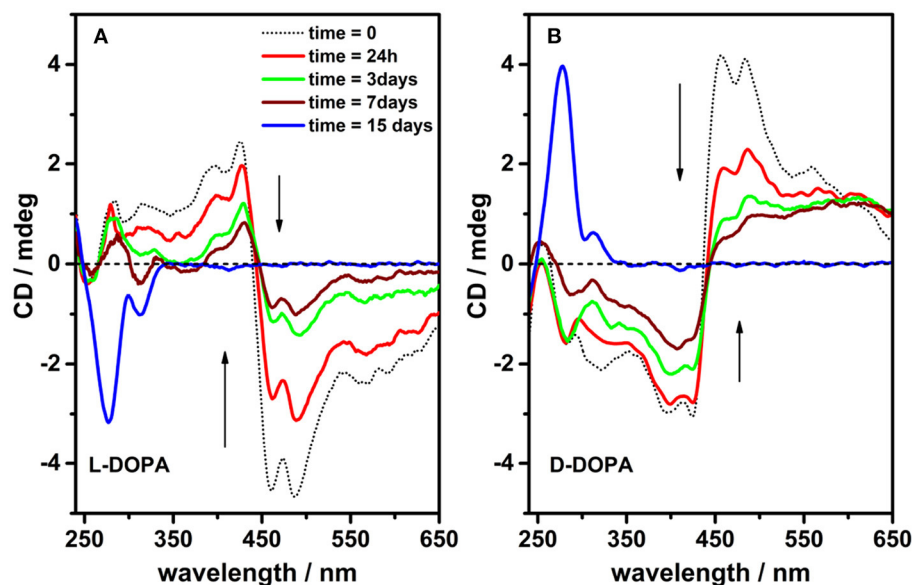


FIGURE 3 | Circular dichroism spectra of incubated solutions [phosphate buffered saline (PBS) buffer, pH = 7.4] containing porphyrin hetero-aggregates [5,10,15,20-tetrakis(4-N-methylpyridyl)porphyrin tetrachloride salt (H_2T4) = 4 μ M, copper(II) 5,10,15,20-tetrakis(4-sulfonatophenyl)porphyrin tetrasodium salt (CuTPPS) = 4 μ M] in the presence of L-3,4-dihydroxyphenylalanine (L-DOPA) 0.5 mM (**A**) and D-3,4-dihydroxyphenylalanine (D-DOPA) 0.5 mM (**B**) as prepared (dotted black curves) and after 24 h, 3, 7, and 15 days (red, green, wine, and blue curves in that order).

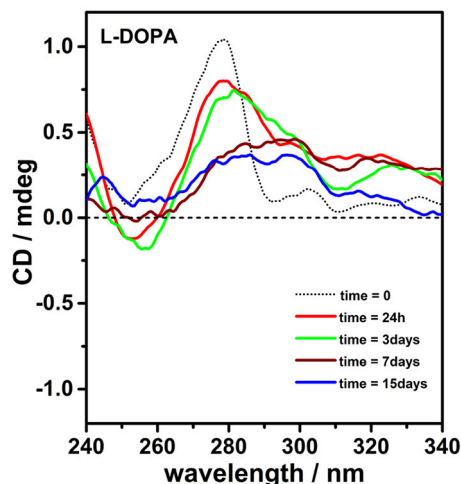


FIGURE 4 | Circular dichroism spectra of L-3,4-dihydroxyphenylalanine (L-DOPA; 0.5 mM) alone in phosphate buffered saline (PBS) buffer (pH = 7.4, 298K) as prepared (dotted black curve) and after 24 h, 3, 7, and 15 days (red, green, wine, and blue curves, respectively).

optics was also measured in order to evaluate the cross-talk contribution to CD.

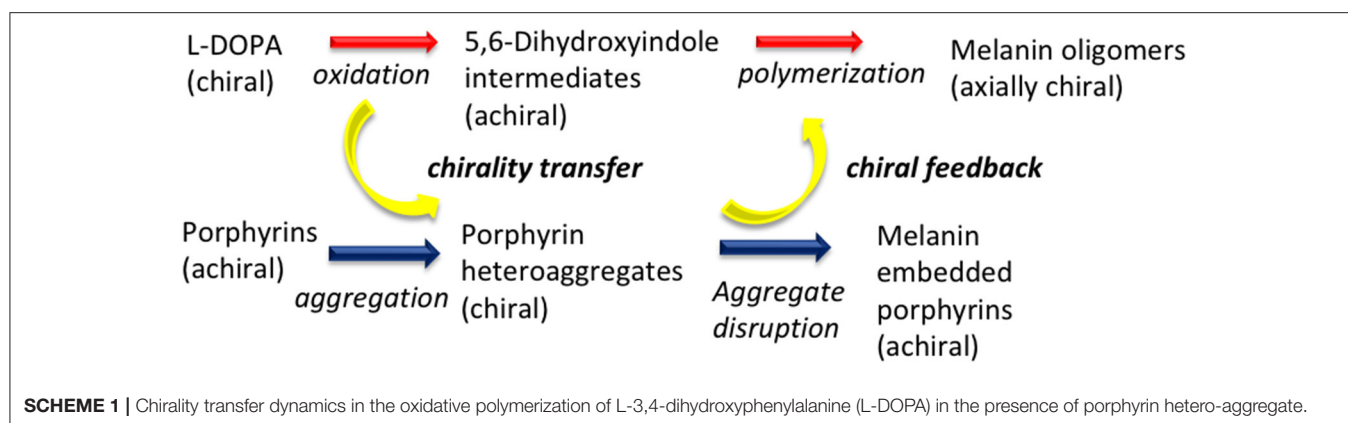
RESULTS AND DISCUSSIONS

In PBS buffer (pH = 7.4), the formation of porphyrin hetero-aggregates from equimolar amounts of tetra-cationic H_2T4 and

tetra-anionic CuTPPS was apparent by both the hypochromic effect and band broadening in the Soret region, as reported in UV/Vis spectrum (**Supplementary Figure 1**). In the absence of chiral inducers in solution and under ultraclean conditions, the building of achiral supramolecular structures, as expected, was denoted by zero optical activity in the porphyrin hetero-aggregate absorption region (**Supplementary Figure 1** inset).

The construction of chiral multicomponent systems requires precise hierarchical rules (Elemans et al., 2003), whereby to prepare chiral porphyrin hetero-aggregates, cationic porphyrin H_2T4 (4 μ M) was to be added to a PBS solution of L-DOPA (0.5 mM) followed by the anionic counterpart CuTPPS (4 μ M). UV/Vis spectra confirm the formation of porphyrin hetero-aggregate, showing a hypochromic effect and broadening of the Soret bands (**Supplementary Figure 2**). Noteworthy in the CD spectra, both a positive single Cotton effect of L-DOPA at about 280 nm and an induced bisignate CD signal in visible region, due to chiral exciton coupling of two porphyrin chromophores in hetero-aggregates, were observed (**Figure 2**). Mirror image was recorded when D-DOPA was used in place of levodopa, confirming that the CD signal in the porphyrin absorption region was induced by the interaction with DOPA via a chirality transfer process (**Figure 2**).

The solutions containing chiral porphyrin hetero-aggregates and single DOPA enantiomers were incubated for 2 weeks in plastic cuvettes rather than in quartz cuvettes in order to minimize the sticking of DOPA-derived melanin products onto cuvette walls. Although the oxidative polymerization of DOPA evolved slowly in PBS buffer at pH 7.4 as is usually the case with catechol and catecholamine compounds (Bernsmann



et al., 2011), after 2 weeks, significant variations in the DOPA absorption and CD spectra were observed. CD and UV spectra of the sample solutions were recorded after 24 h, 3, 7, and 15 days to follow the evolution of DOPA polymerization. In comparison with the initial situation, main changes observed concerned: *i*) the loss of the induced CD signal attributed to the porphyrin hetero-aggregates and, simultaneously, *ii*) a marked change in the dichroic signal of DOPA (Figure 3, Supplementary Figure 3).

Since the chirality transfer mechanism implies a close-range contact between chiral inducer and achiral building blocks (Borovkov et al., 2001; Mammana et al., 2007; Zeng et al., 2009; Randazzo et al., 2019; Ustrnul et al., 2019), the disappearance of the induced chirality may be associated to a de-aggregation of the porphyrin hetero-aggregate owing to the polymerization of DOPA and the associated loss of chirality. In line with this conclusion, the UV/Vis spectra of incubated hetero-aggregates evolved with the growth of the CuTPPS Soret band ($\lambda_{max} = 412$ nm) (Supplementary Figure 3), whereas, conversely, no detectable band associated with H₂T4 ($\lambda_{max} = 423$ nm) was observed (Supplementary Figure 3 inset) presumably due to embedment into the developing melanin matrix whose carboxylate residues are deprotonated (thus anionic charged) at pH value of PBS buffer. Indeed, adding acid solution to melanin precipitate (separated from the solution) in order to protonate the carboxylate residues, a band at 450 nm, ascribable to protonated form of H₂T4, was detected (Supplementary Figure 4). These spectroscopic data suggested that the porphyrin hetero-aggregate in PBS at high ionic strength does not exhibit similar stability as previously demonstrated in water (Mammana et al., 2007; Gaeta et al., 2016). It is likely that ionic strength modulates electrostatic interactions between opposite-charged porphyrins, affecting the stability of the hetero-aggregate in PBS.

Remarkably, drastic changes in the CD signals at 450–500 nm are observed with time (1 week timescale; Figure 3), which are paired to a later increase of the signal at 280 nm (2 weeks timescale). Such profile evolution is a clear signature of the generation of asymmetric structures, likely driven by chirally imprinted porphyrin hetero-aggregates during melanin synthesis, while the original chiral information from DOPA was completely consumed because of its conversion into

5,6-dihydroxyindoles. Noteworthy, contributions from LD are negligible; however, the possibility that a component of differential scattering might affect the measurements owing to the presence of melanin particles cannot be ruled out.

To support the above conclusions, the spectroscopic behavior of L-DOPA in PBS buffer was monitored in the absence of porphyrins. The progress of the oxidative polymerization was denoted by the simultaneous decrease of the absorbance ($\lambda_{max} = 280$ nm) and related CD signal of L-DOPA (Figure 4, Supplementary Figure 5). After several days, the final dark solution did not display almost any residual chirality suggesting the formation of achiral melanin.

Further evidences of the role played by porphyrin hetero-aggregate as chiral templating agent of melanin oligomers have been gained performing a clear-cut experiment, reversing the order of addition of the components. In detail, we added L-DOPA to a solution of preformed achiral porphyrin hetero-aggregate (Supplementary Figure 6). After 1 week, the CD spectrum of L-DOPA looked similar to the CD spectrum of L-DOPA alone in PBS (Supplementary Figure 6 inset), confirming that chiral porphyrin hetero-aggregate plays a key role in inducing chiral melanin oligomer formation.

To conclude, these results disclose a rare example of temporary chiral mediation in which a chirally imprinted aggregate is decomposed while serving in turn as template for the chiral imprinting of developing oligomer aggregates from non-chiral decomposition products of a chiral precursor (Scheme 1).

These results open a new promising area of investigation on the organization of melanin pigments with applications ranging from biology and medicine to nanotechnology and material science.

DATA AVAILABILITY STATEMENT

The raw data supporting the conclusions of this article will be made available by the authors, without undue reservation.

AUTHOR CONTRIBUTIONS

AD^U, Md^I, AP, and RP contributed to the conception and design of the study. Experimental work was carried out by

MG, RR, VV, and NM (CD, UV/Vis, LD, differential scattering) under supervision of AD'U. MG wrote the manuscript and prepared images with contributions of AD'U, Md'I, and AP. All authors participated in the analysis and discussion of obtained results.

FUNDING

Ministero dell'Istruzione, dell'Università e della Ricerca (MIUR) PRIN project code: 2017YJMPZN-005; programma ricerca di

ateneo UNICT 2016-18 linea 1 and 2; Dipartimento di Scienze Chimiche finanziamento giovani ricercatori 2020; programma ricerca di ateneo UNICT 2020-2022 linea 2; Fondi di Ateneo 2020-2022, Università di Catania, linea Open Access.

SUPPLEMENTARY MATERIAL

The Supplementary Material for this article can be found online at: <https://www.frontiersin.org/articles/10.3389/fchem.2020.616961/full#supplementary-material>

REFERENCES

- Angelini, N., Micali, N., Mineo, P., Scamporrino, E., Villari, V., and Vitalini, D. (2005). Uncharged water-soluble Co(II) - Porphyrin: a receptor for aromatic α -amino acids. *J. Phys. Chem. B* 109, 18645–18651. doi: 10.1021/jp052408u
- Bellacchio, E., Lauceri, R., Gurrieri, S., Scolaro, L. M., Romeo, A., and Purrello, R. (1998). Template-imprinted chiral porphyrin aggregates. *J. Am. Chem. Soc.* 120, 12353–12354. doi: 10.1021/ja9820893
- Bernsmann, F., Ball, V., Addiego, F., Ponche, A., Michel, M., Gracio, J. J. D. A., et al. (2011). Dopamine-melanin film deposition depends on the used oxidant and buffer solution. *Langmuir* 27, 2819–2825. doi: 10.1021/la104981s
- Borovkov, V. V., Lintuluoto, J. M., and Inoue, Y. (2001). Supramolecular chirogenesis in zinc porphyrins: mechanism, role of guest structure, and application for the absolute configuration determination. *J. Am. Chem. Soc.* 123, 2979–2989. doi: 10.1021/ja0032982
- Borovkov, V. V., Lintuluoto, J. M., and Inoue, Y. (2002a). Stoichiometry-controlled supramolecular chirality induction and inversion in bisporphyrin systems. *Org. Lett.* 4, 169–171. doi: 10.1021/ol101687oi
- Borovkov, V. V., Lintuluoto, J. M., Sugiura, M., Inoue, Y., and Kuroda, R. (2002b). Remarkable stability and enhanced optical activity of a chiral supramolecular bis-porphyrin tweezer in both solution and solid state. *J. Am. Chem. Soc.* 124, 11282–11283. doi: 10.1021/ja026884z
- Charalambidis, G., Georgilis, E., Panda, M. K., Anson, C. E., Powell, A. K., Doyle, S., et al. (2016). A switchable self-assembling and disassembling chiral system based on a porphyrin-substituted phenylalanine-phenylalanine motif. *Nat. Commun.* 7, 1–11. doi: 10.1038/ncomms12657
- De Luca, G., Romeo, A., Scolaro, L. M., and Pasternack, R. F. (2010). Conformations of a model protein revealed by an aggregating CuII porphyrin: sensing the difference. *Chem. Commun.* 46, 389–391. doi: 10.1039/B918433C
- Della Vecchia, N. F., Avolio, R., Alfè, M., Errico, M. E., Napolitano, A., and d'Ischia, M. (2013). Building-block diversity in polydopamine underpins a multifunctional eumelanin-type platform tunable through a quinone control point. *Adv. Funct. Mater.* 23, 1331–1340. doi: 10.1002/adfm.201202127
- d'Ischia, M., Napolitano, A., Ball, V., Chen, C. T., and Buehler, M. J. (2014). Polydopamine and eumelanin: from structure-property relationships to a unified tailoring strategy. *Acc. Chem. Res.* 47, 3541–3550. doi: 10.1021/ar500273y
- d'Ischia, M., Wakamatsu, K., Napolitano, A., Briganti, S., Garcia-Borrón, J. C., Kovacs, D., et al. (2013). Melanins and melanogenesis: methods, standards, protocols. *Pigment Cell Melanoma Res.* 26, 616–633. doi: 10.1111/pcmr.12121
- Edge, R., d'Ischia, M., Land, E. J., Napolitano, A., Navaratnam, S., Panzella, L., et al. (2006). Dopaguanone redox exchange with dihydroxyindole and dihydroxyindole carboxylic acid. *Pigment Cell Res.* 19, 443–450. doi: 10.1111/j.1600-0749.2006.00327.x
- Elemans, J. A. A. W., Rowan, A. E., and Nolte, R. J. M. (2003). Mastering molecular matter. Supramolecular architectures by hierarchical self-assembly. *J. Mater. Chem.* 13, 2661–2670. doi: 10.1039/B304972H
- Gaeta, M., Oliveri, I., Pietro, Fragalà, M. E., Failla, S., D'Urso, A., Di Bella, S., et al. (2016). Chirality of self-assembled achiral porphyrins induced by chiral Zn(II) Schiff-base complexes and maintained after spontaneous dissociation of the templates: a new case of chiral memory. *Chem. Commun.* 52, 8518–8521. doi: 10.1039/C6CC04018G
- ateneo UNICT 2016-18 linea 1 and 2; Dipartimento di Scienze Chimiche finanziamento giovani ricercatori 2020; programma ricerca di ateneo UNICT 2020-2022 linea 2; Fondi di Ateneo 2020-2022, Università di Catania, linea Open Access.
- Gaeta, M., Raciti, D., Randazzo, R., Gangemi, C. M. A., Raudino, A., D'Urso, A., et al. (2018). Chirality enhancement of porphyrin supramolecular assembly driven by a template preorganization effect. *Angew. Chemie Int. Ed.* 57, 10656–10660. doi: 10.1002/anie.201806192
- Haneda, K., and Watanabe, S. (1971). Synthesis of L-3,4-dihydroxyphenylalanine from L-tyrosine by microorganisms. *Appl. Microbiol.* 22, 721–722. doi: 10.1128/AEM.22.4.721-722.1971
- Helmich, F., Lee, C. C., Schenning, A. P. H. J., and Meijer, E. W. (2010). Chiral memory via chiral amplification and selective depolymerization of porphyrin aggregates. *J. Am. Chem. Soc.* 132, 16753–16755. doi: 10.1021/ja1077602
- Ito, S. (2003). IFPCS presidential lecture: a chemist's view of melanogenesis. *Pigment Cell Res.* 16, 230–236. doi: 10.1034/j.1600-0749.2003.00037.x
- Ito, S., and Wakamatsu, K. (2007). "Chemistry of Melanins," in *The Pigmentary System: Physiology and Pathophysiology: 2nd edn*, eds J. J. Nordlund, R. E. Boissy, V. J. Hearing, R. A. King, W. S. Oetting, J.-P. Ortonne (Oxford: Blackwell Publishing Ltd), 282–310.
- Ito, S., and Wakamatsu, K. (2008). Chemistry of mixed melanogenesis - pivotal roles of dopaquinone. *Photochem. Photobiol.* 84, 582–592. doi: 10.1111/j.1751-1097.2007.00238.x
- Ito, S., Wakamatsu, K., d'Ischia, M., and Napolitano, A. P. (2011). "Structure of melanins," in *Melanins and Melanosomes: Biosynthesis, Biogenesis, Physiological, and Pathological Functions*, eds J. Riley, P. A. Borovansky (Weinheim: Wiley-VCH Verlag GmbH), 167–181. Available at: <https://onlinelibrary.wiley.com/doi/pdf/10.1002/9783527636150#page=185> (accessed October 7, 2020).
- Lauceri, R., Fasciglione, G. F., D'Urso, A., Marini, S., Purrello, R., and Coletta, M. (2008). Kinetic investigation of porphyrin interaction with chiral templates reveals unexpected features of the induction and self-propagation mechanism of chiral memory. *J. Am. Chem. Soc.* 130, 10476–10477. doi: 10.1021/ja803426q
- Mammana, A., D'Urso, A., Lauceri, R., and Purrello, R. (2007). Switching off and on the supramolecular chiral memory in porphyrin assemblies. *J. Am. Chem. Soc.* 129, 8062–8063. doi: 10.1021/ja071447b
- Marchiosi, R., Soares, A. R., Abrahão, J., dos Santos, W. D., and Ferrarese-Filho, O. (2020). "L-DOPA and dopamine in plant metabolism," in *Neurotransmitters in Plant Signaling and Communication. Signaling and Communication in Plants*, eds F. Baluška, S. Mukherjee, A. Ramakrishna (Cham: Springer), 141–167.
- Mason, H. S., and Wright, C. I. (1949). The chemistry of melanin; oxidation of dihydroxyphenylalanine by tyrosinase. *J. Biol. Chem.* 180, 235–247.
- Micali, N., Vybornyi, M., Mineo, P., Khorev, O., Häner, R., and Villari, V. (2015). Hydrodynamic and thermophoretic effects on the supramolecular chirality of pyrene-derived nanosheets. *Chem. Eur. J.* 21, 9505–9513. doi: 10.1002/chem.201500932
- Occhiuto, I. G., Samperi, M., Trapani, M., De Luca, G., Romeo, A., Pasternack, R. F., et al. (2015). Aggregates of a cationic porphyrin as supramolecular probes for biopolymers. *J. Inorg. Biochem.* 153, 361–366. doi: 10.1016/j.jinorgbio.2015.09.013
- Onouchi, H., Miyagawa, T., Morino, K., and Yashima, E. (2006). Assisted formation of chiral porphyrin homoaggregates by an induced helical poly(phenylacetylene) template and their chiral memory. *Angew. Chem.* 118, 2441–2444. doi: 10.1002/ange.200504162
- Panzella, L., Ebato, A., Napolitano, A., and Koike, K. (2018). The late stages of melanogenesis: exploring the chemical facets and the application opportunities. *Int. J. Mol. Sci.* 19, 1753. doi: 10.3390/ijms19061753

- Pezzella, A., Napolitano, A., D'Ischia, M., and Protà, G. (1996). Oxidative polymerisation of 5,6-dihydroxyindole-2-carboxylic acid to melanin: a new insight. *Tetrahedron* 52, 7913–7920. doi: 10.1016/0040-4020(96)00362-6
- Pezzella, A., Vogna, D., and Protà, G. (2003). Synthesis of optically active tetrameric melanin intermediates by oxidation of the melanogenic precursor 5,6-dihydroxyindole-2-carboxylic acid under biomimetic conditions. *Tetrahedron Asymmetry* 14, 1133–1140. doi: 10.1016/S0957-4166(03)00156-3
- Protà, G. (1995). "The chemistry of melanins and melanogenesis," in *Fortschritte der Chemie organischer Naturstoffe. Progress in the Chemistry of Organic Natural Products. Progrès Dans la Chimie des Substances Organiques Naturelles*, eds W. Herz, G.W. Kirby, R.E. Moore, W. Steglich, C. Tamm (Vienna: Springer), 93–148.
- Rananaware, A., La, D. D., Al Kobaisi, M., Bhosale, R. S., and Bhosale, S. V. (2016). Controlled chiral supramolecular assemblies of water soluble achiral porphyrins induced by chiral counterions. *Chem. Commun.* 52, 10253–10256. doi: 10.1039/C6CC04427A
- Randazzo, R., Gaeta, M., Gangemi, C. M. A., Fragalà, M. E., Purrello, R., and D'Urso, A. (2019). Chiral recognition of L- and D-amino acid by porphyrin supramolecular aggregates. *Molecules* 24, 84. doi: 10.3390/molecules24010084
- Raper, H. S. (1927). The tyrosinase-tyrosine reaction: production from tyrosine of 5: 6-dihydroxyindole and 5:6-dihydroxyindole-2-carboxylic acid-the precursors of melanin. *Biochem. J.* 21, 89–96. doi: 10.1042/bj0210089
- Ryu, J. H., Messersmith, P. B., and Lee, H. (2018). Polydopamine surface chemistry: a decade of discovery. *ACS Appl. Mater. Interfaces* 10, 7523–7540. doi: 10.1021/acsami.7b19865
- Simon, J. D., Peles, D., Wakamatsu, K., and Ito, S. (2009). Current challenges in understanding melanogenesis: bridging chemistry, biological control, morphology, and function. *Pigment Cell Melanoma Res.* 22, 563–579. doi: 10.1111/j.1755-148X.2009.00610.x
- Slominski, A., Tobin, D. J., Shibahara, S., and Wortsman, J. (2004). Melanin pigmentation in mammalian skin and its hormonal regulation. *Physiol. Rev.* 84, 1155–1228. doi: 10.1152/physrev.00044.2003
- Slominski, A., Zmijewski, M. A., and Pawelek, J. (2012). L-tyrosine and L-dihydroxyphenylalanine as hormone-like regulators of melanocyte functions. *Pigment Cell Melanoma Res.* 25, 14–27. doi: 10.1111/j.1755-148X.2011.00898.x
- Toyofuku, K., Alam, M. A., Tsuda, A., Fujita, N., Sakamoto, S., Yamaguchi, K., et al. (2007). Amplified chiral transformation through helical assembly. *Angew. Chemie - Int. Ed.* 46, 6476–6480. doi: 10.1002/anie.200701668
- Uemori, Y., Munakata, H., Kitazawa, S., Osada, A., and Imai, H. (2012). Optically active J-aggregate formed from water-soluble porphyrin with phenylalanine. *J. Porphyr. Phthalocyanines* 16, 1285–1292. doi: 10.1142/S1088424612501441
- Ustrnul, L., Kaabel, S., Burankova, T., Martónova, J., Adamson, J., Konrad, N., et al. (2019). Supramolecular chirogenesis in zinc porphyrins by enantiopure hemicucurbit[n] urils (n = 6, 8). *Chem. Commun.* 55, 14434–14437. doi: 10.1039/C9CC07150D
- Zeng, L., He, Y., Dai, Z., Wang, J., Cao, Q., and Zhang, Y. (2009). Chiral induction, memory, and amplification in porphyrin homoaggregates based on electrostatic interactions. *Chemphyschem* 10, 954–962. doi: 10.1002/cphc.200800810
- Zhao, L., Liu, M., Li, S., Li, A., An, H., Ye, H., et al. (2015). Aggregation and supramolecular chirality of 5,10,15,20-tetrakis-(4-sulfonatophenyl)-porphyrin on an achiral poly(2-(dimethylamino)ethyl methacrylate)-grafted ethylene-vinyl alcohol membrane. *J. Mater. Chem. C* 3, 3650–3658. doi: 10.1039/C5TC00037H

Conflict of Interest: The authors declare that the research was conducted in the absence of any commercial or financial relationships that could be construed as a potential conflict of interest.

Copyright © 2020 Gaeta, Randazzo, Villari, Micali, Pezzella, Purrello, d'Ischia and D'Urso. This is an open-access article distributed under the terms of the Creative Commons Attribution License (CC BY). The use, distribution or reproduction in other forums is permitted, provided the original author(s) and the copyright owner(s) are credited and that the original publication in this journal is cited, in accordance with accepted academic practice. No use, distribution or reproduction is permitted which does not comply with these terms.



Polarimetric Measurements of Surface Chirality Based on Linear and Nonlinear Light Scattering

Ankur Gogoi¹, Surajit Konwer² and Guan-Yu Zhuo^{3,4*}

¹Department of Physics, Jagannath Barooah College, Jorhat, India, ²Department of Chemistry, Dibrugarh University, Dibrugarh, India, ³Institute of New Drug Development, China Medical University, Taichung, Taiwan, ⁴Integrative Stem Cell Center, China Medical University Hospital, Taichung, Taiwan

OPEN ACCESS

Edited by:

HiroYuki Miyake,
Department of Chemistry, Faculty of
Science, Osaka City University, Japan

Reviewed by:

Pengyao Xing,
Shandong University, China
Amelia Pilar Rauter,
University of Lisbon, Portugal

*Correspondence:

Guan-Yu Zhuo
zhuo0929@mail.cmu.edu.tw

Specialty section:

This article was submitted to
Supramolecular Chemistry,
a section of the journal
Frontiers in Chemistry

Received: 29 September 2020

Accepted: 31 December 2020

Published: 10 February 2021

Citation:

Gogoi A, Konwer S and Zhuo G-Y
(2021) Polarimetric Measurements of
Surface Chirality Based on Linear and
Nonlinear Light Scattering.
Front. Chem. 8:611833.
doi: 10.3389/fchem.2020.611833

A molecule, molecular aggregate, or protein that cannot be superimposed on its mirror image presents chirality. Most living systems are organized by chiral building blocks, such as amino acids, peptides, and carbohydrates, and any change in their molecular structure (i.e., handedness or helicity) alters the biochemical and pharmacological functions of the molecules, many of which take place at surfaces. Therefore, studying surface chirogenesis at the nanoscale is fundamentally important and derives various applications. For example, since proteins contain highly ordered secondary structures, the intrinsic chirality can be served as a signature to measure the dynamics of protein adsorption and protein conformational changes at biological surfaces. Furthermore, a better understanding of chiral recognition and separation at bio-nanointerfaces is helpful to standardize chiral drugs and monitor the synthesis of adsorbents with high precision. Thus, exploring the changes in surface chirality with polarized excitations would provide structural and biochemical information of the adsorbed molecules, which has led to the development of label-free and noninvasive measurement tools based on linear and nonlinear optical effects. In this review, the principles and selected applications of linear and nonlinear optical methods for quantifying surface chirality are introduced and compared, aiming to conceptualize new ideas to address critical issues in surface biochemistry.

Keywords: membrane, circular dichroism, optical activity, optical rotation, chirality, linear dichroism, second-harmonic generation, sum-frequency generation

INTRODUCTION

Chirality of molecular architectures has become a subject of increasing interest to the chemical, biological, and pharmaceutical science community, largely because of its immense importance in understanding the structure and function of biological systems (Green et al., 2016; Jiang et al., 2017b; Gogoi et al., 2019; Zhao et al., 2020). Chiral compounds or molecules occur in the form of two stereoisomers that are nonsuperimposable mirror images of each other, known as enantiomers. Of particular interest is the homochirality of the left-handed amino acids and right-handed sugars which are the building blocks of the key molecules of life: proteins and nucleic acids, respectively. In fact, such homochiral selectivity is intrinsically linked to all the fundamental biochemical processes of life, including molecular recognition, synthesis, and replication, and is indeed one of the biggest enigmas of contemporary science (Toxvaerd, 2009; Blackmond, 2011; Walker, 2011; Wang et al., 2019a; Zhao et al., 2020). As far as the fullest exploitation of the unique advantages of surfaces at the nanoscale, especially in the fields of enantiomeric recognition and separation is concerned, there is a

pressing need of having a molecular level understanding about how does a (chiral) molecule get adsorbed or bind itself onto a surface, membrane, or interface; whether any kind of surface modification takes place during this process and how much change of the conformation of the (chiral) molecule takes place on the surface (Gautier, 2008). Such studies are also important to shed light on the evolution of chirality across molecular to macroscopic length scales.

On the other hand, a pair of enantiomers of a chiral compound is very difficult to distinguish from each other since they possess exactly same scalar physiochemical properties, for example, density, molecular weight, melting points, boiling points, electronic and vibrational frequencies, reaction rates, and solubilities. Fortunately, their vectorial properties are an exception in the sense that these properties are sign-inverted, and the opposite enantiomers exhibit remarkably distinguishable properties when they interact with other chiral materials (e.g., other biological material, synthetic compounds, or drugs) or polarized light (Tester and Karkalas, 2003; Brunner, 2004; Tang and Cohen, 2010; Lewis, 2013). For example, enantiomers of a chiral molecule have the ability to rotate a plane polarized light by equal amounts, but in opposite directions, leading to optical rotation spectra which are mirror images of each other (Tranter, 2012; Qiu et al., 2016). Depending on the rotation produced in an ideal environment, a chiral molecule can be designated as dextrorotatory (if the rotation is positive or right-handed or clockwise) or levorotatory (if the rotation is negative or left-handed or counterclockwise) enantiomer. This property of a chiral molecule is also known as circular birefringence (CB) since it occurs due to the different indices of refraction for right circularly polarized (RCP) light and left circularly polarized (LCP) light (Liehr, 1964). Likewise, a chiral substance also possesses different absorption cross sections for RCP and LCP, an effect known as circular dichroism (CD) (Fischer and Hache, 2005; Tang and Cohen, 2010). Manifestation of molecular chirality can also be observed in other forms of optical activities, such as Raman optical activity (ROA) and circularly polarized luminescence (CPL).

Admittedly, molecular chiroptical signals are usually weak due to the large difference between the molecular scale and the probing wavelength. Therefore, in addition to molecular chirality, optical activities at surfaces (equivalent to interfaces in this review) are gaining much attention due to the possibility to acquire dramatically enhanced chiroptical interactions and probe chirality and/or changes in chirality at such surfaces (Byers et al., 1994a; Verbiest et al., 1995; Hicks and Petralli-Mallow, 1999; Kneipp et al., 2010; Ben-Moshe et al., 2013). Such studies are also important for their potential to elucidate the underlying process of chiral recognition at surfaces (Ernst, 2006; Gogoi et al., 2019). Although the linear optical activities, as mentioned above, have been used to study surface chirality, they are often limited by surface specificity (or monolayer sensitivity) and concentration, resulting in weak response, that is, surface insensitive. On purpose of compensating the weaknesses of linear optical methods, nonlinear optical methods, including second-harmonic generation (SHG) and sum-frequency generation (SFG), are proposed due to the characteristics of

label-free, noninvasive detection and surface specificity (Shen, 1984; Byers et al., 1994a; Shen, 1994; Shen, 1996; Vogel, 1996; Fischer and Buckingham, 1998; Verbiest et al., 1998). SHG and SFG are contrast mechanisms exclusively sensitive and specific to noncentrosymmetric structures, for example, surface, molecular chirality, and chiral molecules adsorbed on a surface. Thus, using SHG or SFG to study surface chirality is a background-free probe because an achiral liquid cannot contribute to the signal, which is named as C-SHG or C-SFG hereafter. Unlike the OA effects measured by linear optical methods that are mainly contributed from magnetic dipole or quadrupole interactions, C-SHG and C-SFG are electric dipole-allowed transitions (Petralli-Mallow et al., 1993; Byers et al., 1994a; Ji and Shen, 2006), manifesting that they are correlated with a unique molecular structure and a polarized excitation (Simpson, 2002). For this reason, the measurement techniques are designed with specific polarization settings and experimental geometry. Combined with the structural requirements for C-SHG and C-SFG, related techniques are well applicable to selectively probe surface chirality.

Since there are few articles on systematic discussion and comparisons for the abovementioned methods used for the interrogation of surface chirality, in this review, a clear and comprehensive view of polarimetric measurements of surface chirality is presented using several classic articles. The content is started from the linear optical activities, for example, CB, CD, and ROA, and then provides a closer look at the nonlinear optical methods, for example, C-SHG and C-SFG, and their applications. We will deliberately concentrate on the applications of linear and nonlinear chiroptical methods, instead of the development of theory, in studying the chirality at liquid, solid, film, and nanoparticle (NP) surfaces, air/liquid, liquid/liquid, and solid/liquid interfaces, membranes, etc. in the following sections.

Linear Optics on Surface Chirality

Optical techniques offer unique opportunities for the study of multiscale chirality ranging from molecules to surfaces. Notably, the discovery of chiroptical activities dates back to 1848 when Pasteur observed chiral asymmetry in the form of optical rotation in the isomers of tartaric acid (Flack, 2009; Gal, 2013). Over the past century, the constant evolution of chiroptical techniques, such as, optical rotatory dispersion (ORD), electronic circular dichroism (ECD), vibrational circular dichroism (VCD), and Raman optical activity (ROA), has provided unprecedented insight into the chiral signature of molecules, monolayers, or surfaces, especially in the fields of pharmaceutical, agrochemical, and flavor and fragrance technology (Collins et al., 2017; Ozcelik et al., 2020). In addition, there are few other linear optical techniques, such as Rayleigh optical activity (Andrews, 1980; Hoffman et al., 1994; Cameron and Barnett, 2014), circular differential Mie scattering (Yoo and Park, 2015), and Mueller matrix ellipsometry (Podraza et al., 2008), which are used for the interrogation of chiral structures. As yet, despite showing promising results, these techniques have not found widespread applications for the study of surface chirality. This section will cover the fundamentals and highlight the recent applications of

the linear chiroptical techniques that are widely used for interrogating chiral surfaces.

Optical Rotation and Optical Rotatory Dispersion

The optical rotation by a chiral substance is probably the most commonly known chiroptical activity, which is actually the consequence of circular birefringence (CB). Briefly, when a beam of plane polarized light (which may be considered as the resultant of two opposite circularly polarized components of same wavelength and intensity) enters a (optically active) chiral medium, the RCP and LCP experiences different indices refraction resulting in a phase shift between the orthogonal polarizations. Consequently, both the RCP and LCP components will travel at different velocities through the chiral medium, thereby continuously rotating the plane of their resultant electric field vector, a phenomenon similar to linear birefringence (Liehr, 1964; Snatzke, 1968; Kumar and Liz-Marzán, 2019). Now since refractive index is a function of wavelength of the incident light (optical dispersion), optical rotation is also dispersive in nature. Importantly, when measured as a function of incident wavelength, OR is termed as optical rotatory dispersion (ORD). Notably, OR and ORD are represented by specific rotation, α , and molar rotation, M , respectively (Edwards and Jenkinson, 2012).

OR and ORD has been extensively used for stereochemical assignment, determination of enantiomeric purity of products emerging from asymmetric synthesis, glucose concentration, studying molecular structures (particularly secondary structures of large molecules like proteins), etc (Djerassi et al., 1956; Cantor et al., 1966; Magar, 1968; Snatzke, 1968; Chen et al., 1972; Tranter, 2012; Stark et al., 2019). From the instrumentation point of view, several efficient methods for the measurement of optical rotatory dispersion spectrum have been reported (Castiglioni et al., 2011; Han et al., 2014; Jiang et al., 2017a; Goldberg and Weissman, 2019; Liu et al., 2020). Most recently, a novel technique by combining surface plasmon resonance (SPR) and weak value amplification (WVA) was used for high resolution measurements of extremely small optical rotation of chiral molecules in dilute solutions (Xu et al., 2020). In addition to static ORD, several time-resolved ORD experiments have also been demonstrated (Shapiro et al., 1995; Chen et al., 2003; Chen et al., 2007). A number of models have also been developed in the recent past to theoretically predict OR and ORD (Polavarapu, 2002).

Apart from its application in studying molecular chirality, OR and ORD have also been used to study the chirality of nanostructures, membranes, and surfaces. For example, Lenard and Singer, (1966) conducted room temperature ORD measurements to elucidate the structure of membranes made of human red blood cells and of *B. subtilis*. The obtained spectra revealed that a part of the membrane protein is in a helical conformation, while the remainder was primarily in a random coil form. Green et al., (1973) studied the transfer or exchange of cholesterol from phospholipid molecules in liposomes to membranes of human erythrocyte by measuring ORD curves.

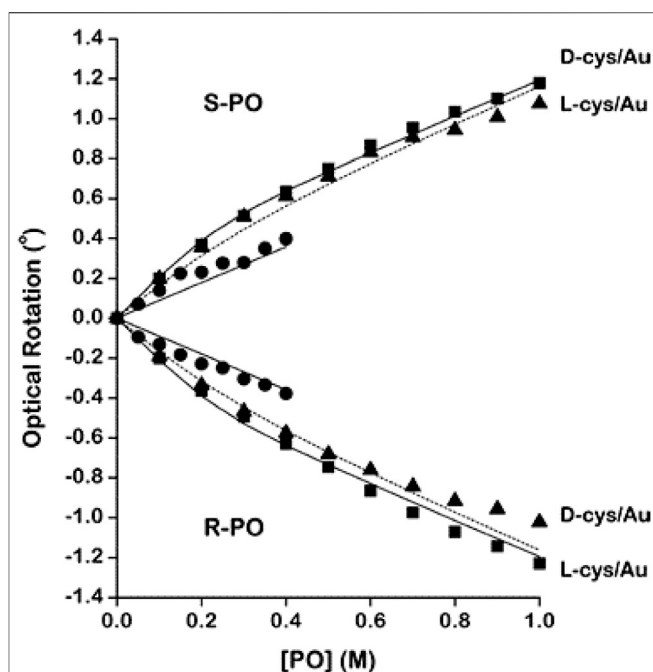


FIGURE 1 | Optical rotation by (R)- and (S)-PO in pure aqueous solutions (●) and in solutions containing Au nanoparticles modified with D- and L-cysteine. The data from the solutions containing the heterochiral pairs ((R)-PO/L-cys and (S)-PO/D-cys) are marked with solid squares (■). The data from solutions containing the homochiral pairs ((R)-PO/D-cys and (S)-PO/L-cys) are marked with solid triangles (▲). The solid and dashed lines mark the fits of the adsorption model described in the text. The deviations between the data for the homochiral and the heterochiral pairs are indicative of the enantiospecific interaction of (R)- and (S)-PO with the chiral Au nanoparticles. The figure and caption have been adapted with permission from Shukla et al., (2010), Copyright © 2010 American Chemical Society.

In a recent work, Esposito et al., (2015) experimentally compared the ORD of different helical nanostructures, such as single helical nanowires (SHN), closely packed single helical nanowires (CP-SHN), and triple helical nanowires (THN). The group observed ORD up to 8° for THN which was independent of the sample orientation with respect to the incoming linear polarization in a broad spectrum ranging from 800 nm to 1050 nm. Conversely, orientation and wavelength-dependent optical activities were observed in cases of SHN. Such tailored chiroptical properties are particularly relevant in the fields of enantio-detection in medical and biological sciences as well as nanophotonics, spintronics, etc. In another work, the ability of polarized near-field scanning optical microscopy (NSOM) in determining the near-field OA of chiral crystal surfaces of enantiomerically pure amino acids was demonstrated (Dressler et al., 2007). Furthermore, Shukla et al. (Shukla et al., 2010; Shukla et al., 2014) used optical rotation measurements to demonstrate the enantioselective adsorption of chiral probes such as R- or S-propylene oxide (PO) by Au NPs coated with D- or L-cysteine (cys). Impressively, the group fabricated chiral Au NPs by modifying the surface with racemic cys or enantiomerically pure D- or L-cys. Subsequently, polarimetry was used to probe the adsorption of racemic PO and enantiopure

R- or S-PO onto these modified Au NPs (Shukla et al., 2010). **Figure 1** shows the OR measurements during the interaction of surface modified Au NPs with R- or S-PO. Moreover, the group studied the influence of wavelength, temperature, and NP size on the magnitudes of optical rotation measurements obtained from the enantiospecific interaction of D- or L-cys-modified Au NPs during addition of racemic (both R-PO and S-PO) PO (Shukla et al., 2015). Advancing their prior works, the group further exploited the capability of OR measurements to demonstrate the enantioselective binding of R- or S-propranolol, one of the well-known pharmaceuticals, onto the chirally modified surfaces of tetrahedral (THH, 24-sided) Au NPs (Shukla et al., 2016). Chirality of chitosan (a type of biocompatible and biodegradable chiral aminopolysaccharide), on the other hand, has attracted much attention in the recent years due to their potential application in medicine, pharmacology, and tissue engineering (Croisier and Jérôme, 2013; Gegel et al., 2018a; Gegel et al., 2018b). For instance, Shipovskaya et al., (2017) reported the optical activity possessed by films of chitosan having a broad range of molecular masses by conducting ORD measurements. The group observed the modulus of optical activity [α] of the films is controlled mainly by chemical structure and molecular arrangement in the film. In addition, significant variation in the measured values of [α] of thermally modified chitosan films was also observed in the study. Following this, the group further reported the optical activity anisotropy of chitosan films (Shipovskaya et al., 2019).

(Electronic) Circular Dichroism

Circular dichroism (CD) is the manifestation of the differential absorption of RCP and LCP by a chiral media. It can occur in all wavelength ranges resulting in electronic circular dichroism (ECD) or vibrational circular dichroism (VCD), depending whether the probing wavelength is in the ultraviolet (UV), visible, or infrared (IR) spectral range, respectively (Zsila, 2010; Tranter, 2012). Notably, OR/ORD and CD are complementary to each other and are interwoven through Kramers–Kronig relations (Emeis et al., 1967; Krykunov et al., 2006; Kumar and Liz-Marzán, 2019). Nevertheless, there is a basic difference between OR/ORD and CD from classical electromagnetic point of view. OR/ORD arises due to the difference in the real part of the complex refractive index which affects the phase velocities of the RCP and LCP of the incident electromagnetic radiation, while the origin of CD can be attributed to the differences in the imaginary part of the refractive index which affects the extinction coefficients (Narushima and Okamoto, 2016; Collins et al., 2017; Kumar and Liz-Marzán, 2019; Yoo and Park, 2019). Importantly, for a medium exhibiting both ORD and CD, the RCP and LCP components of an originally linearly polarized radiation will suffer unequal absorption (i.e., the magnitude of the electric field vectors of the RCP and LCP components leaving the medium will be different), leading to an elliptically polarized resultant beam emerging out of the medium, the major axis of which will define the rotated direction of the new plan of polarization (Liehr, 1964; Snatzke, 1968; Yoo and Park, 2019). Typically, the elliptically polarized beam after suffering CD is

characterized by the ellipticity parameter, θ measured in degrees (Tranter, 2012).

CD is indeed one of the most straightforward yet powerful chiroptical methods due to its unique advantages, such as simple operating procedure, requirement of small concentration (10^{-5} M) of samples, and rapid data acquisition (few milliseconds for single-wavelength measurements) enabling to monitor dynamic events (Zsila, 2010; Rodger, 2013; Petrovic et al., 2015). CD has been used extensively for studying the configurational and conformational features of bioorganic molecular structures (Greenfield, 1999; Berova et al., 2007; Ranjbar and Gill, 2009; Gopal et al., 2012).

Notably, a number of studies aimed at revealing the architecture of biological membranes have been reported (Schneider et al., 1970; Urry et al., 1971; Litman, 1972; Urry and Long, 1974; Long et al., 1977). However, in many cases, application of CD to study the structure and function of biomembranes becomes cumbersome because of the distorted spectra originated due to the scattering by the membrane particulates (Urry and Long, 1974; Gitter-Amir et al., 1976; Long et al., 1977). On the other hand, significant number of efforts have been devoted for the study of structure and function of proteins by using CD, mainly because of its immense importance in the fields of proteomics and structural genomics (Kelly and Price, 2000; Greenfield, 2004; Kelly et al., 2005; Greenfield, 2006; Micsonai et al., 2015). In addition, several online tools and databases have also been developed for the analysis and deposit of CD spectra of protein structures (Whitmore and Wallace, 2004; Whitmore and Wallace, 2008; Abdul-Gader et al., 2011; Whitmore et al., 2011; Micsonai et al., 2015). Of paramount importance are the membrane proteins, which represent approximately 30% of all proteins of human genome sequenced so far. Such proteins take part in vital physiological functions including molecular recognition, cell adhesion, etc., and, most importantly, single-pass membrane proteins alone constitute around 69% of current approved drug targets (Sood and Gross, 2019). Notably, such proteins are not only difficult to crystallize for X-ray crystallographic studies but also a difficult target for nuclear magnetic resonance (NMR) spectroscopy. In this regard, CD spectroscopy has become one of the most reliable choices to uncover valuable information on the structure, function, and dynamics of membrane proteins (Sreerama and Woody, 2004; Siligardi et al., 2014; Matsuo et al., 2016; Miles and Wallace, 2016). In a time-resolved CD spectroscopy measurement, Horn et al. (Horn et al., 2007) successfully studied the kinetic phases of light-harvesting chlorophyll a/b (LHCIIb) protein complex. Dudzik et al., (2013) used far-UV CD spectroscopy to investigate the coordination of copper to the membrane-bound form of α -synuclein (α -syn), a neurological copper-binding protein related to Parkinson's disease. The study revealed that there was no change in the membrane-bound α -syn helicity after binding with a single equivalent of Cu^{2+} at its N-terminus, as shown in **Figure 2**. In another study, combination of vacuum ultraviolet circular dichroism (VUVCD) and linear dichroism (LD) spectroscopy was used to study the conformation as well as the interaction mechanism of

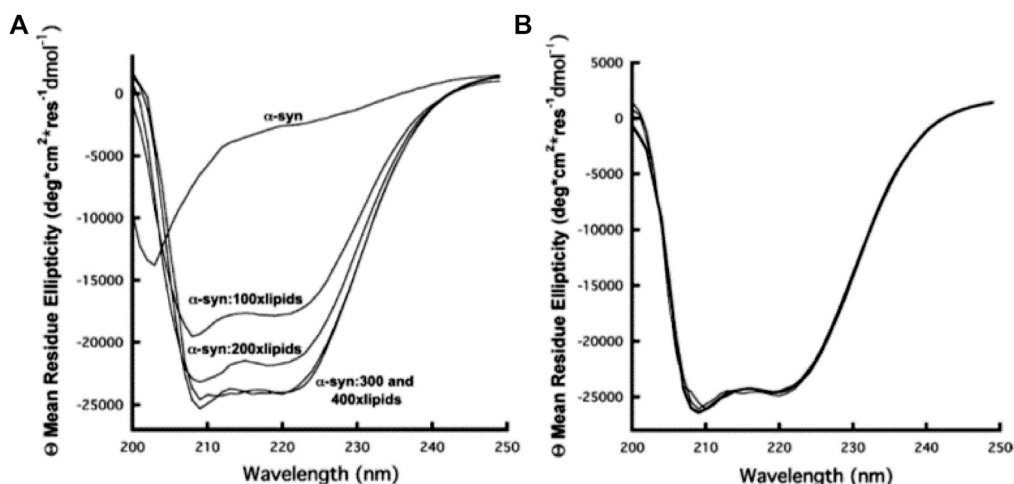


FIGURE 2 | (A) CD spectra of α -syn as a function of addition of lipid in the form of SUVs. From top to bottom, 10 μ M α -syn without lipids, 10 μ M α -syn with 1 mM lipids, 10 μ M α -syn with 2 mM lipids, 10 μ M α -syn with 3 mM lipids, and 10 μ M α -syn with 4 mM lipids, respectively. The CD signal intensity reaches a maximum at a lipid: α -syn molar ratio of 300:1. **(B)** Cu^{2+} titration of the 10 μ M α -syn–3 mM lipid complex. Cu^{2+} concentrations of 0, 10, and 100 μ M give overlapping α -syn CD spectra. The figure and caption have been adapted with permission from Dudzik et al., (2013), Copyright © 2012 American Chemical Society.

phosphatidylglycerol liposome membrane-bound α -lactalbumin (LA), thioredoxin (Trx), and b-lactoglobulin (LG) proteins (Matsuo et al., 2016). Notably, the structure and function of such membrane anchored or adsorbed proteins are inextricably related to each other, and their proper study may lead to the better understanding of the evolution of proteins to have novel and/or specific functions (Thyparambil et al., 2015).

Moreover, a number of CD techniques were reported for interrogating the change of peptide and protein conformation on interacting with different surfaces/monolayers, which can be achieved by comparing the CD spectra before and after interaction (McMillin and Walton, 1974; Vermeer and Norde, 2000; Burkett and Read, 2001; Fears et al., 2009; Sivaraman et al., 2009). For example, McMillin et al. (McMillin and Walton, 1974) demonstrated a CD technique to study the structural change of two blood proteins bovine fibrinogen and clotting factor XII (Hageman factor) adsorbed on a quartz surface. Tanaka et al., (2000) studied blood compatibility of different polymer surfaces, for example, poly(2-methoxyethylacrylate) (PMEA) and poly(2-hydroxyethylmethacrylate) (PHEMA), by using CD to examine the conformational change of surface-adsorbed bovine serum albumin (BSA) and human plasma fibrinogen (FNG). In another work, CD spectra of ultrathin films of the immobilized proteins, RC-b562 and NC-b562, on bare and modified gold surfaces were utilized to study the protein secondary structures. The group found that the secondary structures of the covalently anchored RC-b562 on modified gold substrates were preserved as compared to that of adsorbed NC-b562 molecules, which were found to be aggregated (Shimizu et al., 2003). Moreover, conformation of melectin and antapin antimicrobial peptides was studied in environments simulating eukaryotic and bacterial membranes by using CD spectroscopy (Kocourková et al., 2017). Furusawa and Kan, (2020), on the other hand, evaluated the ECD spectra of a single-layered circular dichroic film constructed by

transferring Au nanospiral structures onto a flexible and transparent polydimethylsiloxane (PDMS) thin film. Excitingly, the results suggested the applicability of the film as a circular dichroic filter having CD peak of -830 mdeg at 630 nm.

Regarding chiral nanostructures, metallic NPs, metal oxide NPs, carbon nanostructures, semiconductor NPs, etc. possess excellent biocompatibility and thus have tremendous potential in biomedical applications (Zhao et al., 2020). Such nanostructures exhibit unique chiroptical properties, including CD which is mainly used to study the conformation and denaturation of surface-adsorbed molecules (Liu and Webster, 2007; Ranjbar and Gill, 2009; Ma et al., 2017; Puri and Ferry, 2017; Lu et al., 2018; Chen et al., 2019; Kuznetsova et al., 2019; Mokashi-Punekar et al., 2019; Zhu et al., 2020). For instance, conformational change of DNA structure due to the interaction with quaternary ammonium-functionalized (Goodman et al., 2006) and amine-terminated cationic (Ghosh et al., 2007) NPs was investigated by CD. Importantly, such studies are of paramount importance in the field of clinical medicine for nucleic acid delivery (Chowdhury and Akaike, 2005). Recently, Slocik et al., (2020), while studying the interaction of chiral peptides with Au NPs by using CD, demonstrated that Au NPs are capable of restructuring the chirality of D-peptides. Most recently, chiroptical properties (CD and CPL) of CdSe/CdS nanocrystals of different anisotropic shapes were investigated to understand the effect of morphology on the surface ligand-induced chirality (Hao et al., 2020).

In addition, NPs strongly interact with biological fluids such as blood, plasma, or intracellular fluids, leading to the creation of protein corona due to the adsorption of proteins on the NP surface (Mahmoudi et al., 2011; Liu et al., 2013; Salvati et al., 2013; Pederzoli et al., 2017). Importantly, the formation of protein corona not only changes the surface properties of NPs but also affects the structure and function of the adsorbed proteins (Wang

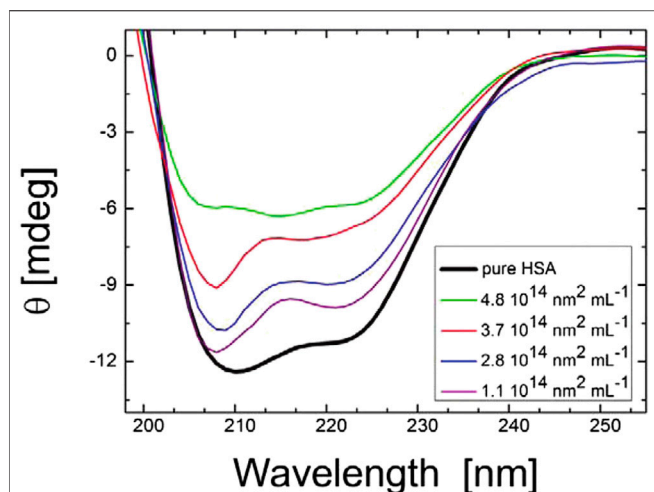


FIGURE 3 | CD spectra of HAS with citrate-stabilized silver nanoparticles (diameter of 36 nm with NP surface site concentrations ranging from 1.1×10^{14} to $4.8 \times 10^{14} \text{ nm}^{-2} \text{ mL}^{-1}$ and a protein concentration of 0.052 mg mL^{-1}). The figure and caption have been adapted with permission from (Gebauer et al., 2012), Copyright © 2012 American Chemical Society.

et al., 2017). In this context, CD has been used extensively to study the changes in the structures of the proteins and their folding and binding properties after forming corona on NP surfaces (Venerando et al., 2013; Fleischer and Payne, 2014; Zhao et al., 2015; Jayaram et al., 2018; ZhangT. et al., 2019; Li and Lee, 2020; Marichal et al., 2020; Park, 2020). Impressively, Gebauer et al., (2012) investigated the protein corona formed by human serum albumin, containing α -helices as predominant secondary structural elements, around citrate-functionalized silver NP surface. As shown in **Figure 3**, CD spectroscopy successfully revealed the structural changes in the adsorbed protein. In another work, Wang et al., (2017) used CD spectroscopy to study the transferrin (Tf) protein corona formation onto the surface of gold NPs (Au NPs), functionalized with D, L, and racemic isomers of penicillamine. The change in the secondary structures of Tf due to the formation of corona on the surface of Au NPs was confirmed by the observed variation in the values of ellipticity and other features of CD spectra.

Moreover, chiral metallic nanostructures possess plasmonic CD (PCD), a unique chiroptical property due to which the enhanced CD signal can be obtained at the frequency of localized surface plasmon resonance (LSPR) (Fan and Govorov, 2012; Collins et al., 2017; Lee et al., 2017; Zhao et al., 2017; Lu et al., 2018; Mokashi-Punekar et al., 2019; Kim et al., 2020). In 2011, Slocik et al., (2011) fabricated optically active metallic NPs by functionalizing achiral Au NPs with peptides of random coil and R-helix secondary structures. The group observed reproducible PCD at $\sim 520 \text{ nm}$ induced by the SPR of the Au NPs for both covalently and non-covalently attached E5 and FlgA3 peptides, respectively (**Figure 4**). Similarly, Cheng et al., (2017) reported the generation of strong CD signals from plasmonic nanostructures fabricated

by grafting spherical Au NPs of different sizes around chiral inorganic silica helical templates. In addition to the inverted CD spectra observed for right- and left-handed helices with sign reversal occurring near the plasmon resonance frequency of the Au nanoparticle, the study also revealed that the amplitude of the CD signal got increased and red shifted with the increase of the diameter of the nanoparticles. Another strategy demonstrated the transfer of chirality of L- or D-cys to cube-shaped Au NPs, resulting in the formation of highly twisted chiral helicoidal structures that displayed strong CD (Lee et al., 2018). Extending this work, the group also studied the evolution of cysteine-induced chirality in film type of assembled helicoid Au NPs by using CD spectroscopy (Lee et al., 2020). Recently, Rajaei et al., (2019) used chiral metasurfaces composed of two-dimensional (2D) planar array of three-dimensional (3D) plasmonic ramp-shaped Au nanostructures to achieve giant CD and dissymmetry factor up to 64% and 1.13, respectively, at the visible range. In another work, Zhang Q. et al. (2019) investigated the origin of PCD possessed by metal NP (Au nanorod)-protein (BSA) complexes at the single-particle level by combining circular differential scattering spectroscopy along with correlated tomographic reconstruction and electromagnetic

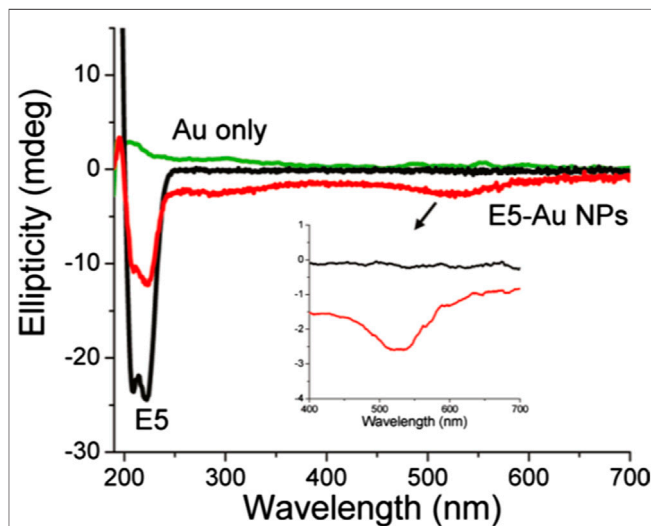


FIGURE 4 | Optical characterization of gold nanoparticles functionalized with the E5 peptide ($5.0 \mu\text{M}$) with 1.14×10^{13} particles/ml. CD spectra of E5 peptide gold nanoparticles with or without E5 peptide. The figure and caption have been adapted with permission from Slocik et al., (2011), Copyright © 2011 American Chemical Society.

simulations. The study revealed that the aggregates exhibit strong PCD, while single nanoparticles did not show any detectable chiroptical activity. Apart from Au-based plasmonic nanostructures, an enhancement of two orders of magnitude of the CD signal was observed from a system of l-glutathione(l-GSH)-coated colloidal silver NPs, further attached to bimane chromophore, due the coupling of metal SPR and molecular electronic transition (Lieberman et al.,

2008). Moreover, plasmon-induced new CD response was observed at LSPR wavelength range (~350–500 nm) in case of silver cube-shaped NPs capped with GSH molecules (di Gregorio et al., 2015). Notably, as far as self-assembly-based plasmonic structures are concerned, Au NPs are chemically stable, while Ag NPs possess better optical properties in terms of extinction cross section and near-field enhancement. To exploit their advantages synergistically, Nguyen et al. (Nguyen et al., 2020) synthesized thiolated DNA functionalized gold–silver core–shell nanoparticles that showed significantly enhanced and blue shifted bisignate CD spectra, as compared to the pristine Au counterparts. Certainly, such results obtained from PCD spectroscopy is of utmost importance for the development of next-generation chiral plasmonic devices.

Vibrational Circular Dichroism (VCD)

As already mentioned, vibrational circular dichroism (VCD) is the differential absorption of RCP and LCP of IR radiation and thus involves the transitions among the vibrational sublevels within the ground electronic state of a chiral substance (Nafie, 2012). Notably, six possible vibrational modes are involved in such transitions (Collins et al., 2017). VCD is relatively young chiroptical technique and was first reported in 1974 by Holzwarth et al. (Holzwarth et al., 1974). It has become one of the most reliable choices for determining the absolute configuration and conformation of chiral molecules due to its inherent advantages, for example, richer spectral information content than ECD spectroscopy, capability of probing molecular interactions and orientation, no requirement of special chromophoric groups, and robust theoretical background (Polyanichko et al., 2011; Petrovic et al., 2015; Kurouski, 2017). A large number of comprehensive reviews are available that highlighted the principle as well as applications of VCD on molecular chirality (Nafie, 2008; Yang and Xu, 2010; Burgueño-Tapia and Joseph-Nathan, 2015; Kurouski, 2017; Nafie, 2018; Krupová et al., 2020).

In addition to its widespread use in probing chirality at molecular scale, VCD has also been used to interrogate chirality at membranes, interfaces, and surfaces (Berthier et al., 2002; Novotná and Urbanová, 2012; Das and Pal, 2017). For instance, in a recent work, Novotná et al., (2014) used model membranes of zwitterionic liposomes from 1,2-dimyristoyl-sn-glycero-3-phosphocholine (DMPC) and sphingomyelin (SPM) liposomes to simulate the phospholipid bilayer and nerve cell membranes, respectively. The group further used VCD to investigate the interaction of bilirubin (BR) with DMPC and SPM model membranes as well as polypeptide poly-L-arginine (PLAG) model membrane proteins, as functions of pH and temperature. The study successfully revealed the strong mutual influence between BR and SPM, which may be related to BR neurotoxicity (Novotná and Urbanová, 2015). Similarly, Kocourková et al. (Kocourková et al., 2017) studied the conformation of antimicrobial peptides melectin and antapin in simulated eukaryotic, bacterial, and nerve cell membranes, where the VCD technique was found to be powerful in differentiating α -helical and polyproline II-type conformations. In another work, interaction of amyloid polypeptide AS_{71–82} with

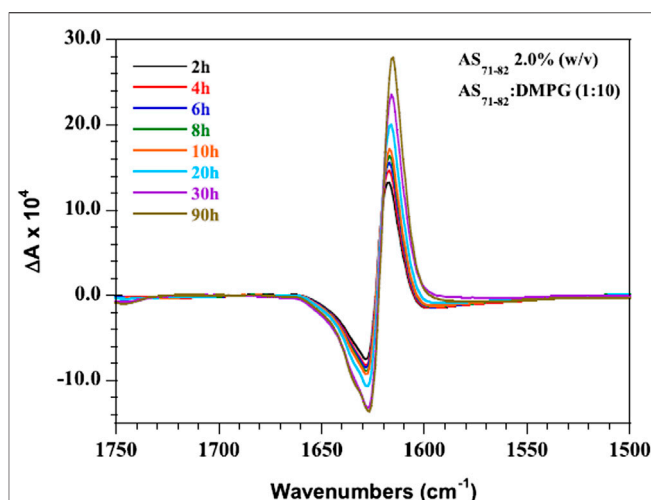


FIGURE 5 | VCD spectra of AS_{71–82} in the presence of DMPG membranes (P:L 1:10, 2.0% AS_{71–82} w/v) recorded as a function of time over a 90 h time period. The figure and caption have been adapted with permission from Martial et al., (2019), Copyright © 2019 American Chemical Society.

anionic membranes was investigated by coupling VCD spectroscopy and IR spectroscopy (Martial et al., 2019). As shown in **Figure 5**, the time-dependent VCD spectra revealed the increase in signal intensity over time, probably indicating the gradual maturation and stabilization of the fibrillar structures. Interestingly, Lizio et al. (Lizio et al., 2018) employed the combination of Raman, ROA, IR, and VCD spectroscopy to elucidate their capability in determining the relative proportion and conformation of α -aminoisobutyric acid (Aib) foldamers in membranes as well as in organic solvents. The VCD spectra of L- or D-Phe capped tetrameric Aib foldamers in the membranes of vesicles revealed the retention of the screw-sense preference of an Aib foldamer even after partitioning into a 1,2-dioleoyl-sn-glycero-3-phosphocholine (DOPC) bilayer. On the other hand, Pazderková et al., (2019) investigated the structural changes of antimicrobial peptide Halictine-1 (HAL-1) due to the interaction with model membranes by combining the use of IR, ECD, VCD, and fluorescence spectroscopies. Here, VCD spectroscopy was specifically used to understand the high concentration-induced structural change of peptides.

Importantly, as far as the experiments to measure VCD spectra are concerned, the major challenge is the relatively weak signals and anisotropy factors. As compared to ECD and IR absorption, VCD signal strength is generally several orders of magnitude smaller (Petrovic et al., 2015; Polavarapu and Santoro, 2020). However, enhanced chiroptical signals can be achieved from high specific surface area material, such as NPs which can be considered as the nanometer-sized analogs of extended flat surfaces (Bieri et al., 2007; Gautier, 2008; Collins et al., 2017; Bhattacharya and Bürgi, 2019). Importantly, in a first-of-its-kind experiment, Gautier et al. (Gautier and Bürgi, 2005) studied the VCD activity of monolayer (N-acetyl-L-cysteine)-protected Au NPs. In another similar work, the group investigated the OA of N-isobutyryl-L-cysteine and N-isobutyryl-D-cysteine molecules

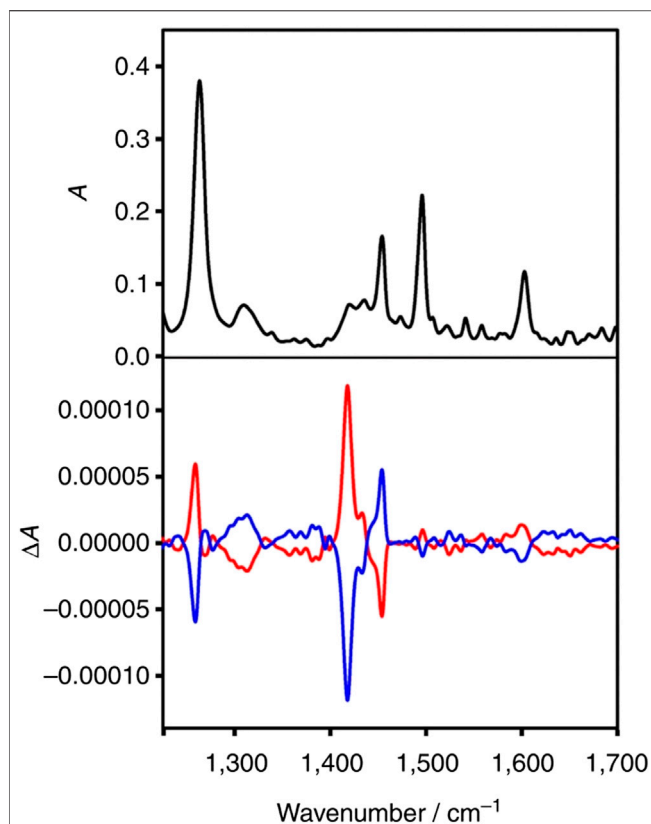


FIGURE 6 | Infrared spectrum of A-Au₃₈(2-PET)₂₄ (black) and VCD spectra of enantiomer 1 (A-Au₃₈(2-PET)₂₄, red) and of enantiomer 2 (C-Au₃₈(2-PET)₂₄, blue). The figure and caption have been adapted with permission from Dolamic et al., (2015), Copyright & 2015 Macmillan Publishers Limited.

adsorbed on the surface of AuNPs by using VCD (Gautier and Bürgi, 2006). Theoretical calculations, conducted in this work, by using density functional theory (DFT) revealed the strong dependence of the VCD spectra on the adsorbed N-isobutyryl-cysteine conformation. In order to explain the mechanism of chirogenesis in metal-based transitions, the group proposed the possible induction of chiral “footprint” due to the double interaction of both acid and thiol groups of N-isobutyryl-cysteine with the metal particle surface. Furthermore, mirror image relationship between the VCD spectra of Au NPs modified by both the enantiomers of 1,1'-binaphthalene-2,2'-dithiol (BINAS) was reported in a recent work (Gautier and Bürgi, 2010). The group observed that the VCD spectrum of adsorbed BINAS is similar to the dithiol form, albeit it appears to be different from its free and disulphide form. Recently, VCD spectroscopy was used to study the conformation and configuration of Au₂₅(PET)_{18–24}((R)-FBINAS)_x cluster (PET = 2-phenylethylthiol, (R)-FBINAS = (R)-5,5',6,6',7,7',8,8'-octafluoro-[1,1'-binaphthalene]-2,2'-dithiol) (Sels et al., 2019). Notably, the study revealed the transfer of chirality of FBINAS to originally achiral PET, which was co-adsorbed within the ligand layer. In another work, Bhattacharyya et al. (Roy Bhattacharyya and Bürgi, 2019) successfully obtained the

enhanced VCD signal from water soluble gold nanocluster Au₂₅(captopril)₁₈ when a small amount of cobalt(II) was added in the aqueous solution.

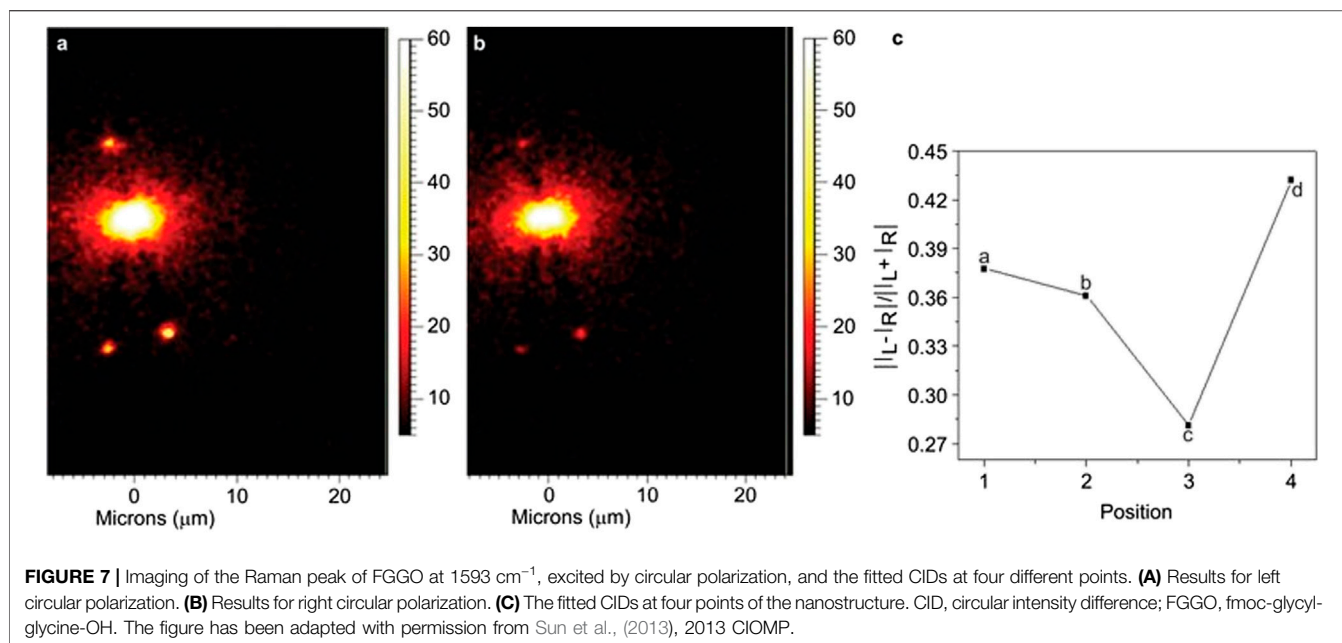
Mostly, VCD measurements involve solution-state samples. Recently, in order to expand its applicability and measure the VCD of different solid samples such as KBr pellets, and films, solid state VCD (SD-VCD) was developed (Sasaki et al., 2013; Mijiddorj et al., 2019; Sato and Kawamura, 2020). In one of the applications, SD-VCD was used to study the mechanism of chiral recognition on a solid clay surface (Sato et al., 2018).

In another interesting work, first direct observation of transfer of chirality from chiral metal cluster to achiral molecules adsorbed on its surface was successfully achieved by VCD spectroscopy (Dolamic et al., 2015). The adaptation of chiral conformation by achiral 2-phenylethylthiolate (2-PET) after getting adsorbed on chiral Au cluster was evidenced by the strong VCD signal from the thiolate moiety. Notably the experimental results were further explained by density functional theory (DFT) calculations. **Figure 6** shows the VCD spectra of the Au₃₈(2-PET)₂₄ cluster enantiomers. On the other hand, Yao et al., (2010) investigated the structure of chiral D-/L-penicillamine ligands adsorbed on silver nanoclusters with mean core diameter ~1.1 nm. The group compared the experimental data with DFT calculations to perform spectral assignments. Accordingly, such studies are important to understand not only the mechanism of chirality transfer but also accurate determination of the configurations and conformations of surface-adsorbed molecules.

Raman Optical Activity (ROA)

Raman optical activity (ROA) is the complementary chiroptical technique of VCD, capable of providing conformational information even for samples that do not have distinct VCD bands (Barron et al., 2007; Krupová et al., 2020). It is the inelastic counterpart of Rayleigh optical activity (Andrews, 1980) and is essentially measured as the difference between the Raman scattering intensities for right and left circular polarized incident or scattered radiation. Accordingly, there are four kinds of linear ROA corresponding to each of the two circularly polarized states of incident and scattered radiation (Collins et al., 2017; Nafie, 2018; Nafie, 2020). Since its first demonstration in 1973 (Barron et al., 1973), it has already become a matured technique and found widespread applications in diverse fields ranging from chiral molecules to viruses (Blanch et al., 2002; Blanch et al., 2003; Zhu et al., 2005; Hoffmann, 2012; Parchaňský et al., 2014; Haraguchi et al., 2015; Gąsior-Głogowska et al., 2016). Notably, ROA is often measured in terms of the dimensionless circular intensity difference (Hoffmann, 2012).

Besides, ROA has also been used in the study of surface chirality. In one of such pioneering works, Hecht and Barron, (1994) worked out the detailed mechanism of incoherent Rayleigh and Raman optical activity from chiral surfaces and predicted that the associated circular and linear polarization optical activity observables could be three orders of magnitude larger than those from bulk samples. The group successfully used differential decomposition of the normal incidence transmission Mueller matrix to determine circular birefringence and dichroism



values. In another work, birefringence-induced ROA in uniaxial crystals with rutile structure was demonstrated by slightly misaligning the incident light with respect to the crystal *c*-axis direction (Hoffman et al., 1994). Recently, scattered circular polarization ROA strategy was used to study the chirality of chiral two-dimensional nanostructured ZnO films and chiral nanostructured ZnO powders (CNZPs) (Duan et al., 2015a). Particularly, the observed ROA revealed the highly crystalline nature of CNZPs.

At this point, it is noteworthy to mention that despite having excellent capability in extracting the absolute configuration and conformation, ROA suffers from weak signal intensities of about 3–5 orders of magnitude smaller than the original Raman scattering intensity, which is already about six orders of magnitude weaker than the incident beam. Obviously, such limitations of spontaneous ROA warrant data acquisition time and higher sample concentration requirement (Abdali and Blanch, 2008; Pour et al., 2018; Krupová et al., 2020). Nevertheless, the advantages of surface-enhanced Raman scattering (SERS) and resonance Raman scattering (RRS) can be utilized to enhance the corresponding ROA intensity (Johannessen et al., 2007; Nagy et al., 2016; Hu et al., 2018). Recently, resonance ROA was utilized to study the enantio-enriched (6,5) single-walled carbon nanotubes (SWNTs) sorted by density gradient ultracentrifugation (Magg et al., 2016).

Notably, the combination of SERS and ROA was first considered almost three decades ago by Efrima, (1983) who predicted that enhanced ROA signals from chiral molecules adsorbed onto metal surfaces can be obtained due to the large electric field gradient that exists near the surface. Efrima also developed the first theoretical framework for explaining the enhancement of ROA of chiral molecules adsorbed on metal surfaces (Efrima, 1985). In spite of these pioneering works and

following theoretical developments, experimental developments for surface-enhanced ROA (SEROA) did not gain sufficient pace during the last decades, mainly because of the difficulties (e.g., large signal-to-noise ratio and complicated spectra) associated with the experiments (Janesko and Scuseria, 2009). However, significant number of efforts have been made in the recent years to revitalize the application of SEROA (Janesko and Scuseria, 2006; 2009; Pour et al., 2011; Ren et al., 2017). For example, Kneipp et al., (2006) successfully obtained stereochemical information of adenine adsorbed on Ag nanoparticles by measuring the SEROA at significantly reduced excitation power, shorter data acquisition time, and lower molecular concentration as compared to classical ROA measurements. In another exciting work, Sun et al., (2013) reported an alternate method of achieving SEROA which can be useful in reducing the artifacts present in SEROA spectra due to the influence of chemical enhancements. The method involved the remote excitation of ROA of chiral fmoc-glycyl-glycine-OH (FGGO) molecules by using chiral Ag nanowires as plasmonic waveguides. The applicability of the method was demonstrated by obtaining ROA image and measuring the ROA spectra as well as circular intensity difference (CID), as shown in Figure 7. Similarly, remote-excited ROA of adenine was realized by surface plasmon propagating along Ag nanowires (Xia et al., 2014). On the other hand, surface-enhanced resonance ROA (SERROA), that involves the coupling of the resonance Raman scattering with surface plasmon enhancement, has also been reported (Abdali et al., 2007; Johannessen et al., 2007). However, SERROA can only be achieved only when there is an overlap between the electronic transition and plasmon resonance frequencies.

Nonlinear Optics on Surface Chirality

Both SHG and SFG are established spectroscopic techniques specifically used to study surface chirogenesis. In theory, these

two nonlinear optical processes can be uniquely described by the second-order susceptibility, $\chi^{(2)}$, tensor (referred to as $\chi^{(2)}$ tensor hereafter) under the point symmetry consideration of C_{∞} when chiral molecules are adsorbed at surface/interface (Maki et al., 1995; Kriech and Conboy, 2003; Mitchell, 2006). Sometimes, the adsorbed molecules should have a certain degree of orientation in order to enhance the C-SHG and C-SFG signal, and thereby, they are structural effects of molecules in response to a polarized field (Simpson, 2002; Mitchell et al., 2005). To derive the nonvanishing $\chi^{(2)}$ tensor elements related to surface chirality, $\chi^{(2)}$ tensor transformation from molecular frame to laboratory frame using the Euler rotation matrix is required, where χ_{xyz} refers to the fact that the direction of the second-order nonlinear polarization flipped (rotated) from the plane of fundamental polarization indicates the chiral-specific component (Petralli-Mallow et al., 1993). Regarding the polarization settings in experiments, the polarization combinations of psp, spp, and pps are responsible for C-SHG and C-SFG, while ssp, sps, pss, and ppp are in charge of achiral contributions at the surface/interface. This section will summarize the arrangement of measurement setup and selected applications of C-SHG and C-SFG in investigating surface chirality.

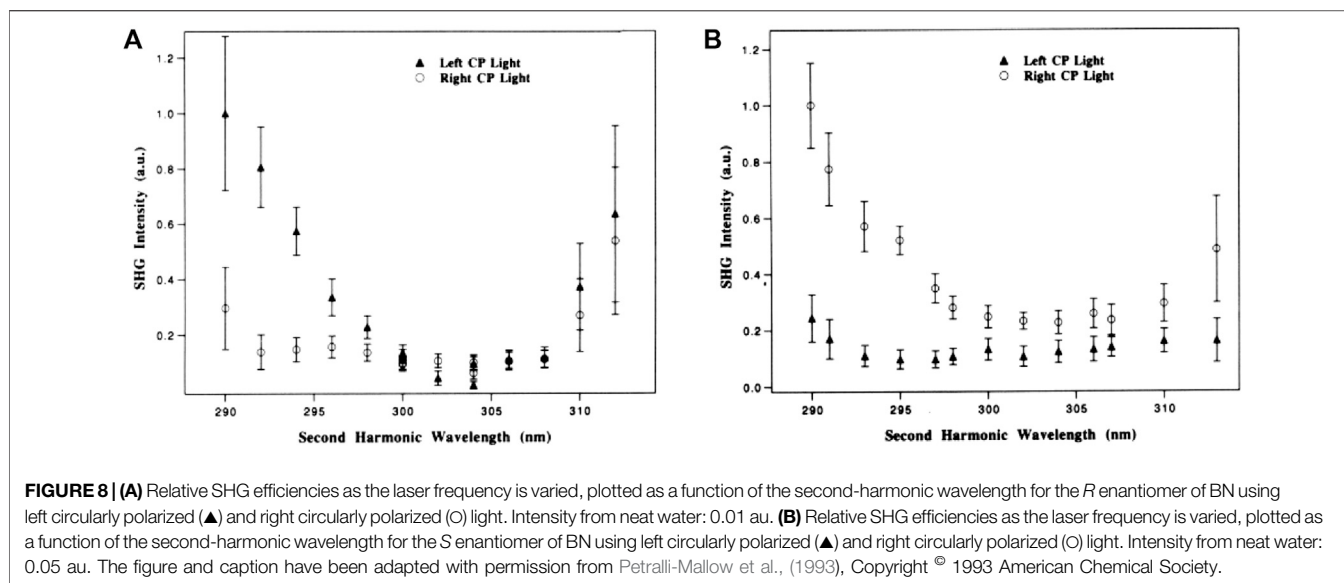
Surface Chirality Measured by Second-Harmonic Generation (SHG)

The scheme for polarimetric measurements of C-SHG can be divided into two main categories: linear polarization to planar surface and circular polarization to planar surface, leading to the optical activities of SHG-CD, SHG-LD, and SHG-ORD. In SHG-CD, first demonstrated by Hicks and coworkers (Petralli-Mallow et al., 1993), chirality results in the SHG intensity difference between the interactions of RCP and LCP, and the signal contrast ratio can be on the order of unity which is more than two orders of magnitude stronger than linear CD (Petralli-Mallow et al., 1993; Hicks et al., 1994). Notably, the sign of SHG-CD ratio (also known as degree of chiral excess, DCE, or enantiomeric excess) indicates the handedness of chiral molecules. Such circular-difference effect is derived from the interference between chiral and achiral components of the $\chi^{(2)}$ tensor (Byers and Hicks, 1994; Fischer and Hache, 2005; Rodriguez et al., 2007). Because the $\chi^{(2)}$ tensor components, oriented normally to the surface, contribute to surface SHG, the arrangement of measurement setup uses a collimated (or weakly focused) laser beam with an angle of incidence (typically 45°) relative to the surface normal to probe the chiroptical effects. Then, the reflected and/or transmitted SHG emitted from the surface is measured. In general, SHG-CD is incorporated with a spectroscopy to have a full view of the resonance effect of the adsorbed molecules (Corn and Higgins, 1994). In SHG-LD, the SHG polarization-dependency curve is measured by rotating the incoming linear polarizations from 0° to 360° using a half-wave plate, with an angle of incidence (typically 45°) relative to the surface normal. The reflected and/or transmitted SHG is detected at s- or p-polarization. The linear-difference effect can be found by comparing the signal at 45° and -45° (or 135°) of the p-direction of the incident beam (Fujiwara et al., 2004; Xu et al.,

2009; Lin et al., 2014). Similar to SHG-CD, the sign of SHG-LD ratio also reflects the handedness of chiral molecules. In SHG-ORD, an oblique incidence of the p-polarized laser beam is used to probe surface/interface, and the direction of SHG polarization is measured with an analyzer to determine the rotation angle in SHG. Similar to SHG-CD, a spectrally resolved measurement is performed to better understand the resonance effect of molecules (Byers et al., 1994a; Hache et al., 2003). In the following, we will lay emphasis on illustrating the selected works of SHG-CD and SHG-LD on surface chirality.

In 1993, a pioneering work conducted by Petralli-Mallow et al. (Petralli-Mallow et al., 1993) successfully revealed the OA effect of 1,1'-binaphthalene-2,2'-diol (BN) at an air/water interface by using SHG-CD spectroscopy. The group observed that the chiroptical response from (R)- and (S)-BN depends on the helicity of incident polarized light, giving rise to opposite CD effects by the two BN enantiomers, as shown in **Figure 8**. Importantly, due to SHG-CD being electric dipole allowed, it is three orders of magnitude stronger than that measured by linear CD spectroscopy. Because SHG intensity is the square of the $\chi^{(2)}$ tensor, this further enhances the difference effect. Moreover, it is observed that without aggregate formation of molecules, a preferred orientation of adsorbed molecules at the surface is hypothesized to be the main contributor to amplify SHG-CD. In 1994, Verbiest et al. (Kauranen et al., 1994) used a Langmuir-Blodgett (LB) film embedded with bacteriorhodopsin molecules for studying surface chirality. The adsorbed molecules present a local ordering in a lattice and randomly oriented on the length scale smaller than an optical wavelength. In the measurement, the incoming polarization on the sample was modulated by a quarter-wave plate (Maki et al., 1997) to continuously change the polarization state from left-circular to linear to right-circular, and subsequently, the surface SHG is recorded at s- and p-polarization in transmission or reflection. Importantly, a theory that includes electric and magnetic dipole contributions to C-SHG was proposed to explain the experimental results. Following this method and accompanying theory, Kauranen et al. (Kauranen et al., 1994; Maki et al., 1995) further included the nonlinear Fresnel factors to accurately describe the C-SHG, and a magnetic dipole contribution $\sim 10\%$ of the electric dipole one was found on the LB monolayers of a synthetic chiral polymer, chromophore functionalized poly(isocyanide). Similarly, Rodriguez et al., (2007) observed OA in thin films of a chiral poly(3-alkylthiophene). In the experiment, the dependency of SH intensity on the rotation angle of the half-wave plate (combined with a quarter-wave plate at fixed angle placed behind it) at a specific laser incidence angle was resolved into s- and p-polarization in transmission and reflection. Notably, a deeper analysis of the susceptibility tensor elements (Rodriguez and Sourisseau, 2002) determined in this work suggested that, analogous to linear CD, the possible origin of the observed chiroptical response could be the interference between electric and magnetic dipole contributions.

Regarding the issue of orientation or structure of molecules on surface, Byers et al. (Byers et al., 1994b) investigated a monolayer of oriented chiral molecules (BN) and found that SHG-CD not



only depends on the handedness of incident polarized light but also on the adsorbed molecules pointing upward or downward from the surface, presenting a positive or negative value of SHG-CD, respectively. Afterward, Sioncke et al., (2001) investigated a chiral, anisotropic LB film of helicenebisquinone, in order to separate the effect of SHG-CD from anisotropy. Results showed that SHG-CD is independent of molecular orientation when sample is rotated, and conversely, the anisotropy depends on the azimuthal angle of the sample, leading to a CD effect. Furthermore, Mitchell et al. observed the OA response from a polypeptide α -helix adsorbed at the air/water interface (Mitchell et al., 2005). In this experiment, poly(γ -benzyl-L-glutamate) (PBLG) and poly(γ -ethyl-L-glutamate) (PELG) were examined, which assisted to form an α -helix of the polypeptide chain. And the effective susceptibilities for C-SHG can be resolved by p- or s-polarization detection while the incident polarization state was continuously varied using a quarter-wave plate, as shown in Figure 9. Result showed that a symmetric or asymmetric SHG polarization dependency represents an achiral or chiral surface, respectively. The most important finding was that a structural effect from the molecular tilting of the individual amide chromophoric subunits with respect to the principal axis of the helix is responsible for surface chirality. Furthermore, Mitchell studied the SHG-OA effect of tryptophan derivative Na-(*tert*-butoxycarbonyl) tryptophan (Boc-Trp) at an air/water interface (Mitchell, 2006). The $\chi^{(2)}$ tensor of chiral and achiral monolayers were determined both experimentally (under two-photon resonant and nonresonant excitation conditions) and theoretically (with ZINDO/S), which agreed quite well with each other. Based on these results, it is concluded that the surface chirality is from a structure effect of the absolute orientation (tilt angle θ and twist angle ψ) of the long axis of indole (polar and achiral) chromophores organized in chiral assemblies at the interface. Moreover, Zou et al., (2006) studied the chirality at polymerized 10,12-tricosadynoic acid (PTDA) LB films on quartz substrate

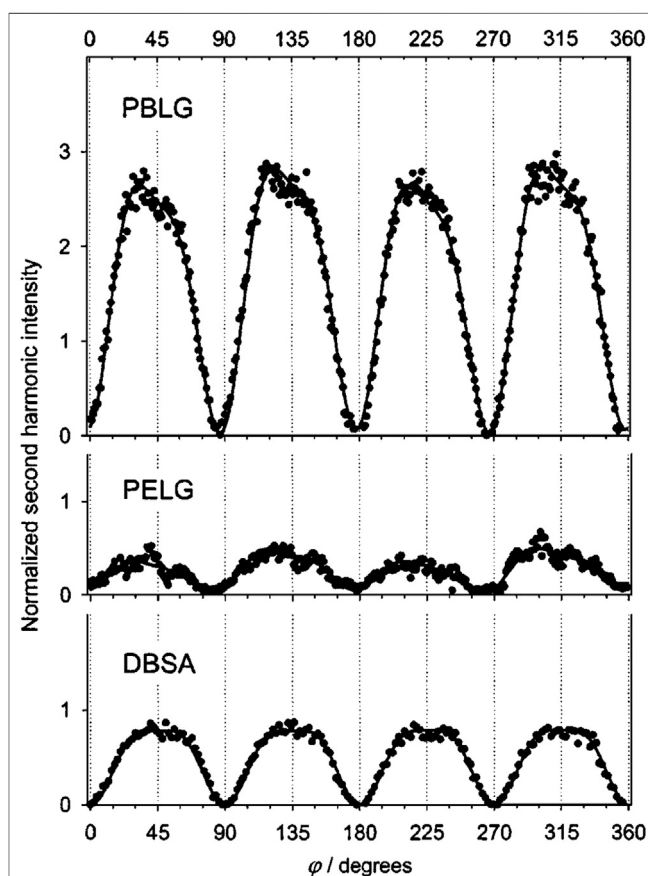


FIGURE 9 | Rotation traces $I_{2\omega}(\phi)$ for the polypeptides PBLG and PELG and for the achiral surfactant DBSA adsorbed at the air/water interface. The solid lines are fits of the data to Eq. (8). Note that the traces for the chiral interfaces PBLG and PELG are asymmetric about $\phi = 180^\circ$, and the trace for the achiral interface DBSA is symmetric. The figure and caption have been adapted with permission from Mitchell et al., (2005), Copyright © 2005 AIP Publishing.

using SHG-CD spectroscopy and polarized angle dependence measurements. It was found that PTDA films showed surface chirality when Cu(II) ions appeared in the subphase solution but did not show surface chirality when the subphase solution contains Cd(II) ions or is pure water. This phenomenon is probably from the metal ions in the subphase solution, which induce a conformational change of the polydiacetylene chain in PTDA films. In addition, the Cotton effect was also observed in the SHG-CD spectra when PTDA films are deposited from Cu(NO₃)₂ subphase, further demonstrating that surface chirality can be formed by a conformational change of achiral molecules.

On the other hand, Fujiwara et al. first studied the chiral molecular aggregates at a liquid/liquid interface by SHG-CD spectroscopy (Fujiwara et al., 2004). The SHG-CD spectra are similar to that measured by linear CD spectroscopy of J-aggregates in bulk solution. One difference from linear CD is that the zero difference effect is not at the absorption maximum of molecules, which may ascribe to the twisted configuration of H₄TPPS²⁻ in J-aggregates. In addition, the asymmetric chiral structure of J-aggregates has been proven to enhance the SHG signal, and the surface chirality can be contributed from the magnetic dipole interactions. Furthermore, in a totally internal reflection (counter-propagating) mode of SHG-CD spectroscopy (Tokunaga et al., 2009), an objective lens was used to shift the position of the incident beam to one side from the lens center and collected the SHG signal at another side. The system was used to discriminate the chirality of molecular aggregates of porphyrin on a glass plate. It is found that the SHG-CD spectra of bilirubin-BSA complex are different from that of racemic bilirubin, manifesting that an M-conformation is appeared in the bilirubin-BSA complex. An advantage of this setup is the easy integration into an SHG-CD microscopy to image surfaces/interfaces and cell membranes. Regarding the protein-membrane interactions, Verbiest et al. (Hicks and Petralli-Mallow, 1999) used an electron transfer protein, cytochrome *c*, to adsorb on self-assembled mono- and bilayers at the solid/liquid interface in order to study the oxidation/reduction state of the protein. It is observed that due to the electrostatic interactions of zwitterions and a net negative charge from the lipid surface, the protein is tightly bonded not reducible by adding ascorbic acid. Afterward, the same group followed the identical experimental conditions and found that the cytochrome *c* protein is reducible by ascorbic acid when adsorbed at alkanethiol self-assembled monolayers but is not reducible at phospholipid/alkanethiol hybrid bilayer membranes (Petralli-Mallow et al., 2000). The phenomenon reveals that cytochrome *c* is reducible by ascorbic acid for negatively charged or hydrophobic monolayers, but not for negatively charged phospholipid and zwitterionic bilayers. This work demonstrates the capability of SHG-CD in monitoring protein-membrane dynamics.

Later on, Huttunen et al., (2009) conducted a simulation work for a different measurement scheme that used a focused circularly polarized laser beam at normal incidence to the surface, holding an azimuthal symmetry about the direction of beam propagation. Notably, this strategy can be used to prevent the interference of SHG by in-plane anisotropy that would produce a chiroptical

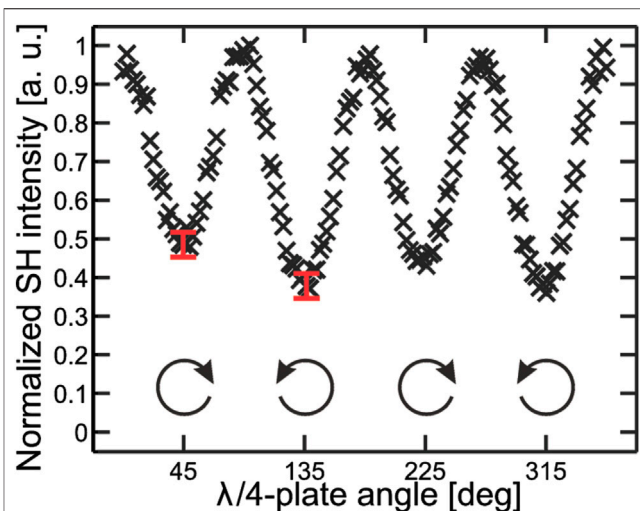


FIGURE 10 | Measured SHG response from a chiral thin film of THBQ as a function of the rotation angle of the QWP. The angles 45°, 135°, 225°, and 315° correspond to CP with varying handedness. The measured SHG-PD response was 0.24. The figure and caption have been adapted with permission from Huttunen et al., (2010), Copyright © 2010 American Chemical Society.

response commonly shown in traditional SHG-CD measurements. Therefore, such measurement is only sensitive to surface chirality isolated from any anisotropy effect of molecules. Another advantage is that it is adaptable to microscopy techniques on surfaces/interfaces due to the normal incidence of the laser beam. Additionally, in the plane wave approximation, the incoming laser beam with an angle between the surface normal can couple the surface nonlinearities offered by the $\chi^{(2)}$ tensor components oriented normally to the surface. Because a circular polarization reveals full vectorial properties within the focal volume, the C-SHG signal is undoubtedly produced from the direction of surface normal. The same group continued to confirm and validate this work using two LB films, one of which was chiral and anisotropic, while the other was achiral and isotropic (Huttunen et al., 2010). The first LB film was fabricated from chiral molecules, tetradodecyloxyhelicenebisquinones (THBQs), that belong to a C₂ point symmetry, while the second film was fabricated from 2-docosylamino-5-nitropyridine (DCANP) molecules with a C_{1h} point symmetry. To confirm the molecular orientation that would make a false interpreting of C-SHG, the two films were measured at different relative directions between the anisotropic axis of the sample and the incident polarization direction. Results showed that there is no SHG-CD response in case of the DCANP film. However, an average SHG-CD value of 0.24 was measured in the THBQs film (Figure 10), confirming the insensitivity of this technique to in-plane anisotropy. Beside the above applications, SHG-CD has been used to study chirality at the air/water interfaces of aqueous (*tert*-butoxycarbonyl)-tryptophan-tryptophan (Boc-Trp-Trp), R- or S-citronelloxy-cyanobiphenyl monolayer (Crawford et al., 1994; Manaka et al., 2005), anisotropic achiral oxidized Si (001) film (Li et al., 2006), glass

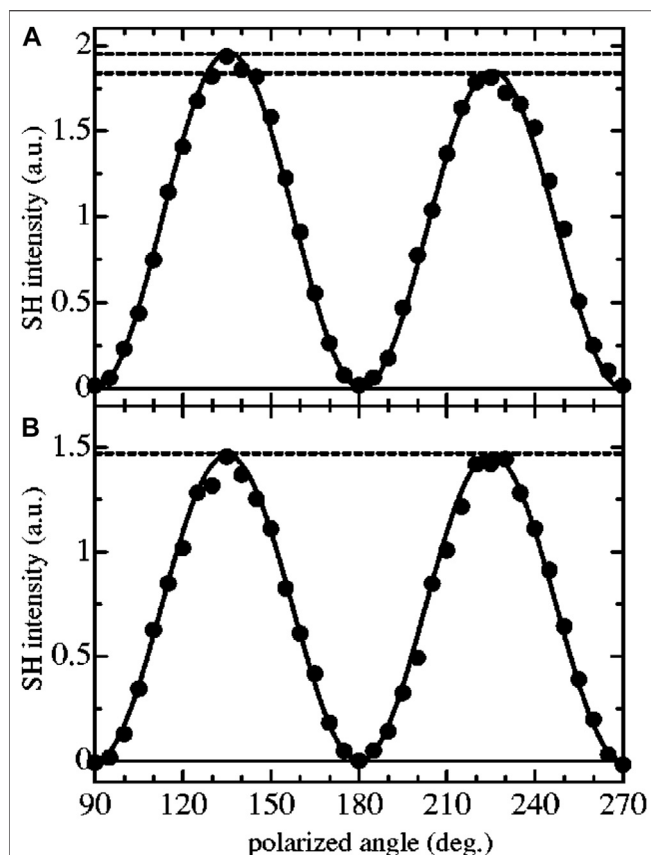


FIGURE 11 | Experimental results for the polarized angle dependence measurement for (A) 6OCB and (B) S-CCB monolayer. SH light was detected for the transmitted direction. In this method, the analyzer angle was fixed and the SH signals were measured as changing the input polarized angle. Solid circles represent the experimental results, and the solid line shows the fitting curves using the appropriate formula $I(2\omega) \propto |S_{15} \sin 2\gamma_i - S_{14} \cos^2 \gamma_i|^2$. The figure and caption have been adapted with permission from Fujimaki et al., (2003), Copyright © 2003 AIP Publishing.

substrate of G-shaped nanostructures (Mamonov et al., 2014), etc. In recent years, by combining the surface specificity and optical sectioning of SHG, SHG-CD has been integrated into nonlinear optical microscopy to image collagenous tissues (Zhuo et al., 2017a; Zhuo et al., 2017b; Schmeltz et al., 2019; Schmeltz et al., 2020). The information of $\chi^{(2)}$ tensor, molecular orientation, polarity, and chirality is extracted with delicate polarimetric measurements and tensor analyses. The corresponding results can be presented in terms of images.

Although the conventional SHG-CD spectroscopy can reveal the chiral information at the surface in a label-free and noninvasive manner, the typical shortcomings are the requirement of a large phase difference between chiral and achiral terms in the $\chi^{(2)}$ tensor and the difficulties in implementing a spectrally resolved measurement. In this context, SHG linear difference (SHG-LD) technique has been successful in investigating surface chirality with rotated linear polarizations to obtain a polarization dependency of SHG. In 1995, Verbiest et al. (Verbiest et al., 1995) first used SHG-LD to

study LB monolayers of the S-enantiomer of a poly(isocyanide) polymer. The measured SHG from isotropic chiral surfaces is different for the linearly polarized excitation at 45° and -45° relative to the p-polarized direction. The difference effect is of the same order of magnitude with SHG-CD but is of orders of magnitude larger than that measured by linear CD. In contrast to SHG-CD, SHG-LD does not require the phase difference between the chiral and achiral susceptibility terms, thereby allowing it to be observed under nonresonant excitation. In general, SHG-LD serves as a partner technique to SHG-CD, both used for studying surface chirality. Some representative works of SHG-LD on surface chirality have been illustrated below.

Fujimaki et al., (2003) have used SHG-LD combined with Maxwell's displacement current measurement to investigate the air/water interface of chiral (S)-4'-citronelloxy-[1,1'-biphenyl]-4-carbonitrile (S-CCB) and achiral 4'-hexyloxy-[1,1'-biphenyl]-4-carbonitrile (6OCB) monolayers. SHG-LD was used to measure the chirality and molecular orientation at surface, while the measurement of Maxwell's displacement current was used to detect the phase transition in monolayers. With the above two measurements, the molecular motion of monolayers on the water surface was monitored and analyzed during compression. Importantly, the hyperpolarizability β_{123} was proven to strongly depend on the molecular chirality, and the ratio of $\chi^{(2)}$ tensor elements, S_{14}/S_{15} , indicated the degree of monolayer chirality. Result showed that an S_{14}/S_{15} ratio of $\approx 1/30$ was obtained for the S-CCB monolayer according to the polarized angle dependence measurement at s-output polarization, as shown in Figure 11. However, the measured ratio was very small for 6OCB monolayer. This result corresponds well with the predication of β_{123}/β_{333} using quantum chemical calculations. Then, Fujiwara et al., (2004) measured a characteristic OA effect from the J-aggregates of achiral porphyrin molecules at heptane/water interface by SHG-LD. In this work, the measurement of SHG polarization dependency was performed by rotating a half-wave plate at the molecular resonance wavelength for excitation. The SHG intensity difference was clearly found between the rotation (polarization) angles at $+45^\circ$ and 45° (referring to p- and s-polarization, respectively). The surface chirality is originated from a helical alignment of the J-aggregates from achiral H_4TPPS^{2-} ion-associated with cetyltrimethylammonium (CTA⁺), which causes a magnetic dipole effect. Following the work of Zou et al., (2006), SHG-LD measurement with s-polarization detection was used to verify the chirality of monolayers, in which an intensity difference was shown at the 45° and 135° polarized angles in the dependency curve. Through the curve fitting under C_{∞} symmetry assumption, the degree of the CD effect, represented by S_{14}/S_{15} , was determined for polymerized TDA monolayers deposited from different solutions. It is interesting to note that surface chirality can be formed with a conformational change of achiral molecules caused by metal ions in the subphase solution.

Furthermore, Xu et al., (2009) used SHG-LD to measure the chirality of Langmuir monolayers formed with achiral 5-octadecyloxy-2-(2-pyridylazo)phenol (PARC18) molecules at the air/water interface. Based on the SHG polarization dependency curve measured at s-polarization, the DCE of the

Langmuir monolayer was determined according to the SHG intensity difference between the polarization angles at 45° and 135° . Results showed that the chirality of the monolayer is correlated with the relative concentration of the two opposite chiral states at different experimental conditions and is mainly from the spontaneous and inhomogeneous aggregation of molecules resulted in symmetry breaking (supramolecular chirality) rather than the compression-induced effects. This study is consistent with Fujiwara et al., (2004) that the surface chirality can be formed by the aggregation of achiral molecules. Following the previous application, Lin et al., (2014) studied the surface chirality of Langmuir monolayers of achiral porphyrins at the air/aqueous interface, which involved the mechanism to form supramolecular chirality with two metal ions, Zn^{2+} and Cu^{2+} , in the subphase solution. The Langmuir monolayers of a tetraphenylporphyrin derivative (TPPA2a), which has two long alkyl (hydrophobic) chains and two ester groups, and a TPPA4 (an analog of TPPA2a but without ester groups) were used to confirm the coordination mechanism. In the SHG-LD result, it is concluded that the chirality is originated from the twisted packing of TPPA2a molecules and Cu^{2+} would change the handedness of the TPPA2a helix. In addition, Zn^{2+} forbids the formation of supramolecular chirality of porphyrin assemblies in contrast to Cu^{2+} that facilitates the chiral formation. And the metal ions have a negative effect to form supramolecular chirality when interact with the central nitrogen of porphyrin rings but have a positive effect when interact with the oxygen atoms of the ester groups. Later on, Lv et al., (2015) performed *in situ* measurements of monolayer chirality at the air/water interface with the C-SHG signal amplified by the amphiphile/tetrakis(4-sulfonatophenyl) porphyrin (TPPS) J-aggregates (supramolecular chirality). Based on the SHG-LD results, the chiral amphiphile-tyrosine derivative (TyrC18) monolayers on water and TPPS solution subphase showed no detectable SHG-LD signals, respectively. Furthermore, the measured DCE ratio was up to 200%, and the absolute chiral configuration can be differentiated by the sign of DCE. It is concluded that the amplification of C-SHG is attributed to asymmetrically molecular orientation and increased hyperpolarizability of the J-aggregates benefited from TyrC18.

A different measurement scheme of SHG-LD is proposed by Matthew et al. (Kriech and Conboy, 2003), who implemented SHG-LD on a setup of counter-propagating beam geometry to study the binding affinity of an amphipathic helical peptide, melittin, to a planar supported lipid bilayer (PSLB) of 2-oleoyl-1-palmitoyl-*sn*-glycero-3-phosphocholine (POPC). This approach is able to isolate C-SHG from those achiral SHG contributions by carefully choosing the input and output polarizations. Due to the measurement geometry, the SHG is coherently built along the direction of surface normal (z-direction), and the SHG of x-polarization corresponds to the magnitude of surface chirality. Results showed that melittin experienced a structural change that formed a well-ordered secondary structure, α -helix, with a net orientation along the surface normal when intercalating into a lipid membrane, as compared to a random coil in solution. Here, the SHG signal was measured at x-polarization while the input

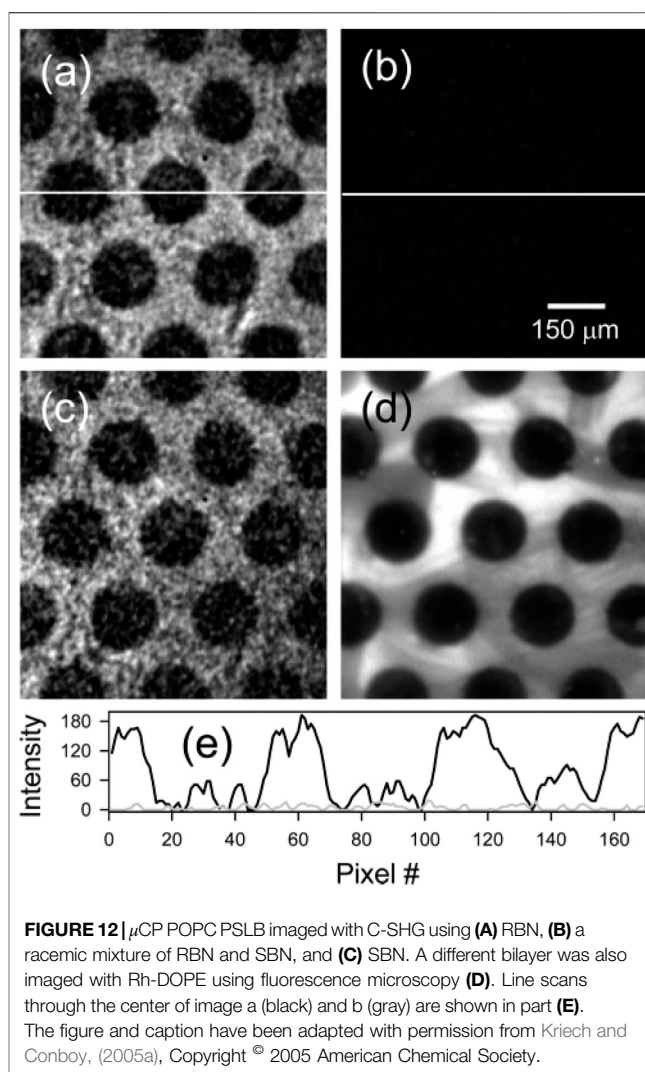
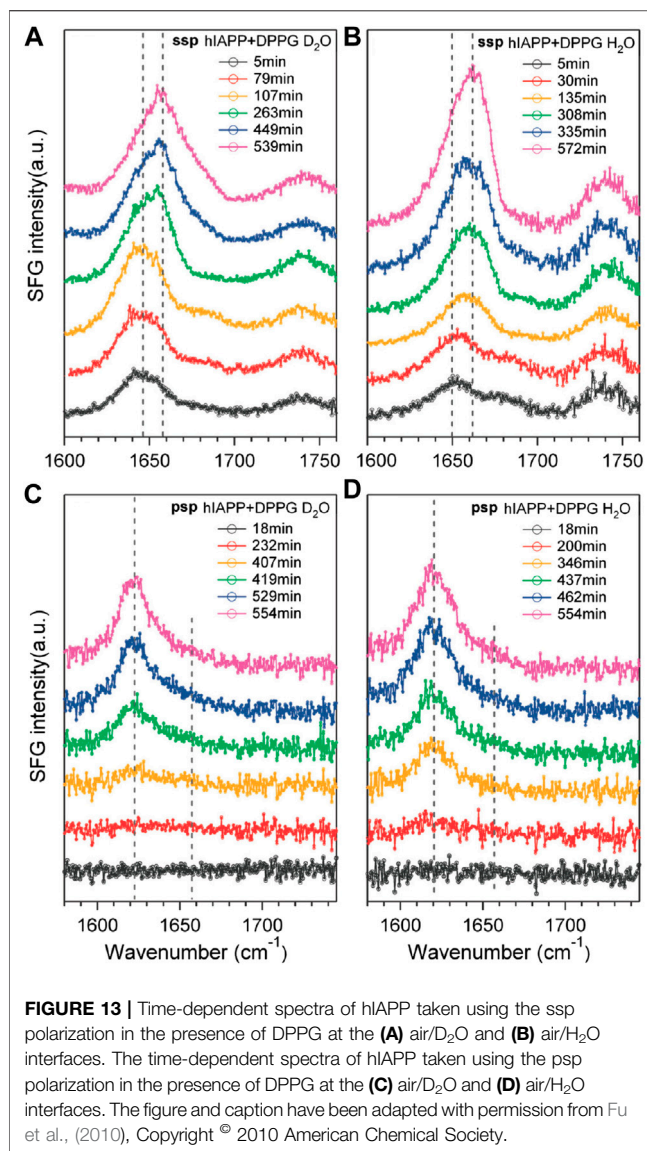


FIGURE 12 | μ CP POPC PSLB imaged with C-SHG using (A) RBN, (B) a racemic mixture of RBN and SBN, and (C) SBN. A different bilayer was also imaged with Rh-DOPE using fluorescence microscopy (D). Line scans through the center of image a (black) and b (gray) are shown in part (E). The figure and caption have been adapted with permission from Kriech and Conboy, (2005a), Copyright © 2005 American Chemical Society.

polarization was continuously changed from 0° to 360° . The same group continued to develop a compact theory to elaborate this counter-propagating detection system (Kriech and Conboy, 2004) and used it to measure the kinetics of *R*- and *S*-1,1'-dinaphthalene-2,2'-diol (RBN and SBN) binding to a POPC bilayer. The enantiomeric excess of RBN and SBN in lipid membranes were also measured, which demonstrates that the two enantiomers undergo complete exchange in the membrane, and the surface enantiomeric excess depends on the enantiomeric composition in the solution (Kriech and Conboy, 2005b). As a novel application of SHG-LD, the same group imaged surface chirality for the first time using the extended form of SHG microscopy, as shown in Figure 12 (Kriech and Conboy, 2005a). In this experiment, the discrimination between the symmetry of RBN and SBN at a PSLB of POPC was achieved, which further provides the spatial distribution information of absorbed molecules on a bilayer. Importantly, without the need for the phase information of $\chi^{(2)}$ tensor elements, χ_{xyz} can be uniquely obtained using the polarization combination of P_{in}/S_{out} . Therefore, by carefully choosing the used polarization setting for



the counter-propagating SHG-LD measurement, the chiral and achiral tensor elements at surfaces can be easily isolated.

Surface Chirality Measured by Sum-Frequency Generation (SFG)

The main difference of SFG from SHG in the arrangement of setup is the use of a tunable IR laser that is organized into a vibrational spectroscopic tool, as the advantage over SHG-related approaches. In general, the measurement of C-SFG uses two polarized laser beams, one is visible and the other is tunable in IR, which are spatiotemporally overlapped at the surface/interface, and the SFG signal is coherently build up from the oriented molecules or chiral structures, which is then detected at the UV in s- or p-polarization by a charge-coupled device (CCD) or a photomultiplier (PMT). Since the chiroptical activities/effects are dispersive in nature, they depend on the probing

wavelength, and thus, the spectrum of their measurements carries the signature of the configuration and conformation of the chiral structures. Similar to SHG-CD spectroscopy, the SFG spectroscopy, being one of the members of surface-specific nonlinear optical spectroscopic techniques, facilitates to record a spectrum for selected molecular bonding in a chiral substance and accurately characterizes the superficial molecular properties with polarized excitations. In this section, we will introduce the polarization-resolved vibrational SFG spectroscopy with literature studies from the following research groups, which have made substantial efforts to implement it on surface chirality.

First, Yan's research group has demonstrated various important experiments using the SFG vibrational spectroscopy in the last decade for the *in situ* and real-time characterization of protein secondary structures at interfaces (Fu et al., 2010; Fu et al., 2011a; Fu et al., 2014a). In these measurements, the secondary structures were investigated in the peptide N-H stretch and amide I bond of a series of model proteins, which were shown in terms of chiral and achiral SFG spectra. Related polarimetric measurement (psp polarization setting) can be used to classify various protein secondary structures and to obtain the orientation and folding kinetics of interfacial proteins. In the studies of amyloid aggregation at the lipid/water interface (Fu et al., 2010; Fu et al., 2011a), it is found that the amyloid protein has relatively disordered structures in normal states, while it aggregates into β -sheet structures (i.e., human islet amyloid polypeptide, hIAPP) on cell membranes in diseased states. The information helps to understand the early stages of amyloid aggregation on membrane surfaces. In experiments, combining C-SFG (psp polarization setting) and achiral SFG (ssp polarization setting) spectroscopic measurements in the amide I region at 1620 cm⁻¹, the aggregation of hIAPP at the air/water interface was observed, as shown in **Figure 13**. Furthermore, the hIAPP solutions in a phosphate buffer with and without negatively charged phospholipid, dipalmitoylphosphoglycerol (DPPG), were used to confirm the induced amyloid aggregation. Result showed that DPPG molecules induce conformational changes in hIAPP instead of rIAPP found in the achiral spectra, while the lipid-induced parallel β -sheet structures can be found in the chiral spectra. It is demonstrated that only proteins folded into chiral secondary structures are able to be observed in C-SFG spectra without the interference of unfolded proteins and water.

On the other hand, the time-dependent chiral and achiral measurements of the interactions between hIAPP and DPPG at the air/water interface were also performed. In one of the experiments, the peptide N-H stretch vibrational band (~ 3200 cm⁻¹) was used to probe the aggregation kinetics (Fu et al., 2011a), in which the chiral specific signal was originated from an intermediate that formed and then disappeared before the parallel β -sheet structures being formed. Moreover, the time-dependent C-SFG signals in the N-H stretch and amide I vibrational regions showed opposite effects upon the addition of DPPG at the air/water interface. In another experiment (Fu et al., 2011a), the C-SFG spectra were obtained from three model systems, LK α 14, pH-low insertion peptide (HLIP), and bovine rhodopsin, and they all showed the N-H stretch vibrational band.

This N-H stretch signal is attributed to the α -helical structure constituted by hIAPP, as an intermediate in the initial aggregation of amyloid on membrane surfaces. Based on the above results, it is concluded that hIAPP shows a disordered structure when adsorbed onto the interface at the initial stage, and then, it is folded into α -helical structures before being converted into β -sheet structures of molecular aggregates.

For the separation of protein secondary structures at interfaces (Fu et al., 2011a; Fu et al., 2011b; Yan et al., 2014), a collection of C-SFG spectra of model peptides and proteins were taken for α -helix, 3_{10} -helix, antiparallel β -sheet, parallel β -sheet (hIAPP), and disordered structures. Result showed that the C-SFG spectra of α -helix and 3_{10} -helix exhibited the N-H stretch band, but no amide I band. However, both N-H stretch and amide I bands appeared in the C-SFG spectra of antiparallel β -sheets. On the contrary, the spectra of hIAPP aggregates only showed the amide I band. Based on the above results, C-SFG has unique selectivity to N-H stretch and amide I bands to distinguish parallel from antiparallel β -sheets and provides specific information for the vibrational structures of protein secondary structures. In addition, there is no amide I band signal from α -helices in C-SFG spectra, and thereby, it is easier to deconvolute the amide I spectra. For other applications, the supramolecular structures, including orientation, symmetry, and chirality, can be extracted by the polarimetric measurements of C-SFG in combination with the analysis of hyperpolarizability tensor elements (Xiao et al., 2012). This kind of study allows for the derivation of amyloid orientation on membrane surfaces, which facilitates to understand the pathogenic mechanism of amyloid-related diseases at the early stages. Furthermore, it is able to shift eye on the C-H stretch vibrational mode (Wang et al., 2013), which is correlated with organic compounds. Therefore, C-SFG promises the observation of surface chirality not only on native membranes but also on synthetic biopolymers. Recently, from another research group, Kocsis et al., (2018) used this technique to discover the chirality induced by the dipolar orientation of confined water in chiral I-quartet artificial channels embedded in supported lipid bilayers similar to aquaporins shown in natural membrane channels. In experiments, achiral HC8 and chiral S-HC8 I-quartets were selected and embedded in supported lipid bilayers for C-SFG measurements on OH and N-H stretch bands. It was found in the chiral psp and spp spectra that a chiral ordering of confined water is formed in both HC8 and S-HC8 channels. Besides, the chirality of HC8 channel is lower than S-HC8 one mainly due to the enantiomeric distribution of the water wires that diminishes the C-SFG signal. In addition, Lu et al., (2019) used SFG vibrational spectroscopy to study the chirality from the peptide- Ca^{2+} ion interfacial interactions when fabricating 2D biomineral nanaosheets. Result showed that the C-SFG signal (psp polarization setting) of amide I band from β -sheet LE10 peptide centered at 1620 cm^{-1} was gradually increased with the interaction time and the CaC_2O_4 mineralization at the last step.

On the other hand, Wang's research group has made a significant contribution to the application of spectrally and polarization-resolved C-SFG measurements. In their studies, a twin polarization angle approach was proposed to quantitatively analyze the surface chirality (Wei et al., 2009). In this approach, both the polarization directions of visible and IR laser beams are

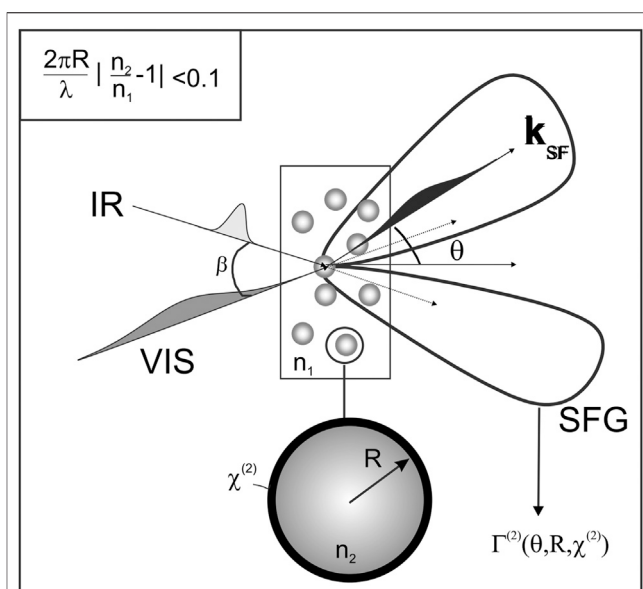


FIGURE 14 | Illustration of a second-order vibrational sum-frequency scattering experiment. The incoming beams generate a nonlinear optical polarization at the interface of a particle. The polarization is the source of the scattered sum frequency light. The magnitude (represented by the scattering lobes) and spectral shape of the scattered field are determined by the molecular properties of the interface, which are contained in the second-order nonlinear susceptibility $\chi^{(2)}$. The angular distribution reflects both the value of the second-order susceptibility and the radius of the particle and the scattering geometry. The criterion used in the Rayleigh-Gans-Debye formalism is depicted in the upper left corner. n_1 and n_2 are corresponding refractive indices. The figure and caption have been adapted with permission from de Beer and Roke, (2007), Copyright © 2007 The American Physical Society.

varied, and the C-SFG signal is detected at s- or p-polarization. The polarization-dependent SFG can be used to precisely measure the sign, relative phase, and absolute values of the chiral and achiral components in the $\chi^{(2)}$ tensor and to identify the surface chirality with a DCE value. In experiments, the S- and R-limonene chiral liquid surfaces were measured, in which the DCE values obtained at 2878 cm^{-1} for S- and R-limonene liquid surfaces are $23.7 \pm 0.4\%$ and $-25.4 \pm 1.3\%$, respectively. It is noted that the detection at s-polarization is only sensitive to the small chiral contributions, similar to SHG-LD. Furthermore, since the C-SFG is sometimes lower than the experimental noise level or influenced by the interplay (leakage) of achiral SFG due to an imperfect polarimetric measurement, which cannot be precisely measured by traditional SFG vibrational spectroscopy, the same group used an interference (or heterodyne) method for the signal enhancement of surface chirality. It is realized by obtaining the interference spectra between the normal chiral and achiral spectrum when a $\pm\theta$ degree of the p-polarization of the visible laser beam is introduced. Such kind of experiment is detailed in Wang et al. (2005), Fu et al. (2014b), Kocsis et al. (2018), Wang et al. (2019b).

An important branch of SFG vibrational spectroscopy is used for the chiral detection of spherical surfaces, that is, NP surfaces (de Beer and Roke, 2007), which is pioneered by Roke et al. When the

discussed geometry is transformed from planar to spherical surfaces, the procedure for deriving effective surface susceptibility should be different because the spatial definition of the incoming wave vectors with respect to the measurement geometry is changed. It indicates a difference in the transformation between the spherical (particle) coordinate of the local susceptibility and the Cartesian coordinate of the effective particle susceptibility. In general, the bulk C-SFG is easily detectable in the transmission mode due to the long coherent length of interaction that is dozens of times larger than that of the reflection mode or at a monolayer in transmission (Belkin et al., 2000), which needs to be enhanced with the help of chiral molecules adsorbed on the surfaces with a preferred orientation. Thus, the increased SFG signal is from certain $\chi^{(2)}$ tensor elements of the adsorbates and the interactions with polarized excitations. Such kind of experiment uses linearly polarized laser beam, following specific polarization combinations as mentioned previously in the experimental scheme, as shown in **Figure 14**. For example, to measure surface chirality, the parameters of β (angle between the two beams) = 45° , θ (scattering angle) = 0° , and polarization combinations of pps, spp, and psp are used. In experiments, the isotropic spherical particles capped with a dielectric film were used, and the molecular interface properties were obtained by measuring the scattering patterns in conjugation with the SFG vibrational spectra. Importantly, the nonlinear Rayleigh–Gans–Debye scattering theory was developed (Roke et al., 2004; de Beer and Roke, 2007) to resolve the chirality and molecular orientation at NP surfaces. Furthermore, by considering the possible effect on the scattering pattern, the effective surface susceptibility as well as the SFG signal can be amplified by adjusting the experimental arrangement, for example, the angle between the two beams, β . Compared to the experiment of planar surfaces, the underlying second-order nonlinear scattering process is dissimilar with an SFG experiment in reflection mode. As a result, the superficial properties such as molecular orientation, composition, and chirality should be managed in a different way. Consequently, C-SFG can not only be used to measure the molecular properties of planar surfaces in reflection mode but also of NP surfaces in an aqueous suspension.

CONCLUSION

In the quest for understanding chirality at different length scales, recent years have witnessed the development of a number of advanced chiroptical strategies, each having its unique advantages for enantiomeric recognition and quantification. In this mini review, we mainly focused on the analytical applications of contemporary chiroptical techniques that have been remarkably successful in interrogating chirality manifested at surfaces,

membranes, and/or interfaces. Undoubtedly, with the capability of probing both molecular and surface chirality, linear chiroptical techniques, for example, ORD, ECD, VCD, and ROA, offer efficient platforms to study not only the identity and the absolute configuration of chiral molecular structures but also the dynamics of surface chirality including its genesis and amplification. That said, we note that a series of technical challenges must be addressed, as elaborated in a number of publications (Petrovic et al., 2015; Collins et al., 2017; Krupová et al., 2020), to further increase the detection sensitivity, acquisition speed, and spectral resolution. In many recent investigations, multimodal spectroscopic techniques have also been used to extract complementary details and/or cross validate the results (Buschhaus et al., 2010; Rivera-Fuentes et al., 2010; Duan et al., 2015b).

On the other hand, nonlinear chiroptical techniques have the potential to open new avenues to the understanding of chirality at surfaces by directly measuring OA effects from molecules localized at surfaces with excellent selectivity and specificity. The spectrally and/or polarization-resolved measurements of C-SHG and C-SFG have shown great potentials and analytical utility in studying surface chirality and dynamics of biological processes. Related applications have been found in chiral molecular recognition at surfaces/interfaces, characterization of protein secondary structures and orientation at interfaces, protein-membrane interactions, kinetics and thermodynamics of protein adsorption/binding at biological surfaces, and molecular aggregations at interfaces. In the near future, we expect that these nonlinear optical surface-specific tools can aid fundamental understanding of disease-induced chiral structure formation, effect evaluation of chiral drug at a particular step, and development of new surface molecular devices for epidemic prevention.

AUTHOR CONTRIBUTIONS

AG, SK, and GZ wrote and edited the manuscript. AG and GZ conceived the work and organized the manuscript.

FUNDING AND ACKNOWLEDGEMENTS

This study was funded by Ministry of Science and Technology (MOST), Taiwan (107-2112-M-039-001 and 109-2112-M-039-001). AG acknowledges the University Grants Commission (UGC), India (Grant No. F.5-376/2014-15/MRP/NERO/2181), and Assam Science Technology and Environment Council, India (Grant No.: ASTEC/S&T/1614/8/2018-19/1159), for their support to the biophotonics research projects at JBC.

REFERENCES

Abdali, S., and Blanch, E. W. (2008). Surface enhanced Raman optical activity (SEROA). *Chem. Soc. Rev.* 37, 980–992. doi:10.1039/b707862p

Abdali, S., Johannessen, C., Nygaard, J., and Nørbygaard, T. (2007). Resonance surface enhanced Raman optical activity of myoglobin as a result of optimized resonance surface enhanced Raman scattering conditions. *J. Phys. Condens. Matter* 19, 285205. doi:10.1088/0953-8984/19/28/285205

- Abdul-Gader, A., Miles, A. J., and Wallace, B. A. (2011). A reference dataset for the analyses of membrane protein secondary structures and transmembrane residues using circular dichroism spectroscopy. *Bioinformatics* 27, 1630–1636. doi:10.1093/bioinformatics/btr234
- Andrews, D. L. (1980). Rayleigh and Raman optical activity: an analysis of the dependence on scattering angle. *J. Chem. Phys.* 72, 4141–4144. doi:10.1063/1.439643
- Barron, L. D., Bogaard, M. P., and Buckingham, A. D. (1973). Raman scattering of circularly polarized light by optically active molecules. *J. Am. Chem. Soc.* 95, 603–605. doi:10.1021/ja00783a058
- Barron, L. D., Zhu, F., Hecht, L., Tranter, G. E., and Isaacs, N. W. (2007). Raman optical activity: an incisive probe of molecular chirality and biomolecular structure. *J. Mol. Struct.* 834–836, 7–16. doi:10.1016/j.molstruc.2006.10.033
- Belkin, M. A., Kulakov, T. A., Ernst, K. H., Yan, L., and Shen, Y. R. (2000). Sum-frequency vibrational spectroscopy on chiral liquids: a novel technique to probe molecular chirality. *Phys. Rev. Lett.* 85, 4474–4477. doi:10.1103/PhysRevLett.85.4474
- Ben-Moshe, A., Maoz, B. M., Govorov, A. O., and Markovich, G. (2013). Chirality and chiroptical effects in inorganic nanocrystal systems with plasmon and exciton resonances. *Chem. Soc. Rev.* 42, 7028–7041. doi:10.1039/c3cs60139k
- Berova, N., Di Bari, L., and Pescitelli, G. (2007). Application of electronic circular dichroism in configurational and conformational analysis of organic compounds. *Chem. Soc. Rev.* 36, 914–931. doi:10.1039/b515476f
- Berthier, D., Buffeteau, T., Léger, J. M., Oda, R., and Huc, I. (2002). From chiral counterions to twisted membranes. *J. Am. Chem. Soc.* 124, 13486–13494. doi:10.1021/ja027660j
- Bhattacharya, S. R., and Bürgi, T. (2019). Amplified vibrational circular dichroism as a manifestation of the interaction between a water soluble gold nanocluster and cobalt salt. *Nanoscale* 11, 23226–23233. doi:10.1039/C9NR07534H
- Bieri, M., Gautier, C., and Bürgi, T. (2007). Probing chiral interfaces by infrared spectroscopic methods. *Phys. Chem. Chem. Phys.* 9, 671–685. doi:10.1039/b609930k
- Blackmond, D. G. (2011). The origin of biological homochirality. *Philos. Trans. R. Soc. Lond. B Biol. Sci.* 366, 2878–2884. doi:10.1098/rstb.2011.0130
- Blanch, E. W., Hecht, L., and Barron, L. D. (2003). Vibrational Raman optical activity of proteins, nucleic acids, and viruses. *Methods* 29, 196–209. doi:10.1016/s1046-2023(02)00310-9
- Blanch, E. W., Hecht, L., Syme, C. D., Volpetti, V., Lomonosoff, G. P., Nielsen, K., et al. (2002). Molecular structures of viruses from Raman optical activity. *J. Gen. Virol.* 83, 2593–2600. doi:10.1099/0022-1317-83-10-2593
- Brunner, H. (2004). “Diastereomers do, what they should not do,” in *Progress in biological chirality*, Editors G. Palyi, C. Zucchi, and L. Caglioti (Oxford: Elsevier), 39–47.
- Burgueño-Tapia, E., and Joseph-Nathan, P. (2015). Vibrational circular dichroism: recent advances for the assignment of the absolute configuration of natural products. *Natural Product Communications* 10, 1785–1795. doi:10.1177/1934578x1501001036
- Burkett, S. L., and Read, M. J. (2001). Adsorption-induced conformational changes of α -helical peptides. *Langmuir* 17, 5059–5065. doi:10.1021/la010156s
- Buschhaus, B., Convertino, V., Rivera-Fuentes, P., Alonso-Gómez, J. L., Petrovic, A. G., and Diederich, F. (2010). Optically active trialkynyl(phenyl)methane: synthesis and determination of its absolute configuration by vibrational circular dichroism (VCD) and optical rotatory dispersion (ORD). *Eur. J. Org. Chem.* 2010, 2452–2456. doi:10.1002/ejoc.201000076
- Byers, J. D., and Hicks, J. M. (1994). Electronic spectral effects on chiral surface second harmonic generation. *Chem. Phys. Lett.* 231, 216–224. doi:10.1016/0009-2614(94)01244-x
- Byers, J. D., Yee, H. I., and Hicks, J. M. (1994a). A second harmonic generation analog of optical rotatory dispersion for the study of chiral monolayers. *J. Chem. Phys.* 101, 6233–6241. doi:10.1063/1.468378
- Byers, J. D., Yee, H. I., Petralli-Mallow, T., and Hicks, J. M. (1994b). Second-harmonic generation circular-dichroism spectroscopy from chiral monolayers. *Phys. Rev. B Condens. Matter* 49, 14643–14647. doi:10.1103/physrevb.49.14643
- Cameron, R. P., and Barnett, S. M. (2014). Optical activity in the scattering of structured light. *Phys. Chem. Chem. Phys.* 16, 25819–25829. doi:10.1039/c4cp03505d
- Cantor, C. R., Jaskunas, S. R., and Tinoco, I., Jr (1966). Optical properties of ribonucleic acids predicted from oligomers. *J. Mol. Biol.* 20, 39–62. doi:10.1016/0022-2836(66)90116-1
- Castiglioni, E., Abbate, S., and Longhi, G. (2011). Experimental methods for measuring optical rotatory dispersion: survey and outlook. *Chirality* 23, 711–716. doi:10.1002/chir.20981
- Chen, E., Gensch, T., Gross, A. B., Hendriks, J., Hellingwerf, K. J., and Kliger, D. S. (2003). Dynamics of protein and chromophore structural changes in the photocycle of photoactive yellow protein monitored by time-resolved optical rotatory dispersion. *Biochemistry* 42, 2062–2071. doi:10.1021/bi020577o
- Chen, E., Swartz, T. E., Bogomolni, R. A., and Kliger, D. S. (2007). A LOV story: the signaling state of the phot1 LOV2 photocycle involves chromophore-triggered protein structure relaxation, as probed by far-UV time-resolved optical rotatory dispersion spectroscopy. *Biochemistry* 46, 4619–4624. doi:10.1021/bi602544n
- Chen, S., Tang, Z., and Xie, J. (2019). Nanoscale chirality. *Part. Part. Syst. Charact.* 36, 1900129. doi:10.1002/ppsc.201900129
- Chen, Y. H., Yang, J. T., and Martinez, H. M. (1972). Determination of the secondary structures of proteins by circular dichroism and optical rotatory dispersion. *Biochemistry* 11, 4120–4131. doi:10.1021/bi00772a015
- Cheng, J., Le Saux, G., Gao, J., Buffeteau, T., Battie, Y., Barois, P., et al. (2017). GoldHelix: gold nanoparticles forming 3D helical superstructures with controlled morphology and strong chiroptical property. *ACS Nano* 11, 3806–3818. doi:10.1021/acsnano.6b08723
- Chowdhury, E., and Akaike, T. (2005). Bio-functional inorganic materials: an attractive branch of gene-based nano-medicine delivery for 21st century. *Cgt.* 5, 669–676. doi:10.2174/156652305774964613
- Collins, J. T., Kuppe, C., Hooper, D. C., Sibilia, C., Centini, M., and Valev, V. K. (2017). Chirality and chiroptical effects in metal nanostructures: fundamentals and current trends. *Advanced Optical Materials* 5, 1700182. doi:10.1002/adom.201700182
- Corn, R. M., and Higgins, D. A. (1994). Optical second harmonic generation as a probe of surface chemistry. *Chem. Rev.* 94, 107–125. doi:10.1021/cr00025a004
- Crawford, M. J., Haslam, S., Probert, J. M., Gruzdkov, Y. A., and Frey, J. G. (1994). Second harmonic generation from the air/water interface of an aqueous solution of the dipeptide Boc-Trp-Trp. *Chem. Phys. Lett.* 230, 260–264. doi:10.1016/0009-2614(94)01142-7
- Croisier, F., and Jérôme, C. (2013). Chitosan-based biomaterials for tissue engineering. *Eur. Polym. J.* 49, 780–792. doi:10.1016/j.eurpolymj.2012.12.009
- Das, D., and Pal, S. K. (2017). Liquid crystal unveiled interactions between melittin and phospholipids at aqueous-liquid crystal interface. *Chemistry Select.* 2, 4779–4786. doi:10.1002/slct.201700604
- De Beer, A. G. F., and Roke, S. (2007). Sum frequency generation scattering from the interface of an isotropic particle: geometrical and chiral effects. *Phys. Rev. B.* 75, 245438. doi:10.1103/physrevb.75.245438
- Di Gregorio, M. C., Ben Moshe, A., Tirosh, E., Galantini, L., and Markovich, G. (2015). Chiroptical study of plasmon-molecule interaction: the case of interaction of glutathione with silver nanocubes. *J. Phys. Chem. C* 119, 17111–17116. doi:10.1021/acs.jpcc.5b03272
- Djerassi, C., Riniker, R., and Riniker, B. (1956). Optical rotatory dispersion studies. VII. Application to problems of absolute Configurations. *J. Am. Chem. Soc.* 78, 6362–6377. doi:10.1021/ja01605a024
- Dolamic, I., Varnholt, B., and Bürgi, T. (2015). Chirality transfer from gold nanocluster to adsorbate evidenced by vibrational circular dichroism. *Nat. Commun.* 6, 7117–7126. doi:10.1038/ncomms8117
- Dressler, D. H., Landau, A., Zaban, A., and Mastai, Y. (2007). Sub-micrometer polarimetry of chiral surfaces using near-field scanning optical microscopy. *Chem Commun (Camb)* 9, 945–947. doi:10.1039/b617139g
- Duan, Y., Han, L., Zhang, J., Asahina, S., Huang, Z., Shi, L., et al. (2015a). Optically active nanostructured ZnO films. *Angew Chem. Int. Ed. Engl.* 54, 15170–15175. doi:10.1002/anie.201507502
- Duan, Y., Han, L., Zhang, J., Asahina, S., Huang, Z., Shi, L., et al. (2015b). Optically active nanostructured ZnO films. *Angew Chem. Int. Ed. Engl.* 54, 15170–15175. doi:10.1002/anie.201507502
- Dudzik, C. G., Walter, E. D., Abrams, B. S., Jurica, M. S., and Millhauser, G. L. (2013). Coordination of copper to the membrane-bound form of α -synuclein. *Biochemistry* 52, 53–60. doi:10.1021/bi301475q

- Edwards, A., and Jenkinson, S. (2012). "8.3 perspective and concepts: overview of techniques for assigning stereochemistry," in *Comprehensive chirality*, Editors E. M. Carreira and H. Yamamoto Netherlands: Elsevier, 39–53.
- Efrima, S. (1985). Raman optical activity of molecules adsorbed on metal surfaces: theory. *J. Chem. Phys.* 83, 1356–1362. doi:10.1063/1.449452
- Efrima, S. (1983). The effect of large electric field gradients on the Raman optical activity of molecules adsorbed on metal surfaces. *Chem. Phys. Lett.* 102, 79–82. doi:10.1016/0009-2614(83)80662-9
- Emeis, C. A., Oosterhoff, L. J., and Vries, G. D. (1967). Numerical evaluation of kramers—krönig relations. *Proc. Roy. Soc. Lond. Math. Phys. Sci.* 297, 54–65.
- Ernst, K. H. (2006). "Supramolecular surface chirality," in *Supramolecular chirality*. (Berlin, Heidelberg: Springer), 209–252.
- Esposito, M., Tasco, V., Todisco, F., Benedetti, A., Tarantini, I., Cusunà, M., et al. (2015). Tailoring chiro-optical effects by helical nanowire arrangement. *Nanoscale* 7, 18081–18088. doi:10.1039/c5nr04674b
- Fan, Z., and Govorov, A. O. (2012). Chiral nanocrystals: plasmonic spectra and circular dichroism. *Nano Lett.* 12, 3283–3289. doi:10.1021/nl3013715
- Fears, K. P., Sivaraman, B., Powell, G. L., Wu, Y., and Latour, R. A., (2009). Probing the conformation and orientation of adsorbed enzymes using side-chain modification. *Langmuir* 25, 9319–9327. doi:10.1021/la901885d
- Fischer, P., and Hache, F. (2005). Nonlinear optical spectroscopy of chiral molecules. *Chirality* 17, 421–437. doi:10.1002/chir.20179
- Fischer, P., and Buckingham, A. D. (1998). Surface second-order nonlinear optical activity. *J. Opt. Soc. Am. B* 15, 2951–2957. doi:10.1364/josab.15.002951
- Flack, H. D. (2009). Louis Pasteur's discovery of molecular chirality and spontaneous resolution in 1848, together with a complete review of his crystallographic and chemical work. *Acta Crystallogr. A, Found Crystallogr* 65, 371–389. doi:10.1107/S0108767309024088
- Fleischer, C. C., and Payne, C. K. (2014). Nanoparticle-cell interactions: molecular structure of the protein corona and cellular outcomes. *Acc. Chem. Res.* 47, 2651–2659. doi:10.1021/ar500190q
- Fu, L., Liu, J., and Yan, E. C. (2011a). Chiral sum frequency generation spectroscopy for characterizing protein secondary structures at interfaces. *J. Am. Chem. Soc.* 133, 8094–8097. doi:10.1021/ja201575e
- Fu, L., Wang, Z., and Yan, E. C. (2011b). Chiral vibrational structures of proteins at interfaces probed by sum frequency generation spectroscopy. *Int. J. Mol. Sci.* 12, 9404–9425. doi:10.3390/ijms12129404
- Fu, L., Ma, G., and Yan, E. C. (2010). *In Situ* misfolding of human islet amyloid polypeptide at interfaces probed by vibrational sum frequency generation. *J. Am. Chem. Soc.* 132, 5405–5412. doi:10.1021/ja909546b
- Fu, L., Wang, Z., and Yan, E. C. (2014a). N-H stretching modes around 3300 wavenumber from peptide backbones observed by chiral sum frequency generation vibrational spectroscopy. *Chirality* 26, 521–524. doi:10.1002/chir.22306
- Fu, L., Zhang, Y., Wei, Z. H., and Wang, H. F. (2014b). Intrinsic chirality and prochirality at Air/R-(+)- and S-(-)-limonene interfaces: spectral signatures with interference chiral sum-frequency generation vibrational spectroscopy. *Chirality* 26, 509–520. doi:10.1002/chir.22337
- Fujimaki, H., Manaka, T., Ohtake, H., Tojima, A., and Iwamoto, M. (2003). Second-harmonic generation and Maxwell displacement current spectroscopy of chiral organic monolayers at the air-water interface. *J. Chem. Phys.* 119, 7427–7434. doi:10.1063/1.1605943
- Fujiwara, K., Monjushiro, H., and Watarai, H. (2004). Non-linear optical activity of porphyrin aggregate at the liquid/liquid interface. *Chem. Phys. Lett.* 394, 349–353. doi:10.1016/j.cplett.2004.07.018
- Furusawa, G., and Kan, T. (2020). Au nanospirals transferred onto PDMS film exhibiting circular dichroism at visible wavelengths. *Micromachines* 11, 641. doi:10.3390/mi11070641
- Gąsior-Głogowska, M., Malek, K., Zajac, G., and Baranska, M. (2016). A new insight into the interaction of cisplatin with DNA: ROA spectroscopic studies on the therapeutic effect of the drug. *Analyst* 141, 291–296. doi:10.1039/c5an02140e
- Gal, J. (2013). Molecular chirality in chemistry and biology: historical milestones. *HCA (Hel. Chim. Acta)* 96, 1617–1657. doi:10.1002/hlca.201300300
- Gautier, C., and Bürgi, T. (2005). Vibrational circular dichroism of N-acetyl-L-cysteine protected gold nanoparticles. *Chem Commun. (Camb)* 43, 5393–5395. doi:10.1039/b509346e
- Gautier, C., and Bürgi, T. (2006). Chiral N-isobutyryl-cysteine protected gold nanoparticles: preparation, size selection, and optical activity in the UV-vis and infrared. *J. Am. Chem. Soc.* 128, 11079–11087. doi:10.1021/ja058717f
- Gautier, C., and Bürgi, T. (2010). Vibrational circular dichroism of adsorbed molecules: BINAS on gold nanoparticles. *J. Phys. Chem. C* 114, 15897–15902. doi:10.1021/jp910800m
- Gautier, C. (2008). "Preparation, size separation and chiroptical properties of chiral gold nanoparticles," Doctoral dissertation. Switzerland: Université de Neuchâtel.
- Gebauer, J. S., Malissek, M., Simon, S., Knauer, S. K., Maskos, M., Stauber, R. H., et al. (2012). Impact of the nanoparticle-protein corona on colloidal stability and protein structure. *Langmuir* 28, 9673–9679. doi:10.1021/la301104a
- Gegel, N., Zhuravleva, Y., Shipovskaya, A., Malinkina, O., and Zudina, I. (2018b). Influence of chitosan ascorbate chirality on the gelation kinetics and properties of silicon-chitosan-containing glycerohydrogels. *Polymers* 10, 259. doi:10.3390/polym10030259
- Gegel, N., Zudina, I., Malinkina, O., and Shipovskaya, A. (2018a). Effect of ascorbic acid isomeric forms on antibacterial activity of its chitosan salts. *Microbiology* 87, 732–737.
- Ghosh, P. S., Han, G., Erdogan, B., Rosado, O., Krovi, S. A., and Rotello, V. M. (2007). Nanoparticles featuring amino acid-functionalized side chains as DNA receptors. *Chem. Biol. Drug Des.* 70, 13–18. doi:10.1111/j.1747-0285.2007.00534.x
- Gitter-Amir, A., Rosenheck, K., and Schneider, A. S. (1976). Angular scattering analysis of the circular dichroism of biological cells. 1. The red blood cell membrane. *Biochemistry* 15, 3131–3137. doi:10.1021/bi00659a029
- Gogoi, A., Mazumder, N., Konwer, S., Ranawat, H., Chen, N.-T., and Zhuo, G.-Y. (2019). Enantiomeric recognition and separation by chiral nanoparticles. *Molecules* 24, 1007. doi:10.3390/molecules24061007
- Goldberg, D., and Weissman, Z. (2019). Accurate, nondifferential, curve-fitted, self-referenced optical rotation polarimeter. *Appl Opt.* 58, 9815–9822. doi:10.1364/AO.58.009815
- Goodman, C. M., Chari, N. S., Han, G., Hong, R., Ghosh, P., and Rotello, V. M. (2006). DNA-binding by functionalized gold nanoparticles: mechanism and structural requirements. *Chem. Biol. Drug Des.* 67, 297–304. doi:10.1111/j.1747-0285.2006.00372.x
- Gopal, R., Park, J. S., Seo, C. H., and Park, Y. (2012). Applications of circular dichroism for structural analysis of gelatin and antimicrobial peptides. *Int. J. Mol. Sci.* 13, 3229–3244. doi:10.3390/ijms13033229
- Green, D. W., Lee, J.-M., Kim, E.-J., Lee, D.-J., and Jung, H.-S. (2016). Chiral biomaterials: from molecular design to regenerative medicine. *Adv. Mater. Interfaces* 3, 1500411. doi:10.1002/admi.201500411
- Green, J. R., Edwards, P. A., and Green, C. (1973). Optical-rotatory-dispersion studies of compounds related to cholesterol in liposomes and the membranes of erythrocyte 'ghosts'. *Biochem. J.* 135, 63–71. doi:10.1042/bj1350063
- Greenfield, N. J. (1999). Applications of circular dichroism in protein and peptide analysis. *Trac. Trends Anal. Chem.* 18, 236–244. doi:10.1016/s0165-9936(98)00112-5
- Greenfield, N. J. (2004). Circular dichroism analysis for protein-protein interactions, *Methods Mol. Biol.* 261, 55–78. doi:10.1385/1-59259-762-9-055
- Greenfield, N. J. (2006). Using circular dichroism spectra to estimate protein secondary structure. *Nat. Protoc.* 1, 2876. doi:10.1038/nprot.2006.202
- Hache, F., Boulesteix, T., Schanne-Klein, M. C., Alexandre, M., Lemerrier, G., and Andraud, C. (2003). Polarization rotation in a second harmonic reflection experiment from an isotropic surface of chiral Träger base. *J. Phys. Chem. B* 107, 5261–5266. doi:10.1021/jp034216+
- Han, Z., Xu, Z., and Chen, L. (2014). New spectroscopic method for the determination of optical rotatory dispersion. *Chin. Optic Lett.* 12, 081202. doi:10.3788/COL201412.081202
- Hao, J., Li, Y., Miao, J., Liu, R., Li, J., Liu, H., et al. (2020). Ligand-induced chirality in asymmetric CdSe/CdS nanostructures: a close look at chiral tadpoles. *ACS Nano* 14, 10346–10358. doi:10.1021/acsnano.0c03909
- Haraguchi, S., Hara, M., Shingae, T., Kumauchi, M., Hoff, W. D., and Unno, M. (2015). Experimental detection of the intrinsic difference in Raman optical activity of a photoreceptor protein under preresonance and resonance conditions. *Angew Chem. Int. Ed. Engl.* 54, 11555–11558. doi:10.1002/anie.201505466

- Hecht, L., and Barron, L. D. (1994). Rayleigh and Raman optical activity from chiral surfaces. *Chem. Phys. Lett.* 225, 525–530. doi:10.1016/0009-2614(94)87122-1
- Hicks, J. M., Petralli-Mallow, T., and Byers, J. D. (1994). Consequences of chirality in second-order non-linear spectroscopy at surfaces. *Faraday Discuss.* 99, 341–357. doi:10.1039/fd9949900341
- Hicks, J. M., and Petralli-Mallow, T. (1999). Nonlinear optics of chiral surface systems. *Appl. Phys. B Laser Optic.* 68, 589–593. doi:10.1007/s003400050669
- Hoffman, K. R., Yen, W. M., Lockwood, D. J., and Sulewski, P. E. (1994). Birefringence-induced vibrational Raman and Rayleigh optical activity in uniaxial crystals. *Phys. Rev. B Condens. Matter* 49, 182. doi:10.1103/physrevb.49.182
- Hoffmann, G. G. (2012). “Spectroscopic analysis: Raman optical activity,” in *Separations and analysis*. Netherlands: Elsevier, 498–519.
- Holzwarth, G., Hsu, E. C., Mosher, H. S., Faulkner, T. R., and Moscowitz, A. (1974). Infrared circular dichroism of carbon-hydrogen and carbon-deuterium stretching modes. Observations. *J. Am. Chem. Soc.* 96, 251–252. doi:10.1021/ja00808a042
- Horn, R., Grundmann, G., and Paulsen, H. (2007). Consecutive binding of chlorophylls a and b during the assembly *in vitro* of light-harvesting chlorophyll-a/b protein (LHCIIb). *J. Mol. Biol.* 366, 1045–1054. doi:10.1016/j.jmb.2006.11.069
- Hu, L., Xi, F., Qv, L., and Fang, Y. (2018). Searching the theoretical ultimate limits of probing surface-enhanced Raman optical activity. *ACS Omega* 3, 1170–1177. doi:10.1021/acsomega.7b02098
- Huttunen, M. J., Erkkilä, M., and Kauranen, M. (2009). Absolute nonlinear optical probes of surface chirality. *J. Optic. Pure Appl. Optic.* 11, 034006. doi:10.1088/1464-4258/11/3/034006
- Huttunen, M. J., Virkki, M., Erkkilä, M., Vuorimaa, E., Efimov, A., Lemmetyinen, H., et al. (2010). Absolute probe of surface chirality based on focused circularly polarized light. *J. Phys. Chem. Lett.* 1, 1826–1829. doi:10.1021/jz100572s
- Janesko, B. G., and Scuseria, G. E. (2006). Surface enhanced Raman optical activity of molecules on orientationally averaged substrates: theory of electromagnetic effects. *J. Chem. Phys.* 125, 124704. doi:10.1063/1.2345368
- Janesko, B. G., and Scuseria, G. E. (2009). Molecule–Surface orientational averaging in surface enhanced Raman optical activity spectroscopy. *J. Phys. Chem. C* 113, 9445–9449. doi:10.1021/jp9025514
- Jayaram, D. T., Pustulka, S. M., Mannino, R. G., Lam, W. A., and Payne, C. K. (2018). Protein corona in response to flow: effect on protein concentration and structure. *Biophys. J.* 115, 209–216. doi:10.1016/j.bpj.2018.02.036
- Ji, N., and Shen, Y. R. (2006). A novel spectroscopic probe for molecular chirality. *Chirality* 18, 146–158. doi:10.1002/chir.20238
- Jiang, S., Jia, H., Lei, Y., Shen, X., Cao, J., and Wang, N. (2017a). Novel method for determination of optical rotatory dispersion spectrum by using line scan CCD. *Opt. Express* 25, 7445–7454. doi:10.1364/OE.25.007445
- Jiang, W., Pacella, M. S., Athanasiadou, D., Nelea, V., Vali, H., Hazen, R. M., et al. (2017b). Chiral acidic amino acids induce chiral hierarchical structure in calcium carbonate. *Nat. Commun.* 8, 15066–15113. doi:10.1038/ncomms15066
- Johannessen, C., White, P. C., and Abdali, S. (2007). Resonance Raman optical activity and surface enhanced resonance Raman optical activity analysis of cytochrome c. *J. Phys. Chem.* 111, 7771–7776. doi:10.1021/jp0705267
- Kauranen, M., Verbiest, T., Maki, J. J., and Persoons, A. (1994). Second-harmonic generation from chiral surfaces. *J. Chem. Phys.* 101, 8193–8199. doi:10.1063/1.468203
- Kelly, S. M., Jess, T. J., and Price, N. C. (2005). How to study proteins by circular dichroism. *Biochim. Biophys. Acta.* 1751, 119–139. doi:10.1016/j.bbapap.2005.06.005
- Kelly, S. M., and Price, N. C. (2000). The use of circular dichroism in the investigation of protein structure and function. *Curr. Protein Pept. Sci.* 1, 349–384. doi:10.2174/1389203003381315
- Kim, H., Im, S. W., Kim, R. M., Cho, N. H., Lee, H.-E., Ahn, H.-Y., et al. (2020). Chirality control of inorganic materials and metals by peptides or amino acids. *Mater. Adv.* 1, 512–524. doi:10.1039/d0ma00125b
- Kneipp, H., Kneipp, J., and Kneipp, K. (2006). Surface-enhanced Raman optical activity on adenine in silver colloidal solution. *Anal. Chem.* 78, 1363–1366. doi:10.1021/ac0516382
- Kneipp, J., Wittig, B., Bohr, H., and Kneipp, K. (2010). Surface-enhanced Raman scattering: a new optical probe in molecular biophysics and biomedicine. *Theor. Chem. Acc.* 125, 319–327. doi:10.1007/s00214-009-0665-2
- Kocourková, L., Novotná, P., Čujová, S., Čefovský, V., Urbanová, M., and Setnička, V. (2017). Conformational study of melectin and antapin antimicrobial peptides in model membrane environments. *Spectrochim. Acta Mol. Biomol. Spectrosc.* 170, 247–255. doi:10.1016/j.saa.2016.07.015
- Kocsis, I., Sorci, M., Vanselow, H., Murail, S., Sanders, S. E., Licsandru, E., et al. (2018). Oriented chiral water wires in artificial transmembrane channels. *Sci. Adv.* 4, eaao5603. doi:10.1126/sciadv.aao5603
- Kriech, M. A., and Conboy, J. C. (2003). Label-free chiral detection of melittin binding to a membrane. *J. Am. Chem. Soc.* 125, 1148–1149. doi:10.1021/ja028577z
- Kriech, M. A., and Conboy, J. C. (2004). Counterpropagating second-harmonic generation: a new technique for the investigation of molecular chirality at surfaces. *J. Optical Soc. America B.* 21, 1013–1022. doi:10.1364/JOSAB.21.001013
- Kriech, M. A., and Conboy, J. C. (2005a). Imaging chirality with surface second harmonic generation microscopy. *J. Am. Chem. Soc.* 127, 2834–2835. doi:10.1021/ja0430649
- Kriech, M. A., and Conboy, J. C. (2005b). Using the intrinsic chirality of a molecule as a label-free probe to detect molecular adsorption to a surface by second harmonic generation. *Appl. Spectrosc.* 59, 746–753. doi:10.1366/0003702054280711
- Krupová, M., Kessler, J., and Bouř, P. (2020). Recent trends in chiroptical spectroscopy: theory and applications of vibrational circular dichroism and Raman optical activity. *ChemPlusChem.* 85, 561–575. doi:10.1002/cplu.202000014
- Krykunov, M., Kundrat, M. D., and Autschbach, J. (2006). Calculation of circular dichroism spectra from optical rotatory dispersion, and vice versa, as complementary tools for theoretical studies of optical activity using time-dependent density functional theory. *J. Chem. Phys.* 125, 194110. doi:10.1063/1.2363372
- Kumar, J., and Liz-Marzán, L. M. (2019). Recent advances in chiral plasmonics - towards biomedical applications. *Bcsj.* 92, 30–37. doi:10.1246/bcsj.20180236
- Kurouski, D. (2017). Advances of vibrational circular dichroism (VCD) in bioanalytical chemistry. A review. *Anal. Chim. Acta.* 990, 54–66. doi:10.1016/j.aca.2017.08.014
- Kuznetsova, V. A., Mates-Torres, E., Prochukhan, N., Marcastel, M., Purcell-Milton, F., O'Brien, J., et al. (2019). Effect of chiral ligand concentration and binding mode on chiroptical activity of CdSe/CdS quantum dots. *ACS Nano.* 13, 13560–13572. doi:10.1021/acsnano.9b07513
- Lee, H.-E., Ahn, H.-Y., Lee, J., and Nam, K. T. (2017). Biomolecule-enabled chiral assembly of plasmonic nanostructures. *ChemNanoMat.* 3, 685–697. doi:10.1002/cnma.201700208
- Lee, H. E., Ahn, H. Y., Mun, J., Lee, Y. Y., Kim, M., Cho, N. H., et al. (2018). Amino-acid- and peptide-directed synthesis of chiral plasmonic gold nanoparticles. *Nature* 556, 360–365. doi:10.1038/s41586-018-0034-1
- Lee, H. E., Kim, R. M., Ahn, H. Y., Lee, Y. Y., Byun, G. H., Im, S. W., et al. (2020). Cysteine-encoded chirality evolution in plasmonic rhombic dodecahedral gold nanoparticles. *Nat. Commun.* 11, 263. doi:10.1038/s41467-019-14117-x
- Lenard, J., and Singer, S. J. (1966). Protein conformation in cell membrane preparations as studied by optical rotatory dispersion and circular dichroism. *Proc. Natl. Acad. Sci. U.S.A.* 56, 1828. doi:10.1073/pnas.56.6.1828
- Lewis, S. (2013). “Techniques, nonchromatographic separation,” in *Encyclopedia of forensic sciences*, Editors J. A. Siegel, P. J. Saukko, and M. M. Houck (Cambridge, MA: Academic Press), 621–626.
- Li, X., Willits, J., Cundiff, S., Aarts, I., Stevens, A., and Dessau, D. (2006). Circular dichroism in second harmonic generation from oxidized Si (001). *Applied Physics Letters - APPL PHYS LETT.* 89, 022102. doi:10.1063/1.2220014
- Li, Y., and Lee, J.-S. (2020). Insights into characterization methods and biomedical applications of nanoparticle-protein corona. *Materials* 13, 3093. doi:10.3390/ma13143093
- Lieberman, I., Shemer, G., Fried, T., Kosower, E. M., and Markovich, G. (2008). Plasmon-resonance-enhanced absorption and circular dichroism. *Angew. Chem. Int. Ed. Engl.* 47, 4855–4857. doi:10.1002/anie.200800231

- Liehr, A. D. (1964). Interaction of electromagnetic radiation with matter. I. Theory of optical rotatory power: topic A. Trigonal dihedral compounds1a. *J. Phys. Chem.* 68, 665–722. doi:10.1021/j100786a001
- Lin, L., Wang, T., Lu, Z., Liu, M., and Guo, Y. (2014). *In Situ* measurement of the supramolecular chirality in the Langmuir monolayers of achiral porphyrins at the air/aqueous interface by second harmonic generation linear dichroism. *J. Phys. Chem. C* 118, 6726–6733. doi:10.1021/jp4106579
- Litman, B. J. (1972). Effect of light scattering on the circular dichroism of biological membranes. *Biochemistry* 11, 3243–3247. doi:10.1021/bi00767a018
- Liu, H., and Webster, T. J. (2007). Nanomedicine for implants: a review of studies and necessary experimental tools. *Biomaterials* 28, 354–369. doi:10.1016/j.biomaterials.2006.08.049
- Liu, W., Rose, J., Plantevin, S., Auffan, M., Bottero, J. Y., and Vidaud, C. (2013). Protein corona formation for nanomaterials and proteins of a similar size: hard or soft corona? *Nanoscale* 5, 1658–1668. doi:10.1039/c2nr33611a
- Liu, X., Yang, J., Geng, Z., and Jia, H. (2020). Simultaneous measurement of optical rotation dispersion and absorption spectra for chiral substances. *Chirality* 32, 23233. doi:10.1002/chir.23233
- Lizio, M., Andrushchenko, V., Pike, S., Peters, A., Whitehead, G. F. S., Vitórica-Yrezábal, I., et al. (2018). Optically active vibrational spectroscopy of α -aminoisobutyric acid foldamers in organic solvents and phospholipid bilayers. *Chemistry* 24, 9399. doi:10.1002/chem.201801121
- Long, M. M., Urry, D. W., and Stoekenius, W. (1977). Circular dichroism of biological membranes: purple membrane of *Halobacterium halobium*. *Biochem. Biophys. Res. Commun.* 75, 725–731. doi:10.1016/0006-291x(77)91532-7
- Lu, H., Schäfer, A., Lutz, H., Roeters, S. J., Lieberwirth, I., Muñoz-Espí, R., et al. (2019). Peptide-controlled assembly of macroscopic calcium oxalate nanosheets. *J. Phys. Chem. Lett.* 10, 2170–2174. doi:10.1021/acs.jpclett.9b00684
- Lu, J. E., Yang, C. H., Wang, H., Yam, C., Yu, Z. G., and Chen, S. (2018). Plasmonic circular dichroism of vesicle-like nanostructures by the template-less self-assembly of achiral Janus nanoparticles. *Nanoscale* 10, 14586–14593. doi:10.1039/c8nr05366a
- Lv, K., Lin, L., Wang, X., Zhang, L., Guo, Y., Lu, Z., et al. (2015). Significant chiral signal amplification of Langmuir monolayers probed by second harmonic generation. *J. Phys. Chem. Lett.* 6, 1719–1723. doi:10.1021/acs.jpclett.5b00472
- Ma, W., Xu, L., De Moura, A. F., Wu, X., Kuang, H., Xu, C., et al. (2017). Chiral inorganic nanostructures. *Chem. Rev.* 117, 8041–8093. doi:10.1021/acs.chemrev.6b00755
- Magar, M. E. (1968). On the analysis of the optical rotatory dispersion of proteins. *Biochemistry* 7, 617–620. doi:10.1021/bi00842a016
- Magg, M., Kadria-Vili, Y., Oulevey, P., Weisman, R. B., and Bürgi, T. (2016). Resonance Raman optical activity spectra of single-walled carbon nanotube enantiomers. *J. Phys. Chem. Lett.* 7, 221–225. doi:10.1021/acs.jpclett.5b02612
- Mahmoudi, M., Lynch, I., Ejtehadi, M. R., Monopoli, M. P., Bombelli, F. B., and Laurent, S. (2011). Protein-nanoparticle interactions: opportunities and challenges. *Chem. Rev.* 111, 5610–5637. doi:10.1021/cr100440g
- Maki, J. J., Kauranen, M., and Persoons, A. (1995). Surface second-harmonic generation from chiral materials. *Phys. Rev. B Condens. Matter.* 51, 1425–1434. doi:10.1103/physrevb.51.1425
- Maki, J. J., Kauranen, M., Verbiest, T., and Persoons, A. (1997). Uniqueness of wave-plate measurements in determining the tensor components of second-order surface nonlinearities. *Phys. Rev. B* 55, 5021–5026. doi:10.1103/physrevb.55.5021
- Mamonov, E. A., Kolmychek, I. A., Vandendriessche, S., Hojeij, M., Ekinci, Y., Valev, V. K., et al. (2014). Anisotropy versus circular dichroism in second harmonic generation from fourfold symmetric arrays of G-shaped nanostructures. *Phys. Rev. B* 89, 121113. doi:10.1103/physrevb.89.121113
- Manaka, T., Fujimaki, H., Ohtake, H., and Iwamoto, M. (2005). SHG and MDC spectroscopy of chiral organic monolayer at the air-water interface. *Colloid. Surface. Physicochem. Eng. Aspect.* 257–258, 79–83. doi:10.1016/j.colsurfa.2004.10.023
- Marichal, L., Degrouard, J., Gatin, A., Raffray, N., Aude, J. C., Boulard, Y., et al. (2020). From protein corona to colloidal self-assembly: the importance of protein size in protein-nanoparticle interactions. *Langmuir* 36, 8218–8230. doi:10.1021/acs.langmuir.0c01334
- Martial, B., Lefèvre, T., Buffeteau, T., and Auger, M. (2019). Vibrational circular dichroism reveals supramolecular chirality inversion of α -synuclein peptide assemblies upon interactions with anionic membranes. *ACS Nano* 13, 3232–3242. doi:10.1021/acsnano.8b08932
- Matsuo, K., Maki, Y., Namatame, H., Taniguchi, M., and Gekko, K. (2016). Conformation of membrane-bound proteins revealed by vacuum-ultraviolet circular-dichroism and linear-dichroism spectroscopy. *Proteins* 84, 349–359. doi:10.1002/prot.24981
- McMillin, C. R., and Walton, A. G. (1974). A circular dichroism technique for the study of adsorbed protein structure. *J. Colloid Interface Sci.* 48, 345–349. doi:10.1016/0021-9797(74)90170-2
- Micsonai, A., Wien, F., Kerna, L., Lee, Y. H., Goto, Y., Réfrégiers, M., et al. (2015). Accurate secondary structure prediction and fold recognition for circular dichroism spectroscopy. *Proc. Natl. Acad. Sci. U.S.A.* 112, E3095–E3103. doi:10.1073/pnas.1500851112
- Mijidodorj, B., Matsuo, Y., Sato, H., Ueda, K., and Kawamura, I. (2019). A comparative study on interactions of antimicrobial peptides L- and D-phenylseptin with 1,2-dimyristoyl-sn-glycero-3-phosphocholine. *Appl. Sci.* 9, 2601. doi:10.3390/app9132601
- Miles, A. J., and Wallace, B. A. (2016). Circular dichroism spectroscopy of membrane proteins. *Chem. Soc. Rev.* 45, 4859–4872. doi:10.1039/c5cs00084j
- Mitchell, S. A. (2006). Origin of second harmonic generation optical activity of a tryptophan derivative at the air/water interface. *J. Chem. Phys.* 125, 044716. doi:10.1063/1.2216696
- Mitchell, S. A., McAloney, R. A., Moffatt, D., Mora-Diez, N., and Zgierski, M. Z. (2005). Second-harmonic generation optical activity of a polypeptide α -helix at the air/water interface. *J. Chem. Phys.* 122, 114707. doi:10.1063/1.1862613
- Mokashi-Punekar, S., Zhou, Y., Brooks, S. C., and Rosi, N. L. (2019). Construction of chiral, helical nanoparticle superstructures: progress and prospects. *Adv. Mater.* 32, 1905975. doi:10.1002/adma.201905975
- Nafie, L. A. (2008). Vibrational circular dichroism: a new tool for the solution-state determination of the structure and absolute configuration of chiral natural product molecules. *Natural Product Communications* 3, 451–466. doi:10.1177/1934578x0800300322
- Nafie, L. A. (2012). “8.25 spectroscopic analysis: vibrational circular dichroism,” in *Comprehensive chirality*. Editors E. M. Carreira and H. Yamamoto (Netherlands: Elsevier Science), Vol. 8, 478–497.
- Nafie, L. A. (2018). “Vibrational optical activity: from small chiral molecules to protein pharmaceuticals and beyond,” in *Frontiers and advances in molecular spectroscopy* Netherlands: Elsevier, 421–469.
- Nafie, L. A. (2020). Vibrational optical activity: from discovery and development to future challenges. *Chirality* 32, 667–692. doi:10.1002/chir.23191
- Nagy, P. R., Koltai, J., Surján, P. R., Kürti, J., and Szabados, Á. (2016). Resonance Raman optical activity of single walled chiral carbon nanotubes. *J. Phys. Chem.* 120, 5527–5538. doi:10.1021/acs.jpca.6b04594
- Narushima, T., and Okamoto, H. (2016). Circular dichroism microscopy free from commingling linear dichroism via discretely modulated circular polarization. *Sci. Rep.* 6, 35731. doi:10.1038/srep35731
- Nguyen, L., Dass, M., Ober, M. F., Besteiro, L. V., Wang, Z. M., Nickel, B., et al. (2020). Chiral assembly of gold-silver core-shell plasmonic nanorods on DNA origami with strong optical activity. *ACS Nano* 14, 7454–7461. doi:10.1021/acsnano.0c03127
- Novotná, P., Goncharova, I., and Urbanová, M. (2014). Mutual structural effect of bilirubin and model membranes by vibrational circular dichroism. *Biochim. Biophys. Acta Biomembr.* 1838, 831–841. doi:10.1016/j.bbmem.2013.12.005
- Novotná, P., and Urbanová, M. (2012). Vibrational circular dichroism study of polypeptide model-membrane systems. *Anal. Biochem.* 427, 211–218. doi:10.1016/j.ab.2012.03.023
- Novotná, P., and Urbanová, M. (2015). Bilirubin, model membranes and serum albumin interaction: the influence of fatty acids. *Biochim. Biophys. Acta Biomembr.* 1848, 1331–1340. doi:10.1016/j.bbmem.2015.02.026
- Ozcelik, A., Pereira-Cameselle, R., Poklar Ulrih, N., Petrovic, A. G., and Alonso-Gómez, J. L. (2020). Chiroptical sensing: a conceptual introduction. *Sensors* 20, 974. doi:10.3390/s20040974
- Parčáňský, V., Kapítan, J., and Bouř, P. (2014). Inspecting chiral molecules by Raman optical activity spectroscopy. *RSC Adv.* 4, 57125–57136. doi:10.1039/C4RA10416A
- Park, S. J. (2020). Protein-nanoparticle interaction: corona Formation and conformational changes in proteins on nanoparticles. *Int J Nanomedicine* 15, 5783. doi:10.2147/IJN.S254808

- Pazderková, M., Maloň, P., Zima, V., Hofbauerová, K., Kopecký, V., Jr., Kočíšová, E., et al. (2019). Interaction of halictine-related antimicrobial peptides with membrane models. *Int. J. Mol. Sci.* 20, 631. doi:10.3390/ijms20030631
- Pederzoli, F., Tosi, G., Vandelli, M. A., Belletti, D., Forni, F., and Ruozzi, B. (2017). Protein corona and nanoparticles: how can we investigate on? *Wiley Interdiscip. Rev. Nanomed. Nanobiotechnol.* 9, e1467. doi:10.1002/wnan.1467
- Petralli-Mallow, T. P., Plant, A. L., Lewis, M. L., and Hicks, J. M. (2000). Cytochrome c model membrane surfaces: exploration via second harmonic generation-circular dichroism and surface-enhanced resonance Raman spectroscopy. *Langmuir* 16, 5960–5966. doi:10.1021/la9913250
- Petralli-Mallow, T., Wong, T. M., Byers, J. D., Yee, H. I., and Hicks, J. M. (1993). Circular dichroism spectroscopy at interfaces: a surface second harmonic generation study. *J. Phys. Chem.* 97, 1383–1388. doi:10.1021/j100109a022
- Petrovic, A. G., Berova, N., and Alonso-Gómez, J. L. (2015). “Absolute configuration and conformational analysis of chiral compounds via experimental and theoretical prediction of chiroptical properties: ORD, ECD, and VCD,” in *Structure elucidation in organic Chemistry*, Editors M.-M. Cid and J. Bravo Germany: Wiley-VCH Verlag GmbH & Co. KGaA, 65–104.
- Podraza, N. J., Pursel, S. M., Chen, C., Horn, M. W., and Collins, R. W. (2008). Analysis of the optical properties and structure of serial bi-deposited TiO₂ chiral sculptured thin films using Mueller matrix ellipsometry. *J. Nanophotonics* 2, 021930. doi:10.1117/1.3062210
- Polavarapu, P. L. (2002). Optical rotation: recent advances in determining the absolute configuration. *Chirality* 14, 768–781. doi:10.1002/chir.10145
- Polavarapu, P. L., and Santoro, E. (2020). Vibrational optical activity for structural characterization of natural products. *Nat. Prod. Rep.* 37, 25. doi:10.1039/d1030np00025f
- Polyanichko, A. M., Andrushchenko, V. V., Bour, P., and Wieser, H. (2011). “Vibrational circular dichroism studies of biological macromolecules and their complexes,” in *Circular dichroism: theory and spectroscopy* Editors D. S. Rodgers (New York: Nova Science Publishers, Inc., 67–126.
- Pour, S. O., Bell, S. E., and Blanch, E. W. (2011). Use of a hydrogel polymer for reproducible surface enhanced Raman optical activity (SEROA). *Chem Commun (Camb)* 47, 4754–4756. doi:10.1039/c0cc05284a
- Pour, S. O., Barron, L. D., Mutter, S. T., and Blanch, E. W. (2018). “Raman optical activity,” in *Chiral analysis Advances in spectroscopy, chromatography and emerging methods*, 2nd Edition, Editor P. L. Polavarapu New York: Elsevier, 249–291.
- Puri, M., and Ferry, V. E. (2017). Circular dichroism of CdSe nanocrystals bound by chiral carboxylic acids. *ACS Nano* 11, 12240–12246. doi:10.1021/acsnano.7b05690
- Qiu, X., Xie, L., Liu, X., Luo, L., Zhang, Z., and Du, J. (2016). Estimation of optical rotation of chiral molecules with weak measurements. *Opt. Lett.* 41, 4032–4035. doi:10.1364/OL.41.004032
- Rajaei, M., Zeng, J., Albooyeh, M., Kamandi, M., Hanifeh, M., Capolino, F., et al. (2019). Giant circular dichroism at visible frequencies enabled by plasmonic ramp-shaped nanostructures. *ACS Photonics* 6, 924–931. doi:10.1021/acsp Photonics.8b01584
- Ranjbar, B., and Gill, P. (2009). Circular dichroism techniques: biomolecular and nanostructural analyses— a review. *Chem. Biol. Drug Des.* 74, 101–120. doi:10.1111/j.1747-0285.2009.00847.x
- Ren, X., Lin, W., Fang, Y., Ma, F., and Wang, J. (2017). Raman optical activity (ROA) and surface-enhanced ROA (SE-ROA) of (+)-(R)-methyloxirane adsorbed on a Ag₂₀cluster. *RSC Adv.* 7, 34376–34381. doi:10.1039/c7ra04949h
- Rivera-Fuentes, P., Alonso-Gómez, J. L., Petrovic, A. G., Santoro, F., Harada, N., Berova, N., et al. (2010). Amplification of chirality in monodisperse, enantiopure alleno-acetylenic oligomers. *Angew. Chem. Int. Ed. Engl.* 49, 2247–2250. doi:10.1002/anie.200906191
- Rodger, A. (2013). “Circular dichroism spectroscopy of biomacromolecules,” in *Encyclopedia of biophysics*. Berlin, Heidelberg: Springer.
- Rodriguez, V., Koeckelberghs, G., and Verbiest, T. (2007). Second-harmonic generation-circular dichroism in thin films of a chiral poly(3-alkyl) thiophene. *Chem. Phys. Lett.* 450, 76–79. doi:10.1016/j.cplett.2007.10.097
- Rodriguez, V., and Sourisseau, C. (2002). General Maker-fringe ellipsometric analyses in multilayer nonlinear and linear anisotropic optical media. *J. Opt. Soc. Am. B* 19, 2650–2664. doi:10.1364/josab.19.002650
- Roke, S., Bonn, M., and Petukhov, A. V. (2004). Nonlinear optical scattering: the concept of effective susceptibility. *Phys. Rev. B* 70, 115106. doi:10.1103/physrevb.70.115106
- Roy Bhattacharya, S., and Bürgi, T. (2019). Amplified vibrational circular dichroism as a manifestation of the interaction between a water soluble gold nanocluster and cobalt salt. *Nanoscale* 11, 23226–23233. doi:10.1039/c9nr07534h
- Salvati, A., Pitek, A. S., Monopoli, M. P., Prapainop, K., Bombelli, F. B., Hristov, D. R., et al. (2013). Transferrin-functionalized nanoparticles lose their targeting capabilities when a biomolecule corona adsorbs on the surface. *Nat. Nanotechnol.* 8, 137–143. doi:10.1038/nnano.2012.237
- Sasaki, T., Hisaki, I., Miyano, T., Tohnai, N., Morimoto, K., Sato, H., et al. (2013). Linkage control between molecular and supramolecular chirality in 2₁-helical hydrogen-bonded networks using achiral components. *Nat. Commun.* 4, 1787. doi:10.1038/ncomms2756
- Sato, H., Tamura, K., Takimoto, K., and Yamagishi, A. (2018). Solid state vibrational circular dichroism towards molecular recognition: chiral metal complexes intercalated in a clay mineral. *Phys. Chem. Chem. Phys.* 20, 3141–3147. doi:10.1039/c7cp05114j
- Sato, H., and Kawamura, I. (2020). Solid-state vibrational circular dichroism studies on the conformation of an amino acid molecule in crystalline state. *Biochim. Biophys. Acta Protein Proteomics* 1868, 140439. doi:10.1016/j.bbapap.2020.140439
- Schmeltz, M., Teulon, C., Latour, G., Ghoubay, D., Borderie, V., Aimé, C., et al. (2019). Implementation of artifact-free circular dichroism SHG imaging of collagen. *Opt. Express* 27, 22685–22699. doi:10.1364/OE.27.022685
- Schmeltz, M., Teulon, C., Pinsard, M., Hansen, U., Alnawaiseh, M., Ghoubay, D., et al. (2020). Circular dichroism second-harmonic generation microscopy probes the polarity distribution of collagen fibrils. *Optica* 7, 1469–1476. doi:10.1364/optica.399246
- Schneider, A. S., Schneider, M. J., and Rosenheck, K. (1970). Optical activity of biological membranes: scattering effects and protein conformation. *Proc. Natl. Acad. Sci. U.S.A.* 66, 793–798. doi:10.1073/pnas.66.3.793
- Sels, A., Azoulay, R., Buma, W. J., Koenis, M. A. J., Nicu, V. P., and Bürgi, T. (2019). Vibrational circular dichroism of thiolate-protected Au₂₅ clusters: accurate prediction of spectra and chirality transfer within the mixed ligand shell. *J. Phys. Chem. C* 123, 22586–22594. doi:10.1021/acs.jpcc.9b05638
- Shapiro, D. B., Goldbeck, R. A., Che, D., Esquerra, R. M., Paquette, S. J., and Kliger, D. S. (1995). Nanosecond optical rotatory dispersion spectroscopy: application to photolyzed hemoglobin-CO kinetics. *Biophys. J.* 68, 326–334. doi:10.1016/S0006-3495(95)80191-8
- Shen, Y. R. (1984). The principles of nonlinear optics. New York, US: John Wiley & Sons.
- Shen, Y. R. (1994). Surfaces probed by nonlinear optics. *Surf. Sci.* 299–300, 551–562. doi:10.1016/0039-6028(94)90681-5
- Shen, Y. R. (1996). A few selected applications of surface nonlinear optical spectroscopy. *Proc. Natl. Acad. Sci. U.S.A.* 93, 12104–12111. doi:10.1073/pnas.93.22.12104
- Shimizu, M., Kobayashi, K., Morii, H., Mitsui, K., Knoll, W., and Nagamune, T. (2003). Secondary structure analyses of protein films on gold surfaces by circular dichroism. *Biochem. Biophys. Res. Commun.* 310, 606–611. doi:10.1016/j.bbrc.2003.09.054
- Shipovskaya, A. B., Shmakov, S. L., and Gegel, N. O. (2019). Optical activity anisotropy of chitosan-based films. *Carbohydr. Polym.* 206, 476–486. doi:10.1016/j.carbpol.2018.11.026
- Shipovskaya, A. B., Fomina, V. I., Kazmicheva, O. F., Rudenko, D. A., and Malinkina, O. N. (2017). Optical activity of films based on chitosan of various molecular masses and modifications. *Polym. Sci. Ser. A* 59, 330–341. doi:10.1134/s0965545x17030154
- Shukla, N., Bartel, M. A., and Gellman, A. J. (2010). Enantioselective separation on chiral Au nanoparticles. *J. Am. Chem. Soc.* 132, 8575–8580. doi:10.1021/ja908219h
- Shukla, N., Ondeck, N., and Gellman, A. J. (2014). Quantitation of enantiospecific adsorption on chiral nanoparticles from optical rotation. *Surf. Sci.* 629, 15–19. doi:10.1016/j.susc.2014.03.011
- Shukla, N., Ondeck, N., Khosla, N., Klara, S., Petti, A., and Gellman, A. (2015). Polarimetric detection of enantioselective adsorption by chiral Au

- nanoparticles - effects of temperature, wavelength and size. *Nanomater. Nanotechnol* 5, 1. doi:10.5772/60109
- Shukla, N., Yang, D., and Gellman, A. J. (2016). Enantiomeric separations of chiral pharmaceuticals using chirally modified tetrahedral Au nanoparticles. *Surf. Sci.* 648, 29–34. doi:10.1016/j.susc.2015.10.061
- Siligardi, G., Hussain, R., Patching, S. G., and Phillips-Jones, M. K. (2014). Ligand- and drug-binding studies of membrane proteins revealed through circular dichroism spectroscopy. *Biochim. Biophys. Acta.* 1838, 34–42. doi:10.1016/j.bbame.2013.06.019
- Simpson, G. J. (2002). Structural origins of circular dichroism in surface second harmonic generation. *J. Chem. Phys.* 117, 3398–3410. doi:10.1063/1.1494423
- Sioncke, S., Van Elshocht, S., Verbiest, T., Kauranen, M., Phillips, K. E. S., Katz, T. J., et al. (2001). Circular-difference effects in second-harmonic generation from thin films. *Synth. Met.* 124, 191–193. doi:10.1016/s0379-6779(01)00441-6
- Sivaraman, B., Fears, K. P., and Latour, R. A. (2009). Investigation of the effects of surface chemistry and solution concentration on the conformation of adsorbed proteins using an improved circular dichroism method. *Langmuir* 25, 3050–3056. doi:10.1021/la8036814
- Slocik, J. M., Govorov, A. O., and Naik, R. R. (2011). Plasmonic circular dichroism of peptide-functionalized gold nanoparticles. *Nano Lett.* 11, 701–705. doi:10.1021/nl1038242
- Slocik, J. M., Dennis, P. B., Govorov, A. O., Bedford, N. M., Ren, Y., and Naik, R. R. (2020). Chiral restructuring of peptide enantiomers on gold nanomaterials. *ACS Biomater. Sci. Eng.* 6, 2612–2620. doi:10.1021/acsbomaterials.9b00933
- Snatzke, G. (1968). Circular dichroism and optical rotatory dispersion- principles and application to the investigation of the stereochemistry of natural products. *Angew. Chem. Int. Ed. Engl.* 7, 14–25. doi:10.1002/anie.196800141
- Sood, V. D., and Gross, A. W. (2019). “Membrane proteins as targets for biological drugs,” in *Advances in membrane proteins: building, signaling and malfunction*, ed. Y. Cao (Singapore: Springer Singapore), 49–65.
- Sreerama, N., and Woody, R. W. (2004). On the analysis of membrane protein circular dichroism spectra. *Protein Sci.* 13, 100–112. doi:10.1110/ps.03258404
- Stark, C., Carvajal Arrieta, C. A., Behroozian, R., Redmer, B., Fiedler, F., and Müller, S. (2019). Broadband polarimetric glucose determination in protein containing media using characteristic optical rotatory dispersion. *Biomed Opt Express* 10, 6340–6350. doi:10.1364/BOE.10.006340
- Sun, M., Zhang, Z., Wang, P., Li, Q., Ma, F., and Xu, H. (2013). Remotely excited Raman optical activity using chiral plasmon propagation in Ag nanowires. *Light Sci. Appl.* 2, e112. doi:10.1038/lsa.2013.68
- Tanaka, M., Motomura, T., Kawada, M., Anzai, T., Kasori, Y., Shiroya, T., et al. (2000). Blood compatible aspects of poly(2-methoxyethylacrylate) (PMEA)--relationship between protein adsorption and platelet adhesion on PMEA surface. *Biomaterials* 21, 1471–1481. doi:10.1016/s0142-9612(00)00031-4
- Tang, Y., and Cohen, A. E. (2010). Optical chirality and its interaction with matter. *Phys. Rev. Lett.* 104, 163901. doi:10.1103/PhysRevLett.104.163901
- Tester, R. F., and Karkalas, J. (2003). “CARBOHYDRATES | classification and properties,” in *Encyclopedia of food sciences and nutrition*. Cambridge, MA: Academic Press, 862–875.
- Thyparambil, A. A., Wei, Y., and Latour, R. A. (2015). Experimental characterization of adsorbed protein orientation, conformation, and bioactivity. *Biointerphases* 10, 019002. doi:10.1116/1.4906485
- Tokunaga, D., Takechi, H., Yin, J. H., Watarai, H., and Ohde, T. (2009). Microscopic measurement of second harmonic generation from chiral surfaces. *Anal. Sci.* 25, 311–314. doi:10.2116/analsci.25.311
- Toxvaerd, S. (2009). Origin of homochirality in biosystems. *Int. J. Mol. Sci.* 10, 1290–1299. doi:10.3390/ijms10031290
- Tranter, G. E. (2012). “Spectroscopic analysis: electronic circular dichroism,” in *Comprehensive chirality*, Editors E. M. Carreira and H. Yamamoto (Netherlands: Elsevier Science), 422–437.
- Urry, D. W., Masotti, L., and Krivacic, J. R. (1971). Circular dichroism of biological membranes. I. Mitochondria and red blood cell ghosts. *Biochim. Biophys. Acta.* 241, 600–612. doi:10.1016/0005-2736(71)90058-7
- Urry, D. W., and Long, M. M. (1974). “Circular dichroism and absorption studies on biomembranes,” in *Methods in membrane biology*. Boston, MA: Springer, 105–141.
- Venerando, R., Miotto, G., Magro, M., Dallan, M., Baratella, D., Bonaiuto, E., et al. (2013). Magnetic nanoparticles with covalently bound self-assembled protein corona for advanced biomedical applications. *J. Phys. Chem. C* 117, 20320–20331. doi:10.1021/jp4068137
- Verbiest, T., Elshocht, S. V., Kauranen, M., Hellemans, L., Snauwaert, J., Nuckolls, C., et al. (1998). Strong enhancement of nonlinear optical properties through supramolecular chirality. *Science* 282, 913–915. doi:10.1126/science.282.5390.913
- Verbiest, T., Kauranen, M., Maki, J. J., Teerenstra, M. N., Schouten, A. J., Nolte, R. J. M., et al. (1995). Linearly polarized probes of surface chirality. *J. Chem. Phys.* 103, 8296–8298. doi:10.1063/1.470714
- Vermeer, A. W., and Norde, W. (2000). CD spectroscopy of proteins adsorbed at flat hydrophilic quartz and hydrophobic teflon surfaces. *J. Colloid Interface Sci.* 225, 394–397. doi:10.1006/jcis.2000.6769
- Vogel, V. (1996). What do nonlinear optical techniques have to offer the biosciences? *Curr. Opin. Colloid Interface Sci.* 1, 257–263. doi:10.1016/s1359-0294(96)80013-6
- Walker, S. I. (2011). “Homochirality,” in *Encyclopedia of astrobiology*. Berlin, Heidelberg: Springer.
- Wang, J., Chen, X., Clarke, M. L., and Chen, Z. (2005). Detection of chiral sum frequency generation vibrational spectra of proteins and peptides at interfaces *in situ*. *Proc. Natl. Acad. Sci. U.S.A.* 102, 4978–4983. doi:10.1073/pnas.0501206102
- Wang, T., Lv, H., Huang, J., Shan, H., Feng, L., Mao, Y., et al. (2019a). Reaction selectivity of homochiral versus heterochiral intermolecular reactions of prochiral terminal alkynes on surfaces. *Nat. Commun.* 10, 1–9. doi:10.1038/s41467-019-12102-y
- Wang, X., Wang, M., Lei, R., Zhu, S. F., Zhao, Y., and Chen, C. (2017). Chiral surface of nanoparticles determines the orientation of adsorbed transferrin and its interaction with receptors. *ACS Nano*. 11, 4606–4616. doi:10.1021/acsnano.7b00200
- Wang, Y., Du, J., Ma, X., Wang, H., Chou, K. C., and Li, Q. (2019b). Chirality discrimination at the carvone air/liquid interfaces detected by heterodyne-detected sum frequency generation. *Heliyon* 5, e03061. doi:10.1016/j.heliyon.2019.e03061
- Wang, Z., Fu, L., and Yan, E. C. (2013). C-H stretch for probing kinetics of self-assembly into macromolecular chiral structures at interfaces by chiral sum frequency generation spectroscopy. *Langmuir* 29, 4077–4083. doi:10.1021/la304954h
- Wei, F., Xu, Y.-Y., Guo, Y., Liu, S.-L., and Wang, H.-F. (2009). Quantitative surface chirality detection with sum frequency generation vibrational spectroscopy: twin polarization angle Approach. *Chin. J. Chem. Phys.* 22, 592–600. doi:10.1088/1674-0068/22/06/592-600
- Whitmore, L., and Wallace, B. A. (2004). DICHROWEB, an online server for protein secondary structure analyses from circular dichroism spectroscopic data. *Nucleic Acids Res.* 32, W668–W673. doi:10.1093/nar/gkh371
- Whitmore, L., and Wallace, B. A. (2008). Protein secondary structure analyses from circular dichroism spectroscopy: methods and reference databases. *Biopolymers* 89, 392–400. doi:10.1002/bip.20853
- Whitmore, L., Woollett, B., Miles, A. J., Klose, D. P., Janes, R. W., and Wallace, B. A. (2011). PCDDb: the Protein Circular Dichroism Data Bank, a repository for circular dichroism spectral and metadata. *Nucleic Acids Res.* 39, D480–D486. doi:10.1093/nar/gkq1026
- Xia, J., Feng, Y., Zhu, L., Zhang, Z., Xia, L., and Liu, L. (2014). Remote excited Raman optical activity of adenine along Ag plasmonic waveguide. *Plasmonics* 9, 673–676. doi:10.1007/s11468-014-9684-5
- Xiao, D., Fu, L., Liu, J., Batista, V. S., and Yan, E. C. (2012). Amphiphilic adsorption of human islet amyloid polypeptide aggregates to lipid/aqueous interfaces. *J. Mol. Biol.* 421, 537–547. doi:10.1016/j.jmb.2011.12.035
- Xu, L., Luo, L., Wu, H., Luo, Z., Zhang, Z., Shi, H., et al. (2020). Measurement of chiral molecular parameters based on combination of surface plasmon resonance and weak value amplification. *ACS Sens.* 10.1021/acssensors.0c00346
- Xu, Y.-Y., Rao, Y., Zheng, D.-S., Guo, Y., Liu, M.-H., and Wang, H.-F. (2009). Inhomogeneous and spontaneous formation of chirality in the Langmuir monolayer of achiral molecules at the air/water interface probed by in situ surface second harmonic generation linear dichroism. *J. Phys. Chem. C* 113, 4088–4098. doi:10.1021/jp810509u
- Yan, E. C., Fu, L., Wang, Z., and Liu, W. (2014). Biological macromolecules at interfaces probed by chiral vibrational sum frequency generation spectroscopy. *Chem. Rev.* 114, 8471–8498. doi:10.1021/cr4006044

- Yang, G., and Xu, Y. (2010). Vibrational circular dichroism spectroscopy of chiral molecules, *Top. Curr. Chem.* 298, 189–236. doi:10.1007/128_2010_86
- Yao, H., Nishida, N., and Kimura, K. (2010). Conformational study of chiral penicillamine ligand on optically active silver nanoclusters with IR and VCD spectroscopy. *Chem. Phys.* 368, 28–37. doi:10.1016/j.chemphys.2009.12.006
- Yoo, S., and Park, Q. H. (2015). Enhancement of chiroptical signals by circular differential mie scattering of nanoparticles. *Sci. Rep.* 5, 14463. doi:10.1038/srep14463
- Yoo, S., and Park, Q.-H. (2019). Metamaterials and chiral sensing: a review of fundamentals and applications. *Nanophotonics* 8, 249–261. doi:10.1515/nanoph-2018-0167
- Zhang, Q., Hernandez, T., Smith, K. W., Hosseini Jebeli, S. A., Dai, A. X., Warning, L., et al. (2019). Unraveling the origin of chirality from plasmonic nanoparticle-protein complexes. *Science* 365, 1475. doi:10.1126/science.aax5415
- Zhang, T., Tang, M., Yao, Y., Ma, Y., and Pu, Y. (2019). MWCNT interactions with protein: surface-induced changes in protein adsorption and the impact of protein corona on cellular uptake and cytotoxicity. *Int J Nanomedicine* 14, 993. doi:10.2147/IJN.S191689
- Zhao, X., Lu, D., Hao, F., and Liu, R. (2015). Exploring the diameter and surface dependent conformational changes in carbon nanotube-protein corona and the related cytotoxicity. *J. Hazard Mater.* 292, 98–107. doi:10.1016/j.jhazmat.2015.03.023
- Zhao, X., Zang, S. Q., and Chen, X. (2020). Stereospecific interactions between chiral inorganic nanomaterials and biological systems. *Chem. Soc. Rev.* 49, 2481–2503. doi:10.1039/d0cs00093k
- Zhao, Y., Sun, M., Ma, W., Kuang, H., and Xu, C. (2017). Biological molecules-governed plasmonic nanoparticle dimers with tailored optical behaviors. *J. Phys. Chem. Lett.* 8, 5633–5642. doi:10.1021/acs.jpclett.7b01781
- Zhu, F., Isaacs, N. W., Hecht, L., and Barron, L. D. (2005). Raman optical activity: a tool for protein structure analysis. *Structure* 13, 1409–1419. doi:10.1016/j.str.2005.07.009
- Zhu, F., Wang, J., Xie, S., Zhu, Y., Wang, L., Xu, J., et al. (2020). L-Pyroglutamic acid-modified CdSe/ZnS quantum dots: a new fluorescence-responsive chiral sensing platform for stereospecific molecular recognition. *Anal. Chem.* 92, 12040–12048. doi:10.1021/acs.analchem.0c02668
- Zhuo, G.-Y., Chen, M.-Y., Yeh, C.-Y., Guo, C.-L., and Kao, F.-J. (2017a). Fast determination of three-dimensional fibril orientation of type-I collagen via macroscopic chirality. *Appl. Phys. Lett.* 110, 023702. doi:10.1063/1.4973885
- Zhuo, G.-Y., Hung, W.-H., and Kao, F.-J. (2017b). Determination of three-dimensional molecular orientation of type-I collagen by circularly-polarized second harmonic generation imaging. Bellingham, Washington: SPIE. doi:10.1117/12.2269427
- Zou, G., Manaka, T., Taguchi, D., and Iwamoto, M. (2006). Studying the chirality of polymerized 10,12-tricosadynoic acid LB films using SHG polarized angle dependence and SHG-CD method. *Colloid. Surface. Physicochem. Eng. Aspect.* 284–285, 424–429. doi:10.1016/j.colsurfa.2005.11.044
- Zsila, F. (2010). “Electronic circular dichroism spectroscopy,” in *Pharmaceutical sciences encyclopedia: drug discovery, development, and manufacturing*. Hoboken, NJ: John Wiley & Sons, Inc., 1–61.

Conflict of Interest: The authors declare that the research was conducted in the absence of any commercial or financial relationships that could be construed as a potential conflict of interest.

Copyright © 2021 Gogoi, Konwer and Zhuo. This is an open-access article distributed under the terms of the Creative Commons Attribution License (CC BY). The use, distribution or reproduction in other forums is permitted, provided the original author(s) and the copyright owner(s) are credited and that the original publication in this journal is cited, in accordance with accepted academic practice. No use, distribution or reproduction is permitted which does not comply with these terms.



Intermolecular Chirality Modulation of Binaphthalene-Bridged Bisporphyrins With Chiral Diamines

Wenxin Lu^{1,2}, Lei Gong², Chaorui Su², Qibao Wang¹, Qing Ling¹, Peng Wang¹, Dongdong Qi^{2*} and Yongzhong Bian^{2*}

¹College of Chemical and Biological Engineering, Shandong University of Science and Technology, Qingdao, 266590, China,

²Beijing Key Laboratory for Science and Application of Functional Molecular and Crystalline Materials, Department of Chemistry, University of Science and Technology Beijing, Beijing, China

OPEN ACCESS

Edited by:

Keiji Hirose,
Osaka University, Japan

Reviewed by:

Takashi Hayashita,
Sophia University, Japan
Paola Rizzo,
University of Salerno, Italy

*Correspondence:

Dongdong Qi
qdd@ustb.edu.cn
Yongzhong Bian
yzbian@ustb.edu.cn

Specialty section:

This article was submitted to
Supramolecular Chemistry,
a section of the journal
Frontiers in Chemistry

Received: 28 September 2020

Accepted: 14 December 2020

Published: 12 February 2021

Citation:

Lu W, Gong L, Su C, Wang Q, Ling Q,
Wang P, Qi D and Bian Y (2021)
Intermolecular Chirality Modulation of
Binaphthalene-Bridged Bisporphyrins
With Chiral Diamines.
Front. Chem. 8:611257.
doi: 10.3389/fchem.2020.611257

A new pair of 2,2'-diamino-1,1'-binaphthyl linked porphyrin dimers, (*R*)-/(*S*)-**H**, were synthesized to study their supramolecular interactions with a pair of chiral diamines ((*R*)-/(*S*)-PPDA) by using UV-Vis absorption, fluorescence and NMR titrations. The spectroscopic titrations indicated that sandwich-type 1:1 complexes were formed at low guest concentration and then transformed to 1:2 open complexes at high guest concentration. The supramolecular interactions afforded sensitive circular dichroism responses, and the CD signs of the 1:1 complexes are decided by the stereostructure of chiral diamine guests. Moreover, due to the shortened linking units, (*R*)-/(*S*)-**H** show more sensitive and predicable CD response than the previously reported hosts (*R*)-/(*S*)-**H1** and this can be reasonably explained by DFT molecular modeling. The present results suggest (*R*)-/(*S*)-**H** are promising for chiral optical sensing.

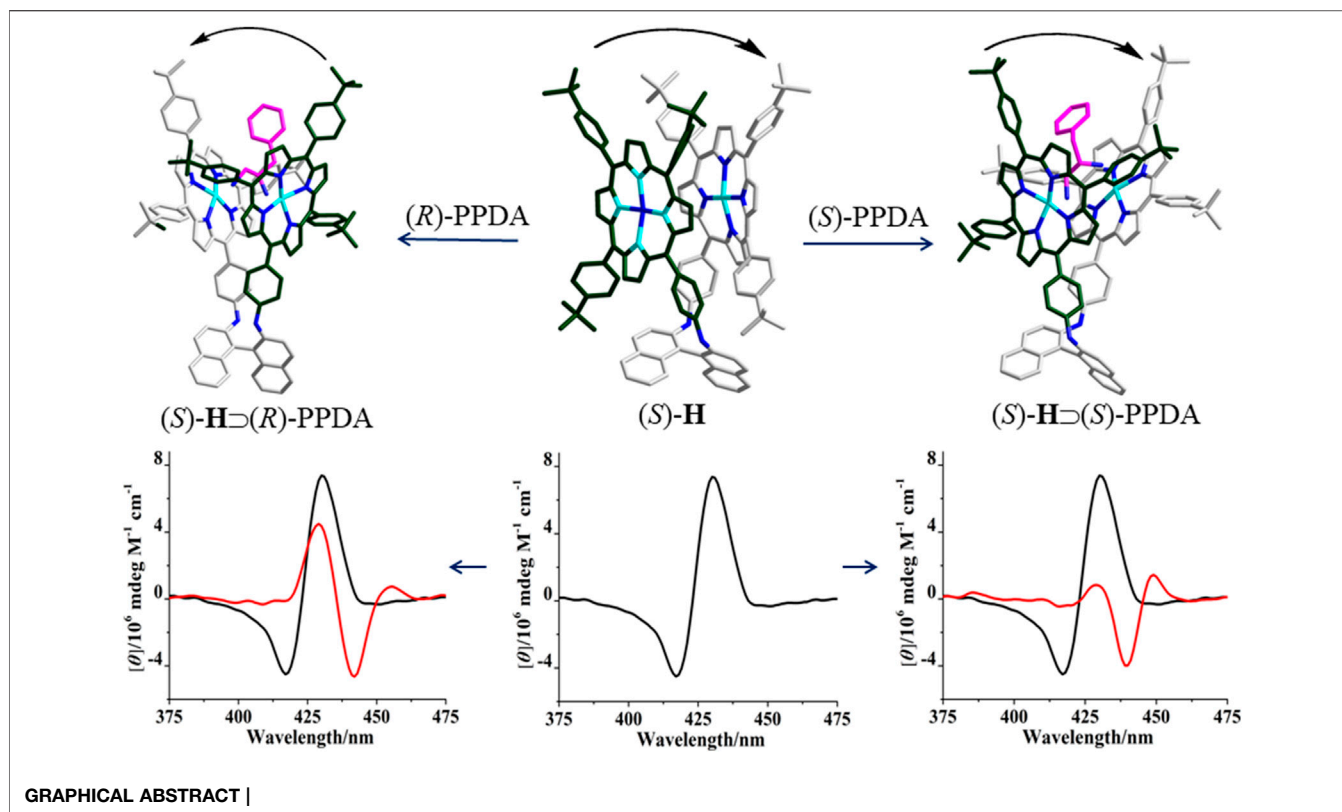
Keywords: porphyrin, diamine, chirality, fluorescence spectroscopy, CD spectroscopy, chiral optical sensor

INTRODUCTION

Chiral phenomenon widely exists in nature such as proteins, polysaccharides and nucleic acids, playing an important role in the development and evolution of life. Modulating the chirality of supramolecular system is pivotal owing to its significance in chemistry (de Jong et al., 2004; Liu et al., 2014; Liu et al., 2015) and material science (Jung et al., 2013; Dou et al., 2020; Wang and Feng, 2018). Supramolecular chirality modulation is crucial for understanding the stereostructure and function of chiral compounds (van Dijken et al., 2014; Liu et al., 2016). In addition, supramolecular chirality modulation has important applications in molecular recognition (Wang et al., 2017; Wu et al., 2019), asymmetric catalysis (Dydie et al., 2011; Hong et al., 2016), chiroptical devices (Wang et al., 2019) and medicines (Weatherly et al., 2017; Li et al., 2019; Ma et al., 2019).

1,1'-binaphthyl derivatives are one of the most important class of C₂-symmetric compound. The pure enantiomers of 1,1'-binaphthyl derivatives have inherent chiral induction abilities due to their rigid C₂ symmetrical structures. In addition, the structures of 1,1'-binaphthyl derivatives are highly tunable since the 2-, 3-, 4-, 6-, 7-, 8- and 9-positions can be systematically modified by introducing functional groups. As a result, they have found extensive applications in the development of optoelectric materials (Yu et al., 2011), optical sensors for molecular recognition (Yu et al., 2013) and asymmetric catalysis (Chen et al., 2003).

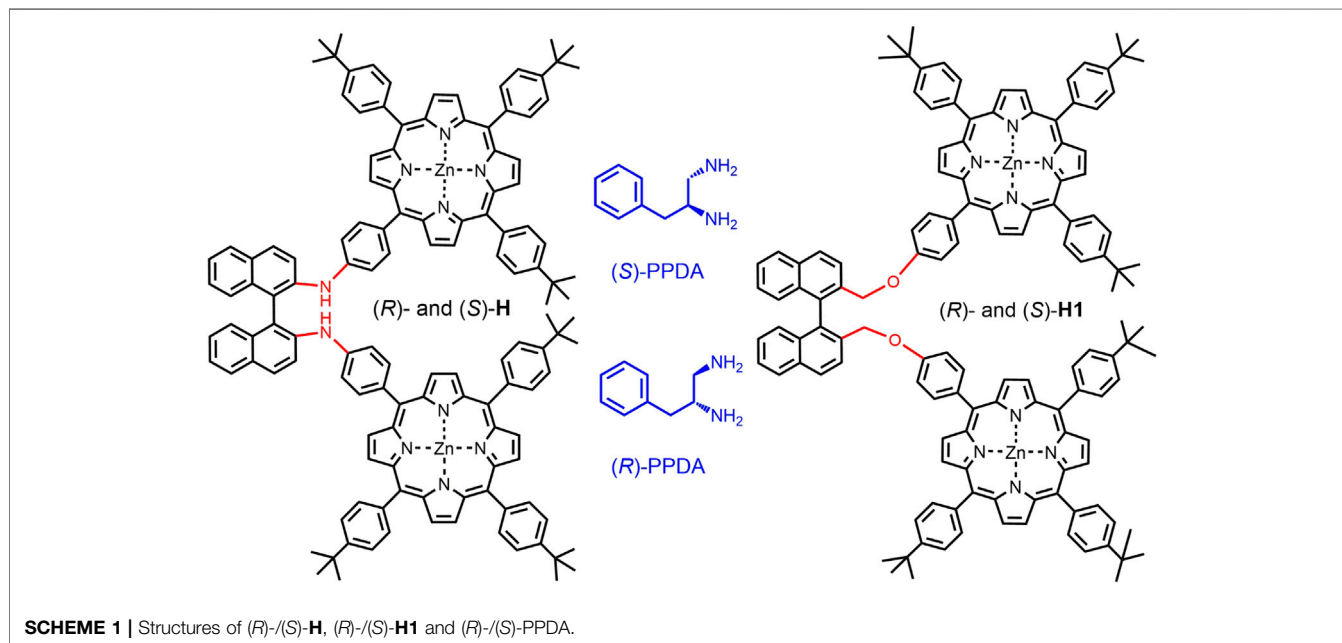
On the other hand, porphyrins are highly involved in supramolecular chirality systems owing to the unique photonic and electronic activities (Peng et al., 2008; Stefanelli et al., 2019; Mondal and



Rath, 2020). In particular, covalently linked bisporphyrin hosts can bind with guest molecules *via* non-covalent interactions, and their CD spectra are sensitive to the corresponding allosteric effects (Hu et al., 2018; Dhamija et al., 2020). As a result, achiral bisporphyrins can be applied to the exciton coupled circular

dichroism (ECCD) protocol for determining the absolute configurations of chiral guest molecules (Hayashi et al., 2015; Hu et al., 2017).

Furthermore, by connecting two porphyrin monomers with chiral spacers, chiral bisporphyrins can be obtained, which are of



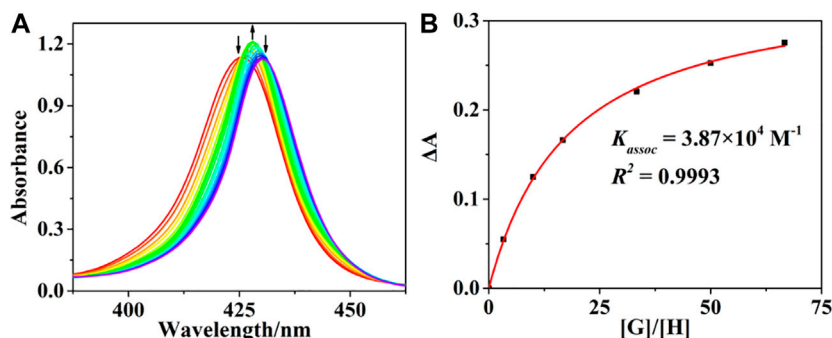


FIGURE 1 | (A) UV-Vis titration profiles of (R)-H with (S)-PPDA. [(R)-H] = 1.5×10^{-6} M; [(S)-PPDA]/[(R)-H] = 0–670. **(B)** Changes in ΔA at 420 nm for evaluating K_{assoc} , the solid line represents the non-linear least square fit for 1:1 complexation.

significance for the development of chiral discrimination systems. In this respect, we reported 1,1'-bi-2-naphthol (BINOL) linked porphyrin dimers for the study of intermolecular chirality modulation and chiral discrimination toward a range of model diamines (Lu et al., 2017a). The results indicated that the enantioselectivity and chiral sensing properties of chiral bisporphyrin hosts can be gradually tuned by varying the connecting units between porphyrin and BINOL moieties.

Herein, we present new dimeric porphyrin hosts (R)-/(S)-H, which were formed by linking two porphyrin units via a (R)- or (S)-2,2'-diamino-1,1'-binaphthyl (**Scheme 1**). The supramolecular complexation and intermolecular chirality modulation with (R)-/(S)-PPDA were studied by electronic absorption, fluorescence, ^1H NMR and CD spectroscopies with the help of DFT calculations. The importance of the linking units in bisporphyrin hosts for chiral recognition was revealed by comparing with the previously reported hosts (R)-/(S)-H1 (Lu et al., 2017b).

RESULTS AND DISCUSSION

Synthesis and Characterization

The new chiral bisporphyrins (R)-/(S)-H were synthesized by Buchwald-Hartwig reaction of (R)- or (S)-2,2'-diamino-1,1'-

binaphthyl with the mono-brominated Zn(II) porphyrinate. The target compounds were obtained with moderate yields (34–35%) and adequately characterized by Mass, NMR and UV-Vis absorption spectral data (see the experimental section and the Supporting Information for details, **Supplementary Scheme S1** and **Supplementary Figures S1,S2**).

UV-Vis Spectrophotometric and Fluorescence Titration

The interactions of (R)-/(S)-PPDA with host (R)-/(S)-H were first monitored by UV-Vis spectrophotometric titration at 298 K in CHCl_3 (**Figure 1** and **Supplementary Figure S3**). Upon adding (S)-PPDA to (R)-H gradually, the B absorption band increased and the absorption maxima redshifted from 425 to 428 nm at the lower guest concentration range (0–67 equiv). An isosbestic point appears at 426 nm, suggesting the domination of a host-guest complex. Considering the ditopic feature of (S)-PPDA and (R)-H, a 1:1 sandwich host-guest complex ((R)-H \supset (S)-PPDA) can be put forward, where a PPDA binds to the two porphyrin moieties by Zn-N coordination (Lu et al., 2017a). The sandwich complexes were found stable up to 67 equiv of (R)-/(S)-PPDA were added, and the association constants (K_{assoc}) of (R)-H \supset (S)-PPDA and (R)-H \supset (R)-PPDA were evaluated as $3.87 \times 10^4 \text{ M}^{-1}$ and $2.88 \times 10^4 \text{ M}^{-1}$, respectively (Thordarson, 2011) (**Figure 1B** and **Supplementary**

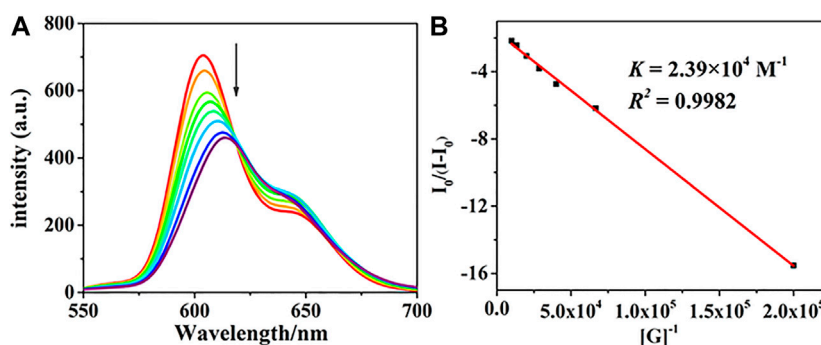


FIGURE 2 | (A) The fluorescence titration profiles of (R)-H with (R)-PPDA [(R)-H] = 1.5×10^{-6} M; [(R)-PPDA]/[(R)-H] = 0–67, λ_{Ex} = 415 nm. **(B)** The Benesi-Hildebrand plot monitored at 604 nm.

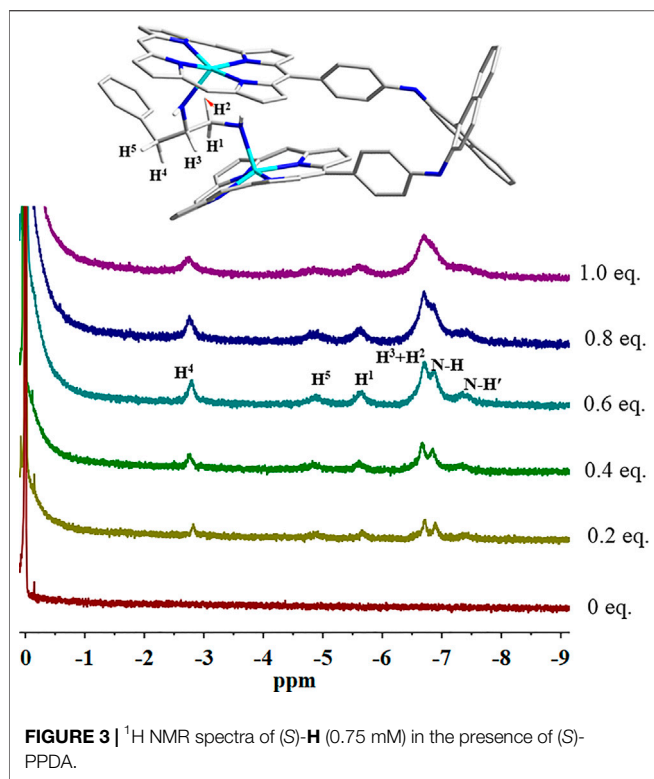


Figure S4). These association constant values are significantly lower than those of the previously reported host **H1** with PPDA (Lu et al., 2017a), which is obviously due to the decreased length and flexibility of the linking units in the present bisporphyrin host **H**. Therefore, further addition of (*R*)-PPDA or (*S*)-PPDA (67–670 equiv) to the host (*R*)-**H** may trigger the conversion to 1:2 open complexes (*R*)-**H**@[(*R*)-PPDA]₂ and (*R*)-**H**@[(*S*)-PPDA]₂ respectively, which can be supported by the further 2 nm redshift of the Soret band and the decrease in its intensity.

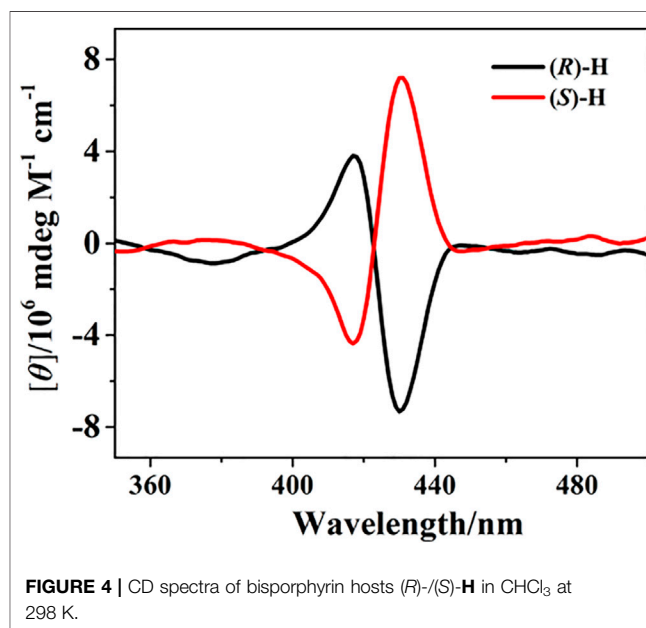
The fluorescence response behaviors of the chiral porphyrin dimer (*R*)-**H** toward (*R*)- and (*S*)-PPDA were also recorded at 298 K in CHCl₃ with the excitation at 415 nm. When a solution of (*R*)-**H** (1.5×10^{-6} M) was treated with (*R*)-PPDA (0–67 equiv), the fluorescence intensity greatly decreased with a redshift from 604 nm to 617 nm (**Figure 2A**). The Benesi-Hildebrand plot (**Figure 2B**) shows a linear relationship in the [G]/[H] range of 0–67 equiv, also suggesting a 1:1 stoichiometry for the stable supramolecular complex (*R*)-**H**⊃(*R*)-PPDA. The K_{assoc} was estimated to be $2.39 \times 10^4 \text{ M}^{-1}$ for (*R*)-**H**⊃(*R*)-PPDA (Hariharan et al., 2007; Jiao et al., 2018). The titration profiles of (*R*)-**H** with (*S*)-PPDA resemble those of (*R*)-**H** with (*R*)-PPDA, and the K_{assoc} for (*R*)-**H**⊃(*S*)-PPDA was obtained as $4.09 \times 10^4 \text{ M}^{-1}$ (**Supplementary Figure S5,S6**). The K_{assoc} values are in good agreement with those obtained from the UV-Vis spectrophotometric titration.

¹H NMR Titration

The binding of (*S*)-PPDA to the chiral bisporphyrin hosts was also probed by ¹H NMR spectroscopy at 298 K in CDCl₃ (**Figure 3** and **Supplementary Figure S7**). Upon the addition of 0.4 equiv of (*S*)-PPDA to (*S*)-**H**, the signals of the free host completely disappeared,

TABLE 1 | ¹H NMR signals of (*S*)-PPDA and the complexation induced shift values ($\Delta\delta = \delta_{\text{bonded PPDA}} - \delta_{\text{free PPDA}}$), at 298 K in CDCl₃.

Proton	Free (<i>S</i>)-PPDA δ /ppm	(<i>S</i>)- H ⊃(<i>S</i>)-PPDA δ /ppm	$\Delta\delta$ /ppm
N-H	1.25	−6.89	−8.14
N-H'	1.25	−7.38	−8.63
H ¹	2.82	−5.63	−8.45
H ²	2.78	−6.68	−9.46
H ³	2.97	−6.68	−9.65
H ⁴	2.55	−2.78	−5.33
H ⁵	2.49	−4.87	−7.36



suggesting the fast exchange between free and bound (*S*)-**H** molecules. Meanwhile, the signals of (*S*)-PPDA moved to high field (from δ 2.97–1.25 to δ −2.78 to −7.38 ppm). The complexation induced shift (CIS) values of the bound guest (*S*)-PPDA ($\Delta\delta = \delta_{\text{bonded PPDA}} - \delta_{\text{free PPDA}}$) are in the range of −5.33 to −9.56 (**Table 1**), which are reasonably close to those of a diamine tweezered by a dimeric Zn(II) porphyrin (Pintre et al., 2012; Lu et al., 2017a). The observations further support the formation of the 1:1 sandwich complex (*S*)-**H**⊃(*S*)-PPDA, where the diamine molecule is shielded by the two porphyrin rings. Compared with the ¹H NMR titration results of (*S*)-**H1** with (*S*)-PPDA (Lu et al., 2017a), the proton signals of PPDA in (*S*)-**H**⊃(*S*)-PPDA were broad and weak due to the low binding affinities of (*S*)-PPDA with (*S*)-**H**. Furthermore, the CIS values ($|\Delta\delta|$) of almost all the (*S*)-PPDA protons were much larger than those in (*S*)-**H1**⊃(*S*)-PPDA, which indicated that the PPDA guest was shielded by stronger ring-current effect from the two porphyrin rings in (*S*)-**H**. These observations can be attributed to the different length and flexibility of the linking units between binaphthalene and porphyrin for (*S*)-**H1** and (*S*)-**H**.

Circular Dichroism Response

The electronic circular dichroism (CD) spectra of (*R*)-**H** and (*S*)-**H** were recorded in chloroform at 298 K. In the porphyrin Soret band

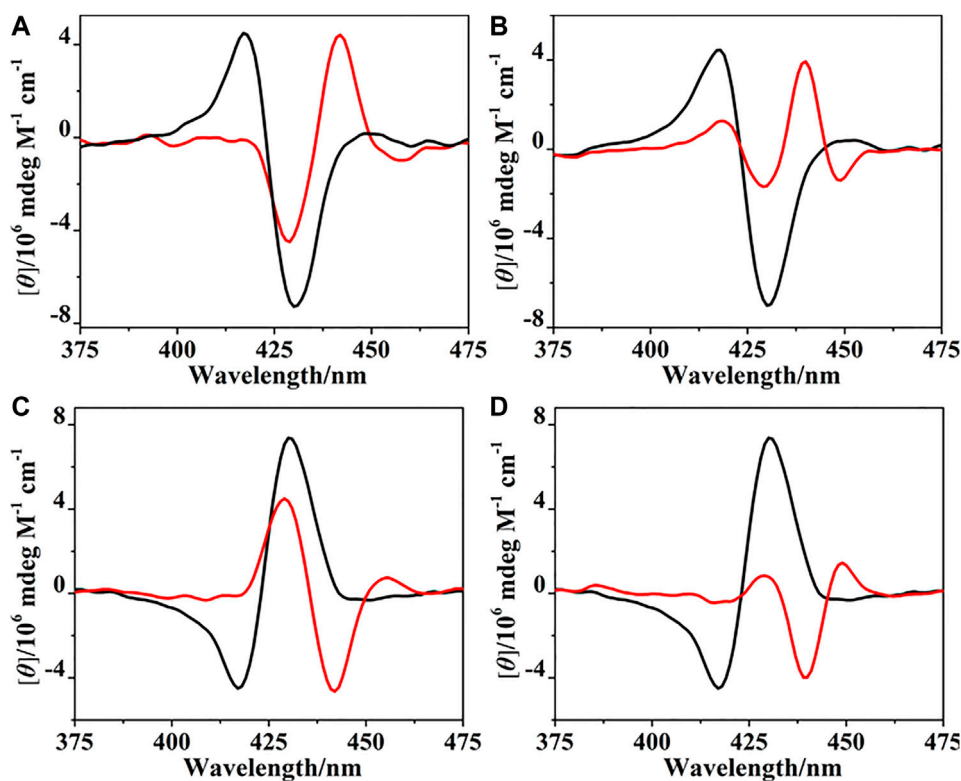


FIGURE 5 | CD spectra of (*R*)-**H** in the absence (black) and presence (red) of PPDA (67 equiv): (A) (*S*)-PPDA, (B) (*R*)-PPDA; CD spectra of (*S*)-**H** in the absence (black) and presence (red) of PPDA (67 equiv): (C) (*R*)-PPDA, and (D) (*S*)-PPDA.

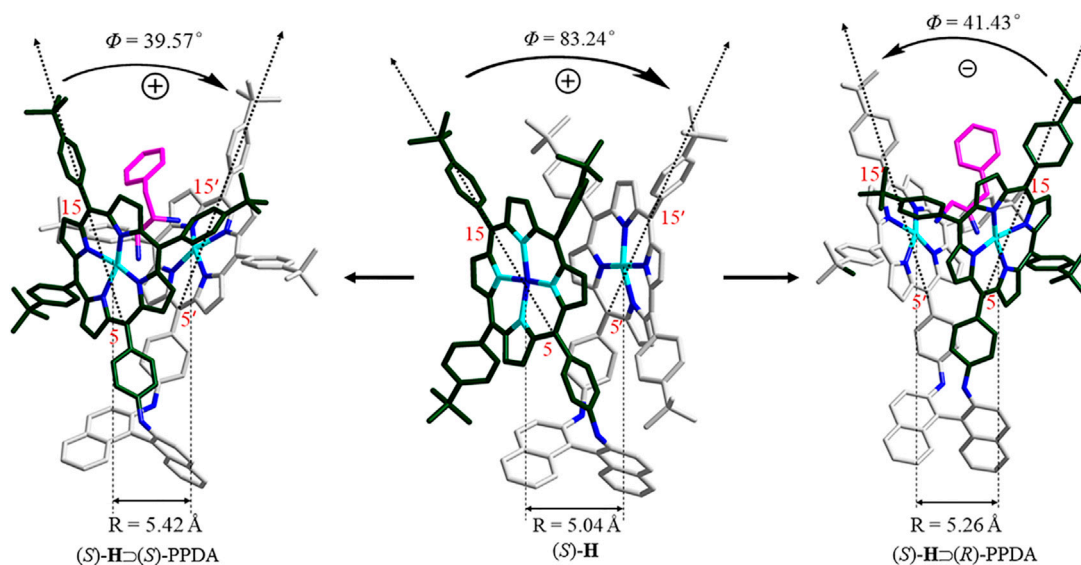


FIGURE 6 | DFT optimized structures of (*S*)-**H**, (*S*)-**H**⊃(*S*)-PPDA and (*S*)-**H**⊃(*R*)-PPDA.

region, split Cotton effects are observed at 430 and 418 nm with opposite signs for (*R*)- and (*S*)-**H**. (*R*)-**H** shows negative CD couplets, while (*S*)-**H** exhibits positive CD couplets, forming perfect mirror images in the CD spectra (Figure 4). The sign of CD couplets can be

directly correlated to the chirality of the linkage by the exciton coupled circular dichroism (ECCD) theory (Pescitelli et al., 2014).

The binding of (*R*)- and (*S*)-PPDA to the bisporphyrin hosts (*R*)-/ (*S*)-**H** was further investigated by CD spectroscopy. Upon addition of

TABLE 2 | Parameters of the optimized molecular structures of (S)-**H**, (S)-**H**⊃(S)-PPDA, (S)-**H**⊃(R)-PPDA, (S)-**H1**, (S)-**H1**⊃(S)-PPDA and (S)-**H1**⊃(R)-PPDA.

Parameter	R (Å)	Φ (°)
(S)- H	5.04	+83.24
(S)- H ⊃(S)-PPDA	5.42	+39.57
(S)- H ⊃(R)-PPDA	5.26	−41.43
(S)- H1 ^a	3.48	+21.22
(S)- H1 ⊃(S)-PPDA ^a	6.10	+50.52
(S)- H1 ⊃(R)-PPDA ^a	5.18	−31.73

^aAdopted from (Lu et al., 2017a).

(S)-PPDA (0–67 equiv) to (R)-**H**, the CD signals at 430 and 418 nm decreased, new signals appeared at 442 and 428 nm (**Figure 5A**). Notably, the negative Cotton effect of (R)-**H** is transformed to a positive Cotton effect with about 10 nm red shift and decreased amplitude. The remarkable CD inversion can be assigned to the binding-induced allosteric effects along with the formation of 1:1 complex (R)-**H**⊃(S)-PPDA. In comparison, the titration of (R)-**H** with (R)-PPDA induced only a red shift and decrease of the negative CD couplets, while no CD inversion was observed along with the formation of (R)-**H**⊃(R)-PPDA (**Figure 5B**). These changes were slightly different with the CD response of (R)-**H1** in the presence of (S)-/(R)-PPDA (Lu et al., 2017a). For (R)-**H1**, when titrated with (S)-PPDA the CD signals transformed to a *positive Cotton effect* with a red shift (13 nm) and increased amplitude, when titrated with (R)-PPDA the CD signals also showed a similar red shift and a remarkably decreased amplitude. The titration results of (S)-**H** with (R)-/(S)-PPDA are similar to that of (R)-**H**. The obtained CD spectra of (S)-**H**⊃(R)-PPDA and (S)-**H**⊃(S)-PPDA are the mirror images of those of (R)-**H**⊃(S)-PPDA and (R)-**H**⊃(R)-PPDA, respectively (**Figure 5**).

According to the CD spectral changes induced by the supramolecular binding for (R)-/(S)-**H** and (R)-/(S)-**H1** (Lu et al., 2017a), it is obvious that (S)-PPDA induces *positive CD couplets*, while (R)-PPDA leads to *negative CD couplets*, thus the final CD signs of the 1:1 host-guest complexes are dominated by the stereostructure of diamines. When the bisporphyrin binds a diamine with different chirality, CD inversion will be observed. Nevertheless, for (R)-/(S)-**H1**, we noted that the formation of (R)-**H1**⊃(R)-PPDA and (S)-**H1**⊃(S)-PPDA resulted in extremely small CD amplitudes, which could make it difficult for determining the CD signs (Lu et al., 2017a). While for (R)-/(S)-**H**, after the formation of (R)-**H**⊃(R)-PPDA and (S)-**H**⊃(S)-PPDA, the CD signals still have moderate intensity and the CD signs can be easily determined, which is favorable for chiral optical sensing.

DFT Molecular Modeling

To further rationalize the CD spectral change, DFT molecular modeling was performed at the B97D/6-31G(D) level. As shown in the optimized molecular structures (**Figure 6** and **Table 2**), the free host (S)-**H** exhibits a clockwise chiral twist (+83.24°) between the coupled effective electric transition moments (EETMs) across the C5/C15 of porphyrin rings, which is in line with the positive CD couplets of (S)-**H** (**Figure 4**). The formation of stable (S)-**H**⊃(S)-PPDA and (S)-**H**⊃(R)-PPDA induces significant changes in the

coupled EETMs. For (S)-**H**⊃(S)-PPDA, the twist angle between the two coupled EETMs decreases from +83.24° to +39.57°, though the clockwise direction is unchanged. In contrast, the twist angle between the coupled EETMs for (S)-**H**⊃(R)-PPDA inverted to anticlockwise (−41.43°), which is consistent with the observed CD inversion phenomenon for this system. Moreover, the relative distance between the two interacting porphyrin moieties (i.e. the Zn-Zn distance) is also altered by the formation of 1:1 complexes. The Zn-Zn distance is increased from 5.04 Å for (S)-**H** to 5.42 and 5.26 Å for (S)-**H**⊃(S)-PPDA and (S)-**H**⊃(R)-PPDA, respectively. The CD amplitude is not only inversely proportional to the square of interporphyrin distance, but also is a function of the twist angle between the two coupled EETMs (Pescitelli et al., 2014). The maximum CD amplitude appears at a twist angle of 70° (Nina et al., 2012). The free host (S)-**H** possesses a larger Zn-Zn distance (5.04 Å) and a twist angle (+83.24°) than the free host (S)-**H1** (3.48 Å and +21.22°), probably due to the relatively short linkage and rigid structure. After the formation of supramolecular complexes with (R)-/(S)-PPDA, the Zn-Zn distances of (S)-**H**⊃(S)-PPDA and (S)-**H**⊃(R)-PPDA get slightly increased while the twist angles get decreased, both leading to the decrease of the corresponding CD amplitude. Thus, the observed decrease in CD intensity for the supramolecular complexes (**Figure 5**) is in accordance with the theoretical prediction.

However, this is not the case for (S)-**H1** (Lu et al., 2017a). Upon binding to (R)-/(S)-PPDA, the Zn-Zn distances increased significantly from 3.48 ((S)-**H1**) to 6.10 ((S)-**H1**⊃(S)-PPDA) and 5.18 Å ((S)-**H1**⊃(R)-PPDA) respectively, which can induce a decrease of the CD amplitude. Meanwhile the twist angles also increased from +21.22° to +50.52° ((S)-**H1**⊃(S)-PPDA) and −31.73° ((S)-**H1**⊃(R)-PPDA) respectively, which may tend to an increase in the CD amplitude. As a result, the prediction of CD amplitude change for (S)-**H1** becomes complicated and uncertain due to the two opposite factors.

CONCLUSION

In summary, we have presented porphyrin dimers (R)-/(S)-**H** and investigated their complexation abilities with (R)-/(S)-PPDA by using UV-Vis absorption, fluorescence and NMR titrations. At low guest concentration (0–67 equiv), 1:1 sandwich host-guest complexes were formed. The intermolecular chirality modulation process has been monitored by CD spectroscopy. The binding process afforded obvious CD spectral change, and the CD signs of 1:1 sandwich host-guest complexes are dominated by the stereostructure of guest molecules. The sensitive CD responses can be attributed to the short linking units and the binding-induced allosteric effects according to the DFT molecular modeling. The present results indicate that the chiral bisporphyrin hosts have great potential as chiral optical probes.

DATA AVAILABILITY STATEMENT

The original contributions presented in the study are included in the article/**Supplementary Material**, further inquiries can be directed to the corresponding authors.

AUTHOR CONTRIBUTIONS

All authors listed have made a substantial, direct, and intellectual contribution to the work and approved it for publication.

ACKNOWLEDGMENTS

Financial support from the National Natural Science Foundation of China (21471015, 21631003 and 21671017), Natural Science Foundation of Shandong Province (ZR2019BB041), Beijing Natural Science Foundation (2202028), Fundamental Research

Funds for the Central Universities (FRF-BD-20-14A), and Scientific Research Foundation of Shandong University of Science and Technology for Recruited Talents is gratefully acknowledged.

SUPPLEMENTARY MATERIAL

The Supplementary Material for this article can be found online at: <https://www.frontiersin.org/articles/10.3389/fchem.2020.611257/full#supplementary-material>.

REFERENCES

- Chen, Y., Yekta, S., and Yudin, A. K. (2003). Modified BINOL ligands in asymmetric catalysis. *Chem. Rev.* 103, 3155–3212. doi:10.1021/cr020025b
- de Jong, J. J. D., Lucas, L. N., Kellogg, R. M., van Esch, J. H., and Feringa, B. L. (2004). Reversible optical transcription of supramolecular chirality into molecular chirality. *Science* 304, 278–281. doi:10.1126/science.1095353
- Dhamija, A., Saha, B., Chandel, D., Malik, H., and Rath, S. P. (2020). Molecule to supramolecule: chirality induction, inversion, and amplification in a Mg(II) porphyrin dimer templated by chiral diols. *Inorg. Chem.* 59, 801–809. doi:10.1021/acs.inorgchem.9b03062
- Dou, X., Mehresh, N., Zhao, C., Liu, J., Xing, C., and Feng, C. L. (2020). Supramolecular hydrogels with tunable chirality for promising biomedical applications. *Acc. Chem. Res.* 53, 852–862. doi:10.1021/acs.accounts.0c00012
- Dydo, P., Rubay, C., Gadzikwa, T., Lutz, M., and Reek, J. N. H. (2011). “Cofactor”-Controlled enantioselective catalysis. *J. Am. Chem. Soc.* 133, 17176–17179. doi:10.1021/ja208589c
- Hariharan, M., Karunakaran, S. C., and Ramaiah, D. (2007). Selective recognition of tryptophan through inhibition of intramolecular charge-transfer interactions in an aqueous medium. *Org. Lett.* 9, 417–420. doi:10.1021/ol062636m
- Hayashi, S., Yotsukura, M., Noji, M., and Takanami, T. (2015). Bis(zinc porphyrin) as a CD-sensitive bidentate host molecule: direct determination of absolute configuration of mono-alcohols. *Chem. Commun.* 51, 11068–11071. doi:10.1039/c5cc03303a
- Hong, L., Sun, W., Yang, D., Li, G., and Wang, R. (2016). Additive effects on asymmetric catalysis. *Chem. Rev.* 116, 4006–4123. doi:10.1021/acs.chemrev.5b00676
- Hu, Q., Zhuo, C., Wang, Y., Hu, C., and Lang, J. (2017). Chirality transfer from chiral monoamines to an m-phthalic diamide-linked zinc bisporphyrinate with a benzylamide substituent. *Inorg. Chem.* 56, 10204–10214. doi:10.1021/acs.inorgchem.7b00815
- Hu, T., Hu, C., Wang, Y., Young, D. J., and Lang, J.-P. (2018). Stoichiometrically controlled chirality inversion in zinc bisporphyrinate-monoamine complexes. *Dalton Trans.* 47, 5503–5512. doi:10.1039/c8dt00326b
- Jiao, J., Tan, C., Li, Z., Liu, Y., Han, X., and Cui, Y. (2018). Design and assembly of chiral coordination cages for asymmetric sequential reactions. *J. Am. Chem. Soc.* 140, 2251–2259. doi:10.1021/jacs.7b11679
- Jung, J. H., Moon, S.-J., Ahn, J., Jaworski, J., and Shinkai, S. (2013). Controlled supramolecular assembly of helical silica nanotube-graphene hybrids for chiral transcription and separation. *ACS Nano* 7, 2595–2601. doi:10.1021/nn306006s
- Li, G., DeLaney, K., and Li, L. (2019). Molecular basis for chirality-regulated A beta self-assembly and receptor recognition revealed by ion mobility-mass spectrometry. *Nat. Commun.* 10. doi:10.1038/s41467-019-12346-8
- Liu, G.-F., Zhang, D., and Feng, C.-L. (2014). Control of three-dimensional cell adhesion by the chirality of nanofibers in hydrogels. *Angew. Chem. Int. Ed.* 53, 7789–7793. doi:10.1002/anie.201403249
- Liu, G.-F., Zhu, L.-Y., Ji, W., Feng, C.-L., and Wei, Z.-X. (2016). Inversion of the supramolecular chirality of nanofibrous structures through Co-assembly with achiral molecules. *Angew. Chem. Int. Ed.* 55, 2411–2415. doi:10.1002/anie.201510140
- Liu, M., Zhang, L., and Wang, T. (2015). Supramolecular chirality in self-assembled systems. *Chem. Rev.* 115, 7304–7397. doi:10.1021/cr500671p
- Lu, W., Li, L., Yang, H., Zhao, L., Qi, D., Bian, Y., et al. (2017a). Intramolecular chirality induction and intermolecular chirality modulation in BINOL bridged bisporphyrin hosts. *Dyes Pigments* 137, 608–614. doi:10.1016/j.dyepig.2016.11.006
- Lu, W., Yang, H., Li, X., Wang, C., Zhan, X., Qi, D., et al. (2017b). Chiral discrimination of diamines by a binaphthalene-bridged porphyrin dimer. *Inorg. Chem.* 56, 8223–8231. doi:10.1021/acs.inorgchem.7b00920
- Ma, X., Kan, Z., Du, Y., Yang, J., Feng, Z., Zhu, X., et al. (2019). Enantioseparation of amino alcohol drugs by nonaqueous capillary electrophoresis with a maltobionic acid-based ionic liquid as the chiral selector. *Analyst* 144, 7468–7477. doi:10.1039/c9an01162e
- Mondal, P., and Rath, S. P. (2020). Cyclic metalloporphyrin dimers: conformational flexibility, applications and future prospects. *Coord. Chem. Rev.* 405. doi:10.1016/j.ccr.2019.213117
- Nina, B., Prasad, L., Koji, N., and Robert, W. W. (2012). *Comprehensive chiroptical spectroscopy: applications in stereochemical analysis of synthetic compounds, natural products, and biomolecules*. Hoboken, NJ: John Wiley & Sons, 2, 1–843
- Peng, X., Komatsu, N., Kimura, T., and Osuka, A. (2008). Simultaneous enrichments of optical purity and (n,m) abundance of SWNTs through extraction with 3,6-carbazolyene-bridged chiral diporphyrin nanotweezers. *ACS Nano* 2, 2045–2050. doi:10.1021/nn800462s
- Pescitelli, G., Di Bari, L., and Berova, N. (2014). Application of electronic circular dichroism in the study of supramolecular systems. *Chem. Soc. Rev.* 43, 5211–5233. doi:10.1039/C4CS00104D
- Pintre, I. C., Pierrefixe, S., Hamilton, A., Valderrey, V., Bo, C., and Ballester, P. (2012). Influence of the solvent and metal center on supramolecular chirality induction with bisporphyrin tweezer receptors. Strong metal modulation of effective molarity values. *Inorg. Chem.* 51, 4620–4635. doi:10.1021/ic202515v
- Stefanelli, M., Magna, G., Zurlo, F., Caso, F. M., Di Bartolomeo, E., Antonaroli, S., et al. (2019). Chiral selectivity of porphyrin-ZnO nanoparticle conjugates. *ACS Appl. Mater. Interfaces* 11, 12077–12087. doi:10.1021/acsami.8b22749
- Thordarson, P. (2011). Determining association constants from titration experiments in supramolecular chemistry. *Chem. Soc. Rev.* 40, 5922–5923. doi:10.1039/c0cs00062k
- van Dijken, D. J., Beierle, J. M., Stuart, M. C. A., Szymanski, W., Browne, W. R., et al. (2014). Autoamplification of molecular chirality through the induction of supramolecular chirality. *Angew. Chem. Int. Ed.* 53, 5073–5077. doi:10.1002/anie.201311160
- Wang, F., and Feng, C.-L. (2018). Stoichiometry-Controlled inversion of supramolecular chirality in nanostructures Co-assembled with bipyridines. *Chemistry-a European Journal* 24, 1509–1513. doi:10.1002/chem.201704431
- Wang, F., Ji, W., Yang, P., and Feng, C.-L. (2019). Inversion of circularly polarized luminescence of nanofibrous hydrogels through Co-assembly with achiral coumarin derivatives. *ACS Nano* 13, 7281–7290. doi:10.1021/acsnano.9b03255
- Wang, L.-L., Chen, Z., Liu, W.-E., Ke, H., Wang, S.-H., and Jiang, W. (2017). Molecular recognition and chirality sensing of epoxides in water using endo-

- functionalized molecular tubes. *J. Am. Chem. Soc.* 139, 8436–8439. doi:10.1021/jacs.7b05021
- Weatherly, C. A., Du, S., Parpia, C., Santos, P. T., Hartman, A. L., and Armstrong, D. W. (2017). D-Amino acid levels in perfused mouse brain tissue and blood: a comparative study. *ACS Chem. Neurosci.* 8, 1251–1261. doi:10.1021/acscchemneuro.6b00398
- Wu, D., Pan, F., Fan, G.-C., Zhu, Z., Gao, L., Tao, Y., et al. (2019). Efficient enantiorecognition of amino acids under a stimuli-responsive system: synthesis, characterization and application of electroactive rotaxane. *Analyst* 144, 6415–6421. doi:10.1039/c9an01692a
- Yu, S., DeBerardinis, A. M., Turlington, M., and Pu, L. (2011). Study of the fluorescent properties of partially hydrogenated 1,1'-Bi-2-naphthol-amine molecules and their use for enantioselective fluorescent recognition. *J. Org. Chem.* 76, 2814–2819. doi:10.1021/jo200226k
- Yu, S., Plunkett, W., Kim, M., Wu, E., Sabat, M., and Pu, L. (2013). Molecular recognition of aliphatic diamines by 3,3'-Di(trifluoroacetyl)-1,1'-bi-2-naphthol. *J. Org. Chem.* 78, 12671–12680. doi:10.1021/jo402277p
- Conflict of Interest:** The authors declare that the research was conducted in the absence of any commercial or financial relationships that could be construed as a potential conflict of interest.

Copyright © 2021 Lu, Gong, Su, Wang, Ling, Wang, Qi and Bian. This is an open-access article distributed under the terms of the Creative Commons Attribution License (CC BY). The use, distribution or reproduction in other forums is permitted, provided the original author(s) and the copyright owner(s) are credited and that the original publication in this journal is cited, in accordance with accepted academic practice. No use, distribution or reproduction is permitted which does not comply with these terms.



Aerobic Oxidations in Asymmetric Synthesis: Catalytic Strategies and Recent Developments

Dzmitry Kananovich*, Gábor Zoltán Elek, Margus Lopp and Victor Borovkov*

Department of Chemistry and Biotechnology, School of Science, Tallinn University of Technology, Tallinn, Estonia

OPEN ACCESS

Edited by:

HiroYuki Miyake,
Osaka City University, Japan

Reviewed by:

Mainak Banerjee,
Birla Institute of Technology and
Science, India
Hideki Sugimoto,
Osaka University, Japan

*Correspondence:

Dzmitry Kananovich
dzmitry.kananovich@taltech.ee
Victor Borovkov
victor.borovkov@taltech.ee

Specialty section:

This article was submitted to
Supramolecular Chemistry,
a section of the journal
Frontiers in Chemistry

Received: 07 October 2020

Accepted: 10 February 2021

Published: 30 March 2021

Citation:

Kananovich D, Elek GZ, Lopp M and
Borovkov V (2021) Aerobic Oxidations
in Asymmetric Synthesis: Catalytic
Strategies and Recent Developments.
Front. Chem. 9:614944.
doi: 10.3389/fchem.2021.614944

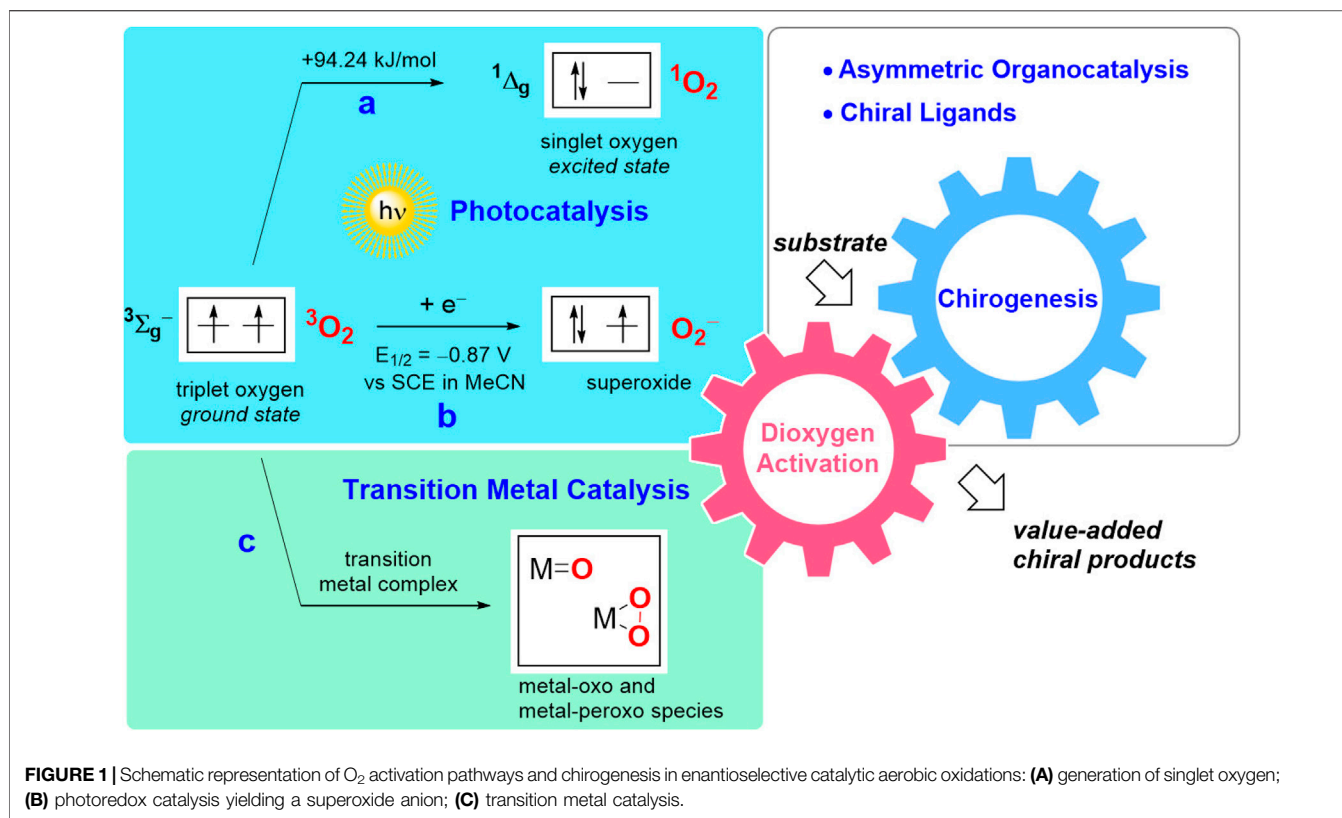
Keywords: oxygen, aerobic oxidation, asymmetric synthesis, enantioselective catalysis, chirality, organocatalysis, transition metals

INTRODUCTION

In modern organic synthesis, asymmetric oxidations are of fundamental importance. The early works of Sharpless, (Katsuki and Sharpless, 1980; Jacobsen et al., 1988; Katsuki and Martin, 2004), Jacobsen (Zhang et al., 1990; Jacobsen et al., 1988) and Shi (Tu et al., 1996) on the stereoselective epoxidation and dihydroxylation of alkenes have established prominent benchmarks, with a strong impact to the whole field of enantioselective catalysis. Owing to the valuable contributions of numerous esteemed research groups, contemporary methods of asymmetric oxidation constitute a powerful and multifunctional tool for the preparation of versatile chiral molecules. However, widespread utilization of hazardous oxidants with poor atom economy (e.g. hypochlorites, iodine(III), and iodine(V) reagents, quinones, peroxy compounds) constitutes a serious shortcoming in the view of current green chemistry paradigm (Anastas and Warner, 1998).

As a consequence, the asymmetric catalytic oxidations with molecular oxygen as a terminal oxidant can be considered as the next Frontier in organic synthesis, (Mukaiyama and Yamada, 1995; Jiao and Stahl, 2019; Sterckx et al., 2019), being especially attractive for large-scale industrial applications (Caron et al., 2006; Hone et al., 2017). Dioxygen itself is an abundant compound presented in air (21% by volume) and vital for the metabolism of aerobic organisms, thus representing an inexpensive and eco-friendly oxidizing agent. It also offers excellent atom economy: as a rule, aerobic oxidation usually produces low molecular weight by-products (e.g. H₂O) or even proceeds with 100% atom efficiency (e.g. formation of peroxides). Hence, atmospheric oxygen nicely fits the green chemistry requirements, being a nearly “ideal” oxidant.

Besides the mentioned green chemistry benefits, recent accomplishments in asymmetric synthesis with atmospheric oxygen often represent prominent examples in the catalytic reaction engineering. Indeed, to ensure reliable stereodiscrimination of a prochiral substrate and enhanced reactivity of



oxygen, the design of enantioselective aerobic oxidation process should commonly comprise two main components: an effective oxygen activation pathway and a proper method of chirality induction (termed “chirogenesis”) (Borovkov et al., 2001).

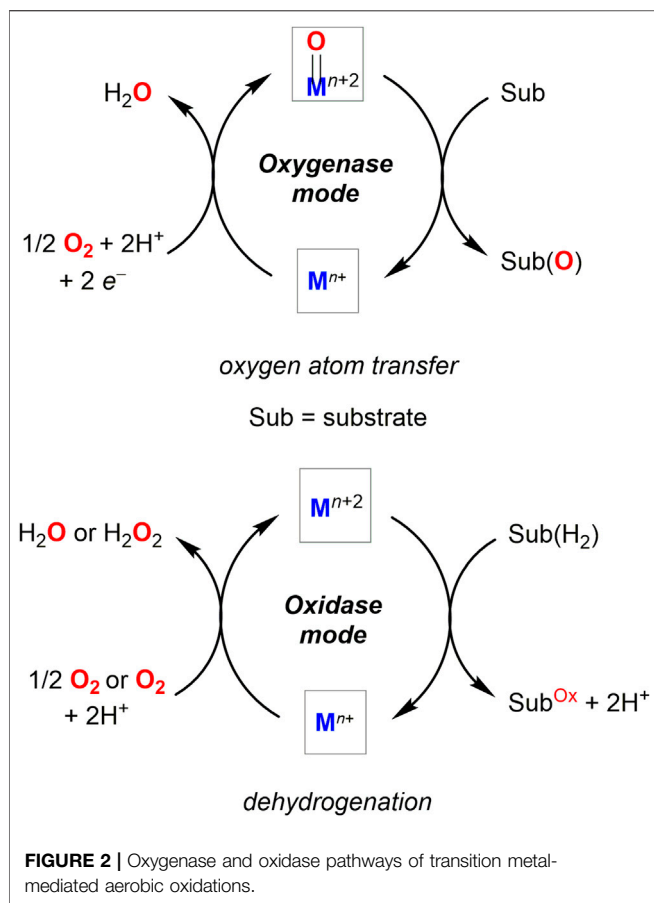
In its ground state, dioxygen molecule represents a stable biradical (triplet oxygen, $^3\text{O}_2$). Although the oxidation of organic compounds is thermodynamically favorable, the reaction of triplet oxygen with usually singlet-state organic molecules is spin forbidden, hence imposing a kinetic limitation on this reaction pathway (Miller et al., 1990). As a consequence, the organic substrates can only be oxidized with triplet oxygen via a radical autoxidation process (Doering and Haines, 1954; Ingold, 1961; Porter, 2013; Poon and Pratt, 2018). Alternatively, transformation of $^3\text{O}_2$ into another type of the oxidative species must be implemented to overcome the corresponding kinetic constraint. As one option, activation of triplet oxygen can be achieved with the aid of photocatalysis, resulting in generation of highly reactive singlet oxygen $^1\text{O}_2$ (Figure 1A) (Zamadar and Greer, 2009; Ghogare and Greer, 2009). Another activation pathway is based on single electron transfer from a photoredox catalyst (Romero and Nicewicz, 2016) (or another monoelectronic reductant) yielding superoxide anion radical O_2^- (Figure 1B). Furthermore, various transition metal complexes can shuttle oxygen atoms even at ambient conditions via generation of the corresponding oxo- and peroxo species, or transfer electrons in the oxidation reactions (Figure 1C) (Miller et al., 1990; Parmeggiani and Cardona, 2012; Allen et al., 2013). The chirogenic process in transition metal-catalyzed

transformations is conventionally induced by a judicious choice of chiral ligand, while photocatalytic approaches are commonly merged with asymmetric organocatalysis.

It is remarkable that the mechanisms outlined above are also relevant for the operation of iron- (Meunier et al., 2004), copper- (Festa and Thiele, 2011), manganese- (Dismukes, 1996), and metal-free flavin-containing enzymes, which provide an inspiration for designing the analogs of the enzymatic reactions (de Gonzalo and Fraaije, 2013; Petsi and Zografos, 2018). Many of these transformations involve synergetic or dual catalytic cycles, featuring masterpieces in the catalytic reaction engineering.

The main aim of the current review is to outline the key catalytic strategies and latest innovative concepts in design of the asymmetric reactions with molecular oxygen as a terminal oxidant. Therefore, the most prominent examples have been judiciously selected among the research works published in the last 20 years. However, for a more detailed overview of the field, especially earlier contributions, a number of comprehensive reviews (Uchida and Katsuki, 2013; Bryliakov, 2015; Bryliakov, 2017; Ottenbacher et al., 2018), and personal accounts (Mukaiyama and Yamada, 1995; Irie and Katsuki, 2004) can be recommended for further reading.

The first part of the review describes transformations mediated by transition metals. Besides asymmetric oxidations mediated by chiral metal complexes, dual catalytic processes are also mentioned, in which the aerobic oxidation step is used solely to generate a prochiral intermediate for the subsequent



asymmetric reaction. The second part focuses on metal-free aerobic oxidations, commonly operating via dual photo-organocatalytic cycles. It worth mentioning that enantioselective oxidations mediated by enzymes, (Endoma et al., 2002; Boyd and Bugg, 2006; Gandomkar et al., 2019), heterogeneous catalysts, (Miyamura et al., 2013), and nanoparticles (Miyamura et al., 2015; Hadian-Dehkordi and Hosseini-Monfared, 2016) also represent an important cluster of valuable synthetic methodologies, however these approaches are out of the scope of this review.

TRANSITION METAL-CATALYZED TRANSFORMATIONS

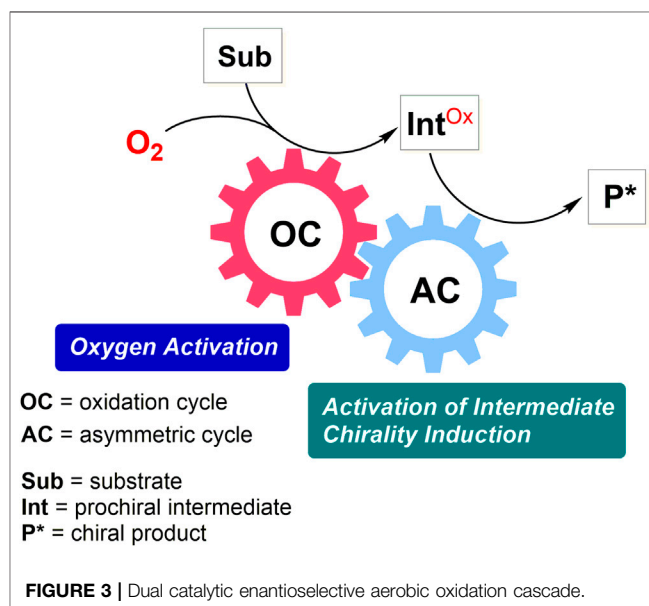
Transition metal-catalyzed transformations constitute the mainstream approach in enantioselective aerobic oxidations. In general, the corresponding catalytic cycles mimic enzymatic activity of metal-containing oxidases and oxygenases (Figure 2), (Bugg, 2003; McCann and Stahl, 2015) with asymmetry typically induced by a chiral environment. Besides being an oxidant, transition metal can also act as a Lewis acid to enable substrate coordination and to facilitate stereodiscrimination of the enantiomeric pairs in oxidative kinetic resolution process.

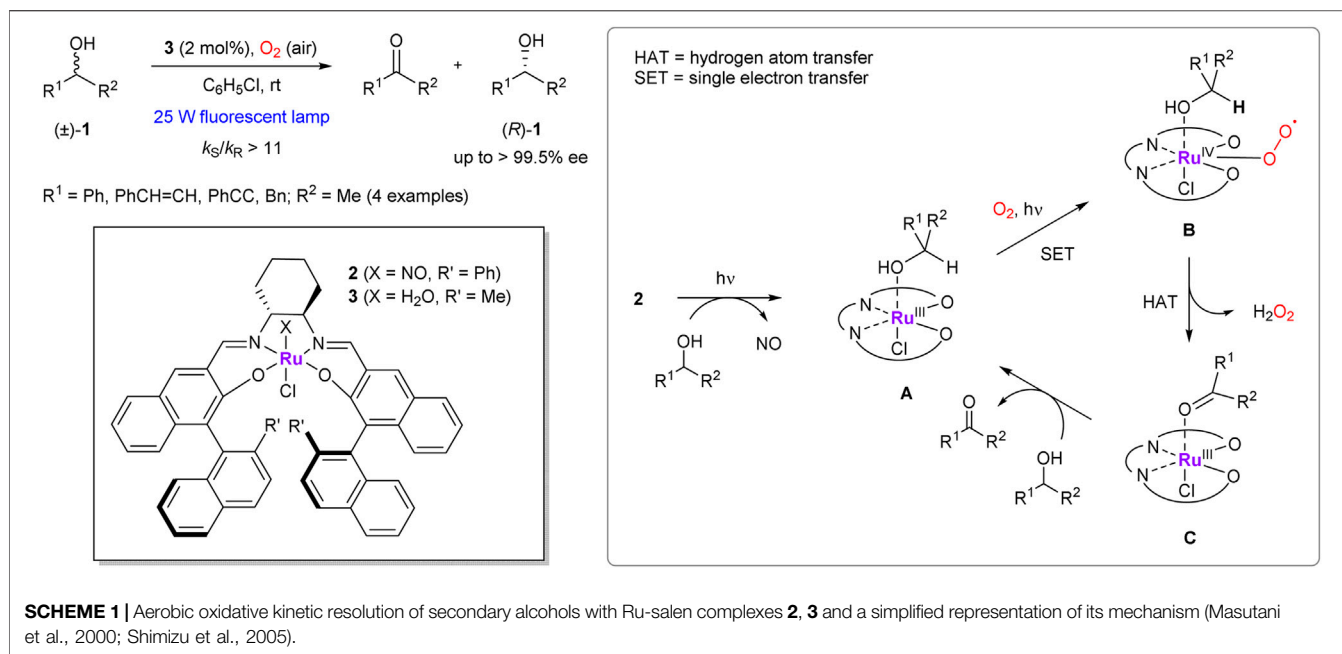
Among the recent advances, synergetic transition metal-photocatalysis (Ding et al., 2017) can be mentioned as a more intricate reaction design, in which photochemically-generated singlet oxygen is exploited.

The transformations presented in this section are subdivided according to the catalytic strategy and origin of chirogenesis. While the majority of enantioselective metal-catalyzed aerobic oxidations relies on the use of a single chiral transition metal catalyst, several cascade or dual catalytic transformations are also known, in which aerobic oxidation cycle is used solely to generate a reactive prochiral intermediate (Figure 3). In the latter approach, chirality is typically induced in an additional catalytic cycle, as presented in the second subsection.

Asymmetric Aerobic Oxidations Mediated by Chiral Metal Complexes

Application of the transition metal complexes as chiral oxygen carriers in asymmetric aerobic oxidations was pioneered by the Mukaiyama's group in 1990s, (Mukaiyama and Yamada, 1995) which designed a number of optically active Mn^{III} complexes to perform the enantioselective epoxidation of olefins (Yamada et al., 1992; Mukaiyama et al., 1993; Nagata et al., 1994; Yamada et al., 1994) and oxidation of sulfides to chiral sulfoxides (Imagawa et al., 1995; Nagata et al., 1995). These keynote contributions were followed by the discovery of chiral nickel (Kureshy et al., 1998) and ruthenium complexes, (Kureshy et al., 1997; Lai et al., 1998), which are capable to mediate the enantioselective aerobic epoxidation of olefins, and works of the Bolm's group on the copper-catalyzed Baeyer-Villiger oxidation of cyclic ketones (Bolm et al., 1994; Bolm and Schlingloff, 1995; Bolm et al., 1997). It should be noted that these prominent early contributions have been extensively discussed in several reviews (Mukaiyama and Yamada, 1995; Bryliakov, 2017; Ottenbacher et al., 2018). The use of chiral metal complexes still represent a





SCHEME 1 | Aerobic oxidative kinetic resolution of secondary alcohols with Ru-salen complexes **2**, **3** and a simplified representation of its mechanism (Masutani et al., 2000; Shimizu et al., 2005).

prevalent approach among the known aerobic oxidation methods.

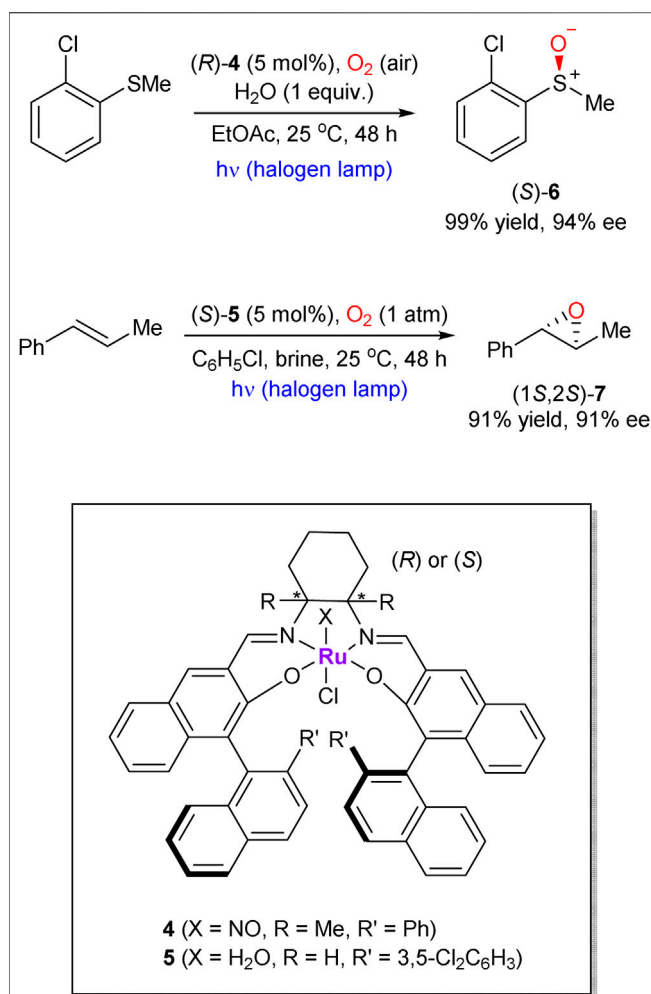
In 2000, Katsuki et al. reported a highly efficient protocol for chemo- and enantioselective aerobic oxidation of secondary alcohols **1** under visible-light irradiation, mediated by optically active (nitroso)-salen ruthenium complex **2** (**Scheme 1**) (Masutani et al., 2000). The reaction mechanism was suggested on the basis of kinetics and kinetic isotope effect studies (Shimizu et al., 2005). It was suggested that irradiation triggers the dissociation of complex **2** and release of NO ligand, thus providing a free coordination site for the alcohol substrate. The produced Ru^{III} complex **A** captures molecular oxygen to afford Ru^{IV} peroxo complex **B**, where the peroxo ligand accepts α -carbynol hydrogen of the alcohol ligand via a hydrogen atom transfer (HAT) process. The resulting ketone-anchoring Ru^{III} species **C** finally recovers the complex **A** via replacement of the ketone ligand with the next molecule of alcohol. In a more recent study the same group demonstrated that a broad range of alcoholic substrates can be employed in aerobic oxidative kinetic resolution even without irradiation, just with the aid of (aqua)-salen ruthenium complex **3** (Mizoguchi et al., 2014). Applications of chiral (NO)Ru-salen complexes in enantioselective aerobic oxidations showed a great potential for further development and have been expanded far beyond the kinetic resolution of alcohols in subsequent works of the same group (Irie and Katsuki, 2004). Thus, similar ruthenium-based catalysts have been successfully used in the enantioselective oxidative couplings of 2-naphthols, (Irie et al., 2000), radical cyclization of 2,2'-dihydroxystilbene, (Masutani et al., 2002), and asymmetric desymmetrization of *meso*-diols (Shimizu et al., 2002; Shimizu and Katsuki, 2003).

Katsuki's chiral Ru-salen complexes are also capable to mediate the "oxygenase type" transformations, such as epoxidation of olefins and oxidation of sulfides (representative

examples **6** and **7** are shown in **Scheme 2**) (Tanaka et al., 2010; Koya et al., 2012). In comparison with early works on the enantioselective Ru-catalyzed aerobic epoxidations of olefins, (Kureshy et al., 1997; Lai et al., 1998), Katsuki's protocol did not require an aldehyde co-reductant or high oxygen pressure and operates at ambient conditions. Interestingly, water was found to be an essential additive, which serves as a proton transfer mediator.

Palladium is one of the most versatile and prominent transition metals in catalysis, including its well-documented role in aerobic oxidative transformations (Stahl, 2004). In 2001, the enantioselective palladium-catalyzed oxidation of secondary alcohols with molecular oxygen was independently reported by Stoltz's (Ferreira and Stoltz, 2001) and Sigman's groups (Jensen et al., 2001) (**Scheme 3**). The chirality was enabled by (–)-sparteine ligand, which also acted as a base. Later, Stoltz and co-workers presented application of this methodology to obtain pharmaceutically potent building blocks (Caspi et al., 2004) and in enantioselective synthesis of several alkaloids (**Scheme 3**) (Krishnan et al., 2008). The precursors **8–11** of the targeted natural products were prepared with exceptional enantioselectivity (90–96% ee) and respectable yields (compared to 50% theoretical maximum), enabling facile preparation of the required chiral motifs. Noteworthy, several functional groups within the substrates (e.g., free hydroxyls, esters) were compatible with the reaction conditions.

In recent decades, investigation of the catalytic reactions with earth-abundant transition metals as sustainable alternatives to precious metal catalysts has become a general trend. Several chiral complexes of the first-row transition metals have been applied in the catalytic oxidative kinetic resolutions of secondary alcohols with molecular oxygen as an oxidant. In these transformations, transition metals acted as oxygen carriers and/or chiral Lewis acids to enable stereodifferentiation of racemic substrates.



SCHEME 2 | Photo-promoted Ru-catalyzed enantioselective sulfide oxidation and alkene epoxidation with molecular oxygen (Tanaka et al., 2010; Koya et al., 2012).

Thus, Chen et al. developed a series of chiral *N*-salicylidene vanadyl carboxylate complexes to perform catalytic kinetic resolution of α -hydroxycarboxylic esters, thioesters, amides (Weng et al., 2006; Chen et al., 2007; Salunke et al., 2011) and α -hydroxyketones (Chen et al., 2011) by using molecular oxygen as the terminal oxidant at ambient conditions. It was found that aerobic oxidation of (*S*)-alcohols proceeds more readily than their (*R*)-counterparts in the presence of vanadium complex **12** and its congeners (Scheme 4). As a notable example illustrating high oxidation selectivity, (*R*)-isomer of *N*-benzylamide **13** was obtained in 50% yield and 98% ee (Weng et al., 2006). Drastically slower rate of the oxidation for (*R*)-isomer ($k_{rel} = 458$) was rationalized based on the results of single crystal X-ray analysis of the corresponding catalyst-substrate adduct **14**. It was found that α -carbinol hydrogen of (*R*)-**13** is shielded with a neighboring *tert*-butyl group of the chiral ligand, thus making it barely accessible for elimination through a two-electron oxidation process (Weng et al., 2006). However, the shielding is absent in the diastereomeric complex with (*S*)-**13**, what results

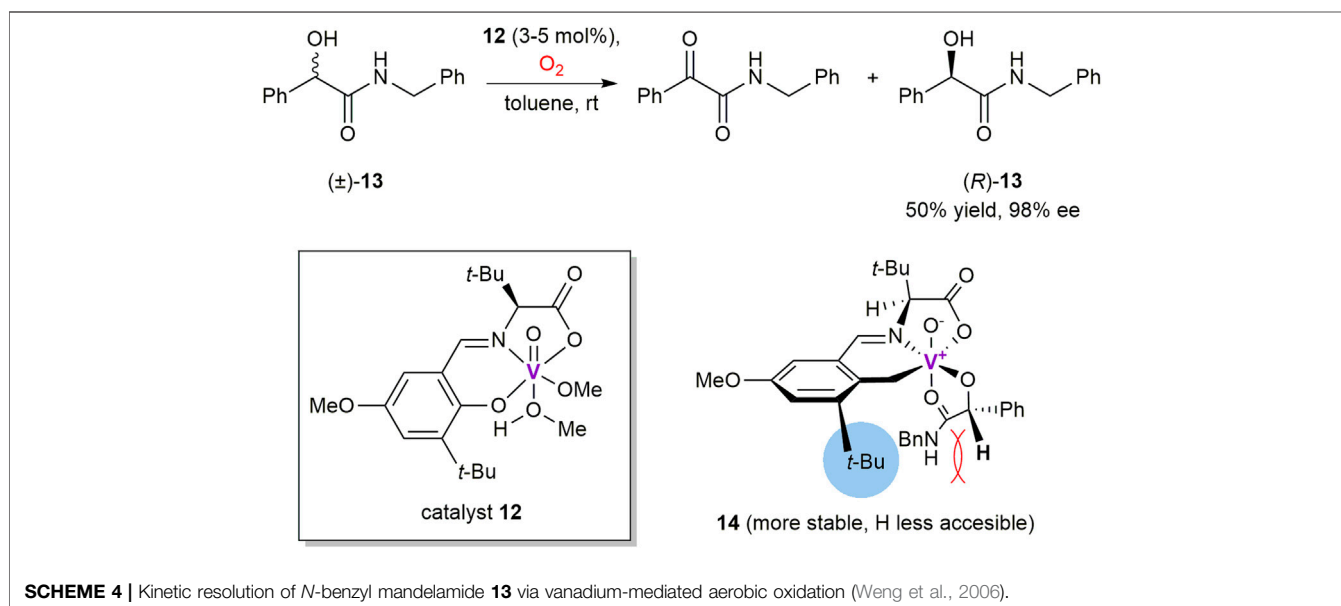
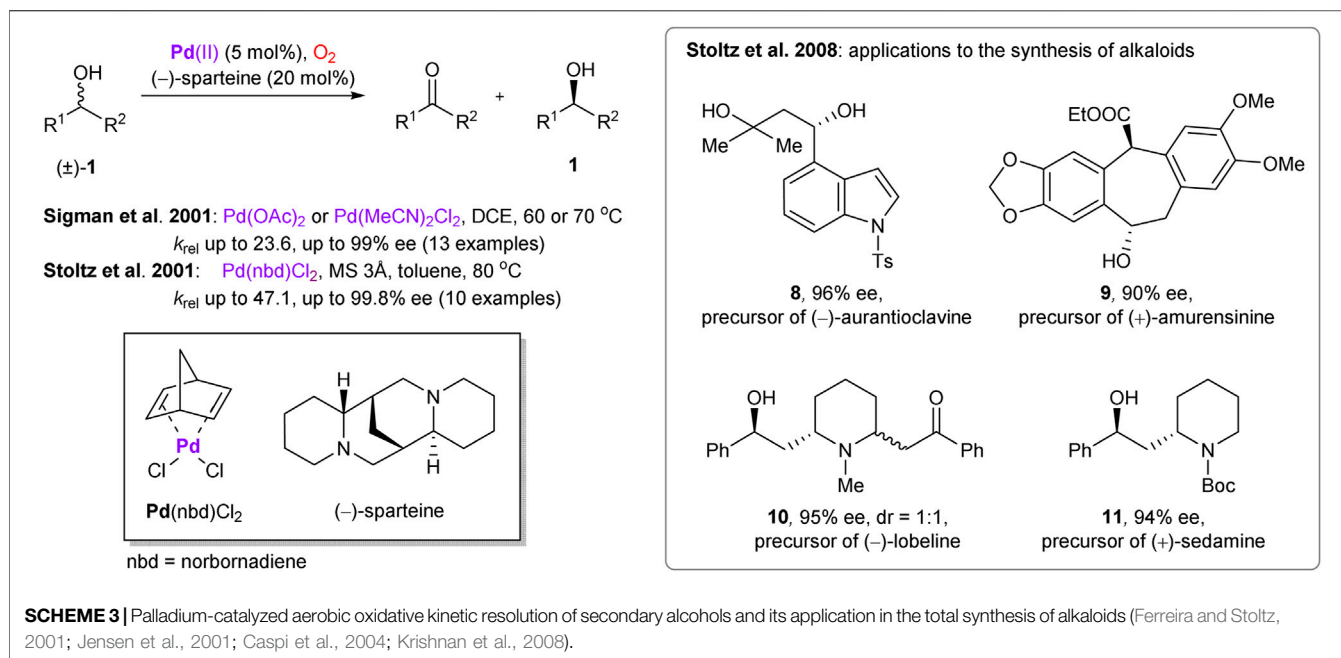
in its fast transformation into the α -ketoamide oxidation product and low-valent vanadium complex. Reoxidation of the latter with molecular oxygen recovers the reactive vanadium (V) species. As a further development, reusable polystyrene-supported vanadium catalysts have also been prepared to promote oxidations of α -hydroxy (thio)esters and amides with enantioselectivities of up to 99% ee (Salunke et al., 2011).

Alamsetti and Sekar reported the first cobalt-catalyzed oxidative kinetic resolution of α -hydroxyesters **15** with molecular oxygen as the sole oxidant (Scheme 5) (Alamsetti and Sekar, 2010). However, 2,2,6,6-tetramethylpiperidin-1-oxyl (TEMPO) was required as a co-catalyst (Wertz and Studer, 2013). Among several cobalt salts and chiral ligands screened, $Co(OAc)_2$ and salen ligand **16** provided the best reaction outcome with racemic methyl mandelate **15** (R = Me, Ar = Ph). The developed conditions were also suitable for a range of α -hydroxyesters, with the maximum selectivity of 99.9% ee achieved for allyl mandelate. Although no mechanistic studies have been performed and a role of cobalt as a potent oxygen carrier has not been manifested, coordination of **15** to the chiral metal complex producing diastereomeric complexes with the different rates of TEMPO-mediated aerobic oxidation could be suggested as a plausible scenario.

The same group applied similar methodology for the kinetic resolution of benzoin **17** via the TEMPO-catalyzed aerobic oxidation in the presence of a chiral zinc complex, generated *in situ* from $ZnSO_4$ and salen ligand **18** (Scheme 6) (Muthupandi and Sekar, 2011). This approach yields enantiomerically enriched **17** with low 43% ee. Since zinc possesses a single stable oxidation state +2 in its compounds, complex **17** could only play a role of chiral Lewis acid, while the oxidation should occur as a nitroxide-catalyzed process (Wertz and Studer, 2013).

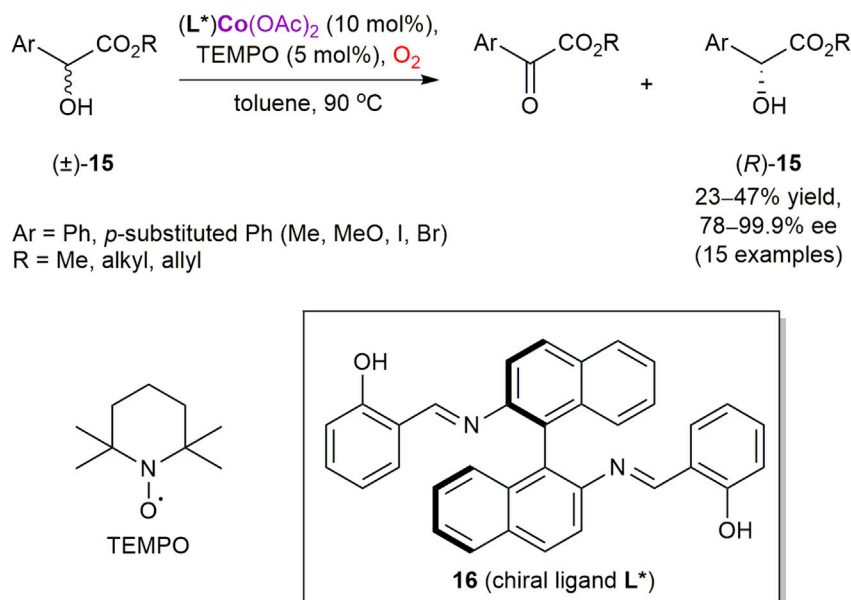
Dioxygen has also been utilized as an oxidant in the asymmetric dehydrogenative C–C coupling reactions. A notable example of such transformation was developed by Egami and Katsuki, who reported in 2009 an aerobic oxidative coupling of 2-naphthols mediated by Fe(salen) complexes (Scheme 7) (Egami and Katsuki, 2009). Chiral iron(III) complex **19** was found to be especially effective for the asymmetric coupling of 3-substituted 2-naphthols **20**, featuring bi-2-naphthols (*R*)-**21** with enantioselectivities greater than 90% ee, with the only exception of methyl-substituted compound (R = Me, 77% ee). The mechanistic studies suggested the coordination of a naphthol substrate to Fe^{III} in a chiral complex, followed by the “oxidase mode” SET oxidation with dioxygen as a rate-determining step. This process generates the radical cationic naphthol species, undergoing subsequent cross-coupling with the anionic 2-naphthol counterpart (Matsumoto et al., 2012; Uchida and Katsuki, 2013).

Chiral binuclear copper oxo-complex **22**, generated *in situ* from (–)-sparteine, $Cu(CH_3CN)_4PF_6$ and molecular oxygen, was introduced by the Porco group to perform asymmetric dearomatization of phenolic compounds (representative example is shown in Scheme 8). The approach was successfully applied as a key step in asymmetric synthesis of natural products, such as azaphilones (Zhu et al., 2005; Zhu and Porco, 2006; Qian et al., 2007; Germain et al., 2011).

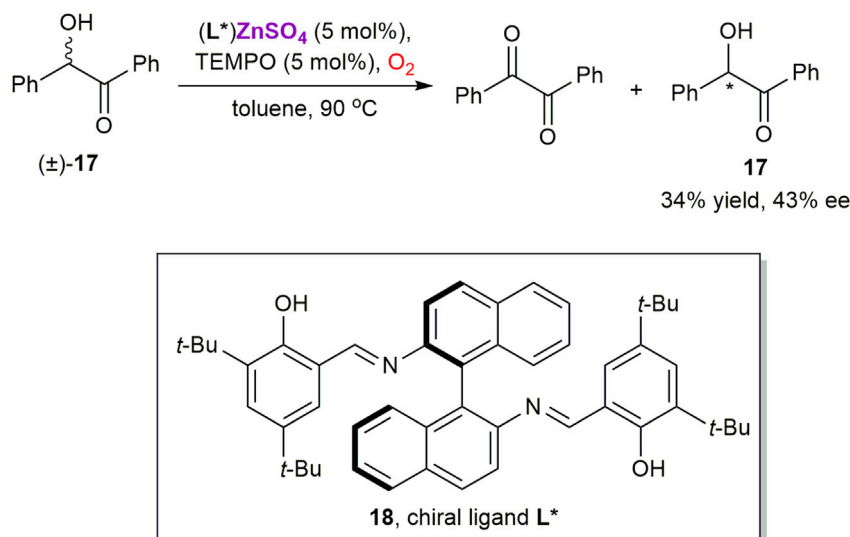


In contrast to the mainstream use of transition metals as oxygen carriers or redox catalysts, Xiao et al. developed a synergetic transition metal-photocatalytic approach, which was applied for highly enantioselective α -hydroxylation of β -ketoesters and β -ketoamides **23** (Scheme 9) (Ding et al., 2017). A family of visible-light-responsive chiral ligands was prepared by grafting a photosensitive thioxanthone motif onto a chiral bisoxazoline scaffold. In the catalytic complex, the thioxanthone motif acts as a triplet-state sensitizer to enable photogeneration of singlet oxygen, while the Ni^{2+} cation acts as a Lewis acid to coordinate β -keto ester substrate **23** in the enolate form. Besides the

preparation of indanone-derived α -hydroxylated esters and amides (e.g. **24a** and **24b**), the reaction protocol was also suitable for α -hydroxylation of heterocyclic and even aliphatic substrates (e.g. **24c** and **24d**). Several functional groups prone to oxidation (alkynyl, vinyl, thiophene, etc.) were inert under the reaction conditions. Asymmetric induction model was proposed, assuming the most preferable coordination of **23** with the most distant position of the bulky adamantyl group (¹Ad) from the chiral ligand. Such mode of the coordination enables the *Re*-face attack of oxidants (either activated ¹O₂ or peroxide **25**), since the *Si*-face is blocked by the rear phenyl groups of



SCHEME 5 | Cobalt-catalyzed enantioselective aerobic oxidation of α -hydroxy esters (Alamsetti and Sekar, 2010).



SCHEME 6 | Oxidative kinetic resolution of (\pm) -benzoin **17** using chiral zinc catalyst (Muthupandhi and Sekar, 2011).

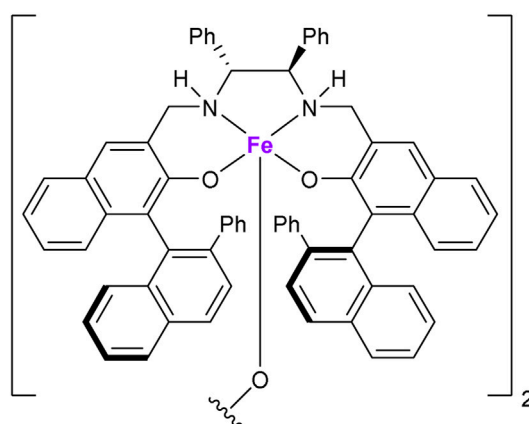
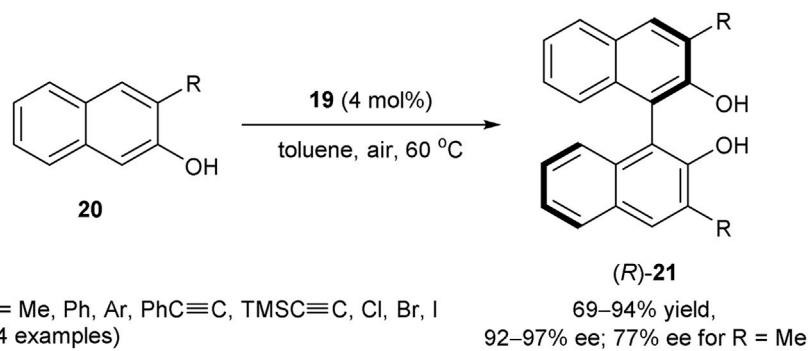
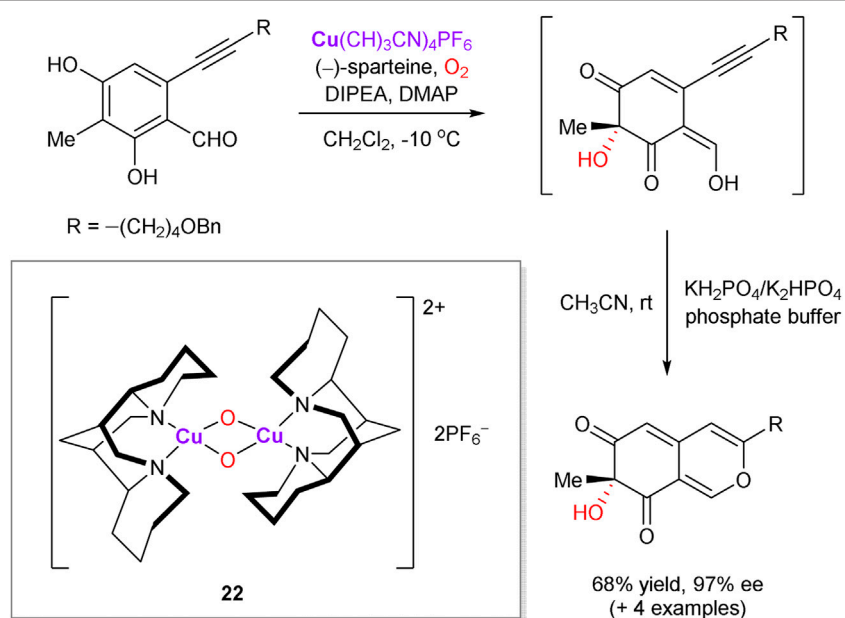
the ligand. The model agrees with the experimentally assigned (*R*)-configuration of product **24a**.

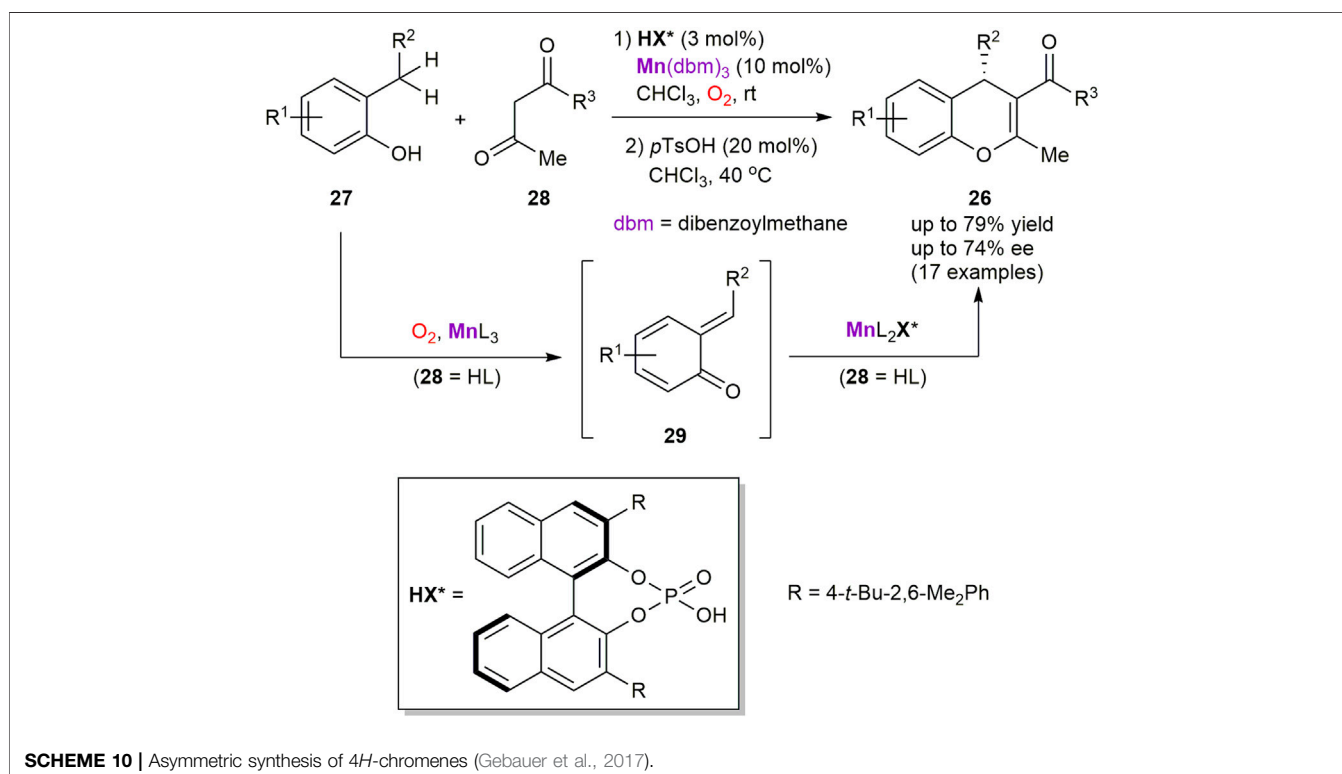
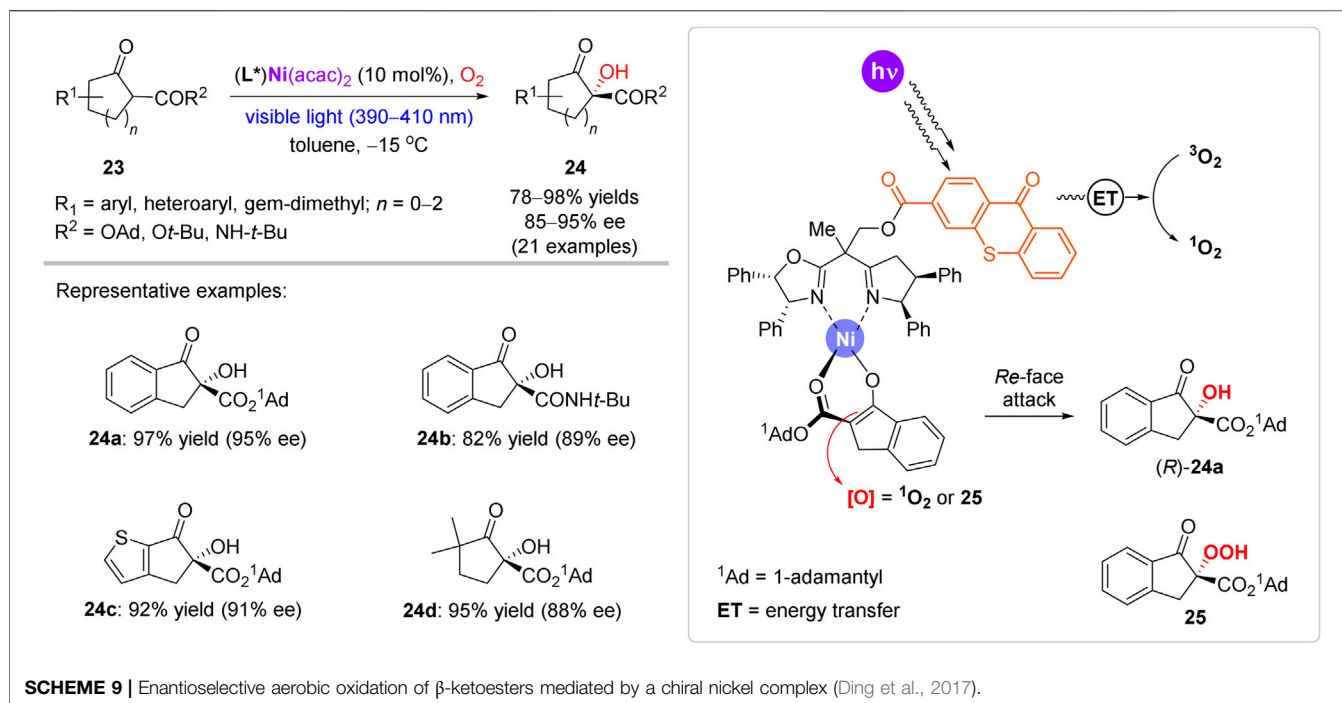
Dual Catalytic Transformations With a Complementary Asymmetric Step

Another important group of synthetic methods is based on the generation of a prochiral oxidized intermediate, which is subsequently involved into a complementary asymmetric catalytic cycle (Figure 3). Commonly, but not necessarily, the

first oxidative catalytic step is transition metal-mediated, while the second asymmetric step is organocatalytic.

Hence, the enantioselective synthesis of 4*H*-chromenes **26** from 2-alkyl-substituted phenols **27** and β -diketones **28** was developed by the Schneider group (Scheme 10) (Gebauer et al., 2017). The process consists of two stages and features a relay catalysis approach with two *in situ* generated manganese catalysts. In particular, the corresponding β -diketonato complexes of Mn^{III} , generated from $\text{Mn}(\text{dbm})_3$ pre-catalyst and β -diketones **28**, were identified as superior oxygen carriers

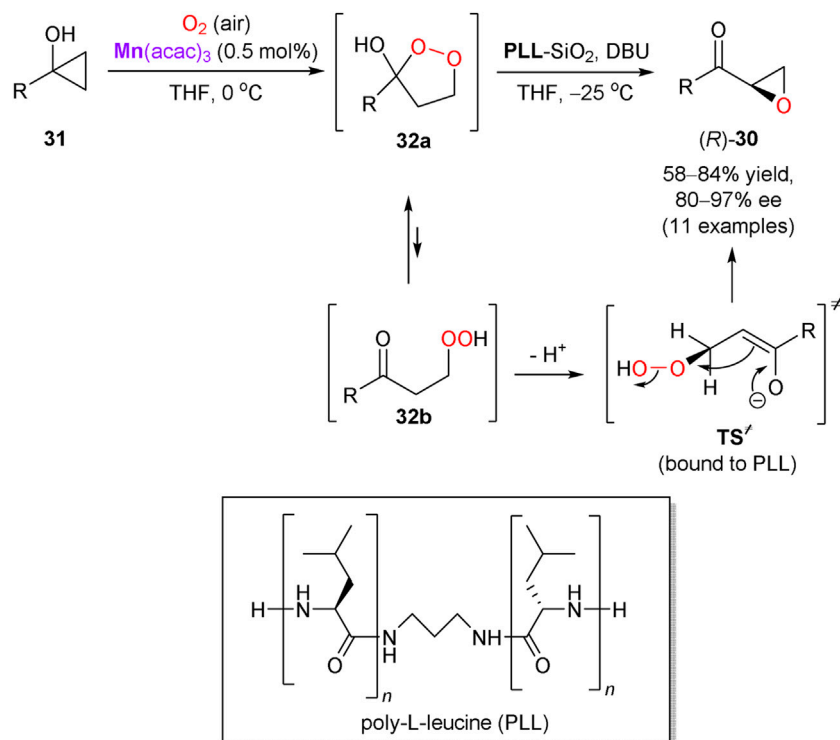
catalyst **19****SCHEME 7** | Iron-catalyzed aerobic oxidative coupling of 2-naphthols (Egami and Katsuki, 2009).**SCHEME 8** | Copper-mediated enantioselective oxidative dearomatization of phenols (Zhu et al., 2005).



to perform *in situ* generation of transient ortho-quinone methides **29** by oxidation of phenols **27**. At the second stage, asymmetric Michael addition of **28** to **29** was occurred and mediated by another type of the chiral Mn^{III} complexes, generated from Mn^{III} diketonates and enantiopure phosphoric

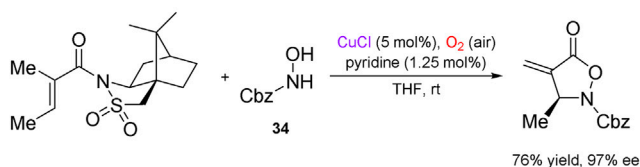
acid HX^* . The process furnished 4H-chromenes **26** in up to 79% yield and 74% ee. However, the reaction outcome was found to be very sensitive to structural changes in the substrates **27** and **28**.

In another representative example, Kananovich's group developed a two-step and one-pot protocol for the asymmetric

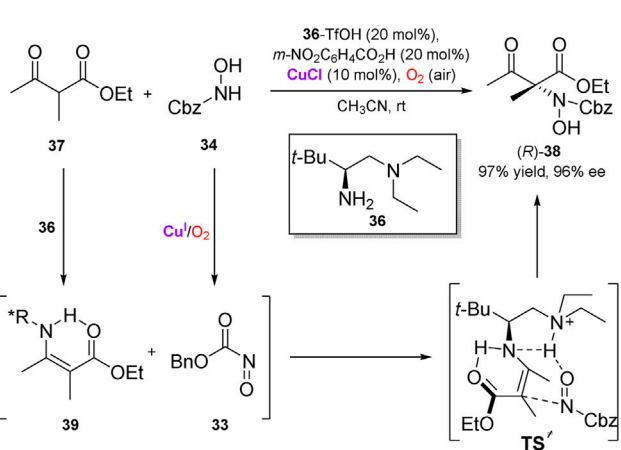


SCHEME 11 | Asymmetric synthesis of epoxy ketones via aerobic oxidation of cyclopropanols (Elek et al., 2017).

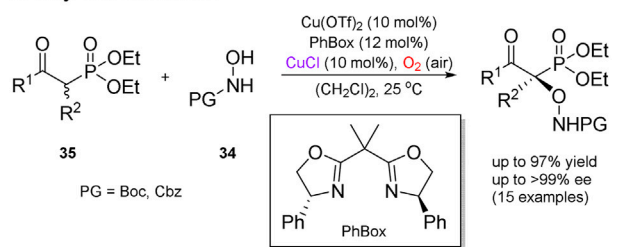
A Alaniz et al.



B Luo et al.



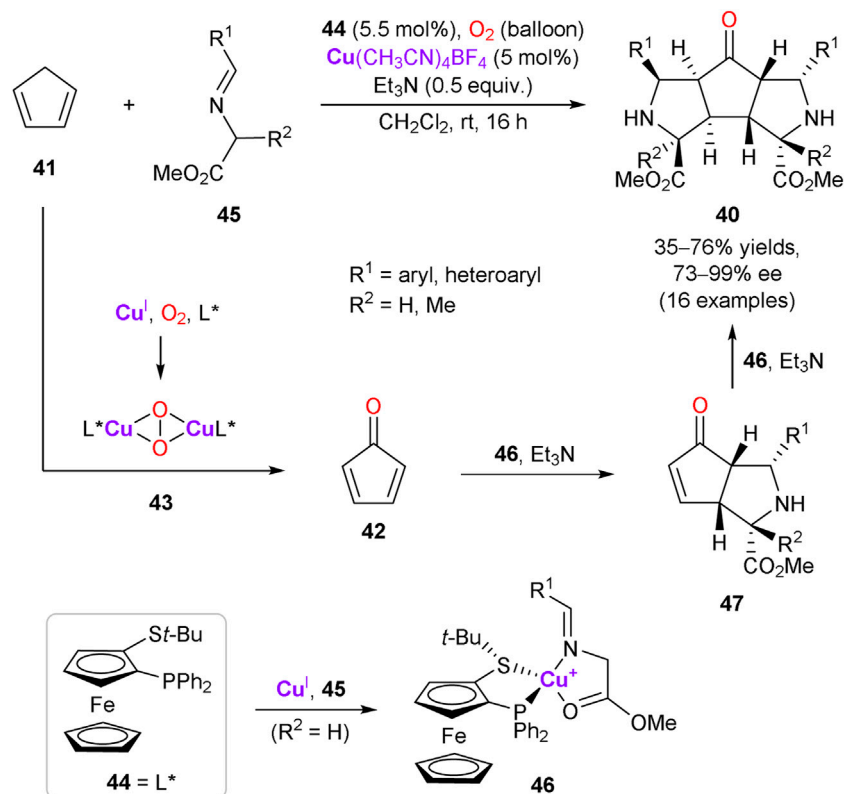
C Maji and Yamamoto



SCHEME 12 | Versatile asymmetric transformations with nitroso compounds generated *in situ* by aerobic oxidation (Frazier et al., 2011; Xu et al., 2014; Maji and Yamamoto, 2015).

synthesis of epoxy ketones **30** from easily available tertiary cyclopropanols **31** (Scheme 11) (Elek et al., 2017). Oxidation of **31** with atmospheric oxygen proceeded readily in THF in the presence of manganese(III) acetylacetonate catalyst, to afford prochiral 1,2-dioxolanes **32a** (equilibrating with β -peroxy ketones **32b**) in nearly quantitative yields. The intermediates

32 were further converted into chiral epoxy ketones **30** by treatment with 1,8-diazabicyclo[5.4.0]undec-7-ene (DBU) in the presence of immobilized on silica gel poly-L-leucine (PLL) catalyst. The experimental protocol is operationally simple and affords **30** in generally high yields and enantioselectivities (80–97% ee). Several functionalities in the



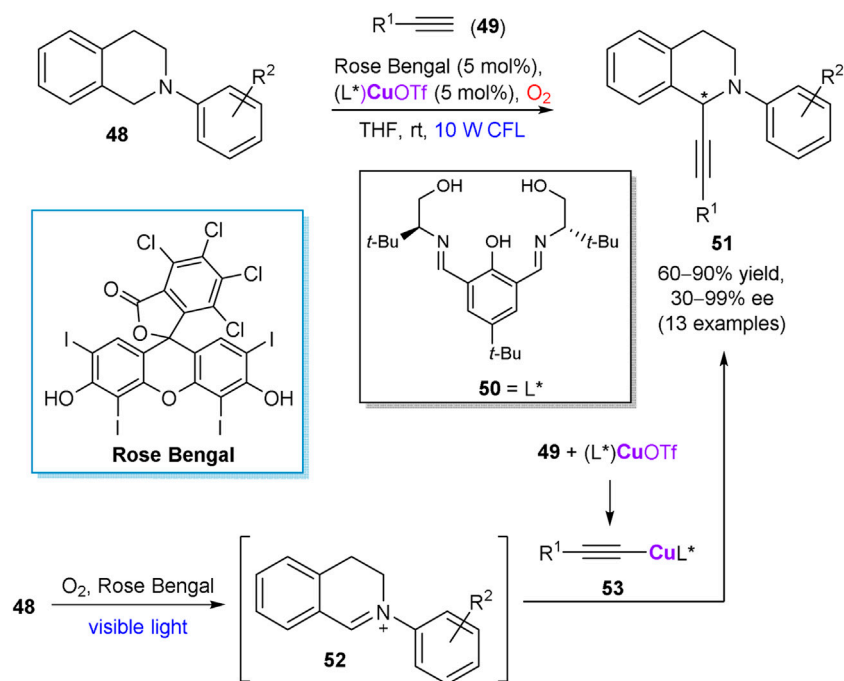
SCHEME 13 | Catalytic aerobic oxidation of cyclopentadiene and tandem enantioselective cycloaddition (Potowski et al., 2015).

R group of **31** tolerate the reaction conditions, except of the metal-coordinating (e.g. amine) and base-sensitive moieties. The α -helical structure of PLL catalyst is responsible for the supramolecular binding of prochiral substrate **32** and favors the corresponding transition state (**TS[‡]**) leading to the *R*-enantiomer of **30** (Kelly and Roberts, 2004; Berkessel et al., 2006). The developed transformation was successfully applied in a short and stereodivergent synthesis of chlamydocin, a natural histone deacetylase inhibitor with chiral epoxy ketone warhead (Elek et al., 2019).

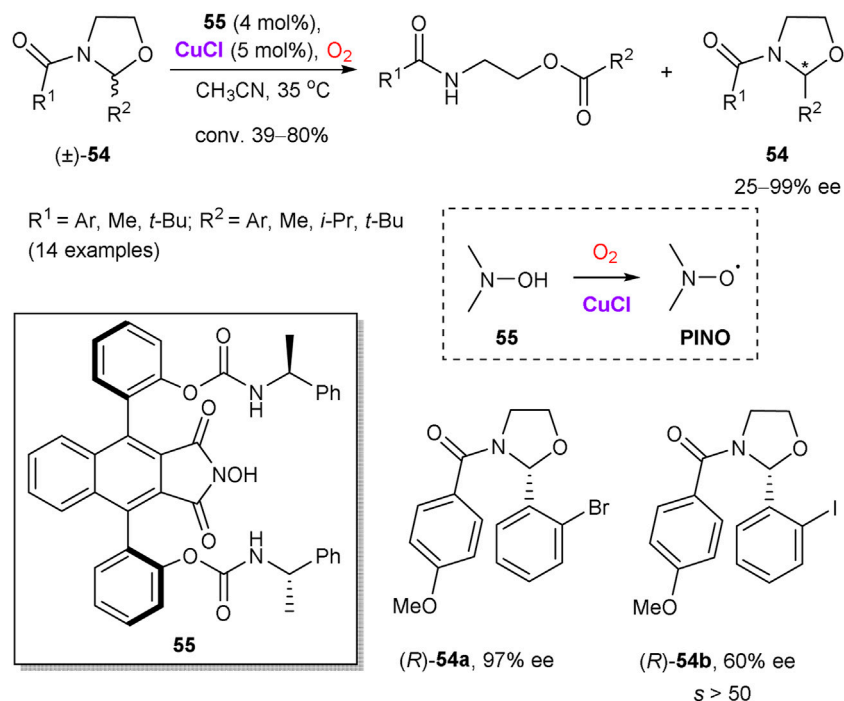
Several enantioselective cascade transformations with reactive intermediates generated by aerobic oxidation in the presence of copper salts have also been reported. Thus, Whiting (Chaiyavej et al., 2011) and Alaniz (Frazier et al., 2011; Frazier et al., 2012) independently disclosed a convenient protocol for the generation of nitrosocarbonyl compounds (e.g. **33**, **Scheme 12B**) by copper-catalyzed aerobic oxidation of *N*-protected hydroxylamines **34**. These reactive electrophilic nitroso compounds have been utilized in a number of robust transformations, including the asymmetric ene reactions (**Scheme 12A**), (Frazier et al., 2011) inter- and intramolecular hetero-Diels–Alder reactions, (Chaiyavej et al., 2011; Frazier et al., 2012) α -amination of silyl enol ethers, (Sandoval et al., 2015) β -dicarbonyl compounds (**Scheme 12B**), (Xu et al., 2014) and α -hydroxylation of β -ketophosphonates **35** (**Scheme 12C**) (Maji and Yamamoto, 2014; Maji and Yamamoto, 2015). The asymmetric α -amination of β -ketocarbonyl compounds

under aerobic conditions, developed by Luo et al., can represent a notable example (**Scheme 12B**) (Xu et al., 2014). In this transformation, aerobic generation of nitrosocarbonyls was beneficially merged with enamine catalysis enabled by a chiral primary amine **36**. The process featured high chemo- and enantioselectivity for a broad range of β -ketocarbonyl substrates, for example β -ketoester **37** furnished the corresponding amination adduct (*R*)-**38** in 97% yield and 96% ee. Based on the absolute configuration of product **38**, as well as X-ray crystal and solution structures of enamine intermediate **39**, the transition state was suggested to account for the observed stereoselectivity, in which the hydrogen-bonding network between **39** and **33** facilitates the *Re*-face attack of enamine to give adduct **38** with the (*R*)-configuration.

An interesting example of the enantioselective assembly of structurally complex 5,5,5-tricyclic products **40** with eight stereocenters via the multicomponent cascade reaction was described (**Scheme 13**) (Potowski et al., 2015). The cascade process is triggered by copper-catalyzed aerobic oxidation of cyclopentadiene **41** to cyclopentadienone **42**. It was supposed that the allylic C–H oxidation of **41** is mediated by the copper peroxo-complex **43**, formed by trapping molecular oxygen by $\text{Cu}(\text{CH}_3\text{CN})_4\text{BF}_4$ in the presence of (*R*)-Fesulphos ligand **44**. The subsequent double catalytic asymmetric 1,3-dipolar cycloaddition of azomethine ylides, derived from glycine ester imines **45**, delivers the final tricyclic product **40**. In turn,



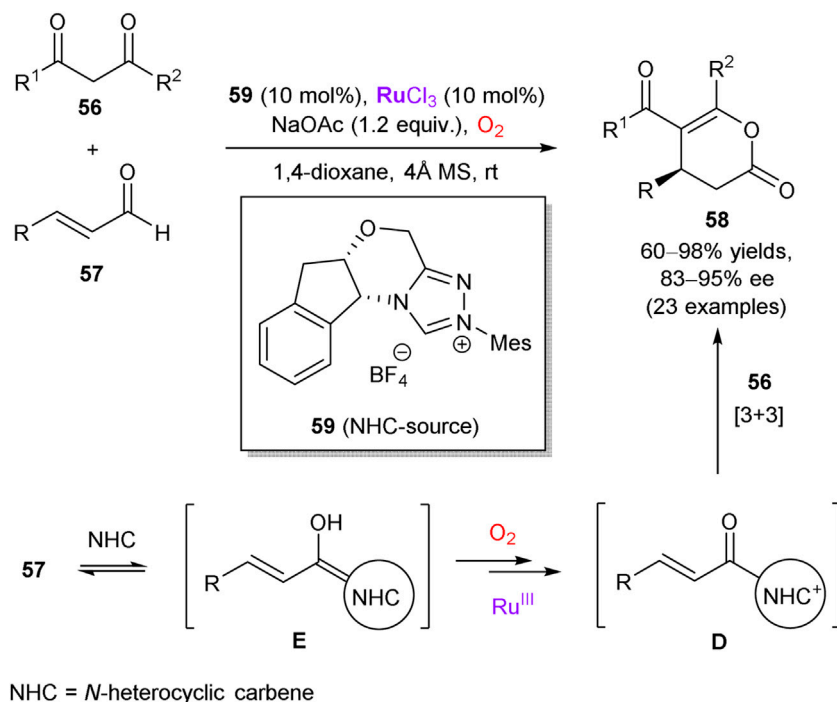
SCHEME 14 | Enantioselective cross dehydrogenative coupling of alkynes **49** with tetrahydroisoquinoline derivatives **48** (Kumar et al., 2017).



SCHEME 15 | Copper-catalyzed oxidative kinetic resolution of oxazolidines **54** (Nechab et al., 2007).

azomethine ylides are generated by deprotonation of the glycine ester imine ligand in the chiral copper complex **46**. The step-wise double cycloaddition proceeds via the *endo* transition state with **42**

(or intermediate **47**) approaching from the *Re*-face of ylide (with respect to C=N) to avoid unfavorable interactions with the *t*-Bu group of the ligand **44**.



SCHEME 16 | Aerobic oxidation/annulation cascade through synergistic catalysis of RuCl_3 and *N*-heterocyclic carbene (NHC) precursor **59** (Wang et al., 2018).

In 2017, Khan et al. described a visible-light enabled enantioselective cross dehydrogenative coupling between tetrahydroisoquinoline derivatives **48** and alkynes **49**, using molecular oxygen as the sole oxidant (**Scheme 14**) (Kumar et al., 2017). The reaction was mediated by *in situ* generated copper complex with chiral salen ligand **50** and Rose Bengal as a complementary photo-redox catalyst, furnishing alkynylation products **51** in up to 90% yield and up to 99% ee. According to the suggested reaction mechanism, prochiral iminium ion **52** is produced by oxidation of **48** in the photo-redox catalytic cycle. In turn, the chiral copper complex (L^*)CuOTf activates terminal alkyne **49** and serves as a precursor of chiral acetylide species **53**, which affords the optically active coupling product **51** after addition to the intermediate imine **52**.

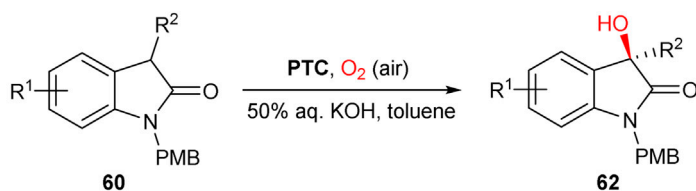
Copper salts are also able to assist in the recovery of catalytically active nitroxide radical species by oxidation with molecular oxygen. Hence, Einhorn et al. disclosed kinetic resolution of oxazolidines **54** by the oxidative ring-opening, catalyzed by chiral *N*-hydroxyphthalimides (NHPI) and copper(I) chloride (**Scheme 15**) (Nechab et al., 2007). Fast reaction rates for the aerobic oxidation of **54** and selectivity factors $s > 20$ were observed for a range of the substrates with the most efficient chiral NHPI catalyst **55**. As notable examples, *o*-bromophenyl-substituted oxazolidine (*R*)-**54a** was obtained in 97% ee at 58% conversion, while *o*-iodophenylloxazolidine **54b** had the ee value of 60% at 39% conversion that corresponds to $s > 50$. The reaction proceeds via intermediate phthalimide *N*-oxyl radical (PINO), which enables a hydrogen atom transfer from the substrate **54**. While a precise role of copper is unclear, it could be attributed to the formation of μ -oxocopper(II) species by the

reaction of CuCl with dioxygen, which are capable to generate PINO from **55** (Nechab et al., 2004).

The last representative example in this subtopic is based on the work of Wang et al., who demonstrated that coordinatively unsaturated RuCl_3 can act as a synergistic co-catalyst in tandem with chiral *N*-heterocyclic carbenes (NHC) (Wang et al., 2018). The authors performed the aerobic [3 + 3] annulation reaction of β -dicarbonyl compounds **56** and enals **57** to access enantiomerically enriched lactones **58** in the presence of carbene precursor **59** (**Scheme 16**). The developed methodology exhibits a broad substrate scope, such as enals with complicated skeletons and diketones with exceptional structural diversity (23 examples in total). The obtained chemical yields were good-to-excellent along with the enantiomeric purity of up to 94% ee. According to the mechanistic studies, the reaction proceeds via acyl azolium intermediate **D**, generated by the ruthenium-catalyzed aerobic oxidation of homoenolate **E**. As a further extension, azolium dienolate intermediates can be generated from β,β -disubstituted enals, which smoothly afford δ -chiral lactones with 80–84% ee upon the [4 + 2] annulation reaction with trifluoromethyl ketones.

METAL-FREE CATALYTIC SYSTEMS

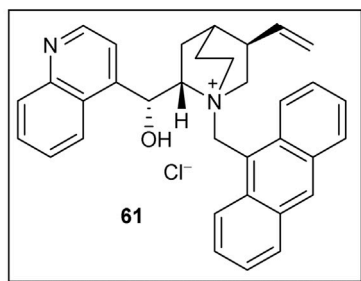
Another important synthetic strategy of asymmetric aerobic oxidations is based on the metal-free catalytic systems. The research activity in this field was commenced in the late 1980s by Shioiri, who described the first α -hydroxylation of achiral ketones with molecular oxygen in a two-phase system, which was



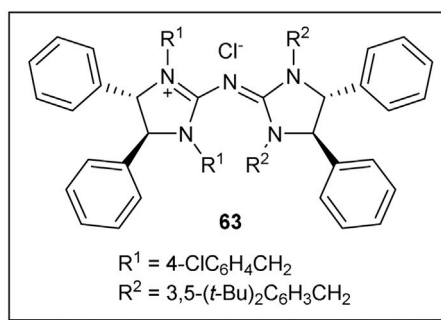
PTC = phase transfer catalyst

Itoh et al. 2008:R¹ = H; R² = allyl, Bn, propargyl, alkyl, etc.PTC = **61** (20 mol%), (EtO)₃P (4 equiv.), -20 °C.

91–100% yields, 67–93% ee (8 examples)

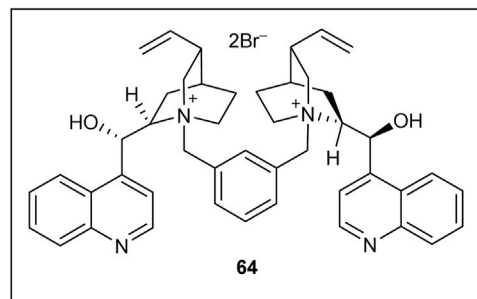
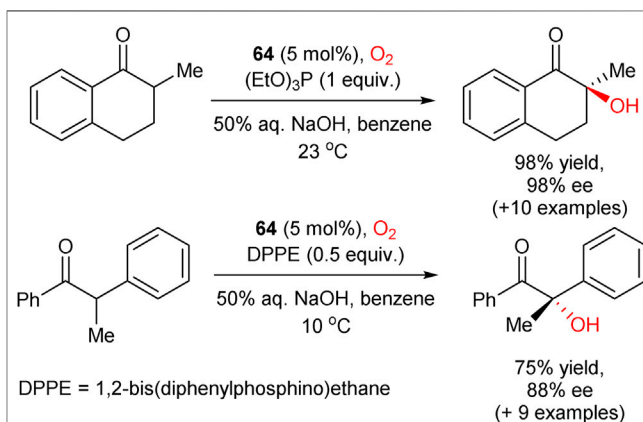
**Tan, Jiang et al. 2012:**R¹ = H, 5-F, 5-OMe; R² = Me, allyl, Bn, propargyl, etc.PTC = **63** (5 mol%), -60 °C.

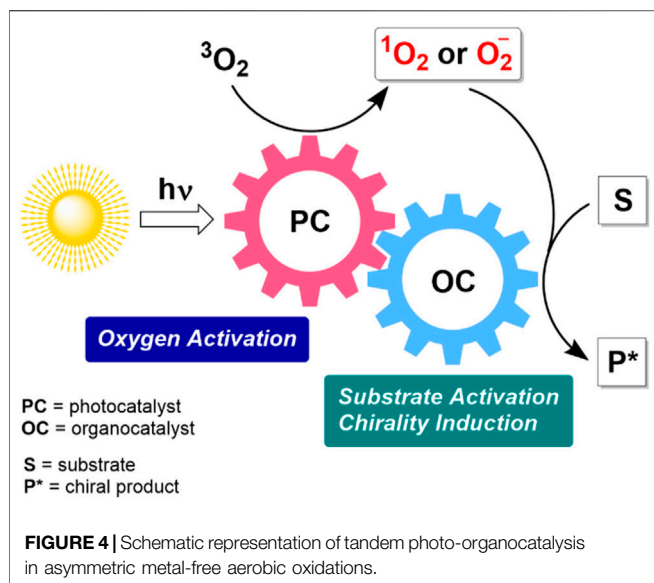
83–93% yields, 85–98% ee (11 examples)

**SCHEME 17** | Asymmetric hydroxylation of oxindoles **60** under phase transfer catalysis (Sano et al., 2008; Yang et al., 2012).

mediated by chiral phase transfer catalysts (PTC) and triethyl phosphite as a co-reductant (Masui et al., 1988). In 1995, Brussee utilized chiral aza-crown ethers for the same purpose (de Vries et al., 1995). The chiral phase transfer catalysis still represent the most frequently exploited approach among the organocatalytic aerobic oxidation methods. Importantly, a specific dioxygen activation process may not be required, since many enolizable carbonyl compounds can readily react with molecular oxygen under basic conditions (Doering and Haines, 1954; Gardner et al., 1968; Konen et al., 1975). As a rule, the organocatalytic methods are tolerant to both air and water what makes them especially attractive for various practical applications.

Following the seminal works of Shioiri (Masui et al., 1988) and Brussee, (de Vries et al., 1995) in 2008, Itoh group reported asymmetric hydroxylation of oxindoles **60** in the biphasic solvent system (toluene/water), mediated by chiral cinchonidine-derived PTC **61** (Scheme 17) (Sano et al., 2008). In this transformation, a set of 3-alkyl-, alkenyl-, and alkynyl-substituted oxindoles **60** were hydroxylated by a simple reaction of oxindole-derived enolates with molecular oxygen and triethyl phosphite, acting as a reductant for peroxide intermediates. The process furnished the corresponding 3-hydroxylated oxindole products **62** in up to quantitative yields and 67–93% enantioselectivities. The (*R*) absolute configuration at the stereogenic center in **62** (for R = allyl) was confirmed by chemical correlation with the known indole compound. In 2012, Tan and Jiang designed similar transformation, utilizing pentanidinium PTC **63** (Yang et al., 2012). In comparison to the Itoh's work, in this case a lower

**SCHEME 18** | Enantioselective α -hydroxylation of cyclic and acyclic ketones (Sim et al., 2015).



catalyst loading (5 mol%) was sufficient and no additional reductant such as triethyl phosphite was necessary. In 2015, Zhao et al. followed a similar phase-transfer catalytic strategy with 1,2-bis(diphenylphosphino)ethane or triethyl phosphite as reductants to perform the aerobic enantioselective α -hydroxylation of cyclic and acyclic ketones with higher yields and enantioselectivities achieved for cyclic ketones (representative examples are shown in **Scheme 18**). Dimeric PTC **64** was utilized and provided excellent stereinduction at only 5 mol% loading (Sim et al., 2015).

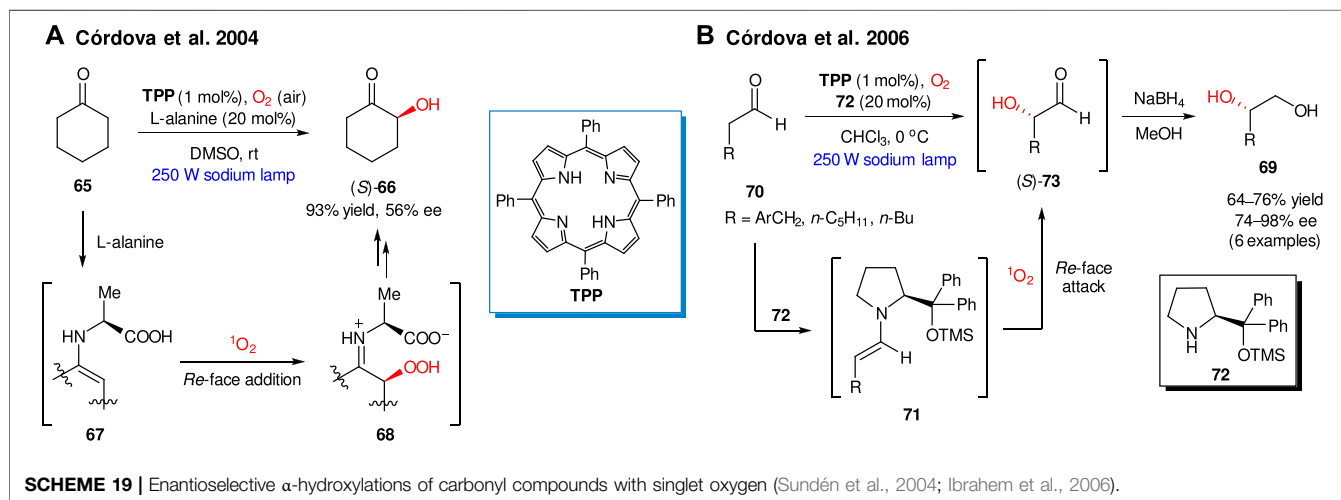
Several recent developments relied on combined photo-organocatalysis to produce more reactive oxygen species, as schematically outlined in **Figure 4**. The photochemical activation of dioxygen delivers highly reactive singlet oxygen in the presence of organic dyes acting as photosensitizers. Alternatively, a photoredox catalytic cycle can be involved. In such a case, the generation of superoxide anion (O_2^-) in an oxidative quenching cycle can be considered as a plausible O_2

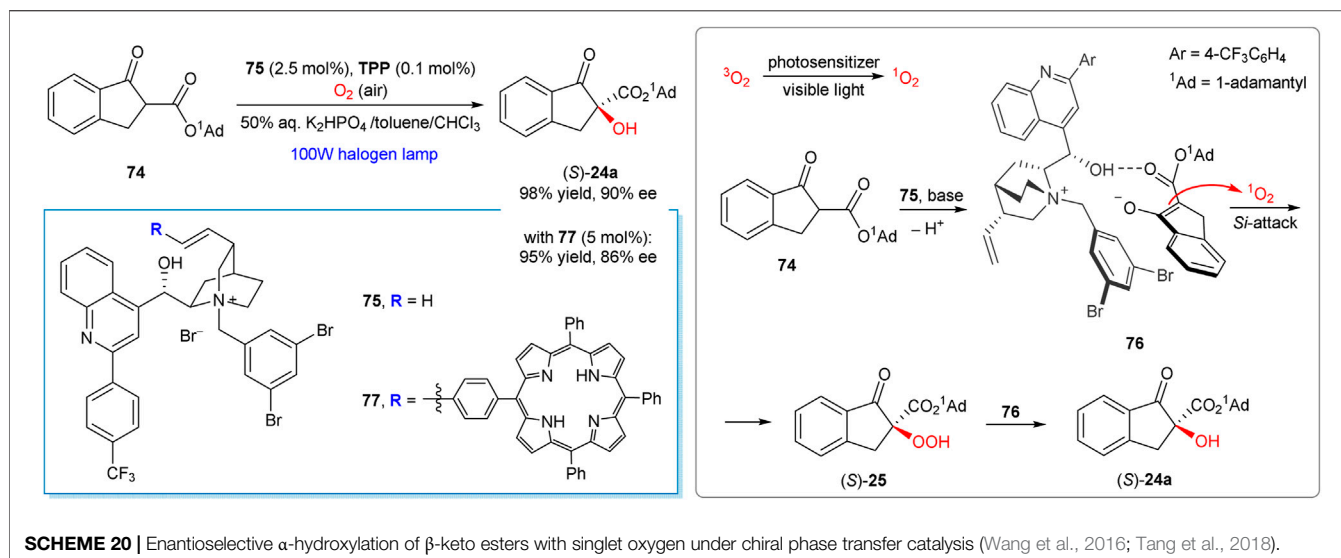
activation pathway. Subsequent asymmetric induction and activation of a substrate take place in a complementary organocatalytic cycle, which may include different types of chiral organocatalytic species, e.g. secondary amines, hydrogen bonding catalysts, phase transfer catalysts. Notable, an organocatalytic molecule and an organic dye can be covalently linked to form a bifunctional catalyst.

The first example of photochemically-driven asymmetric organocatalytic oxidation with singlet oxygen was described by Córdoba group, in 2004 (Sundén et al., 2004). They found that singlet oxygen, generated in the presence of tetraphenylporphyrin (TPP) as a photosensitizer, furnished the enantioselective α -oxidation of ketones in the presence of several natural amino acids as organocatalysts. For example, cyclohexanone **65** produced α -hydroxyketone (*S*)-**66** in 93% yield and 56% ee in the presence of L-alanine (20 mol%, **Scheme 19A**). The key steps of the proposed reaction mechanism imply the intermediate formation of enamine **67**, which undergoes the *Re*-face addition of singlet oxygen producing (2*S*)- α -hydroperoxide intermediate **68**. In the case of a cyclic L-amino acid (e.g. L-proline) the addition of 1O_2 occurred to the *Si*-face of corresponding enamine, thus providing opposite (*R*)-enantiomer of **66**.

As further expansion of the method utility, in 2006 the Córdoba group presented the synthesis of 1,2-diols **69** via organocatalytic enantioselective α -oxidation of aldehydes **70** (**Scheme 19B**) (Ibrahim et al., 2006). The process relies on the generation of enamine species **71**, formed *in situ* from aldehyde **70** and secondary amine organocatalyst **72**. The addition of 1O_2 occurs from the more sterically accessible *Re*-face of enamine **71**. Reduction of produced α -hydroxy aldehydes **73** with $NaBH_4$ furnished 1,2-diols **69** in 64–76% yields and 74–98% ee.

Works of the Meng group represent a notable recent example of chirality induction in the α -hydroxylation reactions by means of phase transfer catalysis and visible light activation of dioxygen (Lian et al., 2012; Wang et al., 2016; Tang et al., 2018; Tang et al., 2019a; Tang et al., 2019b). The method can be considered as complementary to the Ni-mediated transformation developed by the Xiao group (Scheme 9) (Ding et al., 2017). For example, the aerobic oxidation of





ester **74** furnished hydroxylation product **24a** in 98% yield and 90% ee in the presence of 2.5 mol% of phase transfer catalyst **75** (Scheme 20) (Wang et al., 2016). The reaction conditions are mild, being applicable for a range of the β -carbonyl compounds (30 examples in total). Furthermore, the synthetic protocol is scalable and suitable for preparation of **24a** in gram quantities without the loss of enantioselectivity (Wang et al., 2016).

The key step of the suggested reaction mechanism (Scheme 20) implies the addition of singlet oxygen to the chiral enolate-PTC complex **76**, in which ion-pairing, hydrogen bonding and π - π stacking between PTC and substrate were suggested as key supramolecular interactions (Wang et al., 2016). The produced hydroperoxide intermediate **25** then rapidly reacts with the enolate complex **76** furnishing the final product **24a**. The stereochemical outcome of the oxidation could be explained by the *Si*-face attack of $^1\text{O}_2$ or hydroperoxide **25**, since the opposite *Re*-face of enolate in the complex **76** is shielded by 1-adamantyl group.

A bifunctional photo-organocatalyst **77** has also been developed by the same group, with a tetraphenylporphyrin unit grafted to the cinchona alkaloid-derived phase-transfer catalyst (Tang et al., 2018). With the catalyst **77** (5 mol%), visible-light induced aerobic oxidation of **74** afforded (*S*)-**24a** in 95% yield and 86% ee. Further methodological improvements, such as greatly reduced reaction times, were achieved by using a flow photomicroreactor technology (Tang et al., 2019a; Tang et al., 2019b).

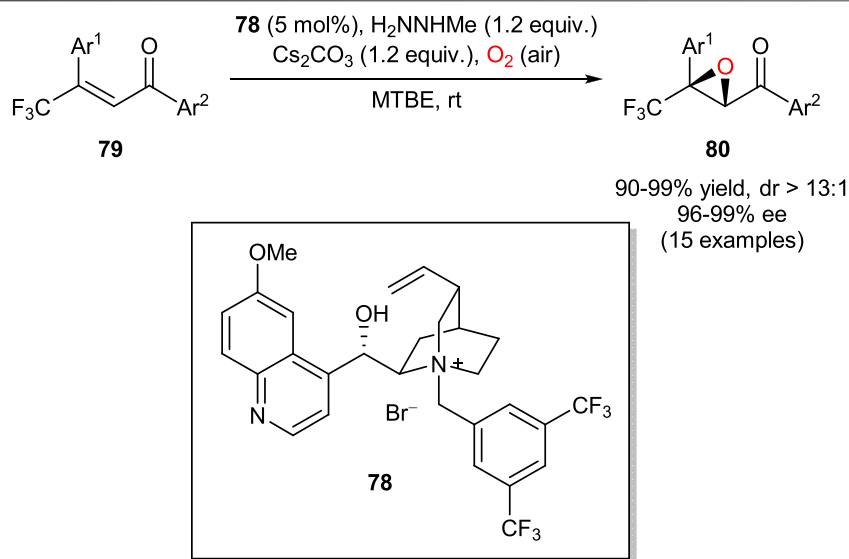
Besides α -hydroxylation of carbonyl compounds, the asymmetric metal-free oxidations with molecular oxygen can also be applied for the synthesis of other valuable chiral products, although such examples are less common.

In 2013, Shibata group reported a highly enantioselective aerobic epoxidation of β -trifluoromethyl β,β -disubstituted enones in the presence of methylhydrazine and catalytic amounts (5 mol%) of cinchona alkaloid-derived PTC **78** (Scheme 21) (Kawai et al., 2013). The use of methylhydrazine was essential to enable a unique dioxygen activation pathway, in

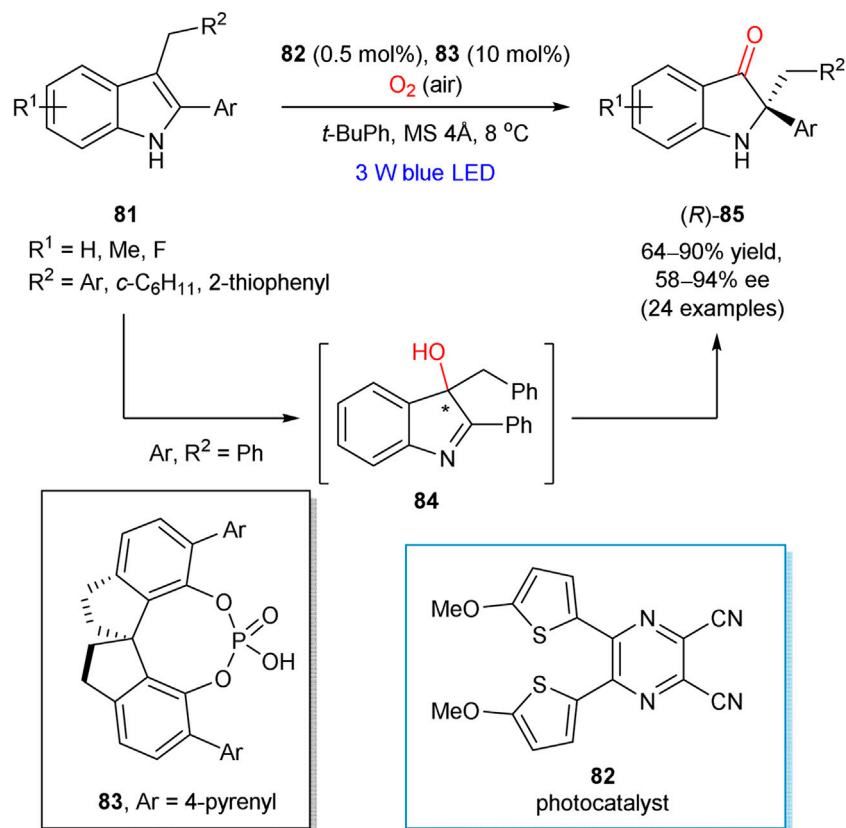
which highly pure hydrogen peroxide was produced *in situ* by reduction of molecular oxygen. The subsequent asymmetric Weitz-Scheffer reaction of enones **79** with H_2O_2 afforded chiral epoxide products **80**.

The enantioselective aerobic oxidation of 2-aryl-3-alkylsubstituted indoles **81**, accompanied with the semipinacol rearrangement, was reported by Zhao and Jiang in 2018 (Scheme 22) (Bu et al., 2018). The developed cooperative catalytic approach involved organophotoredox **82** and hydrogen bonding **83** catalysts. The preliminary mechanistic studies proved the formation of 3-hydroxylated compound **84** at the first step of aerobic oxidation. It was shown that chiral phosphoric acid **83** provided stereocontrol already at the first step, since the intermediate **84** was formed in its enantiomerically enriched form (59% ee at 65% conversion). However, higher enantioselectivity was observed in the subsequent pinacol rearrangement step (92% ee for **85**; Ar = R² = Ph), indicating that the generated 3-hydroxy intermediate **84** could be engaged at this step and hence affected the enantioselectivity of this rearrangement. The reaction mechanism is apparently similar to that mediated by $\text{Ru}(\text{bpy})_3\text{Cl}_2$ as a photocatalyst, which was thoroughly investigated by Xiao and Lu (Ding et al., 2014) and could involve the reaction between photochemically generated indole cation radical and superoxide radical anion, formed from molecular oxygen. While the generation of singlet oxygen cannot be completely excluded, it is unlikely a dominant pathway.

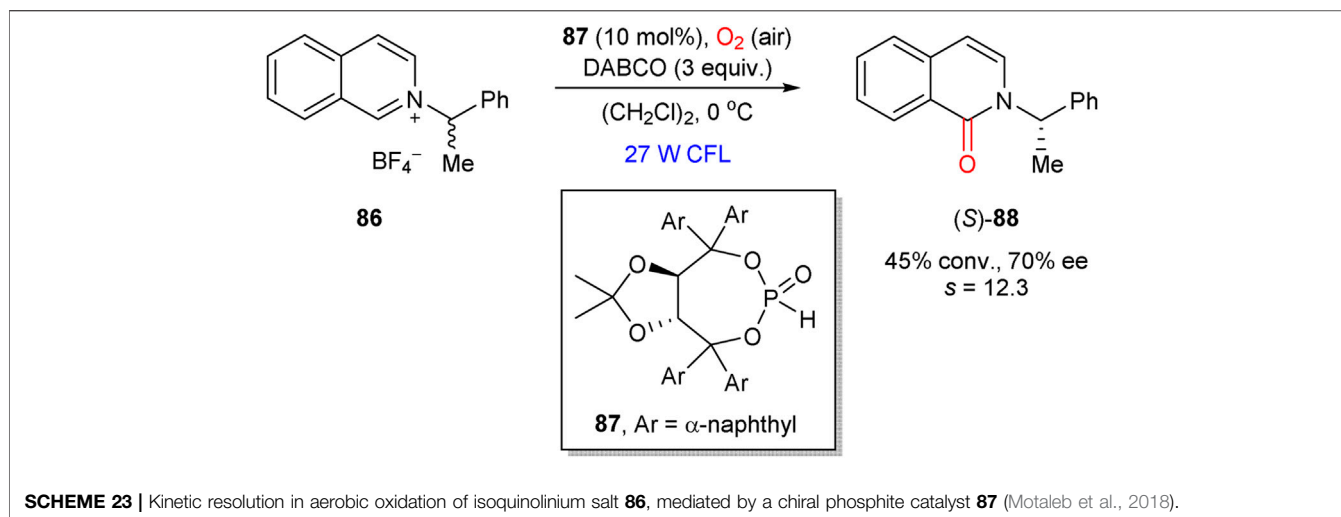
In 2018, Maity et al. presented an example of kinetic resolution in the aerobic visible-light induced oxidation of isoquinolinium salt **86** (Scheme 23) (Motaleb et al., 2018). The process was mediated by the TADDOL-based phosphite catalyst **87**, which led to the oxidation product (*S*)-**88** in 70% ee at 45% conversion (*s* = 12.3). The proposed reaction mechanism implies the initial formation of an adduct between **86** and organocatalyst **87**, which further converts into the organocatalyst-bound α -aminoalkyl radical intermediate. The latter furnishes the oxidation product **88** upon reaction with oxygen or superoxide anion.



SCHEME 21 | Enantioselective aerobic epoxidation of enones **79** (Kawai et al., 2013).



SCHEME 22 | Enantioselective aerobic oxidation of 2-aryl-3-alkylsubstituted indoles **81** (Bu et al., 2018).



CONCLUSION AND OUTLOOK

The progress in enantioselective aerobic oxidations in the last decades clearly demonstrates that molecular oxygen can be considered as a viable oxidant in the asymmetric transformations, being especially attractive for the development of sustainable oxidation protocols. Importantly, an efficient way of chirogenesis must be enabled along with a complementary O_2 -activation cycle to ensure high yields, extended substrate scope, and excellent optical purity of the oxidation products. In turn, the activation of O_2 can be achieved with either transition metal catalysis as a mainstream approach or with the help of photocatalytic methods as another direction. The use of electrosynthesis can also be foreseen (Kawamata et al., 2017; Sambiagio et al., 2017), although it does not have any asymmetric applications yet. Dual catalytic processes have been commonly utilized, as with the aid of custom-designed bifunctional ligands and organocatalysts and with an additional catalytic cycle. Despite the promising potential of tandem catalytic processes for further application, the design of task-specific catalysts and merging two complementary catalytic cycles into a tandem process are still arduous tasks.

For the forthcoming successful developments in the field, several existing challenges must be properly addressed. Although aerobic oxidations themselves are considered as “green-by-design” processes, their safety and energy efficiency characteristics are often not satisfactory for industrial applications. The use of air and especially pure oxygen in the large-scale manufacturing is hampered by incompatibility with flammable solvents, along with accompanying problems such as heat- and mass transfers in a liquid-gas reaction media (Osterberg et al., 2015; Sterckx et al., 2019). Furthermore, non-catalytic radical autooxidation events may represent an additional obstacle (Sterckx et al., 2019). Fortunately, it is possible to attenuate the impact of these negative phenomena with the aid of modern flow chemistry techniques (Gemoets et al., 2016; Hone and Kappe, 2018). Complications for the industrial use of light-driven reactions arise from their significant running cost and high energy demands (Protti et al., 2009) that eventually results in enhanced CO_2 emissions, especially in the case of fossil fuel as a source of energy. This problem can be attenuated and eventually circumvented by further

technology advances, such as design of more energy-efficient light sources, photoreactors, and use of clean energy. As for the latter, direct use of sunlight is especially appealing (Haggiage et al., 2009; Cambié et al., 2017; Cambié et al., 2019). Although the concept is more than a century old (Ciamician, 1912), its renaissance has begun only recently.

Besides the technology-related issues outlined above, chemical diversity of the available transformations must be considerably expanded. Despite rapid progress in the field of aerobic oxidations in general, the contribution of the corresponding asymmetric reactions is rather low and mostly limited to the α -hydroxylation of reactive carbonyl compounds, epoxidations of alkenes, and oxidative kinetic resolutions of secondary alcohols. As one of the solutions, an inspiration for the development of new highly chemo- and enantioselective transformations could arise from enzymatic reactions, of which many have no artificial analogs, such as efficient enantioselective hydroxylation of inactivated C–H bonds (Chang et al., 2000), including hydrocarbons (Adam et al., 2000a; Adam et al., 2000b), and *cis*-dihydroxylation of aromatic compounds (Endoma et al., 2002; García-Urdiales et al., 2005; Boyd and Bugg, 2006).

Albeit the enantioselective oxidation reactions with molecular oxygen are still in their infancy and cannot be considered as dominant among the asymmetric oxidation methods, their sustainable design and prominent potential for environmentally benign chemical industry will certainly stimulate further research activity in the field.

AUTHOR CONTRIBUTIONS

DK and GE performed a literature search and prepared a draft. DK, GE, ML, and VB wrote the paper. All authors contributed to the article and approved the submitted version.

FUNDING

Funding from the Centre of Excellence in Molecular Cell Engineering (Grant 2014-2020.4.01.15-0013), the Estonian Ministry of Education and Research (Grant IUT19-32), and Tallinn University of Technology (Grant B58) is gratefully acknowledged.

REFERENCES

- Adam, W., Lukacs, Z., Harmsen, D., Saha-Möller, C. R., and Schreier, P. (2000a). Biocatalytic asymmetric hydroxylation of hydrocarbons with the topsoil-microorganism *Bacillus megaterium*. *J. Org. Chem.* 65 (3), 878–882. doi:10.1021/jo991725s
- Adam, W., Lukacs, Z., Saha-Möller, C. R., Weckerle, B., and Schreier, P. (2000b). Microbial asymmetric CH oxidations of simple hydrocarbons: a novel monooxygenase activity of the topsoil Microorganism *Bacillus megaterium*. *Eur. J. Org. Chem.* 2000 (16), 2923–2926. doi:10.1002/1099-0690(200008)2000:16<2923::aid-ajoc2923>3.0.co;2-l
- Alamsetti, S. K., and Sekar, G. (2010). Chiral cobalt-catalyzed enantioselective aerobic oxidation of α -hydroxy esters. *Chem. Commun. (Camb)* 46 (38), 7235–7237. doi:10.1039/c0cc01917h
- Allen, S. E., Walvoord, R. R., Padilla-Salinas, R., and Kozlowski, M. C. (2013). Aerobic copper-catalyzed organic reactions. *Chem. Rev.* 113 (8), 6234–6458. doi:10.1021/cr300527g
- Anastas, P. T., and Warner, J. C. (1998). *Green chemistry: theory and practice*. Oxford, United Kingdom: Oxford University Press.
- Berkessel, A., Koch, B., Toniolo, C., Rainaldi, M., Broxterman, Q. B., and Kaptein, B. (2006). Asymmetric enone epoxidation by short solid-phase bound peptides: further evidence for catalyst helicity and catalytic activity of individual peptide strands. *Biopolymers* 84 (1), 90–96. doi:10.1002/bip.20413
- Bolm, C., Khanh Luong, T., and Schlingloff, G. (1997). Enantioselective metal-catalyzed baeyer-villiger oxidation of cyclobutanones. *Synlett* 1997 (10), 1151–1152. doi:10.1055/s-1997-977
- Bolm, C., and Schlingloff, G. (1995). Metal-catalysed enantiospecific aerobic oxidation of cyclobutanones. *J. Chem. Soc. Chem. Commun.* 12, 1247–1248. doi:10.1039/c39950001247
- Bolm, C., Schlingloff, G., and Weickhardt, K. (1994). Optically active lactones from a baeyer-villiger-type metal-catalyzed oxidation with molecular oxygen. *Angew. Chem. Int. Ed. Engl.* 33 (18), 1848–1849. doi:10.1002/anie.199418481
- Borovkov, V. V., Lintuluoto, J. M., and Inoue, Y. (2001). Supramolecular chirogenesis in zinc porphyrins: mechanism, role of guest structure, and application for the absolute configuration determination. *J. Am. Chem. Soc.* 123 (13), 2979–2989. doi:10.1021/ja0032982
- Boyd, D. R., and Bugg, T. D. (2006). Arene cis-dihydrodiol formation: from biology to application. *Org. Biomol. Chem.* 4 (2), 181–192. doi:10.1039/b513226f
- Bryliakov, K. (2015). *Environmentally sustainable catalytic asymmetric oxidations*. Cleveland, OH: CRC Press.
- Bryliakov, K. P. (2017). Catalytic asymmetric oxygenations with the environmentally benign oxidants H_2O_2 and O_2 . *Chem. Rev.* 117 (17), 11406–11459. doi:10.1021/acs.chemrev.7b00167
- Bu, L., Li, J., Yin, Y., Qiao, B., Chai, G., Zhao, X., et al. (2018). Organocatalytic asymmetric cascade aerobic oxidation and semipinacol rearrangement reaction: a visible light-induced approach to access chiral 2,2-disubstituted indolin-3-ones. *Chem. Asian J.* 13 (17), 2382–2387. doi:10.1002/asia.201800446
- Bugg, T. D. H. (2003). Dioxygenase enzymes: catalytic mechanisms and chemical models. *Tetrahedron* 59 (36), 7075–7101. doi:10.1016/s0040-4020(03)00944-x
- Cambié, D., Zhao, F., Hessel, V., Debije, M. G., and Noël, T. (2017). A leaf-inspired luminescent solar concentrator for energy-efficient continuous-flow photochemistry. *Angew. Chem. Int. Ed. Engl.* 56 (4), 1050–1054. doi:10.1002/anie.201611101
- Cambié, D., Dobbelaar, J., Riente, P., Vanderspikken, J., Shen, C., Seeberger, P. H., et al. (2019). Energy-efficient solar photochemistry with luminescent solar concentrator based photomicroreactors. *Angew. Chem. Int. Ed.* 58 (40), 14374–14378. doi:10.1002/anie.201908553
- Caron, S., Dugger, R. W., Ruggeri, S. G., Ragan, J. A., and Ripin, D. H. (2006). Large-scale oxidations in the pharmaceutical industry. *Chem. Rev.* 106 (7), 2943–2989. doi:10.1021/cr040679f
- Caspi, D. D., Ebner, D. C., Bagdanoff, J. T., and Stoltz, B. M. (2004). The resolution of important pharmaceutical building blocks by palladium-catalyzed aerobic oxidation of secondary alcohols. *Adv. Synth. Catal.* 346 (2–3), 185–189. doi:10.1002/adsc.200303188
- Chaiyaveij, D., Cleary, L., Batsanov, A. S., Marder, T. B., Shea, K. J., and Whiting, A. (2011). Copper(II)-catalyzed room temperature aerobic oxidation of hydroxamic acids and hydrazides to acyl-nitroso and azo intermediates, and their Diels-Alder trapping. *Org. Lett.* 13 (13), 3442–3445. doi:10.1021/ol201188d
- Chang, D., Witholt, B., and Li, Z. (2000). Preparation of (S)-N-substituted 4-hydroxy-pyrrolidin-2-ones by regio- and stereoselective hydroxylation with sphingomonas sp. HXN-200. *Org. Lett.* 2 (24), 3949–3952. doi:10.1021/ol006735q
- Chen, C.-T., Bettigeri, S., Weng, S.-S., Pawar, V. D., Lin, Y.-H., Liu, C.-Y., et al. (2007). Asymmetric aerobic oxidation of α -hydroxy acid derivatives by C4-symmetric, vanadate-centered, tetrakisvanadyl(V) clusters derived from N-Salicylidene- α -aminocarboxylates. *J. Org. Chem.* 72 (22), 8175–8185. doi:10.1021/jo70575f
- Chen, C. T., Kao, J. Q., Salunke, S. B., and Lin, Y. H. (2011). Enantioselective aerobic oxidation of α -hydroxy-ketones catalyzed by oxidovanadium(V) methoxides bearing chiral, N-salicylidene-tert-butylglycinates. *Org. Lett.* 13 (1), 26–29. doi:10.1021/ol1024053
- Ciamician, G. (1912). The photochemistry of the future. *Science* 36 (926), 385–394. doi:10.1126/science.36.926.385
- de Gonzalo, G., and Fraaije, M. W. (2013). Recent developments in flavin-based catalysis. *ChemCatChem* 5 (2), 403–415. doi:10.1002/cctc.201200466
- de Vries, E. F. J., Ploeg, L., Colao, M., Brussee, J., and van der Gen, A. (1995). Enantioselective oxidation of aromatic ketones by molecular oxygen, catalyzed by chiral monoaza-crown ethers. *Tetrahedron: Asymmetry* 6 (5), 1123–1132. doi:10.1016/0957-4166(95)00138-f
- Ding, W., Lu, L. Q., Zhou, Q. Q., Wei, Y., Chen, J. R., and Xiao, W. J. (2017). Bifunctional photocatalysts for enantioselective aerobic oxidation of β -ketoesters. *J. Am. Chem. Soc.* 139 (1), 63–66. doi:10.1021/jacs.6b11418
- Ding, W., Zhou, Q.-Q., Xuan, J., Li, T.-R., Lu, L.-Q., and Xiao, W.-J. (2014). Photocatalytic aerobic oxidation/semipinacol rearrangement sequence: a concise route to the core of pseudoindoxyl alkaloids. *Tetrahedron Lett.* 55 (33), 4648–4652. doi:10.1016/j.tetlet.2014.06.102
- Dismukes, G. C. (1996). Manganese enzymes with binuclear active sites. *Chem. Rev.* 96 (7), 2909–2926. doi:10.1021/cr950053c
- Doering, W., and Haines, R. M. (1954). Alkoxide-catalyzed autoxidative cleavage of ketones and esters. *J. Am. Chem. Soc.* 76 (2), 482–486. doi:10.1021/ja01631a044
- Egami, H., and Katsuki, T. (2009). Iron-catalyzed asymmetric aerobic oxidation: oxidative coupling of 2-naphthols. *J. Am. Chem. Soc.* 131 (17), 6082–6083. doi:10.1021/ja901391u
- Elek, G. Z., Borovkov, V., Lopp, M., and Kananovich, D. G. (2017). Enantioselective one-pot synthesis of α,β -epoxy ketones via aerobic oxidation of cyclopropanols. *Org. Lett.* 19 (13), 3544–3547. doi:10.1021/acs.orglett.7b01519
- Elek, G. Z., Koppel, K., Zubrytski, D. M., Konrad, N., Järving, I., Lopp, M., et al. (2019). Divergent access to histone deacetylase inhibitory cyclopeptides via a late-stage cyclopropane ring cleavage strategy. *Org. Lett.* 21 (20), 8473–8478. doi:10.1021/acs.orglett.9b03305
- Endoma, M. A., Bui, V. P., Hansen, J., and Hudlicky, T. (2002). Medium-scale preparation of useful metabolites of aromatic compounds via whole-cell fermentation with recombinant organisms. *Org. Process. Res. Dev.* 6 (4), 525–532. doi:10.1021/op020013s
- Ferreira, E. M., and Stoltz, B. M. (2001). The palladium-catalyzed oxidative kinetic resolution of secondary alcohols with molecular oxygen. *J. Am. Chem. Soc.* 123 (31), 7725–7726. doi:10.1021/ja015791z
- Festa, R. A., and Thiele, D. J. (2011). Copper: an essential metal in biology. *Curr. Biol.* 21 (21), R877–R883. doi:10.1016/j.cub.2011.09.040
- Frazier, C. P., Bugarin, A., Engelking, J. R., and Read de Alaniz, J. (2012). Copper-catalyzed aerobic oxidation of N-substituted hydroxylamines: efficient and practical access to nitroso compounds. *Org. Lett.* 14 (14), 3620–3623. doi:10.1021/ol301414k
- Frazier, C. P., Engelking, J. R., and Read de Alaniz, J. (2011). Copper-catalyzed aerobic oxidation of hydroxamic acids leads to a mild and versatile acylnitroso ene reaction. *J. Am. Chem. Soc.* 133 (27), 10430–10433. doi:10.1021/ja204603u
- Gandomkar, S., Jost, E., Loidolt, D., Swoboda, A., Pickl, M., Elaili, W., et al. (2019). Biocatalytic enantioselective oxidation of sec-allylic alcohols with flavin-dependent oxidases. *Adv. Synth. Catal.* 361 (22), 5264–5271. doi:10.1002/adsc.201900921
- García-Urdiales, E., Alfonso, I., and Gotor, V. (2005). Enantioselective enzymatic desymmetrizations in organic synthesis. *Chem. Rev.* 105 (1), 313–354. doi:10.1021/cr040640a

- Gardner, J. N., Carlon, F. E., and Gnoj, O. (1968). A one-step procedure for the preparation of tertiary α -ketols from the corresponding ketones. *J. Org. Chem.* 33 (8), 3294–3297. doi:10.1021/jo01272a055
- Gebauer, K., Reuß, F., Spanka, M., and Schneider, C. (2017). Relay catalysis: manganese(III) phosphate catalyzed asymmetric addition of β -dicarbonyls to ortho-quinone methides generated by catalytic aerobic oxidation. *Org. Lett.* 19 (17), 4588–4591. doi:10.1021/acs.orglett.7b02185
- Gemoets, H. P., Su, Y., Shang, M., Hessel, V., Luque, R., and Noël, T. (2016). Liquid phase oxidation chemistry in continuous-flow microreactors. *Chem. Soc. Rev.* 45 (1), 83–117. doi:10.1039/c5cs00447k
- Germain, A. R., Bruggemeyer, D. M., Zhu, J., Genet, C., O'Brien, P., and Porco, J. A. (2011). Synthesis of the azaphilones (+)-Sclerotiorin and (+)-8-O-methylsclerotiorinamine utilizing (+)-Sparteine surrogates in copper-mediated oxidative dearomatization. *J. Org. Chem.* 76 (8), 2577–2584. doi:10.1021/jo102448n
- Ghogare, A. A., and Greer, A. (2016). Using singlet oxygen to synthesize natural products and drugs. *Chem. Rev.* 116 (17), 9994–10034. doi:10.1021/acs.chemrev.5b00726
- Hadian-Dehkordi, L., and Hosseini-Monfared, H. (2016). Enantioselective aerobic oxidation of olefins by magnetite nanoparticles at room temperature: a chiral carboxylic acid strategy. *Green. Chem.* 18 (2), 497–507. doi:10.1039/c5gc01774b
- Haggiage, E., Coyle, E. E., Joyce, K., and Oelgemöller, M. (2009). Green photochemistry: solarchemical synthesis of 5-amido-1,4-naphthoquinones. *Green. Chem.* 11 (3), 318–321. doi:10.1039/b816676e
- Hone, C. A., and Kappe, C. O. (2018). The use of molecular oxygen for liquid phase Aerobic oxidations in continuous flow. *Top. Curr. Chem. (Cham)* 377 (1), 2. doi:10.1007/s41061-018-0226-z
- Hone, C. A., Roberge, D. M., and Kappe, C. O. (2017). The use of molecular oxygen in pharmaceutical manufacturing: is flow the way to go? *ChemSusChem* 10 (1), 32–41. doi:10.1002/cssc.201601321
- Ibrahim, I., Zhao, G.-L., Sundén, H., and Córdova, A. (2006). A route to 1,2-diols by enantioselective organocatalytic α -oxidation with molecular oxygen. *Tetrahedron Lett.* 47 (27), 4659–4663. doi:10.1016/j.tetlet.2006.04.133
- Imagawa, K., Nagata, T., Yamada, T., and Mukaiyama, T. (1995). Asymmetric oxidation of sulfides with molecular oxygen catalyzed by β -oxo aldiminato manganese(III) complexes. *Chem. Lett.* 24 (5), 335–336. doi:10.1246/cl.1995.335
- Ingold, K. U. (1961). Inhibition of the autoxidation of organic substances in the liquid phase. *Chem. Rev.* 61 (6), 563–589. doi:10.1021/cr60214a002
- Irie, R., and Katsuki, T. (2004). Selective aerobic oxidation of hydroxy compounds catalyzed by photoactivated ruthenium-salen complexes (selective catalytic aerobic oxidation). *Chem. Rec.* 4 (2), 96–109. doi:10.1002/tcr.20001
- Irie, R., Masutani, K., and Katsuki, T. (2000). Asymmetric aerobic oxidation coupling of 2-naphthol derivatives catalyzed by photo-activated chiral (NO) Ru(II)-Salen complex. *Synlett* 2000 (10), 1433–1436. doi:10.1055/s-2000-7654
- Jacobsen, E. N., Marko, I., Mungall, W. S., Schroeder, G., and Sharpless, K. B. (1988). Asymmetric dihydroxylation via ligand-accelerated catalysis. *J. Am. Chem. Soc.* 110 (6), 1968–1970. doi:10.1021/ja00214a053
- Jensen, D. R., Pugsley, J. S., and Sigman, M. S. (2001). Palladium-catalyzed enantioselective oxidations of alcohols using molecular oxygen. *J. Am. Chem. Soc.* 123 (30), 7475–7476. doi:10.1021/ja015827n
- Jiao, N., and Stahl, S. (2019). *Green oxidation in organic synthesis*. New York, NY: Wiley.
- Katsuki, T., and Martin, V. (2004). Asymmetric epoxidation of allylic alcohols: the katsuki-sharpless epoxidation reaction. *Org. React.* 48, 1–299. doi:10.1002/0471264180.or048.01
- Katsuki, T., and Sharpless, K. B. (1980). The first practical method for asymmetric epoxidation. *J. Am. Chem. Soc.* 102 (18), 5974–5976. doi:10.1021/ja00538a077
- Kawai, H., Okusu, S., Yuan, Z., Tokunaga, E., Yamano, A., Shiro, M., et al. (2013). Enantioselective synthesis of epoxides having a tetrasubstituted trifluoromethylated carbon center: methylhydrazine-induced aerobic epoxidation of β , β -disubstituted enones. *Angew. Chem. Int. Ed. Engl.* 52 (8), 2221–2225. doi:10.1002/anie.201209355
- Kawamata, Y., Yan, M., Liu, Z., Bao, D. H., Chen, J., Starr, J. T., et al. (2017). Scalable, electrochemical oxidation of unactivated C-H bonds. *J. Am. Chem. Soc.* 139 (22), 7448–7451. doi:10.1021/jacs.7b03539
- Kelly, D. R., and Roberts, S. M. (2004). The mechanism of polyleucine catalyzed asymmetric epoxidation. *Chem. Commun.* 18, 2018–2020. doi:10.1039/B404390C
- Konen, D. A., Silbert, L. S., and Pfeffer, P. E. (1975). α -Anions. VII. Direct oxidation of enolate anions to 2-hydroperoxy- and 2-hydroxycarboxylic acids and esters. *J. Org. Chem.* 40 (22), 3253–3258. doi:10.1021/jo00910a020
- Koya, S., Nishioka, Y., Mizoguchi, H., Uchida, T., and Katsuki, T. (2012). Asymmetric epoxidation of conjugated olefins with dioxygen. *Angew. Chem. Int. Ed. Engl.* 51 (33), 8243–8246. doi:10.1002/anie.201201848
- Krishnan, S., Bagdanoff, J. T., Ebner, D. C., Ramtohl, Y. K., Tambar, U. K., and Stoltz, B. M. (2008). Pd-catalyzed enantioselective aerobic oxidation of secondary alcohols: applications to the total synthesis of alkaloids. *J. Am. Chem. Soc.* 130 (41), 13745–13754. doi:10.1021/ja804738b
- Kumar, G., Verma, S., Ansari, A., Khan, N.-u. H., and Kureshy, R. I. (2017). Enantioselective cross dehydrogenative coupling reaction catalyzed by Rose bengal incorporated-Cu(I)-Dimeric chiral complexes. *Catal. Commun.* 99, 94–99. doi:10.1016/j.catcom.2017.05.026
- Kureshy, R. I., Khan, N. H., Abdi, S. H. R., Iyer, P., and Bhatt, A. K. (1998). Aerobic, enantioselective epoxidation of non-functionalized olefins catalyzed by Ni(II) chiral schiff base complexes. *J. Mol. Catal. A Chem.* 130 (1), 41–50. doi:10.1016/s1381-1169(97)00195-7
- Kureshy, R. I., Khan, N. H., Abdi, S. H. R., and Iyer, P. (1997). Chiral Ru(III) metal complex-catalyzed aerobic enantioselective epoxidation of styrene derivatives with Co-oxidation of aldehyde. *J. Mol. Catal. A Chem.* 124 (2), 91–97. doi:10.1016/s1381-1169(97)00076-9
- Lai, T.-S., Zhang, R., Cheung, K.-K., Che, C.-M., Lai, T.-S., and Kwong, H.-L. (1998). Aerobic enantioselective alkene epoxidation by a chiral trans-dioxo(D4-Porphyrinato)Ruthenium(VI) complex. *Chem. Commun.* 15, 1583–1584. doi:10.1039/a802009d
- Lian, M., Li, Z., Cai, Y., Meng, Q., and Gao, Z. (2012). Enantioselective photooxygenation of β -keto esters by chiral phase-transfer catalysis using molecular oxygen. *Chem. Asian J.* 7 (9), 2019–2023. doi:10.1002/asia.201200358
- Maji, B., and Yamamoto, H. (2015). Asymmetric synthesis of tertiary α -hydroxy phosphonic acid derivatives under aerobic oxidation conditions. *Synlett* 26 (11), 1528–1532. doi:10.1055/s-0034-1380290
- Maji, B., and Yamamoto, H. (2014). Copper-catalyzed asymmetric synthesis of tertiary α -hydroxy phosphonic acid derivatives with in situ generated nitrosocarbonyl compounds as the oxygen source. *Angew. Chem. Int. Ed. Engl.* 53 (52), 14472–14475. doi:10.1002/anie.201408893
- Masui, M., Ando, A., and Shioiri, T. (1988). New methods and reagents in organic synthesis. 75. asymmetric synthesis of α -hydroxy ketones using chiral phase transfer catalysts. *Tetrahedron Lett.* 29 (23), 2835–2838. doi:10.1016/0040-4039(88)85224-9
- Masutani, K., Irie, R., and Katsuki, T. (2002). Asymmetric Cyclization via Oxygen cation radical: enantioselective synthesis of 4b,9b-Dihydrobenzofuro[3,2-b]benzofurans. *Chem. Lett.* 31 (1), 36–37. doi:10.1246/cl.2002.36
- Masutani, K., Uchida, T., Irie, R., and Katsuki, T. (2000). Catalytic asymmetric and chemoselective aerobic oxidation: kinetic resolution of sec-alcohols. *Tetrahedron Lett.* 41 (26), 5119–5123. doi:10.1016/s0040-4039(00)00787-5
- Matsumoto, K., Egami, H., Oguma, T., and Katsuki, T. (2012). What factors influence the catalytic activity of iron-salen complexes for aerobic oxidative coupling of 2-naphthols? *Chem. Commun.* 48 (47), 5823–5825. doi:10.1039/c2cc18090a
- McCann, S. D., and Stahl, S. S. (2015). Copper-catalyzed aerobic oxidations of organic molecules: pathways for two-electron oxidation with a four-electron oxidant and a one-electron redox-active catalyst. *Acc. Chem. Res.* 48 (6), 1756–1766. doi:10.1021/acs.accounts.5b00060
- Meunier, B., de Visser, S. P., and Shaik, S. (2004). Mechanism of oxidation reactions catalyzed by cytochrome P450 enzymes. *Chem. Rev.* 104 (9), 3947–3980. doi:10.1021/cr020443g
- Miller, D. M., Buettner, G. R., and Aust, S. D. (1990). Transition metals as catalysts of “autoxidation” reactions. *Free Radic. Biol. Med.* 8 (1), 95–108. doi:10.1016/0891-5849(90)90148-c
- Miyamura, H., Choo, G. C., Yasukawa, T., Yoo, W. J., and Kobayashi, S. (2013). A heterogeneous layered bifunctional catalyst for the integration of aerobic oxidation and asymmetric C-C bond formation. *Chem. Commun. (Camb)* 49 (85), 9917–9919. doi:10.1039/c3cc46204h

- Miyamura, H., Suzuki, A., Yasukawa, T., and Kobayashi, S. (2015). Integrated process of aerobic oxidation-olefination-asymmetric C-C bond formation catalyzed by robust heterogeneous gold/palladium and chirally modified rhodium Nanoparticles. *Adv. Synth. Catal.* 357 (18), 3815–3819. doi:10.1002/adsc.201500529
- Mizoguchi, H., Uchida, T., and Katsuki, T. (2014). Ruthenium-catalyzed oxidative kinetic resolution of unactivated and activated secondary alcohols with air as the hydrogen acceptor at room temperature. *Angew. Chem. Int. Ed. Engl.* 53 (12), 3178–3182. doi:10.1002/anie.201310426
- Motaleb, A., Bera, A., and Maity, P. (2018). An organocatalyst bound α -aminoalkyl radical intermediate for controlled aerobic oxidation of iminium ions. *Org. Biomol. Chem.* 16 (28), 5081–5085. doi:10.1039/c8ob01032c
- Mukaiyama, T., Yamada, T., Nagata, T., and Imagawa, K. (1993). Asymmetric aerobic epoxidation of unfunctionalized olefins catalyzed by optically active α -alkoxycarbonyl- β -ketoiminato manganese(III) complexes. *Chem. Lett.* 22 (2), 327–330. doi:10.1246/cl.1993.327
- Mukaiyama, T., and Yamada, T. (1995). Recent advances in aerobic oxygenation. *Bull. Chem. Soc. Jpn.* 68 (1), 17–35. doi:10.1246/bcsj.68.17
- Muthupandi, P., and Sekar, G. (2011). Zinc-catalyzed aerobic oxidation of benzoin and its extension to enantioselective oxidation. *Tetrahedron Lett.* 52 (6), 692–695. doi:10.1016/j.tetlet.2010.12.004
- Nagata, T., Imagawa, K., Yamada, T., and Mukaiyama, T. (1994). Enantioselective aerobic epoxidation of acyclic simple olefins catalyzed by the optically active β -ketoiminato manganese(III) complex. *Chem. Lett.* 23 (7), 1259–1262. doi:10.1246/cl.1994.1259
- Nagata, T., Imagawa, K., Yamada, T., and Mukaiyama, T. (1995). Enantioselective aerobic oxidation of sulfides catalyzed by optically active β -oxo aldiminatomanganese(III) complexes. *Bull. Chem. Soc. Jpn.* 68 (11), 3241–3246. doi:10.1246/bcsj.68.3241
- Nechab, M., Einhorn, C., and Einhorn, J. (2004). New aerobic oxidation of benzylic compounds: efficient catalysis by N-Hydroxy-3,4,5,6-Tetraphenylphthalimide (NHTPPi)/CuCl under mild conditions and low catalyst loading. *Chem. Commun.* 13, 1500–1501. doi:10.1039/b403004d
- Nechab, M., Kumar, D. N., Philouze, C., Einhorn, C., and Einhorn, J. (2007). Variable C₂-symmetric analogues of N-hydroxyphthalimide as enantioselective catalysts for aerobic oxidation: kinetic resolution of oxazolidines. *Angew. Chem. Int. Ed. Engl.* 46 (17), 3080–3083. doi:10.1002/anie.200603780
- Osterberg, P. M., Niemeier, J. K., Welch, C. J., Hawkins, J. M., Martinelli, J. R., Johnson, T. E., et al. (2015). Experimental limiting oxygen concentrations for nine organic solvents at temperatures and pressures relevant to aerobic oxidations in the pharmaceutical industry. *Org. Process. Res. Dev.* 19 (11), 1537–1543. doi:10.1021/op500328f
- Ottenbacher, R. V., Talsi, E. P., and Bryliakov, K. P. (2018). Catalytic asymmetric oxidations using molecular oxygen. *Russ. Chem. Rev.* 87 (9), 821. doi:10.1070/rcr4825
- Parmeggiani, C., and Cardona, F. (2012). Transition metal based catalysts in the aerobic oxidation of alcohols. *Green. Chem.* 14 (3), 547–564. doi:10.1039/c2gc16344f
- Petsi, M., and Zografos, A. L. (2018). Advances in catalytic aerobic oxidations by activation of dioxygen-monooxygenase enzymes and biomimetics. *Synthesis* 50 (24), 4715–4745. doi:10.1055/s-0037-1610297
- Poon, J. F., and Pratt, D. A. (2018). Recent insights on hydrogen atom transfer in the inhibition of hydrocarbon autoxidation. *Acc. Chem. Res.* 51 (9), 1996–2005. doi:10.1021/acs.accounts.8b00251
- Porter, N. A. (2013). A perspective on free radical autoxidation: the physical organic chemistry of polyunsaturated fatty acid and sterol peroxidation. *J. Org. Chem.* 78 (8), 3511–3524. doi:10.1021/jo4001433
- Potowski, M., Merten, C., Antonchick, A. P., and Waldmann, H. (2015). Catalytic aerobic oxidation and tandem enantioselective cycloaddition in cascade multicomponent synthesis. *Chemistry* 21 (13), 4913–4917. doi:10.1002/chem.201500125
- Protti, S., Dondi, D., Fagnoni, M., and Albini, A. (2009). Assessing photochemistry as a green synthetic method. Carbon-carbon bond forming reactions. *Green. Chem.* 11 (2), 239–249. doi:10.1039/b810594d
- Qian, W. J., Wei, W. G., Zhang, Y. X., and Yao, Z. J. (2007). Total synthesis, assignment of absolute stereochemistry, and structural revision of chlorofusin. *J. Am. Chem. Soc.* 129 (20), 6400–6401. doi:10.1021/ja072225g
- Romero, N. A., and Nicewicz, D. A. (2016). Organic photoredox catalysis. *Chem. Rev.* 116 (17), 10075–10166. doi:10.1021/acs.chemrev.6b00057
- Salunke, S. B., Babu, N. S., and Chen, C.-T. (2011). Asymmetric aerobic oxidation of α -hydroxy acid derivatives catalyzed by reusable, polystyrene-supported chiral N-salicylidene oxido vanadium tert-leucinate. *Adv. Synth. Catal.* 353 (8), 1234–1240. doi:10.1002/adsc.201100062
- Sambiasi, C., Sterckx, H., and Maes, B. U. W. (2017). Electrosynthesis: a new frontier in aerobic oxidation? *ACS Cent. Sci.* 3 (7), 686–688. doi:10.1021/acscentsci.7b00275
- Sandoval, D., Samoshin, A. V., and Read de Alaniz, J. (2015). Asymmetric electrophilic α -amination of silyl enol ether derivatives via the nitrosocarbonyl hetero-ene reaction. *Org. Lett.* 17 (18), 4514–4517. doi:10.1021/acs.orglett.5b02208
- Sano, D., Nagata, K., and Itoh, T. (2008). Catalytic asymmetric hydroxylation of oxindoles by molecular oxygen using a phase-transfer catalyst. *Org. Lett.* 10 (8), 1593–1595. doi:10.1021/ol800260r
- Shimizu, H., Onitsuka, S., Egami, H., and Katsuki, T. (2005). Ruthenium(Salen)-Catalyzed aerobic oxidative desymmetrization of meso-diols and its kinetics. *J. Am. Chem. Soc.* 127 (15), 5396–5413. doi:10.1021/ja047608i
- Shimizu, H., and Katsuki, T. (2003). (Salen)ruthenium-catalyzed desymmetrization of meso-diols (2). Apical ligand effect on enantioselectivity. *Chem. Lett.* 32 (6), 480–481. doi:10.1246/cl.2003.480
- Shimizu, H., Nakata, K., and Katsuki, T. (2002). (Salen)ruthenium-Catalyzed desymmetrization of meso-diols: catalytic aerobic asymmetric oxidation under photo-irradiation. *Chem. Lett.* 31 (11), 1080–1081. doi:10.1246/cl.2002.1080
- Sim, S.-B. D., Wang, M., and Zhao, Y. (2015). Phase-transfer-catalyzed enantioselective α -hydroxylation of acyclic and cyclic ketones with oxygen. *ACS Catal.* 5 (6), 3609–3612. doi:10.1021/acscatal.5b00583
- Stahl, S. S. (2004). Palladium oxidase catalysis: selective oxidation of organic chemicals by direct dioxygen-coupled turnover. *Angew. Chem. Int. Ed. Engl.* 43 (26), 3400–3420. doi:10.1002/anie.200300630
- Sterckx, H., Morel, B., and Maes, B. U. W. (2019). Catalytic aerobic oxidation of C(sp³)-H bonds. *Angew. Chem. Int. Ed.* 58 (24), 7946–7970. doi:10.1002/anie.201804946
- Sundén, H., Engqvist, M., Casas, J., Ibrahim, I., and Córdova, A. (2004). Direct amino acid catalyzed asymmetric α -oxidation of ketones with molecular oxygen. *Angew. Chem. Int. Edition* 43 (47), 6532–6535. doi:10.1002/anie.200460295
- Tanaka, H., Nishikawa, H., Uchida, T., and Katsuki, T. (2010). Photopromoted Ru-catalyzed asymmetric aerobic sulfide oxidation and epoxidation using water as a proton transfer mediator. *J. Am. Chem. Soc.* 132 (34), 12034–12041. doi:10.1021/ja104184r
- Tang, X.-F., Feng, S.-H., Wang, Y.-K., Yang, F., Zheng, Z.-H., Zhao, J.-N., et al. (2018). Bifunctional metal-free photo-organocatalysts for enantioselective aerobic oxidation of β -dicarbonyl compounds. *Tetrahedron* 74 (27), 3624–3633. doi:10.1016/j.tet.2018.05.023
- Tang, X. F., Zhao, J. N., Wu, Y. F., Zheng, Z. H., Feng, S. H., Yu, Z. Y., et al. (2019a). Enantioselective photooxygenation of β -dicarbonyl compounds in batch and flow photomicroreactors. *Org. Biomol. Chem.* 17 (34), 7938–7942. doi:10.1039/c9ob01379b
- Tang, X. F., Zhao, J. N., Wu, Y. F., Feng, S. H., Yang, F., Yu, Z. Y., et al. (2019b). Visible-light-driven enantioselective aerobic oxidation of β -dicarbonyl compounds catalyzed by cinchona-derived phase transfer catalysts in batch and semi-flow. *Adv. Synth. Catal.* 361 (22), 5245–5252. doi:10.1002/adsc.201900777
- Tu, Y., Wang, Z.-X., and Shi, Y. (1996). An efficient asymmetric epoxidation method for trans-olefins mediated by a fructose-derived ketone. *J. Am. Chem. Soc.* 118 (40), 9806–9807. doi:10.1021/ja962345g
- Uchida, T., and Katsuki, T. (2013). Green asymmetric oxidation using air as oxidant. *J. Synth. Org. Chem. Jpn.* 71 (11), 1126–1135. doi:10.5059/yukigoseikyokaishi.71.1126
- Wang, Q., Chen, J., and Huang, Y. (2018). Aerobic oxidation/annulation cascades through synergistic catalysis of RuCl₃ and N-heterocyclic carbenes. *Chem. Eur. J.* 24 (49), 12806–12810. doi:10.1002/chem.201803254
- Wang, Y., Zheng, Z., Lian, M., Yin, H., Zhao, J., Meng, Q., et al. (2016). Photo-organocatalytic enantioselective α -hydroxylation of β -keto esters and β -keto amides with oxygen under phase transfer catalysis. *Green. Chem.* 18 (20), 5493–5499. doi:10.1039/c6gc01245k

- Weng, S. S., Shen, M. W., Kao, J. Q., Munot, Y. S., and Chen, C. T. (2006). Chiral N-salicylidene vanadyl carboxylate-catalyzed enantioselective aerobic oxidation of α -hydroxy esters and amides. *Proc. Natl. Acad. Sci. USA* 103 (10), 3522–3527. doi:10.1073/pnas.0511021103
- Wertz, S., and Studer, A. (2013). Nitroxide-catalyzed transition-metal-free aerobic oxidation processes. *Green. Chem.* 15 (11), 3116–3134. doi:10.1039/c3gc41459k
- Xu, C., Zhang, L., and Luo, S. (2014). Merging aerobic oxidation and enamine catalysis in the asymmetric α -amination of β -ketocarboxylates Using N-hydroxycarbamates as nitrogen sources. *Angew Chem. Int. Ed. Engl.* 53 (16), 4149–4153. doi:10.1002/anie.201400776
- Yamada, T., Imagawa, K., Nagata, T., and Mukaiyama, T. (1994). Aerobic enantioselective epoxidation of unfunctionalized olefins catalyzed by optically active salen-manganese(III) complexes. *Bull. Chem. Soc. Jpn.* 67 (8), 2248–2256. doi:10.1246/bcsj.67.2248
- Yamada, T., Imagawa, K., Nagata, T., and Mukaiyama, T. (1992). Enantioselective epoxidation of unfunctionalized olefins with molecular oxygen and aldehyde catalyzed by optically active manganese(III) complexes. *Chem. Lett.* 21 (11), 2231–2234. doi:10.1246/cl.1992.2231
- Yang, Y., Moinodeen, F., Chin, W., Ma, T., Jiang, Z., and Tan, C. H. (2012). Pentanidium-catalyzed enantioselective α -hydroxylation of oxindoles using molecular oxygen. *Org. Lett.* 14 (18), 4762–4765. doi:10.1021/ol302030v
- Zamadar, M., and Greer, A. (2009). Singlet oxygen as a reagent in organic synthesis. *Handbook Synth. Photochemistry* 16, 353–386. doi:10.1002/9783527628193.ch11
- Zhang, W., Loebach, J. L., Wilson, S. R., and Jacobsen, E. N. (1990). Enantioselective epoxidation of unfunctionalized olefins catalyzed by salen manganese complexes. *J. Am. Chem. Soc.* 112 (7), 2801–2803. doi:10.1021/ja00163a052
- Zhu, J., Grigoriadis, N. P., Lee, J. P., and Porco, J. A. (2005). Synthesis of the azaphilones using copper-mediated enantioselective oxidative dearomatization. *J. Am. Chem. Soc.* 127 (26), 9342–9343. doi:10.1021/ja052049g
- Zhu, J., and Porco, J. A. (2006). Asymmetric syntheses of (–)-mitorubrin and related azaphilone natural products. *Org. Lett.* 8 (22), 5169–5171. doi:10.1021/ol062233m

Conflict of Interest: The authors declare that the research was conducted in the absence of any commercial or financial relationships that could be construed as a potential conflict of interest.

Copyright © 2021 Kananovich, Elek, Lopp and Borovkov. This is an open-access article distributed under the terms of the Creative Commons Attribution License (CC BY). The use, distribution or reproduction in other forums is permitted, provided the original author(s) and the copyright owner(s) are credited and that the original publication in this journal is cited, in accordance with accepted academic practice. No use, distribution or reproduction is permitted which does not comply with these terms.



CD Imaging at High Spatial Resolution at Diamond B23 Beamline: Evolution and Applications

Rohanah Hussain, Tamás Jávorfí and Giuliano Siligardi*

Diamond Light Source Ltd., Harwell Science and Innovation Campus, Didcot, United Kingdom

Circular Dichroism imaging in the 190–650 nm spectral region pioneered at Diamond Light Source B23 beamline, has been made possible by the highly collimated microbeam generated at the beamline and has been used to study the homogeneity of the supramolecular structures of thin films of chiral materials deposited on fused quartz substrates. This facility has been expanded with the installation of a Mueller Matrix Polarimeter, MMP, coupled to the beamlight, of which a preliminary data will be discussed. In the solid state, the measurement of CD related to the supramolecular structure is hampered by the presence of circular birefringence, linear dichroism, and linear birefringence that can only be evaluated using the MMP technique. The ability to characterize the chiroptical property of thin chiral films prepared under a variety of conditions and protocols such as drop cast, spin coating, spray at different temperatures and concentrations will enable the determination of the critical parameters for reproducible, uniform and homogeneous specimen preparation, which is the *sine qua non* for any commercial application. This is of particular importance for optoelectronic materials, but it can also be extended to a broad variety of materials with applications from biosensors to biological tissues.

Keywords: circular dichroism, CD imaging, Mueller matrix polarimetry, nano crystalline cellulose, supramolecular structure

OPEN ACCESS

Edited by:

Victor Borovkov,
Tallinn University of Technology,
Estonia

Reviewed by:

Bart Kahr,
New York University, United States
Honghui He,
Tsinghua University, China

*Correspondence:

Giuliano Siligardi
giuliano.siligardi@diamond.ac.uk

Specialty section:

This article was submitted to
Supramolecular Chemistry,
a section of the journal
Frontiers in Chemistry

Received: 13 October 2020

Accepted: 16 February 2021

Published: 08 April 2021

Citation:

Hussain R, Jávorfí T and Siligardi G
(2021) CD Imaging at High Spatial
Resolution at Diamond B23 Beamline:
Evolution and Applications.
Front. Chem. 9:616928.
doi: 10.3389/fchem.2021.616928

INTRODUCTION

Optical activity is the property of a molecule in the solid state (Arago, 1811) and in solution (Biot, 1815) to rotate the plane of polarized light that pass through it (Biot, 1815).

Circular dichroism (CD) spectroscopy is the technique most often used to characterize optically active chiral molecules. A molecule is chiral if its mirror image forms are nonsuperposable (Pasteur, 1849), like those of L and D amino acids. In general, any entity that is dissymmetric, namely without a plane of symmetry or a center of inversion is chiral. This applies not only to molecules but materials made of large chiral polymers, combined achiral polymers doped with small chiral molecules, and achiral polymers adopting chiral architectures.

Optically active materials show CD that is the difference between the absorption of left and right circularly polarized light passing through the sample (Cotton, 1895).

In a chromophore of a chiral molecule, an electronic transition is an helical displacement of an electron charge induced differently by the left and right circularly polarized light. The quantum-mechanical model of the one-electron mechanism describes the helical displacement of charge generated by the magnetic dipole transition moment as the rotation of charge and the electric dipole transition moment as the linear displacement of charge. Another mechanism is the exciton

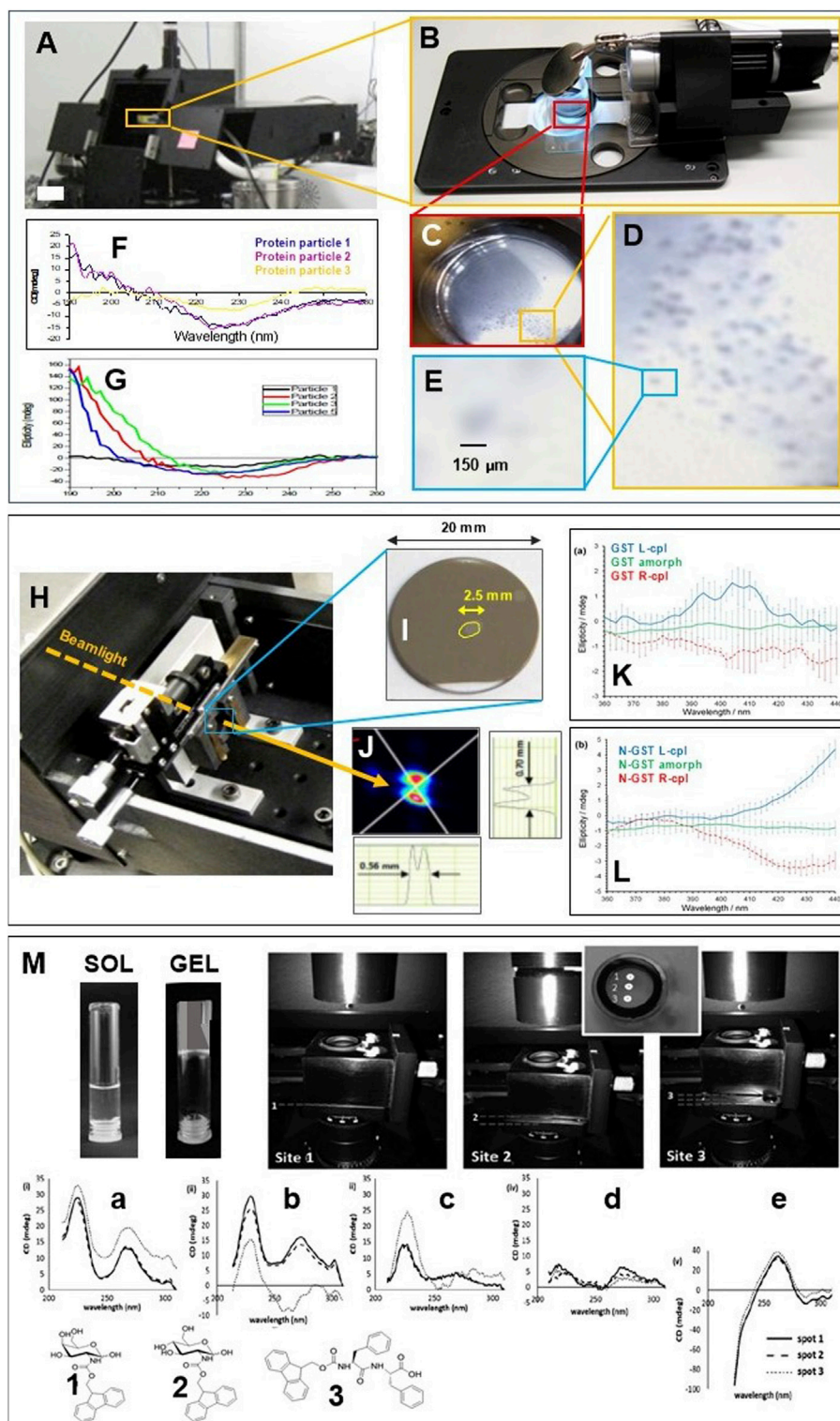


FIGURE 1 | (A) B23 vertical sample chamber of module A. (B) digital camera with mirror at 45° to view the cuvette containing a suspension of protein particles in a physiological solution. (C, E) zoomed images of cuvette cell, particles and single particle with bar size of 150 μm. (F) SRCD spectra of three selected particles of a β-sheet rich protein (Redrawn from 11). (G) a different preparation of the same proteins of (F–H) X-Y mechanical stage enables SRCD to be measured at different spots of the GST yellow circled area investigated using the vertical chamber of B23 module B. (I) Fused silica substrate window coated with a thin film of GST of which the spot of about 2.5 mm in length (circled in yellow for clarity) was sculpted with laser of left- or right-cpl. (J) Beamlight profile of about 600 μm in diameter at the GST (Continued)

FIGURE 1 | specimen measured with beam profile monitor Beamage USB. **(K)** SRCD spectra of GST sculpted with L-cpl (blue), R-cpl (red) and GST outside the spot in **Figure 11**, the amorphous GST (green). **(L)** SRCD spectra of N doped GST sculpted with L-cpl (red), R-cpl (red) and amorphous N-GST (green). All figures redrawn from Borisenko et al. (2015). **(M)** SRCD spectra of five gel specimens prepared from three types of samples: **(A)** GalNHFmoc (1) hydrogel in water triggered thermally (0.01 cm cell); **(B)** GalNHFmoc hydrogel (1) in PBS triggered by sonication (0.02 cm cell); **(C)** GalNHFmoc (1) hydrogel in PBS triggered thermally (0.01 cm cell); **(D)** GlcNHFmoc (2) hydrogel in water triggered thermally (0.02 cm cell); and **(E)** Fmoc-FF (3) hydrogel in PBS triggered by sonication (0.01 cm cell). All samples were gelled in the cuvette cells at a concentration of 2.0 mg ml^{-1} . For each specimen, three different positions were measured as illustrated in the insert [redrawn from Sitsanidis et al. (2018)].

coupling where the helical displacement of charge is generated by the coupling of electric dipole transition moments of two twisted chromophores of the chiral molecule framework (Mason, 1978).

The different velocity at which left and right circularly polarized light travels through chiral materials is called optical rotatory dispersion (ORD) and like the counterpart CD is a manifestation of the optical activity. ORD is generated by circular birefringence that is the difference in refractive index for left and right circularly polarized light (L-cpl and R-cpl) (Fresnel, 1824).

Modern CD instruments use one photoelastic modulator (PEM) to modulate the retardation of the incident linearly polarized light, of which only the quarter wave retardation is selected (Grosjean and Legrand, 1960; Velluz et al., 1965) and measured by a photomultiplier tube (PMT) or an avalanche photo diode (APD) detector (Hussain et al., 2012). The measurement of ORD is achieved by inserting in the CD spectropolarimeter a polarizing prism, the analyser, in between the sample, and the light detector (Lowry, 1935).

The highly collimated micro beamlight generated at B23 beamline for synchrotron radiation circular dichroism (SRCD) (Hussain et al., 2012) enabled the measurements of CD of solid state protein microparticles to assess the conformation homogeneity of their preparation. To our knowledge, that was the first time that CD of individual particles of $150 \mu\text{m}$ in diameter of a β -sheet rich protein was successfully measured without spectral artifacts due to light scattering and birefringence contributions (**Figures 1A–G**) (Gerdova, 2013). To identify and irradiate the single particles with the beamlight (**Figures 1D,E**), a 45° mirror to deflect the beamlight to a digital camera orthogonal to the incident light (**Figure 1B**) demonstrated the feasibility of this method. As the activity of proteins is strictly related to their active conformation, the production of proteins in different foldings than the active one is one of the main causes of reducing the overall protein function and activity. The ability to monitor the protein conformation under a variety of environmental conditions is of paramount importance. It enables the optimization of the protein formulation parameters to obtain reproducible protein particles of retained native activity associated to beta strand-rich folding as illustrated in the example of the particles batch of **Figure 1F** compared to that in **Figure 1G** where significant spectral differences were observed for the same protein particles but prepared with a different method. This proof-of-principle experiment pave the way to expand and extend this approach to many other chiral materials with various applications from Life Science to Physical Sciences.

The use of an X-Y manual stage enabled the measurements of SRCD at different spots of about $600 \mu\text{m}$ in diameter of thin solid state films of pure $\text{Ge}_2\text{Sb}_2\text{Te}_5$ (GST) and N-doped $\text{Ge}_2\text{Sb}_2\text{Te}_5\text{N}$

(N-GST) phase-change memory materials coated on fused silica substrate (**Figures 1H,J**; Borisenko et al., 2015). An area of about 2.5 mm in diameter of amorphous pure and N-doped GST wafer of 22 mm in diameter was pre-irradiated with L-cpl and R-cpl respectively using a powerful laser (**Figure 1H**) that induced a permanent optical activity of opposite chirality (**Figures 1K,L**) due to rapid photo-crystallization of achiral amorphous GST. The sculpted pure or N-doped achiral GST materials with L-cpl or R-cpl laser irradiation has been suggested as a potential method to control the induction of anisotropic optical properties for optoelectronic and photonic applications (Borisenko et al., 2015).

The self-assembly of three different peptide-based compounds, GalNHFmoc (1 in **Figure 1M**), GlcNHFmoc (2 in **Figure 1M**), and Fmoc-FF (3 in **Figure 1M**) from sol to gel state was for the first time investigated using the B23 vertical chamber developed for high throughput CD (HTCD) (Hussain et al., 2016) to probe the homogeneity and uniformity of the supramolecular structure of the three hydrogel materials (Sitsanidis et al., 2018) of different adjacent spots of about $100 \mu\text{m}$ size. This was achieved by using a $10 \times$ objective lens that focused the beamlight to about $100 \mu\text{m}$ in diameter on the sample without creating spectral distortions. The gelation of the peptide compounds from sol state in cylindrical cuvette cells was triggered by two methods: sonication and thermal heating and cooling cycles (**Figure 1M**). In an iterative manner, the method enabled the scientists to induce the gelation by varying one parameter per time in order to find out the optimum protocol for a reproducible homogeneous self-assembling. The benchtop CD instruments would give an average of a much larger area ($2\text{--}3 \text{ mm}$ in diameter) than that with B23.

The use of a $10 \times$ objective lenses transparent down to 190 nm and a motorized X-Y stage in the B23 vertical chamber enabled the CD imaging (CDi) of thin films of chiral materials at high spatial resolution unattainable with bespoke benchtop CD instruments or any other SRCD beamline. The use of B23 CDi tower was first exploited by the Di Bari group for the characterization of the local supramolecular order in thin films of chiral functional conjugated polymers with optoelectronic properties (Zinna et al., 2017).

A spatial resolution of $100 \mu\text{m}$ revealed an inhomogeneous supramolecular structure of the thin film of chiral 1,4-phenylene-based oligothiophene polymer (Albano et al., 2019) (**Figures 2A–H**). The SRCD spectra of that film measured in back side orientation showed opposite sign than the front side that was indicative of linear dichroism (LD) and linear birefringence (LB) contributions to CD and circular birefringence (CB) (**Figures 2A,B**). The fact that the SRCD spectral profiles of both front and back side orientations decreased in overall intensity as a function of time was consistent with a rearrangement of the

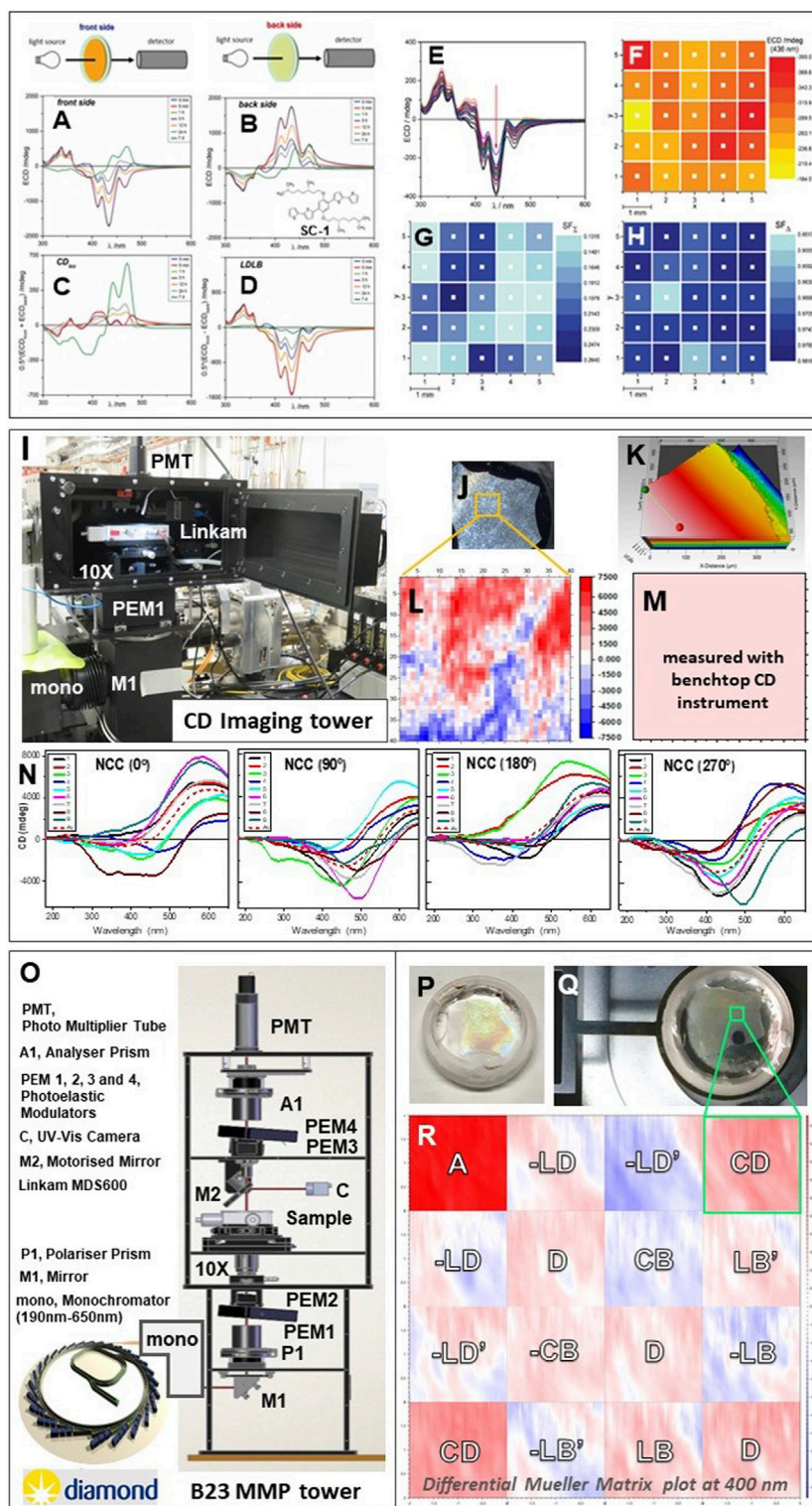


FIGURE 2 | (A) SRCD spectra of a thin film of π -conjugated chiral molecule spin coated (SC-1) on a fused silica substrate measured on the front side orientation as illustrated by the cartoon. **(B)** SRCD spectra of back side orientations. **(C)** Calculated SRCD spectra termed CD_{iso} from the sum of spectra $[(A + B)/2]$. **(D)** Calculated SRCD spectra termed LDLB from the difference of spectra $[(A - B)/2]$. **(E)** 25 CD spectra of front side orientation measured in a 5×5 grid at 1 mm intervals. **(F)** 2D map of SRCD intensities at 436 nm of the 5×5 grid measured in 2E. **(G)** Calculated 2D map of the CD_{iso} intensities at 436 nm of the same 5×5 grid illustrated in F (the back side orientation is not shown). **(H)** Calculated 2D map of LDLB intensities at 436 nm of the 5×5 grid. All figures redrawn from Albano et al. (2019). **(I)** CD imaging (Continued)

FIGURE 2 | tower (CDi) equipped with X-Y motorized Linkam temperature controlled stage MDS600 and a UV transparent 10 × objective lens to map a chiral nematic thin film of NCC (**J**) 90 μm in thickness using a Profilim 3D profilometer (**K**). (**L**) B23 2D map of SRCD intensities of NCC front side orientation measured with a 41 × 41 grid at 50 μm interval steps for a total of 2 mm² area. Note the SRCD intensity range from +7,500 (red) to −7,500 (blue) mdeg. (**M**) 2D map of CD intensity at 480 nm for the same area of 4 mm² measured with Chirascan Plus CD instrument (Applied PhotoPhysics Ltd., United Kingdom). (**N**) SRCD spectra of NCC of a 3 × 3 grid at 1 mm interval steps (total area 2 mm²) as a function of rotation (0, 90, 180, and 270°) around the axis normal to the sample surface (front side) and parallel to the propagation direction of the incident beamlight. (**O**) Optical elements of B23 MMP tower coupled to Diamond light source from bending magnet and B23 double grating subtracting monochromator, mono; M1, 45° plane mirror; P1, linear polarizer; PEM1, PEM2, photoelastic modulators for polarization state generator; 10 ×, objective UV transparent lenses; sample holder; M2, retractable mirror for UV camera; PEM3, PEM4, photoelastic modulators for polarization state analyzer; A1, linear polarizer; PMT, photomultiplier tube detector. (**P**) Zoomed picture of the sample holder with NCC film specimen (**Q**). (**R**) Differential Mueller Matrix plot of the 2 mm × 2 mm area with the 16 elements labeled for the corresponding physical interpretations: CD, circular dichroism; CB, circular birefringence; LD, horizontal linear dichroism; LB, horizontal linear birefringence; LD', 45° linear dichroism; LB', 45° linear birefringence; A, Absorbance; and D, Depolarization (D=A for materials with no depolarization). (Azzam, 1978).

supramolecular structure of the polymer. After 9 days of incubation, however, both front and back side were very similar in terms of profile shape and sign indicating a substantial reduction in LD and LB contributions. This can be better visualized with the sum of the SRCD spectra of the front and back side orientations divided by 2 that corresponds to the CD and CB contributions (**Figure 2C**) while the difference divided by 2 corresponds to the LD and LB elements (Albano et al., 2019) (**Figure 2D**).

For solutions, the solvent is the isotropic component whereas the solute being chiral is the anisotropic component that generates the CD. However, for solutions with macroscopic molecules such as large polymers and solid state films, CD, CB, LD, and LB contributions can be present and must be analyzed quantitatively with the differential Mueller matrix of data measured with MMP (Kuroda et al., 2000; Arteaga et al., 2012). In this paper the Mueller Matrix Ellipsometry is not discussed.

DISCUSSION

For thin films of solid state chiral materials, it is important to remember that all the polarization contributions are additive, and even without LD and LB, the remaining CB contribution will affect the spectral shape hence its accurate interpretation in CD terms.

CD measurements carried out as a function of rotation around the axis normal to the sample surface and parallel to the incident light will show spectral differences if LD and LB contributions are present.

Nanocrystalline cellulose (NCC) obtained from the hydrolysis of cotton-derived cellulose can form chiral nematic liquid crystalline phases with a left helical orientation forming iridescent chiral nematic films upon drying. The SRCD spectra of a 3 × 3 grid of 1 mm interval steps of a thin film of NCC of about 90 μm thick (**Figure 2K**) measured as a function of rotations at 0, 90, 180, and 270° in the B23 vertical chamber equipped with a temperature controlled motorized X-Y linear stage (Linkam MDS600) (**Figure 2I**) revealed unambiguously the presence of LD and LB contributions as substantial spectral differences were observed (**Figure 2N**). The same area of 4 mm² of the 3 × 3 grid at 1mm intervals was re-scanned as a 41 × 41 grid of 50 μm spatial resolution revealing a 2D image with spectral intensity from +7,500 to −7,500 mdeg (**Figure 2L**). It is

important to notice that using a bespoke benchtop CD instrument (Chirascan Plus, APL, United Kingdom), the measured CD illustrated in **Figure 2M** was the average of the same 4 mm² area that did not reveal any of the complexity of the chiroptical properties of the NCC sample of **Figure 2L**. Of course the 2D image measured with B23 in imaging mode (**Figure 2L**) is certainly containing all the four polarization contributions, CD, CB, LD, and LB, for which only the use of a Mueller Matrix Polarimeter (MMP) (Arteaga et al., 2012) would enable the extraction of all those components.

The preliminary differential Mueller matrix plot of the nanocrystalline cellulose (NCC) obtained from the hydrolysis of cotton-derived cellulose (**Figures 2P,Q**) measured with the new B23 MMP tower for imaging facility (**Figure 2O**) confirmed that indeed all polarization contributions, LD, LB, CD, and CB were present in the 2D CDi plot illustrated in **Figure 2L** with the use of B23 CDi tower. The CD elements of the differential Mueller Matrix were analyzed following the method developed by Arteaga of Kahr's group (Arteaga et al., 2012) and Ossikovski group (Arwin et al., 2016). Although the two elements in the anti-diagonal representing the CD maps (**Figure 2R**) were both homogeneous in terms of uniform red colour associated to positive CD, the intensity magnitudes were slightly different due to depolarization (Azzam, 1978). In this case, the average between the two CD elements of the differential Mueller Matrix should be considered revealing that the same area size of 2mm x 2mm of the NCC thin film was indeed homogeneous unlike that observed with the CD imaging tower (**Figure 2I**) that appeared very heterogeneous (negative values in blue and positive in red (**Figure 2L**)). The MMP data (**Figure 2R**) confirmed the presence of the other CB, LD and LB components. This article is not meant to be a full characterisation of thin films of NCC that are known to have complex levels of mesoscale organisation but rather to raise the attention that, for chiral films, the use of differential Mueller Matrix is absolutely necessary in order to achieve a correct spectroscopic data interpretation. In solution, for instance, the conformation of proteins can be tuned by varying the solvent environment, pH, temperature, surfactants, ligands, and concentration and one can assess by CD spectroscopy how big these changes are and how to optimise these parameters in order to achieve reproducible protein formulations (Siligardi and Hussain, 2015). This is also occurring in the solid state, however, the chiroptical spectroscopic assessment of the supramolecular structure to be optimise because it is related to its properties, like for optoelectronic materials where a homogeneous helical

arrangement of the polymer maximises the charge transfer hence the production of current (Naaman et al., 2019), would be hampered and distorted by the presence of CB, LD and LB contributions. That is why the use of the MMP to extract the CD information from the other optical properties of the solid state film is a must.

In here we have described the evolution of Diamond B23 beamline for synchrotron radiation circular dichroism from a powerful light source to push the wavelength boundaries of Xe lamps to the vacuum UV spectral region to chiroptical imaging at higher spatial resolution. The new B23 MMP imaging facility (**Figure 2O**) is the latest tool that enables to see, and hopefully to control the chiroptical properties of materials of which properties rely on their homogeneous supramolecular structure. This will facilitate the identification of the parameters that can optimize such a homogeneity.

INSTRUMENTATION

The SRCD measurements were conducted using two types of B23 vertical sample chambers called towers depending upon the type and size on the sample specimens (Hussain et al., 2012; Hussain et al., 2016). One is equipped with a large X-Y motorized linear stage that can accommodate large samples (maximum $12 \times 8 \text{ cm}^2$) operating at room temperature, and the other with an X-Y motorized and temperature controlled Linkam MDS600 stage (for a maximum of $1.5 \text{ cm} \times 1.5 \text{ cm}$ sample area). The samples were held with appropriate 3D printed sample holders when necessary.

The MMP built by Hinds Instruments (United States) coupled to Diamond B23 light source and the double grating subtractive monochromator (Olis Instruments, United States) operating in the 190–750 nm region is composed of four photoelastic modulators operating simultaneously at different frequencies, two in the polarization state generator and two in the polarization state analyser (**Figure 2O**). The data acquisition and data processing were implemented by Hinds Instruments following the method described in Arteaga et al. (2012).

The MMP was calibrated using aqueous solution of 1S (+) 10-Camphorsulfonic acid (5mg/ml) in a 1cm pathlength cuvette to give a positive CD intensity at 290.5nm of about 1500 mdeg. The other polarization elements of the differential Mueller Matrix were calibrated using a thin film of an optoelectronic material (F8BT:aza [P]) characterised by Mueller Matrix Ellipsometry using a Woollam RC2 (model DI) instrument and reported in Wade et al. (2020). In Wade et al. (2020), the homogeneity of the

supramolecular structure of the thin film of F8BT:aza [P] was assessed at 50 micron spatial resolution by CDi using the B23 vertical chamber of **Figure 2I** as the size of the collimated light beam of the Woollam RC2 ellipsometer was about 3–4 mm in diameter.

The CD spectrum from which **Figure 2M** was generated was measured with Chirscan Plus (Applied Photophysics, United Kingdom). The thickness of the thin film of NCC specimen in **Figure 2K** was measured with the Profilim 3D profilometer (Filmetrics, United States). The MMP was calibrated using aqueous solution of 1S (+) 10-Camphorsulfonic acid (5mg/ml) in a 1cm pathlength cuvette to give a positive CD intensity at 290.5nm of about 1500 mdeg. The other polarization elements of the differential Mueller Matrix were calibrated using a thin film of an optoelectronic material (F8BT:aza [P]) characterised by Mueller Matrix Ellipsometry using a Woollam RC2 (model DI) instrument and reported in Wade et al. (2020). In Wade et al. (2020), the homogeneity of the supramolecular structure of the thin film of F8BT:aza [P] was assessed at 50 micron spatial resolution by CDi using the B23 vertical chamber of **Figure 2I** as the size of the collimated light beam of the Woollam RC2 ellipsometer was about 3–4 mm in diameter.

DATA AVAILABILITY STATEMENT

The original contributions presented in the study are included in the article/Supplementary Material, further inquiries can be directed to the corresponding author.

AUTHOR CONTRIBUTIONS

GS conceived the study and wrote the paper. TJ, RH, and GS developed the CD imaging measurement technique. TJ, and GS performed the MMP spectral measurements. All authors discussed the results.

ACKNOWLEDGMENTS

We would like to thank Prof M. Tiritici of ICL for NCC sample and J. Freudenthal of Hinds Instruments (Hillsboro, Oregon, United States) for his help in calibrating the B23 MMP instrument during B23 beamtime commissioning (CM26447–1).

REFERENCES

- Albano, G., Gorecki, M., Pescitelli, G., Di Bari, L., Javorfi, T., Hussain, R., et al. (2019). Electronic circular dichroism imaging (CDi) maps local aggregation modes in thin films of chiral oligothiophenes. *New J. Chem.* 43, 14584–14593. doi:10.1039/c9nj02746g
- Arago, D. F. J. (1811). "Memoir on a remarkable modification experienced by light rays in their passage through certain diaphanous bodies, and on some other new optical phenomena," in *Mémoires de la classe des sciences mathématiques et physiques de l'Institut Impérial de France. 1st part*. Paris, 93–134.
- Arteaga, O., Freudenthal, J., Wang, B., and Kahr, B. (2012). Mueller matrix polarimetry with four photoelastic modulators: theory and calibration. *Appl. Opt.* 51, 6805–6817. doi:10.1364/ao.51.006805
- Arwin, R., Mendoza-Galvan, A., Magnusson, R., Andersson, A., Landin, J., Järrendahl, K., et al. (2016). Structural circular birefringence and dichroism quantified by differential decomposition of spectroscopic transmission Mueller matrices from *Cetonia aurata*. *Opt. Lett.* 41, 3293–3296. doi:10.1364/ol.41.003293
- Azzam, R.M.A. (1978). Propagation of partially polarized light through anisotropic media with or without depolarization: A differential 4×4 matrix calculus. *J. Opt. Soc. Am.*, 68, 1756–1767.

- Biot, J. B. (1815). Phénomènes de polarisation successive, observés dans des fluides homogènes. *Bull. Sci. Soc. Philomath.*, 190–192.
- Borisenko, K. B., Shanmugam, J., Williams, B. A., Ewart, P., Gholipour, B., Hewak, D. W., et al. (2015). Photo-induced optical activity in phase-changed memory materials. *Sci. Rep.* 1–5, 8770. doi:10.1038/srep08770
- Cotton, A. C. (1895). Absorption inégale des rayons circulaires. *R. Acad. Sci. Paris* 120, 989–991.
- Fresnel, A. (1824). Considérations théoriques sur la polarisation de la lumière. *Bull. Sci. Soc. Philomath.*, 23, 147–158.
- Gerdova, A. (2013). *Absorption flattening correction of circular dichroism spectra of particle suspensions*. Master's thesis. Scotland (United Kingdom: University of Strathclyde).
- Grosjean, M., and Legrand, M. (1960). C R Hebd. *Seances Acad. Sci.* 251, 2150.
- Hussain, R., Javorfi, T., and Siligardi, G. (2016). High-throughput SRCD using multi-well plates and its applications. *Sci. Rep.* 6, 1–6. doi:10.1038/srep38028
- Hussain, R., Javorfi, T., and Siligardi, G. (2012). Circular dichroism beamline B23 at the diamond light source. *J. Syn. Rad.* 19, 132–135. doi:10.1107/S0909049511038982
- Kuroda, R., Berova, N., Nakanishi, K., and Woody, R. W. (2000). “Solid-state CD: application to inorganic and organic chemistry,” in *Circular dichroism: principles and applications*. 2nd Edn Wiley-VCH, New York, 912.
- Lowry, T. M. (1935). Optical rotatory power. *J. Soc. Chem. Ind.* 54, 782. doi:10.1002/jctb.5000543410
- Mason, S. F. (1978). “Optical activity and chiral discrimination,” in *Proceedings of the NATO advanced study institute, Falmer, England, September 10–22, 1978*. Editor S. F. Mason (Falmer, England: University of Sussex), 11–24.
- Naaman, R., Paltiel, Y., and Waldeck, D. H. (2019). Chiral molecules and the electron spin. *Nature Reviews Chemistry* 3, 250–260.
- Pasteur, L. (1849). Relationship which may exist between the crystalline form and the chemical composition and on the cause of rotational polarization. *C. R. Acad. Sci. Paris* 26, 535–538.
- Siligardi, G., and Hussain, R. (2015). CD Spectroscopy: An Essential Tool in Quality Control of Protein Folding. *Structural Proteomics: High-Throughput Methods, Methods Mol. Biol.* (Owens, R.J., ed), Springer NY, 1261, 255–276.
- Sitsanidis, E. D., Piras, C. C., Alexander, B. D., Siligardi, G., Javorfi, T., Hall, A. J., et al. (2018). Circular dichroism studies of low molecular weight hydrogelators: the use of SRCD and addressing practical issues. *Chirality* 30 (15), 708–718. doi:10.1002/chir.22850
- Velluz, L., Legrand, M., and Grosjean, M. (1965). *Optical circular dichroism*. London, New York, NY: Verlag Chemie, 247.
- Wade, J., Hilfiker, J. N., Brandt, J. R., et al. (2020). Natural optical activity as the origin of the large chiroptical properties in p-conjugated polymer thin films. *Nature Communications* 11, 6137–6148.
- Zinna, F., Resta, C., Gorecki, M., Pescitelli, G., Di Bari, L., Javorfi, T., et al. (2017). Circular dichroism imaging: mapping the local supramolecular order in thin films of chiral functional polymers. *Macromolecules* 50, 2054–2060. doi:10.1021/acs.macromol.6b02590

Conflict of Interest: RH, TJ, and GS were employed by Diamond Light Source Ltd.

Copyright © 2021 Hussain, Javorfi and Siligardi. This is an open-access article distributed under the terms of the Creative Commons Attribution License (CC BY). The use, distribution or reproduction in other forums is permitted, provided the original author(s) and the copyright owner(s) are credited and that the original publication in this journal is cited, in accordance with accepted academic practice. No use, distribution or reproduction is permitted which does not comply with these terms.

Advantages of publishing in Frontiers



OPEN ACCESS

Articles are free to read
for greatest visibility
and readership



FAST PUBLICATION

Around 90 days
from submission
to decision



HIGH QUALITY PEER-REVIEW

Rigorous, collaborative,
and constructive
peer-review



TRANSPARENT PEER-REVIEW

Editors and reviewers
acknowledged by name
on published articles

Frontiers

Avenue du Tribunal-Fédéral 34
1005 Lausanne | Switzerland

Visit us: www.frontiersin.org

Contact us: frontiersin.org/about/contact



REPRODUCIBILITY OF RESEARCH

Support open data
and methods to enhance
research reproducibility



DIGITAL PUBLISHING

Articles designed
for optimal readership
across devices



FOLLOW US

@frontiersin



IMPACT METRICS

Advanced article metrics
track visibility across
digital media



EXTENSIVE PROMOTION

Marketing
and promotion
of impactful research



LOOP RESEARCH NETWORK

Our network
increases your
article's readership